NASA/CR—2002-210823/VOL1

EDR No. 18580

Lobed Mixer Design for Noise Suppression

Acoustic and Aerodynamic Test Data Analysis

Vinod G. Mengle and William N. Dalton
Rolls Royce Allison, Indianapolis, Indiana

July 2002

The NASA STI Program Office . . . in Profile

Since its founding, NASA has been dedicated to the advancement of aeronautics and space science. The NASA Scientific and Technical Information (STI) Program Office plays a key part in helping NASA maintain this important role.

The NASA STI Program Office is operated by Langley Research Center, the Lead Center for NASA's scientific and technical information. The NASA STI Program Office provides access to the NASA STI Database, the largest collection of aeronautical and space science STI in the world. The Program Office is also NASA's institutional mechanism for disseminating the results of its research and development activities. These results are published by NASA in the NASA STI Report Series, which includes the following report types:

- TECHNICAL PUBLICATION. Reports of completed research or a major significant phase of research that present the results of NASA programs and include extensive data or theoretical analysis. Includes compilations of significant scientific and technical data and information deemed to be of continuing reference value. NASA's counterpart of peer-reviewed formal professional papers but has less stringent limitations on manuscript length and extent of graphic presentations.

- TECHNICAL MEMORANDUM. Scientific and technical findings that are preliminary or of specialized interest, e.g., quick release reports, working papers, and bibliographies that contain minimal annotation. Does not contain extensive analysis.

- CONTRACTOR REPORT. Scientific and technical findings by NASA-sponsored contractors and grantees.

- CONFERENCE PUBLICATION. Collected papers from scientific and technical conferences, symposia, seminars, or other meetings sponsored or cosponsored by NASA.

- SPECIAL PUBLICATION. Scientific, technical, or historical information from NASA programs, projects, and missions, often concerned with subjects having substantial public interest.

- TECHNICAL TRANSLATION. English-language translations of foreign scientific and technical material pertinent to NASA's mission.

Specialized services that complement the STI Program Office's diverse offerings include creating custom thesauri, building customized data bases, organizing and publishing research results . . . even providing videos.

For more information about the NASA STI Program Office, see the following:

- Access the NASA STI Program Home Page at ***http://www.sti.nasa.gov***

- E-mail your question via the Internet to help@sti.nasa.gov

- Fax your question to the NASA Access Help Desk at 301–621–0134

- Telephone the NASA Access Help Desk at 301–621–0390

- Write to:
  NASA Access Help Desk
  NASA Center for AeroSpace Information
  7121 Standard Drive
  Hanover, MD 21076

NASA/CR—2002-210823/VOL1 EDR No. 18580

Lobed Mixer Design for Noise Suppression

Acoustic and Aerodynamic Test Data Analysis

Vinod G. Mengle and William N. Dalton
Rolls Royce Allison, Indianapolis, Indiana

Prepared under Contract NAS3–27394, Task Order No. 6

National Aeronautics and
Space Administration

Glenn Research Center

July 2002

Acknowledgments

We would like to acknowledge the efforts of several people at NASA Glenn Research Center, Cleveland, Ohio and Allison Advanced Development Company (AADC), Indianapolis, Indiana: Dr. James Bridges and Ms. Kathleen Boyd of NASA Glenn for overseeing and running the acoustic tests at NASA, and for processing all the acoustic data obtained there; Mr. Eugene Krejsa of NASA Glenn for encouragement to do the mixer tests and theoretical modeling and for several discussions during the annual NASA Advanced Subsonic Technology Engine Noise workshops; Mr. Allen Barta, Mr. David Baker, and Dr. Bailey Vittal of AADC for help in the design of lobe mixers and the analysis of plume data; Mr. Frederick Smith and Dr. John Kingsley of AADC for help in mixer geometry definitions using CAD and CFD analysis. The mixer/nozzle models and the static thrust tests were made by Aero Systems Engineering's FluiDyne Laboratories at St. Paul, Minnesota, for which we would like to thank Mr. Randy Merchen and Dr. Dean Long. The first author, Dr. Vinod G. Mengle, was the principal scientific investigator responsible for the concept and design of the new mixers (*"boomerang* scallops" and the *"tongue* mixer"), and analysis of all the acoustic and aerodynamic data. The second author, Mr. William N. Dalton, was the Rolls-Royce Allison program manager for this task. For most of the task-order period (from April 1995 to December 1997) Ms. Kathleen Boyd was the NASA technical monitor and, thereafter (from January 1998 onwards), Dr. James Bridges was the technical monitor.

Note that at the time of research, the NASA Lewis Research Center was undergoing a name change to the NASA John H. Glenn Research Center at Lewis Field. Both names may appear in this report.

Available from

NASA Center for Aerospace Information
7121 Standard Drive
Hanover, MD 21076

National Technical Information Service
5285 Port Royal Road
Springfield, VA 22100

Available electronically at http://gltrs.grc.nasa.gov/GLTRS

Preface

The final report is written in two volumes. In the first volume we present the design philosophy of the new lobe mixers tested, and then analyze the results of various acoustic and aerodynamic tests done at NASA Lewis Research Center, Cleveland, Ohio and Aero Systems Engineering FluiDyne Laboratories, St. Paul, Minnesota over a period of three years (1995-1997). The second volume is a compilation of the plume survey data, the aerodynamic data for the acoustic tests and the acoustic data.

Table of Contents

Volume 1

Preface iii

Summary ix

1. Introduction 1

1.1 Background and Objectives 1

1.2 Overview 2

2. Mixer-Nozzle Designs and CFD Analysis 5

2.1 General Model Assembly and Common Flow Lines 5

2.2 Previous Existing Mixers 7

2.3 New Mixers 9

2.3.1 Conceptual Selection 9

2.3.1.1 Scalloped Family of Mixers 9
2.3.1.2 The Tongue Mixer 14

2.3.2 Design of the New Mixers 18

2.3.2.1 Unscalloped 20 Lobe Mixer 18
2.3.2.2 Implementation of the New Rules for Scalloping 18
2.3.2.3 Design Guidelines for the Tongue Mixer 28

2.4 CFD Analysis of New Mixers 31

2.4.1 Code, Grids and Boundary Conditions 35
2.4.2 Results 38

3. Experimental Program 55

3.1 Acoustic Tests 55

3.2 Aerodynamic Tests 62

3.3 Plume Surveys 68

4. Aerodynamic Results and Analysis 75

4.1 Aerodynamic Performance 75

4.1.1 Definition of Various Terms 75
4.1.2 Thrust Coefficients 77
4.1.3 Nozzle Discharge Coefficients 81
4.1.4 Bypass Ratios 83

4.2 Typical Plume Survey Results 87

4.2.1 Nozzle Exit Plane Survey 87
4.2.2 The Tongue Mixer and Mixer with Cutout Lobes 93
4.2.3 Plume Downstream Evolution 96
4.2.4 Effect of Scalloping 96
4.2.5 Effect of Nozzle-Length 100
4.2.6 Center-line Velocity Comparisons 105

5. Acoustic Results and Analysis 113

5.1 Overview 113

5.2 Mixers with Reference Nozzle Length at Baseline Take-Off Condition 114

5.2.1 Static Free-Jet Data 115

5.2.1.1 12 Lobed Mixers 115
5.2.1.2 Lobe Number Effect 121
5.2.1.3 Effect of Scalloping 126
5.2.1.4 Probable Causes of Noise Reduction 130

5.2.2 Flight Effect: Free-Jet Mach No. 0.2 133

5.2.2.1 12-Lobed Mixers 133
5.2.2.2 Lobe Number Effect 137
5.2.2.3 Effect of Scalloping 141
5.2.2.4 Confluent Mixer Benefits 145

5.2.3 Flight-Effect: Other Free Jet Mach Numbers 146

5.3 Mixers with Reference Nozzle-Length at Higher Nozzle Pressure Ratio Conditions 157

5.3.1 TO # 2 and # 3 with Free Jet Mach No. 0.2 157

5.3.1.1 12-Lobed Mixers 157
5.3.1.2 Lobe Number Effect 160
5.3.1.3 Effect of Scalloping 160

5.3.2 Effect of Free-Jet Mach Number at TO # 3 165

5.4 Diagnosing High-Frequency Source Locations with Changes in Free-Jet Speeds 170

5.4.1 Ray Theory Application 170

5.4.2 The New Diagnostic Method for "Excess" Noise Sources 177

5.4.3 Application to Operating Condition TO # 3 180

5.5 Effect of Nozzle-Length 186

5.5.1 Overall Acoustic Metrics 187

5.5.2 Polar SPL-Spectra 195

5.5.3 Competing Mechanisms for Local Minimum of Noise 206

5.6 Flyover EPNL 208

5.6.1 Effect of Free-Jet Mach Number 209

5.6.1.1 Effect of Observable Angular Limits on EPNL 209
5.6.1.2 Collapse of EPNL Plots 211

5.6.2 Effect of Nozzle Length 219

5.6.3 Comparison of EPNL Between Mixers 226

5.6.4 Quietest Mixer-Nozzle Combinations 232

6. Concluding Remarks 239

7. References 243

Appendices:

A Geometrical Details of Mixers and Nozzles 245

B Refraction Correction Procedure for Free-Jet/Ambient Shear-Layer and Angular Interpolation Scheme 269

C Refraction Angle, Convection Angle and Transmission Coefficient Changes Due to Free-Jet Speed Changes 271

D Comparison of SPL's at Different Free-Jet Mach Numbers and "Shifted" Angles at TO # 3 277

Summary

A comprehensive database for the acoustic and aerodynamic characteristics of several model-scale forced lobe mixers of bypass ratio 5 to 6 has been created for mixed jet speeds up to 1080 ft/s at typical take-off conditions of small turbofan engines. The flight effect is simulated with a free jet surrounding the model nozzle with Mach numbers ranging from 0.0 to 0.3. The static thrust performance and jet plume flow is also examined at typical take-off and cruise conditions. This data is scaled for a nozzle with 29 in. diameter, and the effect of several lobe-mixer and nozzle parameters is examined in terms of flyover noise at constant altitude and, also, noise in the reference frame of the nozzle to understand the changes in the noise-source characteristics.

Several new concepts, mechanisms, methods and findings are reported here for the first time regarding such mixers. The new concepts include a rational method for scalloping lobe sidewalls leading to "boomerang" scallops, and an extreme limit of scalloping leading to the "tongue" mixer. A new diagnostic method to detect "excess" internal noise sources due to fan/core mixing is given; it uses appropriate "shifted" angles for comparison of non-Doppler-shifted noise at several free jet speeds. Another new method is found to extrapolate known flyover noise for lobed mixers from one flight speed to different flight speeds.

The effects of scalloping, number of lobes and mixing-length on noise are systematically examined. Compound effects of lobe penetration and fan-to-core area ratio are also examined. For all forced mixers, the flyover effective perceived noise level (EPNL) is found to scale with "net" thrust when tested at different free jet speeds. Different types of lobe mixers are found to be most effective at different thrust levels to provide maximum noise benefit over a coaxial nozzle. At about 9500 lb net-thrust a maximum of 3 EPNdB noise suppression is accrued with a deeply scalloped lobe mixer having higher number of lobes (20) and higher lobe penetration. However, at a net-thrust of 5000 lb, a maximum of only 1 EPNdB benefit is obtained from a mixer with fewer lobes (12), lower lobe penetration and lobe sidewall cutouts. These benefits increase by about 1 EPNdB when comparison is made on the basis of same mixed jet velocity rather than same net thrust. Thus, for example, at approximately 1060 ft/s, corresponding to the highest thrust levels tested, a maximum noise suppression of 4 EPNdB is achieved by the 20-lobe deeply scalloped mixer. And, in general, the noise benefits increase at higher and higher thrust levels or mixed jet speeds.

Over most of the range of thrusts or jet speeds tested none of the unscalloped lobe mixers are quieter than the coaxial jet. Thus "scalloping" is the most important mixer geometrical parameter identified for reducing noise. Deep scalloping reduces the typical low frequency mixing noise without increasing the annoying mid-to-high frequency noise when compared to the unscalloped mixer, and gives a benefit of 1.8 EPNdB to 3 EPNdB depending on the thrust level. The "gradual" introduction of streamwise vorticity by appropriate scalloping is found to be the key to this behavior. However, scalloping also increases

the bypass ratio. Hence, the effective lobe fan and core areas should be resized appropriately for desired bypass ratios in applications to specific engine cycles. Scalloping also introduces slight thrust-coefficient loss at typical cruise conditions as compared to unscalloped mixers, especially, for mixers with higher number of lobes. Hence, the amount of scalloping should be used as a trading parameter between noise reduction and thrust loss. However, with fewer lobes and lower penetration, even with lobe cutouts (which act like scallops), an improved cruise thrust coefficient is obtained.

One surprising new result regarding the effect of nozzle length is also found: for a given mixer, there exists an "optimal" mixing length or nozzle length that creates a local minimum in noise. A reduction in the mixing-length by 25% gives a noise benefit of as much as 3 EPNdB for the unscalloped mixer compared to the baseline mixing length (which is 1.5 times the nozzle exit diameter). A competing mechanism of acoustic unshielding *vs* aerodynamic unshielding is proposed for this behavior. Using optimal nozzle length can be very helpful in reducing noise with unscalloped mixers if thrust loss due to scalloping is unacceptable. However, its effect on boat-tail angle and cruise thrust coefficient is not examined. Also, the implications of all these lobe and nozzle geometric changes on thrust specific fuel consumption are not examined.

Chapter 1

Introduction

1.1 Background and Objectives

Future commercial applications of the turbofan engine will be required to meet increasingly stringent noise abatement criteria, primarily, due to an increase in aircraft traffic near airports. Many of the current turbofan engines are based on thermodynamic cycles with a bypass ratio of five to six as opposed to the lower bypass ratio of 1.5 or so in older engines. With very high mixed jet velocities for older lower bypass engines, jet-noise is a dominant contributor to total engine generated noise, especially at take-off (TO). However, even with the current higher bypass ratios, and consequently reduced mixed jet velocities, jet noise continues to be a significant contributor.

Reduction of jet noise has been sought earlier by mixing the hot core flow and the cooler fan flow before they exit through the nozzle. A more uniform flow at the nozzle exit plane is supposed to lead to reduced noise levels. Uniform flow at the nozzle exit plane is also known to yield better cruise thrust efficiency thermodynamically than partially mixed flow or separate unmixed flow nozzle systems. In fact, that is the primary reason for mixing the two flows internally. However, the overall noise benefit or penalty incurred due to internal mixing to achieve the uniform exit flow is not well understood. The actual level of noise abatement realized in a specific application must be critically related to the manner and extent to which internal mixing is achieved. Traditionally, the mixing between the hot core flow and the cold fan flow has been achieved with so-called "lobed" mixers which are essentially convolutions at the end of the splitter plate that separates the two flows. However, there does not exist a significant acoustic database for such lobed mixers at higher bypass ratios. In addition, a good correlation between the aerodynamic thrust performance and acoustic performance for such mixers does not exist. This task was conceived to address these two needs as part of NASA's Advanced Subsonic Technology (AST) Program for Engine Noise Reduction, thereby permitting the design of thrust-efficient noise suppression mixers for modern turbofan engines.

Lobed mixers were studied extensively during the mid-seventies and early eighties as a means for improving thrust efficiency, for example, under NASA's Energy Efficient Engine (E^3) Program. Both far field noise data[1] and detailed measurement of fluid-dynamic and aerodynamic properties[2-4] for lobed mixers have been reported in the literature. Previously published noise data [1,5] is typically for low bypass ratio engine cycles (around 1.5) with high ideally-expanded mixed jet velocities of 1330 ft/s or so. Hence, a principal objective of this task was to extend the mixer acoustic data base to higher bypass ratios and operating conditions typical at take-off for modern turbofan engines. At the same time, we also wanted to study the aerodynamic thrust performance at cruise conditions for the same mixers so that the trade-off between take-off noise-suppression

and cruise thrust efficiency loss, if any, can be quantified.

Before entering this program, Rolls-Royce Allison had already designed, fabricated and aerodynamically tested four mixer configurations. These included three lobe mixers and one baseline annular or confluent configuration. Three of these configurations were originally developed under company funding, while the fourth was completed under Task 15 of NASA Contract NAS3-25950. The geometric variations in these mixers were not defined by parametrically varying only one geometric variable to examine its incremental effect on the aerodynamic or acoustic results. However these designs are representative of current technology levels and were included in the current program for their intrinsic value in expanding the experimental database.

Early Rolls-Royce Allison experience with lobed mixers with cutouts in the lobe sidewalls, showed that these cutouts may be acoustically beneficial. This is in line with work done on scalloping of lobes (partial removal of lobe sidewalls) by Pratt & Whitney and General Electric Aircraft Engines. However, no systematic study has been published examining the effect of scalloping on both acoustics and aerodynamic thrust performance especially at high bypass ratios. Hence, one of the objectives of this task was to systematically study the effect of scalloping of lobe sidewalls on noise suppression and thrust performance. This also led us to designing and testing a unique new mixer concept called the "tongue" mixer.

Since the distance between the mixer exit plane and the nozzle exit plane, called the "mixing- length," governs the axial evolution of flow and the consequent noise distribution inside and outside the nozzle it is expected to be an important parameter. Hence, another objective of the program was to examine the relationship between nozzle length and the jet noise generated by the various lobed mixers.

1.2 Overview

The tests in the program were conducted over a period of three years from 1995 to 1997. The acoustic tests were performed in two phases at NASA Lewis Research Center's (now Glenn Research Center) Aeroacoustic Propulsion Laboratory (APL) Nozzle Acoustic Test Rig (NATR) facility. The aerodynamic tests were conducted at Aero Systems Engineering's (ASE) FluiDyne Aerotest Laboratory static thrust stand in St. Paul, Minnesota and were also done in two phases. This report summarizes the principal results of the voluminous data collected from these four different tests and the lessons learned.

For the acoustic tests, data was obtained over a range of free-jet Mach numbers, which simulates the forward motion of the aircraft at take-off. This not only allows us to compare noise benefit at take-off speeds, as opposed to static conditions, but also to approximately locate the different noise sources associated with the different frequency bands, as explained in later chapters. The operating conditions were chosen to cover typical take-off operating conditions for modern turbofan engines. All aerodynamic thrust tests were conducted under static (or no free-jet) conditions, and included both cruise conditions and most of the take-off operating points. Plume surveys outside the nozzle, including total pressure, total temperature and static pressure were also conducted so that possible trends could

be obtained between the acoustic characteristics and the plume evolution.

This volume summarizes the design of a series of lobed mixers developed specifically for this program and the results of the acoustic and aerodynamic tests done for all the mixers. The second volume collates detailed plots obtained from the plume surveys and the aerodynamic data collected during the acoustic tests.

Chapter 2 of this volume discusses the conceptual development and new design rules for the scalloped mixers and the new tongue mixer. It also briefly describes the computational fluid dynamic (CFD) results for some of the new mixers and gives the geometrical properties of all the models tested.

Chapter 3 summarizes the experimental facilities for the acoustic and the aerodynamic tests, and the manner in which the data was processed. It also collates all the test matrices from the different test phases.

Chapter 4 summarizes the aerodynamic test results obtained from the static thrust stand at ASE FluiDyne, as well as those obtained during the acoustic tests at NASA Lewis. Some selected plume surveys are also discussed to facilitate the acoustic data analysis, and the full jet plume data is given in Volume 2.

Chapter 5 summarizes the acoustic test results for all the mixers tested. It discusses the parametric effects of operating conditions, surrounding free-jet Mach number, and nozzle length on each mixer. Comparison between different mixers at the same operating conditions is also presented here to bring out the effect of different geometric parameters such as scalloping and number of lobes. We also present a new way of processing the acoustic data to deduce the presence of excess "internal" mixing noise, that is, noise produced inside the nozzle duct due to the mixing of fan and core flow, as distinguished from the classical jet mixing noise due to sources in the plume outside the nozzle. Certain rules of thumb for improving noise suppression while minimizing the adverse effect on thrust performance are also summarized in this chapter.

Finally, in Chapter 6, we summarize the main conclusions from these tests. Recommendations for implementation in full-scale engines and further useful tests are also given.

The appendices at the end of this volume are intended to supplement the main body of the text by providing additional detailed derivations, data, figures or tables.

Chapter 2

Mixer-Nozzle Designs and CFD Analysis

Under this program, a total of eight mixers were tested. Four of the configurations were existing designs from previous tests, while four new mixers were designed, fabricated and tested. All testing was carried out at model scale. This allowed utilization of an existing test rig for performance measurements at the ASE FluiDyne facility. Additional hardware was fabricated as part of the program to allow adaptation of the mixed nozzle flow rig to the NASA NATR facility.

In this chapter, we briefly outline the history and geometry of the four existing mixers, describe the concepts that led to new rational design rules for scalloping and the unique tongue mixer, and finally present the geometrical details of the four new mixers which were fabricated. The main body of this chapter has the schematic figures (or photos), whereas all detailed geometrical, dimensional figures are collated in Appendix A. The results of a CFD analysis for one of the new scalloped mixers and the tongue mixer are also briefly described to validate the conceptual picture and to help analyze the acoustic data later.

2.1 General Model Assembly and Common Flow Lines

Figure 2.1 shows the general arrangement of the mixer-nozzle configurations and geometrical definitions. All the mixer-nozzle configurations had common inner flow lines for the fan nozzle or shroud. However the outer (external) surface of the fan-nozzle was different for the models tested in the acoustic rig (NATR) and the static thrust stand. This is due to the requirement of providing flight simulation effects via a free-jet surrounding the nozzle in the NATR which demanded a smoother outer surface. Figure A.1 and A.2 show the detailed model assemblies for the acoustic rig and the thrust-stand respectively. Both figures also show the location of the pressure and temperature rakes used at the charging stations and Figure A.2 further shows the additional rake used to measure total pressure (P_T) near the mixer exit plane. The exit P_T rake was removed during thrust measurements.

Figures A.3 and A.4 show the detailed inner flow lines of the baseline or reference fan nozzle downstream of the reference station 0 depicted in Figure A.2. In general, it forms a converging area from about 10.290 in. in diameter at station 0 to 7.245 in. in diameter at the nozzle exit plane (station 57), with a nominal mixing length, L, of 11 in. and gives a baseline mixing length-to-mixing plane diameter ratio (L/D_{mp}) of about 1.10.

Three additional fan nozzles, which were compatible with all the mixers, were also fabricated. Each of these nozzles maintained a constant exit diameter but varied the mixing length (see figure A.5); this varies the axial rate of contraction for each nozzle. The additional mixing lengths tested were 1.363, 0.818, and 0.545, when normalized to the mixing-plane diameter. This corresponds to nominal variations of +25%, -25%, and -50% from the baseline mixing length. The coordinates of the additional nozzles are provided in Figures A.6, A.7 and A.8.

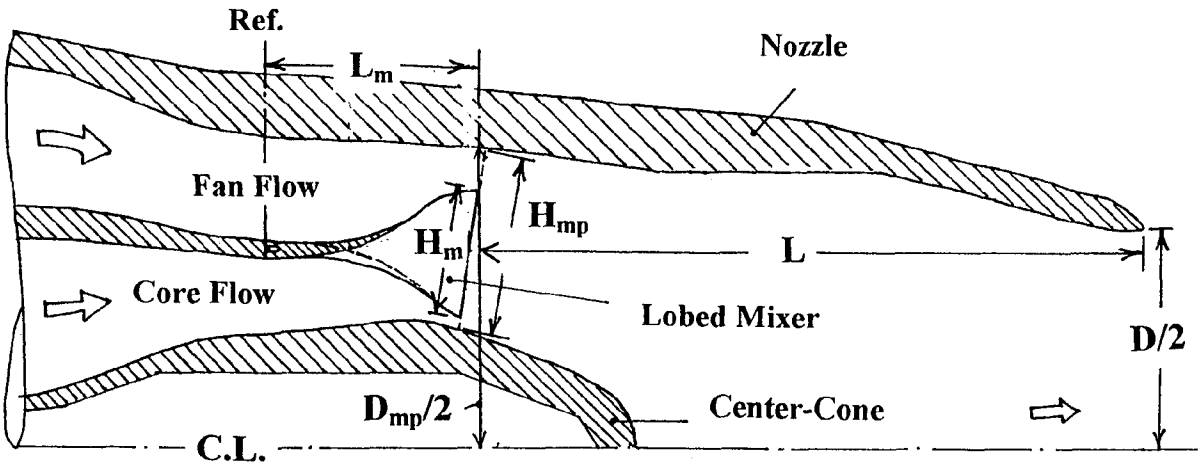

Figure 2.1 Schematic of mixer-nozzle configuration and geometrical definitions.

Mixer	Mixer Code	Lobe No.	Scallop	Lobe Penetration (H_m/H_{mp})	Lobe Length (L_m/D_{mp})	Area Ratio (A_f/A_c)	Mixing Length (L/D_{mp})
Confluent	CONF	-	-	-	-	2.554	1.15
12 Lobe with Cutouts/Low	12CL	12	Triangular Cutouts	0.48	0.33	2.637	1.13
12 Lobe Unscalloped/High	12UH	12	None	0.68	0.34	2.637	1.09
16 Lobe Unscalloped/High	16UH	16	None	0.72	0.34	3.199	1.09

Table 2.1 Previous Existing Mixer Parameters

Two center tailcone configurations were employed. The first shown in Figure A.9, had a length of 5.935 in. and was used with all the lobed mixers. The second one, shown in Figure A.10, was shorter and used only with the confluent nozzle configuration. This tailcone had a length of 4.258 in. and slightly different shape. The two tailcones are shown side-by-side in Figure A.2. The resulting confluent mixer configuration, described below, had a slightly smaller fan-to-core area ratio but was designed such that, after accounting for the boundary-layer thickness, the mass-flow rates would match with the original lobed mixers. From a viewpoint of systematic variation of geometric parameters, it would have been preferable not to have varied the tailcone at all for the confluent mixer, but rather to have varied the confluent mixer geometry itself to match the mass-flow rates or area ratios of the lobed mixers. However, due to the availability of previous aerodynamic, as well as, full-scale acoustic data [6-8] we continued using the old confluent-mixer/tailcone combination instead of building a new one. This fact needs to be borne in mind when comparing acoustic or aerodynamic data of the lobed mixers with that of the confluent mixer. [Note that the uniquely truncated tailcone shown in Figure A.2 (one with cross-hatched cross-section) was a carry-over from an old program and was not used in this task.]

2.2 Previous Existing Mixers

Four existing mixer configurations from previous programs were available. These were:

1. Annular or confluent mixer which acted as the reference configuration.
2. 12-lobed mixer with cutouts in the lobe sidewalls and low penetration (that is, low lobe-height-to-maximum possible lobe height in the duct (H_m/H_{mp} in Figure 2.1)).
3. 12-lobed, unscalloped, high-penetration mixer.
4. 16-lobed, unscalloped, high-penetration mixer.

Figure 2.2 shows the relative shapes of the mixers and Table 2.1 lists their non-dimensional geometric properties as defined in Figure 2.1. As shown in Table 2.1, we will use certain symbols for lobed mixers for convenience: ab c d where ab represents the number of lobes, c represents the type of scalloping or cutouts (U for unscalloped, C for cutouts) and d represents relative lobe-penetration (L for low, H for high lobe penetration).

The two 12-lobed mixers, 12CL and 12UH, differ in two aspects: presence of sidewall cutouts and lobe penetration with fan-to-core area ratio, lobe number, and lobe length held constant. The last two configurations in Table 2.1, 12UH and 16UH, differ in terms of both number of lobes and fan-to-core area ratios, however, they are similar in terms of lobe penetration and lobe length. Between 12UH and 16UH mixer at least two parameters vary from one mixer to the other. As a result, it is not possible to isolate the effect of a particular geometric parameter on the resulting aerodynamic and acoustic data. The detailed geometrical characteristics of these four mixers is provided in Figures A.11 through A.17.

Before discussing the new mixers, let us make a note of some of the characteristics of the original mixers. Firstly, the confluent mixer, CONF, has its own tailcone different from that for all other mixers, as mentioned before. Secondly, only the cut-out version of the 12 lobed, low-penetration mixer (12CL), shown in Figure A.14, was used in

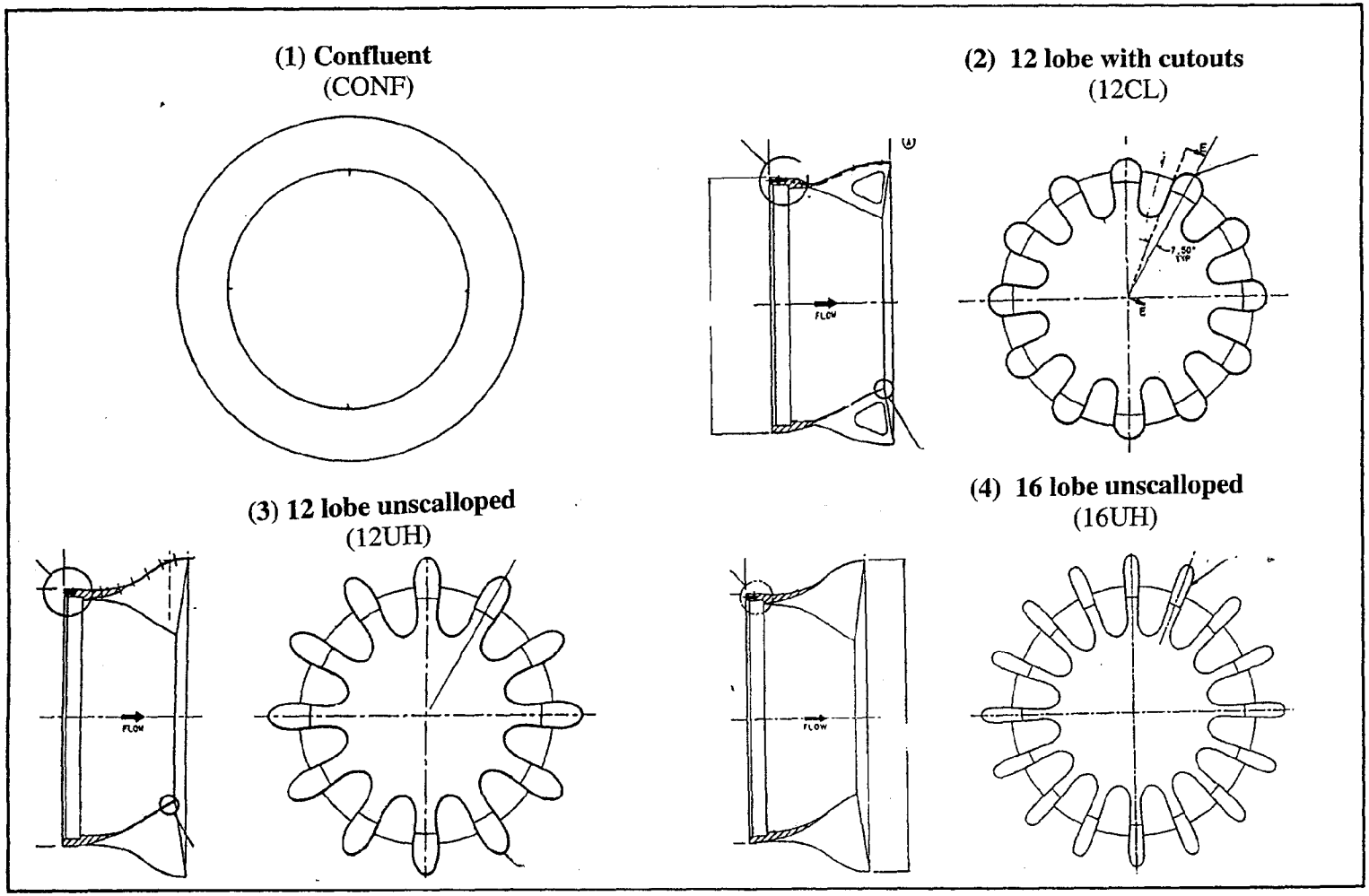

Figure 2.2 Relative shapes of existing mixers.

this program. It was made from a previous uncut version whose flow-lines are given in Figure A.13. The approximate triangular cutouts in the lobe sidewalls of 12CL were made where the sidewalls were flattest. The fillet radii at its 3 apexes were made simply to reduce stress concentrations in the sidewalls. The high-penetration 12-lobe unscalloped mixer, 12UH, was designed earlier to improve thrust mixing efficiency over the uncut, low-penetration 12-lobe mixer. The design philosophy, some CFD results and aerodynamic test results for these three mixers can be found in Booher et al[6] where they are referred to as confluent, baseline (or conventional mixer), and advanced mixer, respectively. The last mixer in Table 2.1, the 16 lobe mixer (16UH), was designed for a different operating point at lower pressure ratios and had a much larger fan-to-core area ratio; consequently, 16UH stands apart from the previous mixers. This should be borne in mind when acoustic comparisons are made later. Results from CFD analysis and comparison with aerodynamic test data for all these four mixers can be found in Barta et al[7] where the 16-lobe mixer is referred to as the acoustic mixer.

2.3 New Mixers

Acoustic data obtained from the four previous existing mixer configurations, in the first phase of this task, confirmed previous observations that aggressive, high-penetration, unscalloped mixer configurations do suppress the low frequency spectrum which is characteristic of unmixed, coaxial turbofan exhausts, but produce secondary spectral peaks at higher frequencies which are heavily weighted in the Perceived Noise Level (PNL) metric. However, the moderate penetration 12 lobe configuration with cutouts in the sidewalls (12CL) produced the low frequency suppression of the more aggressive designs without incurring a penalty at the higher frequencies. Since both the radial lobe penetration and sidewall cutouts were different from the other designs, it was not possible to determine directly from the available data which change was most responsible for the acoustic characteristics. However, data previously presented in the open literature[1] for "scalloped" sidewall mixers for a lower bypass ratio, higher pressure ratio cycle showed similar behavior. From these two results, it is inferred that the sidewall scalloping is the controlling parameter. However, existing data[1,5] defining the acoustic impact of sidewall scalloping was not obtained by parametric variation of a single parameter. For example, the data reported in Reference 1 was obtained on a series of mixers with varying scalloping. However, the variation in scalloping was achieved by *cutting back* the mixer exit plane, introducing an additional variation in the mixer cant angle. To address this shortcoming, three additional mixers were designed and tested in this program which parametrically varied the sidewall scalloping while holding all other parameters fixed. A fourth mixer represents a unique new concept referred to as a "tongue mixer." As part of this effort, a systematic approach to developing the scalloped curves has been defined and rules of thumb for its application developed. Both the process and the resulting designs are described in the following section.

2.3.1 Conceptual Selection

2.3.1.1 Scalloped Family of Mixers

The idea here is to test a family of mixers which have exactly the same geometric properties, except for the amount of scalloping or cutouts in the lobe sidewalls.

This would entail a minimum of two mixers - an unscalloped and a scalloped one. However, to form a trend a third mixer with an "in-between" scallop is required. Then the questions to be answered from an acoustic point of view are:

i) Should we select scallops or cutouts?

ii) Are there preferred shapes, from an acoustic standpoint, for the scallops or cutouts?

iii) How many lobes should we select for this family of mixers?

We invoke certain fluid-dynamic and aeroacoustic principles to answer these questions qualitatively. The precise mechanism of how scalloping may help suppression of noise is not known but what happens to the two flows in the scalloped region must be quintessential to its downstream evolution and noise generation. We present certain new hypotheses which will be used as guidelines to shape the scallops or cutouts.

(i) As compared to an unscalloped forced mixer, it is clear that scalloping, of any type, allows the two streams (fan and core) to interact with each other "earlier" that is, upstream of the corresponding unscalloped mixer exit plane, so that the flows are already partially mixed by the time they reach the original mixer exit plane. Hence, if the two streams are not parallel near the lobe sidewall, then with scalloping, their radial velocity components will give rise to axial or streamwise vorticity right from the start of the scallop. It is well known[9-11] that streamwise vorticity helps enhance mixing of these two flows as opposed to mixing only due to Kelvin-Helmholtz type of vortex-sheet instability. What should be done differently with scalloping is the manner in which vorticity is initially introduced into the flow - earlier and also "gradually". By gradual initial mixing, we mean the axial gradient at which net vorticity is introduced into the flow should be smooth and gradually increasing. This should presumably reduce the relatively high-frequency noise sources, so important to perceived noise level metrics, and which were indeed, found in the unscalloped lobe mixer data of Reference 1, as well as, in phase I of this program. In unscalloped mixers, since the two streams "see" each other for the first time across the "full height" of the mixer exit plane, it is presumably the "sudden" interaction there that shears a larger area of fluid generating the high-frequency noise.

This control over the rate of introduction of vorticity in scalloped lobes can be obtained by gradually increasing the radial height of the scallop starting from zero. This can be verified by referring to the circulation around a loop in the transverse plane enclosing the radial height of the scallop (see Figure 2.3); such a circulation is an integral measure of the axial vorticity at each axial station. The fact that we seek to mix the flows gradually in the beginning may be at odds with the desire that the flows should be fully mixed by the end of the nozzle exit plane because the mixing-length may not be enough. Achievement of a fully mixed flow is desirable from a thermodynamic thrust efficiency point of view and also provides a reduction of low-frequency classical jet mixing noise from the far downstream plume. Obviously, the distance from the mixer exit plane to the nozzle exit plane - the mixing-length - will also play a role in

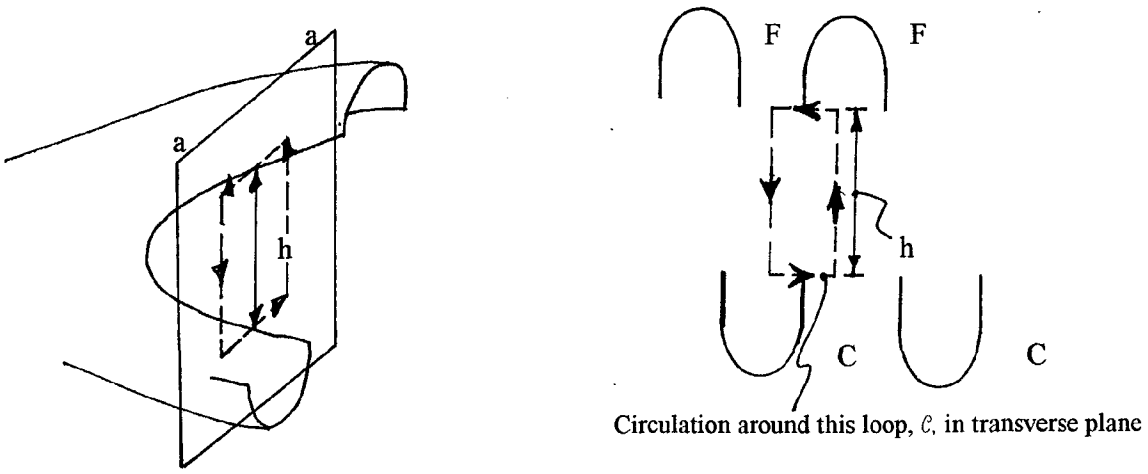

Figure 2.3 Loop in transverse plane for finding circulation at an axial station inside scallops.

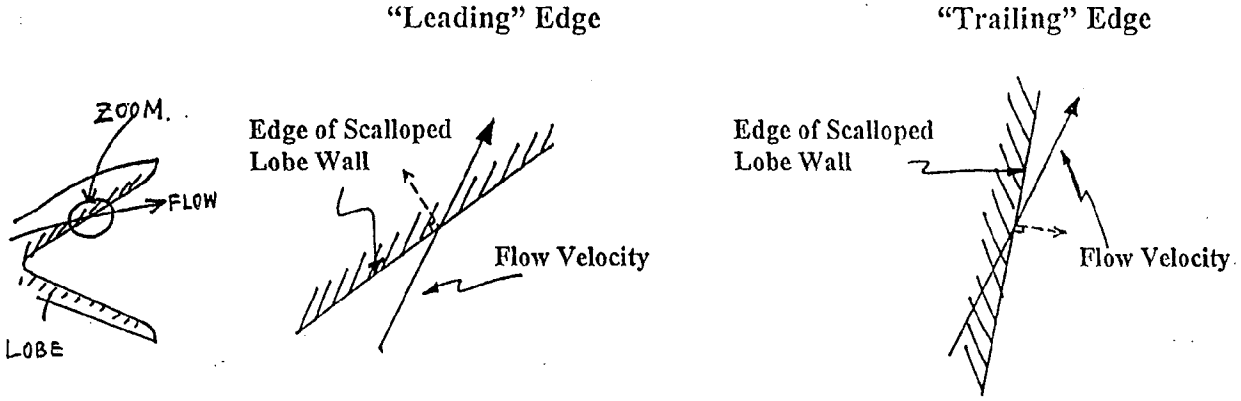

Figure 2.4 Definition of "leading" edge and "trailing" edge of scallop.

how well-mixed the flow is at the nozzle end and how much the low frequency noise is suppressed by a scalloped mixer. So, in fact, we should also test the effect of nozzle length. We also expect a difference in the total pressure loss between scalloped lobes and unscalloped lobe designs.

(ii) The noise mechanism dealt with above is the result of the mixing of two flows and is best represented by the Lighthill "quadrupole" type of noise sources. When we consider flows near scalloped edges we also need to worry about the formation of so-called "dipole" noise sources, which are even more efficient sound generators than quadrupoles. These are the same type of sources that are responsible in fan noise for creating tones when the blade-wakes periodically hit the leading edge of downstream vanes. To be sure, the trailing edge of a splitter plate separating two flows can also act as a dipole source of noise, but of much less magnitude than the corresponding leading edge source. While designing the scallops we must minimize the formation of "dipole" noise sources. Based on the analogy of leading edge dipole sources in the fan blade-vane interaction problem, a design rule is developed for scalloping to minimize dipole formation which will be called the "trailing edge rule."

First a definition for the "leading edge" in a scallop must be developed. Analogous to wing-aerodynamics, we define that part of the scalloped edge as a "leading edge" with respect to a stream if the velocity vector of that stream has the component orthogonal to the edge going "towards" the edge, as shown in Figure 2.4. Conversely, if this orthogonal component is going "away" from the edge then we will define it as a "trailing-edge". To minimize the dipole noise source generation, the scalloped edge should be shaped such that it acts as a trailing edge throughout its length with respect to both the streams (fan and core) around it. This, we will call "the trailing-edge rule for scalloping." In adopting this rule of thumb, it must be remembered that the relative strength of the dipole source relative to the usual quadrupole sources has not been established. It is possible that the dipole source incurred due to scalloping may not be a strong noise source. By avoiding the formation of the dipole, the intent is to simply avoid the formation of additional sources. Based on this guideline, several unacceptable configurations can be immediately identified and are shown in Figure 2.5. For example, the vertical strip at the downstream edge of mixer 12CL violates this rule of thumb.

(iii) Selection of Mixer Lobe Number: In considering the number of lobes to be used in a mixer, it should be remembered that lobe number establishes the wetted perimeter. By increasing the number of lobes in the mixer, the interface area between the two flow streams is increased. This increased area of interaction leads to an overall increase in turbulent mixing. However this process is not entirely straightforward. Since all mixers must fit within the same duct cross sectional area, increasing the number of lobes produces a corresponding decrease in lobe width and the resultant diameter of the axial vortex shed from each lobe sidewall. The resulting changes in vortex growth, diffusion, and interaction

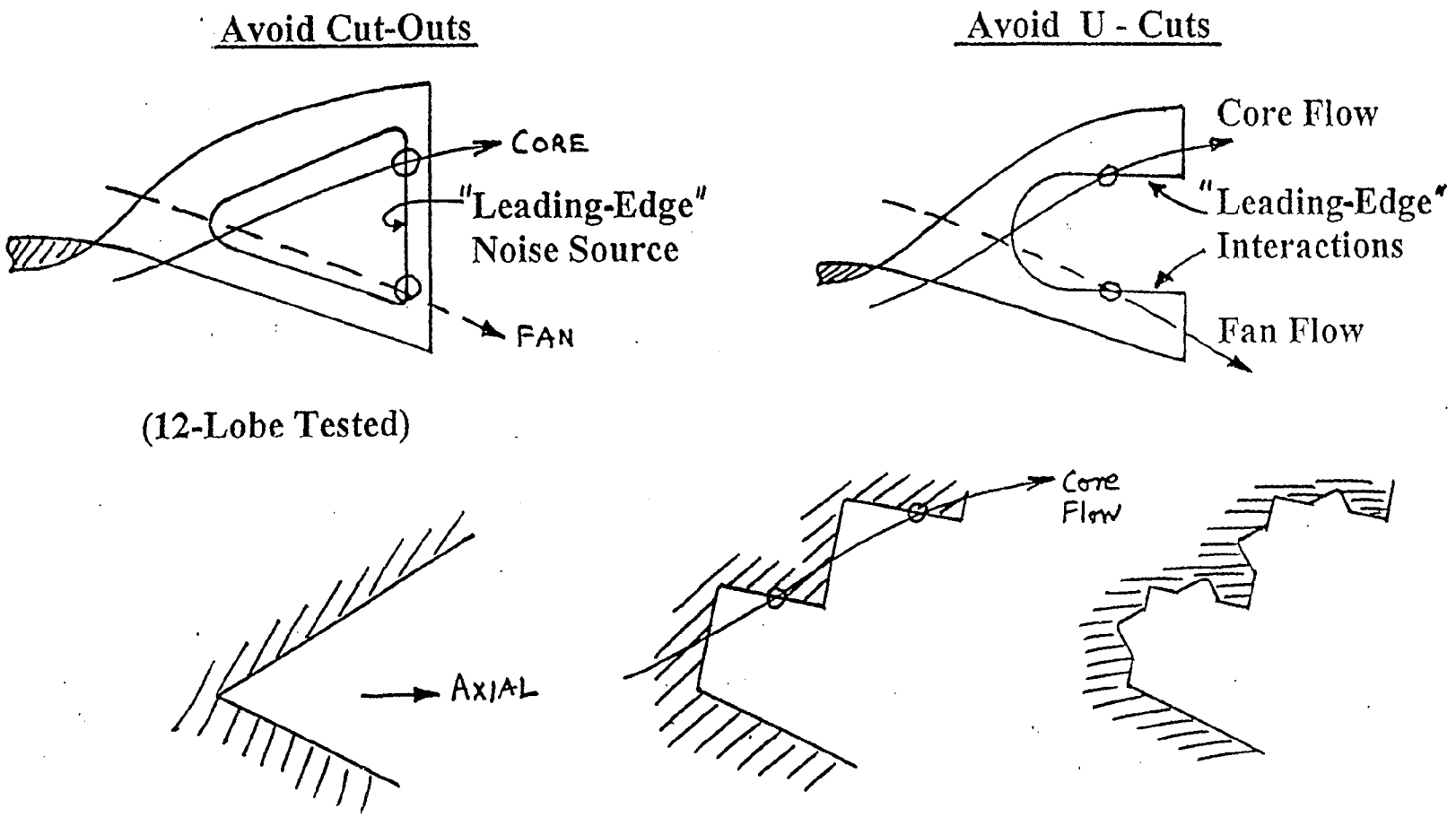

Figure 2.5 Types of scallop-shapes to avoid because of "leading" edge scallops.

will also substantially alter and complicate the mixing process. Unpublished data exists which establishes that an increase in lobe number can be acoustically beneficial under certain operating conditions. However, this acoustic benefit is offset by an increase in skin friction and total pressure loss which will adversely affect thrust production.

It is not easy to place a limit on how high the number of lobes must be from these considerations but other properties like weight, blockage due to lobe metal thickness, and manufacturability of the lobes do come into the picture. Having previously tested mixers with 12 and 16 lobes in the first phase and in order to strike a balance between noise suppression and thrust loss, we selected 20 lobed mixers for the second phase which would be similar to the high-penetration 12 lobe mixers (12UH) in other respects.

2.3.1.2 The Tongue Mixer

As discussed earlier, scallops in forced lobe mixers may be acoustically advantageous if designed properly. Most probably, it is the earlier and more gradual initiation of streamwise vorticity due to the scallops that is helpful in reducing high-frequency noise. Suppression of the low frequency portion of the spectrum is enhanced as the flow approaches a uniform state at the nozzle exit. By letting the scallops become deeper and deeper both these processes can be accentuated, although we then lose control of the cross-sectional areas for the two streams and, hence the flow properties between the lobe sidewalls. It is also possible that for a given shape and number of lobes in a lobe mixer, there exists an optimal depth of scallop from a noise suppression point of view. If we take this scalloping to its ultimate limit, that is, scallop all of the lobe sidewall, only the lobe crests and valleys remain. This bare skeleton of fully scalloped lobes will look like multiple tongues of metal deflected towards the outer nozzle wall and the nozzle center-line - hence, the name "tongue" mixer. If the two streams are subsonic and if the two streams flowing along their respective tongue surfaces still do not separate then the process of formation of a streamwise vortex between the two tongues will still exist and enhance mixing. However, without the lobe sidewalls to guide the two streams the tongue surfaces will now have to be modified from the corresponding unscalloped lobed mixer geometry. In fact, the older rules of designing forced lobe mixers may not be applicable to the tongue mixer.

This concept of the tongue mixer as an extreme limit of scalloping actually can be viewed as one of the steps bridging the gap between the confluent mixer (splitter plate) and a scalloped lobe mixer, as shown in Figure 2.6. Here, the conceptual variations between the tongue mixer and the confluent mixer, called the "comb" mixer and the "screen" mixer are obtained by reducing the width of the tongues and then adding a transverse grid. The comb and the screen mixers will simply generate small-scale eddies downstream, where the mixing between the two streams will proceed due to turbulent diffusion alone and will not be efficient. However, a tongue mixer, if designed properly, may stand to benefit acoustically. It may also have advantages in terms of manufacturability, weight and cost.

The principle of operation for the tongue mixer, thus, still remains the earlier and gradual generation of axial vorticity by

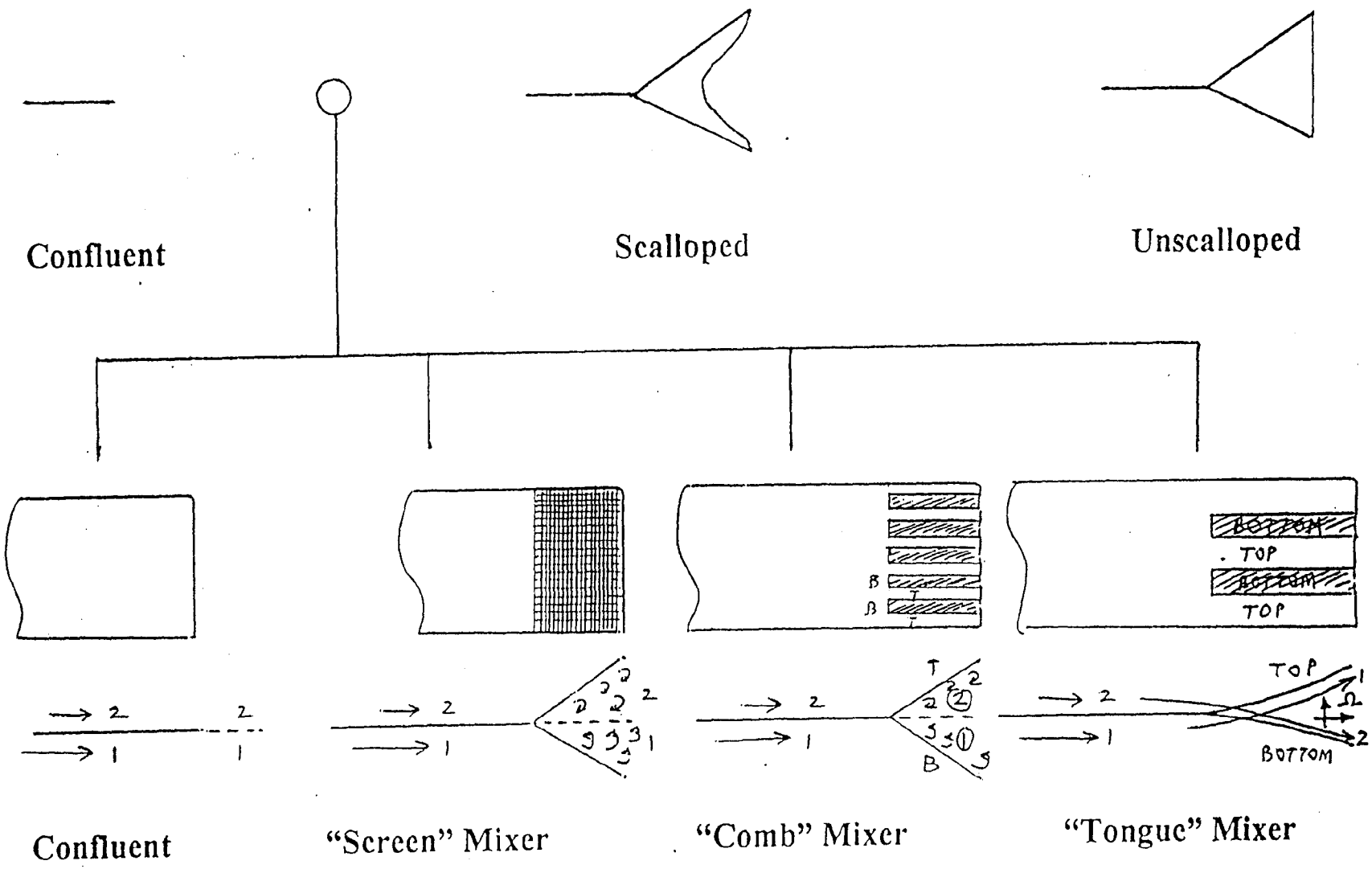

Figure 2.6 Spectrum of subsonic mixers bridging the gap between confluent and lobed mixers.

guiding each stream in its own tongue such that the mixing between them occurs across the vortex sheet which replaces the lobe sidewalls. This vortex sheet has both axial and radial vorticity components due to differences in, respectively, the radial velocity components and the axial velocity components of the two streams. The axial vorticity component is known to enhance mixing in lobed mixers by increasing the interface area between the two flows by curling the vortex-sheet, and thus introducing the "engulfing" process which is far superior to mixing due to viscous diffusion occurring in a confluent nozzle. This same enhanced mixing process will now occur in the region between any two adjacent tongue edges and continue downstream with interaction between the adjacent vortex sheets. With axial vorticity first ingested at the "root" of the tongues (that is, where the two neighboring tongues first start diverging from each other) and with axial vorticity at downstream stations being possibly strongest midway between the two tongues, this vortex-sheet will curl at mid-height and the central vortices will grow in size as they convect downstream. In this regard it is interesting to note that Elliott et al [9] at M.I.T. have suggested through their CFD studies that for lobed mixers maximum mixing contribution due to axial vorticity can be obtained if the axial vorticity is highest or concentrated at the mid-height of the lobes. The hypothesized vorticity dynamics for the tongue mixer is shown in Figure 2.7.

We will embody these considerations as three basic principles, to be stated below, around which we can base our design guidelines for tongue mixers. First, since we are talking about a new concept, let us clearly define some of the new terminology we have adopted for the tongue mixer:

(a) *Top* tongue or core tongue refers to the radially *outward* tongue (as we go downstream); *bottom* tongue or fan tongue for the radially *inward* one.

(b) *Internal* stream or surface, for a given tongue, refers to the flow or surface that would be inside the unscalloped lobe from which this tongue can be thought to be made of; the *external* stream or surface would be the one outside that lobe. Thus for a conventional two-stream nozzle with fan flow surrounding the core flow, for the *top* tongue (which can be thought of as being made up of the *crest* of a core lobe) the internal stream is the core stream and the external stream is the fan stream; whereas, for the *bottom* tongue the internal stream is the fan stream and the external stream is the core stream.

The three basic fluid-dynamics and acoustic principles for the tongue mixer to work are:

P1. The internal flow on the tongue should not separate.

P2. The external flow over the tongue should not go around it towards its internal side displacing the internal flow and forming wake like eddies.

P3. The dipole noise-source due to the interaction of tongue and external flow should be minimized while achieving the desired goals of mixing performance.

Thus, for any tongue geometric parameter under consideration it should be designed such that the above three principles are satisfied. We will refer to these principles as P1, P2 and P3. There may be other rules of thumb which may improve the non-acoustic

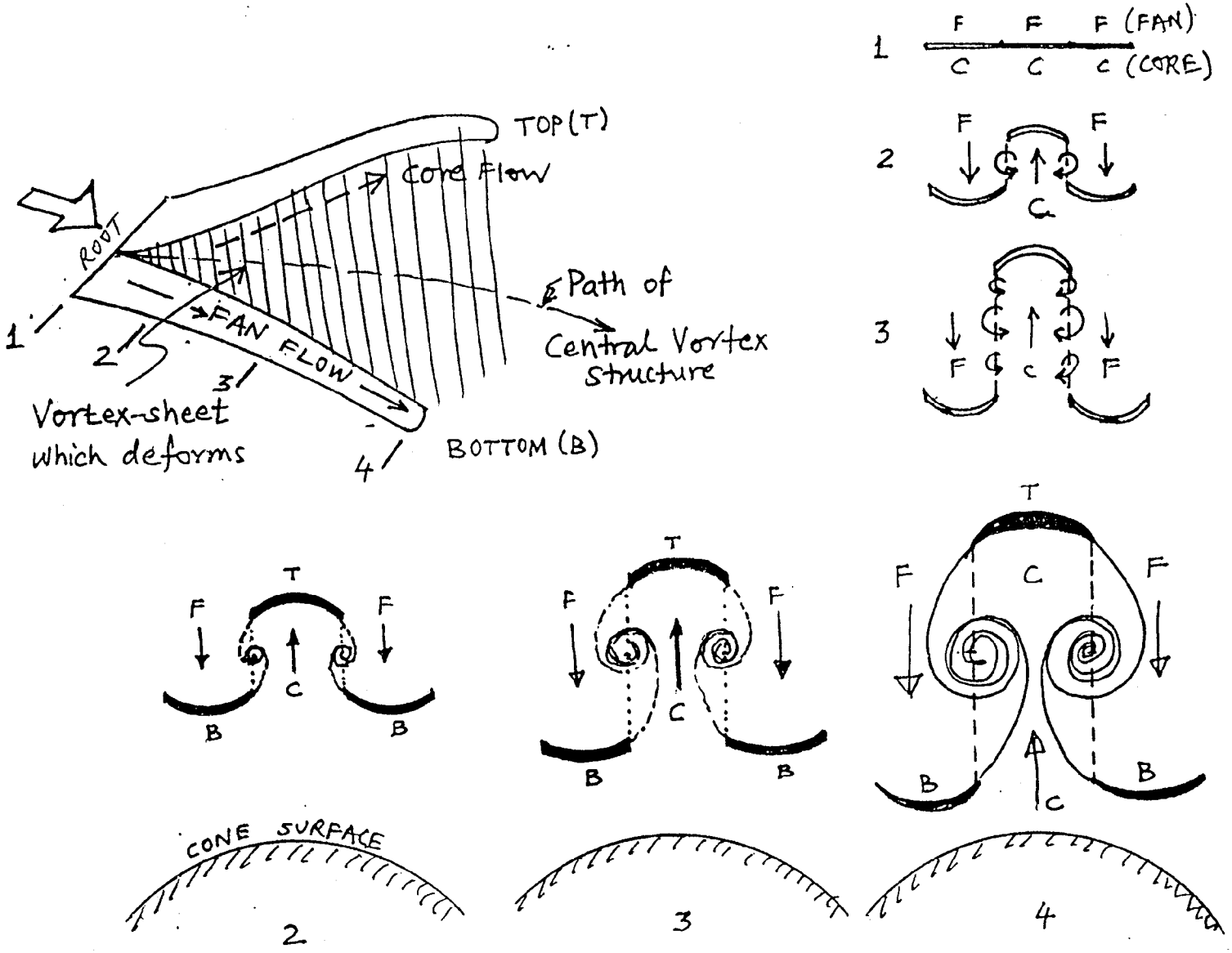

Figure 2.7 Expected flow development in tongue mixer using vorticity dynamics.

performance, such as aerodynamic thrust, and should be incorporated, if possible, without violating the above principles.

2.3.2 Design of the New Mixers

2.3.2.1 Unscalloped 20-lobe mixer

The 12 lobe, high penetration mixer (12UH), 12 lobe low penetration mixer (12CL), and the confluent mixer (CONF) configurations of Table 2.1 were designed to have equal bypass ratio. For the parametric study of the effects of scalloping, a 20 lobe configuration was selected. The unscalloped 20 lobe baseline was designed to have an identical area ratio, lobe penetration and lobe length as the 12UH configuration. In this way, it would be possible to isolate the effect of lobe number on acoustics and aerodynamics. The angular coordinates of the new 20 lobe mixer (denoted 20UH) were initially derived by symmetrically compressing the 12UH coordinates on either side of the crest centerline by the lobe ratio (12/20). This initial profile was then modified by increasing the radius of curvature of the crest and decreasing the radius of curvature of the keel, as viewed in the transverse plane. In addition, it was necessary to re-contour the crest surface in the meridional plane to suppress a small region of separated flow. Some CFD results are discussed later in section 2.4.2. The final configuration is shown in Figure A.18.

2.3.2.2 Implementation of the New Rules for Scalloping

In the previous section, we developed two general guidelines for designing scalloped edges for a given lobe mixer:

(i) the radial height of the scallop should *gradually* increase from zero to some value.

(ii) the scalloped edge should be a "trailing-edge" all along its length with respect to both fan and core flows.

These guidelines do not address the selection of the axial depth of the scallop or the specific curve defining the edge of the scallop. Additional criteria for selecting these parameters must be defined.

Since the flow inside the lobes and close to the lobe surface closely follow the shape of the crest or keel (depending on whether it is core flow or fan flow respectively) it appears, at first sight, that a simple V-shaped deep scallop in the lobe sidewall (with the V pointing upstream) will satisfy both the geometrical principles mentioned above. This appears satisfactory for lobes with monotonic radially diverging crest and keel lines, or scallops with relatively shallow axial depth. However it can fail in cases where either the crest or the keel line has an inflection point, especially, when the scallop is axially deep. We will show how that limitation can be removed and give a general method to obtain a first-order scalloped edge satisfying the two rules. This will be done by building approximate flow lines purely from the given geometry of the unscalloped lobe and without the use of any CFD tools. Any further refinements will of course necessitate CFD tools; however, in most cases, the first order estimate of the scalloped edge should be adequate.

While discussing the geometry of a scalloped edge on the lobe wall it is convenient to consider a reference meridional plane rx (r being the radial direction and x being the axial flow direction) in the case of a circular nozzle and rotate all the corresponding lines (such as, the lobe crest or keel lines) from meridional planes at different azimuthal angles on this

one reference plane. We will call the straight line joining the top of the lobe crest and the bottom of the lobe keel in this reference meridional plane as the "unscalloped" trailing edge of the lobe. This line may be canted and not necessarily radial. Any deviation of the actual trailing edge of the lobe from this straight line will be considered as scalloping.

It is convenient to use local mixer axes (ξ,η) as parallel and orthogonal to this "unscalloped" lobe trailing edge. Figure 2.8 shows one selection of these axes (with origin O) with ξ-axis along the unscalloped edge and η-axis passing through the intersection of the crest and keel lines (point C). Some of the geometrical terms we have introduced to describe the scalloped edge characteristics are also shown. Thus the depth, height and offset of the scallop broadly describe its geometry and the type of the curve tells its shape. Notice that the depth FH is defined here to be in the η-direction which may not be necessarily in the axial direction due to a possible cant angle of the unscalloped edge. The scallop depth, FH, can be expressed as a percentage of the maximum depth, CO, that can be achieved for the given lobe; thus, 100*FH/CO is the percentage depth. The offset of the scallop apex F is defined from a point G which in some way defines the "mid-height point" at that depth. With the local axes defined as in Figure 2.8, it is natural to define the mid-height point G as the mid-point of a line parallel to the unscalloped edge and passing through the apex F. The offset can then be quantified as a percentage of the maximum offset achievable at that depth as 100*FG/GI. However, note that it may be possible to define the locus of "mid-height points" as the locus of centers of circles inscribed between the lobe crest and keel lines (see Figure 2.9(a)). In this latter sense the point p in Figure 2.9(a) is equi-distant from the two neighboring crest and keel surface lines (pq = qr); whereas, in the previous sense (as shown explicitly in Figure 2.9(b)) it still is equidistant from these two surface lines but on a given canted line pqr parallel to the unscalloped edge. We define the zero offset line as the simpler-to-draw mid-height line CC' of Figure 2.9(b). Lastly the scallop height DE can also be defined as a percentage of the maximum scallop height possible AB as 100*DE/AB.

When constructing the scalloped edge one can ask the broadest question: "What is the scallop depth, offset, height and type of curve that should be selected to reduce noise?" We do not know the answer to this question and how indeed noise varies with these parameters. It does not appear that such a question has ever been posed at all or answered in the open literature to our knowledge. It appears that the most dominant parameters amongst these may be the *depth* of the scalloped curve. The effect of scallop depth is what will be studied here. Thus a reasonable question that we propose to answer is "Given the scallop apex location F (that is depth and offset) how do you construct the scalloped edge so as to satisfy the two rules (given at the beginning of this sub-section)?"

The "trailing-edge (t.e.) rule" requires an estimate of the flow direction on both sides of the corresponding unscalloped lobe sidewall. If we can obtain a simple approximation to the flow velocity direction near the crest and keel lines then that would indeed help in constructing at *least deep scallops whose edges are close to the crest and keel lines* and which satisfy the t.e. rule. From two-dimensional inviscid flow analysis results we know that, for example,

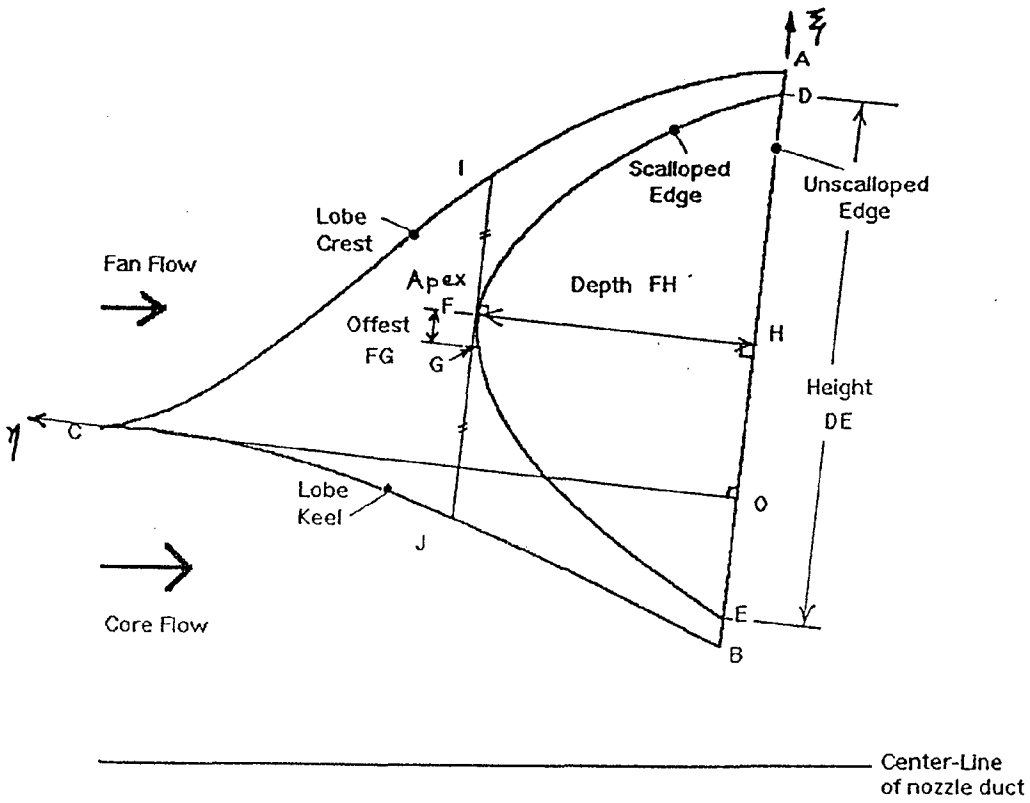

Figure 2.8 Geometrical definitions for describing a scalloped edge on a lobe mixer sidewall.

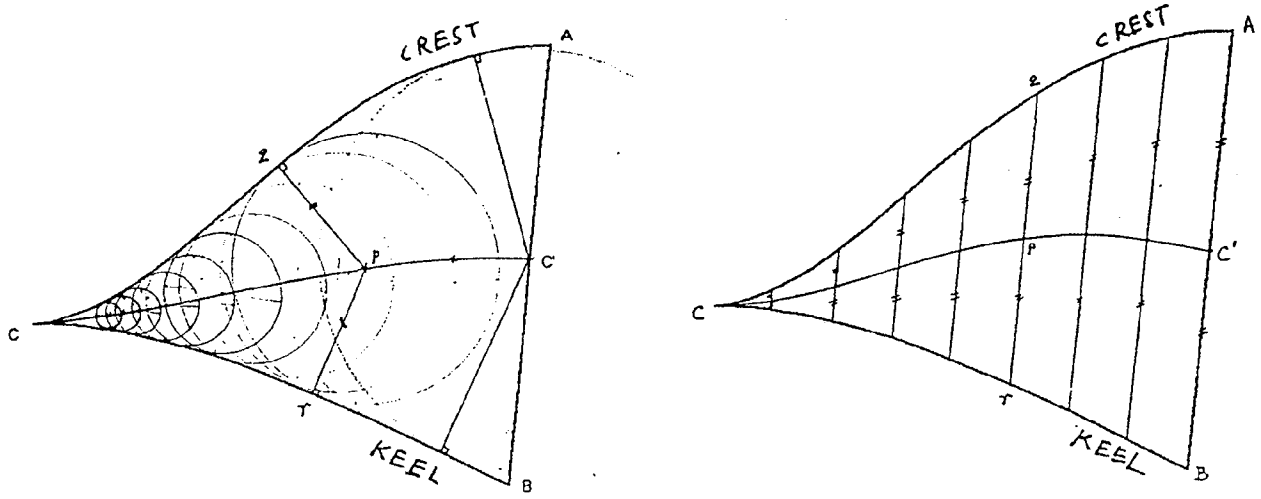

(a) Locus of centers of inscribed circles

(b) Mid-heights of lines parallel to (canted) unscalloped edge

Figure 2.9 Two possible methods of prescribing the mid-height locus for a lobed mixer.

the steady streamlines near a surface and away from stagnation points and separated regions are very nearly "locally parallel" to that surface. But there is an ambiguity when we say that two curves are locally parallel because we can translate a given curve horizontally or vertically or in any other direction and consider any of these translated curves to be "parallel" to the curve in its original location. So we need to be more precise. We assume, as a first order estimate for obtaining the flow velocity direction at a point, P, near a solid line that the flow velocity there is influenced most by the point, Q, close to P on that line and the slope of the line at the point Q. The closest point Q to a line from a point P in the flow is of course obtained by dropping a perpendicular from P to that line as shown in Figure 2.10. Then we assume that the flow velocity direction at P is the same as the tangent to the solid line at Q. Of course, this procedure fails when point P in the flow region is equidistant from two or more solid lines or in general is influenced more or less equally by two or more nearby surfaces. However, in our application if we consider the core flow velocity component in the meridional plane, say, at the azimuthal center of the core-lobe, the two influencing solid surfaces of interest are the lobe crest and the plug surface, with the plug exerting little influence on the velocity direction near the crest line. Similarly, the fan flow velocity component in the meridional plane at the center of the fan lobe, which is bounded by the keel and the nozzle wall is influenced more by the keel surface than the nozzle wall when P is near the keel surface. So it appears reasonable to apply this approximation to the flow velocity direction near the crest and keel surfaces which is all that is needed for satisfying the t.e. rule. Once the local flow velocity direction is known at a point then it is easy to verify whether a proposed scalloped edge near that point P is a "trailing" or "leading" edge, as shown in Figure 2.10.

Using this construction we can easily find the upper and lower radial *bounds* on the scalloped edge corresponding to a give apex location which does not violate the t.e. rule. First note that if we draw a circle with diameter PQ (see Figure 2.10) then the tangents to it at P and Q give the direction of the flow velocity at P and Q. So if we roll this circle on the crest line then the envelope of the rolling circles will correspond to the streamline or the pathline of the particle passing through point P in this approximation. Figure 2.11 shows these "rolling-ball envelopes" corresponding to a given scallop apex location F. There are two of them, one corresponding to the core flow and the other to the fan flow. Consider for the moment the *upper* core flow particle path passing through F. If the downstream portion of the tangent to the scalloped edge at F lies *below* the rolling ball envelope then obviously it would be a "leading" edge. Hence, any scalloped edge which lies wholly below this rolling ball envelope will violate the t.e. rule at least in regions close to F. In this sense the rolling ball envelope from F gives a "lower" radial bound for the scalloped edge on the upper side. Similarly the lower rolling ball envelope from F gives the "upper" radial bound for the scalloped edge on the lower side. Thus, for example, even a straight scalloped edge (which can be considered as upper part of a V-scallop) from F which lies wholly below the upper rolling ball envelope will not satisfy the t.e. rule. Further, even if a portion of the upper straight scalloped edge near F is below the upper envelope then it will still violate the t.e. rule.

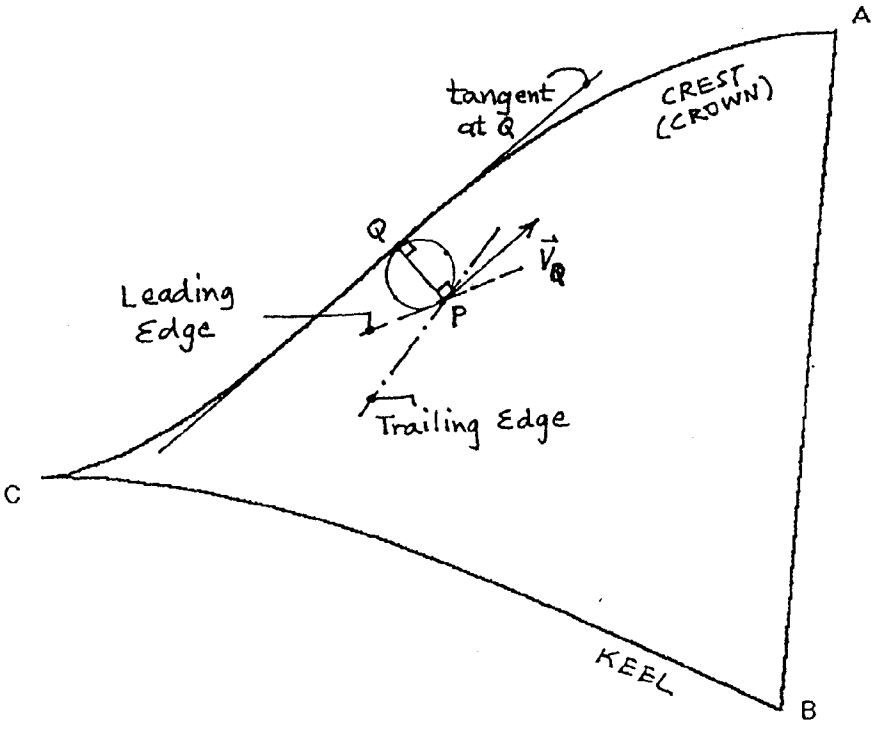

Figure 2.10 Approximate estimate of the direction of flow velocity vector at point P near the crest-line and the relative location of a trailing or a leading edge of a scallop near P.

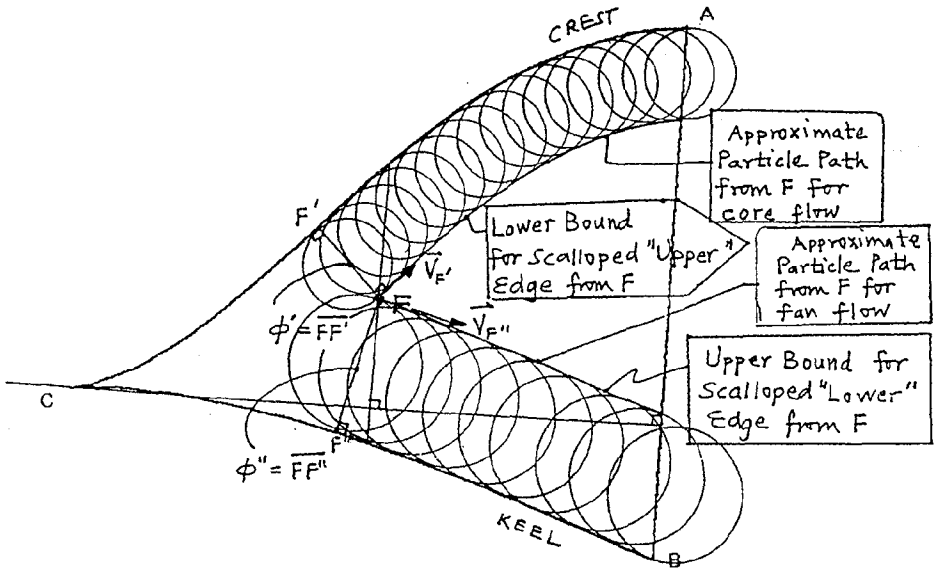

Figure 2.11 Rolling ball envelopes as approximate particle paths corresponding to the apex, F, of the scallop on two sides of a lobe wall and the corresponding bounds for the scalloped edge.

Since the rolling ball envelope gives one of the bounds for the scalloped edge it is pertinent to ask if *any* curve which is wholly above that envelope (we are referring to the *upper* scalloped edge here) satisfies the t.e. rule. The answer is no because if, for example, the scalloped edge "approaches" the crest line and then "recedes" from it, it is possible that the t.e. rule is locally violated somewhere in-between. However, one family of curves which is wholly above the rolling ball envelope appears to be promising, namely, the envelope formed by circles of monotonically decreasing diameters and touching the crest line, as shown in Figure 2.12(a). In general, with the chords between the tangency points of consecutive circles decreasing monotonically ($P_1P_1' > P_2P_2' > P_3P_3'$ etc.), the two curves (the crest line and the scalloped edge) can be defined to be converging. In the special case of a *straight* crest line and another converging *straight, concave or convex* line (which can be thought as the envelope of circles with monotonically decreasing diameters with linear, more than linear and less than linear rate of decrease respectively) we can easily see from Figure 2.12(b) that the converging scalloped edge line indeed satisfies the t.e. rule. We also observe from Figure 2.12.(b) that for such a special case not only the chords but also the perpendiculars drawn from the scalloped edge on the crest line are monotonically decreasing. Such perpendiculars are easy to construct for two given curves on an interactive CAD program. Without having proven it for the general case of converging curves, as in Figure 2.12(a), we will take it as a rule of thumb that if the lengths of the perpendiculars from the given scalloped edge on the crest or keel lines form a monotonically decreasing sequence as we go downstream then it will very likely satisfy the t.e. rule.

In practice it may be easier not only to check for this decreasing sequence of perpendiculars but also to simply double check at several points whether the t.e. rule is satisfied or not by drawing the approximate flow velocity directions as in Figure 2.10 and then iterating on the scalloped curve if needed. It turns out that this sort of iterative geometrical method is extremely fast when implemented on an interactive computer program and is the method of choice. We further note here that if the flow separates from the surface, say, at the crest-line then the application of the above rule of thumb becomes even more conservative because in that case the flow velocity near the scalloped edge will diverge away from the crest surface.

Figure 2.13 shows one such construction for the scalloped edge of the 20 lobed mixer. Here we have arbitrarily selected the location of the scalloped-apex as one with *about* 58% depth and 0% offset. This gives us a sufficiently deep scallop (much deeper than conventional scallops) without any danger of a structurally weak lobe sidewall and with a reference offset of zero. In order to obtain "converging" curves the endpoints of the scalloped height, namely, D and E are originally selected well above the limits imposed by the rolling ball envelopes from the apex F. The scallop height DE is also chosen initially to be large so that the two flows can interact in the scalloped area as much as possible forming nascent axial vortices inside the scalloped region before going downstream of the unscalloped edge AB. The initial scalloped height chosen was about 92% with AD = BE. Having thus located the points F, D and E the problem is of obtaining a scalloped edge passing through these points and satisfying the t.e. rule. One other condition imposed is the avoidance of sharp corners on the scalloped

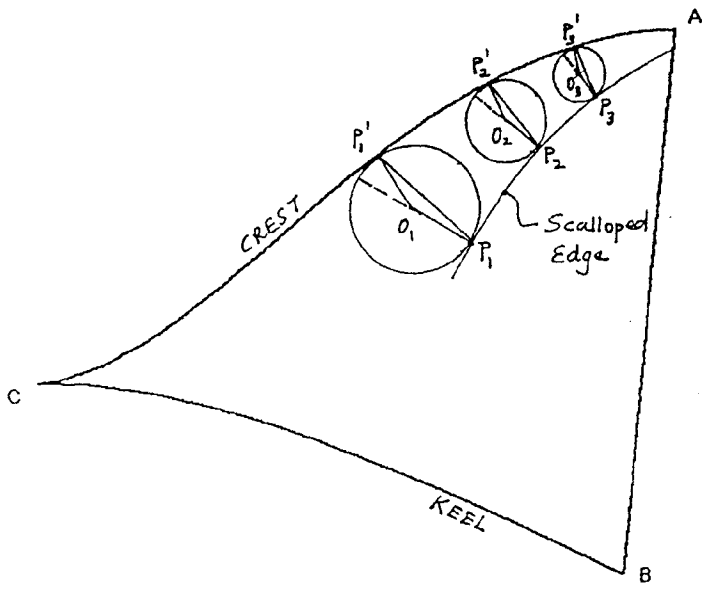

Figure 2.12(a) Envelope formed by circles of monotonically decreasing diameters and touching the crest line. The chords between points of tangency also decrease leading to "converging" curves.

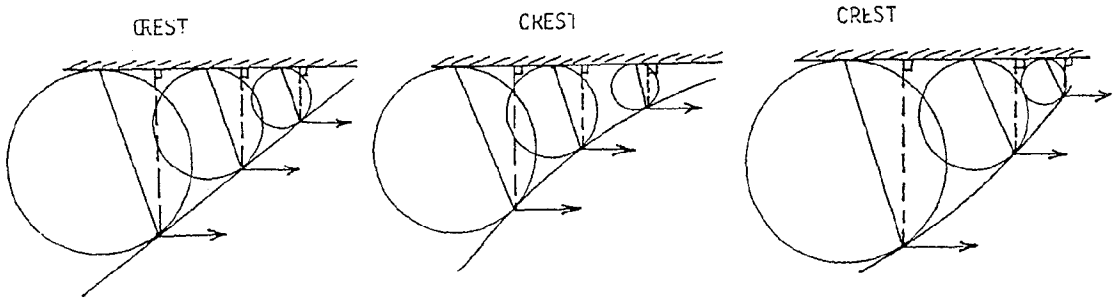

(a) Straight edge (b) Concave edge (c) Convex edge

Figure 2.12(b) Satisfaction of the "trailing-edge rule" when the crest is a straight line and the scalloped edge is converging whether straight, concave or convex.

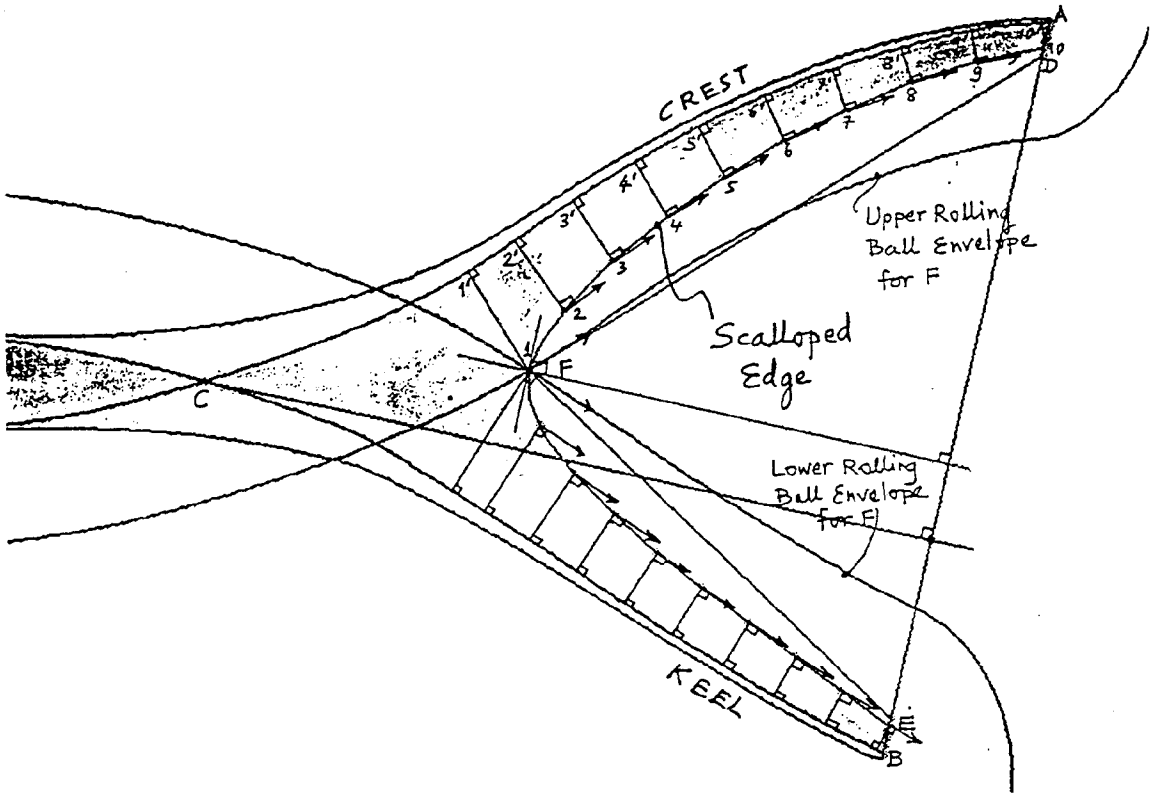

Figure 2.13 Checking the construction of a proposed scalloped edge with monotonically decreasing perpendiculars drawn from that edge to the appropriate nearest lobe surface (crest or keel).

edge so as to avoid points of high stresses on the lobe skin and also to avoid secondary corner vortices which can lead to total pressure losses.

This process of constructing the scalloped edge is broken into two pieces - the upper and the lower edges with respect to the apex. Let's focus on the upper portion. First note that a simple straight edge FD will indeed violate the t.e. rule near F because it is below the corresponding upper rolling ball curve as mentioned before. The two portions will also have to meet smoothly at the apex which implies that both the portions have a common tangent at the apex F which is parallel to the unscalloped edge AB. With three properties of the upper curve fixed, namely, two points (F and D) and the tangent at one of those points (F) we can let a unique three parameter curve pass through those points. However, we have more freedom for the shape of the curve if we use a four parameter curve with one parameter left free. B-splines with four parameters (poles) are easily available and easy to construct in typical CAD applications and, hence, were selected. The fourth parameter, it turns out, controls the angle of the tangent at the remaining point D. After selecting this fourth parameter such that the slope at D is slightly higher than at A one can draw the proposed scalloped edge passing through F and D, and use the rule of thumb of decreasing perpendiculars (which can be equally spaced on the scalloped edge) to check if the t.e. rule is satisfied. After going through this iteration a couple of times and satisfying the t.e. rule of thumb we further pulled the point D upward to point 10 (see Figure 2.13) to make the curves more converging and increase the margin of safety. The decreasing perpendiculars on this final curve are shown in Figure 2.13 and so is the double verification of the t.e. rule by drawing the approximate local velocities on the scalloped edge as lines orthogonal to these perpendiculars. A similar process was used to draw the lower portion of the scalloped edge, FE. In order to avoid the sharp corners at D and E large fillet radii were used there. Since the crest and keel lines of the corresponding 20-lobe unscalloped mixer are diverging radially from each other, the scalloped edge, constructed as above, also automatically satisfies the first design rule of gradually increasing radial distance between the upper and the lower edges of scallop. Projection of these curves back on to the three-dimensional lobe surface gives the final scalloped lobe. Scallops obtained in this manner are seen to have a "boomerang" shape. Hence, we will call them "boomerang scallops." Figure A.19 shows the details of the final geometry of the 20 lobe deeply scalloped mixer of high-penetration (called 20DH).

We have also applied this process to obtain a family of moderately deep scallops as shown in Figure 2.14. For a systematic study of the effect of the depth of scallop on noise we have selected a scallop of depth equal to half of the previous one but of the same scallop height. As before with B-splines we still have a non-unique choice of several curves. Six of these are shown in Figure 2.14 ranging from a V-cut (curve 1) to a very concave line 6 where the fourth poles of the B-spline are equally spaced on the tangent line at the apex F. Since the depth is deemed shallow it appears that all of these will easily satisfy the t.e. rule and no check is needed in this case. Each curve, however, gives a different scalloped area. Notice that if we had V-cut scallops in both cases then with half-depth and same height the moderate scallop would have half of the

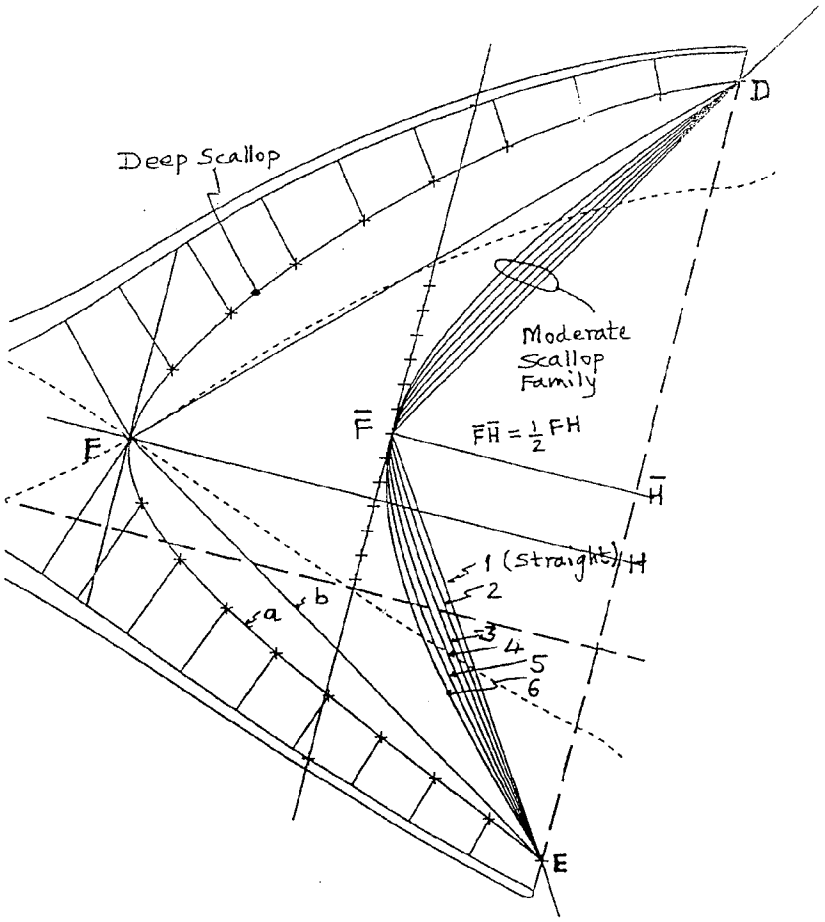

Curve #	% Area
1	39.4
2	41.1
3	42.9
4	44.7
5	46.5
6	48.5

Figure 2.14 Family of scalloped edges with depth equal to half of the deeply scalloped mixer (20DH) but same scallop height. The scalloped areas differ and are shown as percentages of the deeply scalloped one in the inset table. Curve 6 was selected for 20MH mixer.

Table 2.2 New Mixer Parameters

Mixer	Code	Lobe No.	Scallop	Lobe Penetration (H_m/H_{mp})	Lobe Length (L_m/D_{mp})	Area Ratio (A_f/A_c)	Mixing Length (L/D_{mp})
20 Lobe Unscalloped	20UH	20	None	0.67	0.34	2.637	1.10
20 Lobe Moderately Scalloped	20MH	20	Moderate	0.67	0.34	2.637	1.10
20 Lobe Deeply Scalloped	20DH	20	Deep	0.67	0.34	2.637	1.10
Tongue	12TH	12 pairs	Tongue type	0.56	0.34	1.765	1.10

scalloped area as the deeper one. Hence, we have finally selected the curve which gives approximately half of the scalloped area as the previous deep scallop, namely, curve 6 which has a scalloped area equal to 48.5% of that for the deeply scalloped case. Figure A.20 shows the 20 lobe, moderately scalloped, high-penetration mixer (termed 20MH). Table 2.2 lists the non-dimensional geometric properties of these 20 lobe mixers.

2.3.2.3 Design Guidelines for the Tongue Mixer

The design guidelines given here are those which were used more in the spirit of building a proof-of-concept tongue mixer model adhering to the three principles, P1, P2 and P3 discussed in the previous section 2.3.1.2. Time constraints did not permit optimization of the tongue contours through the use of CFD analysis. Primarily, basic fluid dynamic principles and engineering judgment were used to pin down the flow lines for a proof-of-concept tongue mixer. We give below a description of the selection for its major parameters, namely, the number of tongues, the internal and external flow lines in profile, and the transverse cross-sections.

(i) Number of Tongues

As a baseline design we start with all top tongues of one shape and all bottom tongues of another shape. Principle P3 suggests that we should not have too many tongues lest there be considerable dipole type noise from the tongues themselves. The root-widths of the tongues, although independent parameters, go hand-in-hand with the number of tongues and are considered together. Principle P2 suggests that the tongue widths should not be too thin, that is, the number of tongues should not be too large. This selection can be partially resolved by using the arguments developed from vorticity dynamics as described earlier.

The interface area for mixing due to engulfment depends on the largest diameter that can be achieved by the two adjacent vortex structures shown in Figure 2.7 and that is limited by the *smallest* tongue width. This width will govern when adjacent vortices touch each other and begin interacting. Hence, if we have unequal tongue widths then the vortices will grow to a smaller size than if the tongue-widths were equal. This would suggest equal tongue widths.

Examination of the three original lobed mixers shows that the only mixer with equal lobe-width at the root was the conventional mixer with cutouts (12CL). This has 12 lobes. The 12CL mixer may serve as a comparison point if we also select 12 pairs of tongues for the tongue-mixer. Any larger number will make the widths thinner with more chance of violating Principle P2. Also we already have a *deeply* scalloped mixer with 20 lobes (20DH) which will provide some indication as to what happens to a tongue mixer with thinner widths. Hence, in order to conservatively satisfy P2 for a proof-of-concept study, we selected 12 pairs of tongues, with both top and bottom tongues of equal widths. With an average radius of about 3.284 in. at the adapter ring where the roots of these tongues will be located, this leads to about 0.86 in. width at the root of the 24 tongues. This is deemed conservatively wide for the core and fan flow velocities to be considered, so that Principle P2 is not violated.

(ii) *Internal Flow Lines in Profile*

Consider the tongues in a longitudinal cross-section view along their center-lines in a meridional plane. Clearly avoidance of

separation (Principle P1) governs the internal flow-lines. It is possible that as a first step of iteration one could start with the corresponding flow lines of the keel and the crest lines of a comparable lobed mixer for the bottom and the top tongue respectively. However, without the sidewalls the internal flow will probably have a larger tendency to separate for the same surface angle.

Consider first the flow line of the *bottom* tongue over which the fan-stream flows. The axial static pressure distribution along the keel line of a lobed mixer shows that after a short initial rise it generally decreases. The pressure distribution along the internal side of the bottom tongue may not be so favorable. Its maximum angle should be somewhere between that used for tailcones (which is an axi-symmetric body) and that used for advanced mixer lobes, perhaps even more on the conservative lower side, so as to satisfy Principle P1. This implies that $22^{\circ} < \max(\theta_{bot}) < 30^{\circ}$. The flow line itself can be made up of a simple circular arc and straight line combination with the fan flow exiting at the maximum angle at its tip which may be made almost parallel to the tailcone. An angular value lower than that for the corresponding lobed mixer with the same length would now imply that the distance between the tongue's tip and the tailcone has increased or, in other words, that the corresponding penetration of the tongue has decreased. Increased penetration increases the height of the vortex sheet or the interfacial mixing area and is deemed beneficial from a mixing effectiveness point of view. (Increased mixing effectiveness is believed to increase thrust coefficient and reduce low frequency noise contribution.) This can be achieved by either increasing the length of the tongue or being more aggressive on the maximum angle. This first choice would go against Principle P3 and must be weighted against satisfaction of Principle P1.

Now consider the *top* tongue flow-line internal to which the higher speed core stream flows. The GE E^3 mixer lobe data shows that the axial static pressure distribution on the crown's core side decreases as we go downstream (*favorable* pressure gradient). For the top tongue we still need to be cautious so as not to violate Principle P1. We again conservatively establish the tongue angles to be below the maximum angles typically used for the crown side of lobes. As before, smooth circular-arc/straight-line combinations can be used with the exit angle for the core-flow being kept axial so as to minimize thrust losses due to non-axial discharge. With smaller maximum angles we again face the issue of reduced penetration, which can be resolved as suggested above.

Overall it is believed that a longer tongue may be preferable to a higher angle in order to increase penetration. That is, it is more important to follow P1 than P3 for the concept to work at all. Also it should be noted that for the tongue mixer the angle between the line joining the tips of adjacent tongues and the vertical (or radial) line - the *scarf or cant angle* in lobe mixers - is not so relevant because the flows have already started mixing. So the length of the tongues should <u>not</u> be adjusted according to this scarf angle.

(iii) External Flow Lines in Profile

Once the internal flow lines are defined, then the external flow lines for the center cross-sectional view of the tongues in the meridional plane is not so much an acoustic issue as a structural and aerodynamic issue. Aerodynamically, the space between the external and the internal flow lines of a

given tongue defines the blockage created by the bottom and the top tongue respectively for the core and the fan flow. This blockage thickness should be minimized. The minimum thickness at any axial station, on the other hand, is governed by the structural stiffness required to withstand the applied stresses and assure that fatigue failures due to vibration do not occur.

For the proof-of-concept model, individual tongues were machined from bar stock and attached to an adapter ring to form an assembly. To reduce base drag at the tongue tip, it must be as thin as possible. A simple thickness distribution shape which tapers monotonically from that prescribed at the root by the mixer adapter ring thickness (0.298 in.) to a thin machinable edge (0.010 in.) at the tip of the tongue was deemed adequate.

(iv) Transverse Cross-sections

Transverse cross sections were developed by prescribing an internal arc and an external arc at a given axial station once its center thickness had been decided from previous rules. Aerodynamically, the tongues should not act as blunt bodies to the external flow over them lest they increase the ram drag. Also for them to function as envisaged earlier through vorticity dynamics they should not violate Principle P2. Thus on a cylindrical surface of the streamlines of the external flow (that is, whose normal is more or less in the radial direction and not in the axial one) their external surface should appear streamlined like the leading edge of an airfoil. If we further prescribe that the external flow on the tongue should leave its edges axially and, hence, that the tangent to the external arc at the edge should be axial, then this would demand a deep curve for the external arc and unless matched similarly on the internal side with another deep curve will lead to very thick tongues which are undesirable from blockage and weight points of view. Both these criteria can be met by something like a super ellipse but it is obviously more blunt and perhaps difficult to machine than a simple circular arc. Also the angle at which the external flow will leave the tongue edge is determined more directly by the shape the vortex sheet takes *due to balance of pressure* in the two streams and not so much from the metal cross-sectional angle. Thus if we remove the condition that the external arc should have an axial tangent at its edge this leaves a wide variety of arc shapes at our disposal to satisfy the streamlined criterion. For simplicity of machining, circular arcs were selected for both the external and the internal curves such that the thickness at the edge is again as thin as possible and then chamfered. (Knife edges are not preferred from machining viewpoint although they are preferred aerodynamically.)

Unless the width of the tongue is defined at each axial station this still does not uniquely define the circular arcs. The consideration for width-distribution of the tongue can be made by looking at its top-view (or actually radially towards the center from outside the nozzle) which will also be reflected in its ALF (aft-looking-forward) view. Each tongue can be made of constant width throughout its length or tapered (convergent or divergent). Here the principle that applies is P2. Constant width is probably adequate, however, it will lead to more blockage and ram drag (clear in ALF view). Tapering will reduce some of this blockage but the minimum width at the tip should again be governed by Principle P2. Again with simplicity in mind, we decided on the width distribution that follows from selecting radial lines for the tongue edges when seen in ALF view. The final selection gives a

convergently tapered bottom tongue and a slightly divergent top tongue.

This still leaves a wide variety of shapes for both the arcs of the transverse cross-section. Approached sequentially the arcs can be constructed as follows:

- known values are center-line thickness, tongue-width and edge thickness
- the arbitrariness is then in only one of the arcs
- select some "appropriate" circular radius for the external arc which will pass through the external surface point
- the tongue-width then automatically defines the edges for that external arc
- with prescribed tongue edge thickness and the internal point (due to the center-line tongue thickness) the internal arc is now uniquely prescribed by the three points
- determination of the arbitrary external curve radius should also consider that the internal arc needs to be *concave* for following Principles P1 and P2 except perhaps for some transition region near the root of the tongue, in addition to the previous aerodynamic discussion.
- another aerodynamic consideration, which would be apparent from the side view, is that any sharp corners should be avoided, lest they introduce secondary corner vortices which may increase losses.

It is possible that there are other machining issues that can make the cross-section shape simpler and should be incorporated after keeping all the above principles in mind. This procedure basically defines all the flow lines for the tongues and should be a good place to start for CFD iterations.

The tongue mixer penetration, as defined in Table 2.2 and Figure 2.1, was set at 0.56, which is between the corresponding values for the lobed mixer configurations 12CL and 12UH. This was selected to provide an improvement in mixing effectiveness compared to 12CL. As previously mentioned the root width of both the inward and outward projecting tongues were set equal. This results in a considerable reduction in the area ratio (A_f/A_h), projected on the transverse plane, compared to either the 12 or 20 lobe mixer designs (see Table 2.2). This selection was expected to result in a considerable bypass ratio reduction compared to the 12 or 20 lobe mixers, but was made purposely to satisfy the vortex dynamics arguments discussed earlier

Figure A.21(a) through A.21(c) show the geometrical details of the final tongue mixer as fabricated. It's non-dimensional geometric properties are included in Table 2.2 Figure 2.15 shows the relative locations and shapes of the tongue mixer and the 20 lobe deeply scalloped mixer (20DH) for comparison. Note that attaching the tongue mixer to the upstream cylinder required an extra adapter ring. In order to maintain the relative location of the tongue mixer inside the nozzle, we have had to fabricate additional adapter rings for the outer nozzle and the center-cone, as shown in Figure 2.15.

Figures 2.16(a) and (b) are photos of all eight mixers included in the test program.

2.4 CFD Analysis of New Mixers

Computational fluid dynamics (CFD) analysis was done on three of the new mixers as part of this task, namely the 20 lobe unscalloped (20UH), 20 lobe deeply scalloped (20DH) and the tongue mixer (12TH). The mixers were analyzed with the

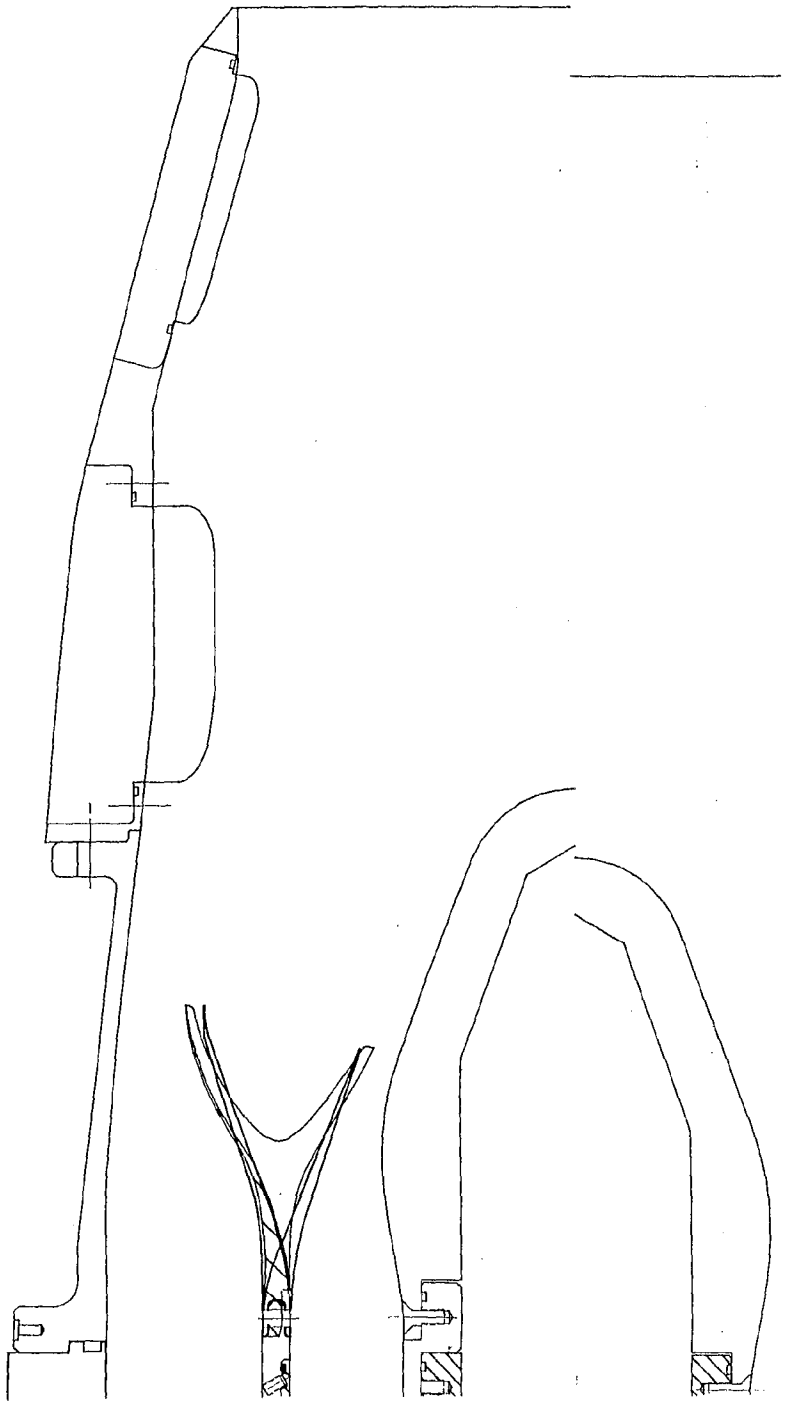

Figure 2.15 Relative location of the tongue mixer (12TH) with respect to the deeply scalloped mixer (20DH).

Figure 2.16(a) The confluent mixer (CONF), the 12-lobe mixers (12CL, 12UH) and the tongue mixer (12TH).

Figure 2.16(b) The 16-lobe mixer (16UH) and the 20-lobe mixers (20UH, 20MH, 20DH).

purpose of qualitatively validating our fluid-dynamic concepts and to help explain some of the aerodynamic and acoustic data. We only briefly touch upon some of the results from the analysis for the traditional unscalloped 20UH mixer but expand more on the CFD results for the other two non-traditional mixers.

2.4.1 Code, Grids and Boundary Conditions

Numerical Modeling

A 3D, viscous CFD analysis was conducted using the NPARC analysis code. The NPARC code, Version 3.0, (Ref. 12) solves the full three-dimensional Reynolds-averaged Navier-Stokes equations in strong conversation form using the Beam and Warming approximate factorization scheme to obtain a block tri-diagonal system of equations. Pulliam's scalar penta-diagonal transformation provides for an efficient solver. The code has several turbulence models available including: the Baldwin-Lomax, RNG, Baldwin-Barth, Spalart-Almaras, and k-ε turbulence models. The calculations presented in this study use the Chien low Reynolds number k-ε turbulence model. The implicit scheme uses central-differencing with artificial dissipation to eliminate oscillations associated with the use of central differences. The code allows the use of structured, multiple grid blocks. Tri-linear interpolation is used to transfer information at the grid block interfaces. The NPARC code has been used previously to predict the internal and external flows related to other mixer/nozzle exhaust systems.

Grid Generation

The mixers are composed of identical pairs of lobes which are spaced at equal angular intervals. This symmetric geometry is exploited to reduce the computational requirements resulting in a grid which extends circumferentially between the centerline of one lobe pair. The GRIDGEN code, Version 11.2 (Reference 13), was used to generate the computational grid. The distance of the first grid point off a viscous surface is 0.001. The blocks are made with contiguous interfaces and extend from a station far upstream of the mixer exit plane to the nozzle exit plane. In order to save time, simulation outside the nozzle (for the jet plume) was not done but the downstream boundary conditions were adjusted appropriately, as discussed later.

The computational grid for the 20 lobe unscalloped mixer (20UH) is shown in Figure 2.17. The grid consists of 6 blocks and approximately 500,000 points. The highlighted grid contains the mixer region of the grid. The grid for the 20 lobe deep-scallop mixer (20DH) is shown in Figure 2.18. The grid consists of 5 blocks and approximately 1,000,000 points. The additional points were needed to resolve the scalloped region of the mixer. The computational grid for the 12 pair internal tongue mixer is shown in Figure 2.19 and consists of 6 blocks and approximately 1,000,000 points.

Boundary Conditions

Inside the nozzle, the fan and core upstream total pressures and temperatures are specified. The walls are modeled as no-slip adiabatic surfaces. The downstream boundary at the nozzle exit plane has an "extrapolated static pressure gradient." The centerline is modeled as an axis of symmetry. The flow variables are mass-averaged along this axis. Symmetry conditions were used along the sides of the computational domain which are the meridional planes in the center of each lobe.

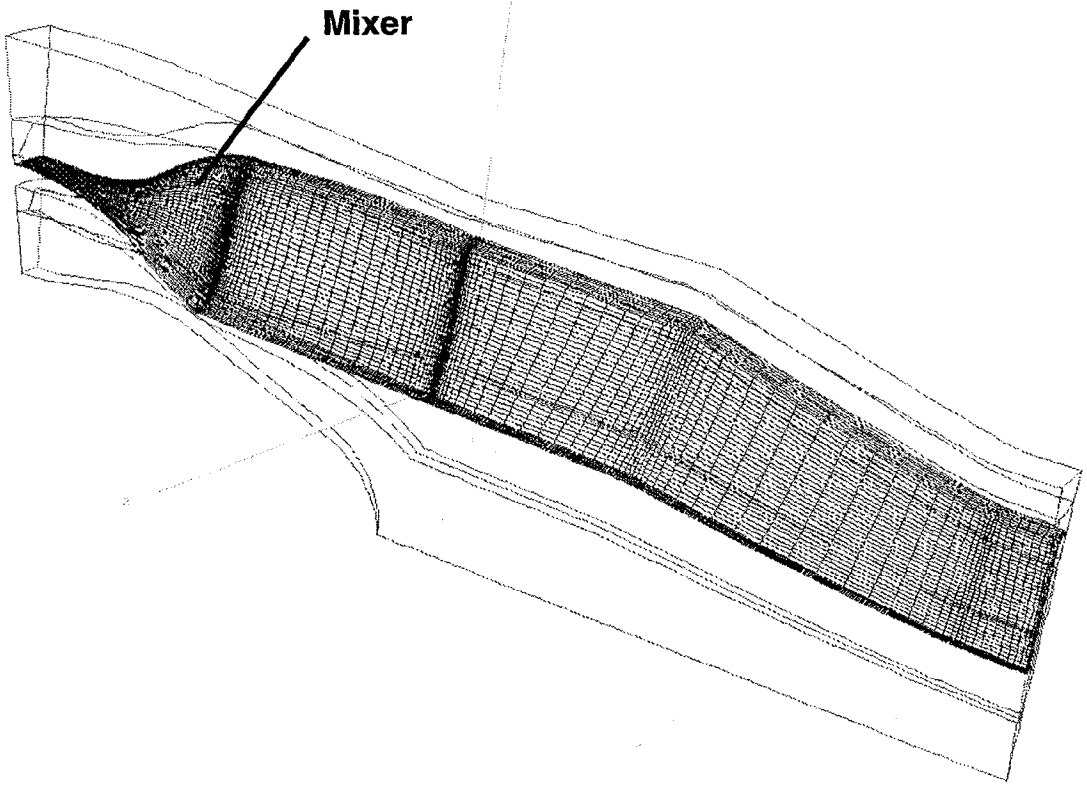

Figure 2.17 Partial grid for the 20-lobe unscalloped mixer (20UH) inside the nozzle.

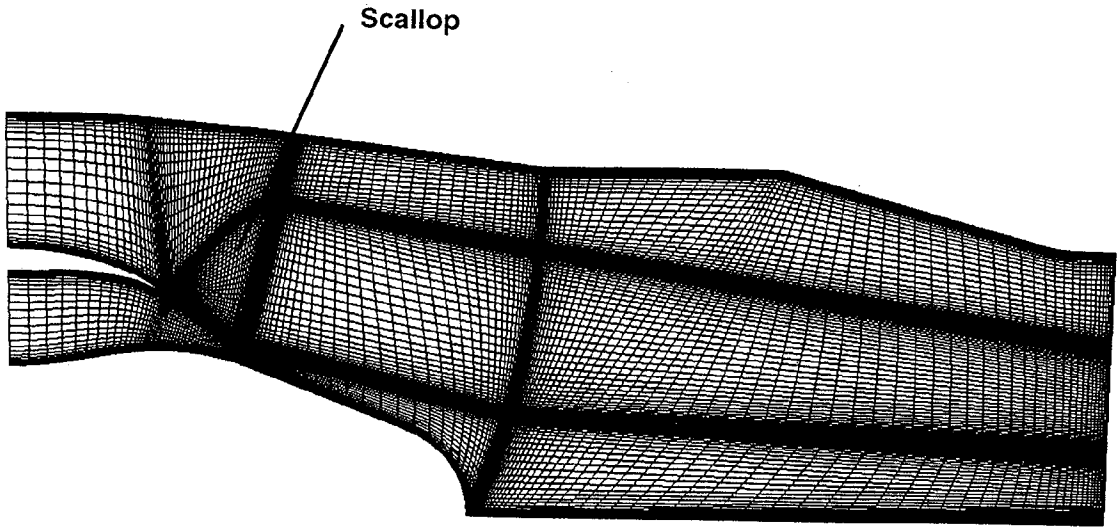

Figure 2.18 Partial grid for the 20-lobe deeply scalloped mixer (20DH) inside the nozzle.

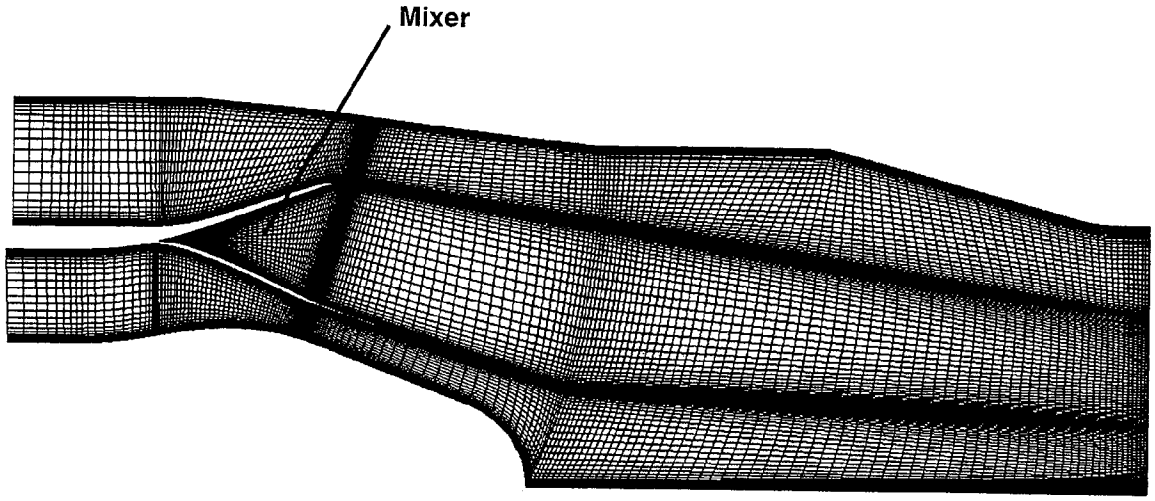

Figure 2.19 Partial grid for the tongue mixer (12TH) inside the nozzle.

The extrapolated static pressure gradient is implemented by extrapolating all primitive variables (density, velocities, energy). The static pressure gradient which is determined from the total energy distribution is scaled by a user provided pressure which controls the mass-flow rate. This boundary condition allowed a vortex to exist through the exit of the computational domain and improved convergence of the solution as compared to using a constant exit static pressure field boundary condition. The converged solution produces global mass conservation within the nozzle to within 1% of the inlet value. A slight radial static pressure gradient remained at the exit plane in the converged solution. This is not unusual and similar behavior was observed in the plume experimental survey.

2.4.2 Results

(a) 20 Lobe Unscalloped Mixer (20UH)

CFD runs on the first version of the 20-lobed mixer, which was simply an angularly compressed version of the previous 12-lobed high penetration (12UH) mixer, were made. It was found that in the upper half region of the underside of the lobe crest a strong adverse pressure gradient existed which led to separation of the core flow. A refined analysis of 12-lobed unscalloped mixer (12UH) (designed some six years ago) also revealed an adverse pressure gradient and some separation in the same region which was not resolved by the grid used during the original effort. Although a comparison of the measured pressure on this mixer (12UH) at the core crest centerline showed this feature, the location of the beginning of the adverse pressure gradient was further downstream, thus confining the separation to a small region at the core crest tip. This is possibly due to a very aggressive core flow line deflection angle at the inflection point of the lobe crest line - which was done to maintain a high penetration (0.68) in a small length of the mixer. Hence, to alleviate separation in the 20-lobed mixer the core crest line maximum angle was decreased while maintaining the lobe penetration by slightly increasing the lobe length and thus introducing a slightly larger cant angle of the mixer exit plane.

As an example, Figure 2.20 shows the flow velocity vectors just outside the boundary layers on two sides of the lobe wall. First, observe that there is now no separation of the core flow at the crest, or of the fan flow at the keel. Secondly, note that the core flow close to the crest and the fan flow close to the keel on the lobe sidewall are "almost parallel" to the crest and keel lines respectively, as assumed in Section 2.3.2.2 (see Figure 2.10). Moreover, slightly away from the crest and the keel lines, the core and the fan flow direction on the lobe sidewall are such that the rules of thumb given in Section 2.3.2.2 for satisfying the t.e. rule become even more conservative. This puts the previous design rules for scalloping on a firmer ground.

(b) 20 Lobe Deeply-Scalloped Mixer (20DH)

Typical cross-sectional results for the 20 lobe deep scalloped mixer (20DH) are given in Figures 2.21 to 2.23 for the total temperature (T_T), axial vorticity (Ω) and the turbulent kinetic energy (k) in terms of non-dimensionalized quantities for axial locations both inside the scallop and outside the mixer up to the nozzle exit plane. In these figures, X is measured positive downstream of the mixer exit plane, L_S is the axial length of the scallop and L is the mixing length (from the mixer exit plane to

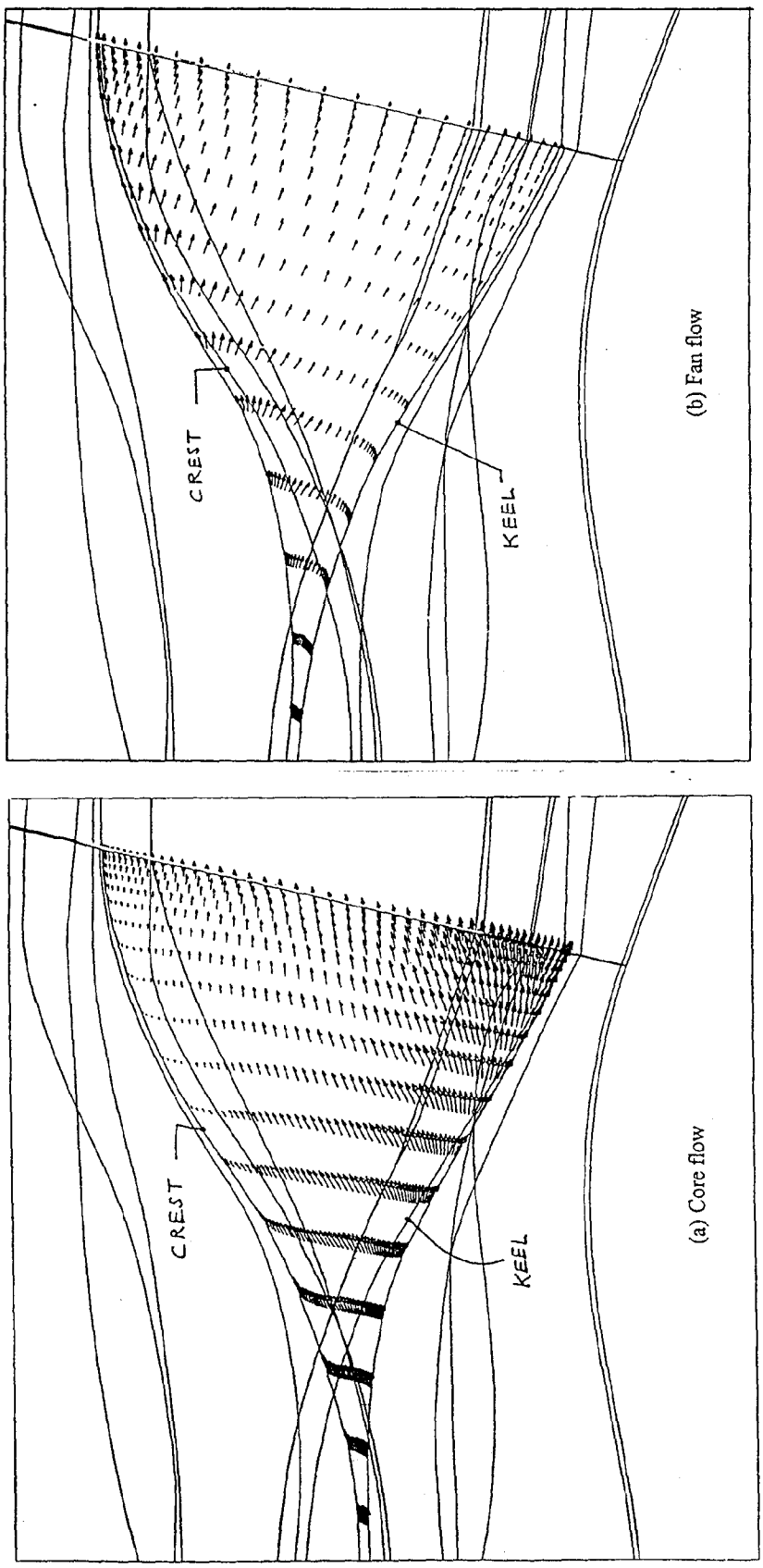

Figure 2.20 Flow velocity vectors just outside the boundary layers on two sides of the lobe-wall of 20UH mixer.

Figure 2.21(a) Total temperature contours for 20DH mixer in the transverse plane up to the mixer exit plane.

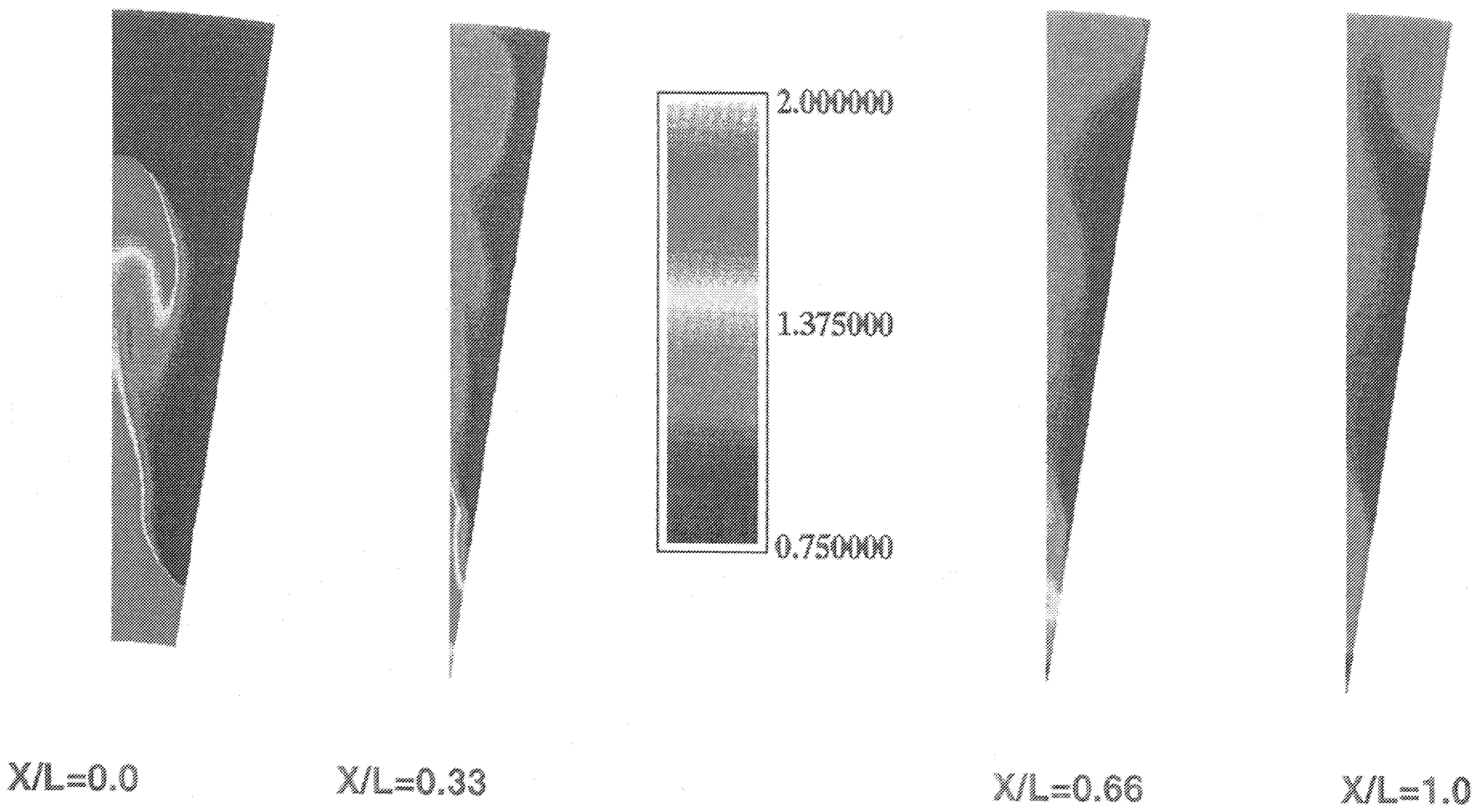

Figure 2.21(b) Total temperature contours for 20DH mixer in the transverse plane from the mixer exit plane to nozzle exit plane.

Figure 2.22(a) Axial vorticity contours for 20DH mixer in the transverse plane up to the mixer exit plane.

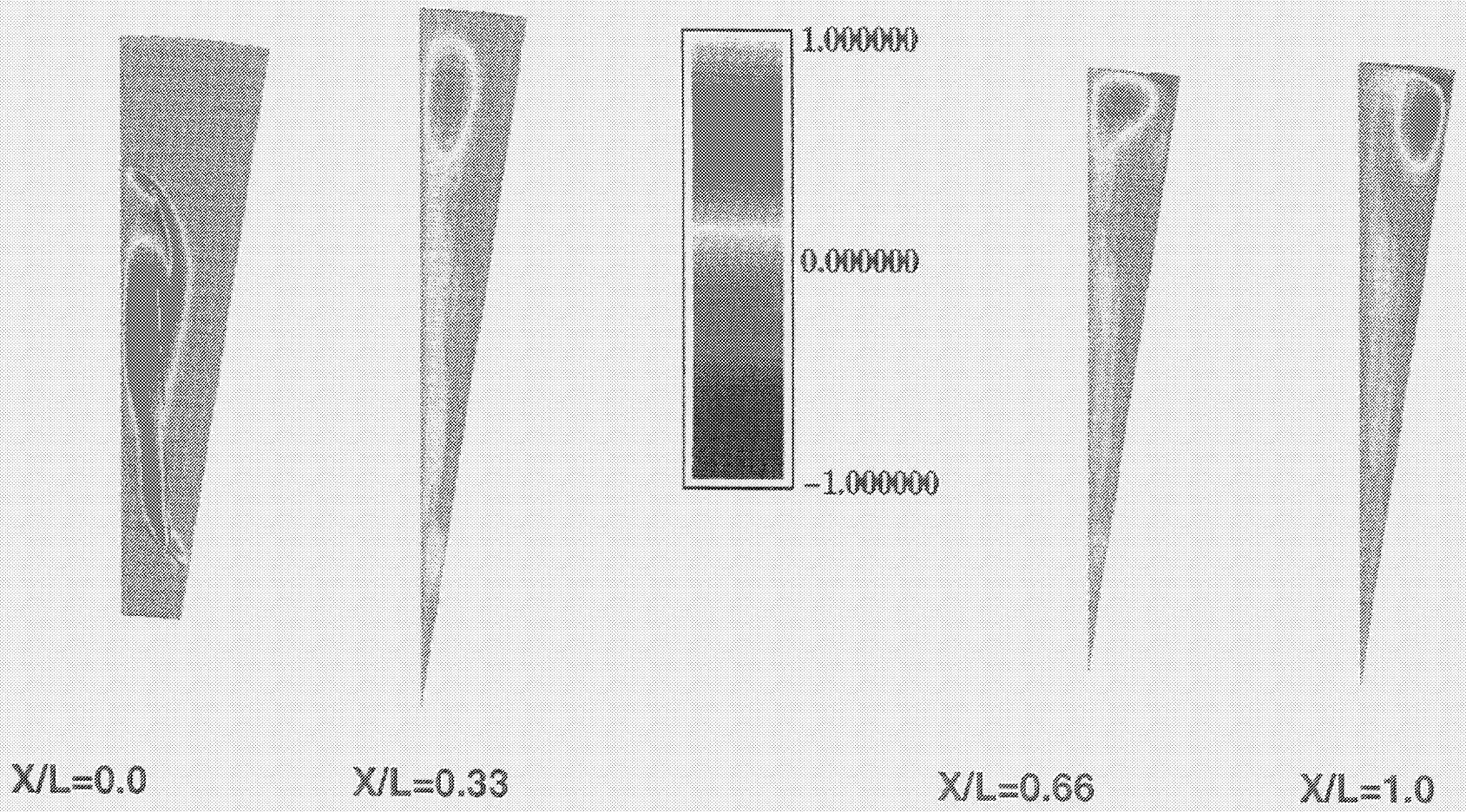

Figure 2.22(b) Axial vorticity contours for 20DH mixer in the transverse plane from the mixer exit plane to nozzle exit plane.

Figure 2.23(a) Turbulent kinetic energy contours for 20DH mixer in the transverse plane up to the mixer exit plane.

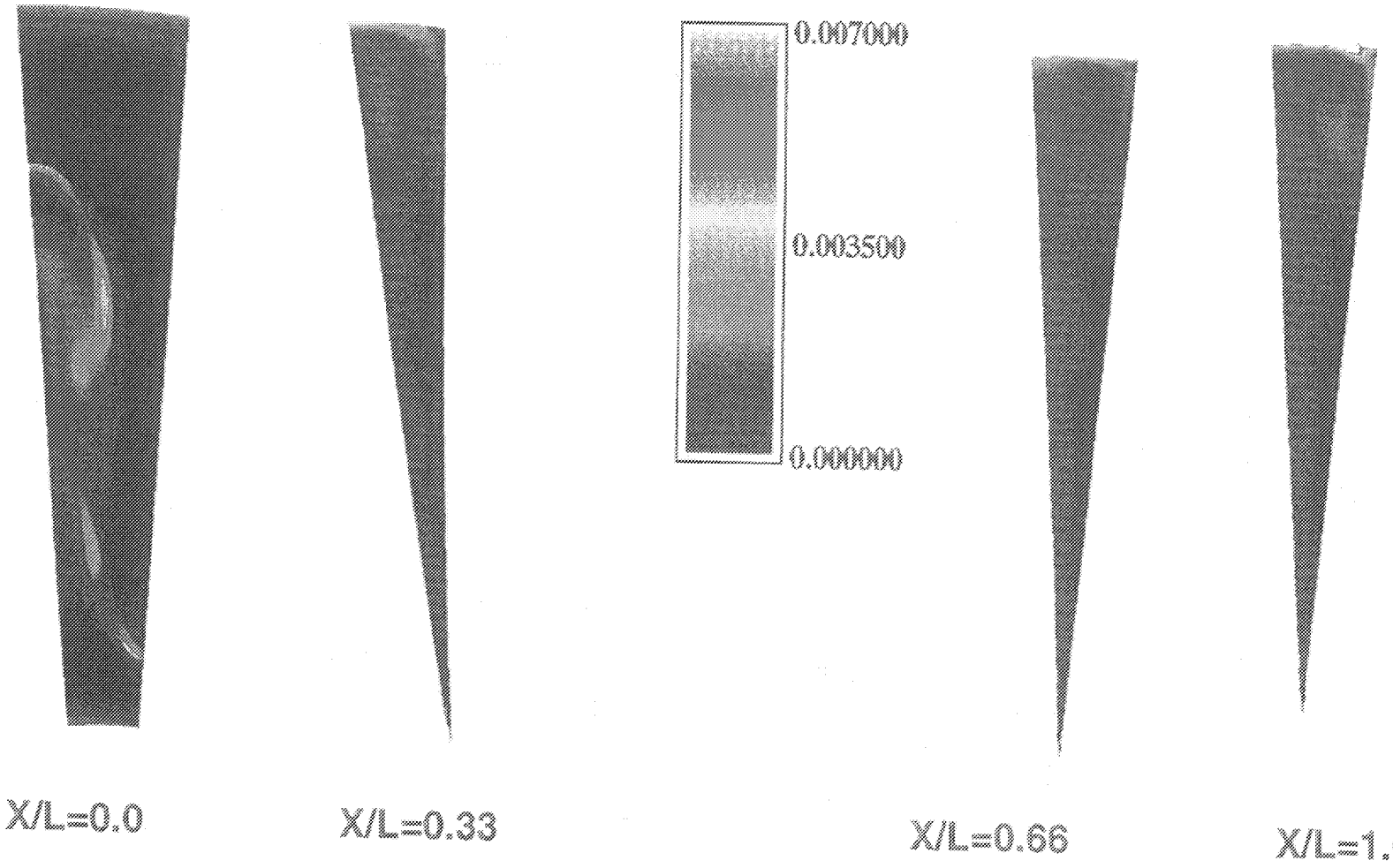

Figure 2.23(b) Turbulent kinetic energy contours for 20DH mixer in the transverse plane from the mixer exit plane to nozzle exit plane.

the nozzle exit plane). The operating condition is NPR_f = 1.457, NPR_c = 1.375, T_{tc}/T_{tf} = 2.296 with free-jet Mach number, M_{fj} = 0. The data presented in the plots is non-dimensionalized in the following manner:

$T_{non} = T/(\gamma_{ref}/T_{ref})$,
$\Omega_{non} = \Omega x_{ref}/a_{ref}$,
$k_{non} = k/a_{ref}^2$

where γ_{ref} = 1.4, T_{ref} = 533 °R, x_{ref} = 1/12 ft, $a_{ref} = \sqrt{\gamma_{ref} R T_{ref}}$ and R = 1716 ft-lb/(slug-°R).

From these figures, we observe that strong nascent vortices begin to form immediately inside the scallop, as expected, and continue to form a tighter vortex downstream of the mixer which quickly migrates to the nozzle wall (within the first one-third distance of the mixing-length), and finally interacts and merges with the neighboring similar vortex by the end of the nozzle exit plane. By the time the flow has reached the mixer exit plane the interface between the core flow and the fan flow has already been increased tremendously as compared to the unscalloped case, which leads to better mixing. The turbulent kinetic energy magnitude does not appear to be significant and is fairly uniform in the cross-sectional plane close to the nozzle exit. All these features appear to be in the direction expected earlier and validates the rules of thumb used in designing the scallops, at least from the point of view of flow physics. It should also be observed that no indications of separation were noted on the inside of the lobes with the introduction of the deep scallop.

(c) The Tongue Mixer

Similar results from the CFD analysis for the tongue mixer (12TH) with baseline nozzle-length are given in Figures 2.24-2.26. This particular solution corresponds to the same conditions for which results were presented for the 20-lobe deeply-scalloped mixer (20DH) so that comparison with it can be done.

From these figures it can be seen that:

(i) Mixing does indeed begin vigorously right from the beginning at the first station shown (X/L_s = -0.66) where the tongues have already diverged from each other (Figure 2.25(a)). This is as expected and is similar to the behavior in 20DH mixer at the start of the scallop.

(ii) By the time the core and fan streams have reached the tongue-tip exit plane (x/L_s = x/L = 0) considerable axial vorticity is already formed, similar in intensity to that form 20DH but a with larger area of coverage due to the broader tongue widths.

(iii) Downstream of the tongues, an isolated vortex is immediately formed similar to that in 20DH. However, unlike 20DH, it lingers at the same radial height for a longer axial distance and does *not* immediately convect to the outer duct wall. The radial convection velocity of this vortex is governed by the average radial velocity components of the core and the fan streams in the tongues. This is probably much smaller than in 20DH due to smaller angles of divergence of the tongues as compared to the aggressive lobe crown- and keel-angles of 20DH.

(iv) At the nozzle exit plane, (x/L = 1), the total temperature (Figure 2.24(b))is fairly uniform except for the annular hot ring near the central axis. This shows that the core flow over the center-cone is not as well mixed as in mixer 20DH. The vortex (Figure 2.25(b))is less intense and further

Figure 2.24(a) Total temperature contours for 12TH mixer in the transverse plane up to the mixer exit plane.

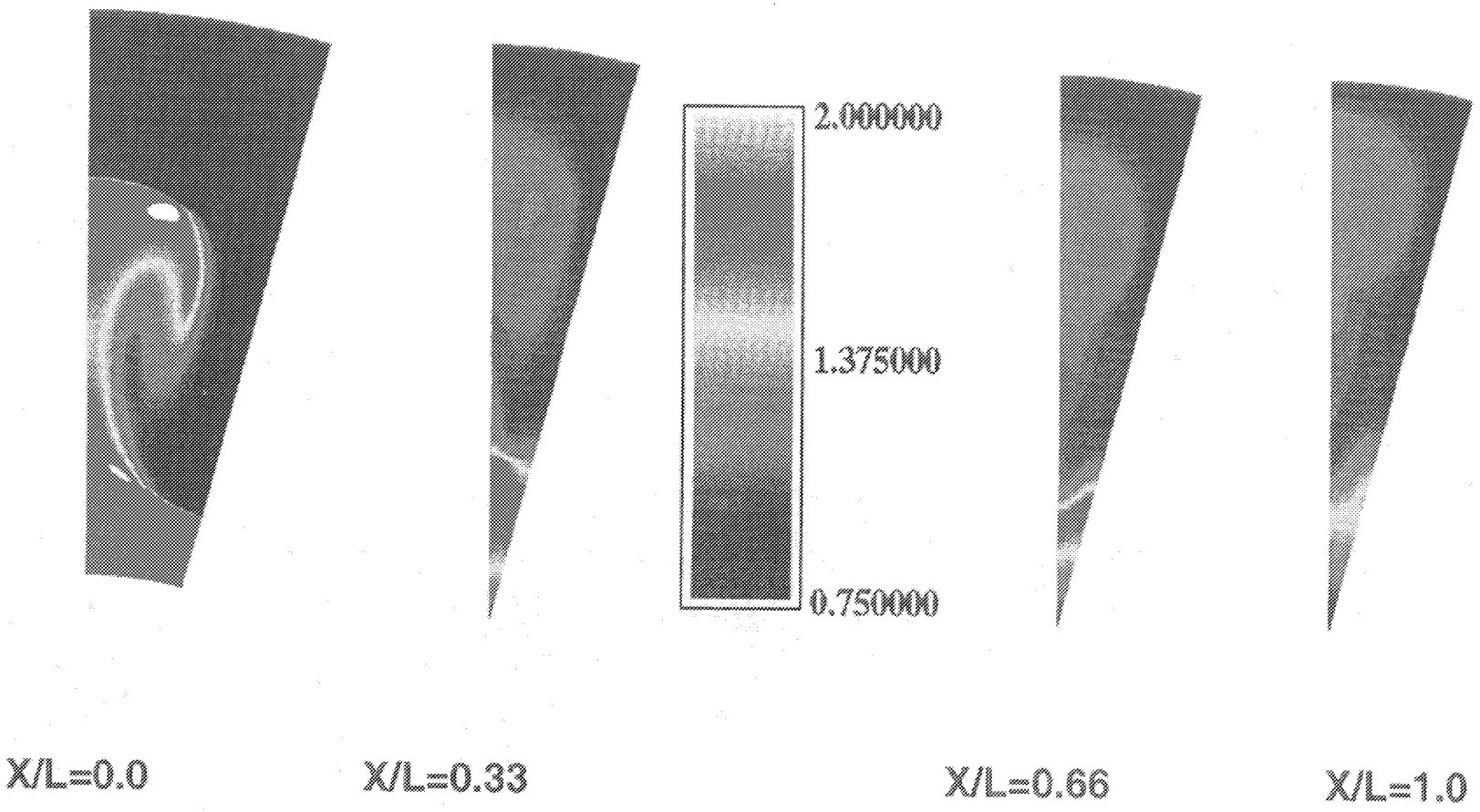

Figure 2.24(b) Total temperature contours for 12TH mixer in the transverse plane from the mixer exit plane to nozzle exit plane.

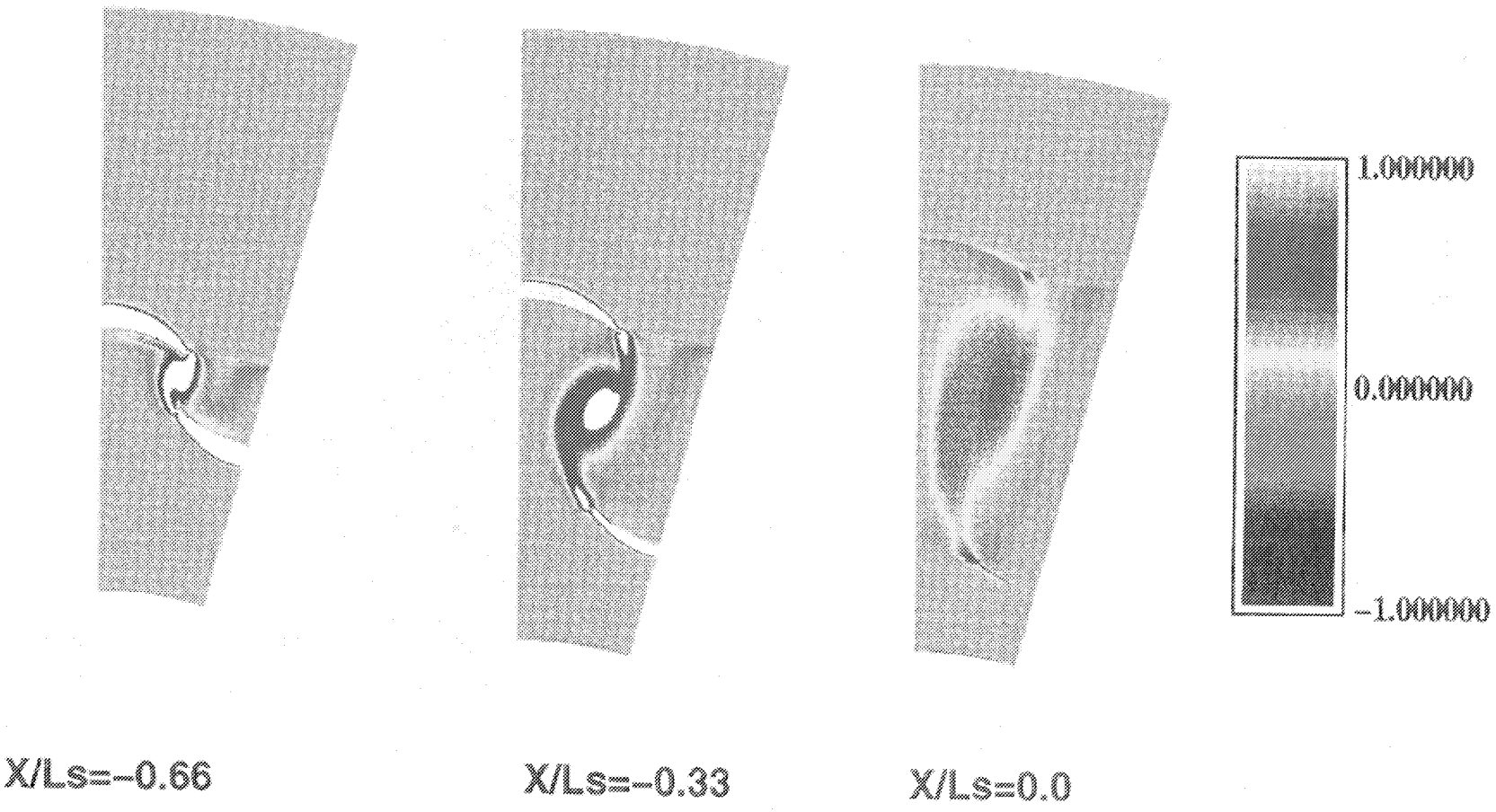

Figure 2.25(a) Axial vorticity contours for 12TH mixer in the transverse plane up to the mixer exit plane.

Figure 2.25(b) Axial vorticity contours for 12TII mixer in the transverse plane from the mixer exit plane to nozzle exit plane.

Figure 2.26(a) Turbulent kinetic energy contours for 12TH mixer in the transverse plane up to the mixer exit plane.

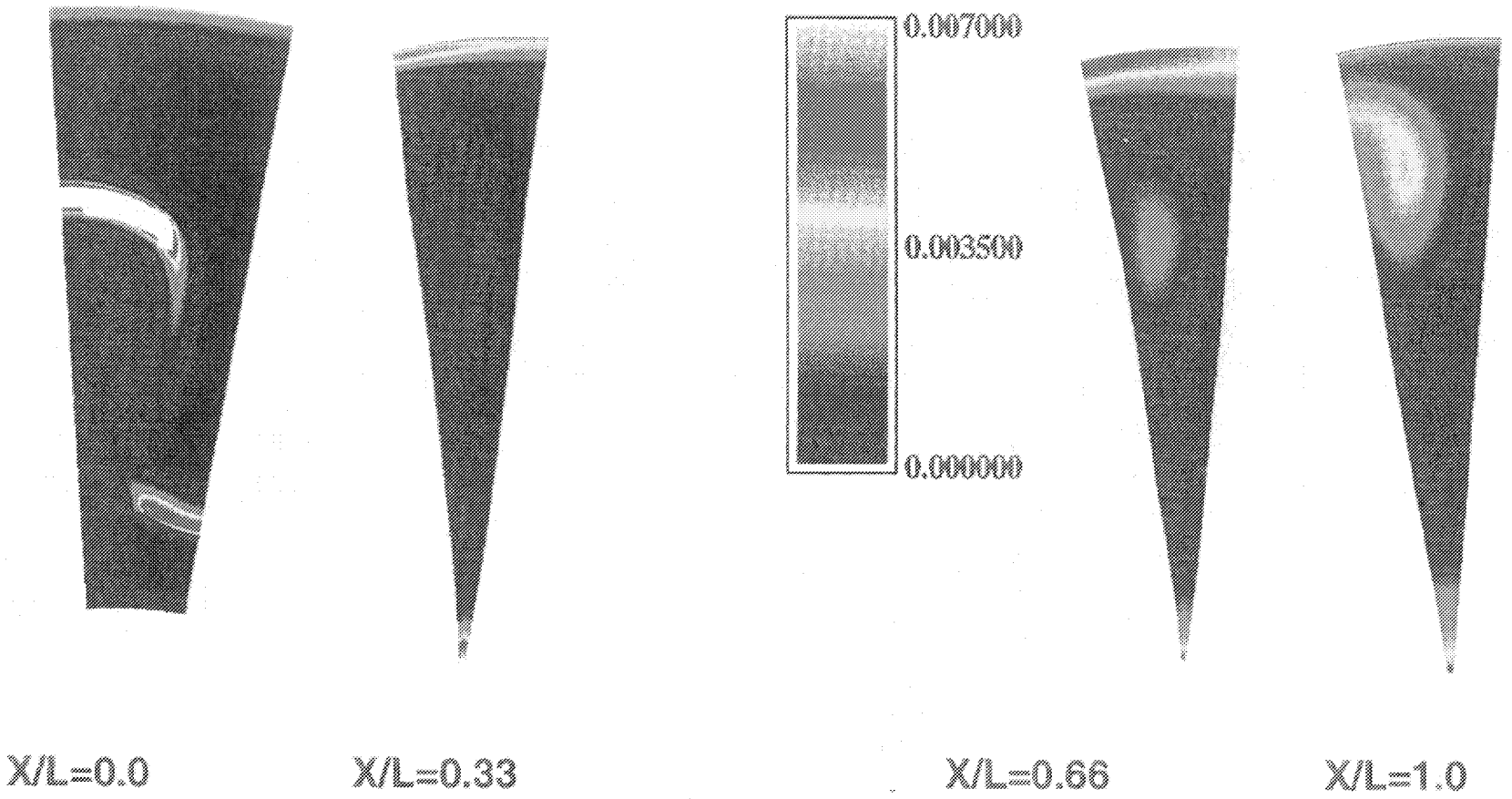

Figure 2.26(b) Turbulent kinetic energy contours for 12TH mixer in the transverse plane from the mixer exit plane to nozzle exit plane.

away from the nozzle wall than in 20DH but the turbulence intensity (Figure 2.26(b)) suddenly seems to have grown inside this vortex. It appears that in 12TH the boundary layer on the nozzle wall is growing much faster than in 20DH (compare turbulence intensity contours at x/L = 0.66 in Figures 2.26(b) and 2.23(b)) and the axial vortex has sucked into itself a large part of this wall boundary layer by induction by the time it reaches the nozzle exit plane. Whether this is an artifice of the turbulence modeling used in the CFD code or a real physical effect is not known. One acoustic effect that such higher turbulence intensity can have is an increase in amplitude of the higher frequency portion of the sound spectrum due to the small length scales of these axial vortices. The relative amplitude of the hot spots and the hotter central core should also be observable in the plume survey. This verification will be done later. One of the important items verified by the CFD analysis was the absence of flow separation on the inside surface of both the tongues as required by the design principles in Section 2.3.2.2. We will keep these CFD observations in mind when we compare the acoustic results for the tongue mixer later.

Finally, Figure 2.27 shows a comparison of the non-dimensional axial velocity contours at the nozzle exit plan for all the three mixers analyzed in this CFD study: 20UH, 20DH and 12TH (normalization is with respect to the reference speed of sound, a_{ref}, mentioned earlier). This figure shows that, overall, the unscalloped mixer, 20UH, has a much higher axial velocity throughout, whereas, both the deeply scalloped 20DH mixer and the tongue mixer (12TH) have lower overall velocity but are not as uniformly mixed as the unscalloped mixer.

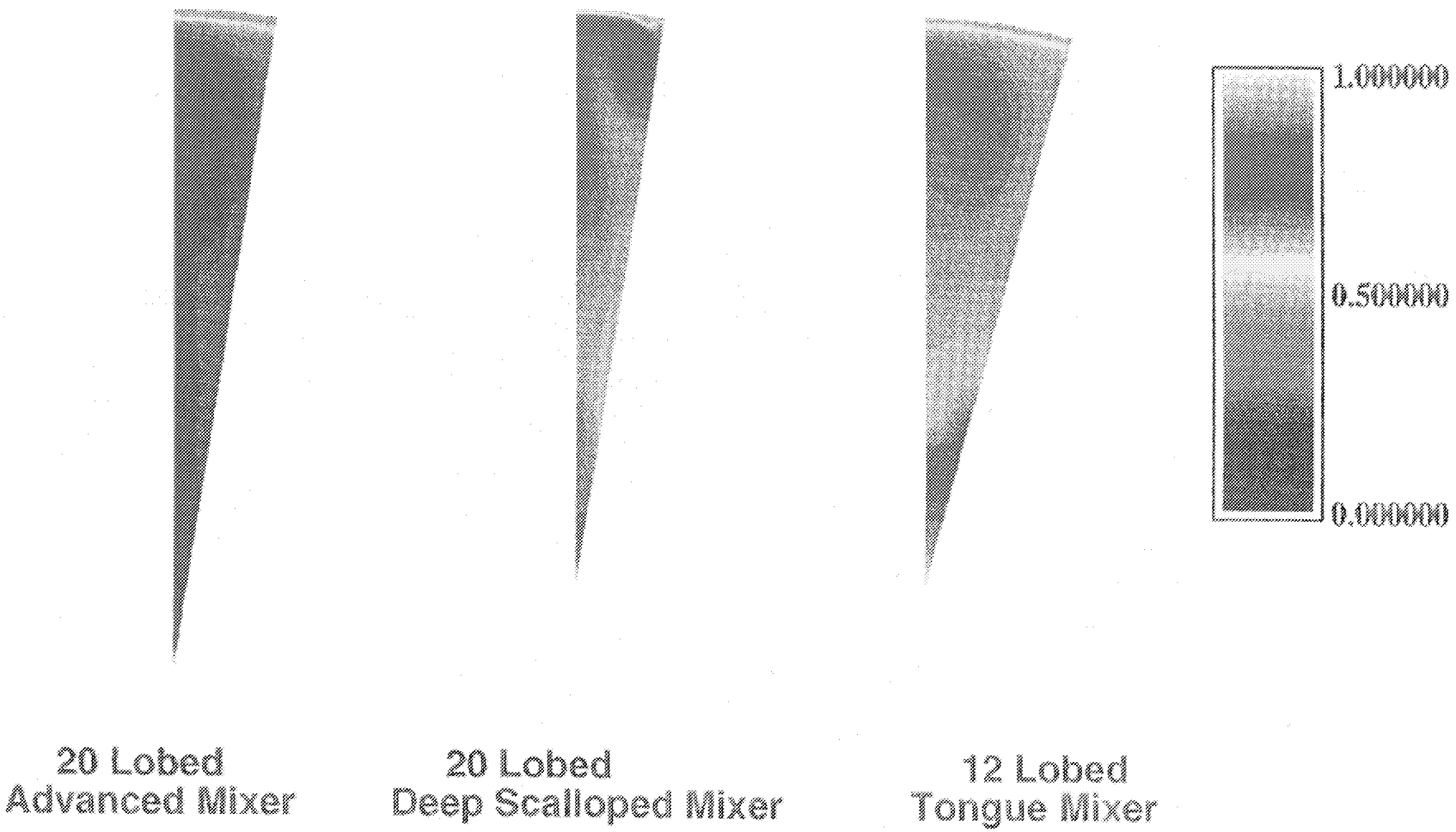

Figure 2.27 Axial velocity contours at the nozzle exit plane for 20UH, 20DH and 12TH mixers (from left to right).

Chapter 3

Experimental Program

A comprehensive experimental program was carried out which included measurement of far-field acoustic levels, nozzle aerodynamic performance, and jet plume aerodynamic surveys. Due to the specialized requirements for obtaining some of this data, two separate facilities were used. A description of these facilities and the experimental apparatus employed are provided in the following sections. In addition, the test matrix for each phase of the program is presented along with a description of the experimental procedure and data reduction methods employed.

3.1 Acoustic Tests

Test Facility

All acoustic tests were carried out in NASA's Aerocoustic Propulsion Laboratory (APL) at Lewis Research Center. This facility is a 65 ft. radius, acoustically treated, hemispherical geodesic dome (see Figure 3.1). The walls of the dome are treated with acoustic wedges as is approximately half of the floor area. Within the confines of the dome is the Nozzle Acoustic Test Rig (NATR). The schematic floor plan of APL with NATR is shown in Figure 3.2. The NATR duct work is acoustically lined (inside and outside) and extends from an annular air ejector system to a plenum and bellmouth transition section which is an ASME long-radius nozzle followed by a free-jet nozzle duct having an exit internal diameter of 53 in. and a nozzle centerline approximately 10 ft. above the floor. This arrangement provides a free-jet Mach number capability up to 0.3 to simulate forward flight effects on the noise source. An acoustically treated wall installed in the APL near the NATR exit plane and extending aftward along the length of the jet exit rig and test article shields the test vehicle noise source from the untreated floor region to prevent reflections from unrelated test rig equipment residing in this vicinity.

Downstream of the NATR is the Jet Exit Rig (JER). Test models are installed on the aft end of the JER, and the movable JER is positioned axially relative to the NATR exit plane at the desired location (generally a distance which aligns the test model nozzle exit approximately 24 in. downstream of the NATR exit plane) to appropriately utilize the 48 ft. arc microphone array of the APL. The JER is the structure through which airflow is delivered to the test article via connections to facility compressed air supplies. Exhaust gases from the JER/NATR are expelled through the 43 ft. high by 55 ft. wide APL exhaust door. More detailed information relative to the APL facility, its test rigs and support system is available in Reference 14.

The jet rig provides two stream flows whose flow rates are measured by choked Venturi-meters. The total pressure and total temperature are monitored in the model nozzle at a charging station just upstream of the mixer exit plane (see Figure A.1). In the first phase of this program, in November 1995, it was found that the desired high nozzle pressure ratios in the secondary (fan) stream could not be achieved. Hence, a year later, the jet rig was modified to provide supplementary air and the desired nozzle pressure ratios acquired in the second phase of this task.

Figure 3.1 NASA's Aeroacoustic Propulsion Laboratory at Lewis Research Center, Cleveland, Ohio.

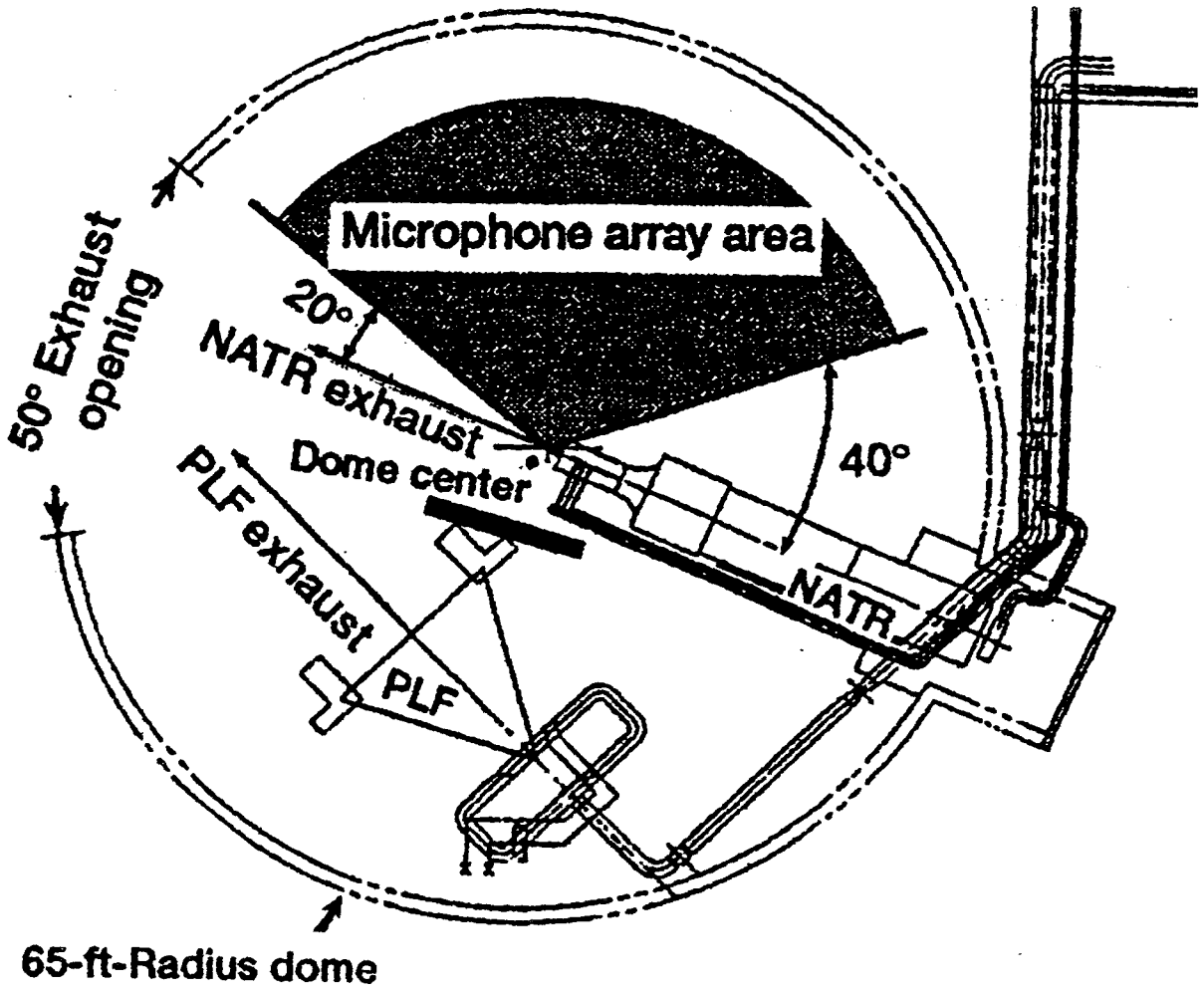

Figure 3.2 Floor plan of APL showing location and orientation of NATR and PLF facilities in dome footprint.

Figures 3.3 and 3.4 show the mixer-nozzle models installed in the jet exit rig. With a nozzle exit diameter of 7.25 in., the ratio of the diameter of the free-jet nozzle to the model nozzle is 7.31 and is deemed appropriate for the range of frequencies of interest. The merging of the free-jet/ambient shear layer with the model-jet/free-jet shear layer occurs several diameters downstream of the noise producing region of interest in the model and is not a concern in this test. Narrow band acoustic data was acquired using ¼ in. Bruel & Kjaer microphones positioned on a 48 ft. radius from the nozzle exit center in a horizontal plane through the nozzle axis. Twenty-five microphones were positioned in the upstream and downstream quadrants of the jet ranging from an angle of $\theta = 45°$ with respect to the inlet axis to $\theta = 165°$. [Note that the angle θ used in this report is with respect to the jet inlet axis, rather than the jet exit axis.] This is deemed to be the range of observable angles away from the diffraction/shadow lip effect of the free-jet nozzle in the upstream quadrant and outside the free-jet in the downstream quadrant.

Test Procedure and Data Processing

Acoustic testing was conducted by establishing the initial desired free-jet Mach number in the NATR. An acoustic test for the background noise with free-jet flow was done. Following this, generally, the test point conditions for the lowest pressure ratio and temperature were fixed. When conditions stabilized, acoustic data was acquired. Fan and core flows were then adjusted to the pressure and temperature conditions corresponding to the power setting for the next highest pressure ratio test point. After conditions stabilized, acoustic data was again acquired. This procedure was repeated in the order of increasing pressure ratio until acoustic data was acquired for all power setting simulations at the first free-jet Mach number. Once this was accomplished, the free-jet Mach number was changed and the procedures described above repeated in reverse order (decreasing pressure ratio) until acoustic data was acquired at all desired power settings associated with the second Mach number. This cycle was repeated for all free-jet Mach numbers of interest.

The acoustic and aerodynamic performance data for the test program was provided by NASA LeRC to Allison Engine Company in electronic data base format for further analysis. The acoustic data processing scheme used at NASA LeRC is outlined in Figure 3.5. Its final goal is to produce noise data on the ground below the flight path for a flyover at an altitude of 1500 ft. This method takes into account, broadly speaking, microphone calibrations, free-jet shear layer refraction, atmospheric and spherical spreading attenuation, data scaling, Doppler shifting for flyover data and standard day meteorological corrections. The free-jet background noise was subtracted from the measured acoustic data for test points simulating flight conditions.

Some details regarding the specific method used for free-jet shear layer refraction are given in Appendix B. It is essentially an adaptation of Amiet's method described in Ahuja et al[15] and extended to narrow-band spectra. With no prior knowledge of the location of sources in the different frequency band, they are all assumed to be at the nozzle exit plane center. This assumption is valid at higher frequencies but may introduce some error at relatively low frequencies, which are hopefully below the full-scale low frequency range.

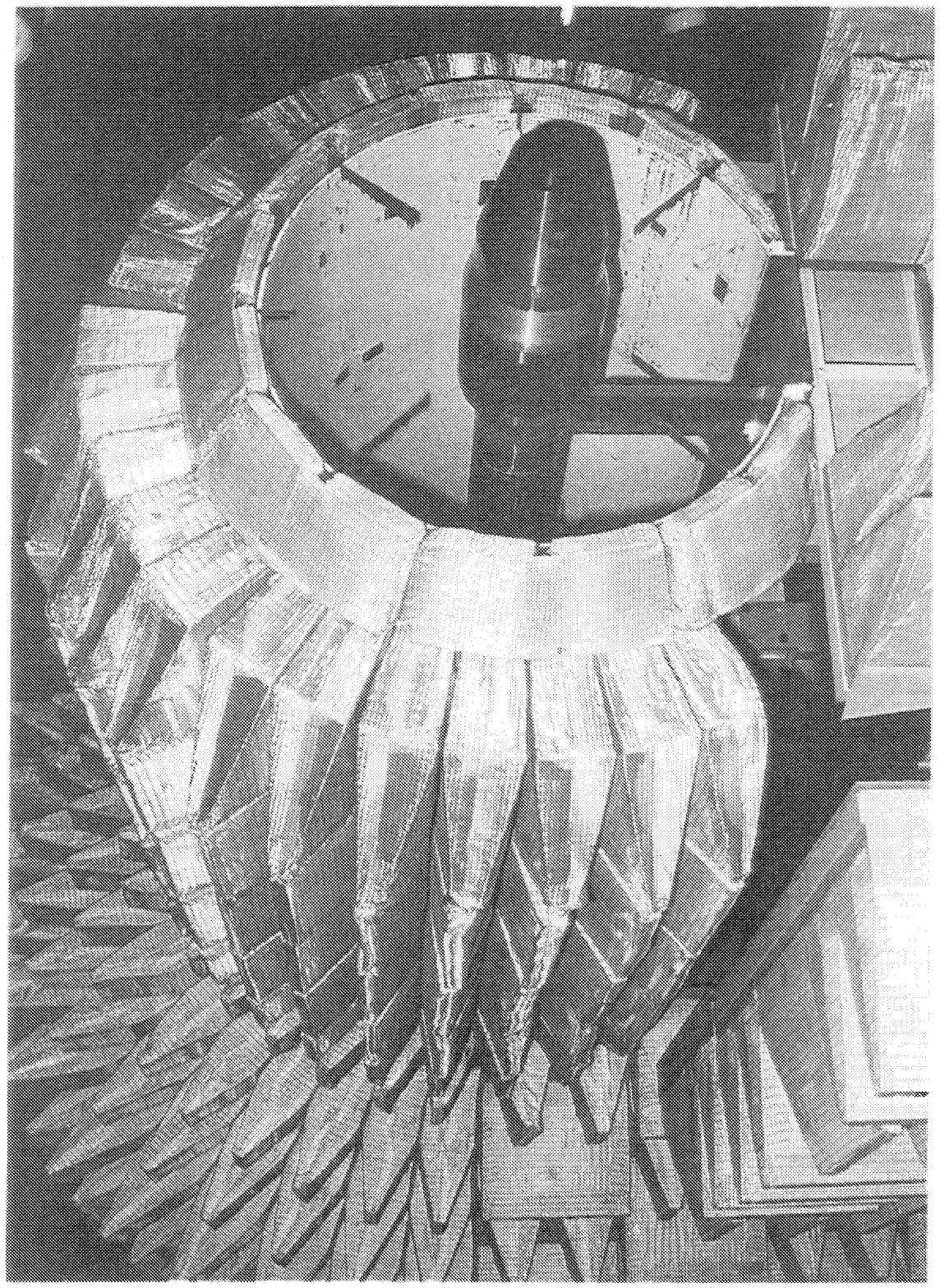

Figure 3.3 Mixer-nozzle model installed in the NATR jet rig which is lined with acoustic wedges.

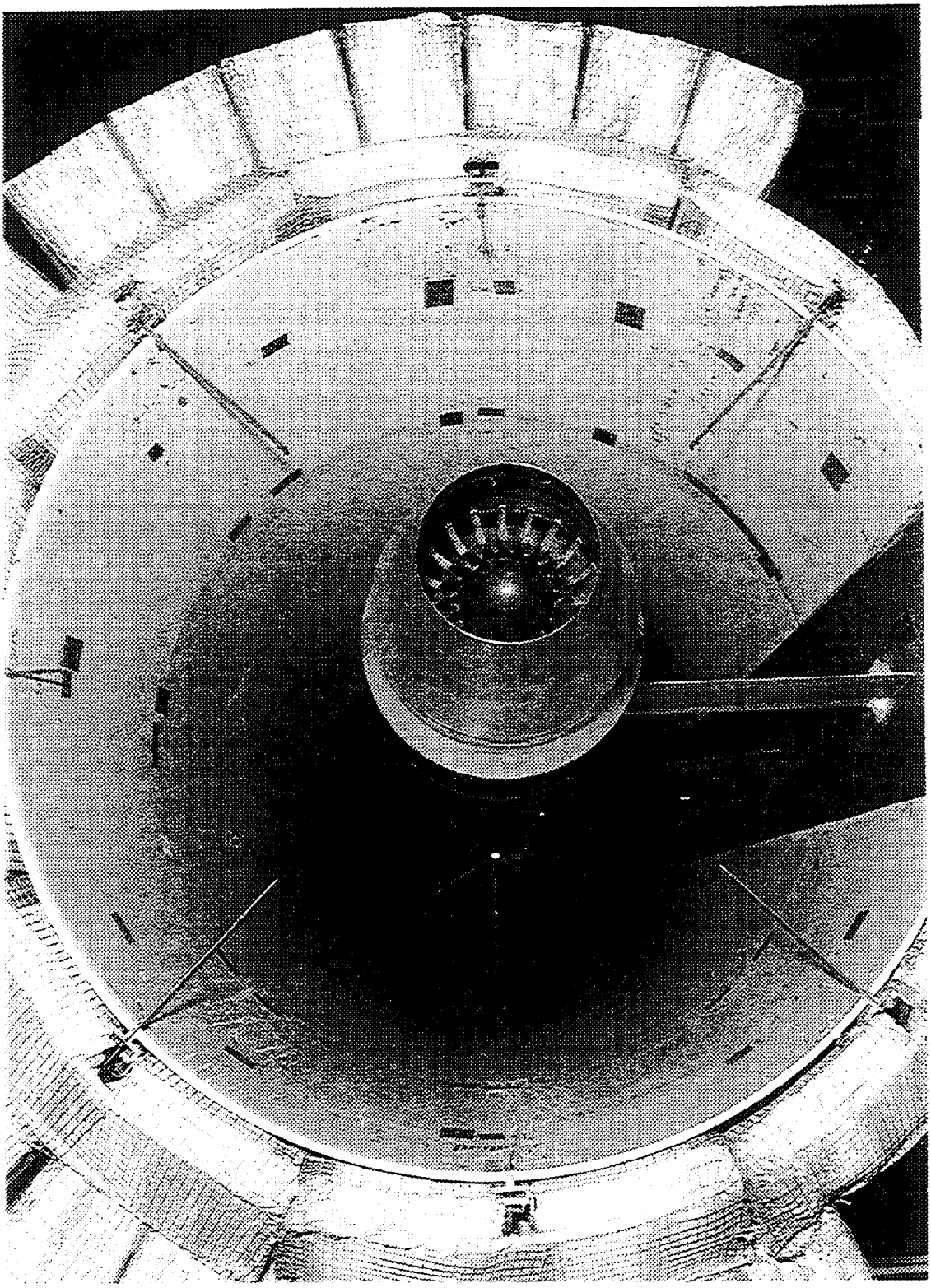

Figure 3.4 A close-up view of the mixer-nozzle model installed inside the free-jet wind-tunnel.

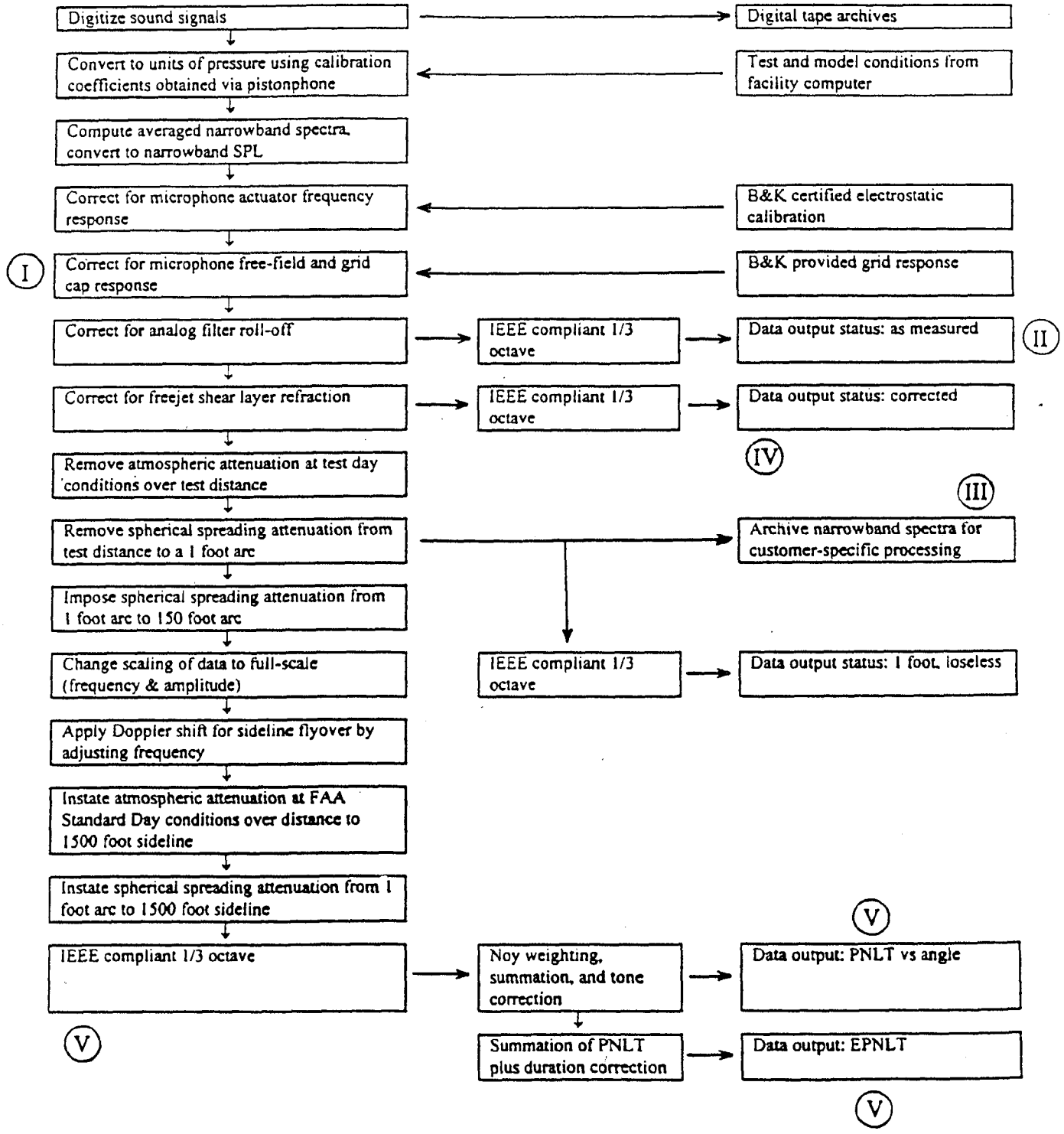

Figure 3.5 NASA LeRC acoustic data processing scheme.

The final acoustic data provided by NASA LeRC to Rolls-Royce Allison was in the following form, scaled to a nozzle with 660.5 in^2 throat, at standard day conditions (77°F and 70% relative humidity):

(1) 150 ft. polar data: 1/3 rd octave-band sound pressure level (SPL re. $2*10^{-5}$ N/m^2) spectra (80 hz to 10,000 hz) and overall SPL (OASPL) at angles ranging from 55° to 165° in increments of 5° in the reference frame of the nozzle; 1/3rd octave-band sound power spectrum (PWL re. 10^{-12} W) and overall power (OAPWL) were also provided. All of this data was found for ambient static pressure of 14.3 psi.

(2) 1500 ft. flyover data: Doppler shifted 1/3rd octave-band SPL spectra, OASPL directivity, PWL spectra, OAPWL, Tone Corrected Perceived Noise Level (PNLT) and the Effective Perceived Noise Level (EPNL). The flyover data was found for an ambient static pressure of 14.7 psi.

In particular, note that the 150 ft. polar data in the reference frame of the nozzle is *not* Doppler-shifted, whereas, the 1500 ft. flyover data is, indeed, Doppler-shifted using the free-jet Mach no. as the flyover Mach number and both are in the free-field. There are no corrections for extra ground attenuation, multiple jet shielding or airframe shielding/reflections.

The aerodynamic data provided by NASA LeRC to Rolls-Royce Allison for these acoustic tests included the actual operating conditions (that is, fan and core nozzle pressure ratios and total temperature ratio), the free-jet Mach number, the test-cell ambient conditions and measured mass-flow rates in the two streams.

Test Matrix

The test conditions at which data were obtained are listed in Table 3.1. Data was obtained over a range of fan and core pressure ratios typical of those observed in current engines at approach and take-off. Initial acoustic testing, carried out in 1995, revealed that fan pressure ratios above 1.44 could not be reached due to JER air-supply limitations. During the 1995 test program, data was acquired at four values of free-jet Mach numbers (0, 0.1, 0.2, and 0.3). Following modification of the rig air delivery system, a second test program was carried out in 1996. During this test, data was acquired at all intended nozzle operating conditions but measurements at the free-jet Mach number of 0.1 were deleted from the test matrix, as shown in Table 3.1. Thus, there is significant overlap of operating conditions between the two tests done a year apart and, generally speaking, the results of the second test were considered to have superceded those of the first test. It is the results of the 1996 test that are reported and analyzed here. Table 3.2 lists the mixer-nozzle configurations tested in 1995 and 1996. Note that only the four original mixers were tested in 1995; whereas, in 1996, all the eight mixers were tested but no data was obtained for the nozzle with 25% increased length.

3.2 Aerodynamic Tests

Test Facility

Static thrust and nozzle performance measurements were obtained in the blowdown facilities at ASE FluiDyne Test Group's St. Paul, Minnesota Laboratory. Tests were carried out in 1995 on the four original mixers in FluiDyne's Channel 14. Selected results from this sequence are presented in this report. A second series of tests were carried out in 1997 in Channel 11.

Condition Code	M_{fj} (Free-Jet Mach No.)	NPR_f (P_{tf}/P_{amb}) (fan)	NPR_C (P_{tc}/P_{amb}) (core)	TTR (T_{tc}/T_{tf})	Operating Condition
A	0.0	1.21	1.17	2.21	Approach
B	0.0	1.44	1.39	2.34	T.O. #1
C	0.0	1.61	1.54	2.62	T.O. #2
D	0.0	1.82	1.74	2.79	T.O. #3
E	0.2	1.21	1.17	2.21	Approach
F	0.2	1.44	1.39	2.34	T.O. #1
G	0.2	1.61	1.54	2.62	T.O. #2
H	0.2	1.82	1.74	2.79	T.O. #3
I	0.3	1.21	1.17	2.21	Approach
J	0.3	1.44	1.39	2.34	T.O. #1
K	0.3	1.61	1.54	2.62	T.O. #2
L	0.3	1.82	1.74	2.79	T.O. #3

Table 3.1 Acoustic Test Matrix

	Mixing-Length Change (ΔL/L)			
Mixer Code	0%	-25%	-50%	+25%
CONF	OX	O	O	O
12CL	OX	O	OX	O
12UH	OX		OX	
12TH	X	X	X	
16UH	OX	O	OX	O
20UH	X	X	X	
20MH	X		X	
20DH	X	X	X	

Table 3.2 Mixer Nozzle Configurations for Acoustic Tests

(O = 1995, X = 1996)

Hardware in the second test program included the 4 new mixer designs and selected repeat runs for some of the original mixers. Both these channels are two-temperature flow static thrust stands in which the nozzle thrust is determined from force measurement with a strain-gage force balance. The general arrangement of Channel 14 and Channel 11, as well as, the station notations are shown in Figure 3.6, 3.7 and 3.8 respectively.

The airflows for both the cold and hot passages of a test nozzle are obtained from the facility 500 psi dry air storage system. Air for the cold passage is throttled, metered through a long-radius ASME nozzle, ducted to the cold passage of the test nozzle, and finally exhausted to atmosphere. Air for the hot passage is throttled, passed through a regenerative storage heater, mixed with unheated bypass flow to achieve a desired temperature, metered through a long-radius ASME nozzle, ducted to the hot passage of the test nozzle, and finally exhausted to atmosphere.

The model assembly is supported by a 3-component strain-gage force balance and is isolated from the facility piping by two elastic seals (see schematic in Figure 3.8) The ASME meter at Station 1 is water-cooled to protect the elastic seal from thermal effects. Since the cooling water is confined to the upstream (i.e. non-metric) hardware only, no tare forces are introduced by the water supply lines. Facility implementation was provided to calculate mass flow rates at Stations 1 and 4 (Figure 3.8) and to calculate the exit thrust produced by the test nozzle. The data were recorded with the laboratory digital data acquisition system. For the 1997 test in Channel 11, charging station instrumentation in the core duct consisted of four 5-probe total pressure rakes (P_{t8}), two 4-probe and two 2-probe total temperature rakes (T_{t8}). Also associated with each total pressure rake was on outer wall static pressure tap (P_{s8}). Charging station instrumentation for the fan passage consisted of four 12-probe area-weighted rakes (P_{t7}) and three 5-probe thermocouple rakes (T_{t7}). An inner and outer wall static pressure tap (P_{s7}) was also associated with each total pressure rake in the fan duct.

Test Procedures

Two types of tests were done: "hot" when the core flow is heated up to approximately 860°F and "cold" when the core flow was nominally at 70°F, same as the fan flow temperature for all tests. For all hot nozzle tests, T_{t7} and T_{t8} were calculated as an average from thermocouples at each charging station (12 for the core, 15 for the fan). For all cold nozzle tests T_{t7} and T_{t8} were calculated form T_{t4} and T_{t1}, respectively, by subtracting the temperature drop due to adiabatic throttling of flow between the meter station and the nozzle charging station. The charging station total pressures were defined as the area-weighted average from all the available probes in each duct (20 in core and 48 in fan).

The fan and core mass flow rates through the test nozzle were determined using choked ASME long-radius metering nozzles. These values were used to determine the effective thrust areas (discharge coefficient * reference duct-area) for each duct and the whole nozzle.

To evaluate the axial and vertical thrust components, the force balance was first calibrated. The force balance calibration determined the output characteristics of the three force balance flexures and the two elastic seals between the metric model

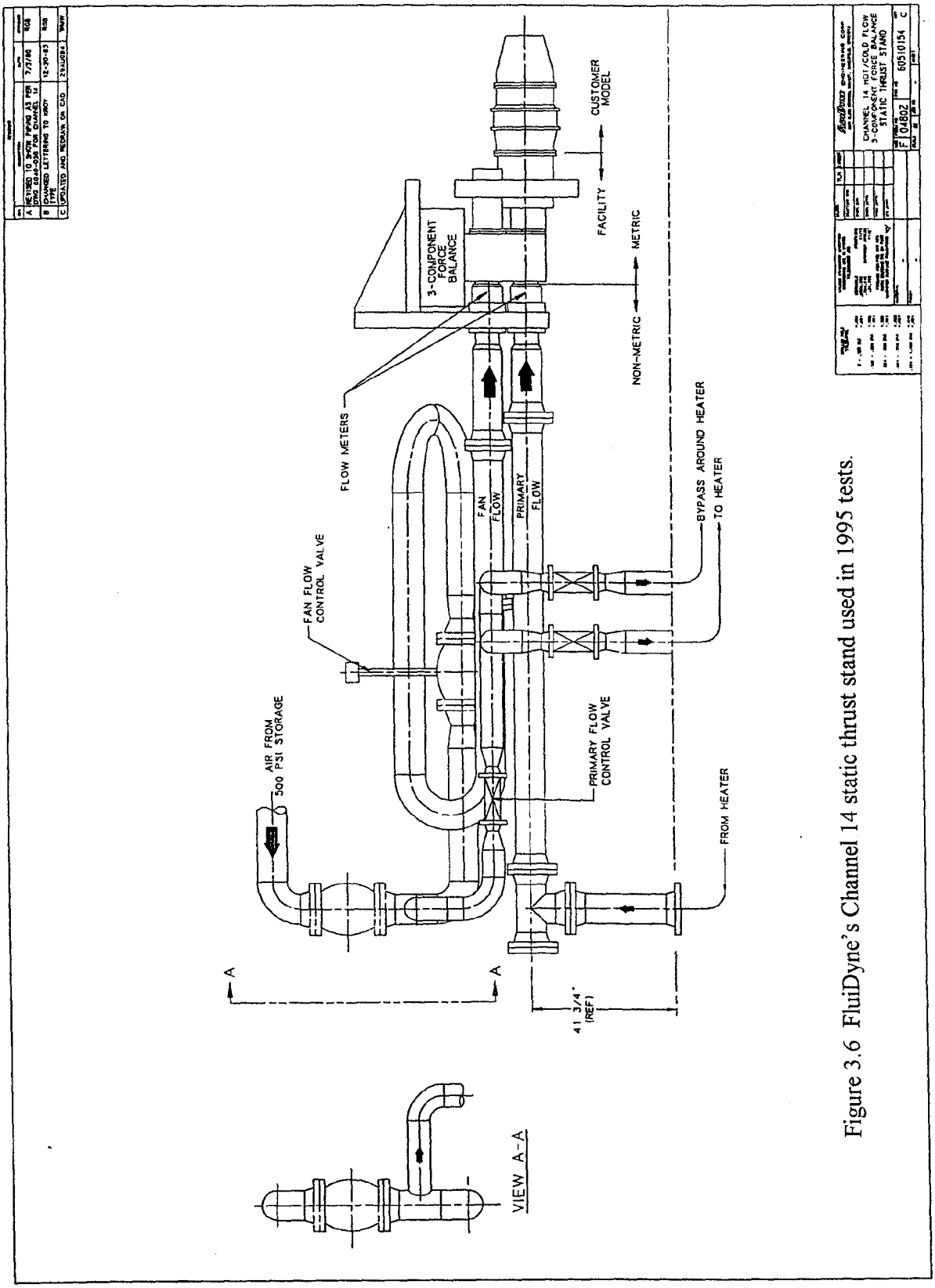

Figure 3.6 FluiDyne's Channel 14 static thrust stand used in 1995 tests.

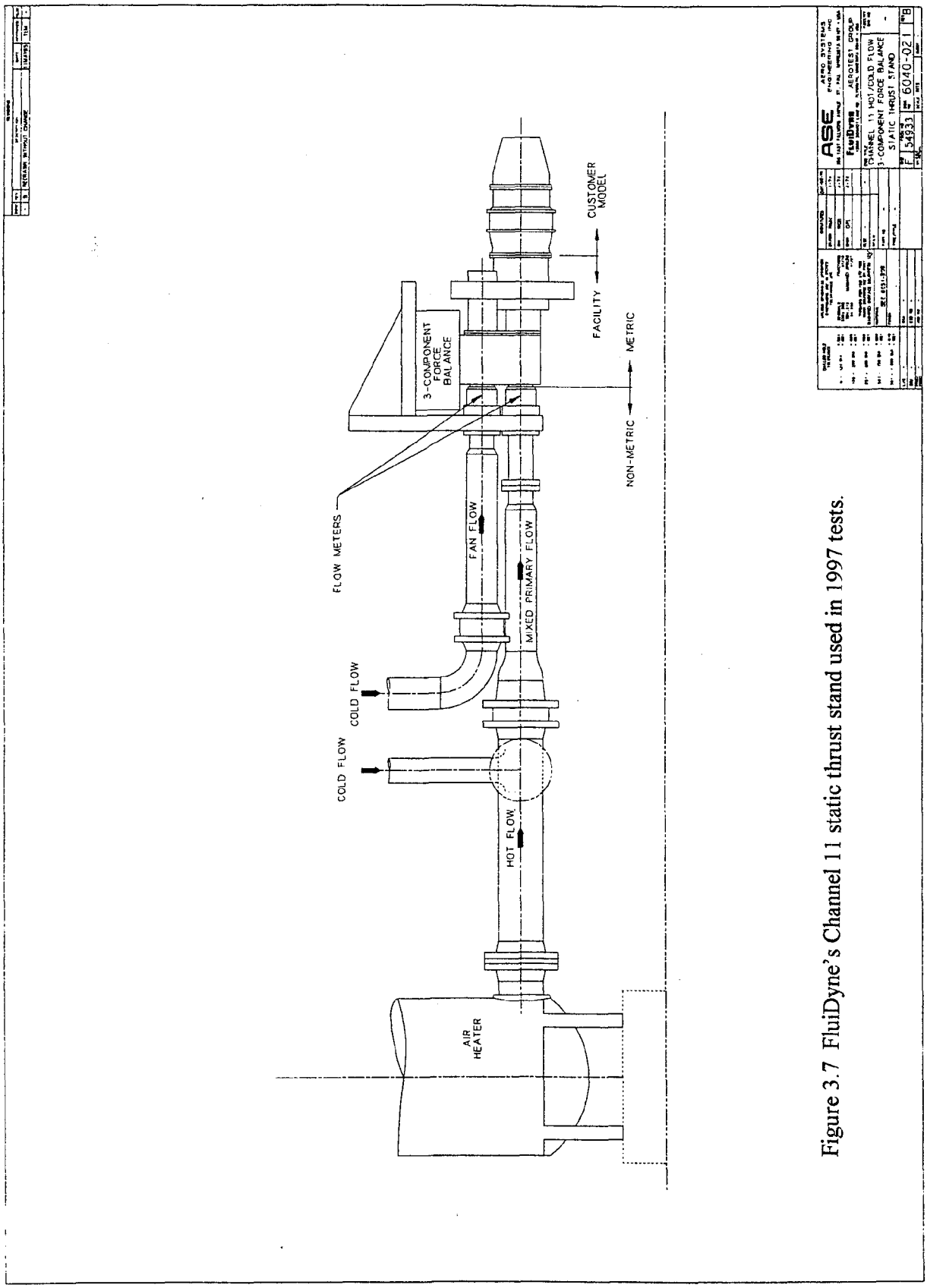

Figure 3.7 FluiDyne's Channel 11 static thrust stand used in 1997 tests.

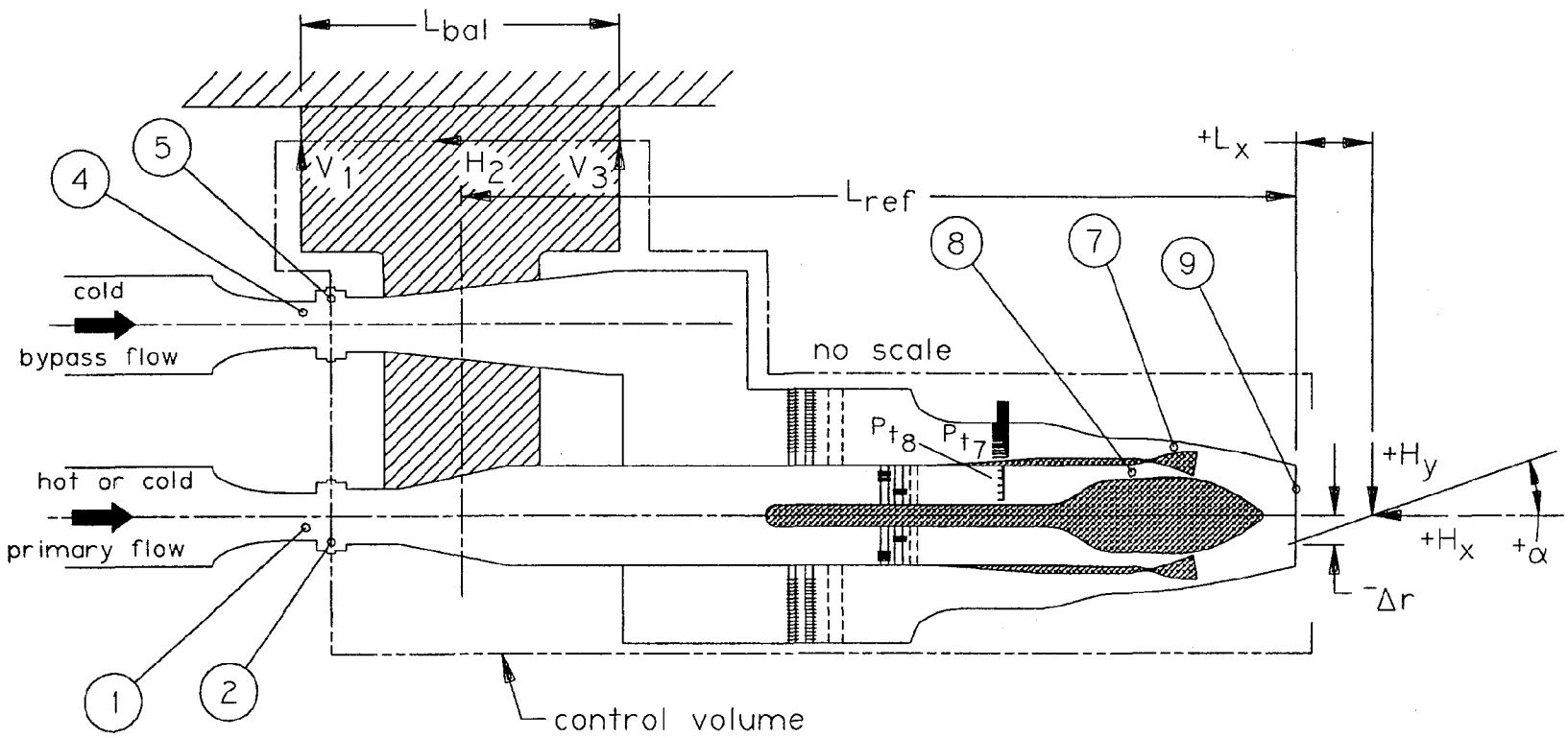

Station	Description
1	ASME meter throat (core flow)
2	Flexible seal (core flow)
4	ASME meter throat (fan flow)
5	Flexible seal (fan flow)
7	Fan nozzle
8	Core nozzle
9	Final nozzle throat

Figure 3.8 FluiDyne's station notation for model tests in Channel 11.

assembly and the non-metric facility structure. The elastic seals produce a small tare force, largely due to radial seal deflections necessary to support the static pressure differential across the seal. The seal and balance assembly were calibrated under simulated operating conditions of load and seal differential pressures. This procedure yields the thrust vector (magnitude, angle and location), thrust coefficient, fan and core effective throat areas, fan and core mass flow rates, and overall nozzle discharge coefficient. Standard ASME long-radius flow nozzles were tested before and after each test program to demonstrate facility accuracy in determining the discharge coefficient and the thrust coefficient of test nozzles. The test results were compared with predicted (target) values which are based on semi-empirical equations and were found to be very accurate in general.

Test Matrices

The purpose of these tests was to compare the aerodynamic performance of the mixers at cruise and take-off conditions. Since the facility had a limit on the maximum allowable temperature in the core flow of 860°, the desired "cruise" total temperature ratio of 2.79 could not be achieved, but a maximum of 2.50 was used instead. Also, in order to assist the evaluation of thrust mixing efficiency, which effectively captures the effect of temperature on thrust, additional "cold" tests were performed where the core flow was kept at the same temperature as the fan-flow. Aerodynamic tests were done only on selective mixers in 1997 after results from the acoustic tests were known. Tables 3.3 and 3.4 give the nominal test matrices for which data was obtained in the 1995 and 1997 tests respectively for the various mixer configurations with baseline nozzle-length and no free-jet.

3.3 Plume Surveys

Limited jet plume aerodynamic surveys were carried out in 1995 and 1996 in the NASA APL/NATR facility following the acoustic tests, with the data used to correlate noise with flow properties.

A unique multi-sensor rake assembly, shown schematically in Figure 3.9, was used to measure total pressure (P_t), static pressure (P_s), and total temperature (T_t). The rake assembly was mounted in a frame which allowed horizontal traversing of the plume in the axial and the transverse directions. This assembly was positioned at a series of axial locations downstream of the nozzle plane, providing a cross sectional survey of the aerodynamic properties in the plume at each location.

The axial distance X (downstream of the nozzle exit plane), for which good data could be taken varied from 0.2D to 10D (D = nozzle exit diameter) . A "full" axial survey consisted of X/D = 0.2, 0.5, 1.0, 3.0, 5.0, 7.5 and 10. At each X/D location a lateral sweep of the rectangular array across the plume was made in ¼ in. steps in the Y direction (see Figure 3.9 for definition of X, Y, Z). The data was acquired in an over-lapping manner such that a corresponding measured P_t T_t and P_s value was obtained for each data point location in the transverse XY measurement plane. A "full" transverse survey typically swept from Y = -4.75 in. to Y = +4.75 in., whereas a "center" transverse survey, done to conserve testing time, typically varied from Y = -0.75 in. to Y = +0.75 in.. The extent of the vertical, "Z", sweep was constant from Z = -5.0 in. to Z = +5.0 in. with ¼ in. spacing between adjacent

Table 3.3 1995 Nominal Aerodynamic Test Matrix

Mixer	NPR_f	NPR_c	TTR
CONF	1.44	1.40	1.0/2.34
	1.80	1.76	1.0/2.50
	2.38	2.30	1.0/2.50
12CL	1.44	1.40	1.0/2.34
	2.38	2.30	1.0/2.50
16UH	1.44	1.40	1.0/2.34
	2.38	2.30	1.0/2.50

Table 3.4 1997 Nominal Aerodynamic Test Matrix

Mixer	NPR_f	NPR_c	TTR
12CL	1.44	1.39	2.34
	1.62	1.54	2.50
	1.82	1.74	2.50
	2.40	2.32	2.50
12UH	1.44	1.39	1.0/2.50
	1.62	1.54	1.0/2.50
	2.40	2.32	1.0/2.50
12TH	1.44	1.39	2.34
	1.62	1.54	2.50
20UH	1.44	1.39	2.50
	1.62	1.54	2.50
	2.40	2.32	1.0/2.50
20DH	1.44	1.39	2.50
	1.62	1.54	2.50
	2.40	2.32	1.0/2.50

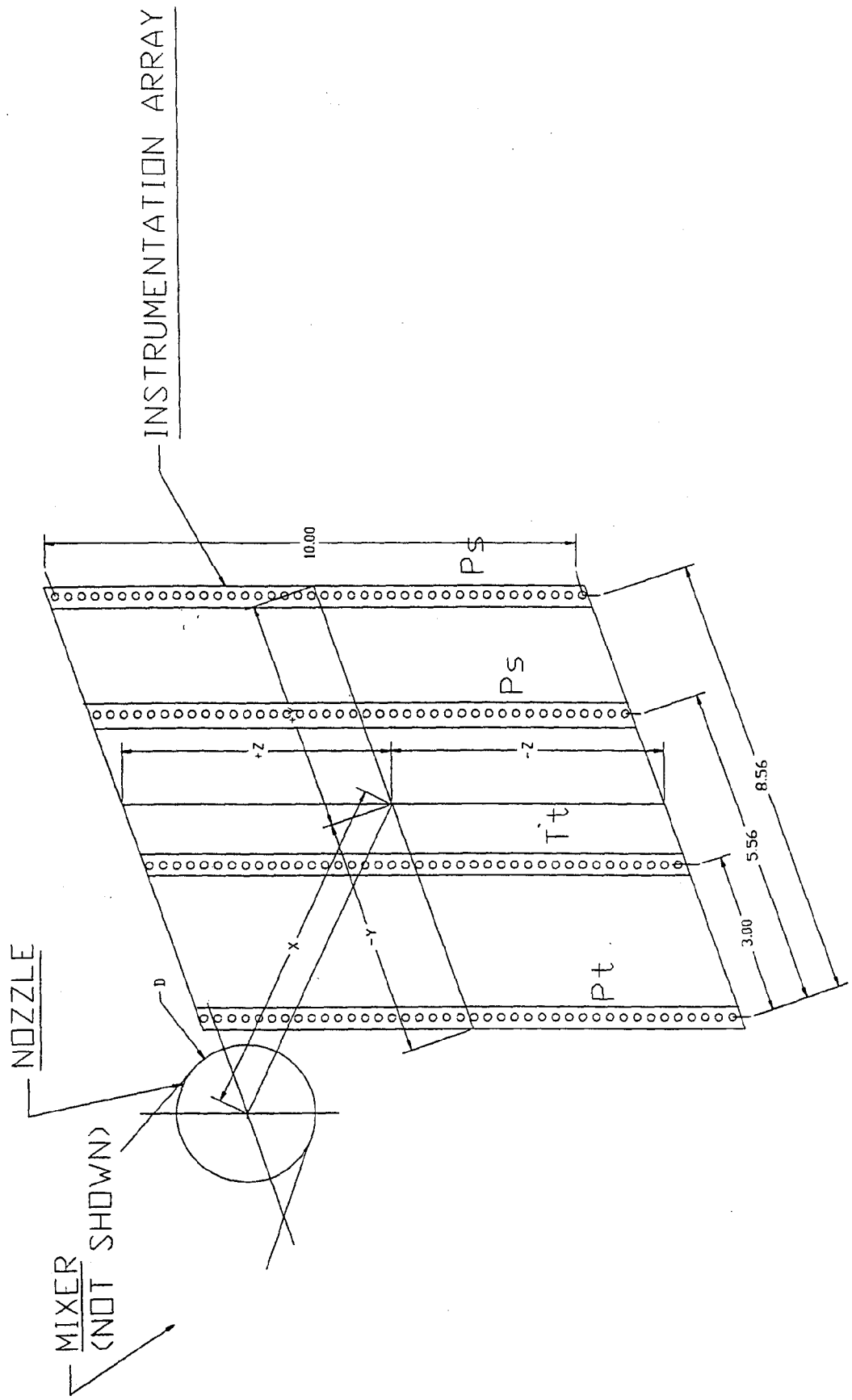

Figure 3.9 NASA plume traversing rake sketch and axis definition.

probes. The total and static pressures and the total temperature at a given point were used to calculate the local plume velocity by using the isentropic relations. This data could then be used to examine the distribution of the various aerodynamic quantities within a slice of the plume or track the axial evolution of a parameter at various locations relative to the centerline. Table 3.5 shows the test matrix for which plume survey data was obtained. The test sequence employed four of the available mixers, the baseline length nozzle, fan pressure ratios of 1.44 and 1.6, and free-jet Mach number of 0.2. A few selected additional points were also considered as time permitted.

During the 1995 aerodynamic performance tests at FluiDyne Laboratories, exit rake surveys for total pressure (P_t) obtained at the mixing plane and T_t at the nozzle exit plane were obtained using a rotating (gear-driven) survey rake assembly (see Figure A.2). Figure 3.10 and 3.11 show the details of the 15 probe P_t-rake and T_t-rake respectively. Typically, data was taken radially at angles ranging from 0° to 25° in increments of 2.5° after the blow-down facility had stabilized for each angle. This test employed the four original mixer configurations (CONF, 12CL, 12UH, 16UH) and the baseline length nozzle.

The test-matrix covered the reference point of NPR_f = 1.44, NPR_C = 1.39, TTR = 2.35 and the "hot" cruise point of NPR_f = 2.4, NPR_c = 2.32, TTR = 2.50. These correspond to the operating points for which full plume data was also obtained (see Table 3.5).

Mixer	Nozzle-Length Change	Operating Condition*						
		$M_{fj} = 0$			$M_{fj} = 0.1$	$M_{fj} = 0.2$		
		B	C	D	BF**	F	G	H
CONF	0%				O			
12CL	0%, -50%				O	X	X	X
12UH	0%				O			
12TH	0%	X	X	X		X	X	X
16UH	0%				O			
20UH	0%					(X)		
20MH	0%							
20DH	0%					X	X	X

* See Table 3.1 for definition of operating condition codes B, C, etc.

** BF is same NPR, TTR as B or F but with $M_{fj} = 0.1$

O = 1995, X = 1997, (X) = Partial Survey

Table 3.5 NASA Plume Survey Test Matrix

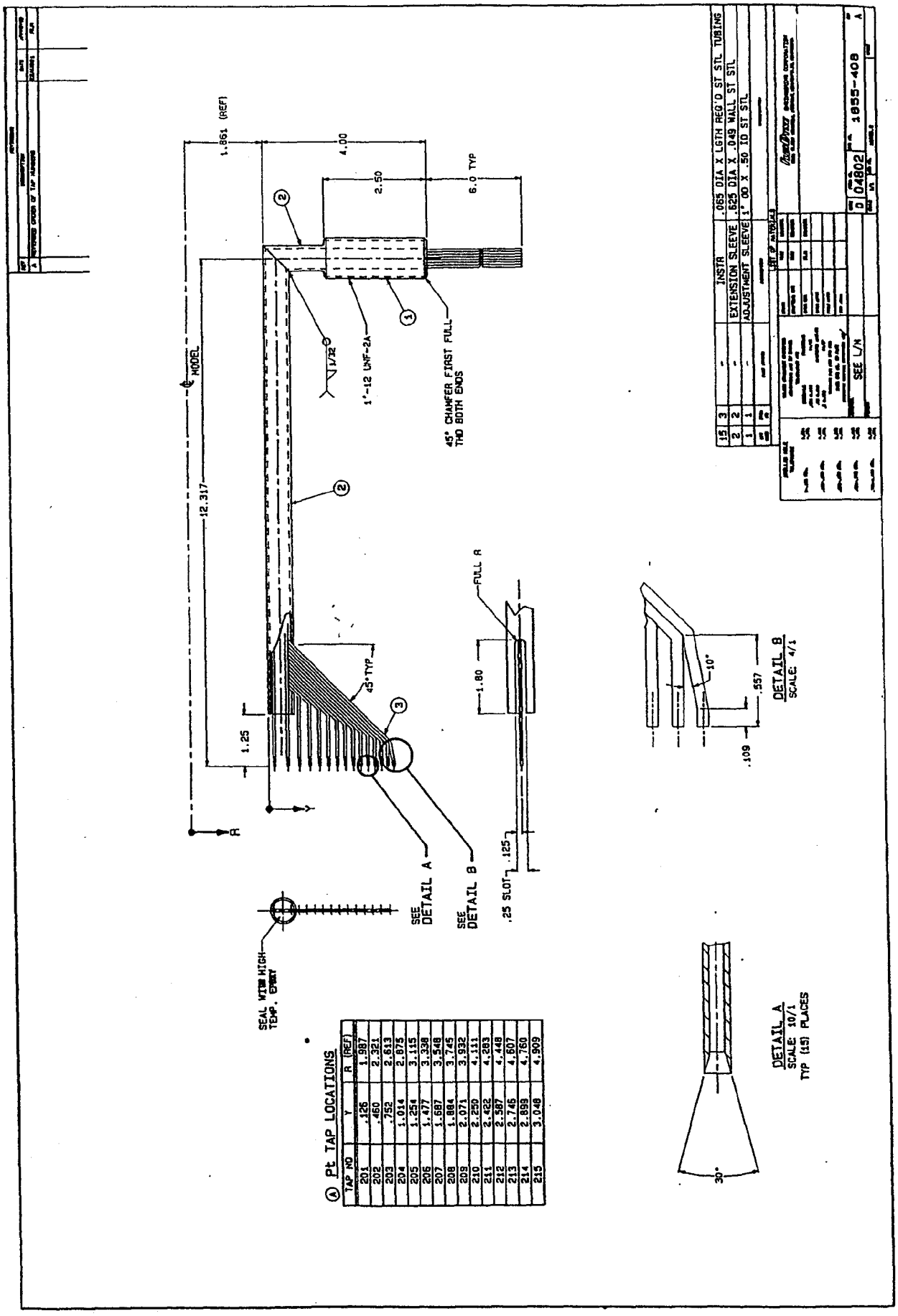

Figure 3.10 FluiDyne's 15 probe P_t rake.

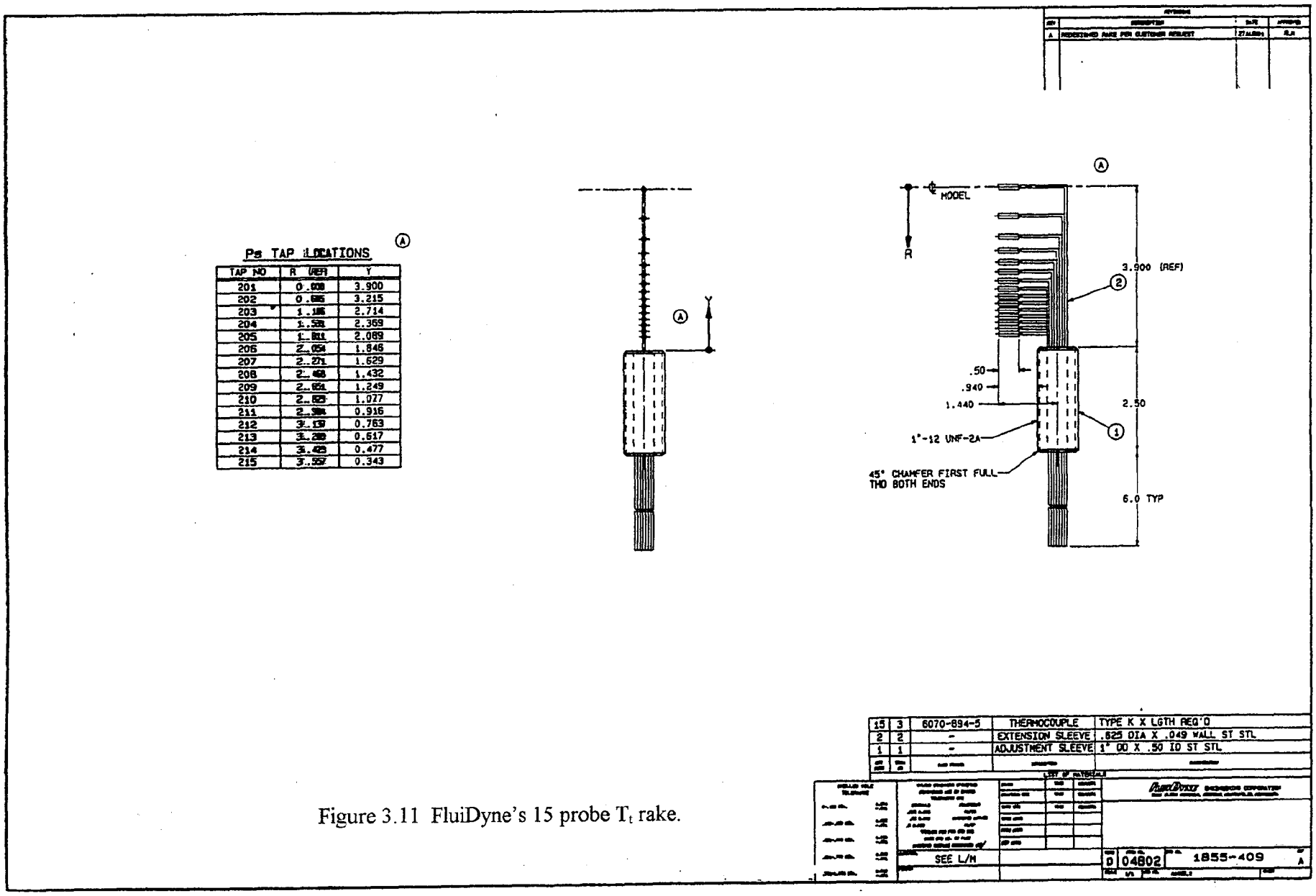

Figure 3.11 FluiDyne's 15 probe T_t rake.

Chapter 4

Aerodynamic Results and Analysis

In this chapter, we present the aerodynamic performance data and plume survey results for some of the mixer-nozzle configurations tested. Aerodynamic performance is presented in terms of mass-flow rates, bypass ratio, nozzle-discharge coefficients, and the thrust coefficient at various operating conditions. The plume survey data is presented in terms of total temperature and local velocity distribution across transverse cross-sections of the jet from the nozzle exit plane to ten diameters downstream and also along the center-line of the jet. The plume surveys help bridge the gap later between the plume flow physics and the acoustic properties of the jet. The aerodynamic performance data, on the other hand, provides the metric for thrust efficiency, both at take-off and cruise, to compare against the noise suppression ability of the mixers.

4.1 Aerodynamic Performance

Table 4.1 summarizes the aerodynamic performance data collected for the various mixer-nozzle configurations from the static thrust-stand tests at FluiDyne. We will first define the various terms appearing in this table and then discuss the results.

4.1.1 Definition of Various Terms

For a given operating condition, the data is divided into three broad categories:

(i) Mass-Flow Rates: These are the actual values, as obtained at test-day conditions, for the fan passage (m_f), core passage (m_c), the total mass-flow rate ($m_{total} = m_f + m_c$) and the bypass ratio (BPR, defined as m_f/m_c).

(ii) Nozzle Discharge Coefficients: The discharge coefficients for the fan and the core nozzles (C_D), are defined as the ratio of actual mass-flow rate to the ideal isentropic mass-flow rate discharging to the ambient test-cell conditions for the given nozzle pressure ratio (NPR). These coefficients are given in terms of the "effective throat area" for the individual nozzles, $C_{Df}A_f$ and $C_{Dc}A_c$, respectively. Individual flow discharge coefficients cannot be found because the individual throat areas A_f and A_c are not known for all the mixers, especially, mixers with scalloped or cutout lobes (20MH, 20DH and 12CL) and the tongue mixer (12TH). The ratio of these two terms $(C_{Df}A_f)/(C_{Dc}A_c)$, provides the "effective area ratio" between the fan and the core streams. In addition, an "overall" nozzle discharge coefficient, $C_{Dnozzle}$, defined as the ratio of [total effective throat-area of fan and core-nozzles] to [the nozzle-throat-area] or $(C_{Df}A_f + C_{Dc}A_c)\ /A_{nozzle\text{-}throat}$, is also presented. The inspected cold nozzle exit area, $A_{nozzle\text{-}throat}$, of 41.2233 in^2 was used.

(iii) Thrust Related Terms: The measured model-scale value of net static axial component of thrust, H_x, is presented first. This thrust component is defined

Table 4.1 Static Aerodynamic Performance Results (FluiDyne Tests).
(Model scale, 100% Nozzle-length)

Mixer	Operating Conditions			Mass-Flow Rates				Nozzle-Discharge Coefficients				Thrust Related Terms				
	NPR_f	NPR_c	T_{Tc}/T_{Tf}	m_f lbm/s	m_c lbm/s	m_{total} lbm/s	BPR[1]	$C_{Df}A_f$ in^2	$C_{Dc}A_c$ in^2	Eff. Area Ratio [2]	$C_{Dnozzle}$[3]	H_x lbf	H_x*[4] lbf	V_{mix}[5] ft/s	C_{tr}[6]	eta[7]
CONF	1.438*	1.404	0.997	13.4837	4.2453	17.7290	3.18	30.3390	9.9160	3.0596	0.9765	426.85	7068.09	775.3	0.9922	-
	1.439*	1.393	2.345	13.5033	2.6036	16.1069	5.19	30.4590	9.5380	3.1934	0.9703	423.12	7011.75	845.9	0.9951	0.2923
	1.803*	1.738	0.994	18.3657	5.4600	23.8257	3.36	30.8880	9.5290	3.2415	0.9804	720.07	11923.43	973.2	0.9930	-
	1.792*	1.735	2.513	17.9255	3.4901	21.4156	5.14	30.4250	9.8150	3.0998	0.9761	710.80	11778.23	1068.7	0.9962	0.3223
	2.373*	2.292	0.993	24.1787	7.2644	31.4431	3.33	30.8200	9.5520	3.2265	0.9793	1134.51	18784.71	1161.8	0.9961	-
	2.376*	2.295	2.500	23.9448	4.5987	28.5435	5.21	30.5380	9.7030	3.1473	0.9761	1135.37	18813.51	1280.8	1.0000	0.3915
12CL	1.441*	1.394	1.008	13.3896	4.2242	17.6138	3.17	30.0020	10.0390	2.9885	0.9713	422.55	6984.59	772.5	0.9866	-
	1.440*	1.399	2.336	13.0808	2.7551	15.8359	4.75	29.3880	9.9760	2.9459	0.9549	419.41	6933.66	852.8	0.9952	0.8717
	1.443	1.391	2.345	13.3837	2.6784	16.0621	5.00	29.7180	9.7260	3.0555	0.9568	422.15	6938.48	846.3	0.9932	-
	1.618	1.548	2.505	15.7228	3.0090	18.7318	5.23	30.0040	9.7080	3.0906	0.9633	565.51	9339.79	972.1	0.9941	-
	1.822	1.741	2.511	18.1385	3.4743	21.6128	5.22	30.0050	9.6560	3.1074	0.9621	724.06	11898.20	1078.7	0.9953	-
	2.378*	2.296	1.006	23.6189	7.6725	31.2914	3.08	30.0680	10.1470	2.9632	0.9755	1131.45	18702.44	1164.3	0.9933	-
	2.377*	2.299	2.503	23.1539	4.7881	27.9420	4.84	29.5070	10.0840	2.9261	0.9604	1125.89	18613.15	1297.5	1.0055	1.2282
	2.403	2.320	2.509	23.6542	4.8182	28.4724	4.91	29.6530	10.0140	2.9612	0.9622	1148.05	18872.05	1298.4	1.0013	-
12UH	1.443	1.389	1.007	13.4310	4.1852	17.6162	3.21	29.8840	9.9500	3.0034	0.9663	419.67	6926.76	767.1	0.9834	-
	1.443	1.392	2.483	13.0148	2.6490	15.6638	4.91	29.0950	9.9660	2.9194	0.9475	415.53	6864.21	854.2	0.9925	0.9254
	1.613	1.541	1.008	15.9160	4.8561	20.7721	3.28	30.2640	9.8470	3.0734	0.9730	562.09	9278.75	871.3	0.9844	-
	1.613	1.541	2.501	15.4465	3.0487	18.4952	5.07	29.5100	9.8580	2.9935	0.9550	556.07	9183.24	968.1	0.9943	1.0057
	2.400	2.319	1.009	23.8893	7.7744	31.6637	3.07	29.9790	10.1410	2.9562	0.9732	1141.40	18853.66	1160.7	0.9897	-
	2.406	2.323	2.507	23.2280	4.8882	28.1162	4.75	29.2670	10.2060	2.8676	0.9575	1141.10	18863.28	1306.8	1.0042	1.4651
12TH	1.441	1.390	2.339	12.6354	2.8164	15.4518	4.49	28.4555	10.3515	2.7489	0.9414	404.26	6703.94	842.4	0.9818	-
	1.613	1.543	2.515	14.9493	3.1659	18.1152	4.72	28.7595	10.3147	2.7882	0.9479	544.84	9039.67	968.5	0.9870	-
16CL	1.439*	1.391	1.016	14.5770	2.8991	17.4761	5.03	32.8930	6.9760	4.7152	0.9671	417.19	6950.21	768.7	0.9836	-
	1.442*	1.393	2.333	14.2397	1.8868	16.1265	7.55	32.3340	6.9640	4.6430	0.9533	415.15	6942.78	828.9	0.9912	0.7727
	2.389*	2.316	1.004	25.9513	5.4662	31.4175	4.75	32.9760	7.1800	4.5928	0.9741	1133.96	18889.96	1162.2	0.9928	-
	2.398*	2.319	2.504	25.3230	3.4115	28.7345	7.42	32.3630	7.2090	4.4892	0.9599	1130.56	18906.98	1266.9	1.0043	1.1583
20UH	1.441	1.388	2.502	12.9366	2.6050	15.5416	4.97	29.0446	9.8972	2.9346	0.9447	411.75	6810.86	853.1	0.9937	-
	1.614	1.539	2.508	15.4115	3.0236	18.4351	5.10	29.4904	9.8251	3.0015	0.9537	556.33	9203.69	971.7	0.9970	-
	2.404	2.321	1.002	23.8363	7.8773	31.7136	3.03	29.8577	10.2295	2.9188	0.9724	1143.36	18904.62	1160.9	0.9910	-
	2.405	2.322	2.509	23.0957	4.9111	28.0068	4.70	29.1327	10.2671	2.8375	0.9558	1136.85	18818.15	1307.1	1.0048	1.3925
20DH	1.442	1.392	2.503	13.3155	2.3635	15.6790	5.63	29.8187	8.9265	3.3405	0.9399	410.96	6801.62	844.0	0.9900	-
	1.616	1.544	2.503	15.8532	2.7362	18.5894	5.79	30.2660	8.8372	3.4248	0.9486	554.11	9172.12	959.8	0.9927	-
	2.410	2.324	1.001	24.7133	6.9678	31.6811	3.55	30.9330	9.0474	3.4190	0.9699	1138.94	18860.71	1157.6	0.9867	-
	2.403	2.320	2.504	23.9245	4.3493	28.2738	5.50	30.1662	9.0796	3.3224	0.9520	1128.07	18684.65	1284.7	1.0010	1.4493

(1) BPR = Bypass Ratio (2) Effective Area Ratio = $(C_{Df}A_f)/(C_{Dc}A_c)$ (3) $C_{Dnozzle} = (C_{Df}A_f + C_{Dc}A_c)/A_{nozzle\text{-}throat}$

(4) $H_x^* = 16^*H_x^*(P_{ref}/P_{amb})$, P_{ref} = 14.7 psi, normalized FULL-SCALE Axial Thrust

(5) $V_{mix} = H_x/m_{total}$, effective mixed velocity (6) C_{tr} = Measured Thrust/Ideal Separate Flow Thrust, Thrust Coefficient

(7) eta = $100(C_{trhot} - C_{trcold})/C_{trcold}$, Measure of Thrust Mixing Effectiveness * 1995 Test Data; Unmarked is 1997 Test Data

as the axial exit momentum of the exhaust flow, plus the excess of exit pressure over ambient pressure times the projected nozzle exit area. Next, the corresponding "full-scale" value (with scale-factor of 4) of this axial thrust component, normalized to a reference ambient pressure of P_{ref} = 14.7 psi, and defined as $H_x^* = 16H_x(P_{ref}/P_{amb})$ is given. The effective mixed velocity, defined as the ratio of measured axial thrust to measure total mass-flow rate and given by $V_{mix} = H_x / m_{total}$, and sometimes used for comparisons between mixer acoustic results, is presented next. Finally we present the thrust coefficient, C_{tr}, defined as the ratio of measured total thrust to the ideal separate flow or unmixed thrust. The latter is defined as the sum of ideal thrusts obtained from the fan and core streams when each stream, with the measured mass-flow rate, is ideally expanded to the ambient pressure from the given total pressure and temperature without mixing with the other stream. In addition, to understand how the thrust-coefficient changes with core-to-fan temperature ratio we also present a measure of percentage thrust-mixing efficiency, eta, defined by

$$eta = 100\left(C_{tr_{hot}} - C_{tr_{cold}}\right) / C_{tr_{cold}} .$$

Here "hot" stands for hot core flow and "cold" stands for cold core flow at the same temperature as the fan stream. Recall that there was a limit on the highest temperature that the core-stream could achieve at FluiDyne which prevented it from achieving the core-to-fan associated with some of the operating points. Hence, a knowledge of the thrust-mixing efficiency allows us to extrapolate, to the first order, the value of the thrust-coefficient to higher core temperatures than could be achieved in the test facility.

Some of the important terms used in Table 4.1 are also defined in the footnotes below it for convenience. This table includes the results of two tests done at FluiDyne. The first, completed in 1995, included only the original four mixers (CONF, 12CL, 12UH and 16UH) marked with an asterisk in the NPR_f column. The second was completed in 1997 and used a mix of the original and the new mixers. All results are for the baseline or 100% nozzle-length, and under static conditions (M_{fj} = 0). Also note that the "cruise" conditions differ slightly between the 1995 and the 1997 tests.

4.1.2 Thrust Coefficients

Figure 4.1 shows a plot of the static thrust-coefficient, C_{tr}, as a function of NPR_f for all mixers tested at all operating conditions. The margin of error in C_{tr}, from repeatability tests, is around 0.15%. In general, we observe that C_{tr} increases with nozzle pressure ratio, as expected. A better perspective is obtained for comparison between different mixers and between "hot" and "cold" results for a given mixer by focusing individually on different operating conditions. Figures 4.2(a) and (b) show C_{tr} in bar-chart form for the cruise condition and the reference takeoff condition, TO #1 (see Table 3.1 for definition of TO conditions).

We first note that at "hot cruise" (Figure 4.2(b)) all the lobed mixers produce a higher thrust coefficient than the confluent mixer (CONF), which has a C_{tr} = 1.0000. The CONF-mixer also has the lowest thrust mixing efficiency, as measured by eta in Table 4.1. This increase in thrust coefficient for lobed mixers at cruise is, of course, the primary reason for using them rather than the confluent mixer for internal exhaust nozzles.

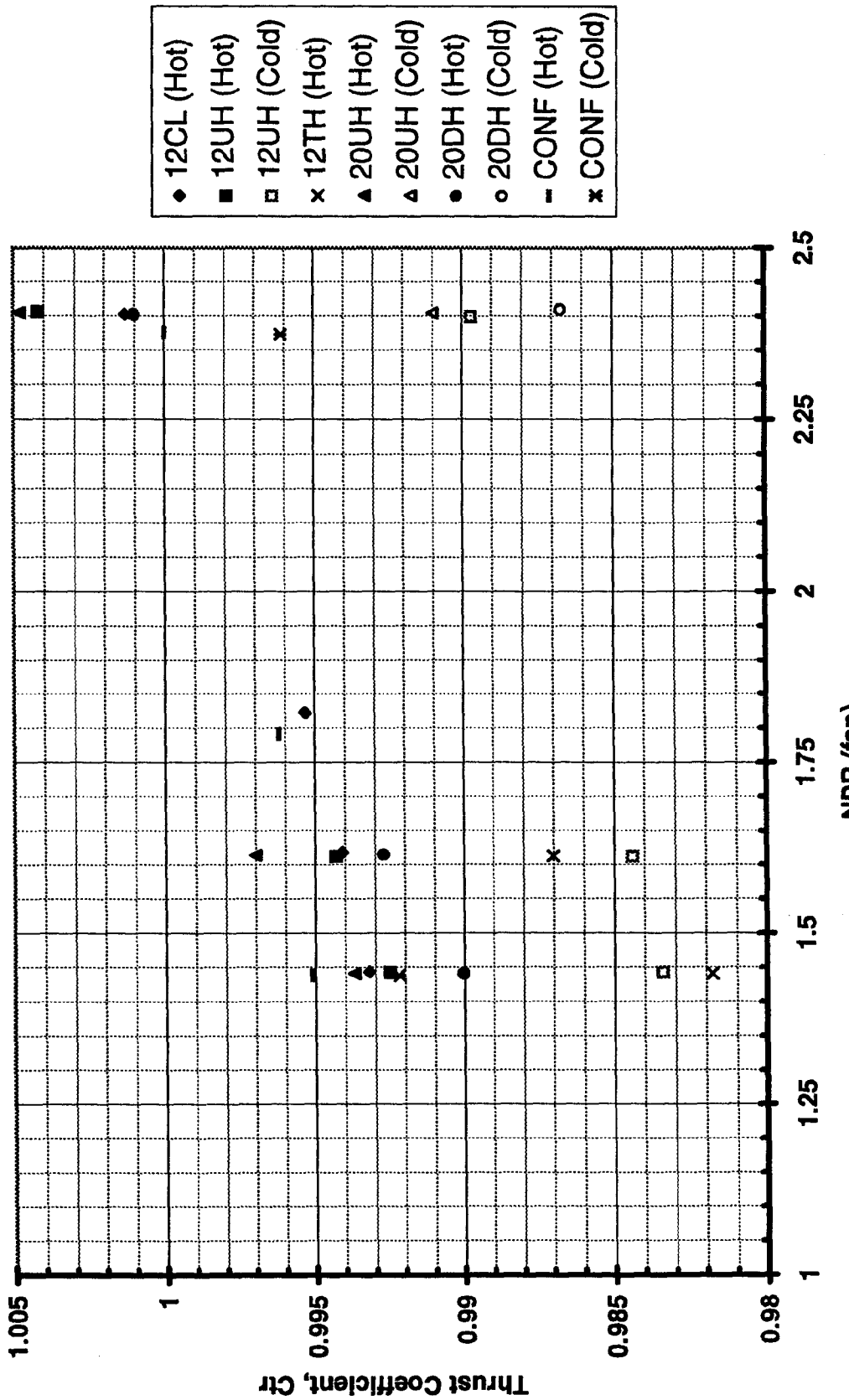

Figure 4.1 Static thrust coefficient for all mixers.

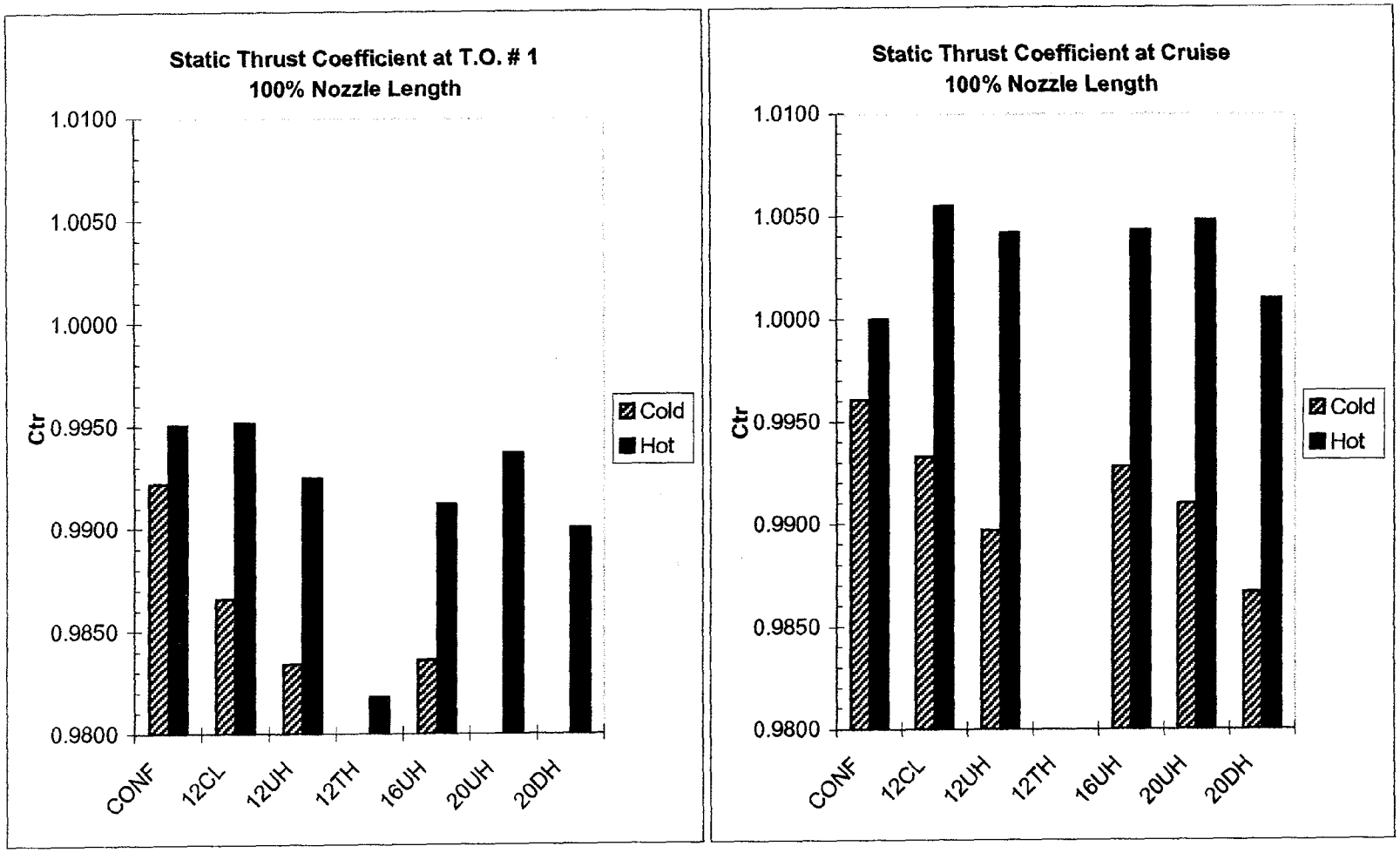

Figure 4.2 Static thrust coefficient with 100% nozzle-length at (a) T.O. # 1 and (b) Cruise

At cruise, the 12-lobe mixer with cutouts (12CL) shows one of the highest thrust-coefficients, 1.0055, in the 1995 tests. However, note from Table 4.1 that when this same mixer was tested in 1997, its C_{tr} reduced to 1.0013. This apparent decrease in C_{tr}, which is above the margin of error, is probably due to the "test-hardships" that mixer 12CL went through during the two-year period between the two FluiDyne tests. Some nicks and dents on the thin walls of 12CL were, indeed, observed during the 1997 tests at FluiDyne.

The unscalloped, high-penetration 20-lobe mixer (20UH) has the next highest cruise thrust coefficient of 1.0048 which is significantly higher than its deeply scalloped counterpart (20DH) which has C_{tr} = 1.0010. This shows that deep scalloping implies thrust and total pressure losses at cruise as compared to unscalloped lobe walls and should be kept in mind when comparing its noise benefits, if any, at take-off. Both the 20-lobe mixers (20UH, 20DH) have fairly high thrust-mixing efficiencies as measured by eta (last column in Table 4.1). This means the increase in their thrust coefficients with an increase in core temperature, say, to the actual core temperature demanded at cruise conditions, will also be higher than other mixers with lower eta values.

The 12-lobe unscalloped, high-penetration mixer (12UH) produces a cruise C_{tr} of 1.0042, which is comparable to 20UH. It also has the highest thrust-mixing efficiency, eta, which is comparable to that of 20DH.

The cruise thrust coefficient of the remaining unscalloped mixer with 16 lobes, 16UH, is 1.0043 and is comparable to 12UH, but it has a much lower eta value. Recall that 16UH has a very different (larger) fan-to-core area ratio than the rest of the lobed mixers (see Tables 2.1 and 2.2), so that its mass-flow rates would be very different leading to a different (larger) bypass ratio, actual thrusts etc, even though it is operating at the same pressure and temperature ratio as the other mixers. Thus, when comparisons are made later for noise characteristics at constant thrust, we need to consider not only the thrust-coefficient of the mixer-nozzle configuration but also its different mass-flow rate characteristics.

Most of the observations made above for cruise conditions also hold good at lower pressure ratios, like TO #1, shown in Figure 4.2(a), with a few exceptions. At this condition, the confluent mixer (CONF) has one of the highest C_{tr} = 0.9951, but still the lowest thrust mixing efficiency. The tongue mixer (12TH) has the lowest C_{tr} = 0.9818 implying larger total pressure losses due to the strong mixing produced by its streamwise vortices found earlier in the CFD simulations (see Figure 2.25). However, like 16UH, the tongue mixer (12TH) also has a very different projected fan-to-core area ratio (see Table 2.2), much lower than the other mixers. This would lead to different mass-flow rates (lower bypass ratio) and different thrust at the same operating conditions. Comparing the lobed mixers tested at TO #1, the *relative* values of C_{tr} remain similar to those at cruise: 12CL has the highest C_{tr}, 20UH has the next highest, 20DH is lower than 20UH, and so on. However, it should be noted that at TO #1, a slight difference in the total temperature ratio exists between the tests done in 1995 and those done in 1997. For configurations CONF, 12CL, 16UH, the 1995 tests set T_{tc}/T_{tf} at 2.34. For configurations 12UH, 12TH, 20UH and 20DH, the 1995 tests were conducted at T_{tc}/T_{tf} = 2.51. Also note that the reduction

in C_{tr} for mixer 12CL observed at cruise was also observed at the lower NPR when comparing the 1997 and 1995 results (C_{tr} = 0.9932 in 1997 as compared to C_{tr} = 0.9952 in 1995).

In summary, among the lobed mixers, 12CL consistently has the highest static thrust coefficient, with 20UH a close second. The unscalloped lobe mixers with high penetration (12UH, 16UH) have comparable performance at cruise with reference to 20UH. The deep scalloping present in 20DH introduces significant thrust coefficient losses at both the cruise and takeoff conditions. The tongue mixer (12TH) suffers the strongest losses at pressure ratios typical at take-off.

4.1.3 Nozzle Discharge Coefficients

Figures 4.3(a) and (b) show that the static nozzle discharge coefficients, $C_{Dnozzle}$, for the various mixers at TO #1 and cruise conditions respectively. The discharge coefficient at "hot" conditions is lower than "cold" conditions, as usual, for all the mixers.

With no metal blockage, the confluent mixer (CONF) predictably shows the highest discharge coefficient. Mixer 12CL which has the fewest number of lobes and lowest penetration with cutout lobes, shows the next highest discharge coefficient, as might be expected from a metal blockage point of view. Mixer 20UH, which has the highest number of lobes, shows the lowest value of discharge coefficient of all the unscalloped configurations. However, mixer 16UH, with large fan-to-core area ratio, shows the highest value. Deep scalloping (20DH) affects the discharge coefficient adversely both at cruise and TO The tongue mixer (12TH), with the lowest fan-to-core area ratio, also has one of the lowest discharge coefficient for both TO #1 and TO #2 (see Table 4.1).

An examination of the effective area ratios for the different mixers (see Table 4.1) also reveals a correspondence with their geometric area ratios (see Tables 2.1, 2.2). For example, all mixers with similar geometric area ratios (12CL, 12UH, 20UH) also show similar "effective area ratios". The effective area ratio does not change much with nozzle pressure ratio.

On the other hand, deep scalloping (20DH) definitely increases the effective area ratio. This is in spite of the fact that the individual fan and core flow areas, as axially projected on a transverse plane at the mixer-exit, are the same as its unscalloped counterpart, 20UH. A closer examination of the individual effective areas for 20DH and 20UH shows that the increase in effective area ratio is due to a larger decrease in effective core flow area compared to the smaller increase in effective fan flow area. For example, at cruise, with deep-scalloping, the effective core flow area is reduce by 11.6%, whereas, the effective fan-flow area increases by only 3.5%. Recall that although the static pressure at the scalloped edge of a lobe must be balanced between the fan and the core flows, the ratio of their total pressures, P_{tfan}/P_{tcore} is greater than 1 (about 1.036). The fan stream, with higher total pressure head, appears to "pinch" or narrow down the flow area available for the core stream, as is also seen in the CFD-simulations of the total temperature contours in Figure 2.21(a). Although the absolute changes in the effective areas of the core and fan streams due to scalloping are of the same order of magnitude, for a high bypass ratio mixer-nozzle such as these, the change in

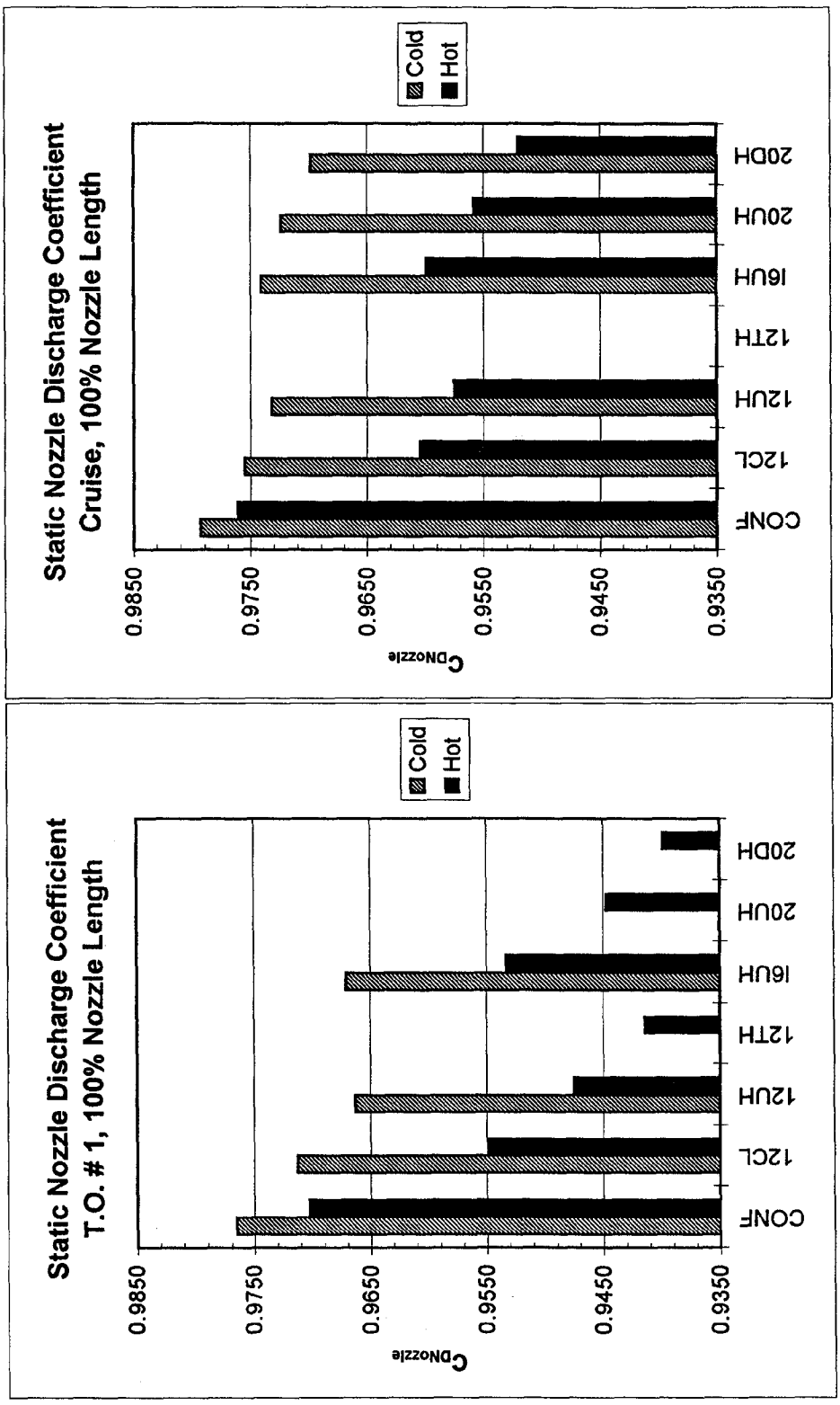

Figure 4.3 Static nozzle discharge coefficient with 100% nozzle-length at (a) T.O. # 1 and (b) Cruise.

core area on a percentage basis is larger than that in fan area.

4.1.4 Bypass Ratios

Static Case

Figure 4.4 shows the measured bypass ratio (BPR) for all mixers tested at FluiDyne under all operating conditions. For all mixers, the change in BPR due to operating condition is not large. However, for the lobed mixers bypass ratio does peak at an intermediate nozzle pressure ratio and then decrease to a minimum at the cruise condition. Comparing the various lobed mixers, configurations 12UH and 20UH, which have the same fan-to-core area ratio, have comparable BPR's at all pressure ratios. Mixer 12CL, which has cutouts in the lobes but the same fan-to-core area ratio as 12UH, has a slightly higher BPR than 12UH. By comparison, mixer 16UH, with the highest fan-to-core area ratio, has the highest BPR. Similarly, mixer 12TH, with the smallest fan-to-core area ratio, has the smallest BPR. Deep scalloping (20DH) increases the BPR compared to 20UH at all operating conditions, as expected from previous discussions.

All the tests at FluiDyne were performed under static conditions, that is with a free-jet Mach number of 0.0 and with the baseline (100%L) nozzle-length. Hence, the effect of M_{fj} or nozzle-length on the aerodynamic performance parameters cannot be determined from the FluiDyne test data.

However, the acoustic tests done at NASA's APL did vary M_{fj} and nozzle-length, but were restricted to the measurement of the mass-flow rate and not the thrust or the discharge coefficients. Since both M_{fj} and nozzle-length turn out to have significant effects on the noise characteristics of mixers, a brief look at least at their bypass ratios is useful.

Effect of Free-Jet Mach No.

Figure 4.5 shows the effect of free-jet Mach number, M_{fj}, on BPR at performance condition TO #3 for mixers with 100% nozzle-length using data obtained during acoustic tests done at NASA. The overall trends in terms of bypass ratio at static conditions, amongst the different mixers is the same as found in the FluiDyne tests (Figure 4.4) That is, the static BPR's of 12UH, 20UH are comparable to each other while 12CL is slightly higher than both. As before, 16UH has the highest BPR while 12TH has the lowest. The addition of scalloping increases the BPR, with the additional information from the 20MH mixer that BPR is in some sense also proportional to the scalloped area. (Compare BPR's of 20UH, 20MH and 20DH.) However, the absolute values of BPR are slightly different between the NASA and FluiDyne tests at the same operating conditions, and with the NASA tests consistently showing a slightly larger BPR value than the corresponding FluiDyne data. The difference is most likely attributable to the differences in the measuring instruments and the data processing methods at the two facilities. Since we are interested in studying the effect of M_{fj} on BPR from tests done at one facility, the difference in BPR-values are of primary importance rather than their absolute values. From Figure 4.5 we can see that the effect of changing M_{fj} from 0.0 to 0.3 on the bypass ratio is generally not much. Two exceptions are noted: a significant increase in bypass ratio is observed in the confluent configuration as the free jet Mach number increases; however, mixer 12CL experiences a

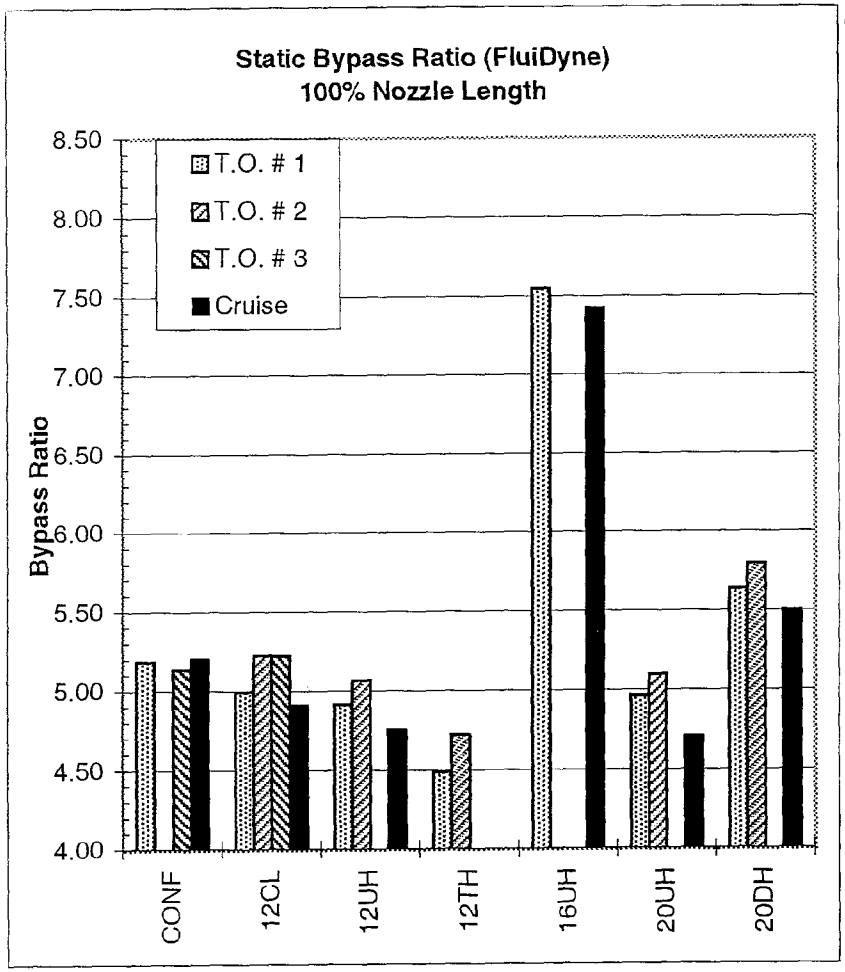

Figure 4.4 Effect of operating condition on static bypass ratio with 100% nozzle-length.

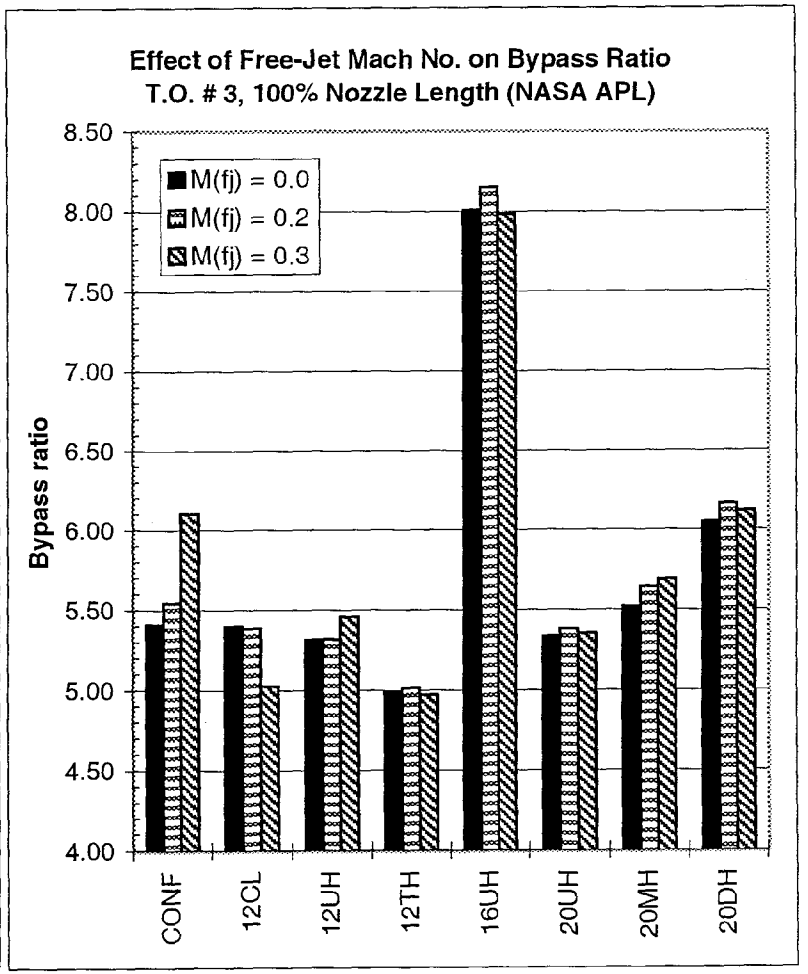

Figure 4.5 Flight-effect on bypass ratio at 100% nozzle-length.

reduction in bypass ratio between free jet Mach numbers of 0.2 and 0.3.

Effect of Nozzle Length

Figures 4.6(a) and (b) show the effect of decreasing nozzle length (100%L to 50%L) on BPR for the mixers at M_{fj} = 0.2 and performance conditions TO #1 and #3, respectively. Three of the lobed mixers (12TH, 20UH and 20DH) also had data taken with the 75%L nozzle. In general, it is observed that bypass ratio decreases with decreasing nozzle length, for both performance conditions. This trend is monotonic over the range of nozzle lengths tested.

In order to understand the reasons for this monotonic decrease in BPR with decreasing nozzle length, the changes in the individual fan and core flow-rates and total flow rates need to be scrutinized. These comparisons will be made at standard day conditions to remove the effects of changes in ambient conditions through the use of "corrected" flow rates. The corrected mass flow rates are defined, as in the turbomachinery literature:

$$m_{corr} = \frac{m_{measured}\sqrt{T_t / T^*_{ref}}}{P_t / P^*_{ref}}$$

where

$T^*_{ref} = 518.7^\circ R$

$P^*_{ref} = 14.7 psi.$

Figure 4.7 first shows the bypass ratio defined in terms of individual corrected flow. The previously observed trend does not change when corrected flow is used to determine bypass ratio: the corrected bypass ratio also decreases as the nozzle-length is decreased for all mixers. Figure 4.8 shows the individual corrected mass-flow rates for fan and core streams in a comparative bar-chart form for several mixers. A general trend for all the mixers is that the fan flow rate decreases when the nozzle-length decreases and, with the exception of 12UH, the core flow rate increases simultaneously so as to approximately maintain the same total flow rate.

We will attempt to list the possible ingredients of the mechanism to explain the above mass-flow rate data, however, the complete aerodynamic mechanism is not fully understood at this point. Recall that the reduction in mixing length was achieved by preserving both the nozzle throat area (or the nozzle exit diameter) and the mixing plane diameter. This reduction in mixing-length has the effect of "squeezing" the nozzle duct flow in a shorter axial distance and "releasing" it to ambient pressure at the nozzle lip "earlier" than a longer nozzle. This reduction in mixing-length would imply less mixed flow at the nozzle exit plane. "Squeezing and early releasing" would imply faster axial expansion rate and higher acceleration of the subsonic mixed flow inside the shorter nozzle than that in the longer nozzle. For the shorter nozzle, the aft half of the flow outside the nozzle dominated by axial vorticity, is now in an "unbounded' region rather than in the "bounded" duct environment. All of these processes downstream of the nozzle must affect the axial evolution of fan/core flow mixing upstream at the mixer exit plane. However, both the subsonic streams must have the same static pressure at the trailing edge of the mixer (Kutta condition). This common static pressure can be different for the two nozzles and can change the effective throat areas for the fan flow and the core flow while keeping the sum of their areas the same due to the same duct cross-sectional area near the mixer exit plane. This

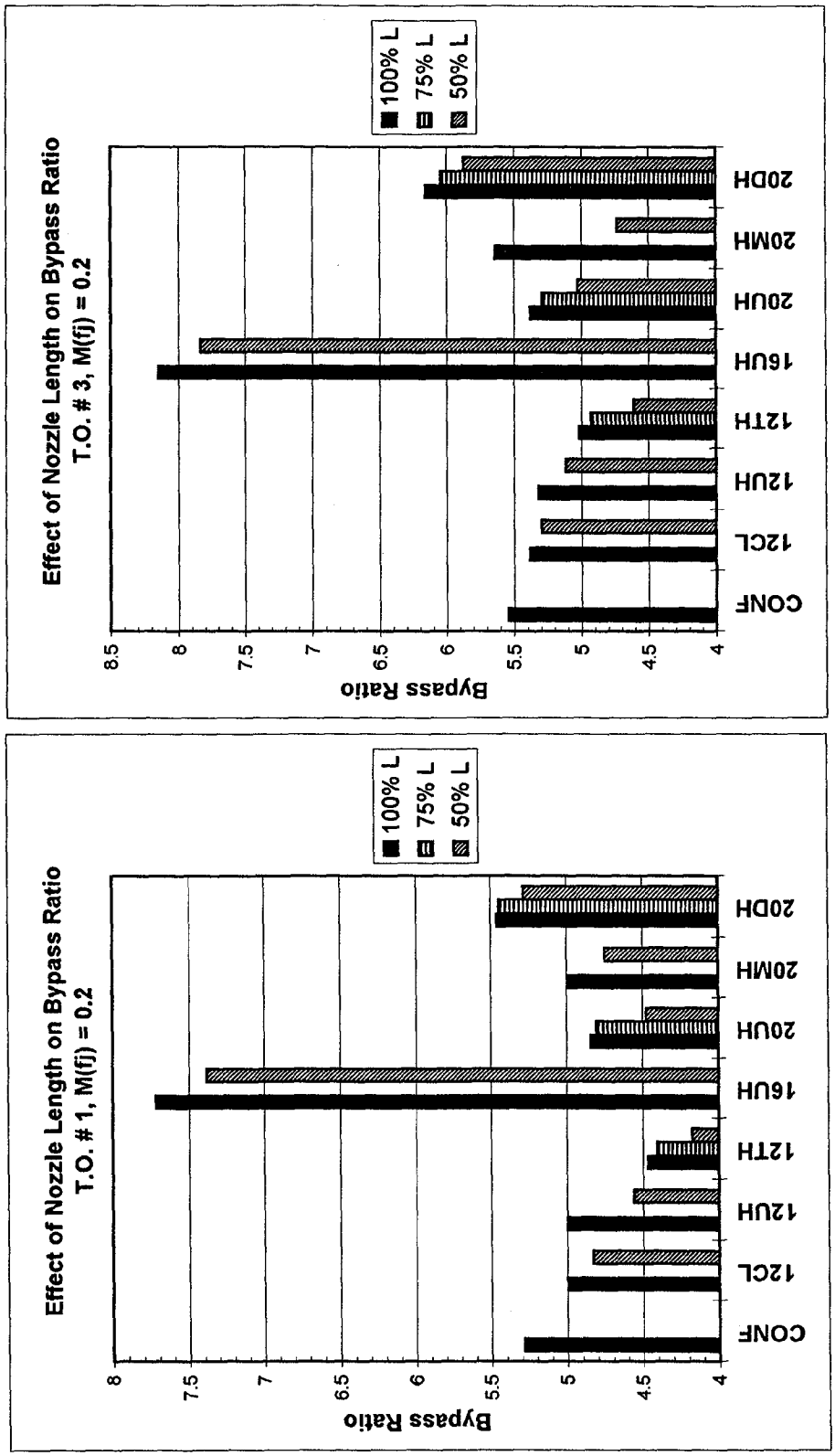

Figure 4.6 Effect of nozzle-length on bypass ratio at $M_{fj} = 0.2$ for (a) T.O. # 1 and (b) T.O. # 3.

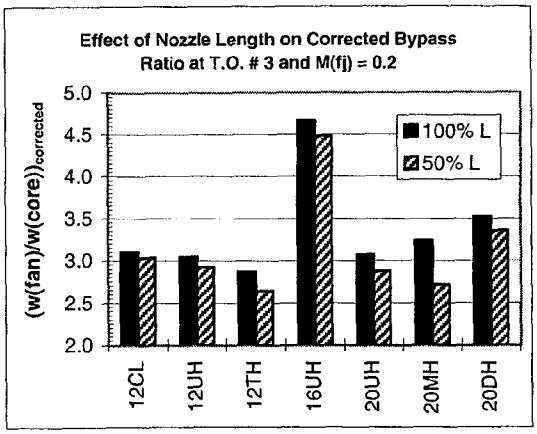

Figure 4.7 Effect of nozzle length on corrected bypass ratio

can explain the simultaneous rise in one mass-flow rate (core flow) and decrease in the other (fan flow) with the total mass-flow rate remaining the same. Also based on one dimensional ideal-mixing arguments, which is independent of the mixing length, the total flow rate of two streams should not change with nozzle length when their pressure ratios and temperature ratio are not changed. This is partly what is observed in Figure 4.8, except for the 12UH mixer. However the internal mixing is by no means ideal and both streams suffer different total pressure losses when the nozzle-length is decreased.

A possible mechanism for the decrease of fan mass flow rate when the nozzle length is decreased is that the axial vortices (which migrate radially outward inside the nozzle as seen in the CFD simulation in Figures 2.21, 2.22 or 2.24, 2.25) close to the aft convergent part of the nozzle partly block the fan flow near the duct wall. How far radially these axial vortices move depends on the lobe penetration and their radial convection velocity. As a result, the higher the penetration the more the fan blockage due to these axial vortices. This is partly borne out in the observed differences in fan flow changes between 12CL and 12UH or 20UH. In all mixers, it turns out that all these mechanisms collude to decrease the fan flow rate when the nozzle-length is decreased. It appears then, that to maintain approximately the same total mass flow rate, as demanded form the 1-d ideal mixing analysis, the core flow rate must increase.

Further deeper investigation is needed to fully understand this aerodynamic effect of shortening the nozzle length.

4.2 Typical Plume Survey Results

In this section, typical plume survey results are presented as obtained in static tests at FluiDyne and in tests done at the NASA APL with a free jet flow. Several of these plume surveys are collated in Volume 2 as plots of total temperature or local velocity distribution, and Table 4.2 gives overall guidance to those figures for each mixer tested. The purpose of this section is to selectively discuss some of these plume survey plots so that a better understanding can be obtained regarding the plume flow physics and its connection to the far field noise which is presented in the next chapter.

4.2.1 Nozzle Exit Plane Survey

Figure 4.9(a) shows the total temperature contours for a section at the nozzle exit plane for the four original mixers (CONF, 12CL, 12UH 16UH) with the baseline nozzle-length (100%L), at performance condition TO #1 and $M_{fj} = 0$ (static case). Figure 4.9(b) shows the radial temperature profiles for the same case and compares

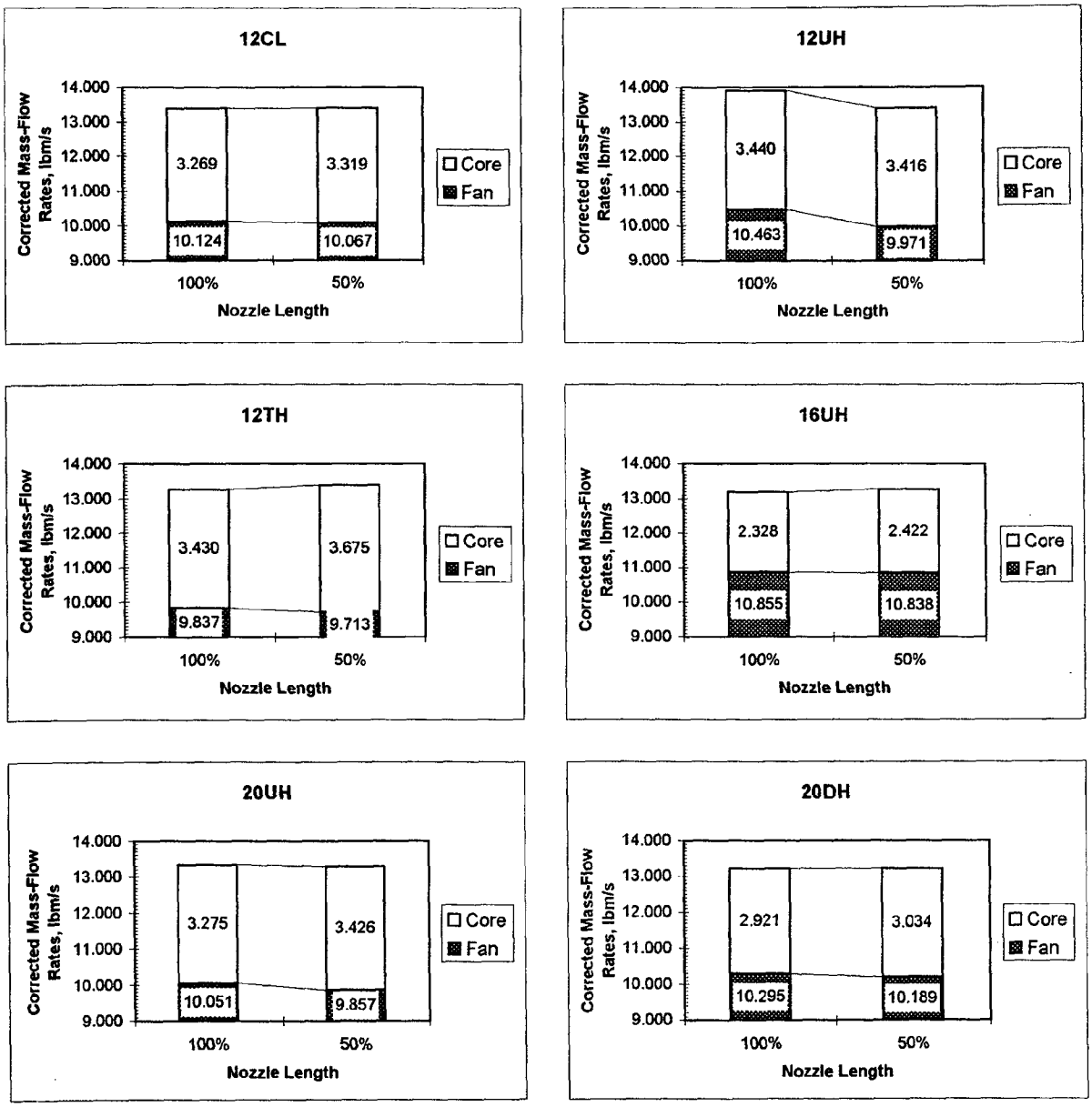

Figure 4.8 Effect of nozzle-length on "corrected" mass-flow rates at M_{fj} = 0.2 and T.O. # 3.

Table 4.2 Guide to Plume Survey Data as plotted in Vol. 2 (parts 1, 2) and FluiDyne Tests#

MIXER	T.O. # 1										T.O. # 2									
	Velocity				Total Temperature						Velocity					Total temperature				
	x/D=0.2	1	>1.0	C.L.**	0.1	0.2	0.5	1	>1.0	C.L.**	0.2	0.5	1	>1.0	C.L.**	0.2	0.5	1	>1.0	C.L.**
CONF					FD(M=0)*															
					8 (M=0.1)				**30(M=0.1)**	**45(M=0.1)**										
					27(M=0.1)		**28(M=0.1)**		**31(M=0.1)**											
					29(M=0.1)															
12CL					FD(M=0)*															
100%L	12	20		1	**9(M=0.1)**					61	15		24		2, 5					
	13				**32(M=0.1)**		**33(M=0.1)**	**34(M=0.1)**	**35(M=0.1)**	**12***	33	34	35	36	**17***					
							36			**45(M=0.1)**				37						
														38						
														39						
12CL				1						61	14									
50%L										**12***										
12UH					FD(M=0)*															
					10(M=0.1)					**45(M=0.1)**										
					37(M=0.1)		**38(M=0.1)**	**39(M=0.1)**	**40(M=0.1)**											
12TH	18			1						61						65				
				3 (M=0)						**12***						**14*,23***				
16UH					FD(M=0)*															
					41(M=0.1)		**42(M=0.1)**	**43(M=0.1)**	**44(M=0.1)**	**45(M=0.1)**										
					11(M=0.1)															
20UH				1						61										
						25*				**12***										
20DH	9	19		1		63				61	11	27	25	29	2. 4	64, 66	67	68	69	62
	10					**24***				**12***	26		28	30	**17***				70	**13***
			60 (Jet Wake)											31					71	
														32					72	

Notes: # Plume survey figure numbers are for free-jet Mach no. (M) of 0.2 unless mentioned; Light References = Figure nos. in Part 1, Vol. 2;
Bold references = Figure nos. in Part 2, Vol. 2 FD = 1995 FluiDyne surveys: All Temperature surveys are at nozzle-exit plane;
FluiDyne tests also have total pressure survey plots at the mixer exit plane for the same conditions as the corresponding total temperature surveys
* = Non-dimensional ** C.L. = Center-Line Traverse

Table 4.2 (continued) Guide to Plume Survey Data as plotted in Vol. 2 (parts 1, 2) and FluiDyne Tests

MIXER	T.O. # 3								Cruise
	Velocity					Total Temperature			Total Temperature
	0.2	0.5	1	>1.0	C.L.**	0.2	0.5	C.L.**	Nozzle-Exit
CONF									FD(M=0)*
12CL	17		23		2, 8	1	5	15*	FD(M=0)*
100%L	16		22		18*	19*			
	40	41	42	43					
				44					
				45					
				46					
12CL	47	48	49	50	2, 7	2	6	15*	
50%L				51		20*			
				52					
				53					
12UH									FD(M=0)*
12TH						3	4	15*	
						21*			
16UH									FD(M=0)*
20UH									
20DH			21		2, 6		7	15*	
		54	55	56	18*		22*		
				57					
				58					
				59					

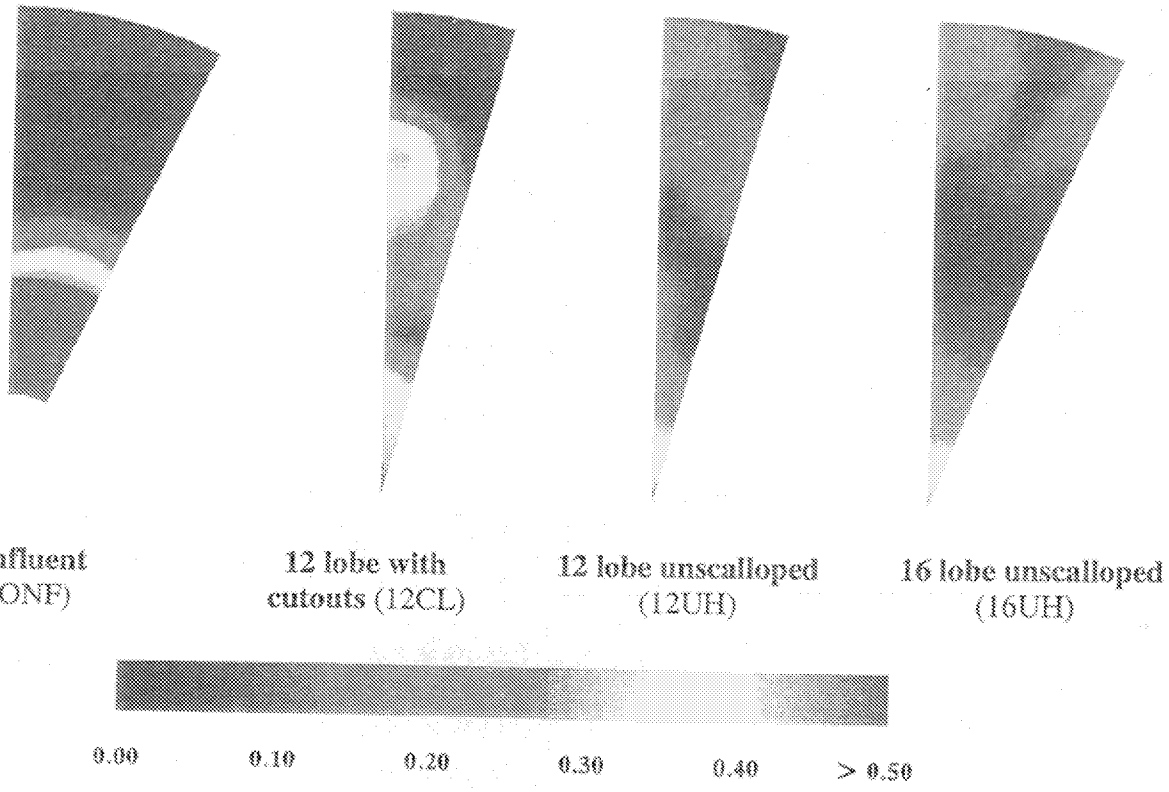

Figure 4.9(a) Total temperature contours at the nozzle-exit plane (FluiDyne).

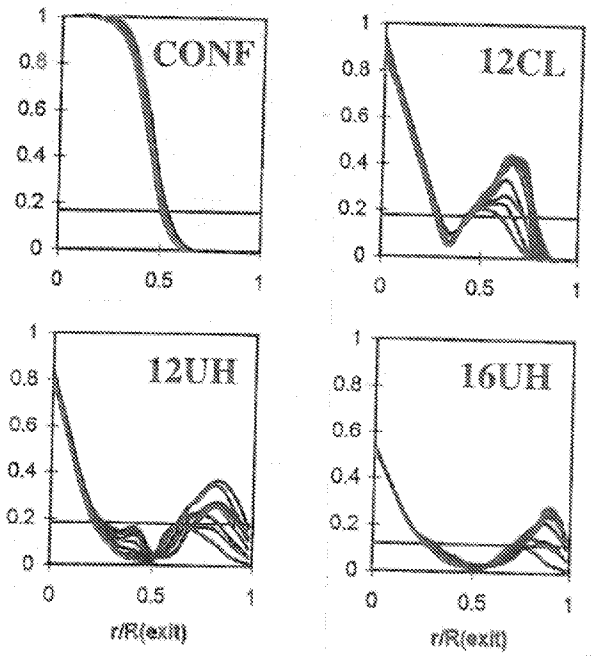

Figure 4.9(b) Total temperature radial profiles at different azimuthal angles and ideally mixed total temperature (horizontal line).

them to the ideally mixed temperatures found from the known mass flow rates and the enthalpy conservation equation for each mixer. The total temperature is shown in a non-dimensional form defined by $T_t^* = \left(T_t - T_{t\,fan}\right) / \left(T_{t\,core} - T_{t\,fan}\right)$ so that $T_t^* = 1$ implies core temperature and $T_t^* = 0$ corresponds to the fan temperature.

We make the following observations:

(i) The confluent mixer (CONF) shows hardly any mixing between the core and the fan flow, as expected. Viscous mixing is the dominant mechanism available in this configuration and it is obviously not effective in the available mixing-length. The Kelvin-Helmholtz instability which occurs in vortex sheets or thin shear-layers and which increases the interface area between the two streams, is apparently not a strong mixing mechanism for the confluent mixer which has a fairly high fan-to-core velocity ratio (V_f/V_c= 0.7).

(ii) The forced lobe mixers, on the other hand, produce much better mixing than the confluent, as can be seen from the smaller deviation of the local temperature from the ideally mixed temperature (Figure 4.9(b)). One can also qualitatively say from these figures that 16UH is much better mixed than 12UH, which in turn is better mixed than 12CL. The mechanism for enhanced mixing in forced lobe mixers is by now well known: It is largely attributable to the streamwise or axial vorticity generated by the difference in radial velocity components of the core and the fan flows near each lobe sidewall. This axial vorticity generated downstream of the lobe sidewalls rotates the two flows around each other in tight spirals, increasing the interface area, and producing better mixing though the "engulfment' process. The relative strength of the vortices generated and their convection in the radial direction depends on the lobe geometry as given by parameters such as the angle between the two flows at the mixer exit plane, lobe penetration, and number of lobes.

(iii) The effect of lobe penetration on the radial location of these vortices at the nozzle exit plane is clearly captured in these figures by the location of "hot spots". The local peaks in temperature are created by the partially mixed hot core stream and are typically found in the central core region of an axial vortex as seen in the previous CFD-simulations (see Figures 2.21, 2.22 or 2.24, 2.25). Thus, we observe that 12CL, with low lobe penetration, has its hot spots and, hence, axial vortices closer to the central axis than 12UH and 16UH mixers which have higher lobe penetration. Since the nozzle exit radius is also smaller than the radial height of the lobe crests in 12UH or 16UH, it appears that these axial vortices may even be interacting with the nozzle duct wall at the very aft end. This data also gives some credence to the fan-flow blockage mechanism discussed earlier in Section 4.1.4 for the shorter nozzle.

(iv) Figure 4.9(b) shows that, even in the lobed mixers, the region near the central axis is not well mixed. However, the mixing improves as we go from 12CL to 12UH to 16UH.

Mixing in the central region is believed to be controlled by the gap at the mixer exit plane between the lowest part of the lobe and the tail-cone surface, as well as how closely the fan flow exit angle matches with the tail-cone angle. An improvement in mixing can be obtained in this region by decreasing the gap as much as practical and aligning the fan parallel to the tail-cone surface at the mixer exit plane. Further confirmation of the relative mixing efficiencies between these four mixers is also obtained from Figures 8 through 11 in Volume 2, pt. 2 where the free-jet Mach number is set to $M_{fj} = 0.1$ for the same TO #1 operating condition. These plots tend to imply that higher lobe number and higher penetration are conducive to faster mixing. Both these geometrical features increase the interface area between the fan and the core streams and enhances mixing. However, we should also bear in mind that 16UH has a larger fan-to-core area ratio than the other mixers, and 12CL has cutouts, so that there may be secondary compound effects when compared with 12UH.

4.2.2 The Tongue Mixer and Mixer with Cutout Lobes

The effect of the tongue mixer (12TH) on total temperature mixing near the nozzle exit plane (X/D = 0.2 where X = axial distance from nozzle exit plane and D = nozzle exit diameter) is shown in Figure 4.10(a) where it is also compared with 12CL (Figure 4.10(b)) at the higher NPR of TO #3 and M_{fj} = 0.2. The total temperature is given in degrees Fahrenheit. Here again we observe that the hot-spots for the tongue mixer, which has high penetration, have migrated to the outermost extremities of the nozzle circumference and even beyond, since at X/D = 0.2 the hot spots can penetrate the nozzle-lip shear layer. For the tongue mixer the central region remains unmixed as in the previous mixers and, at this higher temperature ratio condition, the "stems" of the mushroom-type axial vortices are still visible, denoting less azimuthal mixing there. However the temperature of the peripheral hot-spots in the tongue-mixer are less than half of that in the 12CL mixer (compare Figures 4.10(a) and 4.10(b)). This means that the tongue-mixer has much more vigorous mixing and dissipation than 12CL.

We can also compare this data with the CFD-simulation of the tongue-mixer at a *lower* nozzle pressure and temperature ratio in Figure 2.24(b) at the nozzle-exit ("X"/L = 1.0 where "X" is from the mixer exit plane and L is the mixing length). Some similarities and some dissimilarities are observed. For example, the size and location of the outer hot-spot and its "stem" are well-captured -- the hot-spot is expected to radially migrate further when it reaches X/D = 0.2, as in Figure 4.10(a). However, the central hot-spot is not captured in the CFD-simulation, where, instead, CFD-results show a thin hot annular ring and a cold spot at the center. This is probably due to the problems in CFD simulation near the central axis of the cylindrical domain of computation.

Figure 4.10(b) for mixer 12CL can also be compared to the static case for 12CL at lower pressure ratios (Figure 4.9(a)). This comparison shows that, even at higher nozzle pressure and temperature ratios the radial location of the axial vortices has not changed much, implying that the vortex position is strongly dictated by the lobe penetration at all operating conditions. In addition, the central hot-spot has not

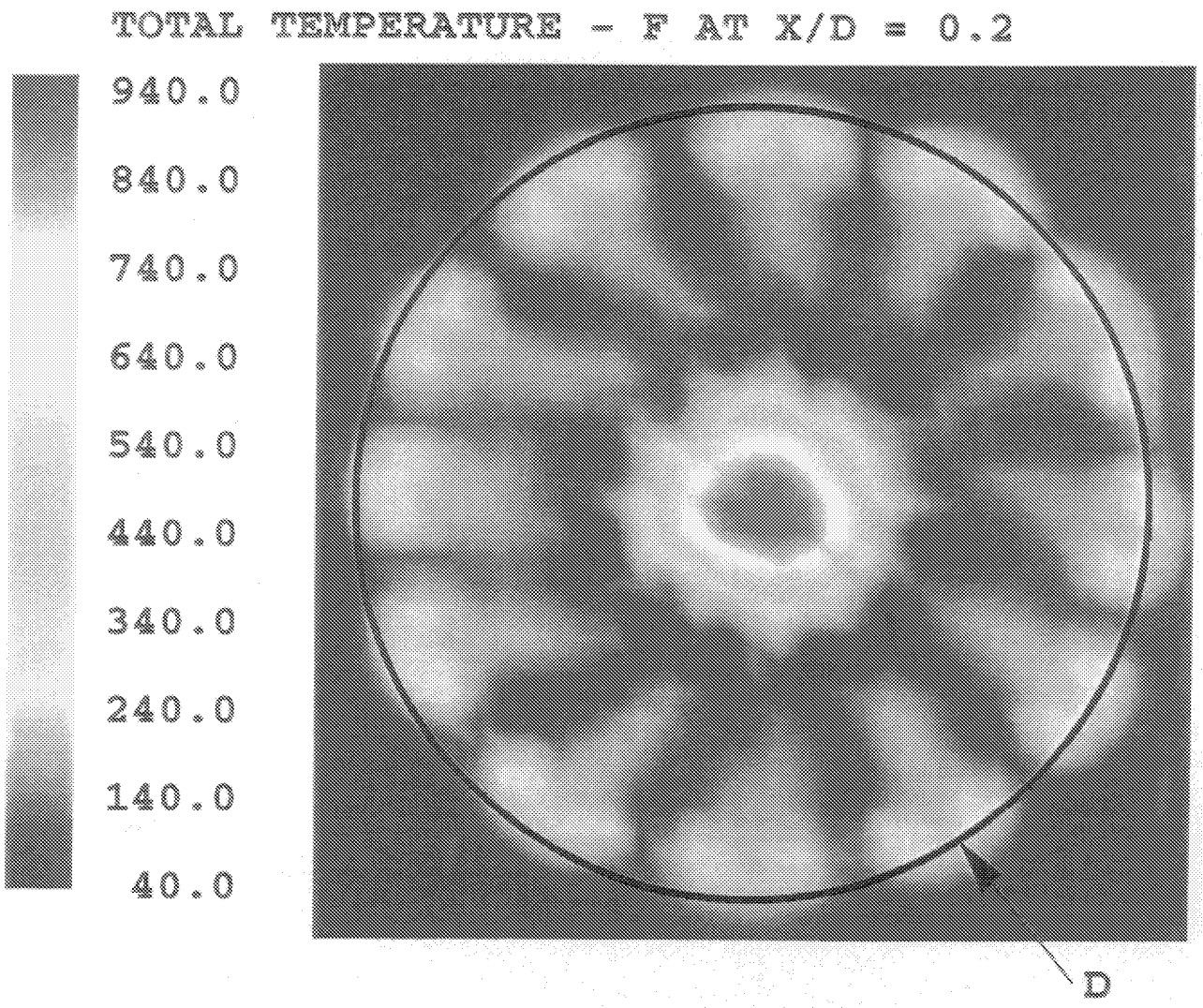

Figure 4.10(a) Total temperature contours for the tongue mixer with 100% nozzle-length at X/D = 0.2.

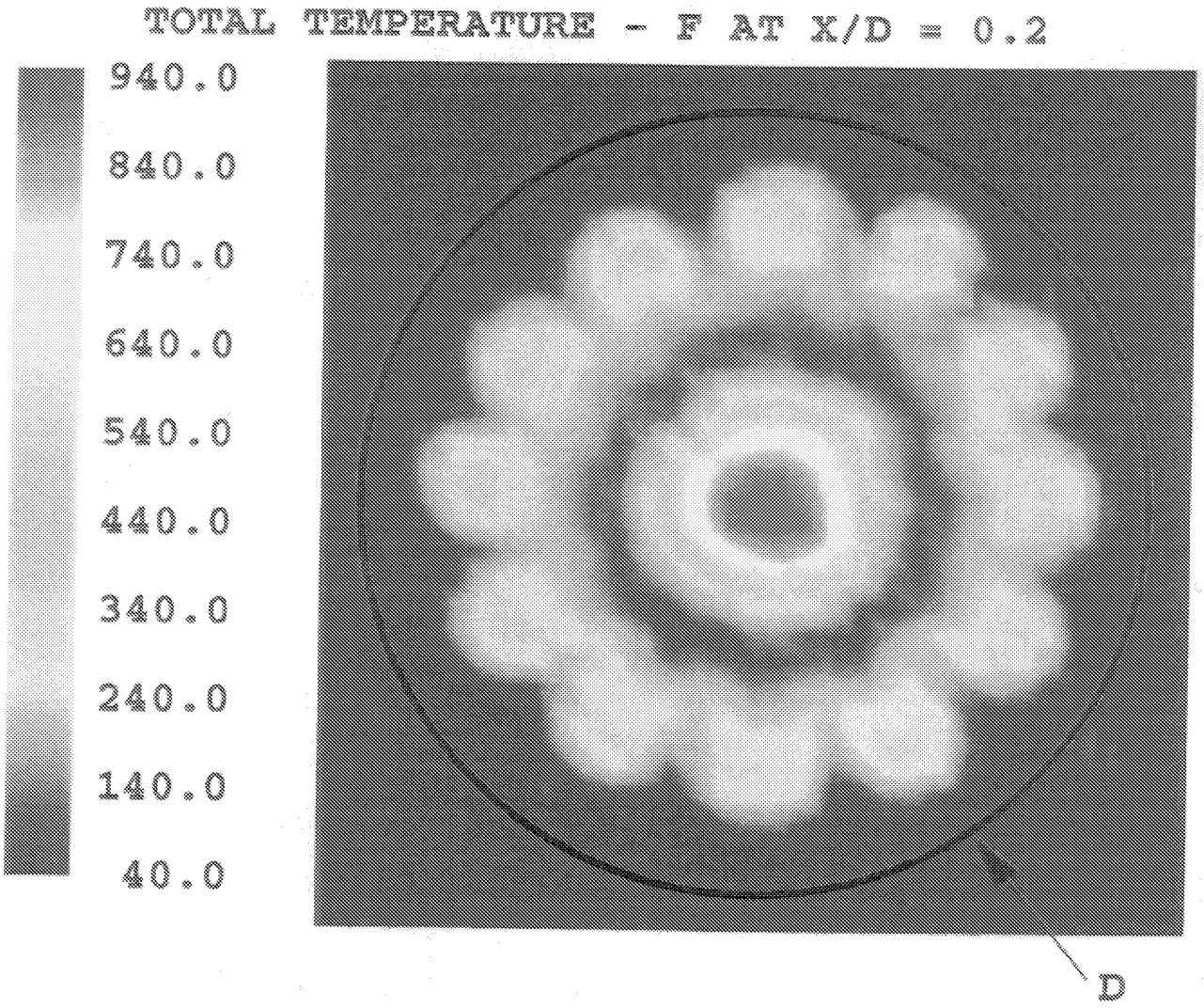

Figure 4.10(b) Total temperature contours for 12CL mixer with 100% nozzle-length at X/D = 0.2.

diffused at all at this axial station. Note that in both mixers (12CL and 12TH), since a "core" lobe is at the 12 o'clock position and there are 12 hot-spots in Figure 4.10, the axial vortices from the neighboring lobe sidewalls of a "core" lobe, although of opposite signs, coalesce first rather than those from a "fan" lobe. It is only further downstream that all these 12 hot-spots merge azimuthally to form an annular ring of higher temperature implying that the jets will quickly become axisymmetric. This axisymmetry will be more evident in the next section. The radial temperature gradients, however, are also unsteady entropy regions and, thus, generators of extra noise beyond that created by radial gradients in velocity. It should also be noted that although a free jet flow is present (M_{fj} = 0.2) the overall hot-spot structure has not changed much from the static case (Figure 4.9(a)), presumably because with low lobe penetration the axial vortices are still away from the growing nozzle-lip shear layer.

4.2.3 Plume Downstream Evolution

The downstream evolution of the plume velocity profile for mixer 12CL at operating condition TO #3 and M_{fj} = 0.2 is shown in Figure 4.11 at Y = 0.0 and several downstream stations. [Note that the measurements are obtained on a rectangular Cartesian grid with Y in the horizontal direction in the transverse plane and Z in the vertical direction in this plane. Hence, plots for constant Y-values are along vertical "chords" lines and not radial lines. Y = 0 with variable Z values represents measurements along a vertical diameter which passes through the top and bottom "core" lobes.] The plume velocity is calculated from the measured P_t, P_s and T_t values and the isentropic relations.

Some general observations follow from Figure 4.11:

(i) The initial complicated structure of the velocity profiles at lower X/D-values quickly gives way to a simpler plume further downstream. Although not shown here but evident from the detailed profiles shown at various Y-values in Vol. 2, part 1, figures 40 - 46, the plume quickly becomes axisymmetric further downstream.

(ii) The radial gradients in axial velocity govern part of the turbulence intensity and, hence, are strong sources of noise. Thus, the plume will generate noise not only from the radial gradient in velocity at the nozzle-lip shear-layer but also from these axial vortex structures, hot-spots and the central velocity peak. These are "excess" noise sources, in the sense, that they will not occur in a jet with an equivalent uniform velocity and temperature profile at the nozzle-exit plane.

(iii) The thickening of the lip shear-layer downstream is evident from the decreasing radial slope of the velocity profiles near Z = ± 3.625 in.

The center-line velocity decay will be examined in a later section where it will be compared with other mixers.

4.2.4 Effect of Scalloping

Figures 4.12(a) and (b) show the typical effect of scalloping on the total temperature profiles at X/D = 0.2 for the lower nozzle pressure ratio condition of TO #1 with M_{fj} = 0.2. The peripheral hot-spots in the unscalloped mixer (20UH) diffuse out into

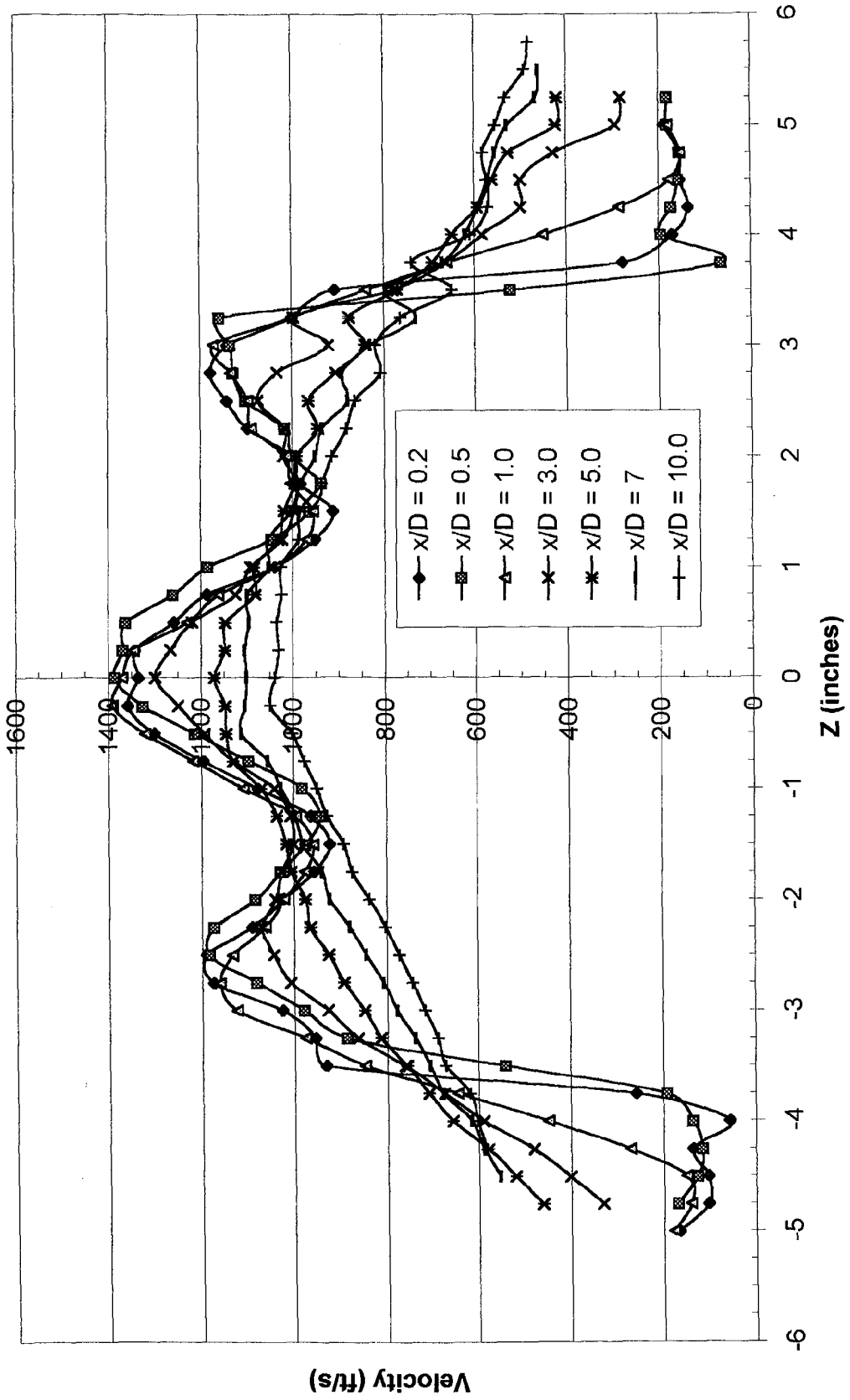

Figure 4.11 Typical radial plume survey for axial evolution of velocity profile at Y = 0.0 in. for 12CL mixer with 100% nozzle-length.

Figure 4.12(a). Non-dimensional total temperature profiles for 20UH mixer with 100% nozzle length at X/D=0.2 for TO #1 at M(fj)=0.2. [The vertical axis is zoomed in to amplify the peripheral hot-spot structure. Highest central axis eta is 0.887.]

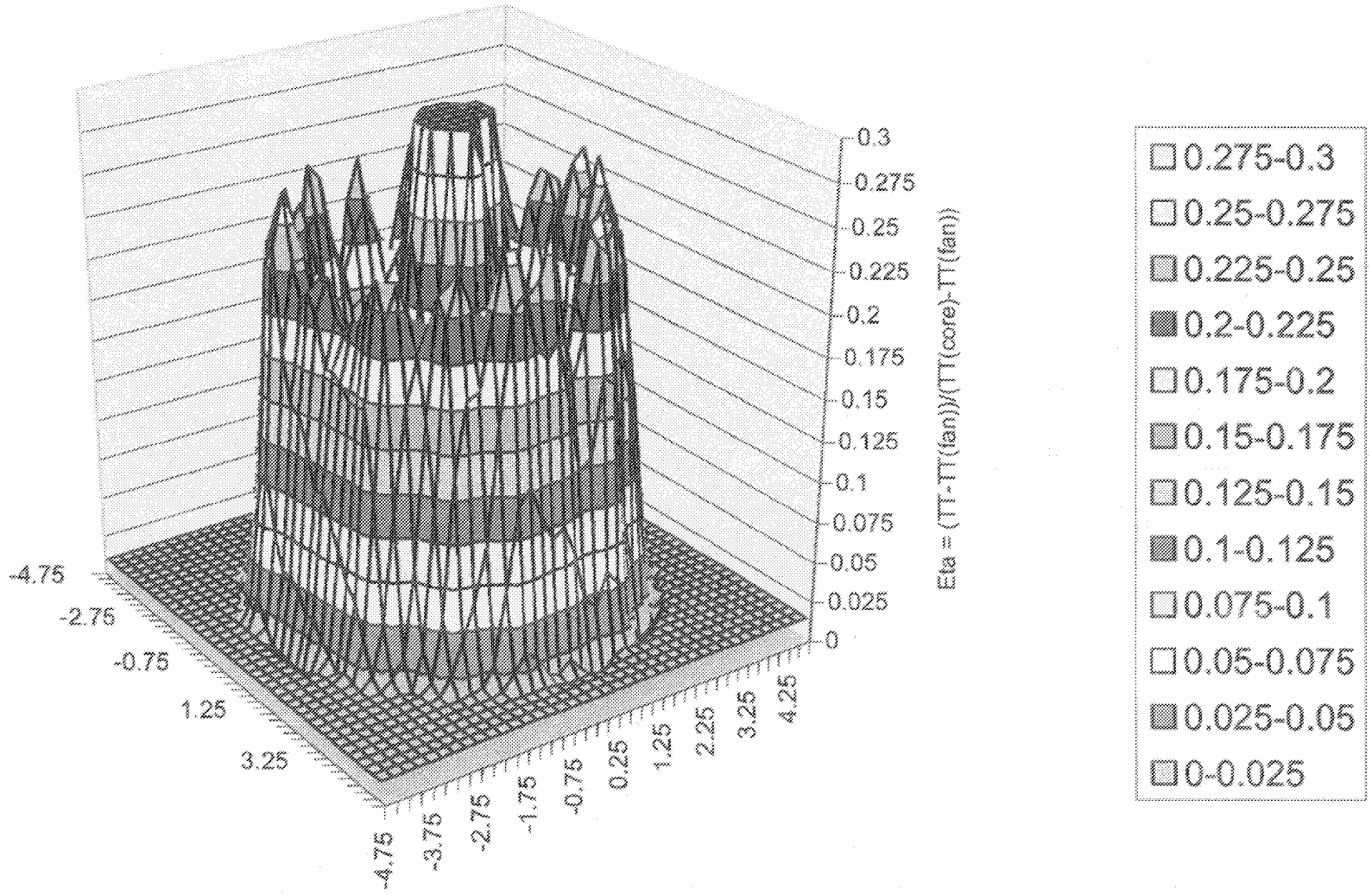

Figure 4.12(b). Non-dimensional total temperature profiles for 20DH mixer with 100% nozzle length at X/D = 0.2 for TO #1 at M(fj) = 0.2. [The vertical axis is zoomed in to amplify the peripheral hot-spot structure. Highest central axis eta is 0.9216.]

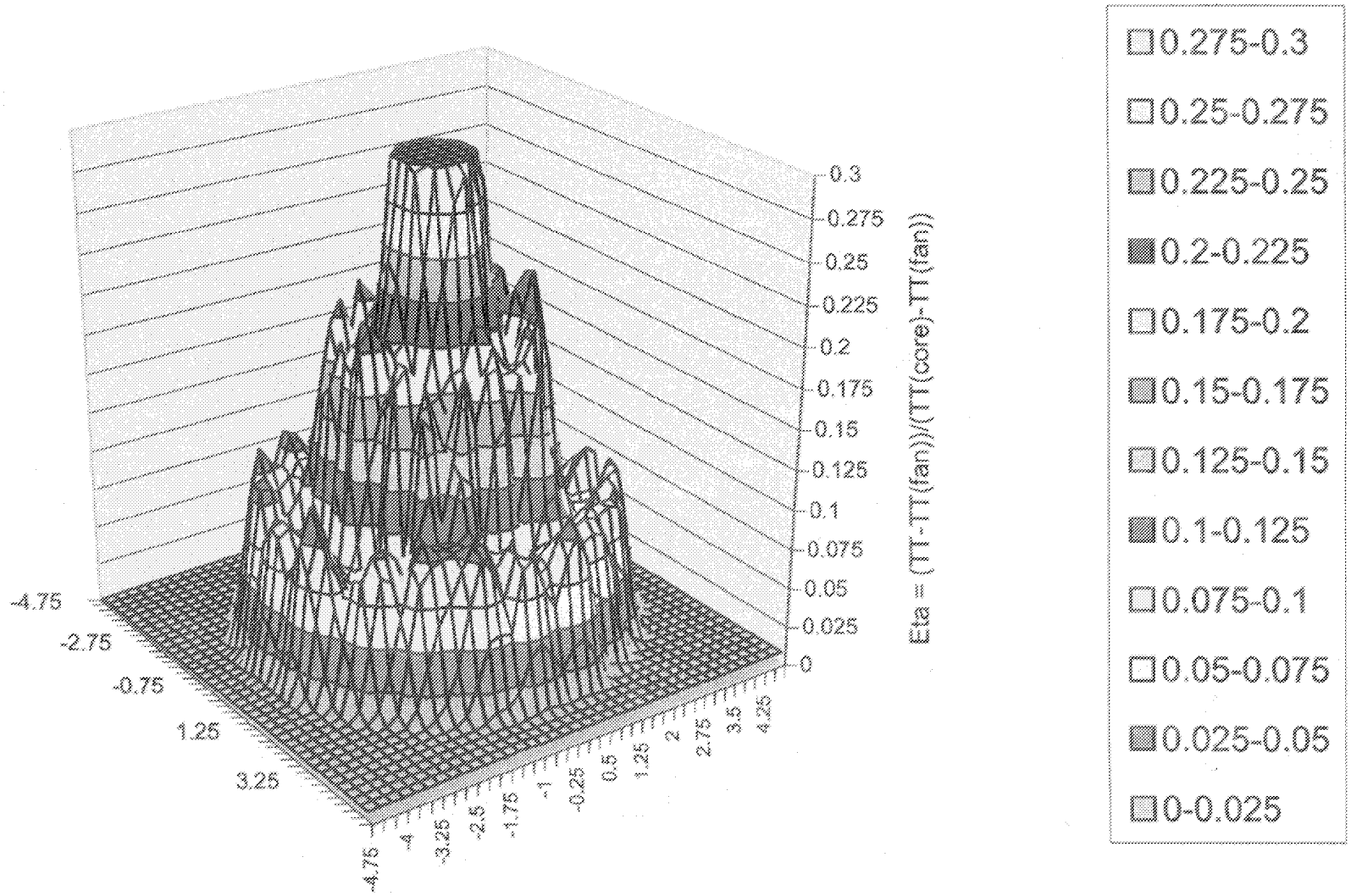

two smaller humps for the deeply scalloped mixer (20DH). Comparing the data of Figure 4.12(b) with the CFD simulation for the 20DH mixer configuration in Figure 2.21(b), it appears that the hot-spot of 20UH at Z= ± 3.0 in. has actually migrated radially outward in the 20DH mixer and is reduced in strength. At the same time, the second inward hot-spot in 20DH at Z = ±1.75 in. with strength *Eta* = 0.2 is from the "stem" of the mushroom vortex seen in Figure 2.21(b). In any case, although scalloping appears to weaken the outer hot-spots, the central hot-spot is not affected. The central hot-spot, as mentioned earlier, is primarily a function of the gap between the lowest portion of the lobes and the tailcone surface and which is the same in 20UH and 20DH.

Figure 4.13 shows the velocity profile for the deeply scalloped mixer (20DH) at the axial location X/D = 0.2. The peripheral velocity is very well-mixed as compared to that of mixer 12CL (Figure 4.11(a)). The unscalloped mixer (20UH), with larger peripheral humps in the temperature, is not expected to be as uniform as 20DH. The central region in Figure 4.13, on the other hand, still shows a small hump in the velocity profile of 20DH which would, indeed, act as an "excess" noise source due to shear.

4.2.5 Effect of Nozzle-Length

We compare the effect of halving the mixing-length using data for the 12CL mixer. Since reducing the nozzle-length from 100%L to 50%L for 12CL also surprisingly reduced noise (Section 5.6.2) we will study the plume profiles for these two nozzle lengths in more detail.

Figure 4.14 shows the total temperature contours at X/D = 0.2 for the 12CL mixer with a 50% nozzle length at performance condition TO #3 and M_{fj} = 0.2. Compare this with 100%L at same X/D = 0.2 (Figure 4.10(b)). It appears that 50%L is not as well-mixed as 100%L as expected. In the 50%L case, the "stems" of the mushroom axial vortices are still visible, the hot-spots on the periphery are still well separated azimuthally, and the central hot-spot is slightly larger. Further downstream at X/D=0.5 the same differences between 100%L and 50%L are still observed (see Figures 5, 6 in Volume 2, part 2). Thus, with a shorter mixing-length we can safely conclude that the flow is not as well mixed as with the longer mixing-length at the same distance from the nozzle exit-plane.

Comparison of velocity profiles for the two nozzle lengths at X/D = 0.2 for operating condition TO #3 is shown in Figures 4.15 (a) and (b). The local velocity peaks at the periphery for the 50% nozzle-length appears higher than for 100%L (compare Z = -2.25 in.) implying less mixing with the shorter nozzle-length.

The above comparisons were done at the same distance from the nozzle exit plane. Since mixing between the fan and the core streams begins at the mixer exit plane as opposed to the nozzle-exit plane, it is more instructive to compare the flow profiles between the two nozzle lengths at same distance from the mixer exit plane. This will also bring out the effect of removing the nozzle-duct in the aft portion of the mixing-length and exposing the partially mixed flow to the ambient pressure sooner. In both nozzle-length cases, since data was taken only at discrete axial locations (X/D-values of 0.2, 0.5, 1.0, 3.0, 5.0, 7.5 and 10.0) and L/D = 1.555 for the baseline nozzle, it turns out that there is only one axial location where data exists at approximately the same

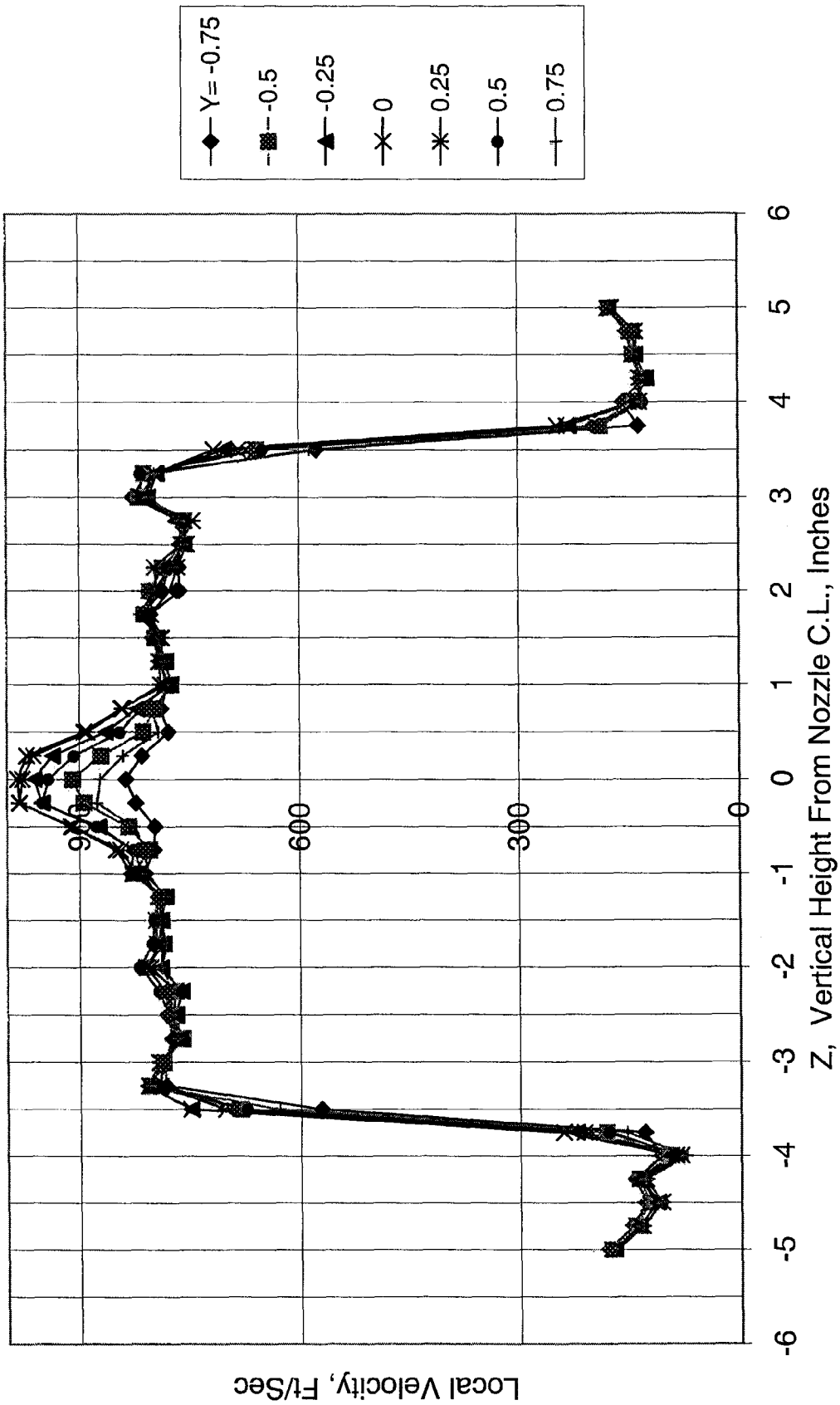

Figure 4.13(a) Vertical chordwise velocity profiles for 20DH mixer with 100% nozzle length at X/D=0.2 for TO #1, M(fj) = 0.2.

Figure 4.13(b). 3d velocity profiles for 20DH mixer with 100% nozzle length at X/D=0.2 for TO #1, M(fj) = 0.2.

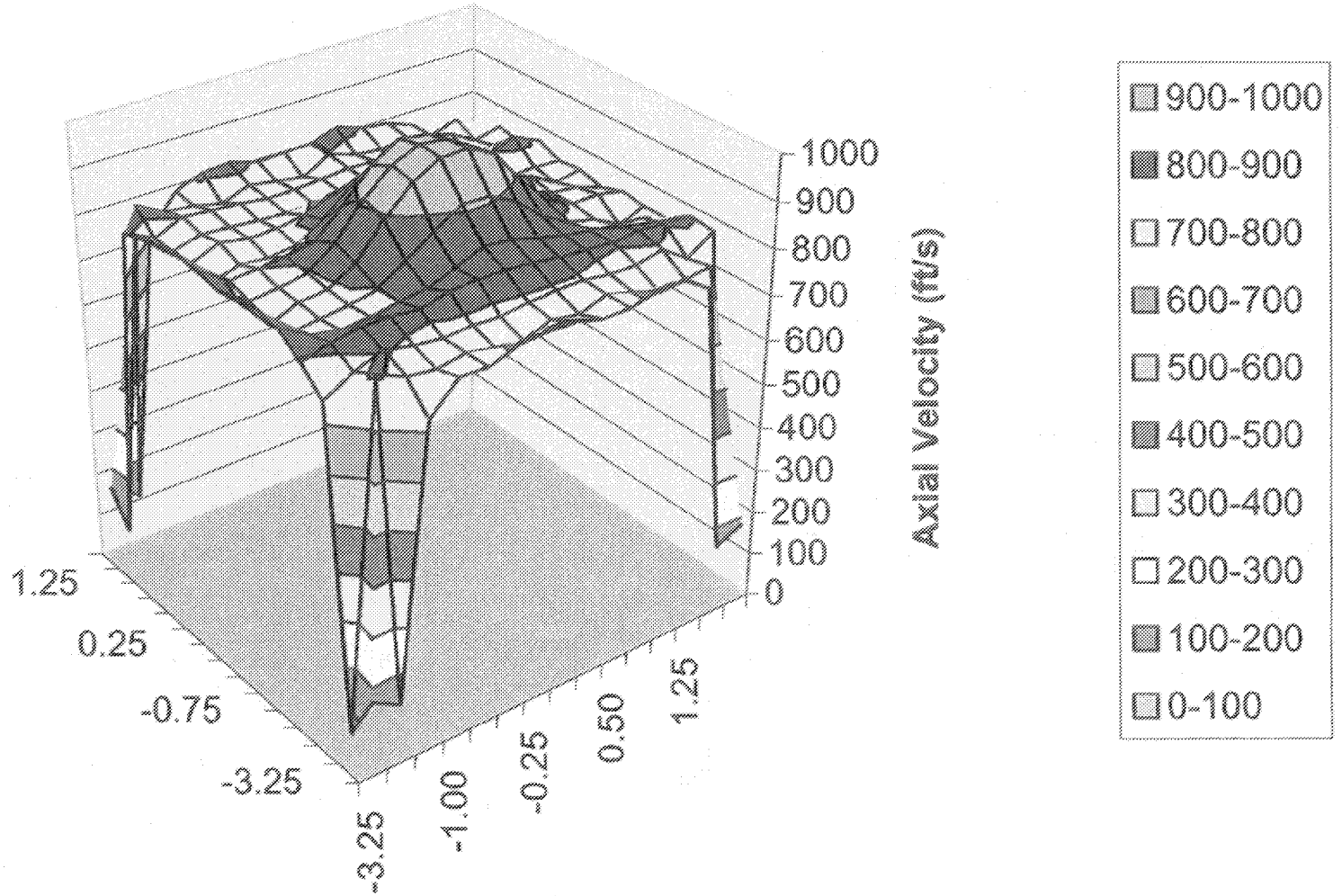

Figure 4.15(a) Vertical chordwise velocity profiles for 12CL mixer with 100% nozzle length at X/D=0.2 for TO #3 at M(fj) = 0.2.

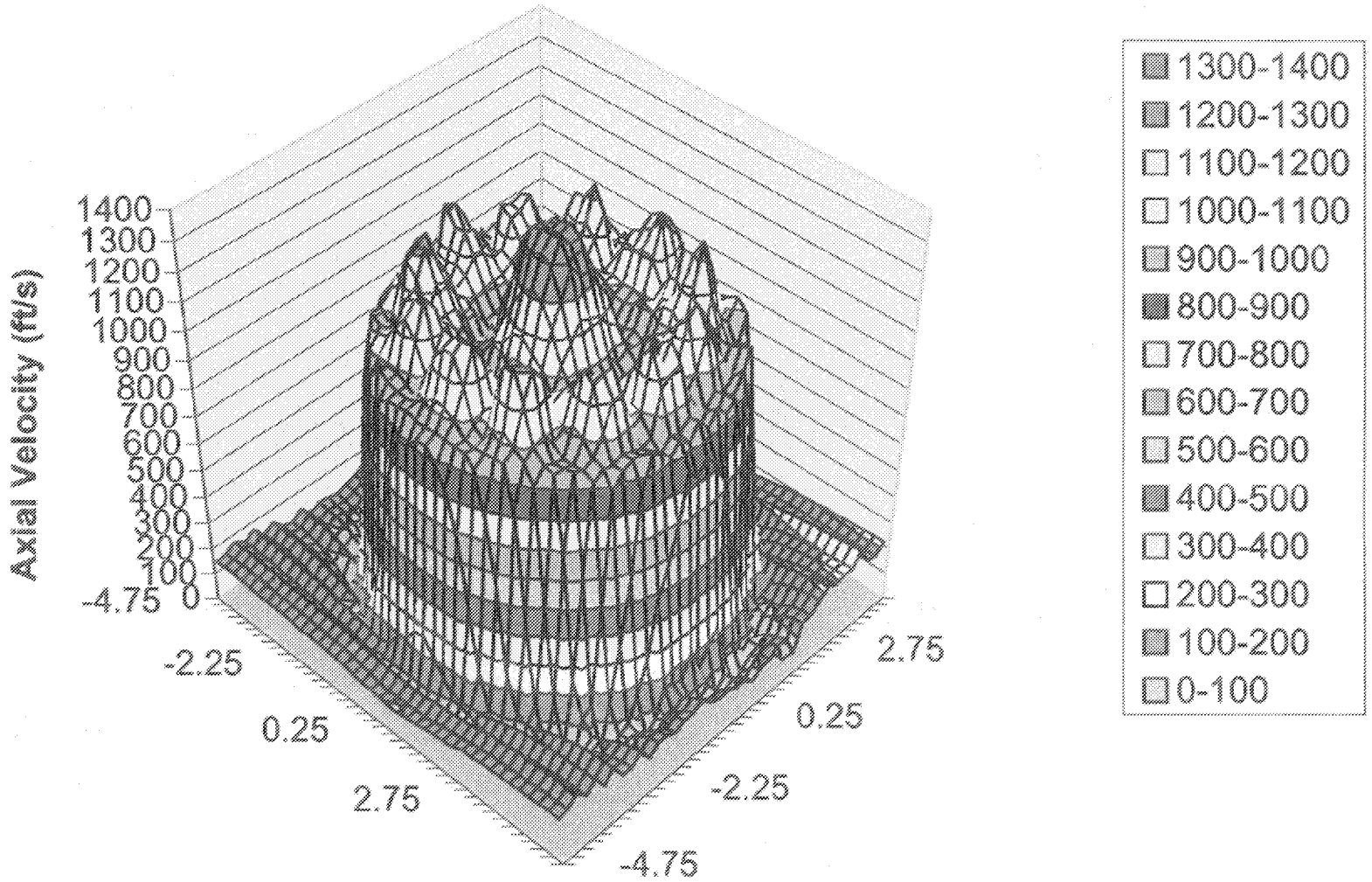

Figure 4.15(b) 3d velocity profiles for 12CL mixer with 50% nozzle length at X/D = 0.2 for TO #3 at M(fj) = 0.2.

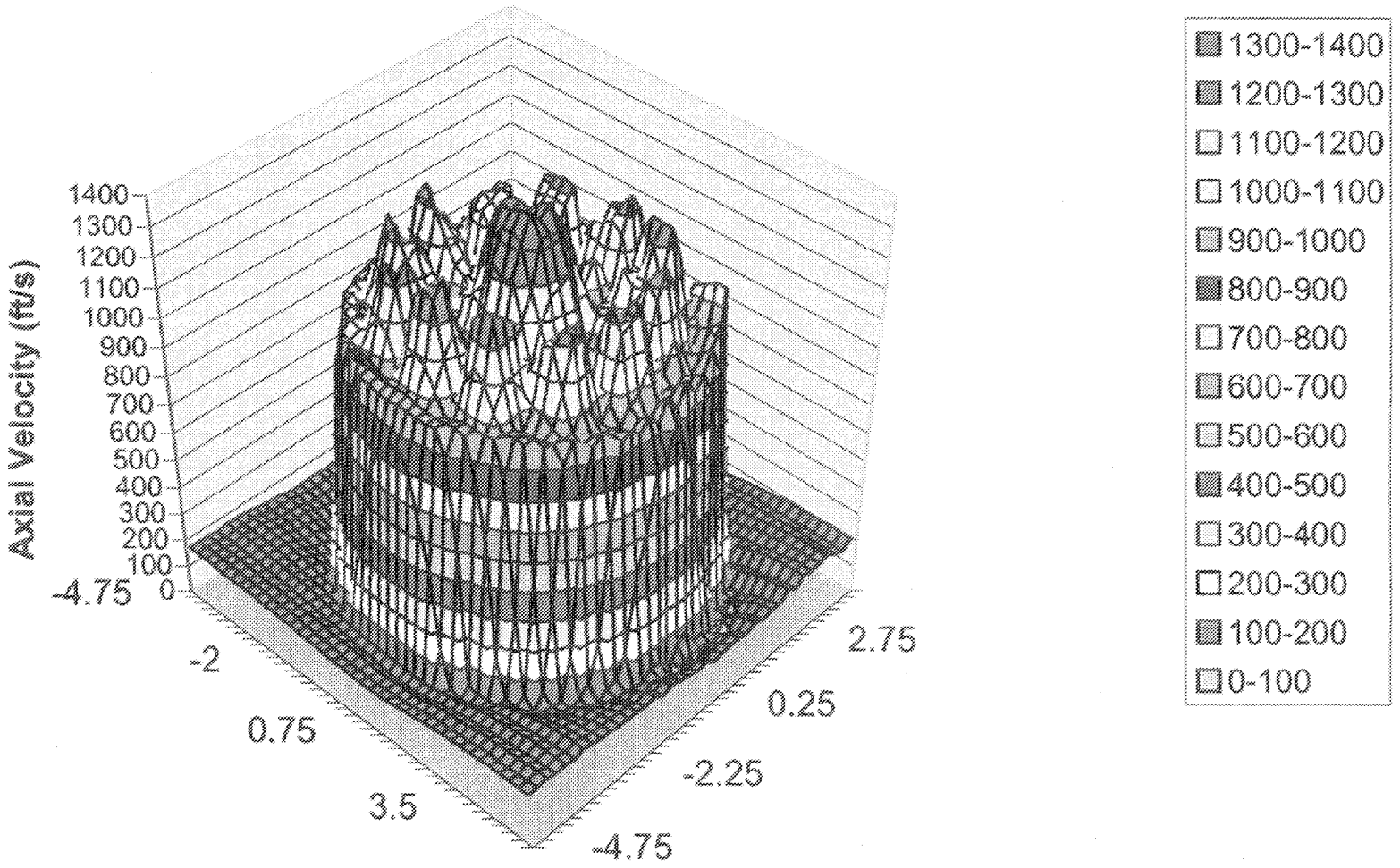

distance from the mixer-exit plane for the 100%L and 50%L configurations. An axial location of X/D = 0.2 for the 100%L nozzle corresponds approximately to X/D = 1.0 for the 50%L nozzle. Figures 4.16 (a) and (b) show a comparison of the velocities at these two axial locations at different values of Y in the transverse plane for the two nozzle-length configurations with mixer 12CL installed. It is very interesting to see that the mean velocity profiles, at all Y-locations shown, match very well indeed - except for a small shift in the Z-direction for local peaks.

Since the flow at X/D = 0.2 for the 100%L nozzle is still adjusting to the ambient pressure, having only been recently released from the nozzle, there may be statistical variations even in the measured mean flow. Hence, it may be better to compare the flow profiles for these two configurations with different nozzle-lengths further downstream when flows from both the nozzle-configurations have had sufficient time to adjust to the surrounding environment. However, as mentioned earlier, we do not have comparable data for both cases further downstream at the same distance from the mixer exit plane. Hence, we will compare only the center-line velocities for these two cases after appropriately shifting their axial locations so that now they are referenced from the mixer exit plane. Figure 4.17 shows this comparison for the center-line velocities where simple linear interpolation is used between data points. Apart from the initial small variations, the center-line velocities for 100%L and 50%L match rather well for $X_{\text{mixer exit plane}}/D \geq 4.0$.

Figures 4.16 and 4.17 imply the following:

(i) The appropriate axial distance when comparing flows from mixer-nozzle configurations of different mixing-lengths is not relative to the nozzle-exit plane, but is rather from the mixer-exit plane.

(ii) Removing the aft-half of the duct length in the internal mixing region for mixer 12CL has little effect on the mean velocity profiles at the same distance from the mixer-exit plane when compared downstream of the longer nozzle. Hence the noise radiating from the far downstream portion of the two nozzles ought to be similar, whereas the difference in the noise spectra between the two nozzles should be attributed to stations upstream of at least X/D = 0.2 (with reference to baseline nozzle), that is, to stations close to the nozzle exit plane both inside and outside the nozzle duct.

As will be seen in the next chapter, this is borne out for the two nozzles, respectively, in the *similarity* of the low frequency spectra radiating mainly from the large eddies in the far downstream region and the *dissimilarity* of the high frequency spectra corresponding to the small-scale eddies near the nozzle exit plane

4.2.6 Center-line Velocity Comparisons

In these lobed mixers we have seen that the initial non-axisymmetric flow profiles become axisymmetric a short distance downstream of the nozzle exit due to the good azimuthal mixing produced by the axial vortices. Hence, a center-line velocity decay comparison can give a fair idea of the overall relative noise levels produced by these mixers, especially the plume decay far downstream where larger eddies govern the low frequencies. With this in mind, we compare the "center-line" velocities for a few mixer-nozzle configurations in Figure

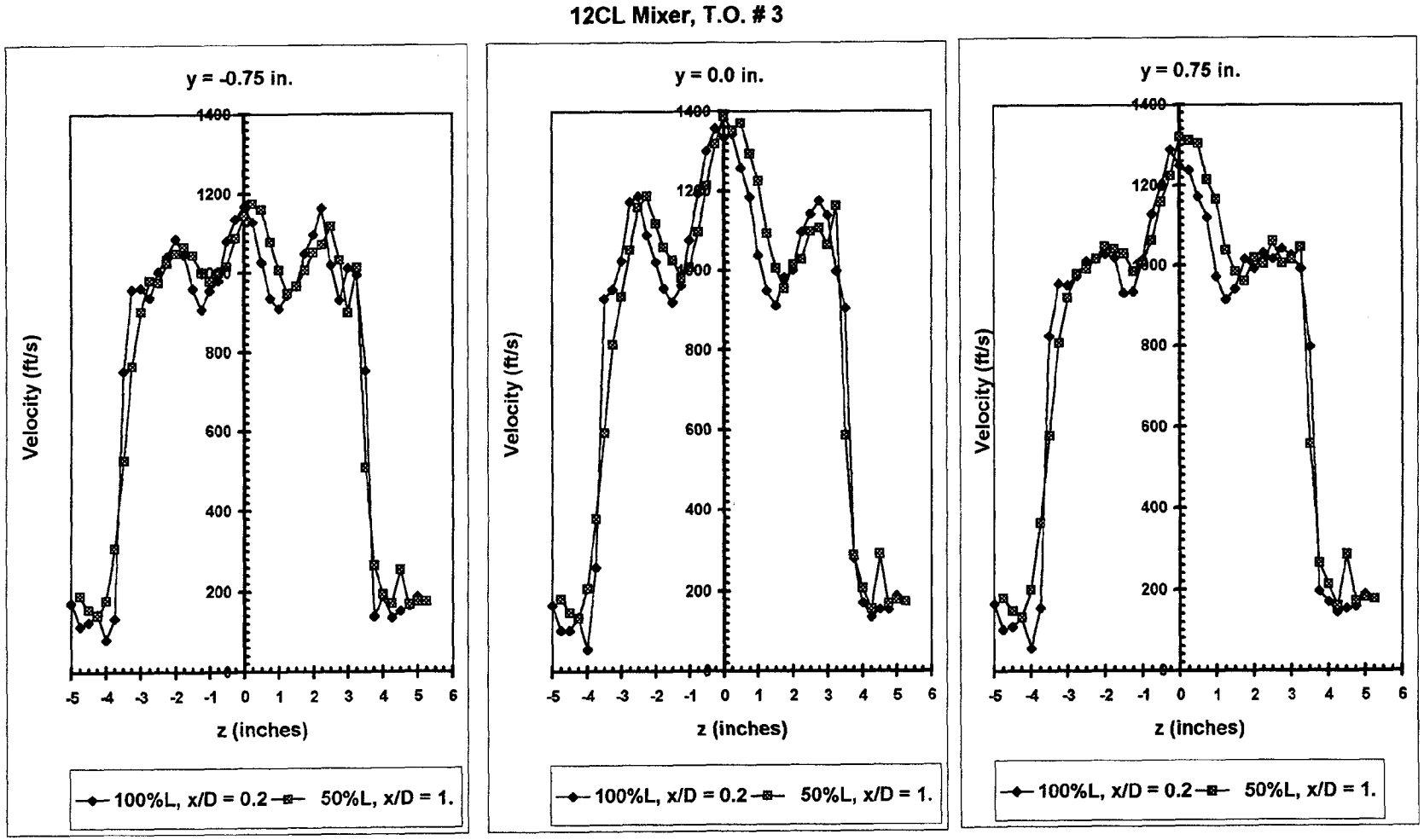

Figure 4.16(a) Comparison of velocity profiles for different nozzle-lengths at same distance from the mixer exit plane for 12CL mixer at T.O. # 3 at M_{fj} = 0.2 at y = - 0.75 in., 0.0 in. and +0.75 in.

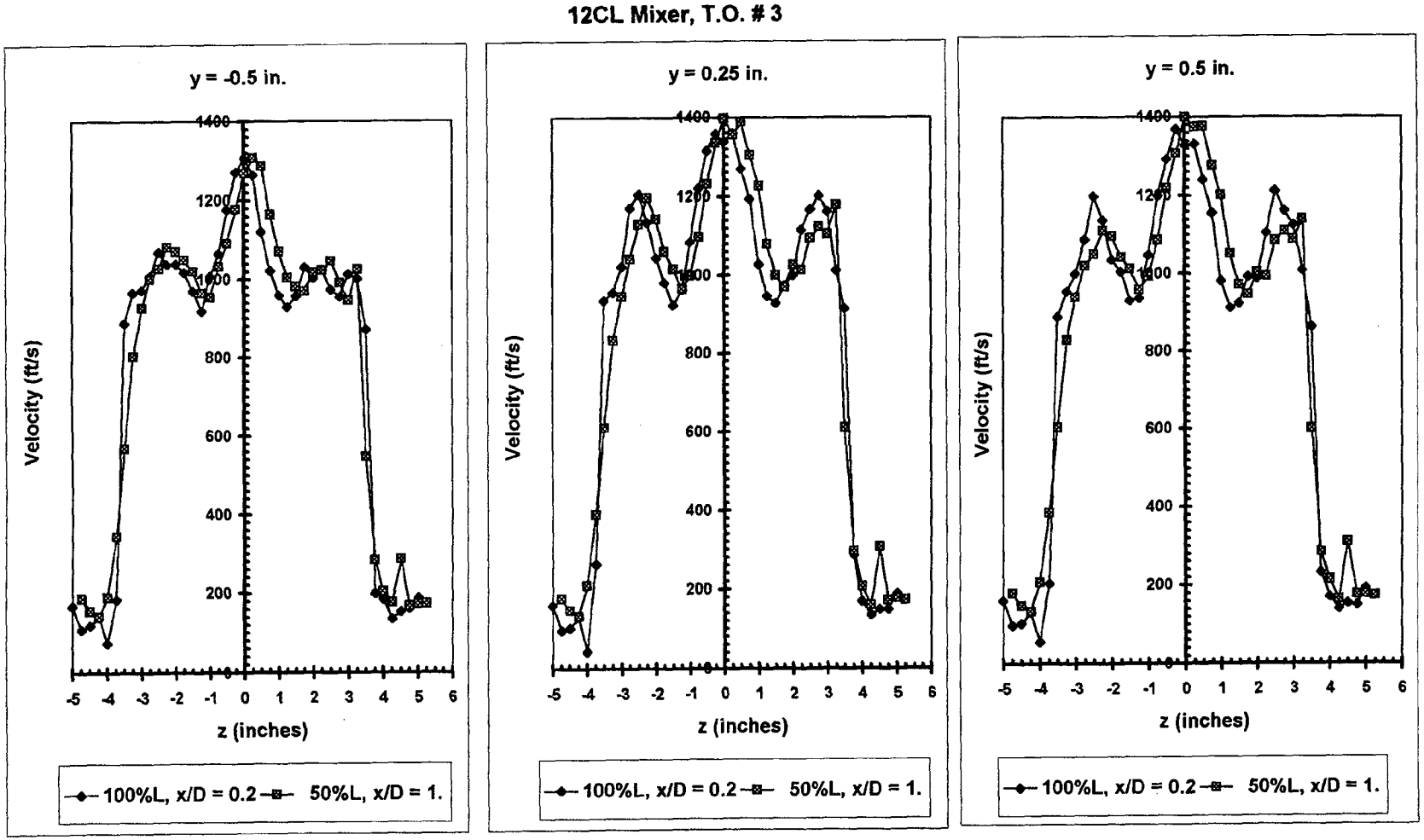

Figure 4.16(b) Comparison of velocity profiles for different nozzle-lengths at same distance from the mixer exit plane for 12CL mixer at T.O. # 3 at M_{fj} = 0.2 at y = - 0.5 in., 0.25 in. and +0.5 in.

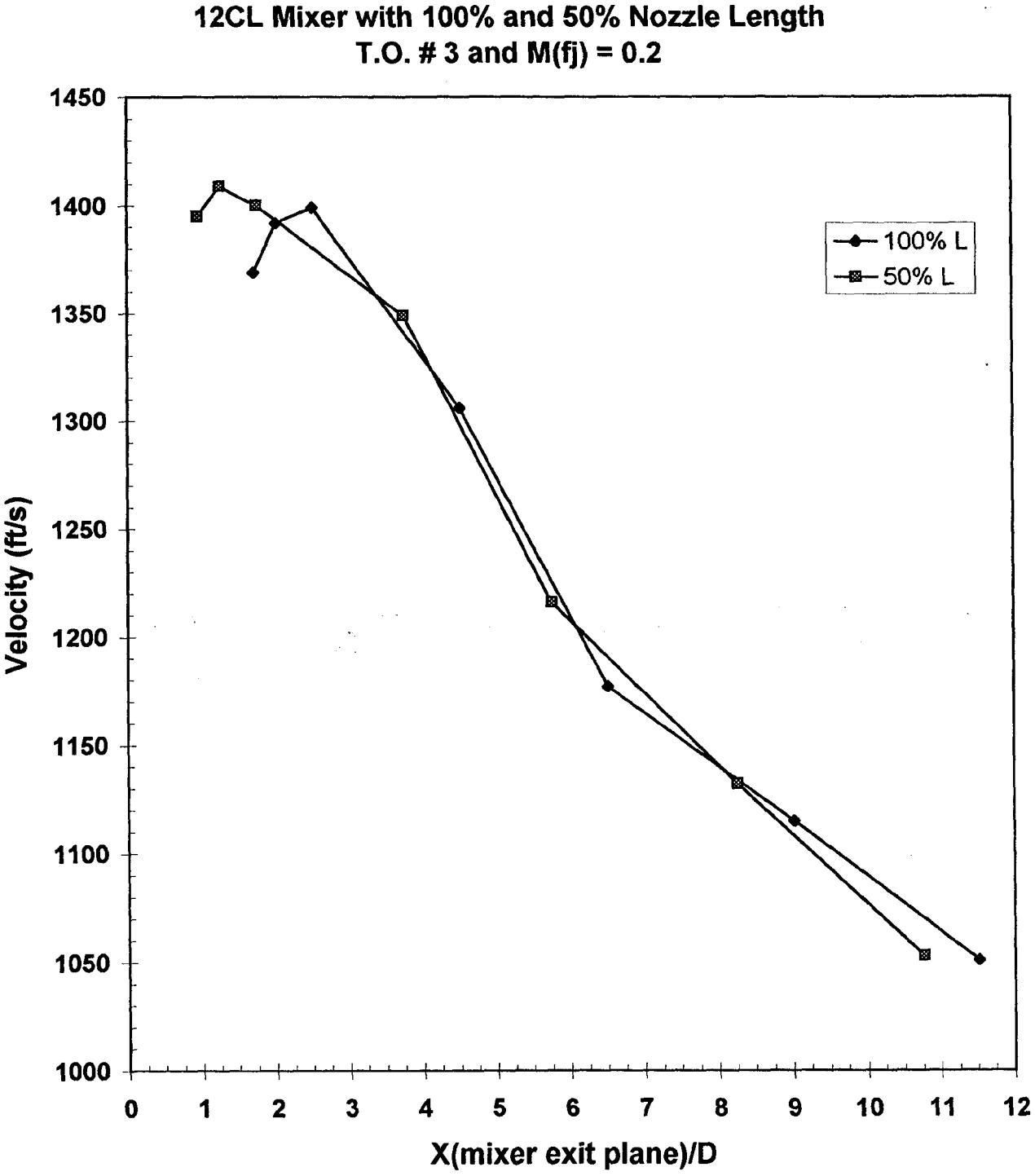

Figure 4.17 Comparison of center-line velocities at same distance from the mixer exit plane for nozzles with different lengths.

4.18 with semi-log axes for performance condition TO #1 and Figure 4.19 for TO #2 and #3 at $M_{fj} = 0.2$.

From Figure 4.18 we observe that for all mixers there is only a very short-distance ($X/D \leq 1.0$), beyond the nozzle exit plane, where the center-line velocity is constant, downstream of this location it starts decaying. This does not represent a "potential" core in the normal sense, as we have seen in Figures 4.11, 4.13 or 4.15, but simply a small portion of the hot core fluid which flows over the tail-cone and which quickly mixes with the surrounding fan flow downstream. The center-line velocities between the 12-lobed mixers and the 20-lobed mixers are distinctly different in the beginning with a reduction in magnitude of about 50 ft/s for the 20-lobed mixers. However, further downstream, around X/D of 8, all the mixers seem to have similar center-line velocities. It should be noted that if the 100%L and 50%L configurations for 12CL are shifted to correspond to the distance from the mixer-exit plane, they overlap as before in Figure 4.17.

Figure 4.19 for the higher nozzle pressure ratios shows similar trends, however with larger differences in the initial magnitudes which decay to the same levels at $X/D = 8$.

We have discussed in this section only some of the most pertinent plume-survey data. Volume 2 contains the rest of the data collected and should be referred to as the need arises in understanding the acoustic data discussed in the next chapter.

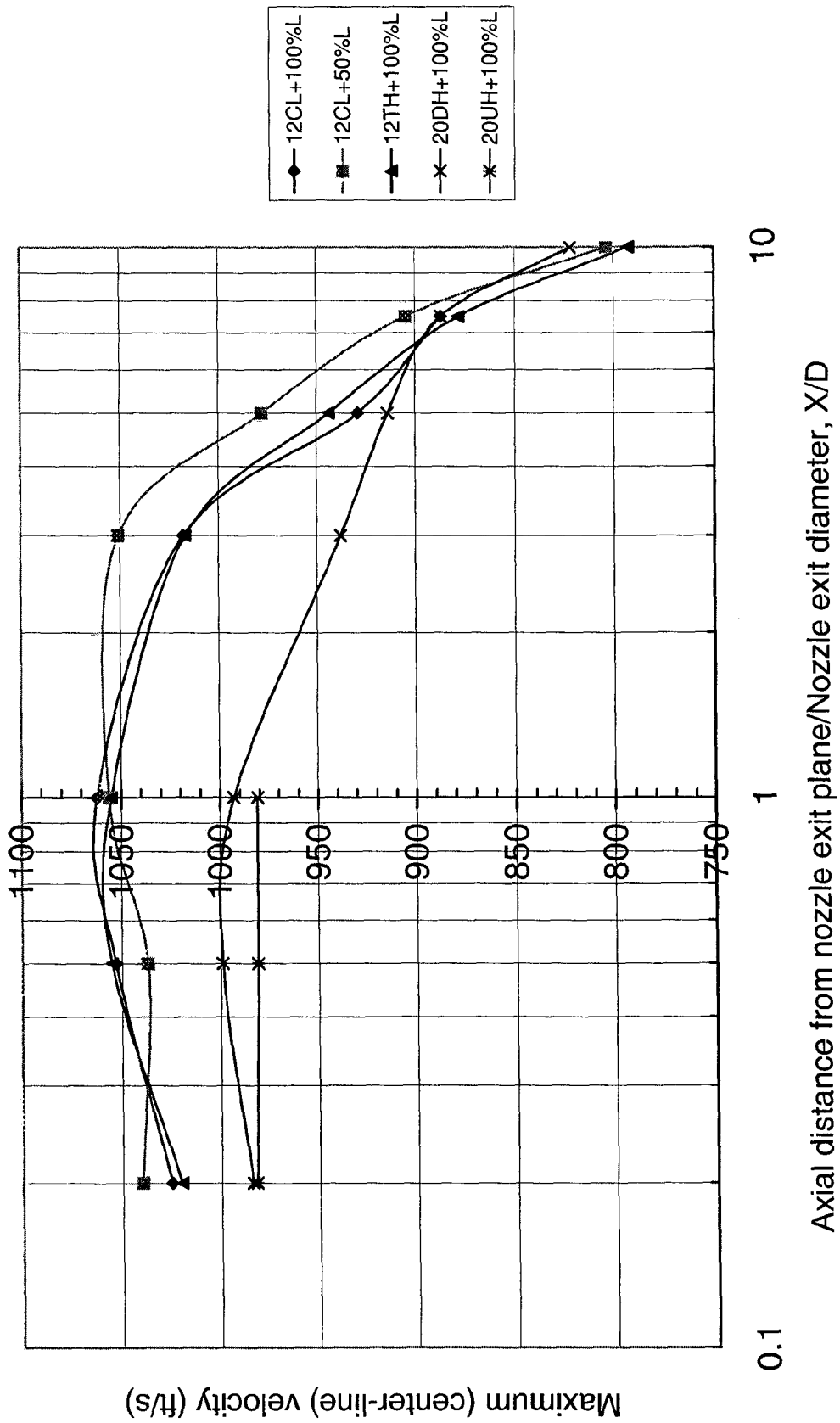

Figure 4.18 Comparison of maximum (center-line) velocity decay for several mixers at TO#1 and M(fj) = 0.2.

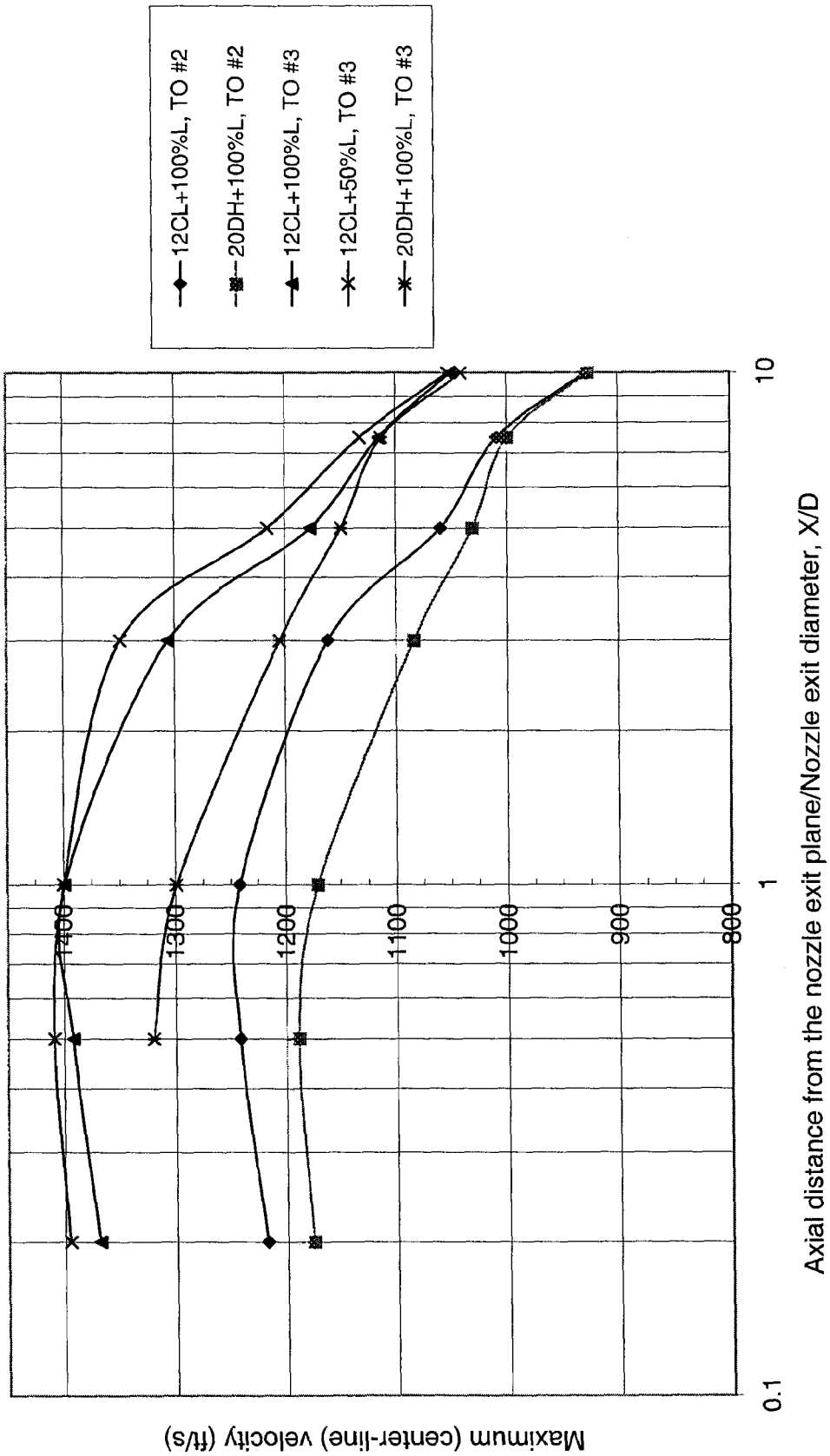

Figure 4.19 Comparison of maximum (center-line) velocity decay for 12CL and 20DH mixers at TO #2 and TO #3 at M(fj) = 0.2

Chapter 5

Acoustics Results & Analysis

5.1 Overview

The acoustic results for the various mixers are presented and analyzed in this chapter. Due to the vast amount of data collected, representing variations in a number of different parameters including both operating conditions and mixer-nozzle geometry, systematic presentation of results to isolate parametric trends was a major challenge.

In order to capture the effects of mixer geometry between the two sets of lobed mixers (the original four designs from 1995 and the new configurations from 1996), results will be presented in terms of 3 general groupings (see Tables 2.1 and 2.2 for nomenclature and mixer properties):

Group 1. All 12 lobed configurations (12CL, 12UH, 12TH).
Group 2. All unscalloped configurations (12UH, 16UH, 20UH).
Group 3. All 20 lobed configurations (20UH, 20MH, 20DH).

Group 1 examines the compound effects of penetration and sidewall cutouts (with the tongue mixer configuration (12TH) representing, in some sense, the limiting case of deep scalloping). Group 2 examines the importance of lobe number, while Group 3 isolates the effect of sidewall scalloping. In addition, comparisons between members of different groupings are also used to illustrate particular points. In all cases, the confluent or coaxial mixer (CONF) is taken as the baseline configuration.

Initially, comparisons between the mixer configurations will be made with the reference nozzle length (100%L) and free-jet Mach number of 0.2. In the second phase, the effects of free-jet speed on far-field noise will be examined. In that section, a new method for diagnosing the location of high-frequency noise sources is presented and its importance examined. Finally, the effect of nozzle length on the noise produced by each of the mixer configurations is examined, with some new and interesting findings presented. All results presented are for a nozzle with an exit cross sectional area of 660.5 in^2 (or 29 inches diameter), representing a scale factor of four.

While analyzing these acoustic results, two questions arise: (a) How and why do the "noise source characteristics" change with the parameter being examined? (b) How "important" is that parametric effect? The first question is answered by examining the far field noise characteristics in the "reference frame of the nozzle". By this, we mean the sound pressure or sound power spectra whose directivity characteristics have been adjusted to remove the refraction effects which occur across the shear layer at the free-jet/ambient interface. This data is presented on a circle of 150 ft radius whose center is coincident with the center of the nozzle exit plane. All such polar data has been corrected to reference conditions of 14.3 psi, 77°F and 70% relative humidity. The polar spectrum has no Doppler-shift corrections applied. The second question, relating to the "importance" of a particular parameter, is examined using perceived

noise level (PNL) and effective perceived noise level (EPNL) and the corresponding sound pressure level as observed by a ground based observer during a simulated flyover of the test nozzle at a fixed altitude of 1500 ft For this flyover simulation, the SPL spectra is appropriately adjusted for slant distance propagation effects, standard day atmospheric attenuation, Doppler shift due to aircraft motion relative to the observer, and an ambient pressure at standard day of 14.7 psia. For the Doppler shift, the aircraft is assumed to fly at the velocity of the free jet appropriate to the test point considered. In addition, the ground around the observer is assumed to be non-reflecting.

As mentioned earlier, the second acoustic test done at NASA in 1996 repeated most of the data-points done in 1995 and added many more operating points, and thus, in many ways, superseded the previous test data. We present and analyze in this report only the 1996 acoustic test results. Some of the 1995 acoustic test results have been reported in Mengle et al[16] and should be consulted for the sake of completeness.

A few general things to be kept in mind while considering these data are:

(i) When comparing acoustics of different mixers at the same operating conditions we may not necessarily obtain the same mass-flow rates or thrust. These aerodynamic quantities are functions of the geometrical parametric changes, as studied in the previous chapter, and are themselves independent objects of study. Hence, the purpose of these inter-mixer acoustic comparisons at the same operating conditions is primarily to establish the "relative shape" of their acoustic/noise spectra, rather than some global integral acoustic metric. At the end of the chapter, a comparison is presented of their global acoustic metrics, like flyover EPNL, on a consistent basis such as constant thrust, so that an objective measure can be obtained for their acoustic suppression benefits. But that can be done only if data is available at several operating conditions and interpolation of data is assumed. On the other hand, if the mixers differ widely in their geometric properties, for instance area ratio (compare 12UH versus 12TH versus 16UH in Tables 2.1, 2.2), then their mass-flow rates and bypass-ratios are widely different, and inter-mixer comparisons, even though at the same operating conditions, are not apt.

(ii) Effects of other "non-mixer" parameters on a given mixer, such as, nozzle-length or free-jet speed or operating condition can, however, be legitimately studied from an acoustics point of view, although these parameters may change the mass-flow rates, etc.

5.2 Mixers with Reference Nozzle Length at Baseline Take-off Condition

In this section we examine the noise characteristics of the various mixer configurations with the reference (100%) nozzle-length (nominal mixing length L/D_{mp} = 1.10) at a baseline operating condition, TO #1 (nominal NPR_f = 1.44, NPR_c = 1.39 and T_{tc}/T_{tf} = 2.34). Initially, we will concentrate on the noise produced under static (no free jet flow) conditions. At static conditions there is no correction for free-jet/ambient shear-layer refraction and the Doppler effect is not present. Thus a "basic acoustic datum" is created for later comparisons.

5.2.1 Static Free-Jet Data

5.2.1.1 12 Lobed Mixers

Figures 5.1 (a), (b), and (c) present, respectively, (a) the 150 ft polar overall sound pressure level directivity (OASPL) and sound pressure level (SPL) spectra for selected angles, (b) sound power spectra (PWL) and sound pressure level directivity for selected frequencies, and (c) PNL directivity and flyover SPL spectra at selected angles for mixer Group 1 (12 lobe configurations).

The following characteristics stand out in this group under static conditions:

(i) All lobed mixers are quieter for angles between 125° and the jet axis than the confluent (CONF) mixer, as seen in the OASPL data (Figure 5.1(a)).

(ii) With the exception of 12CL, they do this at the expense of increasing OASPL in the upstream quadrant.

(iii) At shallow angles, like 150°, the low frequencies (100-300 Hz) dominate for all mixers as seen in the polar SPL spectra in Figure 5.1(a). This familiar result is produced by the refraction of sound waves *away* from the jet exit axis as they propagate through the negative radial gradient of the axial velocity in the plume. This effect is much stronger for higher frequencies than for lower frequencies. This is a feature typical of all such jets in the similarity region far downstream of the nozzle-exit plane as seen in Chapter 4 plume data. As a result, at 150 ° even though 12UH and 12TH are louder for mid-to-high frequencies (higher than, say, 700 Hz), it is the large decrease in low frequency SPL observed with these mixers that drives their OASPL below that of the confluent or 12CL configuration.

(iv) "Low" frequencies are associated with the strength of "large" eddies which exist far downstream of the nozzle exit. The observation that the SPL spectra for 12UH and 12TH show a reduction in low frequency amplitudes for all angles (60°, 90°, 125° and 150°) implies that these two mixers have the weakest large eddies amongst the Group 1 mixers. This is intimately related to the thoroughness of the mixing achieved between the fan and the core flow, and how that flow subsequently mixes with the ambient. This will be explored in somewhat more detail later.

(v) The reduction in low frequency noise achieved in 12UH and 12TH is also captured in the PWL-spectrum of Figure 5.1(b).

(vi) The distinguishing feature of the SPL spectra of configurations 12UH and 12TH for angles away from the jet axis, as shown in Figure 5.1(a), is the dramatic increase in noise level for mid-range frequencies (approximately 1500-2000 Hz), producing a "hump" in the spectra. In fact, at all these angles (60°, 90°, 125°) these humps are also the "global" peaks or the most dominant frequencies. Their peak SPL frequencies shift slightly to higher values as we go closer to the jet exit axis. The high-frequency noise contributions (5000 Hz and above) of 12UH and 12TH are also higher than CONF or 12CL. Hence, it must be the large mid-to-high frequency contributions of 12UH and 12TH that make their OASPL larger than CONF or 12CL for angles upstream of 110°.

(vii) "Mid-to-high" range frequency noise is attributable to "smaller" eddies which predominates near the nozzle exit plane or even inside the nozzle. These small scale eddies are produced in lobed or tongue mixers by the

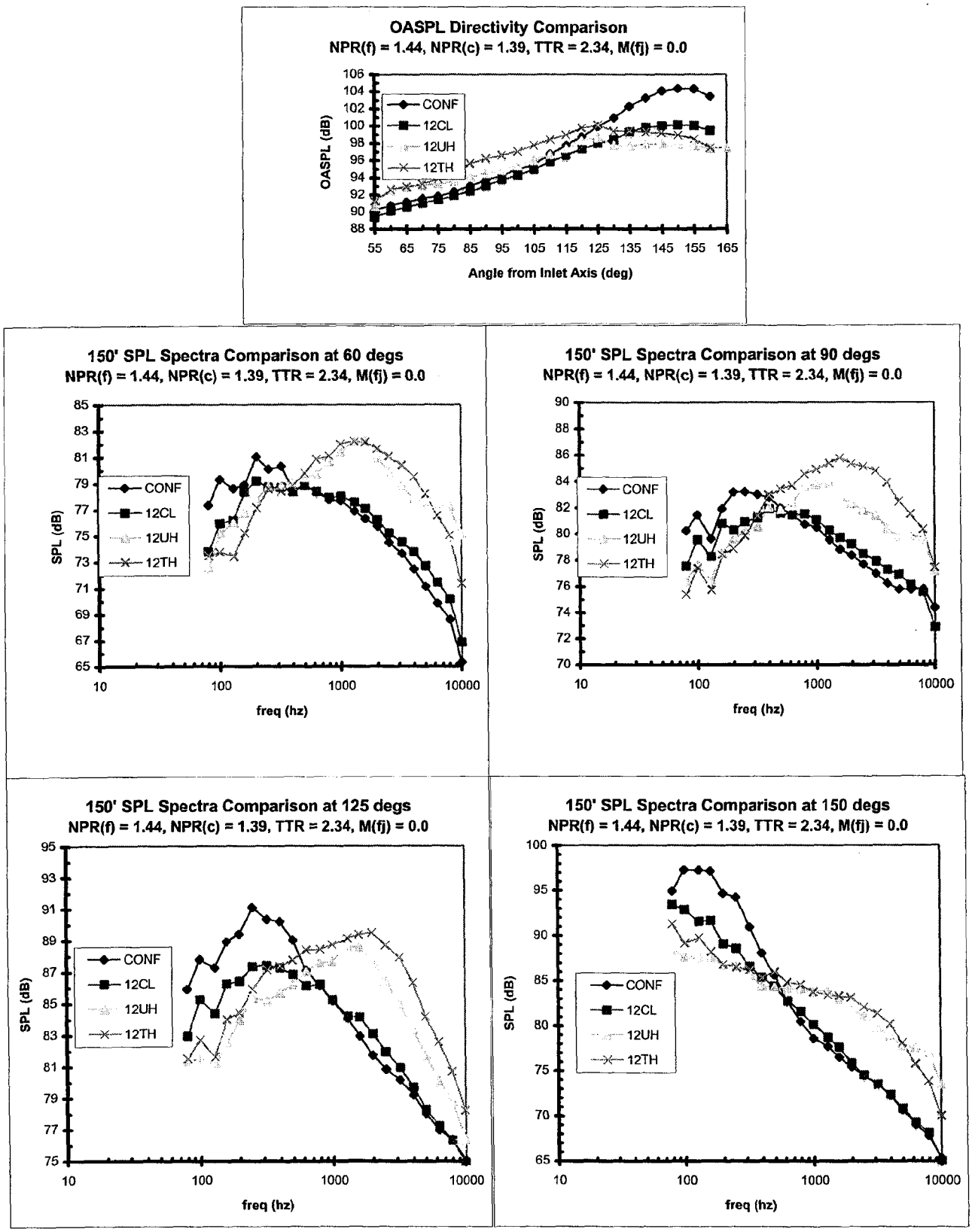

Figure 5.1 (a) OASPL directivity and SPL spectra for CONF, 12CL, 12UH and 12TH at T.O. # 1, M(fj) = 0.0

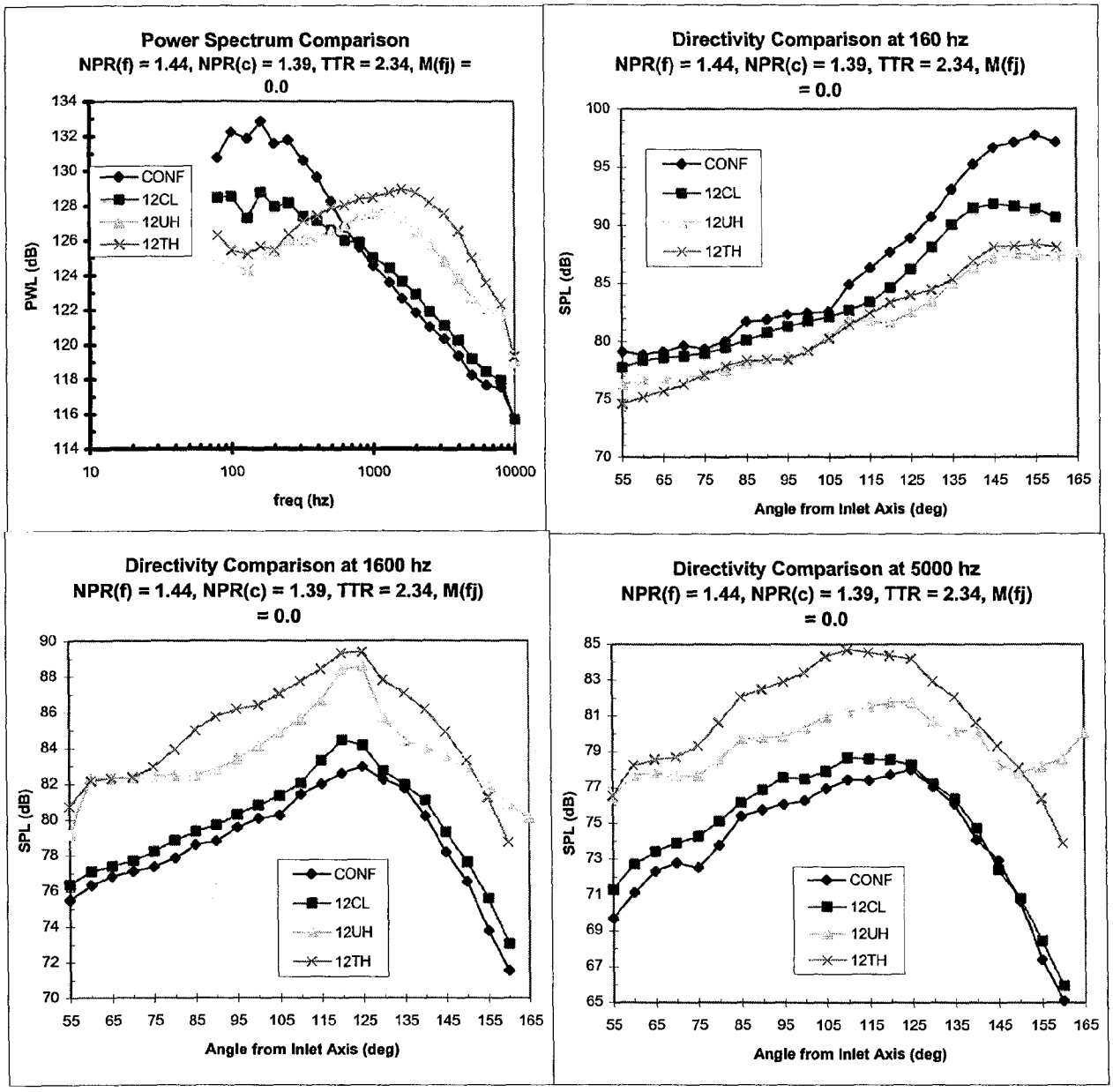

Figure 5.1 (b) Power spectrum and SPL directivity for CONF, 12CL, 12UH and 12TH at T.O. # 1, M(fj) = 0.0

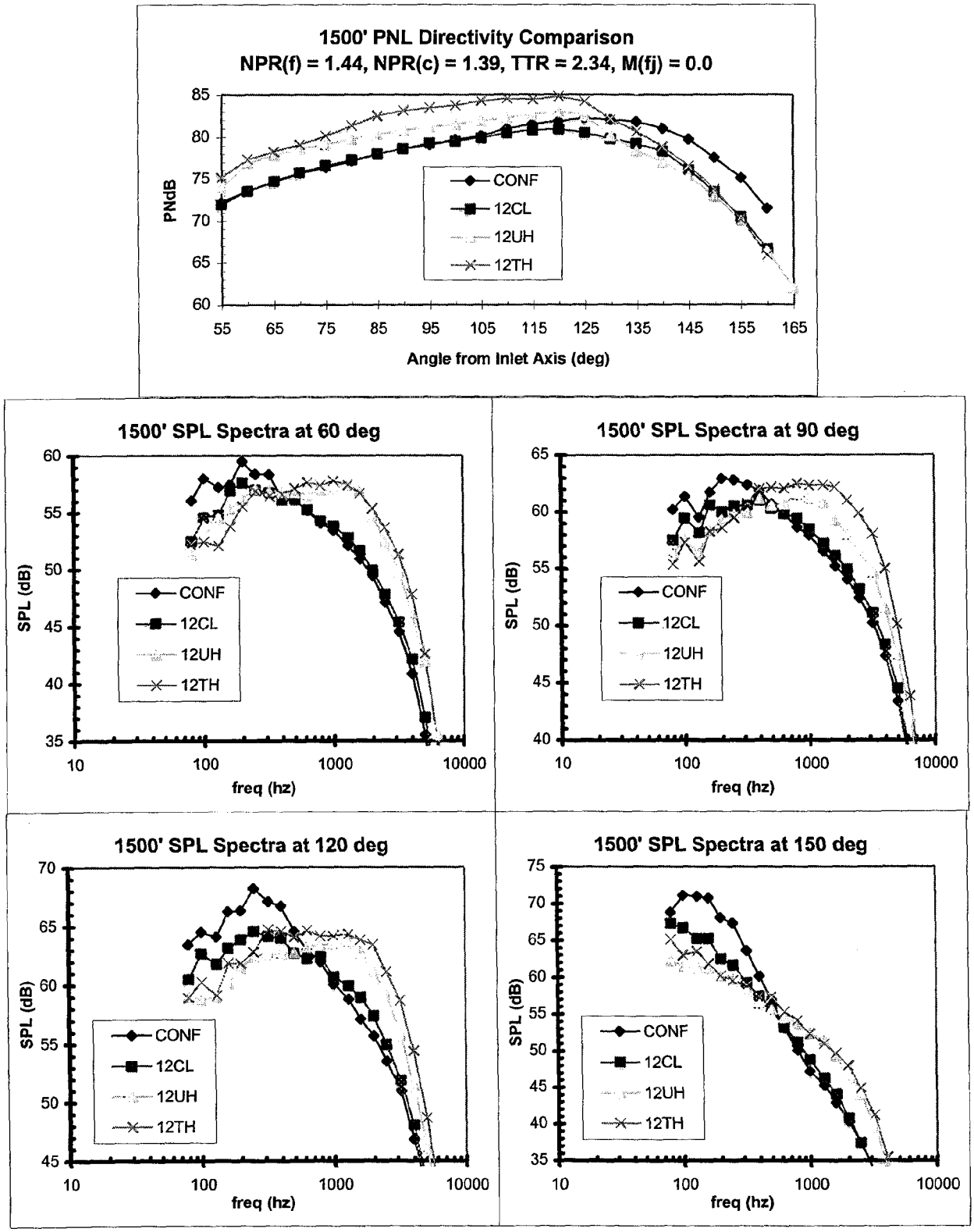

Figure 5.1(c) Flyover PNL directivity and SPL spectra for CONF, 12CL, 12UH and 12TH at T.O. # 1, M(fj) = 0.0

mixing of fan and core flows which emerge from the lobes/tongues with widths much "smaller" than the nozzle diameter. This issue will also be explored later in more depth.

(viii) The mid-frequency hump and larger high-frequency output of 12UH and 12TH are also captured in PWL-spectrum of Figure 5.1(b).

(ix) It appears from the PWL-spectrum of Figure 5.1(b) that the 12UH and 12TH mixers suppress low frequency sound far better than a confluent configuration, but at the expense of increasing the mid-to-high frequency spectrum. It is interesting to note that although both have relatively high lobe penetration (12UH has 0.68 and 12TH has 0.56 compared to 12CL's 0.48), 12UH is unscalloped, whereas 12TH represents the limit of deep scalloping. The fact that they still appear to have similar noise signatures may be related to their widely differing area ratios which have led to totally different bypass ratios and thrusts, as seen in Chapter 4.

(x) As opposed to the 12UH and 12TH mixers, the acoustic signature of the 12-lobe low penetration mixer with cutouts (12CL) is quite different. Its OASPL is lower than the confluent design at all angles. Although its high-frequency SPL is comparable to the confluent mixer at all angles, the low-frequency SPL is much lower than CONF (although slightly higher than 12UH or 12TH). This is also reflected in its power spectrum in Figure 5.1(b).

(xi) Thus, it appears that the compound effect of cutouts and low lobe penetration has benefited 12CL tremendously in terms of reducing low frequency sound without increasing the high-frequency sound compared to CONF. This must be a result of how the fan/core flow mixing progressed inside the nozzle and outside it while mixing with the ambient. This is an issue which will be taken up later. It also hints that in this case at least the noise benefits of cutouts overcome any excess noise produced by the dipole-type noise made by the leading edge of the aft end of the cutouts mentioned in Chapter 2.

(xii) Figure 5.1(b) also shows the directivity of particular frequencies for all mixers: 160 Hz (corresponding to peak PWL for configurations CONF and 12CL), 1600 Hz (where peak PWL of 12UH and approximately of 12TH occurs) and a relatively high frequency component at 5000 Hz. For any of these frequencies, the SPL directivity for all mixers is similar in shape. The low frequency SPL monotonically increases as we approach the jet exit axis (up to around 150°) and then decreases as has been observed in single-stream nozzles. However, the mid-to-high frequency SPL peak occurs more upstream, at around 120°-125°. This is due to the refraction effect of the sheared jet flow described earlier which leaves a "relative zone of silence" near the jet exit axis. On the other hand, for any given lobed mixer, the peak moves upstream with increasing frequency. As in single-stream nozzles, we expect the different frequency scales to originate at different axial portions of the jet. The higher frequencies, associated with small-scale eddies, originate more upstream; the lower frequencies, associated with larger eddies, originate further downstream in the plume. This is, indeed, reflected in the coaxial jet model of Fisher et al[17] and Balsa & Gliebe[18]. Hence, returning to the SPL-directivities of Figure 5.1(b), the

relative amplitudes of the SPL's between different mixers at a given frequency tell us how the source strengths, corresponding to these frequencies and located at similar relative axial positions in the jet, differ between mixers. However, without specific source-location data, such as might be obtained with multi-microphone phased arrays, we cannot further pinpoint the source-locations for a given frequency. In a later section, however, we develop a technique which indicates the location of some high-frequency sources in an approximate sense.

(xiii) The community noise impact of the spectral and directivity differences between the various mixers is clearly shown by the 1500 ft PNL directivity of Figure 5.1(c). The increase in frequency of the SPL peak observed in configurations 12UH and 12TH is seen to produce a significant increase in the peak value of PNL compared to either the confluent baseline or 12CL. This increase in peak PNL is totally the result of the frequency weighting of the NOY scale, since little or no difference in the amplitude of the maximum value of SPL is observed between the configurations. The PNL penalty incurred by configurations 12UH and 12TH persists for all angles upstream of the peak. A different trend is observed for mixer configuration 12CL. This configuration displays the lowest peak PNL of any of the configurations and this behavior is also observed for all angles upstream of the peak. This result again ties back to the spectral characteristics of this mixer which shows a reduction in the low frequencies without a corresponding increase in the higher frequencies. The spectral range between 1000 Hz and approximately 4000 Hz controls the observed PNL behavior. As alluded to earlier, frequencies below 1000 Hz are not so heavily weighted in the NOY calculation. Although frequencies above 4000 Hz are heavily weighted in the NOY calculation, atmospheric attenuation of these frequencies is very high. The SPL spectra at 1500 ft show a substantial fall off in the highest frequencies and this trend becomes stronger for angles away from 90° due to the larger propagation distances involved. For this static case ($M_{fj} = 0$), the propagation and atmospheric attenuation effects display a symmetry relative to the 90° directivity angle. Since there is no Doppler shifting of the frequency between the front and aft quadrants due to relative motion between the source and the observer, any asymmetry observed in the PNL directivity around 90° at static conditions is solely due to the true source asymmetry. When aircraft motion is present, this result changes. This effect will be examined later.

In conclusion, the 12 lobe mixer with cutouts and low lobe penetration (12CL) appears quieter than the other 12-lobed mixers (12UH, 12TH) or the confluent mixer because it reduces the low frequency noise without raising the mid-to-high frequencies which are heavily noy weighted. The tongue mixer (12TH), although it decreases the low frequency noise, is heavily penalized due to the increase in mid-to-high frequency noise it creates. The tongue mixer's low bypass ratio of 4.55 (compared to 4.95 of 12CL or 4.71 of 12UH) under static conditions and consequent higher effective jet velocity accentuates its noise too. Thus, the effects of scalloping/sidewall-cutouts, which

produced a noise benefit for 12CL, were overwhelmed by other effects in the tongue mixer.

Mixer configuration 12UH produced the second highest noise, as measured by PNL, of all the configurations. This configuration was designed to have an identical hot stream/cold stream area ratio as compared to 12CL. However, configuration 12UH has a higher penetration than 12CL and lacks the sidewall cutouts. It is not possible to determine the relative importance of these two differences on the generation of jet noise from the data presented in this section.

Although the 12-lobe unscalloped mixer (12UH) proved to be noisier, the lack of scalloping usually leads to a better thrust coefficient at cruise. Hence, from the viewpoint of keeping balance between cruise thrust efficiency and takeoff noise reduction, it is expedient to first study unscalloped mixers but vary the number of lobes with the hope of "improving" mixing and noise characteristics. This is done next.

5.2.1.2 Lobe Number Effect

Figures 5.2(a), (b), (c) show, respectively, the polar OASPL-directivity, PWL-spectra, flyover PNL-directivity, and the corresponding SPL-spectra or directivity for 12UH, 16UH and 20UH mixers, and the baseline confluent (CONF) mixer. Since 12UH and 20UH have all lobe parameters approximately equal, except for lobe number, we will pay special attention to the difference in noise signatures created by these two mixers. The 16-lobe mixer, 16UH, is unique in that it has a much larger fan to core area ratio than the other configurations in the group. It has been included in this group because of its similarities in other parameters (lobe penetration,, non-scalloped, lobe length) of 12UH and 20UH. General trends observed within this group are:

(i) The 150 ft polar SPL spectra of the 20-lobe mixer is lower in the mid-to-high frequency range than the 12-lobe mixer at all angles (Figure 5.2(a)). This is also reflected in the power spectrum (PWL of Figure 5.1(b) and the flyover SPL's in Figure 5.1(c)). However, 20UH does not suppress the lower frequency SPL's as much as 12UH does; this can also be seen in PWL and flyover SPL's.

(ii) The decrease in high frequency and increase in low frequency of 20UH as compared to 12UH is reflected in the OASPL directivities as a relative decrease for angles upstream of peak PNL which occurs at 120° and a relative increase in the angles downstream of the peak PNL angle.

(iii) Although the OASPL of 20UH at shallower angles (closer to the jet axis) is higher than 12UH, the flyover PNL (Figure 5.2(c)) for both the mixers at those angles is the same. This is the result of the difference in weighting between the two metrics. Since each frequency band is equally weighted, the value of OASPL at a particular angle is determined by the band with the highest amplitude. For both 12UH and 20UH, the lower frequencies are dominant at the shallow angles. Since the peak of the SPL spectrum is larger for 20UH than 12UH, the OASPL of 20UH will also be larger. The preferential NOY weighting of the higher frequencies in computing PNL changes this trend. Although 12UH displays a larger peak SPL in the important 1-4 kHz range in the 150 ft polar than does 20UH, the atmospheric

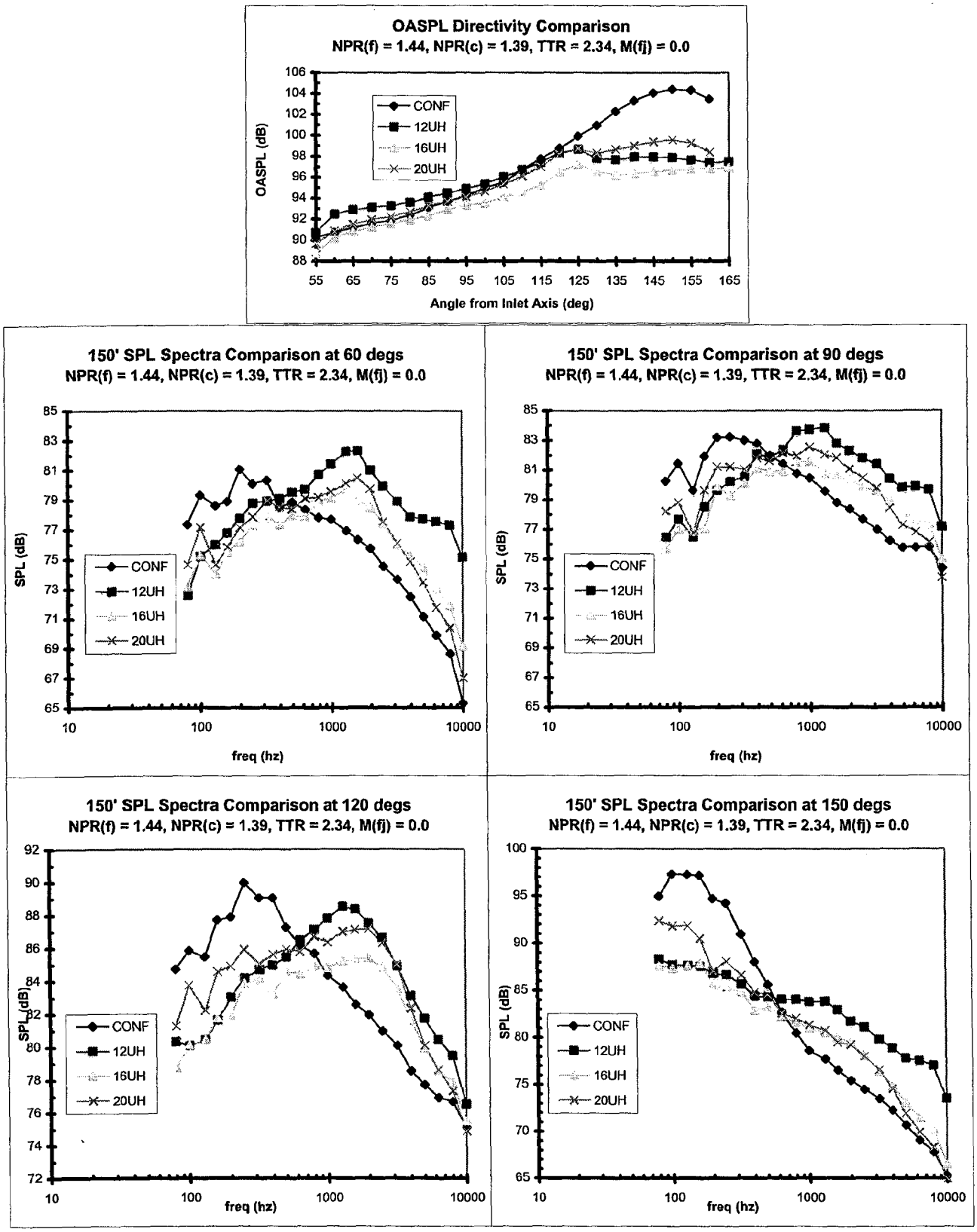

Figure 5.2 (a) Effect of lobe number on OASPL directivity and SPL spectra at T.O. # 1 and M(fj) = 0.0.

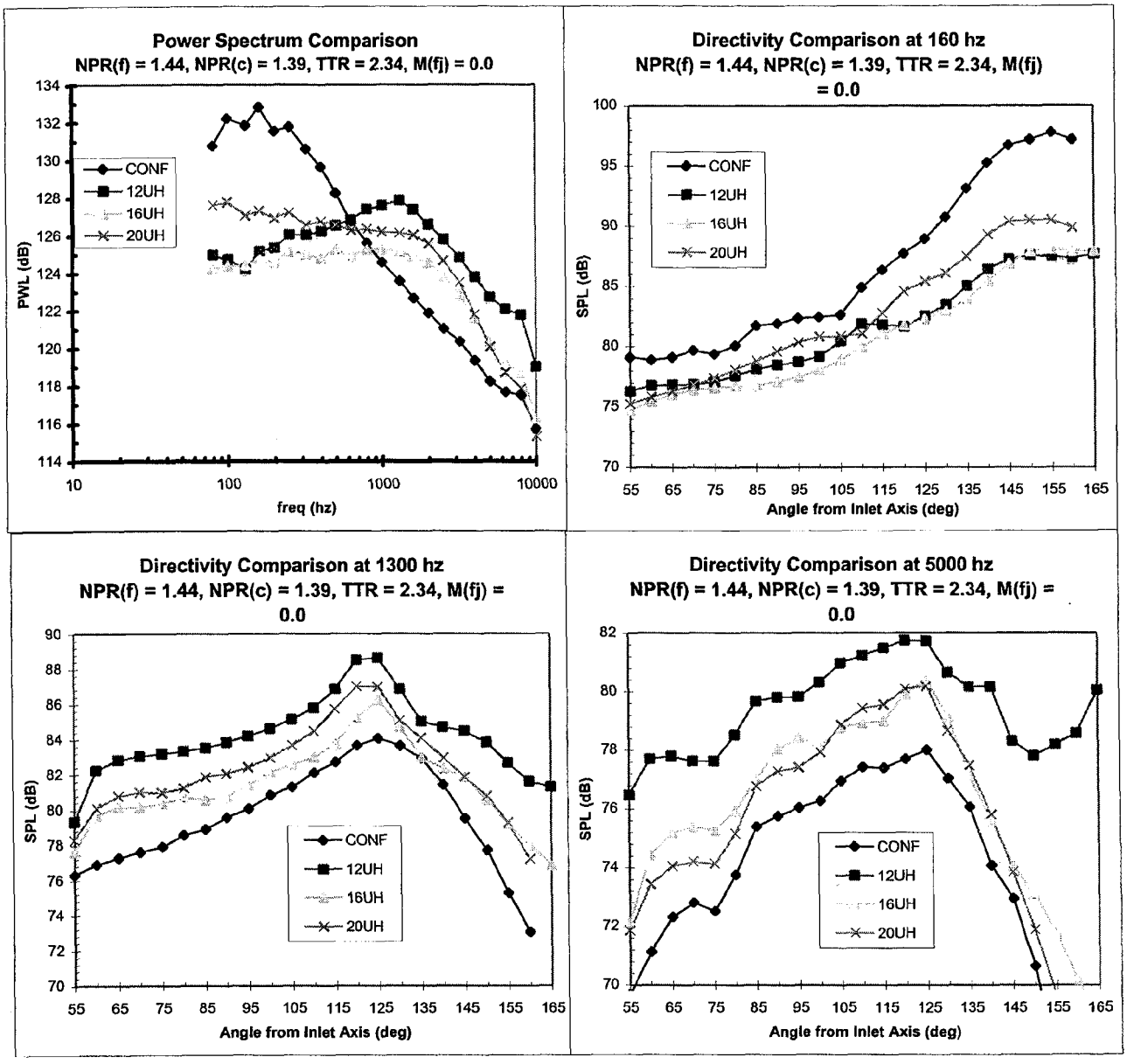

Figure 5.2 (b) Effect of lobe number on power spectrum and SPL directivity at T.O. # 1 and M(fj) = 0.0.

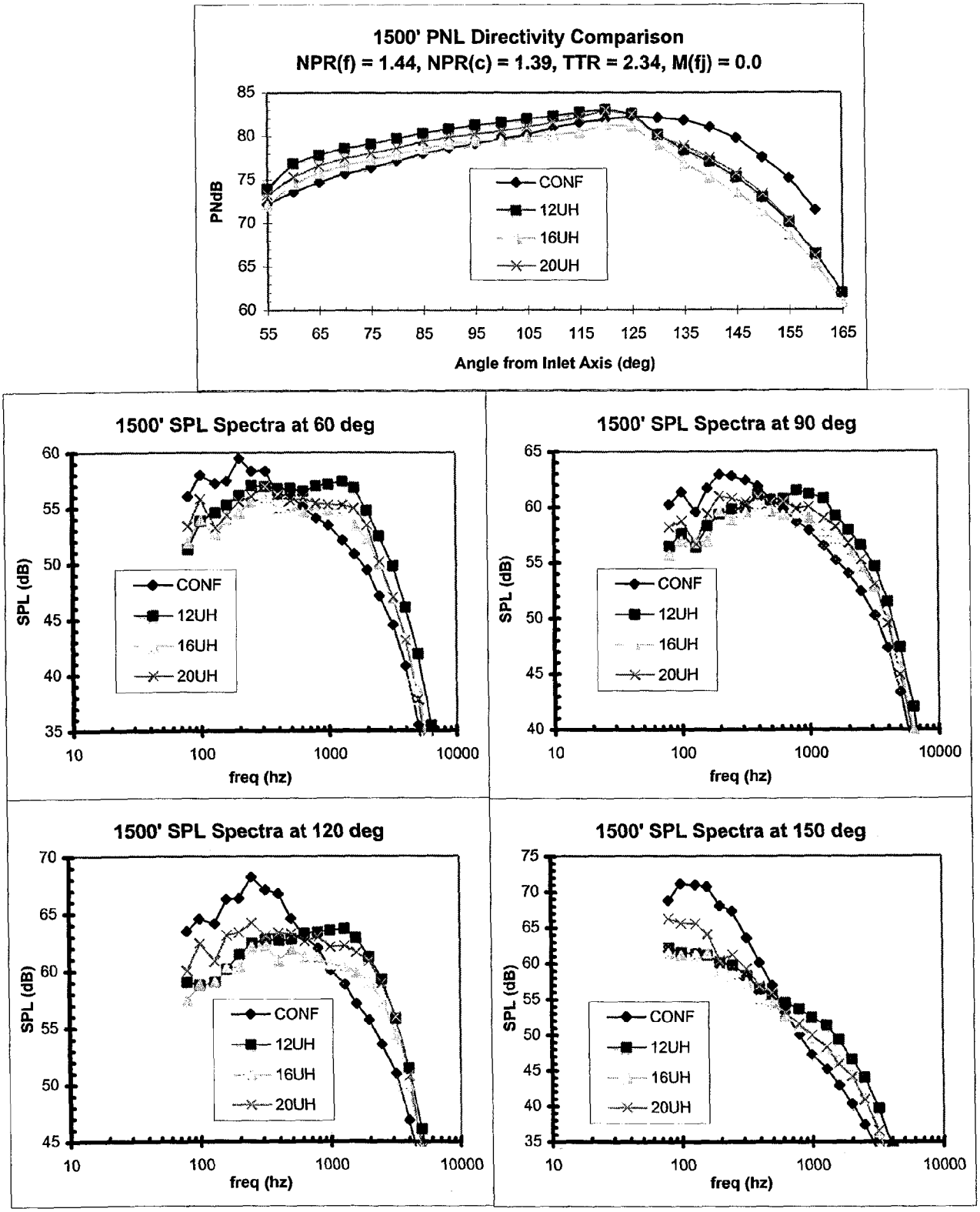

Figure 5.2 (c) Effect of lobe number on flyover PNL and SPL spectra at T.O. # 1 and M(fj) = 0.0.

attenuation that occurs during the propagation to the 1500 ft sideline is sufficient to result in nearly equal PNL for the two configurations at the shallow angles.

(iv) For all angles less than or equal to the peak PNL angle of 120°, the 20 lobed mixer is definitely quieter than the 12 lobed design. On an overall integral basis this would make the mixer with higher numbers of lobes (20UH) quieter than one with fewer lobes (12UH). However, this does not necessarily make the 20 lobe mixer quieter than the confluent mixer on an overall basis and we will have to await for the EPNL comparisons (with the nozzle moving) in a later section.

(v) Turning our attention to the 16-lobe mixer (16UH) with the higher fan-to-core area ratio, we find that it radiates the least power at all frequencies, produces the lowest OASPL at all angles, the lowest peak PNL, and generally the lowest PNL directivity of all the mixers in this group. This would, of course, make it the quietest mixer in the group for a fixed operating condition. As a result of the difference in area ratio, the 16 lobe mixer has a much larger bypass ratio (7.64) than 12UH (4.95) or 20UH (4.8) and consequently much lower effective jet velocity. This change in bypass ratio is accompanied by a change in thrust for a fixed fan and core operating conditions. Since a flight application would require maintaining a fixed thrust, the above comparisons are not totally appropriate. On the other hand, it also shows that a decrease in noise can be made by increasing the fan-to-core area ratio, but a change in the cycle condition would be needed to maintain thrust.

(vi) It is noteworthy that for a given polar angle, the frequency associated with the maximum polar SPL value (Figure 5.2(a)) does not shift systematically with lobe number for these unscalloped mixer configurations, although the use of one-third octave bands may mask some of the details. That is to say, the peak frequencies do not appear to be correlated with the widths of the mixer lobes which, in turn, set the scale the diameter of the axial vortices. However, the maximum SPL amplitudes do decrease with an increase in the number of lobes.

(vii) The angle at which a particular frequency band peaks is approximately the same for the confluent configuration and all the lobed configurations. For example, the peak amplitude for 1300 Hz occurs at approximately 120° for all the mixers discussed in this section. Of course, the relative strength of a particular frequency band does vary between the mixers.

In conclusion, we see that an increase in the number of lobes produces a decrease in the overall noise at static conditions. This is primarily achieved by reducing the mid-to-high frequency noise in the angular range upstream of the peak PNL angle while changing the flyover noise at the shallower angles only minimally. Note that the low frequency polar SPL for the higher lobe-count mixer is, however, slightly higher than a low lobe-count mixer. This observation, combined with a similar observation for the previous group of mixers, implies that reducing the mid-to-high frequency spectra may be more important to overall noise

reduction than large reductions in low frequency noise alone. The paradigm in mixer-design in the past has been to mix fan and core flows as fast as possible so that a nearly uniform flow forms by the nozzle exit plane. It was reasoned that this would lead to faster plume decay and reduce low frequency noise. The current data shows that this strategy may not be the optimum because the mid-to-high frequency noise generated by the faster fan/core mixing may upset the overall balance. Since the presence of a moving free stream surrounding the nozzle is known to suppress the low frequency portions of the jet noise spectra for a single round jet, these observations may be modified when flight effects are included. This will be examined in detail in a later section. Prior to this, the subtle effects of scalloping will be discussed in the next section.

5.2.1.3 Effect of Scalloping

Figures 5.3(a), (b), (c) show the polar OASPL directivity, the sound power spectra (PWL), the flyover PNL-directivity, and the associated SPL-spectrum or directivity for the 20UH, 20MH and 20DH mixers. All results are again presented for stationary surroundings ($M_{fj} = 0$) and for a reference operating point with a fan pressure ratio of 1.44, core pressure ratio of 1.39 and a core-to-fan total temperature ratio of 2.34. Recall that the moderately scalloped mixer (20MH) has half the scalloped area of the 20DH (see Table 2.2).

(i) The primary difference between the deeply scalloped mixer (20DH) and the unscalloped design (20UH) is a reduction in amplitude of the mid-to-high frequencies (approximately 1-4 kHz) as shown in the 150 ft polar SPL spectra of Figure 5.3(a). This improvement is observed over all directivity angles. At the same time, the substantial low frequency suppression produced by the aggressive mixing of the 20 lobe unscalloped configuration is not reduced. A small increase in the highest frequencies (greater than 4 kHz at 90°) is observed for 20DH compared to 20UH, but the increase is small enough to be of no practical concern. The moderately scalloped configuration (20MH) produces similar trends, but the suppression of the mid-range frequencies is significantly less than observed for 20DH. The OASPL directivity, PWL spectrum, and PNL directivity, as shown in Figures 5.3 (a), (b) and (c), for configuration 20MH are all bounded above and below by the corresponding results for 20UH and 20DH, respectively. However, the correlation between noise reduction and scalloped area, although monotonic, is not simple.

(ii) All this is reflected in the lowest OASPL directivity as well as the lowest PNL directivity at all angles for the deeply scalloped mixer, 20DH, making it the quietest mixer in the group.

(iii) As in the coaxial jet model of Fisher et al[17] there appear to be at least two dominant regions of frequency in lobed mixers (Figure 5.3(a)). One is the low-frequency peak governed by the fully-mixed region far downstream and the other is the mid-to-high frequency peak governed by the shear-layer between the ambient and the partially mixed fan/core flow close to nozzle exit. The geometry of the lobed mixer and changes to the mixing process can be used beneficially to

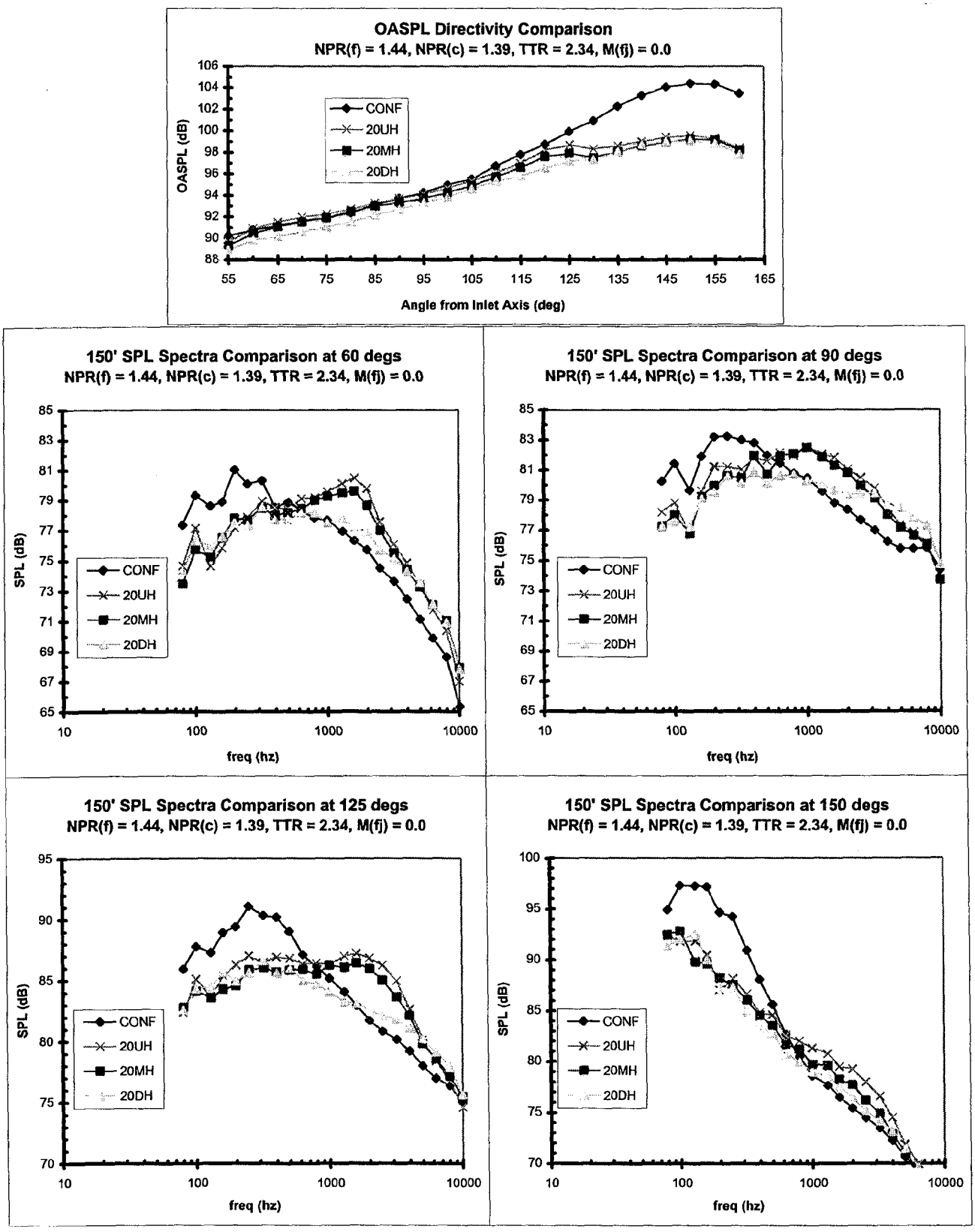

Figure 5.3 (a) Effect of scalloping on OASPL directivity and SPL spectra at T.O. # 1, $M_{fj} = 0.0$

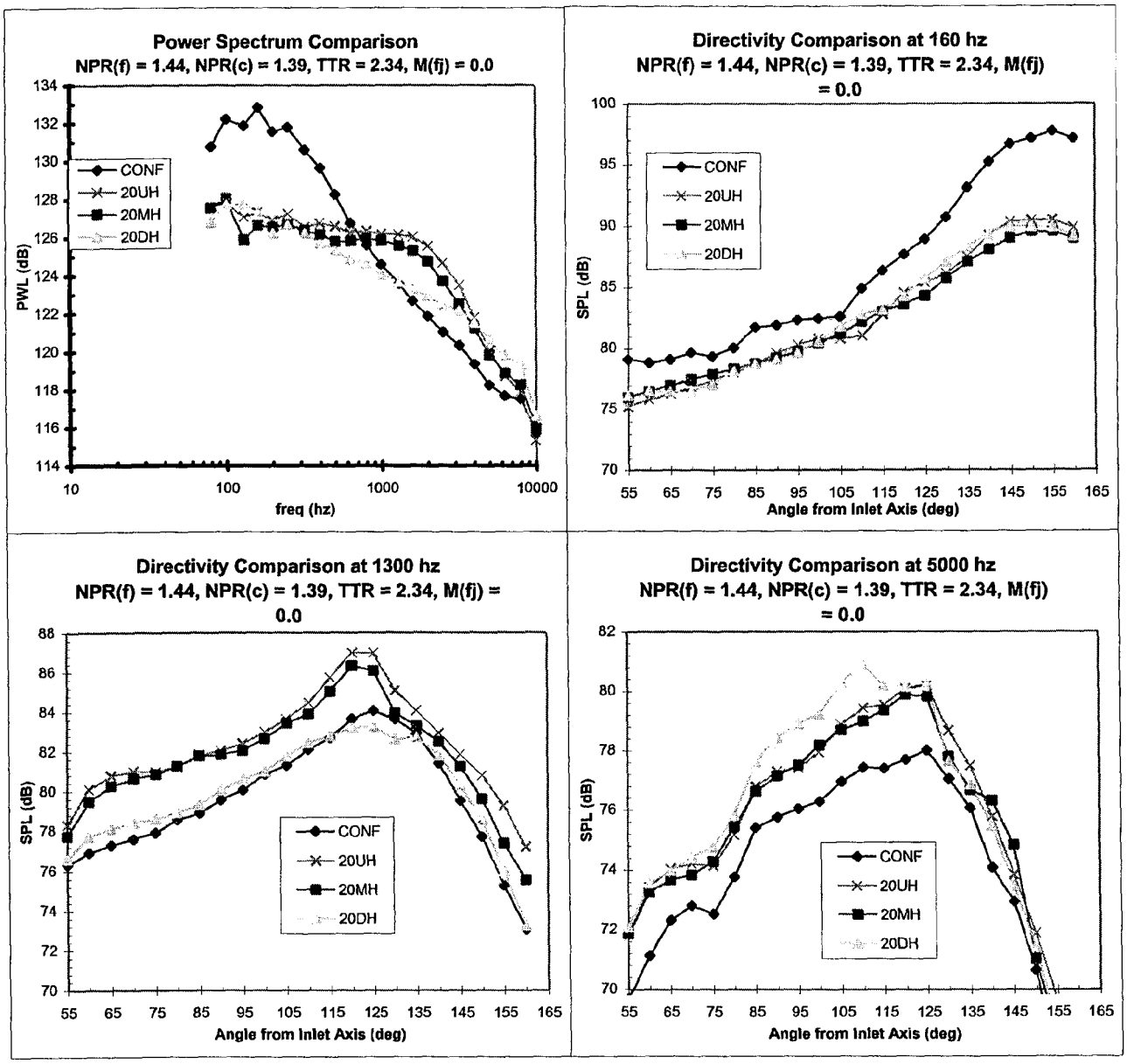

Figure 5.3 (b) Effect of scalloping on power spectrum and SPL directivity at T.O. # 1, $M_{fj} = 0.0$

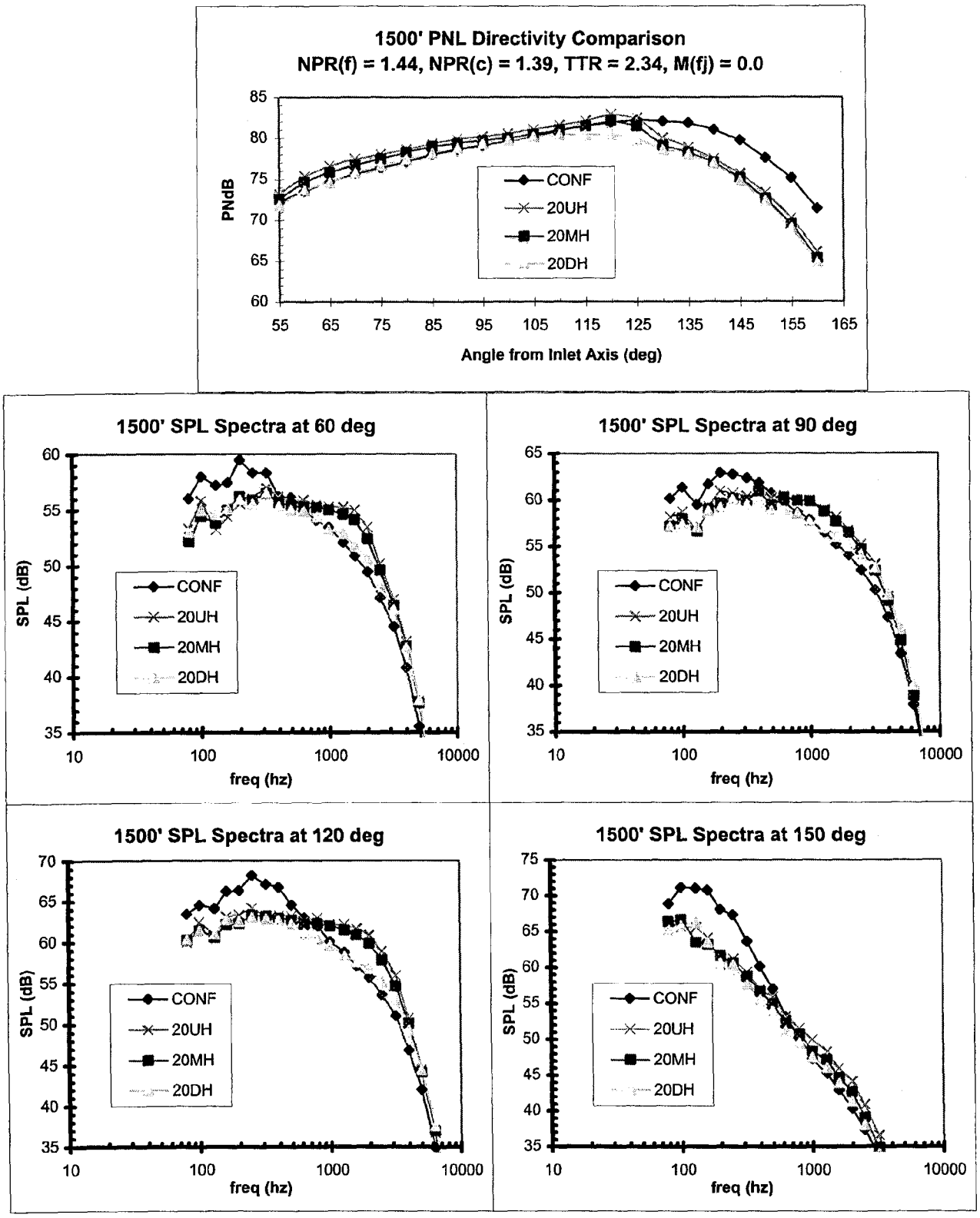

Figure 5.3 (c) Effect of scalloping on flyover PNL directivity and SPL spectra at T.O. # 1, $M_{fj} = 0.0$

control one or the other of these peaks. The unscalloped 20-lobe mixer produces a substantial reduction in the low frequency noise at the peak PNL angle compared to the confluent design, but a large increase in the mid-frequencies is observed. Introducing sidewall scallop improves the low frequency suppression at the peak PNL angle and significantly reduces the higher frequency penalty.

(iv) It also appears that the SPL-directivity at 1300 Hz, (Figure 5.3(b)) for the unscalloped and the moderately scalloped mixers has a more rapid decay away from the peak than the deeply scalloped mixer ("beaming" characteristics); whereas, the very high frequency (5000 Hz) SPL directivity for 20DH shows a slight increase over 20UH or 20MH for all angles upstream of the peak PNL angle.

In conclusion, deep scalloping helps overall noise suppression by reducing the mid-to-high range frequencies without any increase in the low frequency spectra and only a small inconsequential increase in the very high frequencies compared to unscalloped mixer. However, we also saw in Chapter 4 how deep scalloping can cause higher thrust losses at both takeoff and cruise conditions. We also note here that noise suppression does not appear to follow a linear relation with the scalloped areas. It is possible that there is some "critical" scalloped area after which one begins to reap noise benefits. However, it is also possible that for a given mixer there exists an "optimal" scalloped area beyond which no additional noise benefits occur. This second possibility can not be proven, but is hinted at by the poor acoustic performance of the tongue mixer in § 5.2.1.1, even after accounting for its area ratio difference as compared to the other mixers.

Before moving on to the case of non-zero free-jet speed, which represents the flight effect, we digress briefly to the possible causes of noise reduction observed in some of these mixers even under static conditions. The flight-effect will, of course, complicate the matter further by changing some of the sources discussed in the next section.

5.2.1.4 Probable Causes of Noise Reduction

In the previous three sections we have seen that noise can be reduced by the compound effect of lobe cutouts and low penetration or by increasing the number of lobes or by deep scalloping, at least for static operation and with the relatively low jet speed (830 ft/s) characteristic of the baseline operating point. Out of these effects only the second and third effects are parametrically captured in our acoustic data base. Hence, we discuss the scalloping effect first, which in a way captures some of the "cutout" effects, and then the lobe number effect.

Scalloping Effect

The probable mechanism for the scalloping effect, from the fluid-dynamic point of view, has already been discussed in Chapter 2 (Section 2.3.1) in fair amount of detail and this understanding is embedded in our scalloped lobe design philosophy. Briefly, it was concluded in Section 2.3.1 that "boomerang" type scalloping, as in 20DH, will "introduce axial vorticity *gradually*" into the flow beginning at an earlier axial location so that the fan/core flow mixing proceeds more "gently" than the unscalloped mixer and the most intense turbulence spots are acoustically shielded by the nozzle duct. This may or may not lead to a more uniform velocity/temperature profile by the time the two flows reach the nozzle exit plane (that

depends on how long the mixing length is), but it will tend to reduce the mid-to-high frequency noise component generated by the internal mixing and by the interaction of the partially mixed flow with the ambient. Some of the CFD results for 20DH mixer in Figures 2.21-2.23 have captured the low turbulent kinetic energy generated during this internal mixing with axial vorticity. In a later section, it is shown that the noise in this frequency range for 20UH originates primarily in the region close to the nozzle exit plane.

It would have been useful to have comparable plume survey data for 20UH and 20DH at static baseline conditions but from Table 3.5 we see that although data exists for 20DH at Mfj = 0.2 only a partial data set was collected for 20UH at the three axial stations, X/D = 0.2, 0.5, 1.0. Although a non-zero free-jet speed changes the shear-layer properties between the nozzle-jet/free-jet, the arguments given here are independent of it. Comparison of total temperatures for 20UH and 20DH (see Figures 4.12 (a) and (b)) in the transverse plane at X/D = 0.2 shows that deep scalloping caused the outer hot-spot of 20UH (at Z $\approx \pm$ 3 in.) to reduce in intensity and move outward, but at the same time another less intense hot-plateau was formed closer to the axis (at Z $\approx \pm$ 1.75 in.). Scalloping appears thus to encourage azimuthal mixing of axial vortices and to reduce the radial gradient of total temperature in the outer periphery which itself leads to another source of noise. The central hot-spot intensity and size has not changed much and the center-line traverse of total temperature (see Figure 61 in Vol. III, pt. 1) looks similar for both unscalloped and scalloped mixers. On the other hand, the velocity profile for the scalloped mixer at X/D = 0.2 (see Figure 4.13) appears fairly uniform with only a small local maximum at the center, corresponding to the hot-spot from the core stream. The corresponding velocity profile for 20UH is not available, but it is expected that it will be less uniform at the periphery due to the larger hot-spots. This would imply an increased shear in this region for the unscalloped mixer, making it an additional source of noise. The center-line velocity traverse out to one diameter (see Figure 4.18) is similar for scalloped and unscalloped mixers. Plume data is not available for X/D greater than 10 for 20DH, a region which is expected to govern the low frequency noise behavior. However, from the polar SPL data (Figure 5.3(a)) which shows similar low frequency behavior at all angles for both unscalloped and scalloped mixers (20UH and 20DH) we can inversely deduce that the far-field plume decay must be similar for both mixers. Beyond this we cannot really pin-point the process that leads to noise reduction due to scalloping with the available data.

Packman & Eiler[1] describes the differences in flow-fields and noise of unscalloped and scalloped mixers for a very low bypass ratio nozzle for Pratt & Whitney's JT8D engine. Although some of their observations and conclusions are applicable here, some are not. For example, as in our case, they also found scalloping to decrease noise in the mid-to-high frequency range. However, their scalloped mixer was concluded to have less nozzle exit uniformity and there was no central hump. Although the details may differ with scale and operating conditions the final outcome relative to noise was similar: scalloping reduces noise. Another recent paper by Yu et al[19] attempts to describe the fluid-dynamic effects of scalloping but no connection to noise production is made. All the processes described in Yu et al[19] may not be applicable to the mixers used in our study due to different lobe/nozzle geometry and

operating conditions.

In summary, scalloping appears to produce less intense hot spots by encouraging azimuthal and radial mixing between axial vortices which reduces the mid-to-high frequency noise without changing much of the far-field plume decay produced by an unscalloped design. A more detailed plume flow study is needed to uncover more of the physics connecting the scalloped mixer flow to the noise that it generates.

All the arguments that apply to the noise benefit of scallops can be extended to cutouts as used on the 12CL mixer. Since it was shown to be quieter than 12UH it is likely that the "leading-edge dipole source" from the lobe-wall strip downstream of the cutouts on 12CL, mentioned earlier in Chapter 2, is a less important noise source than the mixing of the flows downstream. However, 12CL also had a lower lobe penetration than 12UH. Penetration plays some role in the radial migration of the axial vortices generated by the mixers (as also seen in the CFD simulations, Figures 2.22(b), 2.25(b)). This change in radial migration will determine whether the vortices interact with the outer nozzle-duct wall and, hence modify the ambient/jet shear-layer, thus generating more or less noise. We unfortunately cannot distinguish the lobe-penetration effect on noise from this data directly other than noting that for high-penetration the high-speed core flow, which is radially thrown outwards, immediately interacts with the shear-layer between the jet and the ambient flow close to the nozzle-exit plane, possibly increasing the shear, and hence, increasing the mid-to-high frequency sound. A low-penetration mixer, such as 12CL, keeps the axial vortices closer to the jet-axis. This prevents the high-speed core flow from immediately interacting with the ambient shear layer, reducing shear there and, hence, also reducing the mid-to-high frequency noise from that region. However, these same low-penetration axial vortices will continue to modify the flow further downstream, what Fisher et al[17] call the "interaction" region for noise production, and modify the noise characteristics.

Lobe Number Effect

Now, consider the effect of increasing the number of lobes (20UH versus 12UH). This obviously increases the interface area between the fan and the core flows and decreases the length-scale (diameter) of the axial vortices which are now more numerous. This should enhance mixing between the two flows. A decrease in the length-scale of the axial vortices would seem to imply an increase in the dominant frequency, but this is true only if their strengths remained the same. As the number of lobes increases, the number of vortices occupying the space within the nozzle must also increase. This promotes earlier azimuthal interaction between the vortices. This can, indeed, reduce their strengths. It will be shown later that the mid-to-high frequency sound of mixers 12UH and 20UH is associated with these axial vortices and their interaction with the jet/ambient shear layer. In Figure 5.2(a), the mid-frequency content of the 20 lobe mixer, 20UH, is less than that of the comparable 12 lobe mixer, 12UH. This seems to imply that an increase in the lobe count produces a reduction in the strength of the axial vortices and the jet/ambient shear layer due to better azimuthal mixing of the axial vortices. On the other hand, the 20 lobe mixer, 20UH, is less effective in reducing the low frequency portion of the spectrum which is typically associated with the far downstream plume characteristics. It is inferred that the larger diameter and stronger axial vortices produced by the 12 lobe mixer, 12UH,

probably promote more rapid decay of the plume through viscous diffusion.

In summary, increasing the number of lobes produces a decrease in mid-to-high frequency sound. Greater lobe count increases the interface area between the fan and core streams and promotes a less intense initial mixing region aided by more numerous smaller and, perhaps, less intense axial vortices. However, this type of initial mixing does not appear to promote rapid far-field plume decay. This results in a slight increase in low-frequency sound over a mixer with fewer lobes. More definitive work is needed to understand the reasons for the latter half of this story.

5.2.2 Flight-Effect: Free-Jet Mach No. 0.2

This section examines the comparative acoustics results for the various mixers with the reference 100% nozzle-length, at baseline operating condition TO #1 when the free-jet Mach number is set to 0.2. This is representative of aircraft speeds at take-off for today's regional and business jet applications. As before, the data presentation will be in terms of different groups of mixers in order to isolate specific effects. Instead of analyzing all the details, as in the previous section, the focus in this section will be on the differences in noise signatures between mixers caused by the non-zero free-jet Mach number.

5.2.2.1 12-Lobed Mixers

Figures 5.4(a), (b), (c) show the polar OASPL directivity, power spectrum and flyover PNL-directivity with the corresponding SPL-spectra or SPL-directivity for 12CL, 12UH, 12TH and CONF mixers for a free jet Mach No. of 0.2 at TO # 1. Compare these figures with Figures 5.1(a), (b), (c) respectively where the free-jet Mach No. was zero.

(i) The major difference observed in the OASPL with a non zero free-jet speed is that 12UH and 12TH appear much louder that either the baseline CONF or 12CL configurations for angles less than or equal to 130°. For example, at 90° the difference in OASPL of 12UH and CONF is almost 3.5 dB as opposed to 1.5 dB at static conditions.

(ii) Over this angular range, the polar SPL spectra of the lobed mixers in this group are dominated by the mid-to-high frequency range, as shown clearly in Figure 5.4(a). Similar trends are observed when comparing the PWL spectra of Figure 5.4(b) and 5.1(b). Using 2000 Hz as an example, the difference in sound power between configurations 12UH and CONF is 8.5 dB with a free jet Mach No. of 0.2 as opposed to 4.5 dB at static conditions. It is important to note that the presence of the free jet flow produces a decrease in the PWL spectra for both the lobed mixers and the confluent configuration but the confluent is more affected. Similar trends hold for the tongue mixer. Similar local trends are observed in the SPL spectra for the various directivity angles.

(iii) With the free jet operating, the difference in sound power spectra between the confluent configuration and the forced mixers 12UH and 12TH is larger in the mid-to-high frequency bands than the difference in the low frequency bands (less than 500 Hz). Comparing the PWL of 12UH and CONF at M_{fj} = 0.2, the difference is 8.0 dB at 2000 Hz versus 6.0 dB at 100 Hz; whereas, in the static case the corresponding differences are 4.5 dB

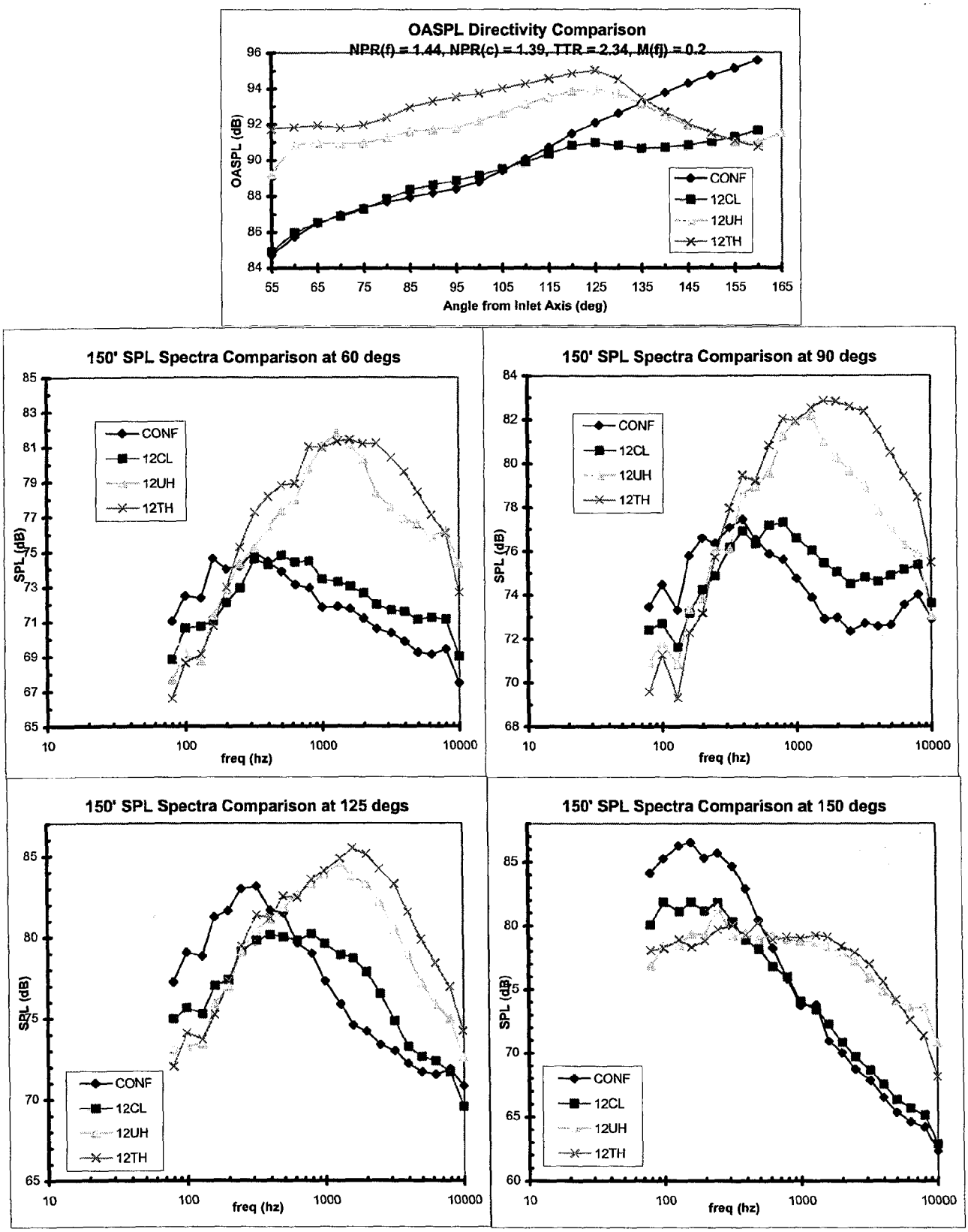

Figure 5.4(a) OASPL directivity and SPL spectra of CONF, 12CL, 12UH, 12TH mixers at T.O. # 1, $M_{fj} = 0.2$

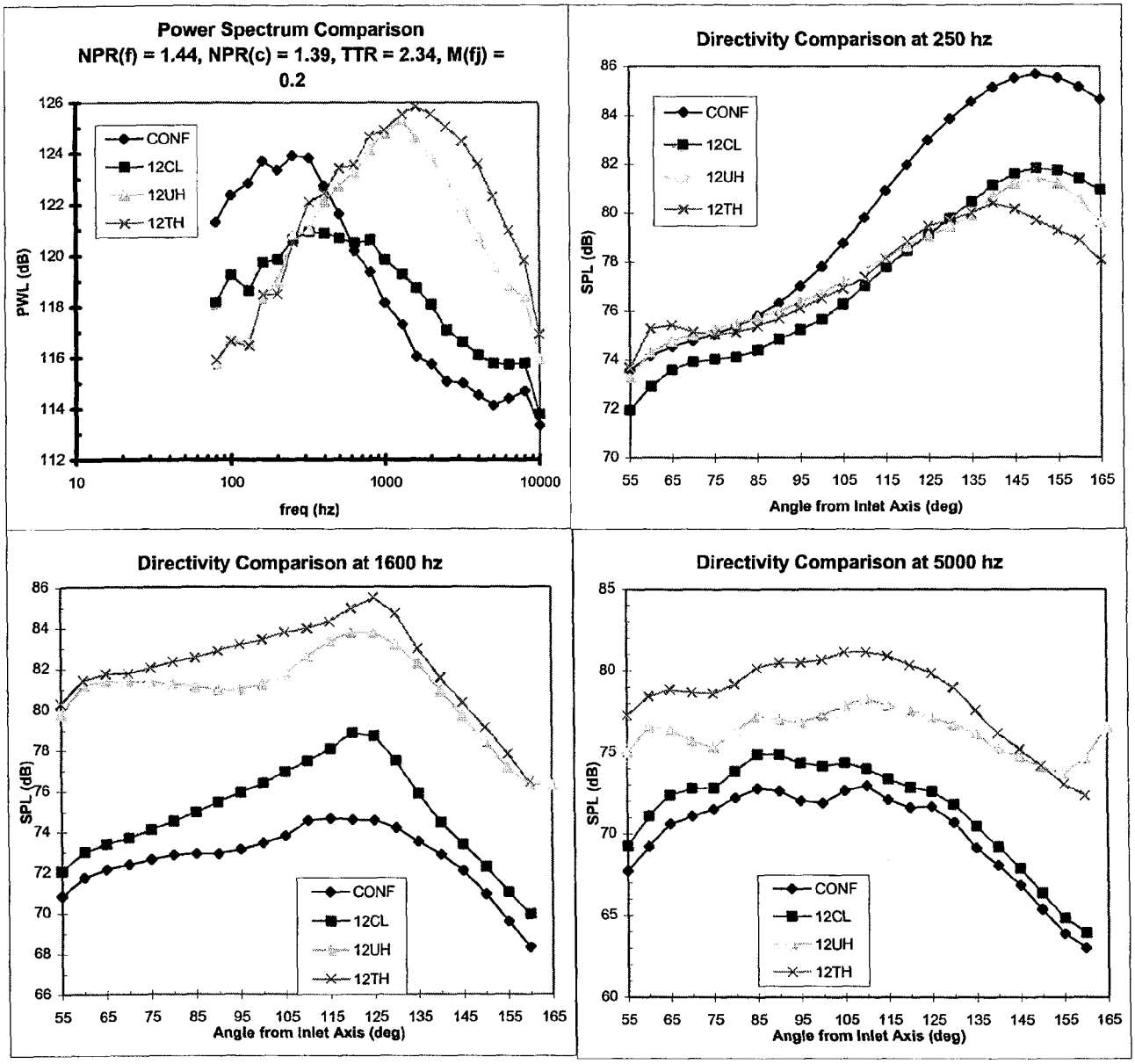

Figure 5.4(b) Power spectrum and SPL directivity of CONF, 12CL, 12UH, 12TH mixers at T.O. # 1, $M_{fj} = 0.2$

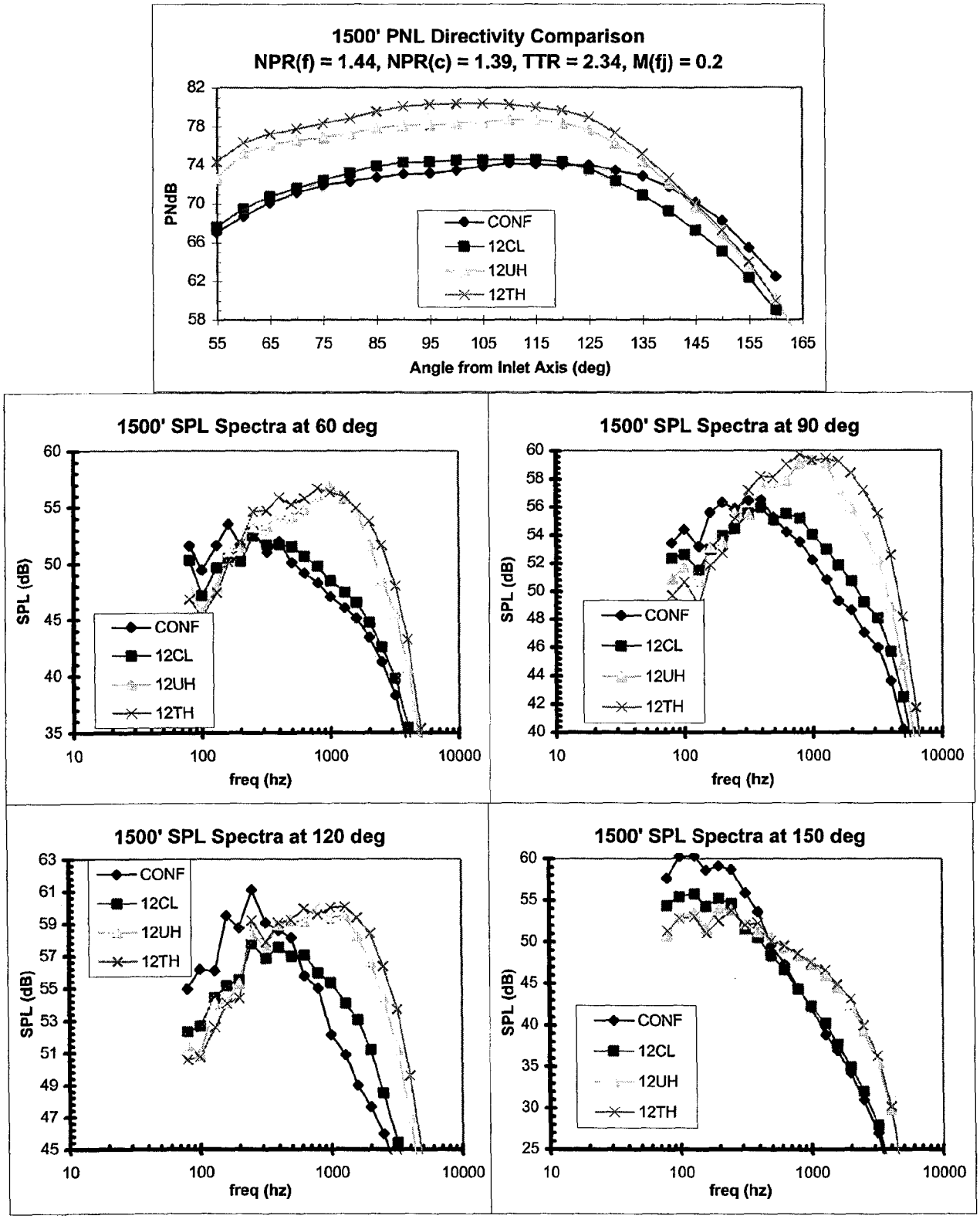

Figure 5.4(c) Flyover PNL directivity and SPL spectra of CONF, 12CL, 12UH, 12TH mixers at T.O. # 1, Mfj = 0.2.

at 2000 Hz versus 7.5 dB at 100 Hz.

(iv) From the similarity of dB-difference at low frequencies, whether the free jet flow is on or off (compare SPL's in Figure 5.4(a) and 5.1(a)), it is concluded that the low frequency spectra of both the forced mixers and the confluent mixer are generated in similar locations within the jet plume and respond similarly to an external flow. This is not true for the higher frequency portion of the spectrum.

(v) Under static conditions, the 150 ft polar SPL spectra for configuration 12UH and 12TH show very similar trends. This similarity is not altered when a free jet flow is present. This implies a similarity in source distribution between the two configuration which will be examined in more detail in a subsequent section.

(vi) At 125°, where lobed mixers have a local OASPL peak, the relative magnitudes of the peak SPL's between 12UH (or 12TH) and CONF (or 12CL) change drastically with external flows. Under static conditions, CONF has a larger peak SPL than 12UH peak SPL at this angle. With a free jet flow present, the magnitudes are reversed. The reduction in peak SPL of CONF or 12CL due to a free jet flow is typically larger than that for 12UH or 12TH at all angles upstream of 125°. That is, the free-jet appears to benefit CONF and 12CL more than it does 12UH or 12TH.

(vii) The noise benefits of the free-jet Mach No. for configurations CONF or 12CL over 12UH or 12TH are most clearly captured in the flyover PNL (Figure 5.(c). Note that both 12CL and CONF are now quieter than 12UH or 12TH at all angles. In particular, the decrease in noise at shallow angles for CONF or 12CL is significantly greater than that for 12UH or 12TH. The reason for this will be discussed later.

(viii) As a result of the spectral changes produced by the free jet flow, the confluent mixer, CONF, produces a lower PNL than the 12 lobe configuration with cutouts, 12CL, for angles less than or equal to the peak PNL angle of 120° or so. A very different result was observed under static conditions. In that situation, configuration 12CL produced a lower PNL for all angles than CONF.

In summary, forward flight-effect or non-zero free-jet speed benefits the confluent mixer and 12CL much more than it does either 12UH or 12TH. As a result, CONF and 12CL are now much quieter at <u>all</u> angles than 12UH or 12TH. Mixer CONF now even competes with 12CL for overall quietness but the EPNL discussion will be postponed to a later section. This appears mainly due to larger relative reductions in the mid-to-high range frequency sound for CONF and 12CL than those for 12UH and 12TH; the low frequencies are affected similarly for all the mixers.

5.2.2.2 <u>Lobe Number Effect</u>

Figures 5.5(a), (b), (c) show the polar OASPL, PWL, flyover PNL and corresponding SPL's for 12UH, 16UH and 20UH for a free jet Mach number of 0.2 at TO # 1. Primary attention will be paid to the difference between the results for 12UH and 20UH, recalling that 16UH has a much higher fan to core area ratio. The comparable plots for free jet flow are in Figures 5.2 (a), (b) and (c).

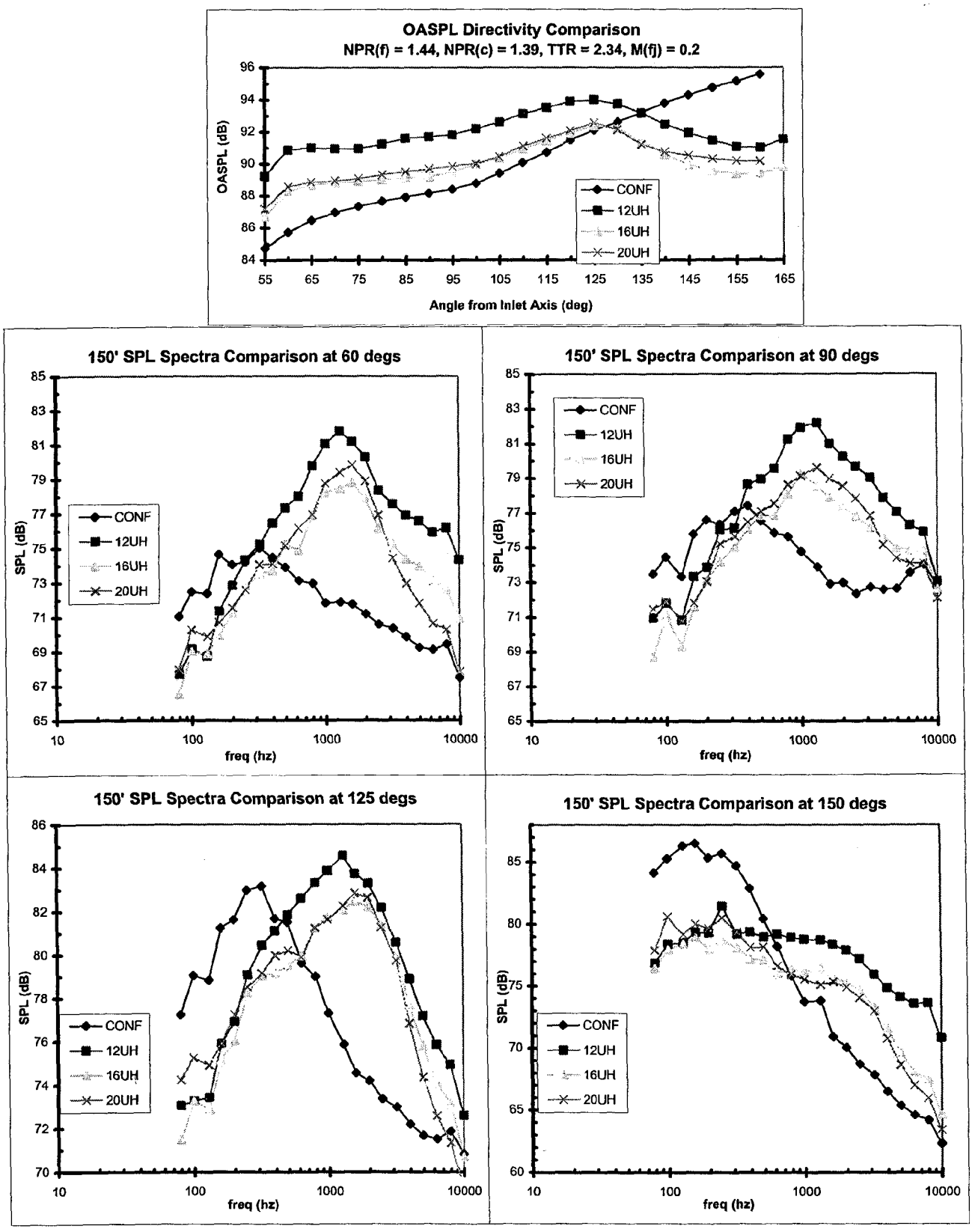

Figure 5.5(a) Effect of lobe number on OASPL directivity and SPL spectra at T.O. # 1, Mfj = 0.2

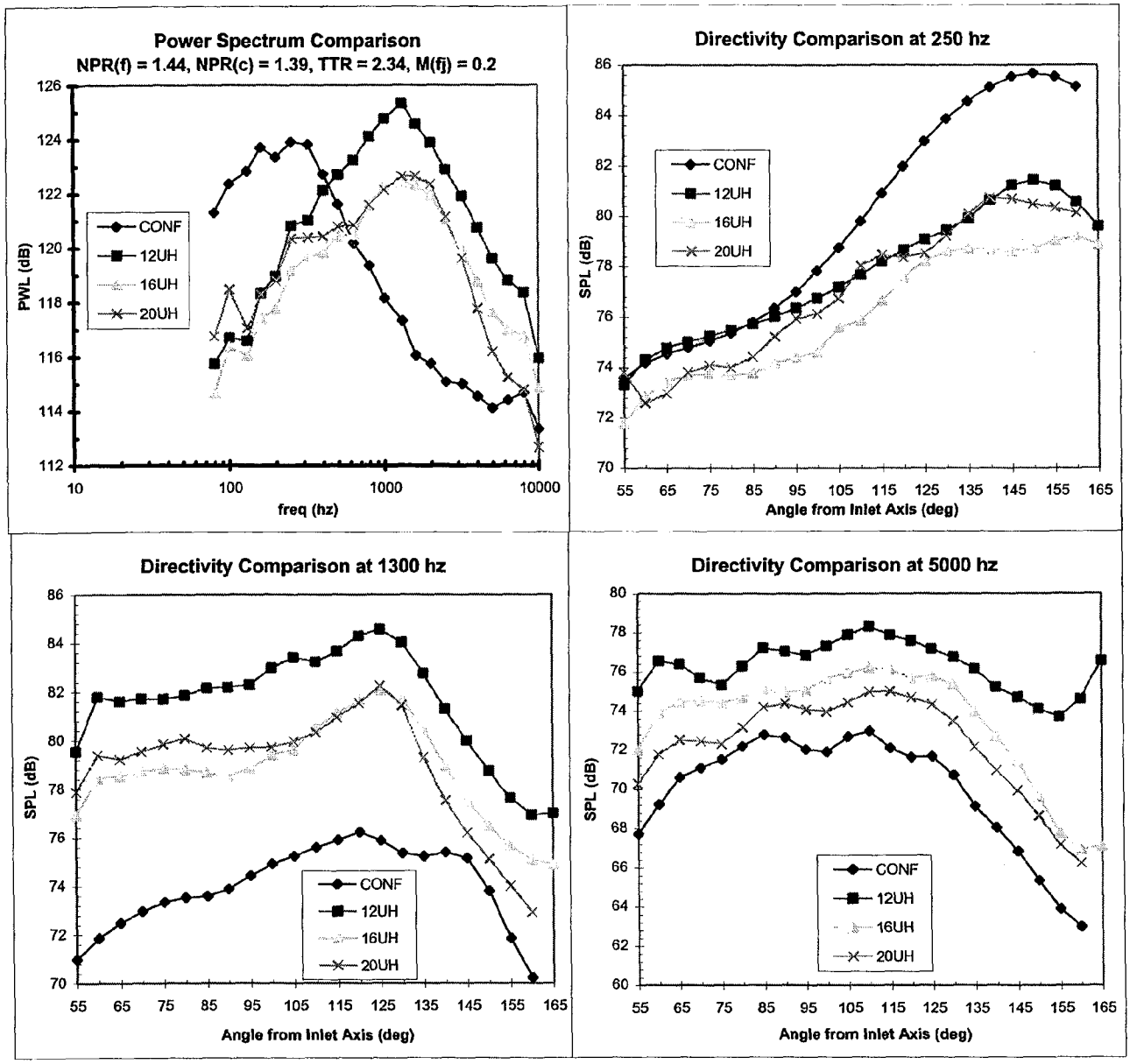

Figure 5.5(b) Effect of lobe number on power spectra and SPL directivity at T.O. # 1, $M_{fj} = 0.2$

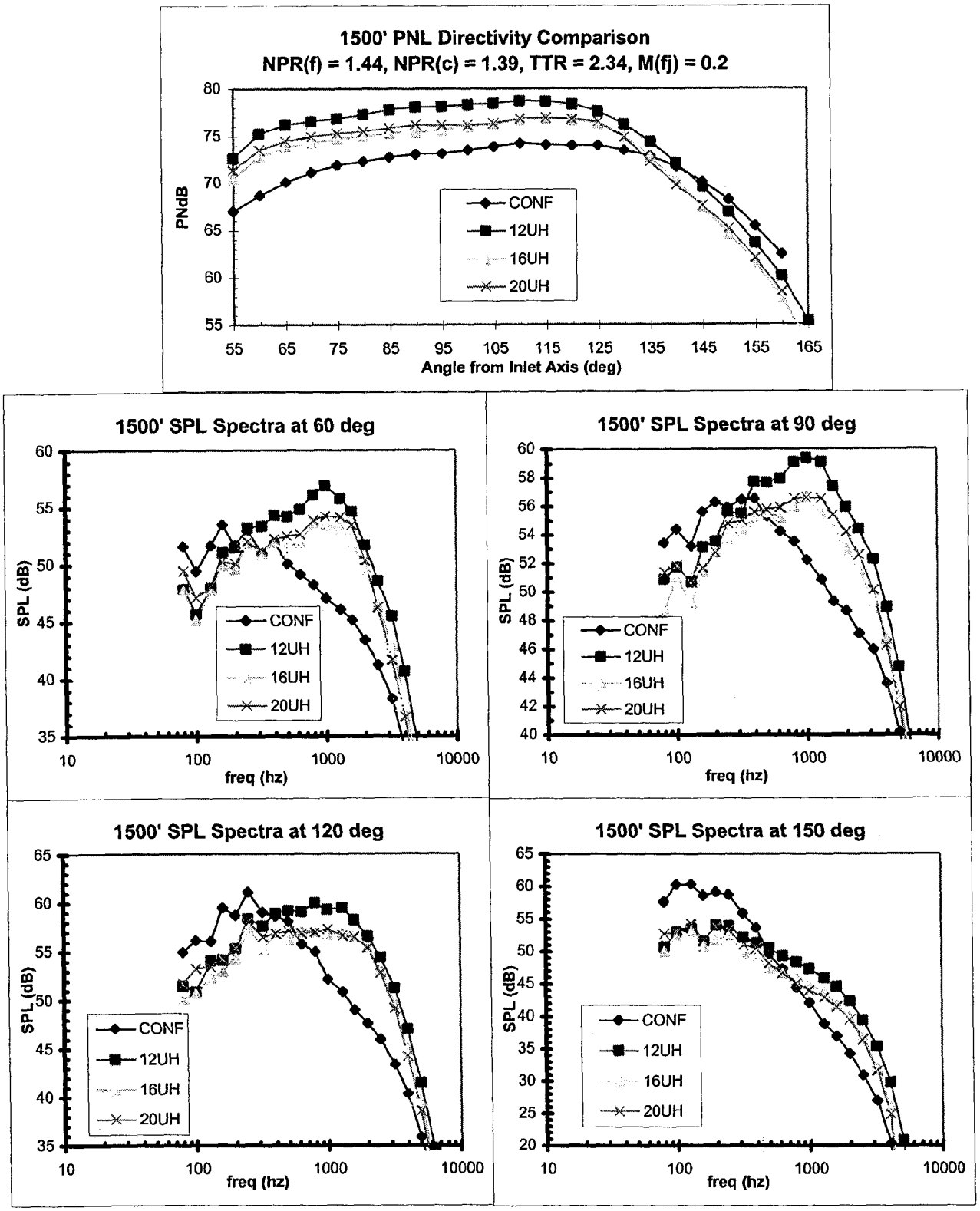

Figure 5.5(b) Effect of lobe number on flyover PNL directivity and SPL spectra at T.O. # 1, $M_{fj} = 0.2$

(i) For a free-jet Mach No. of 0.2, the OASPL of 20UH is lower than that of 12UH at all angles rather than just upstream of the local peak OASPL angle of 125° as was true for the static case. The spectral results of Figures 5.2(a) and 5.5(a) provide the explanation for this change in behavior. For the static case in Figure 5.2(a), the 12 lobe configuration, 12UH, was more effective in suppressing low frequencies for angles near the jet axis than was the 20 lobe design, 20UH. In the presence of an external flow, both designs produce essentially equal low frequency sound pressure levels; at higher frequencies, the free jet flow affects both configurations equally for all angles, with the overall result that the 20 lobe configuration remains quieter than the 12 lobe configuration.

(ii) The improved low frequency suppression of mixer 20UH in the presence of an external flow is also observed in the PWL spectra of Figure 5.5(b). It is now seen that the PWL of 20UH and 12UH are very similar at low frequencies as opposed to the static case (Figure 5.2(b)) where 20UH produced more power output.

(iii) From the flyover noise point of view, Figure 5.5(c) shows that now 20UH is quieter than 12UH at all angles rather than just upstream of the peak PNL angle as occurred in the static case (Figure 5.2(c)). The Doppler-shifted SPL in Figure 5.5(c) also show how, at even shallow angles, 20UH now matches 12UH at low frequencies and is, of course, always quieter at mid-to-high frequencies as in the static case.

(iv) However, with a free jet flow, both 12UH and 20UH produce higher PNL than the confluent baseline for angles less than or equal to 135°. As a result, the confluent configuration will be quieter than any of the unscalloped mixers in flight as will be seen in the EPNL values later.

In summary, when flight effects are included, increasing the lobe count makes the mixer-nozzle quieter at all angles, especially due to larger relative decreases in low frequencies as compared to smaller relative decrease in mid-to-high frequency spectra.

5.2.2.3 Effect of Scalloping

Figures 5.6 (a), (b), (c) show the polar OASPL, PWL, flyover PNL with the corresponding SPL-spectra or directivities for 20UH, 20MH and 20DH mixers for a free jet Mach number of 0.2 and at the reference operating condition TO #1. Comparable no free jet flow plots are shown in Figures 5.3 (a), (b) and (c).

(i) The presence of a free jet flow produces only a minor relative change in the OASPL directivity for the scalloped mixers compared to the static results in Figure 5.3(a). Both the polar SPL spectra (Figure 5.6(a)) and sound power spectra (Figure 5.6 (b)) of the scalloped mixers continue to show that free jet flow primarily affects the lowest frequencies. Little or no effect on the differences between mixer configurations is introduced by a free jet flow at higher frequencies as illustrated by comparison of Figure 5.3(a) and Figure 5.6(a) at an angle of 125° and a frequency of 2000 Hz for mixers 20UH and 20DH.

(ii) From a flyover noise viewpoint (see

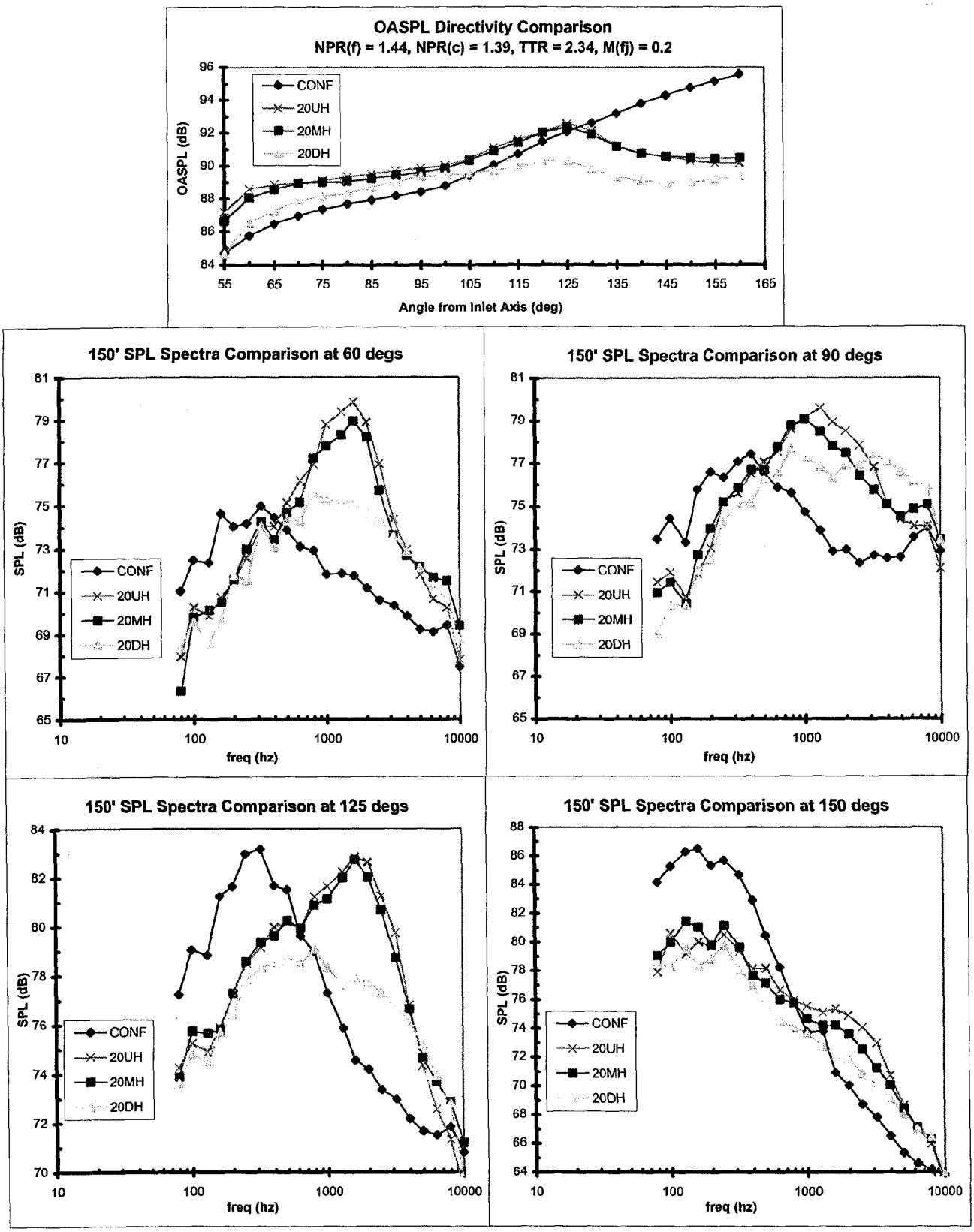

Figure 5.6(a) Effect of scalloping on OASPL directivity and SPL spectra at T.O. # 1, $M_{fj} = 0.2$

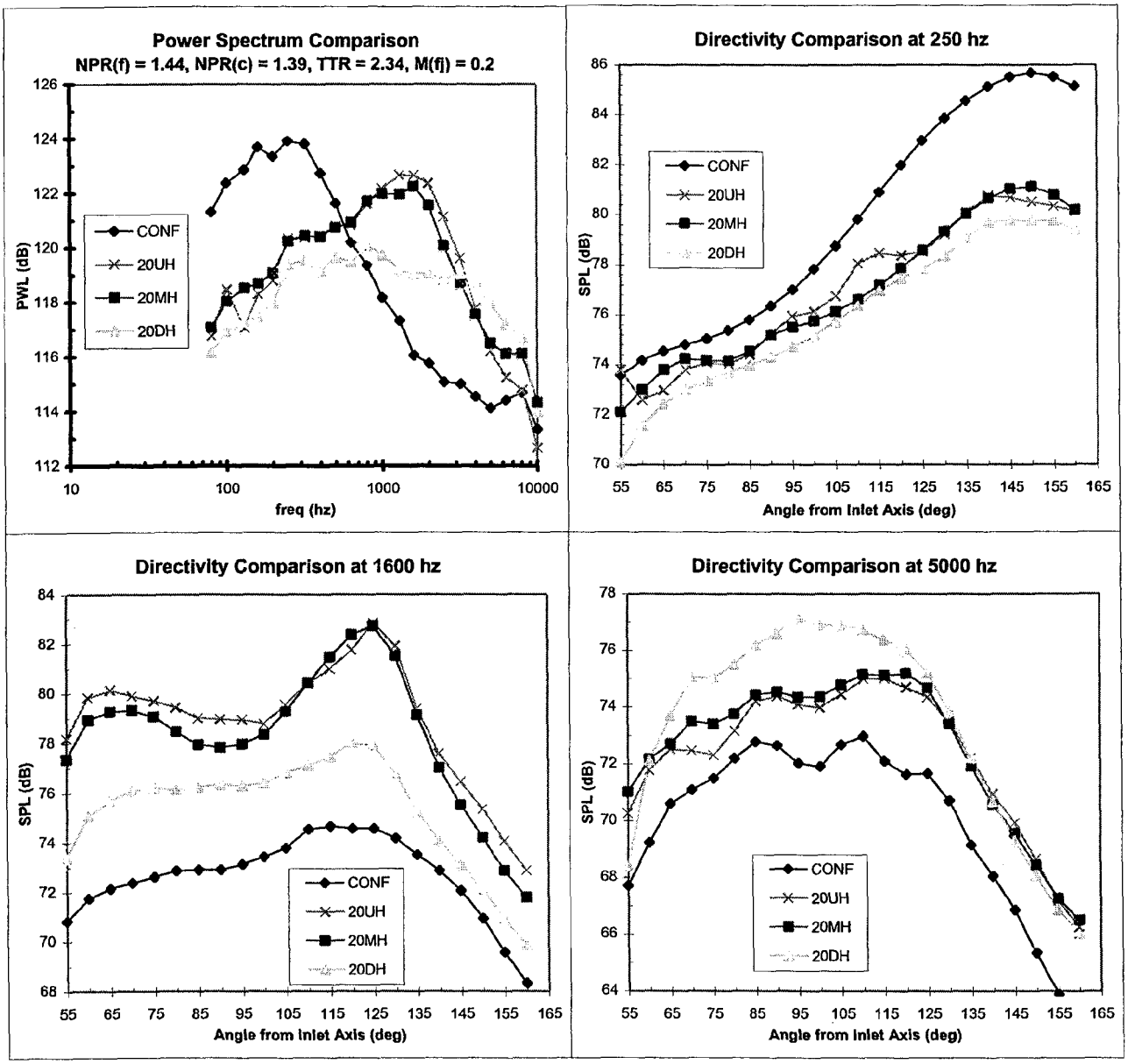

Figure 5.6(b) Effect of scalloping on power spectra and SPL directivity at T.O. # 1, $M_{fj} = 0.2$

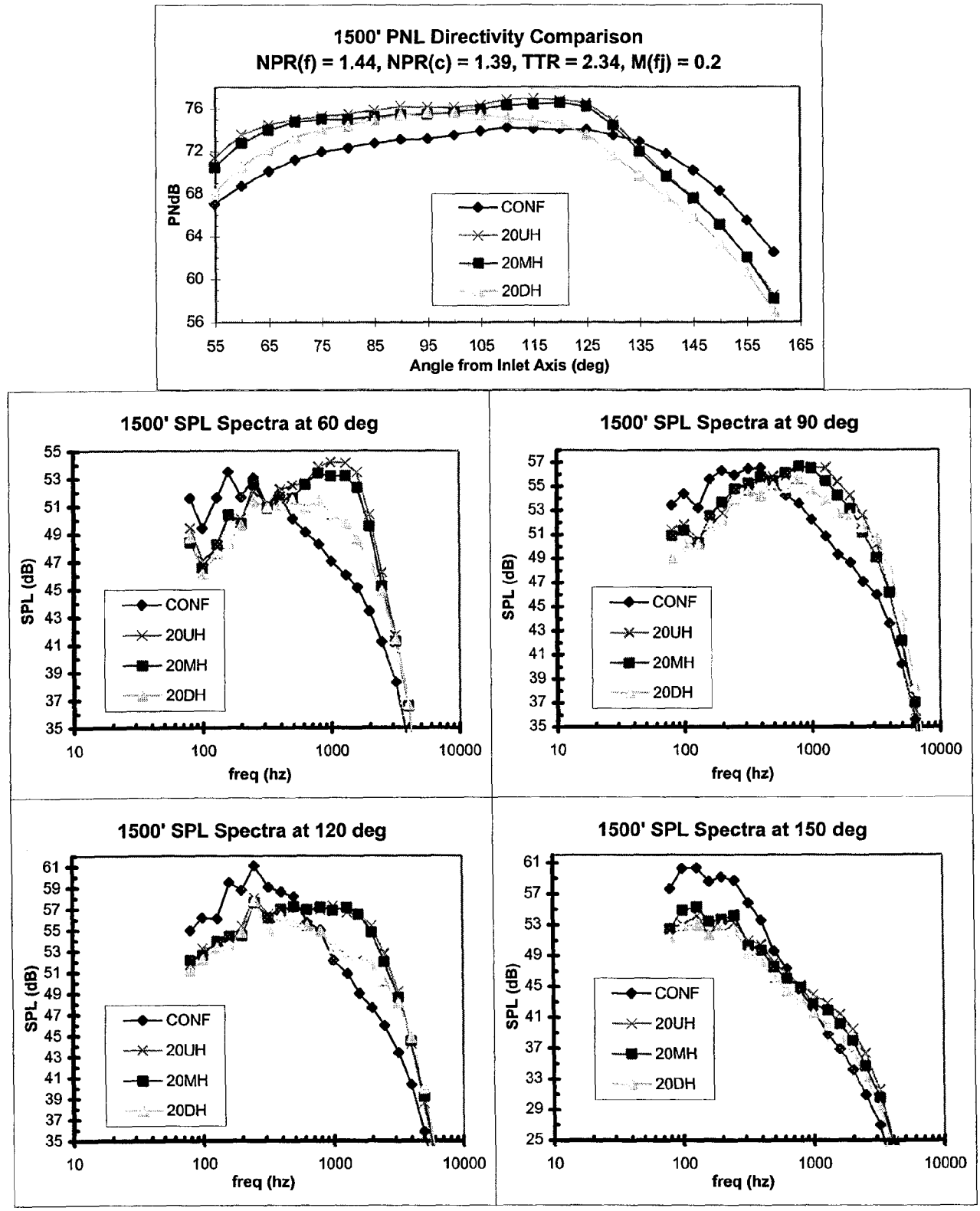

Figure 5.6(c) Effect of scalloping on flyover PNL directivity and SPL spectra at T.O. # 1, $M_{fj} = 0.2$

PNL directivity Figure 5.6(c)) the scalloped mixer remains quieter than the unscalloped mixer at all angles in the presence of a free jet flow. At shallow angles near the jet exit axis, the difference between scalloped and unscalloped designs increases slightly when a free-jet flow is present.

(iii) In terms of peak PNL, the confluent mixer is superior to even the quietest scalloped, lobed mixer (20DH) with a free jet flow present for the low power operating condition under consideration. This superiority is also observed for angles less than the angle for peak PNL. This difference in PNL continues to be driven by the higher levels observed in the mid-to-high frequency sound for the lobed mixers. The penalty incurred in this frequency range by lobed mixers is reduced with scalloping but not removed whether a free jet flow is present or not.

In summary, the beneficial effects of scalloping are not influenced by the presence of an external flow-field. The scalloped designs tested in this program were equally effective under static conditions and with a free jet flow present.

5.2.2.4 Confluent Mixer Benefits

In the above section, it was found that the confluent configuration produced lower PNL values than any of the scalloped designs for angles less than or equal to the peak PNL angle when an external flow is present. Comparison of the spectral characteristics of the confluent mixer with the lobed designs showed that the lobed designs produced excess energy in the 1-4 KHz frequency band. This spectral shift for the lobed mixers has been related to the presence of the turbulence generated by the strong axial vortices induced by these devices. The confluent design produces no axial vorticity, relying solely on the formation of Kelvin-Helmholtz vortex sheet instability and consequent turbulent transport between the primary and the secondary flow streams to accomplish mixing of the two streams. This type of mixing does not produce intense turbulence in the length scales associated with acoustic radiation in the mid-frequency ranges. This type of viscous mixing is also much less effective than that induced by the strong axial vortices of forced lobe mixers and the plume does not decay as fast as a fully mixed jet. As a result, the confluent mixer becomes a strong source of low frequency noise under static conditions. The presence of the free jet produces a reduction in shear downstream of the primary potential core, as will be analyzed later. Since this area is the primary source of low frequency noise in a jet, the reduced shear will result in reduced low frequency noise. This is particularly important for the confluent mixer, since its spectra is dominated by low frequencies. The external flow has little or no impact on the mid-spectral bands, which dominate the radiated noise from the lobed mixer configurations.

Directivity differences between the lobed and confluent mixers also affect integrated metrics like EPNL. The confluent mixer produces it maximum polar levels at shallow angles near the jet axis. During flyover type calculations, increases in slant propagation distance and source convective de-amplification associated with shallow angle radiation further benefit the confluent design. Lobed designs tend to produce maximum polar levels closer to 90° and as a result do not see the same propagation distance benefits. Based on comparison at the fixed operating condition TO #1, only mixer configuration 12CL provides a PNL

benefit over a confluent mixer when flight effects are included. Consideration of detailed EPNL trends will be deferred to a later section. However it is possible to draw some conclusion at this point related to flyover noise suppression. It has been shown that the noise levels in the low frequency portions of the jet mixing spectrum are significantly reduced as the flight speed increases. Lobed mixers produce a dramatic decrease in the low frequency spectrum at static conditions but this is accompanied by an increase in higher frequency bands. Forward flight does not significantly influence this high frequency hump. Removing portion of the mixer sidewall through the use of cutouts or scalloping, increasing the number of lobed mixers and possibly reducing the lobe radial penetration reduces the increase in the higher frequency band sound produced by lobed mixers, but not to the levels observed on a confluent configuration. As a result, with flight effect, lobe mixers produce only a minimal reduction in jet noise when jet velocities are low.

An important general lesson learned regarding flyover noise suppression at low jet speeds is the following: any mechanism that produces less of the "annoying" mid-to-high frequency noise is usually preferable even if it does not significantly reduce the less annoying low frequency noise; flight effect helps reduce the low frequency noise anyway.

In the next section, results at additional free jet Mach numbers will be presented. This data provides insight into the axial location of the sources producing the mid-to-high frequency range noise associated with lobed mixers, prompted by the observations in this section that free jet flow affects some frequencies less than others.

5.2.3 Flight-Effect: Other Free Jet Mach Numbers

Data was acquired over a range of free-jet Mach numbers, varying from 0.0 to 0.3. The effect of varying this parameter on the PWL spectrum, polar OASPL directivity, and flyover PNL directivity is presented and discussed for each mixer in this section. Figures 5.7 to 5.14 show these acoustic metrics for, respectively, CONF, 12CL, 12UH, 12TH, 16TH, 20UH, 20MH, and 20DH mixers. Note that the vertical-axis scale for a given metric may vary between mixers. This should be borne in mind when comparing changes in a given metric from one mixer to the other.

Increasing the free-jet Mach number produces the following effects for every mixer:

(i) All acoustic metrics (PWL, OASPL and PNL) decrease.
(ii) The reduction in low frequency PWL is much greater than that at mid or high frequency.
(iii) The decrease in aft quadrant OASPL is much greater than that in the front quadrant.
(iv) Similarly the decrease in the aft quadrant flyover PNL is much larger than that in the front quadrant.
(v) The angle at which the peak PNL occurs moves upstream with increasing free-jet speed.

All these effects were noted in the previous section when studying $M_{fj} = 0.2$ and are now seen to be extended also to $M_{fj} = 0.3$. But the additional decreases due to a change of M_{fj} from 0.2 to 0.3 are typically not as drastic as those from $M_{fj} = 0.0$ to $M_{fj} = 0.2$.

The fact that noise, in general, decreases with increases in free-jet Mach numbers is

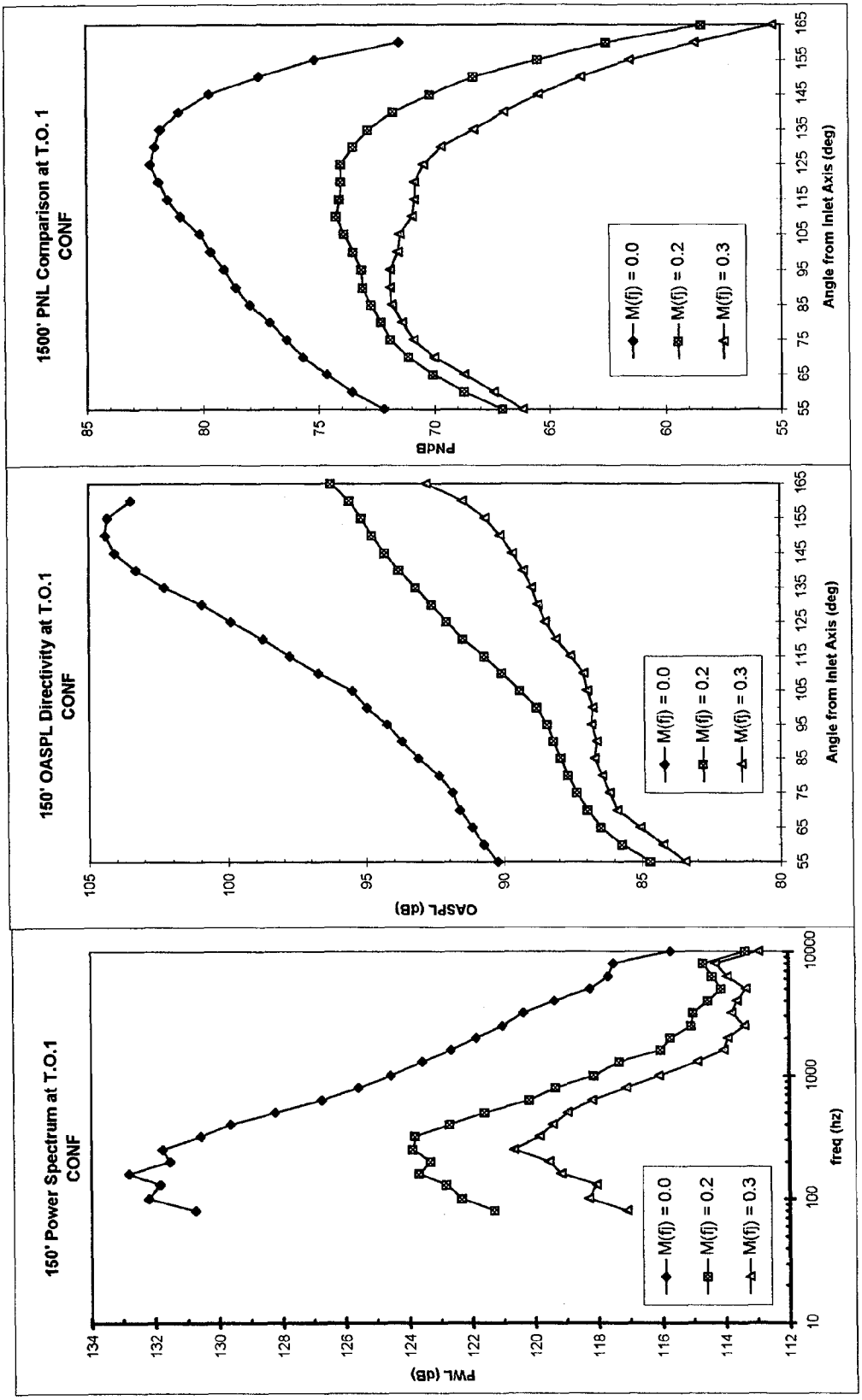

Figure 5.7 Effect of Mfj on power spectrum, OASPL directivity and flyover PNL directivity for CONF mixer at T.O. # 1

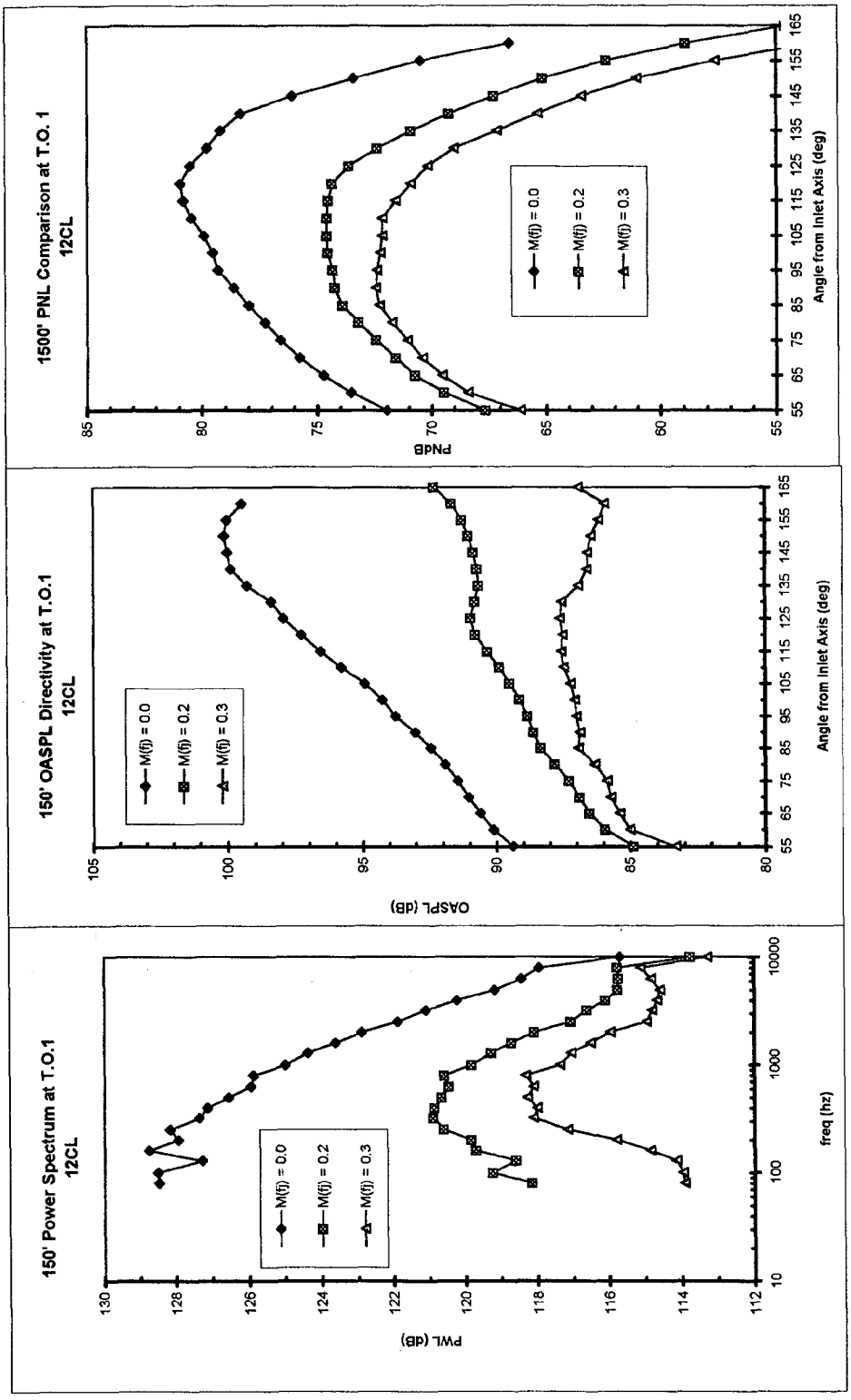

Figure 5.8 Effect of M_{fj} on power spectrum, OASPL directivity and flyover PNL directivity of 12CL mixer at T.O. # 1

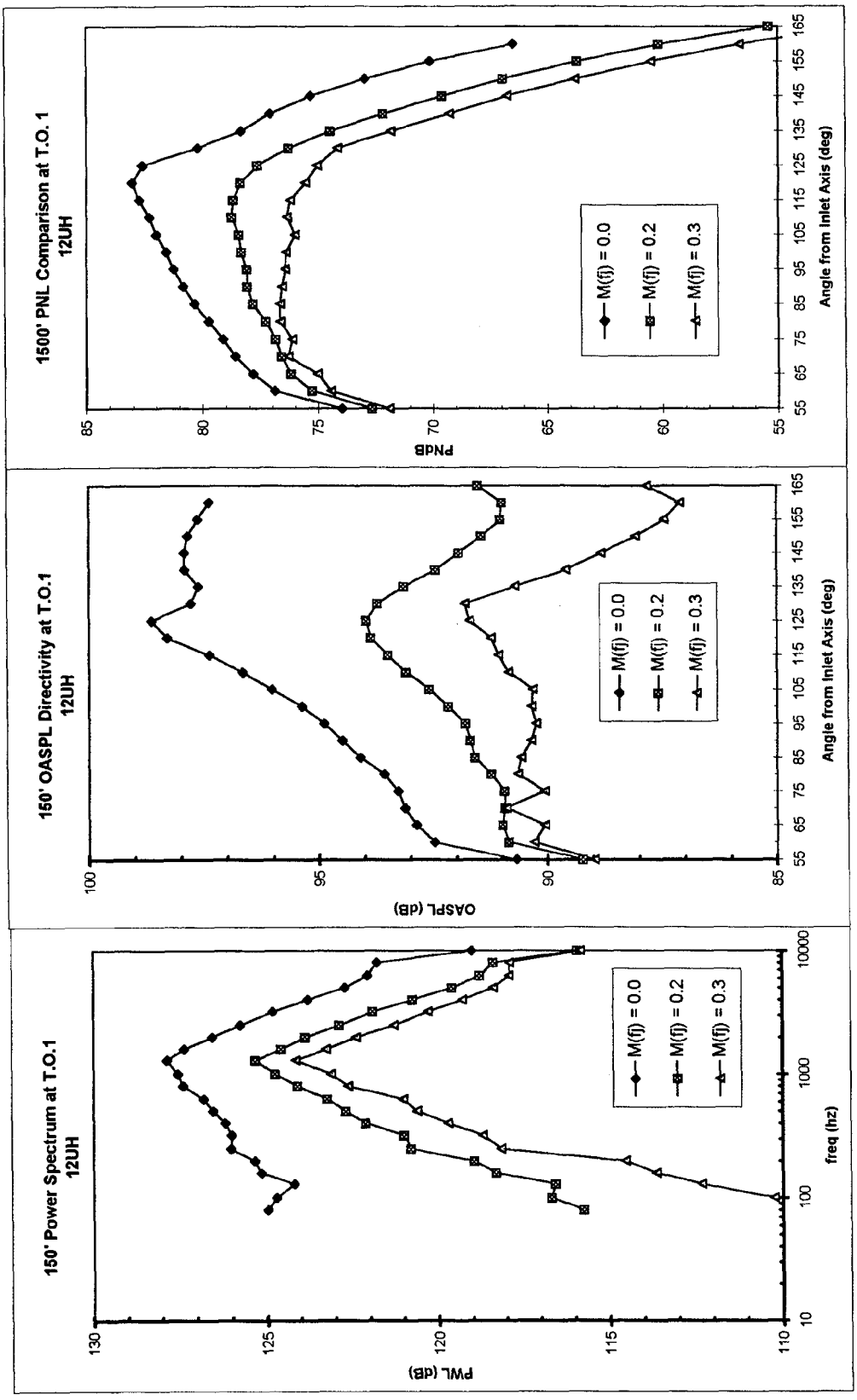

Figure 5.9 Effect of M_{fj} on power spectrum, OASPL directivity and flyover PNL directivity of 12UH at T.O. # 1

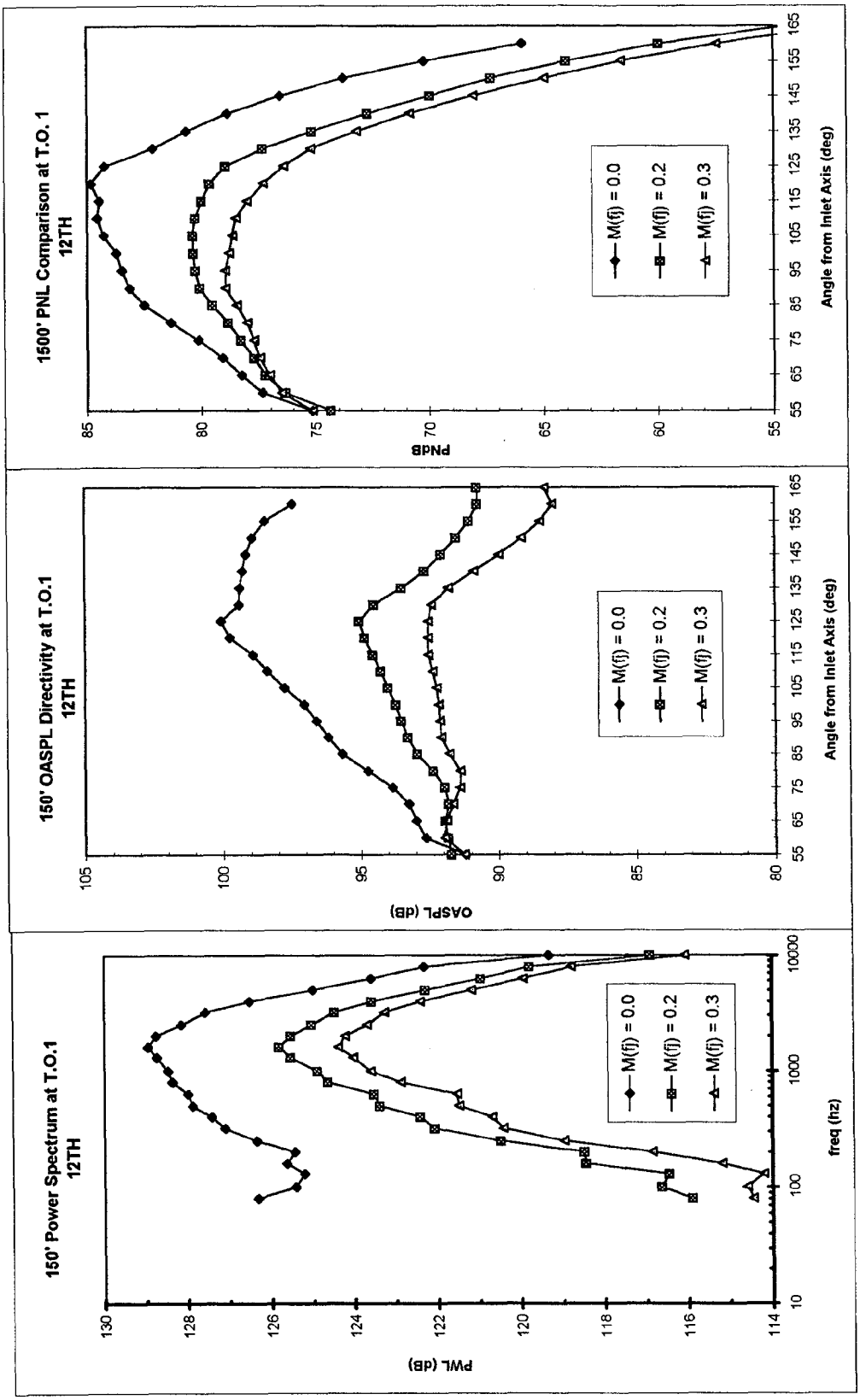

Figure 5.10 Effect of M_{fj} on power spectrum, OASPL directivity and flyover PNL directivity of 12TH mixer at T.O. # 1.

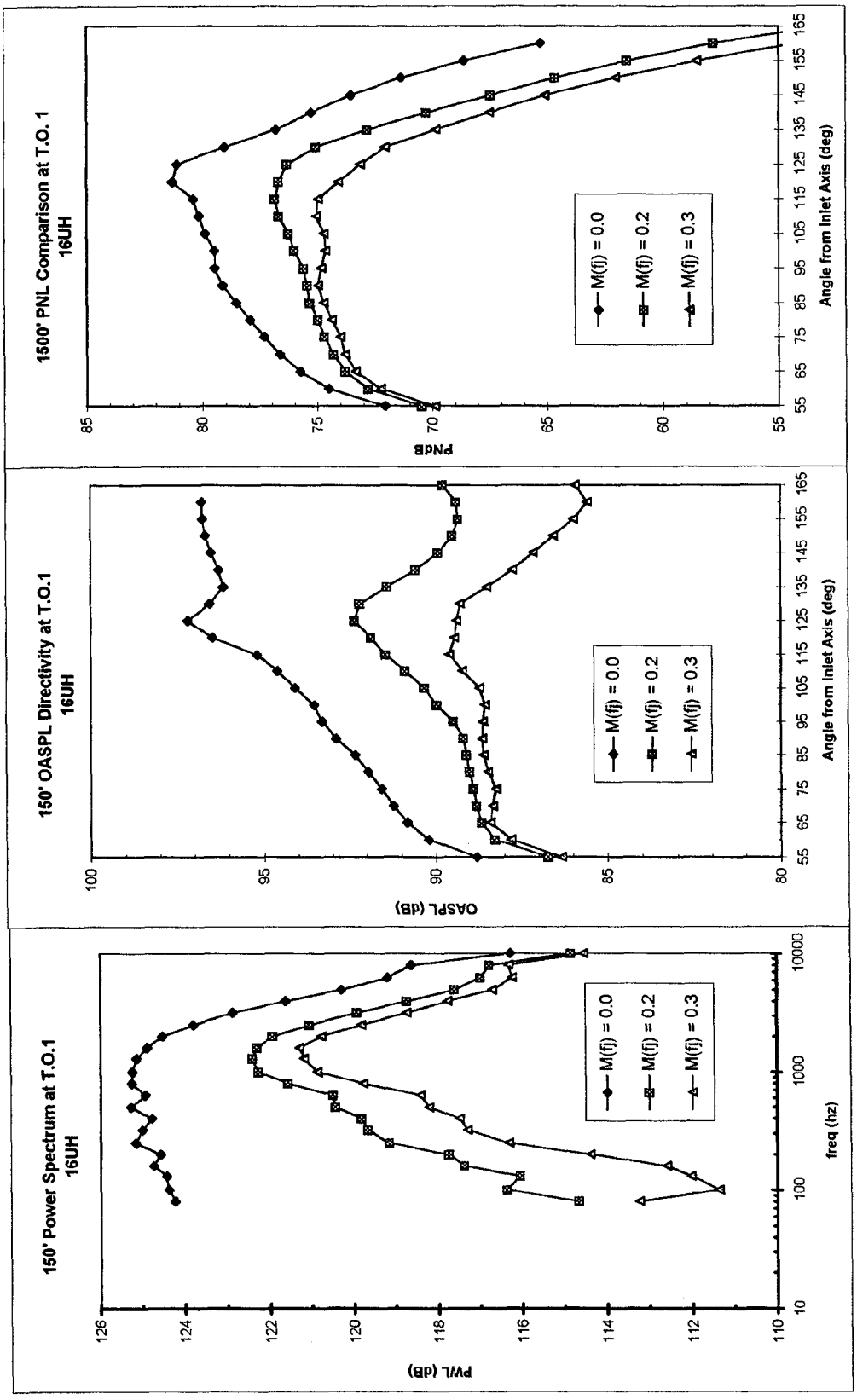

Figure 5.11 Effect of Mfj on power spectrum, OASPL directivity and flyover PNL directivity of 16UH mixer at T.O. # 1.

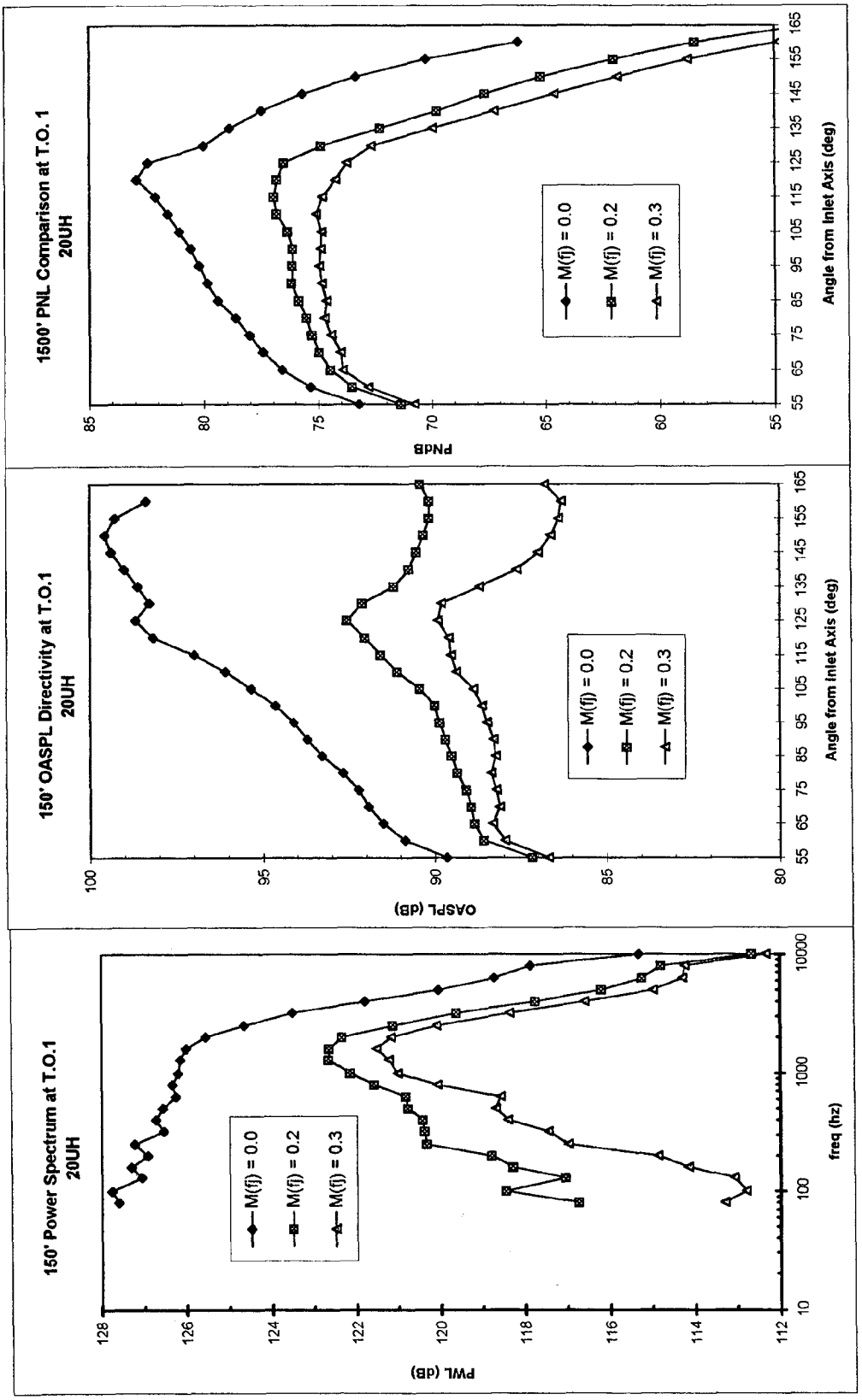

Figure 5.12 Effect of M_{fj} on power spectrum, OASPL directivity and flyover PNL directivity of 20UH mixer at T.O. # 1.

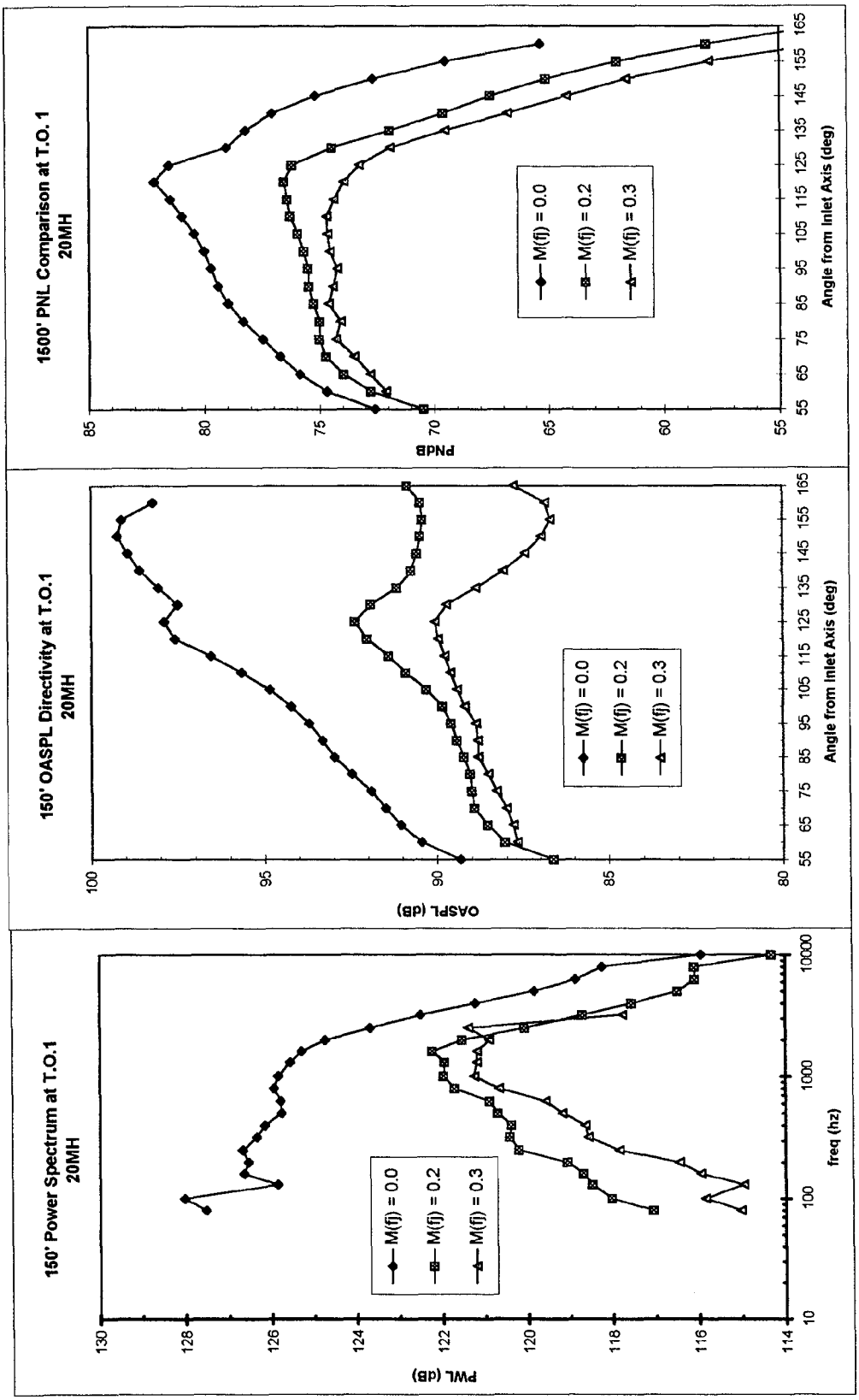

Figure 5.13 Effect of M_{fj} on power spectrum, OASPL directivity and flyover PNL directivity of 20MH mixer at T. O. # 1.

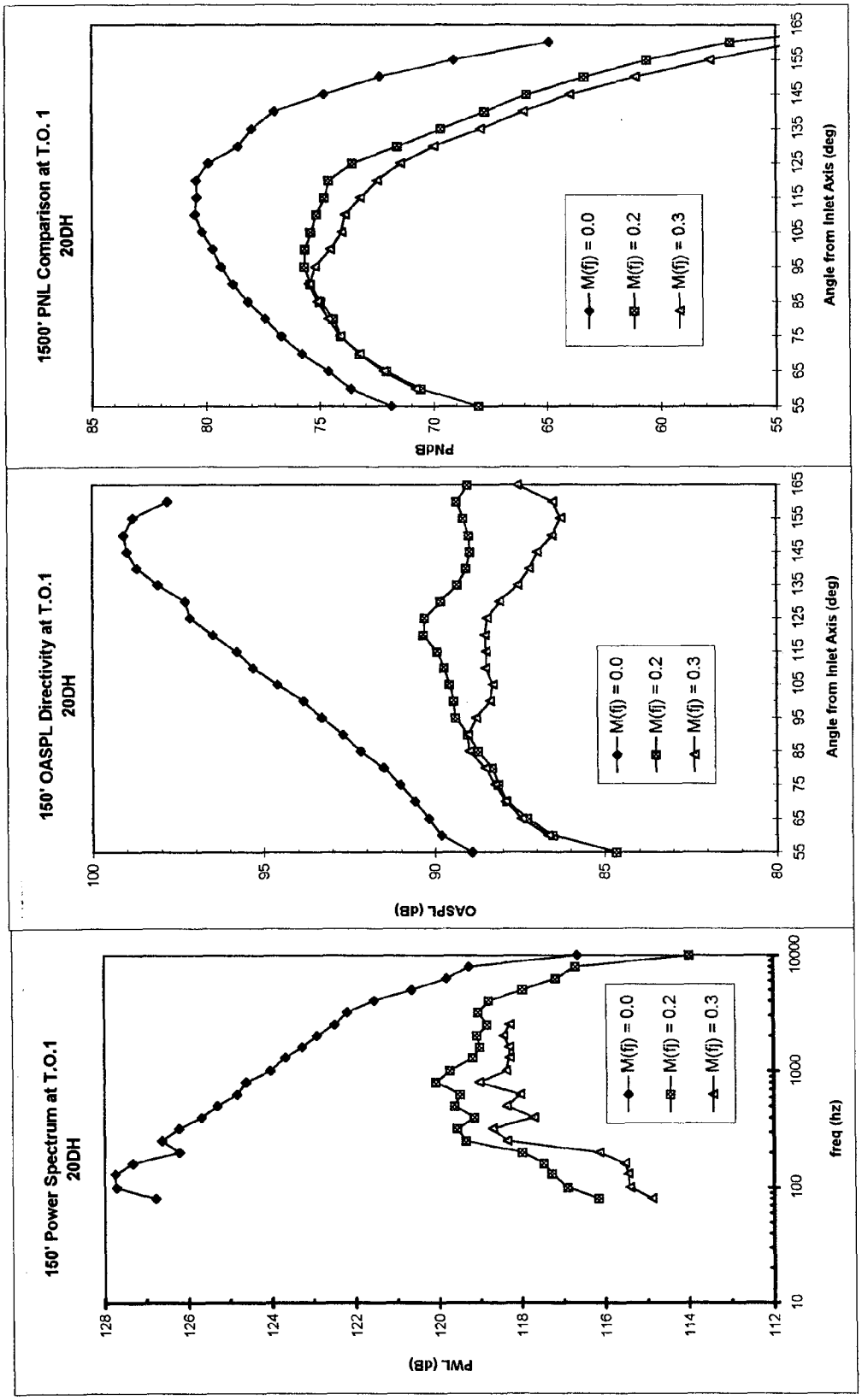

Figure 5.14 Effect of Mfj on power spectrum, OASPL directivity and flyover PNL directivity of 20DH mixer at T.O. # 1.

well known experimentally for single-stream nozzles and the same reason must apply to at least fully-mixed nozzles with uniform exit flow. A new and simple mathematical explanation is given below using Abramovich's theory of turbulent jets[20].

An increase in free-jet speed reduces the shear-layer thickness, δ, and increases the potential core length. The highest turbulence intensity and the dominant noise source is known to be just downstream of this potential core where the shear-layers surrounding it interact most vigorously. The magnitude of the radial gradient of axial velocity, $|\partial U/\partial r|$, governs the dominant noise source intensity and the jet diameter there governs the source volume and, hence, its net contribution to noise. A first-order estimate of these quantities can be obtained by using

$$\frac{\partial U}{\partial r} \approx \frac{U_{free-jet} - U_{jet}}{\delta}.$$

The shear layer thickness at the end of the potential core, δ_C, can be estimated by using, for simplicity, Abramovich's expression for incompressible, axisymmetric cold turbulent jets (which assumes self-similarity in the velocity in the initial portion of the jet/ambient mixing layer), namely,

$$\delta_c = R / \sqrt{a + bm}$$

where R is nozzle-exit radius, $m = U_{free-jet} / U_{jet}$ and a, b are universal constants with values of 0.214 and 0.144 respectively.

The above two formulae for $\partial U/\partial r$ and δ_C immediately show that the ratio of $|\partial U/\partial r|$ at the end of the potential core with a free-jet present to that with no free-jet is

$$\eta = |1 - m| \sqrt{1 + \frac{b}{a} m}.$$

This ratio can be easily shown to decrease with increase in m for $0 \leq m \leq 1$. For observed self-similar velocity profiles[20] it can be shown that, η, as given above, is also the ratio of the maximum axial velocity gradients in the flow at this location. Thus, when the free-jet speed increases, the potential core length increases and the shear at its end decreases, leading to a decrease in turbulence intensity. In addition the volume of the noise sources at this location, characterized by the radius δ_C, is also reduced. This decrease in turbulence intensity, as well as, the volume of turbulent source, leads to a decrease in the peak far-field noise. For hot jets, with jet-to-ambient density ratio other than one, the above argument can be extended by using more complicated expressions for the shear-layer growth given in Abramovich[20]. With some modifications this argument can also be extended to coaxial jets where the ambient/jet shear layer increases the annular fan potential core length with an increase in free-jet speed but not the central primary potential core length.

The above explanation is applicable only for the "peak" noise producing regions outside the nozzle for fully-mixed or single-stream nozzles. It cannot explain, for example, the observed differences in sensitivity of high and low frequency noise to free-jet speed changes, since these originate in different portions of the jet. Abramovich's theory[20] can be applied similarly to the upstream end of the jet (jet/ambient shear layer or the "initial' region of Fisher et al [17]) to study the high-frequency noise, as well as, to the far downstream self-similar region of the jet ("mixing" region of Fisher et al[17]) to study low-frequencies. However, we do not embark on that analysis here.

Returning back to Figures 5.7 to 5.14 we note that, as discussed before, the smaller

changes in higher frequencies in the PWL spectra with increasing M_{fj} are related to smaller changes in OASPL and PNL in the upstream angles where these frequencies dominate. Similarly, the larger changes in the low frequency PWL spectra with increasing M_{fj} are related to larger changes in the downstream angles for OASPL, PNL where low frequencies dominate.

The flyover PNL directivity is influenced by several additional effects due to aircraft motion, which are not present in the polar OASPL directivity and which are worth emphasizing again. First is the source convective amplification effect which amplifies sound in the upstream quadrant and decreases it in the downstream quadrant solely due to the motion of the source with respect to the observer. This tends to rotate the PNL-θ curves clockwise around 90°. Secondly, in a horizontal flyover above the observer, the slant distances from the source to the observer and the Doppler shift in frequency change with angle. The directionality of the Doppler frequency effect produces an increase in the observed frequency spectrum, as the source approaches the observer and a corresponding decrease in the observed spectrum as the source moves away from the observer. As a result, the atmospheric absorption applied to a particular frequency band in the front and rear quadrants will relate to different portions of the original source spectrum. This creates further asymmetry in PNL directivity around 90° than the true source asymmetry captured in the polar OASPL directivity in the reference frame of the nozzle. These effects combined with the overall decrease in peak noise source amplitude, discussed earlier, leads to the observed downward shift in PNL-directivity with clockwise rotation around 90° when the free-jet speed is increased.

As noted before, the effects discussed above produce a steep decrease in flyover PNL at shallow angles. Since EPNL is a temporal integration of PNL (corrected for tones), but only extends over the interval when the PNL is within 10 dB of the peak value, reductions in noise at shallow angles may have little effect on EPNL since the levels at these angles are near or below the 10 dB down points. For example, note that at Mfj = 0.2 this happens at 160° for CONF, 155° for 12CL, and about 145° for the rest of the mixers. The spectra associated with these angles are dominated by low frequencies whose strengths are in turn governed by the rate of plume decay. Thus, devices which promote only rapid plume decay near the jet axis for the purpose of reducing noise levels will not significantly reduce EPNL unless they also reduce the mid-to-high frequency noise at other angles.

A far more effective strategy is to focus on reducing the PNL for angles less than or equal to the peak. There are several reasons for this. First, the rate of decrease of PNL is lower for angles upstream of the peak than downstream. As a result, the majority of the "duration" correction for EPNL is associated with angles upstream of the peak PNL angle for the forced mixers. In addition the spectra at the upstream angles peak at frequencies with a higher annoyance weighting.

Perhaps the most striking feature of Figures 5.7 to 5.14 is the difference in sensitivity of the PWL, OASPL, or PNL to free-stream Mach number changes when we compare one mixer against the other. For example, all the lobed mixers show smaller changes in high frequency PWL or upstream OASPL or PNL than the confluent mixer when free stream Mach number is changed. However, mixer 12CL shows remarkably similar changes to CONF as free stream Mach number changes, except for the OASPL

signature at shallow angles. The noise signatures of all the "unscalloped" mixers (12UH, 16UH and 20UH) are also remarkably similar to each other and markedly different than CONF. The deeply scalloped mixer, 20DH, has distinctly different noise signatures than the rest of the lot. (Note that the high-frequencies recorded by the 55° microphone for the 20DH mixer test were in error and are not shown in Figure 5.14.) Its PWL appears closest to that of 12CL but not its OASPL or PNL. The tongue mixer, 12TH, also has its own distinct noise signatures but is, perhaps, most similar to 12UH, as noted before.

Before leaving this section, we make two final notes.

(i) If mid-to-high frequency sound is affected less by free-jet Mach number changes then the sources that produce them may be hidden or shielded away from the effects of the free-jet/nozzle-jet shear layer.

(ii) Since changes in free-jet speed produce changes in the direction of the ray coming out from the jet (because acoustic group velocity (ray) in the free-jet is the vector sum of phase velocity and free-jet velocity), in order to study the change in the noise source due to free-jet effects one needs to study polar SPL's not at the same angles in the far-field inside the free-jet, but at angles obtained after removing the additional refraction changes in the transmitted rays.

The effect of a free jet flow on the corresponding polar SPL's will be examined in depth in a later section.

5.3 Mixers with Reference Nozzle-Length at Higher Nozzle Pressure Ratio Conditions

It is expedient to examine how the noise signatures of different mixers compare at the two higher growth TO conditions with higher thrusts or jet speeds.

We first examine the acoustic results at M_{fj} = 0.2 for the two higher pressure ratio TO conditions for the various groups of mixers. Although corresponding static results are available, it is the case with a free jet flow present (simulating aircraft motion), that is the more realistic one from a flyover noise point of view. Secondly, since we found in the last section how important noise source information can be obtained by studying the effect of various free-jet Mach numbers, we will examine that effect for the highest pressure ratio condition (TO #3) in detail.

5.3.1 TO #2 and #3 with Free-Jet Mach Number 0.2

The overall spectral information is captured in the polar PWL-spectrum, whereas, the flyover noise is best captured in the flyover PNL directivity. For the sake of brevity, we will present the PWL-spectra and flyover PNL-directivity including the polar SPL-directivity of the most energetic component and flyover SPL-spectra at only the peak PNL angle. These four plots, which summarize the most important noise signatures at any give free-jet Mach number, will be presented in this section for each group of mixers.

5.3.1.1 12-Lobed Mixers

Figures 5.15 and 5.16 show PWL, PNL and SPL for the 12-lobed mixers and the confluent baseline (Group 1) at TO #2 and TO #3 respectively. Comparison of PWL

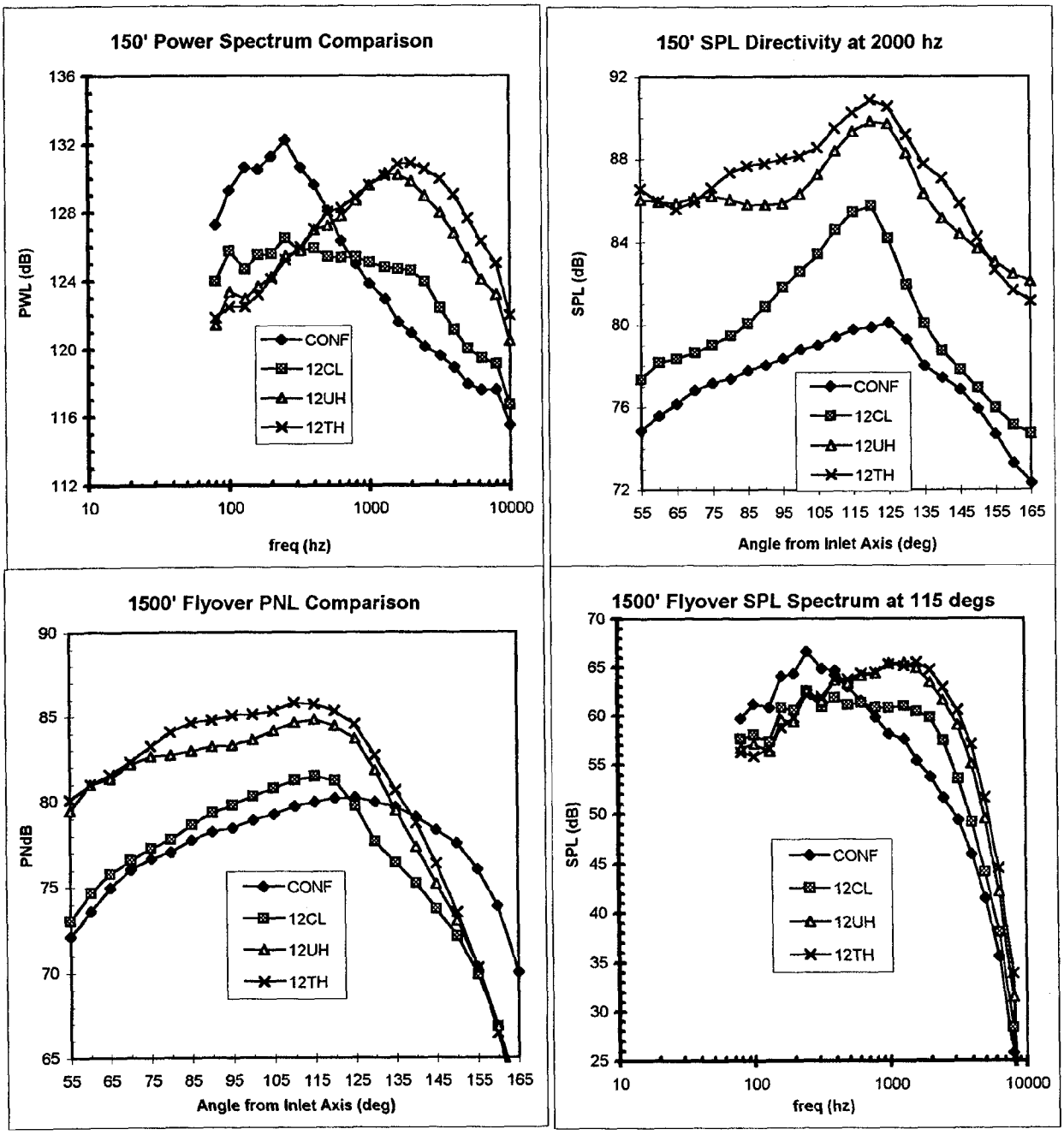

Figure 5.15 Power Spectrum and Flyover PNL Comparison of Mixers at T.O.#2 and M(fj) = 0.2 (12 Lobed Mixers)

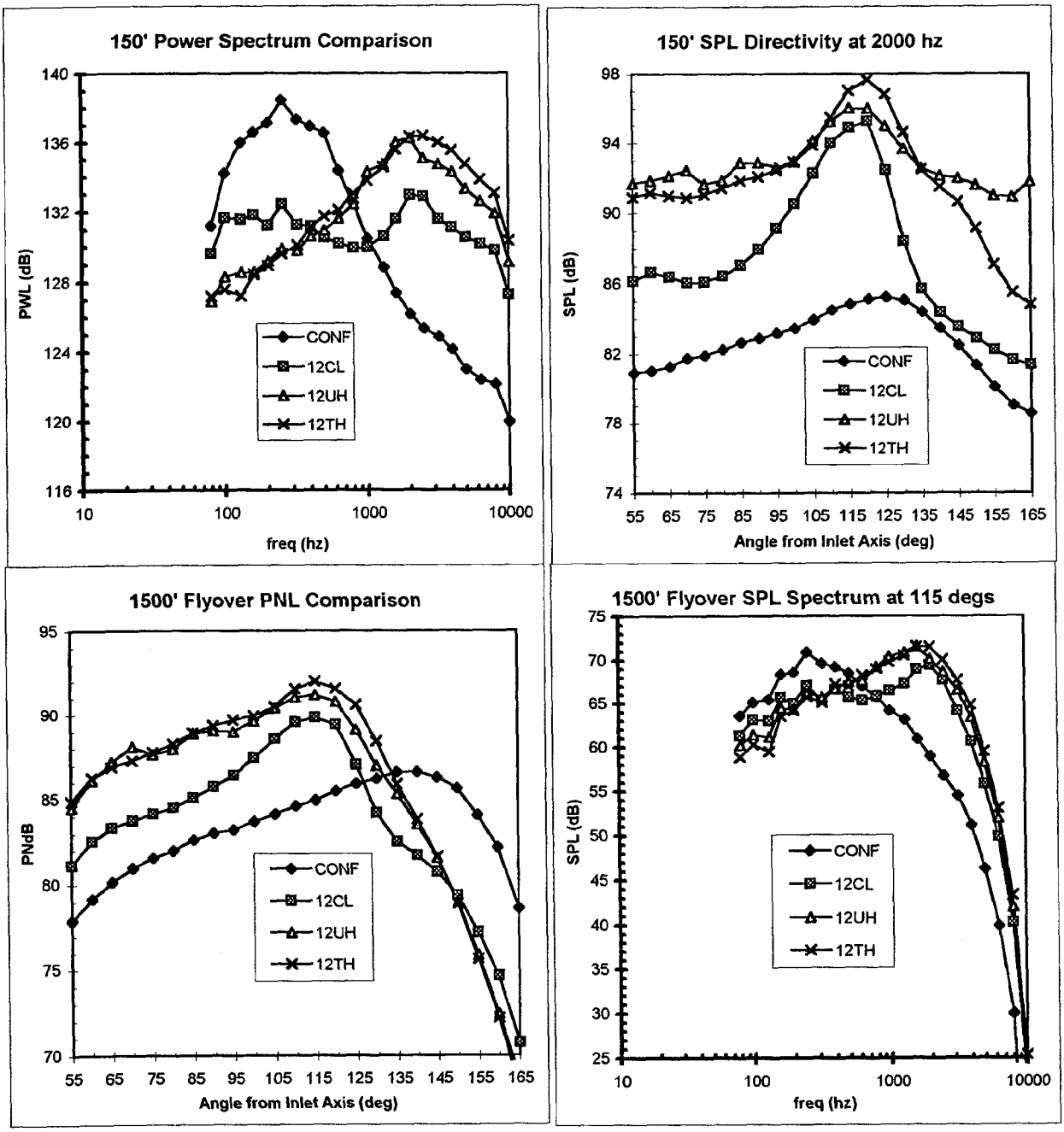

Figure 5.16 Power Spectrum and Flyover PNL Comparison of Mixers at T.O.#3 and M(fj) = 0.2
(12 Lobed Mixers)

shows how the CONF low frequency peak rises above the high frequency peaks of 12UH and 12TH as nozzle pressure increases. The lack of mixing in CONF starts hurting it at these high pressure or thrust conditions. Although the relative ranking of the mixers remains the same for a given frequency, a secondary peak near 2000 Hz emerges for 12CL at TO #3 which was not present in TO #1 or TO #2. The decibel increase in this secondary peak between TO #2 and TO #3 is considerably larger than the increase in the low frequency peak. The comparison of SPL directivity at 2000 Hz at TO #3 between different mixers in Figures 5.16 clearly shows how 12CL approaches the other two mixers near peak PNL angle of 115°.

This implies that at very high nozzle pressure ratios the axial vortices and their interaction with the ambient, which was seen to produce the mid-to-high frequency peaks, become even more important. This is especially true for 12CL where its low frequency peak is already higher than either the 12UH or 12TH mixers. The inability of the CONF mixer to reduce low frequencies due to inferior mixing is accentuated at higher pressure, as seen at the shallow angles of the PNL-directivity (compare Figures 5.15 and 5.16 with Figure 5.4(c)). At TO #3, the peak PNL is shifted downstream for CONF to 140° from 125° at TO #1. In addition, the PNL associated with angles downstream of the peak are still within 10 PNdB of the peak and, hence, still important as opposed to the TO #1 case. The mid-frequency spectral peak of 12CL produces a prominent PNL peak at 115° directivity which was not present at TO #1. This is also, of course, captured in the flyover SPL spectra at 115°.

In summary, 12UH and 12TH are still noisier than 12CL or CONF at higher NPR's, especially at angles upstream of 130°. The inferior mixing of the confluent configuration starts hurting it significantly at shallower angles although it is still quieter at angles upstream of 125°., A previously unseen strong mid-to-high frequency peak emerges in the spectrum of 12CL at an angle of 115°. This new peak is the result of an increase in the strength of the axial vortices produced by this mixer due to the higher pressure ratio.

5.3.1.2 Lobe Number Effect

Figures 5.17 and 5.18 show PWL, PNL and SPL for 12UH, 16UH and 20UH mixers at TO #2 and TO #3 respectively. The overall relative behavior in terms of PWL spectrum appears to have remained similar for all the three mixers with changes in operating condition, with perhaps 20UH producing a slight increase in the high frequencies, similar to those of 12UH at TO #3. The peak PWL of 20UH appears to have shifted by a couple of frequency-bands at TO #3. The relative PNL-directivities of these mixers also have not changed much.

In summary, increasing the lobe count has the same effect at higher NPR's as at lower NPR's with a small relative increase in the high frequency power output.

5.3.1.3 Effect of Scalloping

Figures 5.19 and 5.20 show PWL, PNL and SPL for 20UH, 20MH and 20DH mixers at TO #2 and TO #3 respectively. Again deep scalloping (20DH) appears to suppress noise in terms of PWL as efficiently as at low NPR's (Figure 5.6(b)) at all frequencies. Even the mid-to-high frequencies attributable to turbulence in the axial vortices, shows only a minor peak PWL at 3200 Hz for TO #3 for mixer 20DH. Actually the competition between the low

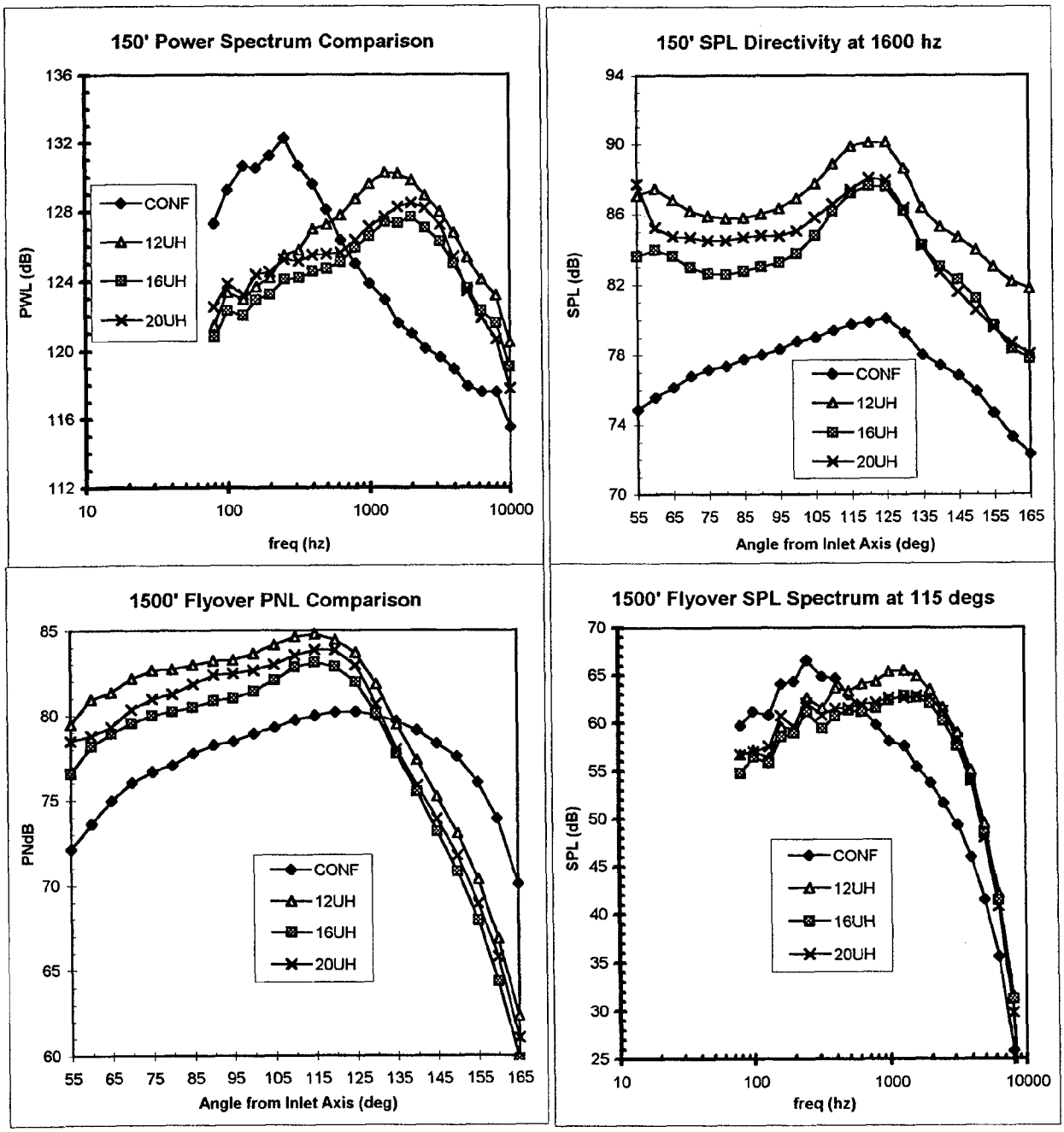

Figure 5.17 Power Spectrum and Flyover PNL Comparison of Mixers at T.O.#2 and M(fj) = 0.2
Effect of Number of Lobes

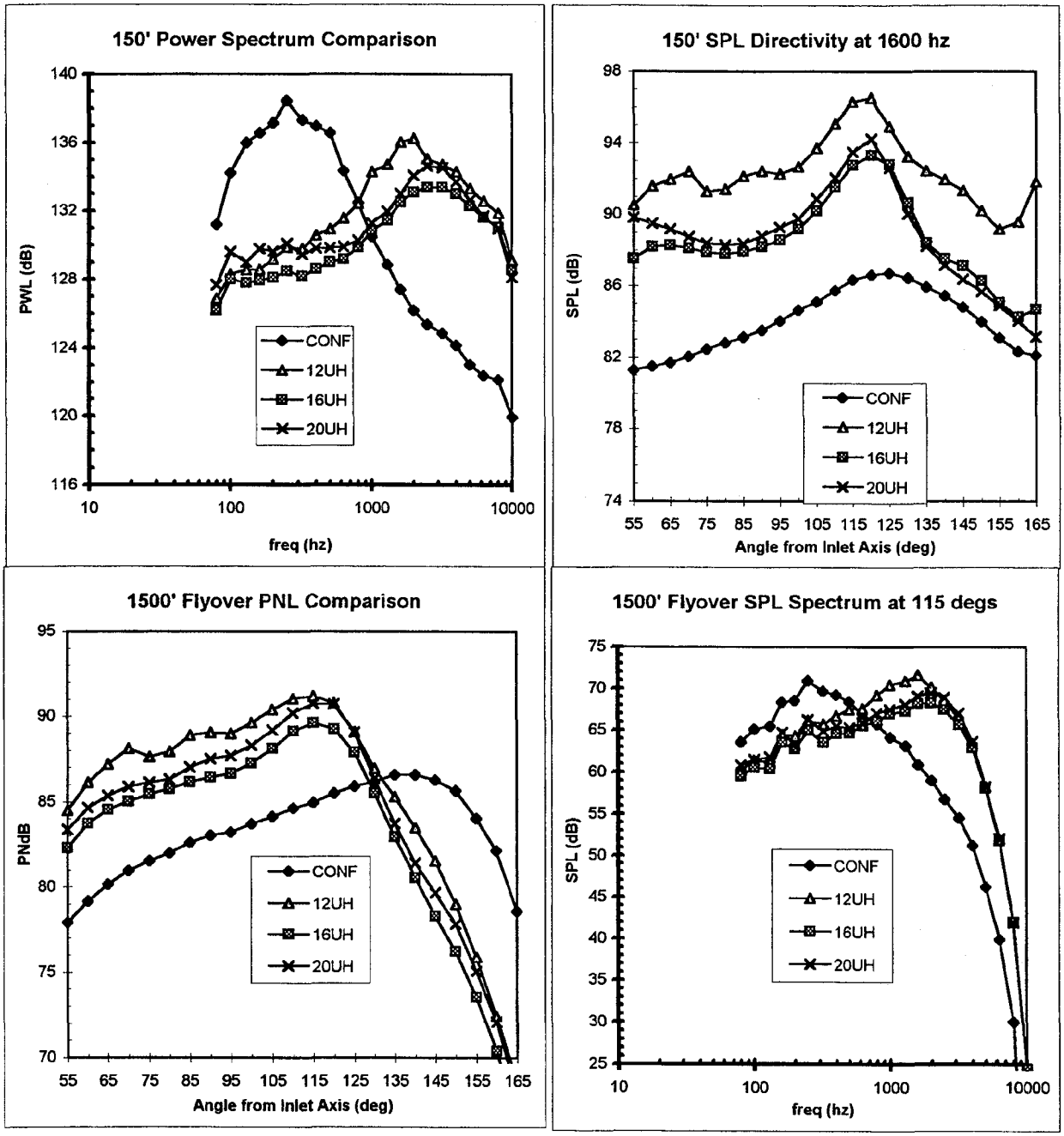

Figure 5.18 Power Spectrum and Flyover PNL Comparison of Mixers at T.O.#3 and M(fj) = 0.2. Effect of number of lobes.

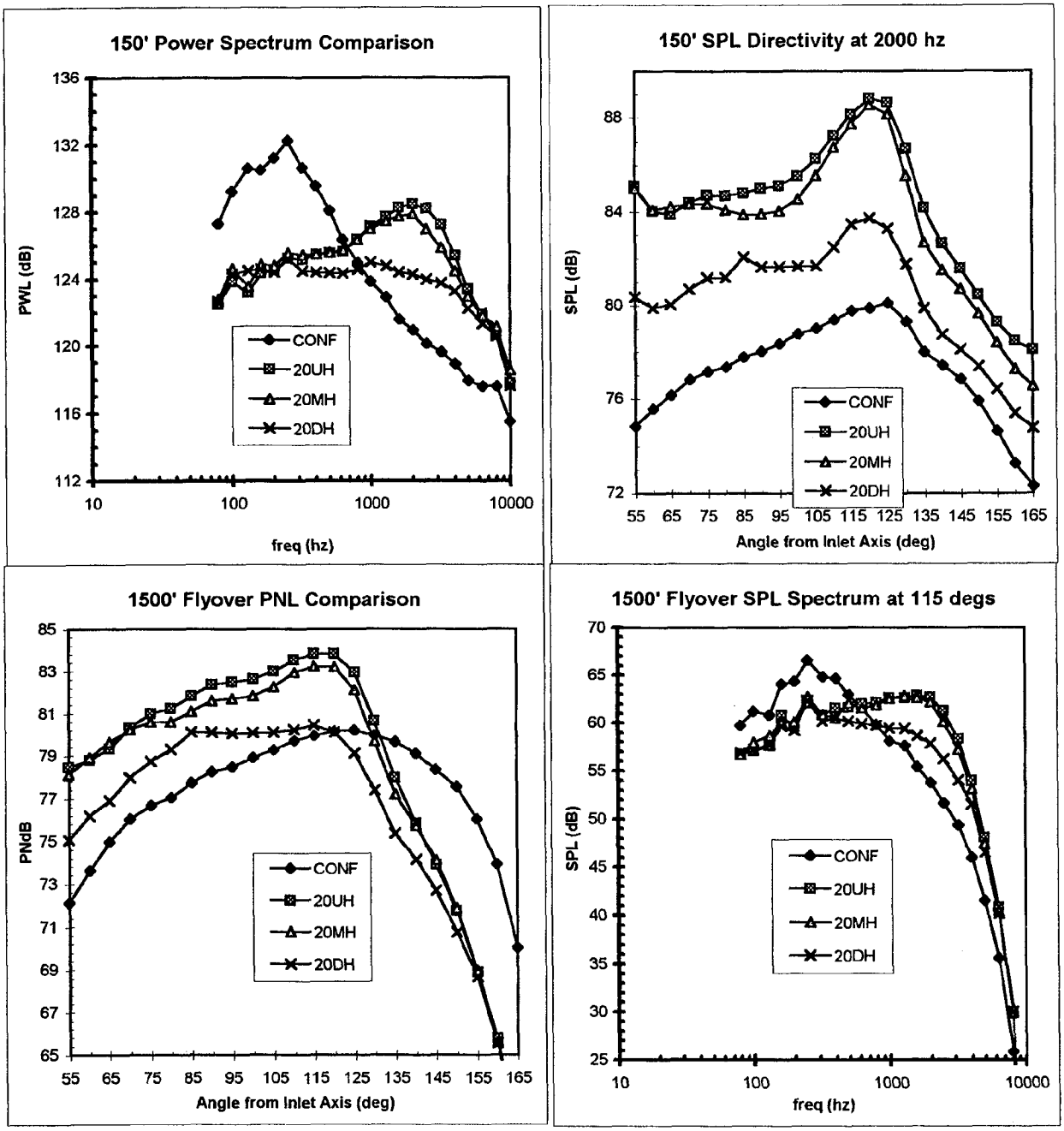

Figure 5.19 Power Spectrum, Flyover PNL & SPL Comparison of Mixers at T.O.#2 and M(fj) = 0.2. Effect of scalloping.

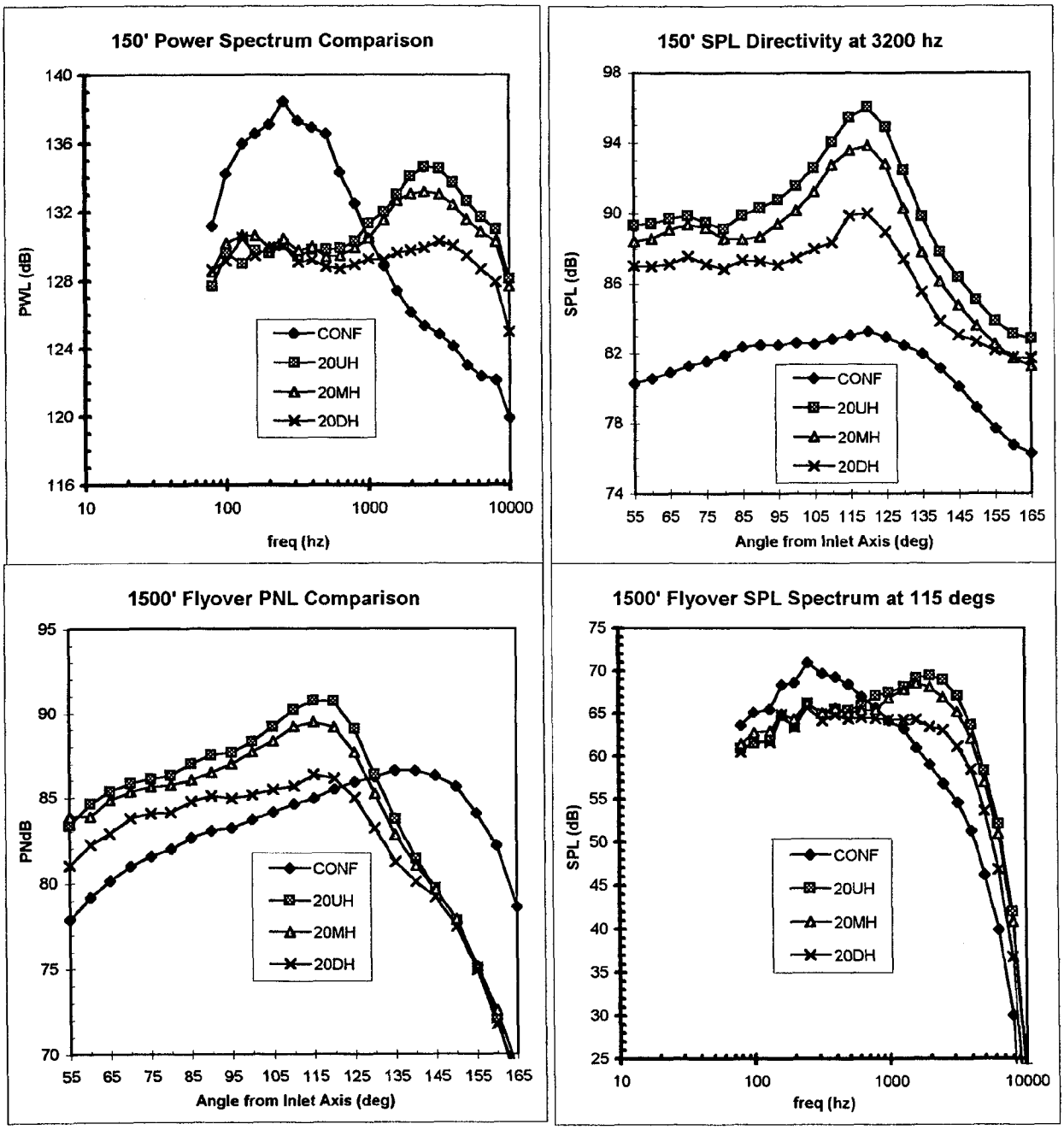

Figure 5.20 Power Spectrum, Flyover PNL & SPL Comparison of Mixers at T.O.#3 and M(fj) = 0.2. Effect of scalloping.

and the high frequency mechanisms of 20DH is made quite apparent in the double humped nature of the PWL at TO #3 and the plateau at TO #2 versus the single hump at low frequencies for TO #1 (Figure 5.6(b)). This also reflects in the flyover PNL of 20DH as a peak at 115° for TO #3, a plateau from 90° to 115° for TO #2 and a peak at 100° for TO #1 (Figure 5.6(c)). From the PNL comparison between 20DH and CONF at TO #3, it appears that the PNL peak of 20DH is smaller than that of CONF, and due to the steep reduction in noise for angles higher than the peak angle the 20DH will be much quieter than CONF on an EPNL basis at these higher NPR-conditions. The same can be said at TO #2. However, we will defer the actual EPNL calculation for now. On the other hand, the SPL-directivity at 3200 Hz for the moderately scalloped mixer 20MH now shows a larger reduction relative to the unscalloped 20 lobe design than at low NPR's. That is, unlike at low NPR's, even moderate scalloping is now beneficial. In addition the frequencies associated with peak PWL increase with increasing NPR.

In summary, the effect of scalloping become more pronounced as nozzle pressure ratio increases. Even moderate scalloping produces a noise benefit at the highest pressure tested, a result not observed at the lowest NPR. Deep scalloping produces a considerable noise reduction relative to the confluent baseline at the higher NPR's tested. This is the result of producing significant low frequency reduction with only a moderate increase in the mid spectral bands. A cross-comparison between all eight mixers will be done later on EPNL basis. However, for now we will examine the effect of different free-jet Mach numbers at the highest NPR condition TO #3.

5.3.2 Effect of Free-Jet Mach Number at TO #3

The purpose of making a comparison at different free-jet Mach numbers (0.0, 0.2 and 0.3) is to see the relative spectral changes at high and low frequencies, and also at upstream and downstream angles as in Section 5.2.3, but for the highest NPR tested for a given mixer so that we can understand the source location characteristics. Hence, we focus on only the changes in the power spectrum (PWL) and OASPL-directivity, in the reference frame of the nozzle, as opposed to changes in flyover PNL, due to M_{fj}. For convenience of comparison across mixers we will present each group on one sheet for each group of mixers. Figures 5.21, 5.22, 5.23 and 5.24 show the effect on PWL-spectrum and polar OASPL-directivity for, respectively, CONF, Group 1 (12CL, 12TH, 12UH), Group 2 (12UH, 16UH 20UH) and Group 3 (20UH, 20MH, 20DH) mixers. Compare this with similar plots at TO #1 (Figures 5.7 to 5.14).

The confluent mixer (Figure 5.21) shows similar behavior at all free jet conditions with a more uniform decrease in PWL over the whole frequency spectra and in OASPL for all angles than observed for all the lobed mixers. All lobed mixers at this high NPR condition show a marked insensitivity in certain regions to free jet conditions.

(i) PWL for the mid-to-high frequencies changes very little with changes in free-jet speed. However significant changes in PWL are observed at the lower frequencies with changes in the free jet flow. This is more evident at TO #3 than at TO #1.

(ii) Similarly, the OASPL for upstream angles does not change much with a change in free-jet speed, especially

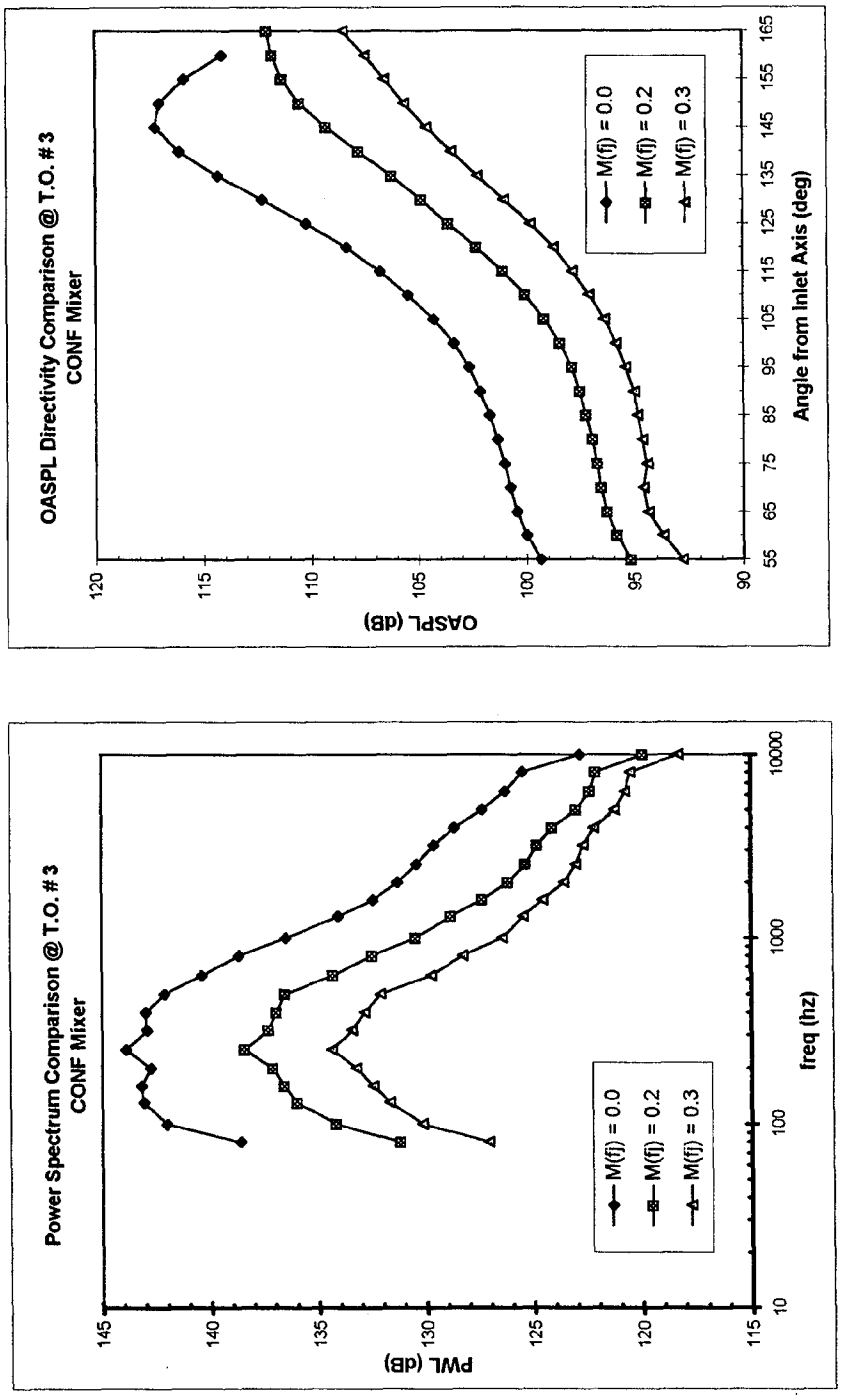

Figure 5.21 Effect of free-jet Mach number on 150 ft PWL spectrum and OASPL directivity at T.O. # 3.

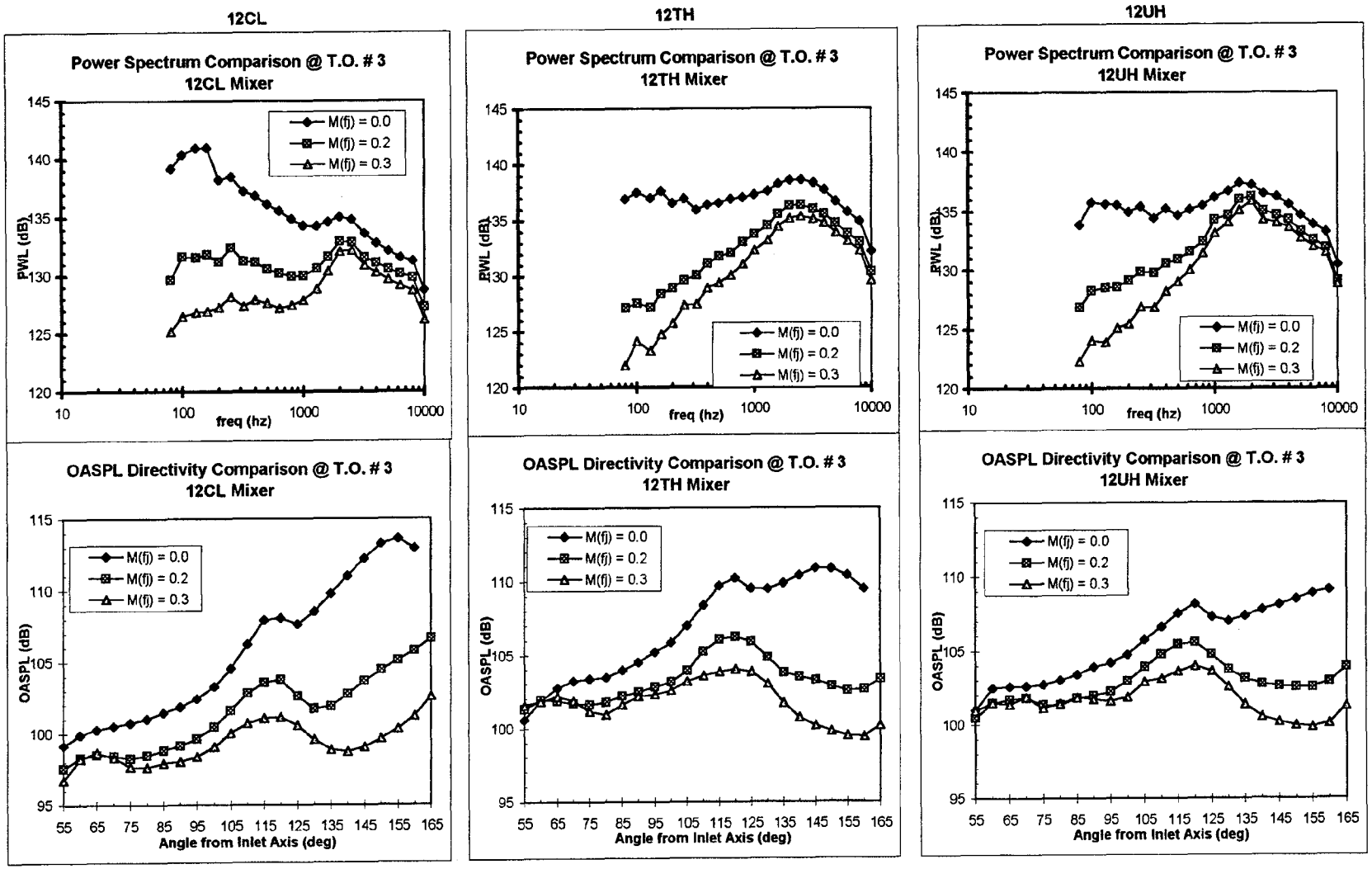

Figure 5.22 Effect of free-jet Mach number on 150' PWL spectrum and OASPL directivity at T.O. # 3 of 12 lobed mixers (Group 1).

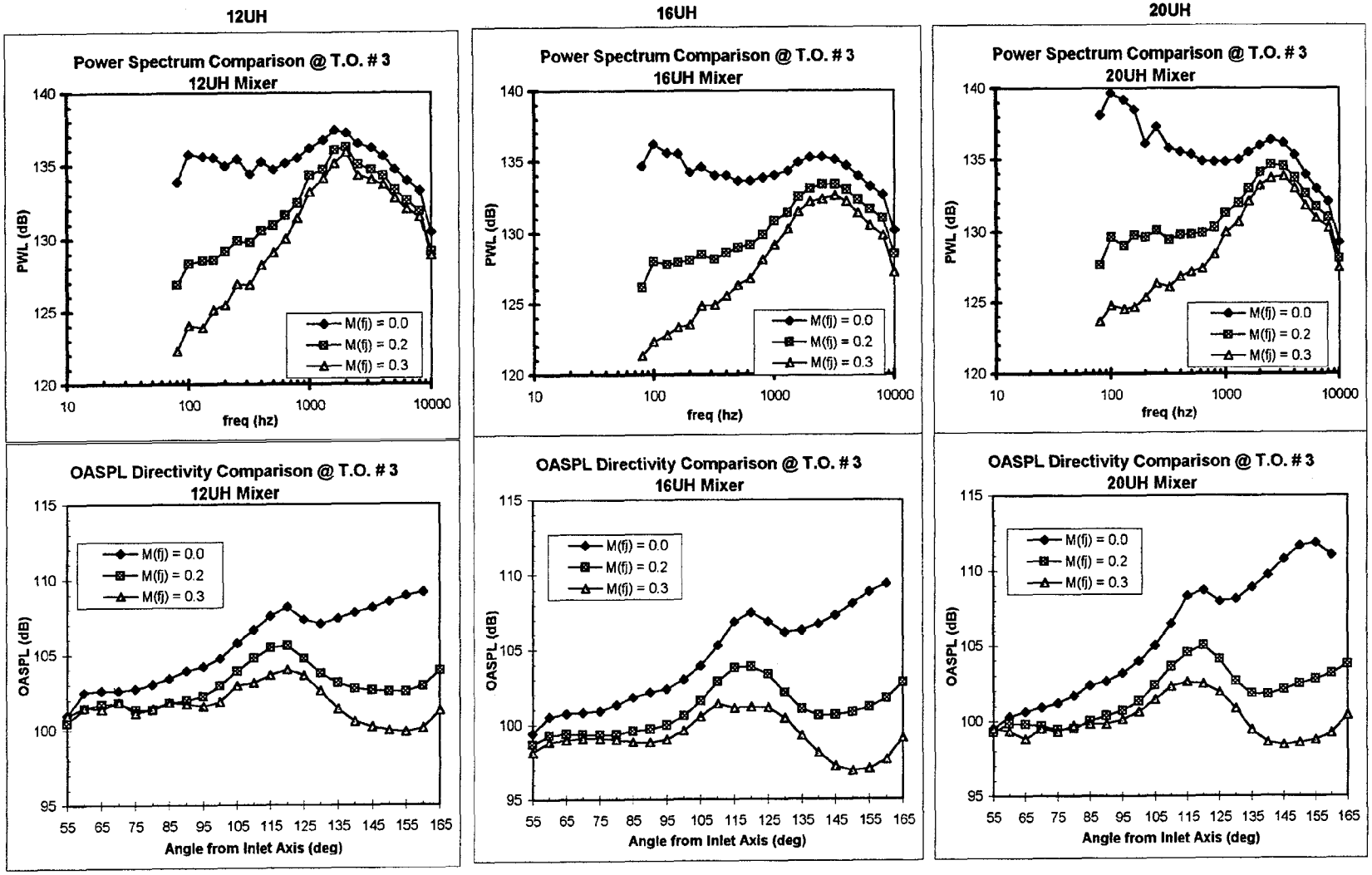

Figure 5.23 Effect of free-jet Mach number on 150' PWL spectrum and OASPL directivity at T.O. # 3 of 12UH, 16UH, 20UH (Group 2).

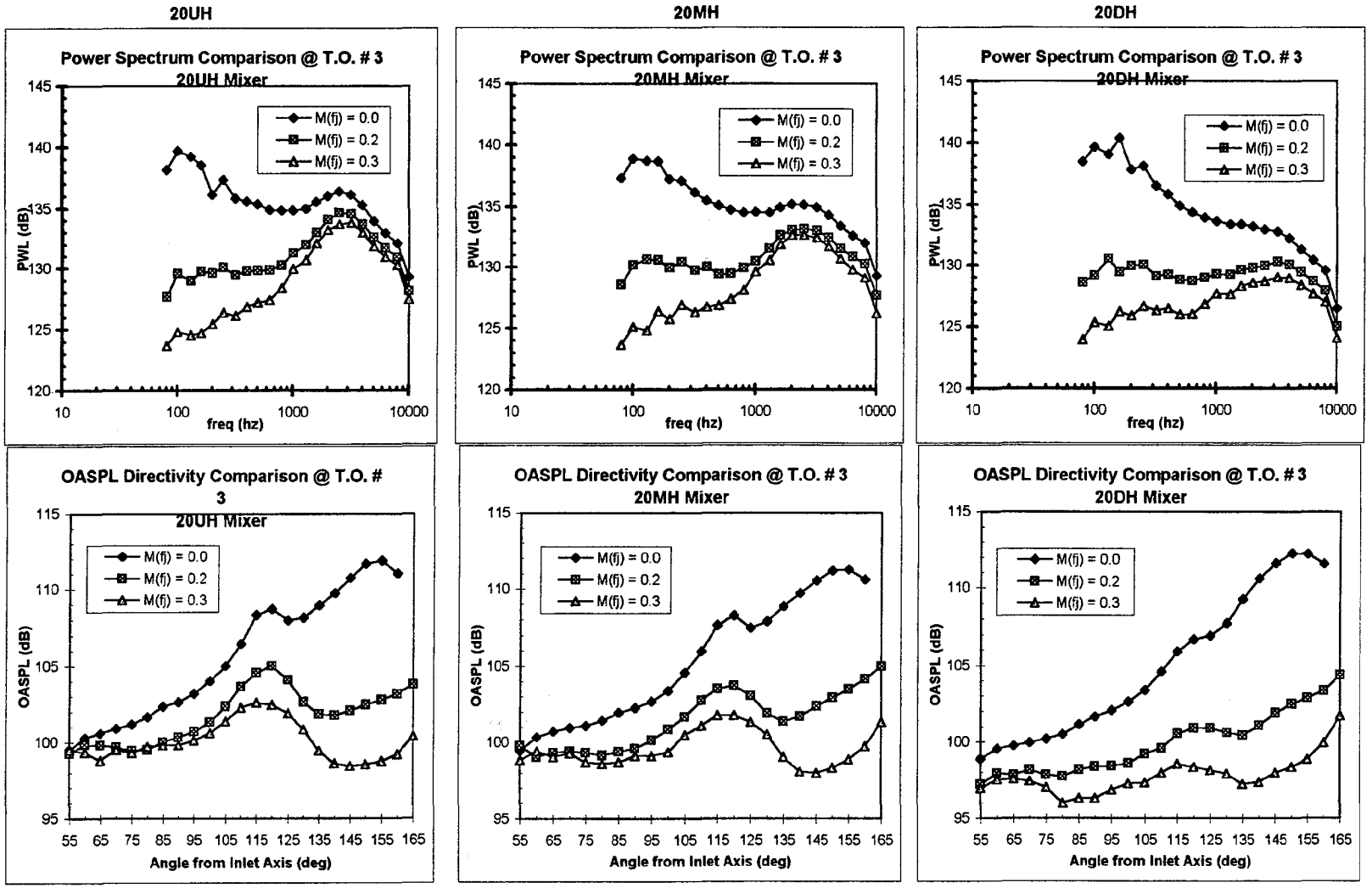

Figure 5.24 Effect of free-jet Mach number on 150' PWL spectrum and OASPL directivity at T.O. # 3 of 20UH, 20MH, 20DH (Group 3)

compared to the larger changes at downstream angles. This, too, is more evident at TO #3 than at TO #1.

It is remarkable to note that local secondary peaks in the mid-to-high frequency range for mixers 12CL and 20DH start to become the predominant features in the PWL-spectra as the free-jet Mach number increases at this high NPR condition. This was not evident at the low NPR conditions of TO #1. So whatever mechanism is causing that high frequency peak now controls the noise suppression ability of these two mixers. For all other lobed mixers this mechanism was dominant even at low NPR conditions. We have remarked repeatedly in the past that this peak at higher frequency must represent the effect of turbulence intensity due to axial vorticity and mixing of fan and core flows both inside and outside the nozzle. We examine this in more depth in the next section by analyzing the SPL-spectra at various angles.

5.4 Diagnosing High-Frequency Source Locations with Changes in Free-Jet Speed

This analysis was prompted by the observations in the previous sections that the sound power spectrum, PWL, does not change much in the mid-to-high frequencies for lobed mixers when the free-jet speed is changed. This is also reflected in the relative insensitivity to free-jet speed of the polar OASPL and the flyover PNL directivities at angles upstream of peak PNL. It is important to understand the reason behind this trend because the PNL associated with angles near 90° is within 2-3 PNdB of the peak PNL value, which would imply a significant contribution to EPNL. This observation was not found to hold good for the CONF mixer, which re-enforces the suspicion that the turbulence in the axial vortices of the forced lobed mixers may be the cause of the high frequency noise. We proceed to explore the polar SPL-spectra at different free-jet Mach numbers in detail in this section.

5.4.1 Ray Theory Application

Since our interest principally lies in relatively "high" frequencies, we will use ray theory or geometric acoustics. Consider an acoustic ray radiating from a source inside the jet at some angle to the jet axis and coming out through the shear-layer between the model-jet and the free-jet with the observer inside the free-jet. When the free-jet speed is changed, the outgoing ray in the free-jet will change its direction due to a change in the *refraction* of the wave-number vector and also due to a change in the *convection* speed of the wave-fronts at the altered free-jet speed. Hence, if we want to study the change in the source characteristics due to a change in the free-jet speed, then we should compare the rays coming from the jet for different free-jet speeds, not at the same angle in the free-jet, but at different refracted ray angles corresponding to the same incident ray from the source. Also, in such a comparison we are ultimately interested in the direction of the rays, and not of the wave-number vectors, because acoustic energy transmitted to an observer inside the free-jet is carried at the group velocity along the ray directions [22,23]. In a moving media, ray direction is not the same as the wave-number vector direction or normal to the wave-fronts.

Further, in the geometric acoustics limit there is no reflection of the incident ray from the shear layer and the incident ray is fully transmitted. However, it is known from Candel's planar wave analysis[21] that the amplitude of the wave that is transmitted through a shear-layer discontinuity can be

different than the amplitude of the incident wave (their ratio being characterized by the "transmission coefficient") and, importantly, it varies with the incident wave-normal angle. Hence, we also need to estimate the changes in the transmission coefficient with changes in free-jet speed for a given incident wave amplitude so that we can account for the differences if they are large enough.

The results for the angular relationships due to *refraction* and *convection*, and the amplitude changes due to *transmission coefficient* changes are given in this section from two-dimensional considerations assuming planar waves. This is an extension of Candel's wave analysis[21] to moving flows on *both* sides of a shear-layer. Consider the geometry of the angles on either side of the shear-layer between the free-jet and the model-jet. This shear layer is modeled, for convenience, as a thin planar vortex-sheet on the nozzle lip-line, as shown in Figure 5.25. The model-jet flow, assumed to be uniform, on one side of the lip-line is labeled as region 1. The free jet flow on the other side, also assumed to be a uniform flow, is labeled region 2. The source S, located inside the model jet and assumed stationary, radiates a wave at local speed of sound c_1 with wave-normal angle ϕ_1 with the jet inlet axis. This wave-front convects downstream with the local flow speed $U_1 = M_1 c_1$ to give the direction of the incident ray from the source, as shown using the velocity triangle. Such angular relationships between the wave-front normals and the ray directions in moving media through velocity triangles are well-known and can be found, for example, in Lighthill[22]. This incident wave-front is refracted through the thin vortex-sheet. When the free-jet speed is zero, the transmitted wave-front normal subtends an angle of ϕ_{20} with the inlet axis and the wave travels in region 2 at the local speed of sound, c_2, as shown in Figure 5.25. This is also the direction of the transmitted ray when the free-jet speed is zero. However, when the free-jet speed is non-zero then the change in the propagation angle of the transmitted ray can be conveniently broken into two parts:

(i) *refraction* of the corresponding wave-front normal, denoted by angular change of $\Delta\phi_r$,

(ii) *convection* of the wave-fronts using velocity triangle, denoted by angular change of $\Delta\phi_c$.

This leads to the final transmitted ray angle of

$$\Phi_2 = \phi_{20} + \Delta\phi_r + \Delta\phi_c .$$

(Note: We will use lower-case Greek symbols for wave-normal angles and upper-case Greek symbols for corresponding ray angles.) From the detailed analysis given in Appendix C we obtain:

$$\cos\phi_2 = \frac{{}^{c_2}\!/_{c_1}\cos\phi_1}{1-\cos\phi_1(M_1 - {}^{c_2}\!/_{c_1} M_2)}$$

$$\tan\Delta\phi_c = \frac{M_2\sin\phi_2}{1-M_2\cos\phi_2}$$

where

$$\phi_2 = \phi_{20} + \Delta\phi_r .$$

is the angle of the wave-normal in the free jet. Hence, ϕ_{20}, which is ϕ_2 at $M_2 = 0$, is given by

$$\cos\phi_{20} = \frac{{}^{c_2}\!/_{c_1}\cos\phi_1}{1-M_1\cos\phi_1}$$

By using the above formulae, we can directly relate ϕ_2 to ϕ_{20} without referring to the model jet (or flow 1) properties:

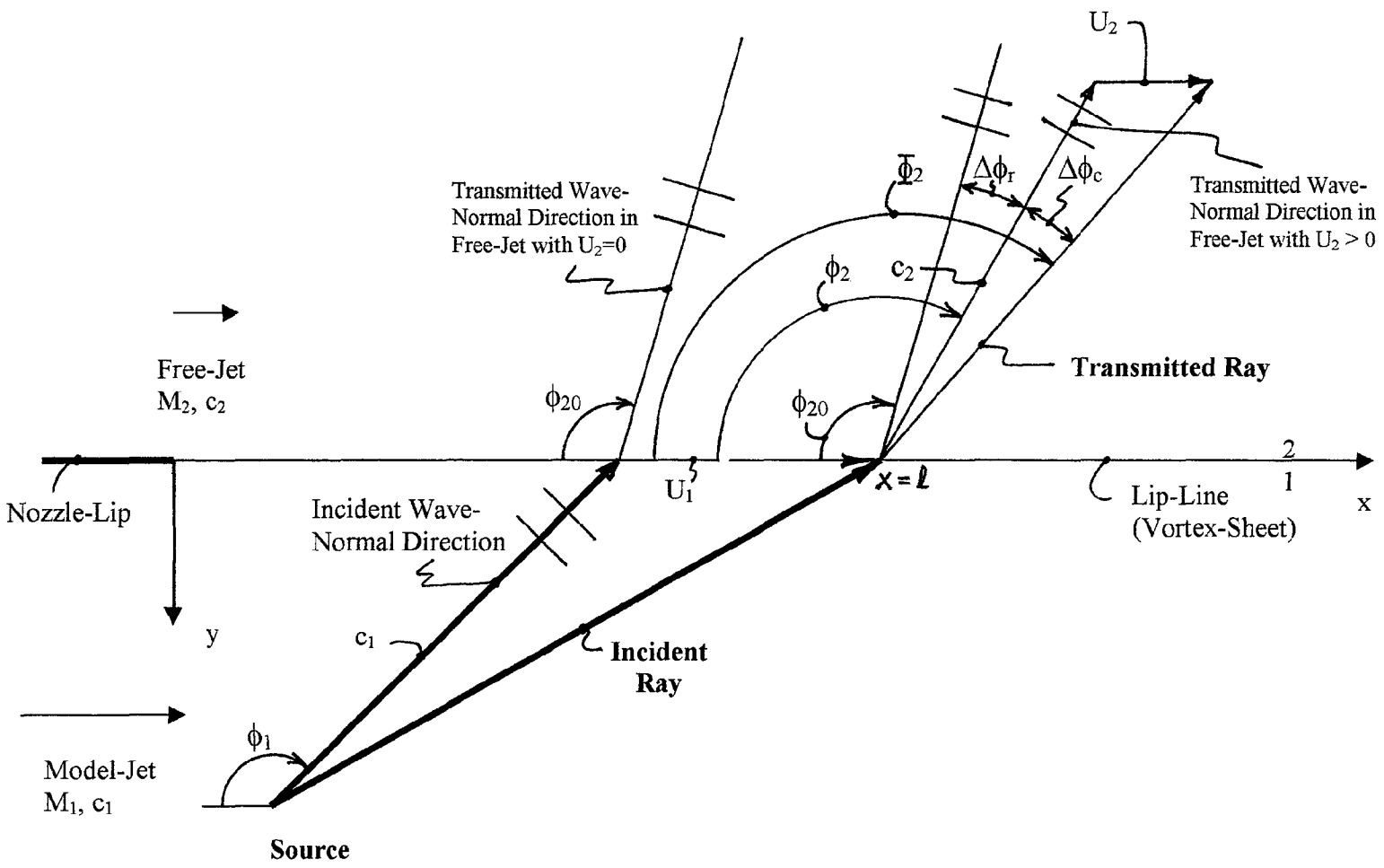

Figure 5.25 Refraction & Convection of Wave-Fronts due to Free-Jet

$$\cos\phi_2 = \frac{\cos\phi_{20}}{1 + M_2\cos\phi_{20}}$$

This relationship only requires knowledge of the free-jet Mach number M_2 , without involving the model-jet properties, M_1 and c_1. Thus given ϕ_{20} and M_2 we can find $\Phi_2 = \phi_2+\Delta\phi_c$ from the above equations without knowing M_1 and c_1.

Since rays radiate from different portions of the jet, it would be difficult to utilize these results in the geometric near-field. However, as the distance R from the jet to the observer becomes sufficiently large (geometric far-field), some simplifications occur. For these simplifications to be valid, R must meet two conditions: firstly, R must be large compared to the distance from the nozzle-lip to the point where the incident ray crosses the shear layer, denoted by l in Figure 5.25; secondly, R must be large compared to the nozzle exit radius, r_{exit}. It is clear from Figure 5.26, which depicts this situation, that in the *geometric far-field* inside the free jet flow when $l/R << 1$ and $r_{exit}/R << 1$:

$$\theta_{20} \cong \phi_{20}$$
$$\Delta\theta \cong \Delta\phi$$

where θ_{20} is measured from the center of the nozzle-exit plane, as usual, and $\Delta\phi$ is change due to refraction or convection at the lip-line. This can also be proven mathematically very easily. Thus, instead of using ϕ_{20} and $\phi_{20} + \Delta\phi$ one can use θ_{20} and $\theta_{20} + \Delta\theta$ at a sufficiently long distance R inside the free-jet. In other words, in the geometric far field we can refer to observer distances and angles from the center of the nozzle exit rather than from the apparent source locations.

At full-scale under study, r_{exit} = 1.208 ft and R = 150 ft, so that r_{exit}/R = 0.008. For mid-to-high frequencies of interest in such comparisons, the responsible sources are not too far from the nozzle-exit plane making l of the order of r_{exit}. Even taking the worst case of $l = 10r_{exit}$ gives l/R = 0.08 which creates hardly any error by using θ_{20} and $\Delta\theta$ instead of ϕ_{20} and $\Delta\phi$, respectively. Recall from Chapter 3 that the polar SPL data at 150 ft with a free jet flow has been obtained from a free jet of finite diameter after first correcting for the refraction effect from the shear layer between the free jet and the ambient using Ahuja et al[15] type of method (see Appendix C). This polar 150 ft SPL data corresponds to the angle of the wave-normals, θ_2 (or the "emission" angle[15]) inside the free-jet and in the reference frame of the nozzle.

Table 5.1 lists the final refracted ray angle Θ_2 ($=\Phi_2$) and the refracted wave-normal angle, θ_2 ($= \phi_2$) for a range of input "static" free-jet angles θ_{20} ($= \phi_{20}$) at two different free-jet Mach numbers of interest, M_{fj} = 0.2 and 0.3. The intermediate angles which go into this calculation are also given, namely, the pure refraction angular change Δ_{refr} ($= \Delta\phi_r$) and the pure convection angular change Δ_{conv} ($= \Delta\phi_c$). The blank spaces for the shallow angular range (larger values of θ_{20}) give complex values of Θ_2 and correspond to the "zone of silence," which begins at slightly different values of θ_{20} for the two free-jet Mach numbers. Figure 5.27 shows the two angular changes, $\Delta\phi_r$ and $\Delta\phi_c$ as functions of ϕ_{20}. Thus note that at 90° there is no refraction effect on the wave-normals and the bending of the rays is purely due to convection of the wave-fronts. This is also true approximately for angles near 90°. For very small angles and angles just before the zone of silence begins the refraction effect is much larger than the convection effect.

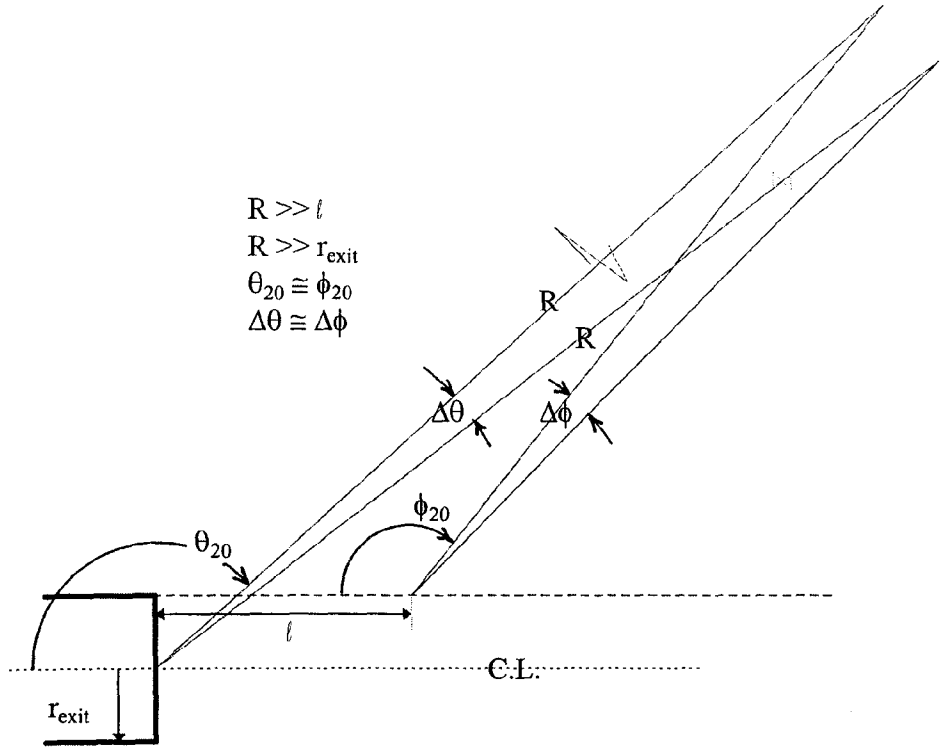

Figure 5.26 Angular simplifications in the geometric far-field

Table 5.1 Refraction & Convection Effects with Free-Jet On

$M_{fj} = 0$	$M_{fj} = 0.2$				$M_{fj} = 0.3$			
θ_{20}	θ_2	Δ_{refr}	Δ_{conv}	Θ_2	θ_2	Δ_{refr}	Δ_{conv}	Θ_2
0	**33.56**	33.56	7.56	41.11	**39.72**	39.72	13.99	53.71
5	**33.83**	28.83	7.61	41.44	**39.92**	34.92	14.04	53.95
10	**34.64**	24.64	7.75	42.39	**40.52**	30.52	14.17	54.69
15	**35.95**	20.95	7.98	43.92	**41.50**	26.50	14.38	55.89
20	**37.72**	17.72	8.27	45.99	**42.86**	22.86	14.66	57.52
25	**39.89**	14.89	8.62	48.51	**44.56**	19.56	14.99	59.54
30	**42.42**	12.42	8.99	51.42	**46.57**	16.57	15.35	61.92
35	**45.26**	10.26	9.39	54.65	**48.89**	13.89	15.73	64.61
40	**48.37**	8.37	9.78	58.16	**51.47**	11.47	16.10	67.57
45	**51.72**	6.72	10.16	61.88	**54.31**	9.31	16.45	70.77
50	**55.28**	5.28	10.51	65.79	**57.39**	7.39	16.78	74.17
55	**59.03**	4.03	10.82	69.86	**60.70**	5.70	17.05	77.75
60	**62.96**	2.96	11.09	74.05	**64.23**	4.23	17.26	81.49
65	**67.07**	2.07	11.30	78.36	**67.97**	2.97	17.40	85.37
70	**71.33**	1.33	11.44	82.77	**71.93**	1.93	17.46	89.39
75	**75.75**	0.75	11.52	87.28	**76.10**	1.10	17.42	93.53
80	**80.34**	0.34	11.53	91.87	**80.50**	0.50	17.29	97.79
85	**85.09**	0.09	11.46	96.55	**85.13**	0.13	17.05	102.18
90	**90.00**	0.00	11.31	101.31	**90.00**	0.00	16.70	106.70
95	**95.09**	0.09	11.08	106.16	**95.13**	0.13	16.22	111.36
100	**100.36**	0.36	10.75	111.12	**100.56**	0.56	15.62	116.17
105	**105.84**	0.84	10.34	116.18	**106.30**	1.30	14.87	121.17
110	**111.54**	1.54	9.83	121.37	**112.40**	2.40	13.98	126.38
115	**117.49**	2.49	9.23	126.72	**118.95**	3.95	12.91	131.86
120	**123.75**	3.75	8.51	132.26	**126.03**	6.03	11.65	137.68
125	**130.38**	5.38	7.68	138.06	**133.85**	8.85	10.15	144.01
130	**137.53**	7.53	6.71	144.24	**142.78**	12.78	8.33	151.12
135	**145.44**	10.44	5.56	151.01	**153.83**	18.83	5.95	159.78
140	**154.78**	14.78	4.13	158.90	**174.06**	34.06	1.37	175.43
145	**168.42**	23.42	1.92	170.34	*	*	*	*
150	*	*	*	*	*	*	*	*
155	*	*	*	*	*	*	*	*
160	*	*	*	*	*	*	*	*
165	*	*	*	*	*	*	*	*
170	*	*	*	*	*	*	*	*
175	*	*	*	*	*	*	*	*
180	*	*	*	*	*	*	*	*

θ_{20} = Angle of wave-front normal with inlet axis in the static free-jet ($M_{fj} = 0$)
θ_2 = Angle of wave-front normal with inlet axis in the free-jet purely due to refraction
$\Delta_{refr} = \theta_2 - \theta_{20}$, Pure refraction effect without convection
Δ_{conv} = Purely convection effect after accounting for refraction effect
$\Theta_2 = \theta_{20} + \Delta_{refr} + \Delta_{conv}$, Final angle of the ray in the free-jet
* = Gives complex values of θ_{20} corresponding to "zone of silence"

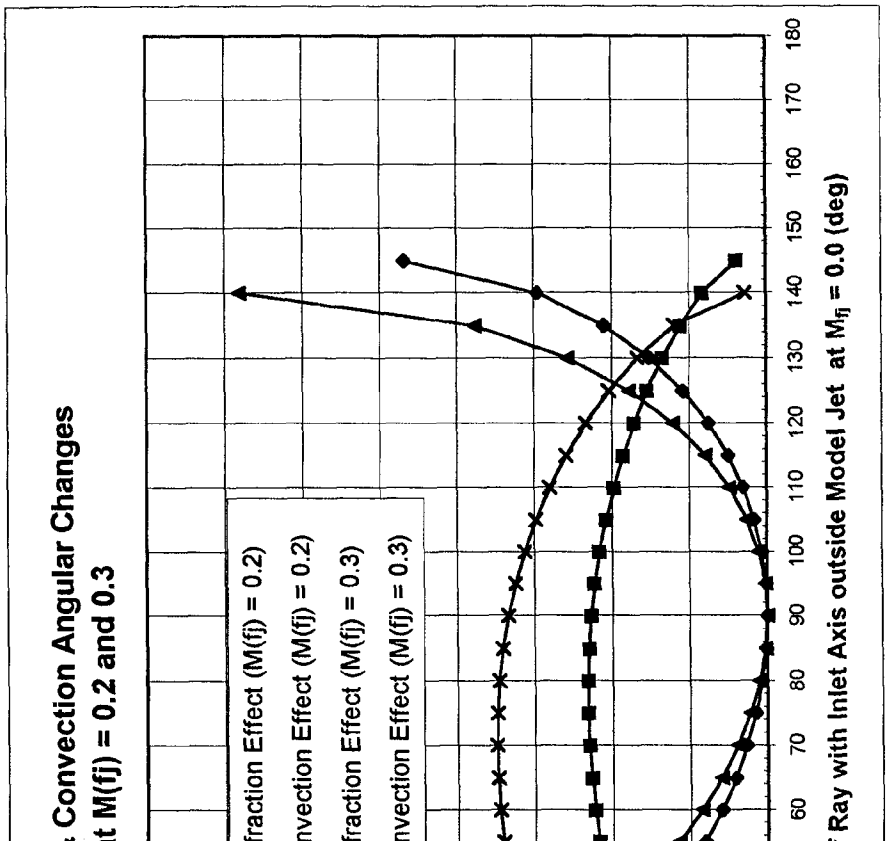

Figure 5.27 Refraction and convection angular changes due to free-jet flow at M_{fj} = 0.2 and 0.3.

The relationships between the various angles given above are not restricted by the assumption of plug flow in the model jet or the thin vortex-sheet model of the free-jet/model-jet shear layer but are also applicable when there is variation in the flow properties in the vertical direction and the shear-layer is thicker. This is true so long as the static pressure in the vertical direction remains fixed. In that case the model-jet flow properties in the above relations, namely, M_1 and c_1 are to be replaced by the local model-jet flow properties *at the source location.* The final relation between Φ_2 and ϕ_{20} or ϕ_2 and ϕ_{20} is, however, independent of model-jet flow properties, as mentioned earlier.

Further, these relationships between angles are applicable not only to *planar* two-dimensional flows but also to the *cylindrical* case if the two flows are assumed uniform, the thin vortex-sheet is a cylindrical surface and the point source is on its axis. In this case, any incident ray from the source is always in the meridional plane, rx (containing the radial direction r and the axial streamwise direction x), whence, its local interaction at the cylindrical vortex-sheet can be considered as if both the vortex-sheet and the incident wave-fronts are *locally* planar. This results in the transmitted ray being in the same meridional plane as the incident ray. That is, Figure 5.25 can be interpreted as if it is drawn in the meridional plane of the incident ray and all the angular relationships remain the same as derived before for the planar case.

Next we tackle the issue of "transmission coefficient" changes at different free-jet Mach numbers and the corresponding observation angles. The detailed analysis and results are again given in Appendix C. These results show that for a range of "static" free-jet angles θ_{20} not too far from 90° the changes in the SPL of the transmitted ray-tube due to changes in the free-jet Mach number up to 0.3 are *at most* of the order of ± 0.4 dB. The errors are less in the aft quadrant than in the front quadrant and for hot jets the errors are even smaller. This is small enough for our purposes of comparison and, hence, can be neglected if we restrict ourselves to that angular range. Recall that, in any case, in the geometric acoustics limit the rays are not reflected and our analysis will be consistent if we indeed neglect the transmission coefficient changes.

5.4.2 The New Diagnostic Method for "Excess" Sources

Let's say that we know the 150 ft polar SPL data inside the free jet at different "emission" angles, θ_2 (= ϕ_2, see Figure 5.25) for different M_{fj}, as in our data base. Then in order to study the effect of free-jet Mach number on the high-frequency source characteristics we should compare the far-field polar SPL of $M_{fj} = 0$ at angle θ_{20} with that of $M_{fj} > 0$ at angle $\theta_2 = \theta_{20}+\Delta\theta_r$ as given in Table 5.1. Thus, we will compare the far-field polar SPL's of different M_{fj}'s at corresponding "shifted" angles, denoted by the following pairs:

$$(M_{fj} = 0, \theta_{20}) \leftrightarrow (M_{fj}>0, \theta_2).$$

If the 150 ft polar SPL data inside the free jet is referred to the ray angle, Θ_2, or "reception" angle[15] then comparison of SPL's at different M_{fj}'s should be made at the corresponding shifted ray angles, also to be found in Table 5.1, and this relationship is denoted by:

$$(M_{fj} = 0, \Theta_{20}) \leftrightarrow (M_{fj}>0, \Theta_2).$$

It is possible that the polar SPL data is available at only certain angles, as in our case, from $\theta_2 = 55°$ to 165° with 5° interval.

In that case, data may not be available exactly at the angle θ_2 demanded by Table 5.1 for different M_{fj}. As an approximation, SPL data at the closet available angle will be used. With data available at 5° intervals the maximum error in angle will be 2.5°. When we actually compare data we will select angles which will minimize this error for the available M_{fj} of 0.2 and 0.3.

Since our whole analysis here was driven by the observation that the sound power in the mid-to-high frequencies does not change much with free-jet speed, let us see from the viewpoint of source location, what this may mean. Figure 5.28 shows several source-locations for a jet with internal mixing and a table listing if those sources should change in intensity due to free-jet speed changes. Generally speaking a change in free-jet speed changes the mixing characteristics between the nozzle-jet and the free-jet at the lip shear-layer and further downstream where the two lip-shear layers from diametrically opposite ends of the nozzle interact as well as in the far downstream plume flow-field. However, if there are any other sources of noise away from the free-jet related shear-layers then their turbulence intensity will not be modified much due to changes in the free-jet speed, if we neglect "back-reaction" on those sources due to an impedance change at the lip shear-layer.

For example, source 1 in Figure 5.28 is inside the nozzle and may arise due to internal fan-core flow mixing and hence, not change in strength due to changes in free-jet speed with a fixed ambient pressure at the lip. Similarly source 2 in that Figure, shown away from the lip shear-layer, can arise due to fan and core flows not being completely mixed at the nozzle-exit plane and will not change in strength due to changes in free-jet speed. Back-reaction on both these sources can be neglected. Both these sources, 1 and 2, are in some sense "excess" noise sources. The first is an "internal" excess noise source and the second an "external" excess noise source. These are "excess" noise sources in the sense that they will not occur in a single stream nozzle with "uniform" exit jet velocity producing the same thrust. In the case of forced lobed mixers these are driven by axial vorticity, have small length-scales, and hence, are candidates for mid-to-high frequency noise sources.

On the other hand, sources in locations 3, 4 and 5 in Figure 5.28 are in direct interaction regions with the free jet flow and will change their strengths as M_{fj} changes. For example, earlier in Section 5.2.3 we had shown how the radial gradient of velocity at the end of the potential core near region 4 decreases with an increase in M_{fj} thus reducing noise in fully mixed jets. However, this should not be taken to imply that effects of axial vorticity are only confined to source locations 1 and 2. For example, in the case of high lobe penetration the axial vortices may not completely diffuse internally, and will then interact with the lip-shear layer at location 3. For low-lobe penetration these vortices can continue to convect all the way up to location 4. From the table in Figure 5.28, we can conclude that if we find that the far-field high-frequency SPL's for different free-jet Mach numbers at the appropriately "shifted" angles do not change, then they probably are coming from "excess" sources either from source location 1, inside the nozzle or from source location 2, close to the nozzle exit plane and away from the lip-shear layer. Further, if we have flow data at the nozzle exit plane which shows uniform flow (velocity and temperature) then it would mean that there are no "external" excess sources at 2 and the burden of invariant SPL-data will completely fall upon "internal" excess noise sources. In the case

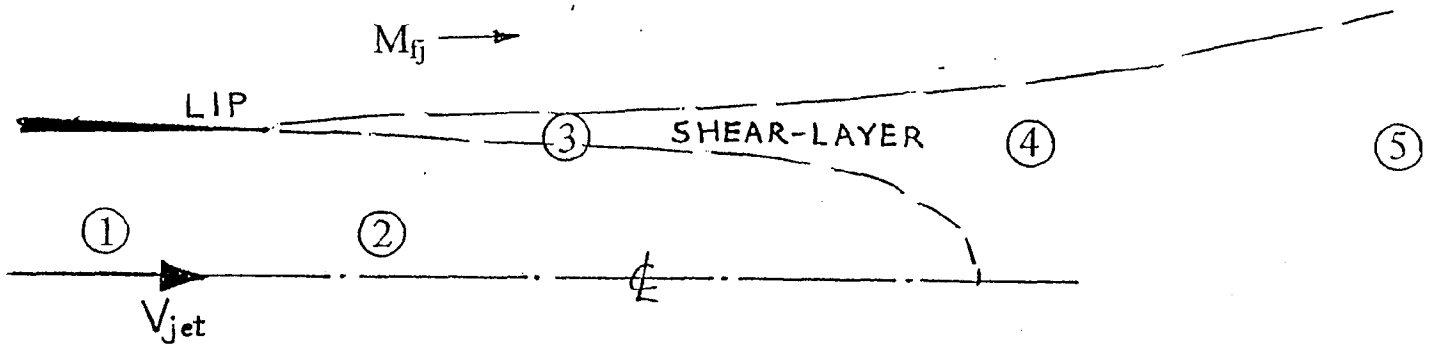

Source Location	Source should change in intensity due to free-jet speed changes	
	NO	YES
1	X	
2	X	
3		X
4		X
5		X

Figure 5.28 Source location and possible insensitivity to free-jet speed changes.

of forced lobe mixers, these are nothing but the turbulence generated by the dominant axial vortex structures. On the other hand, if the SPL's at shifted angles do change then this method fails to say anything definite about the excess noise sources.

It should be noted that internal sources of noise can also radiate to the far-field upstream quadrant. This is illustrated in Figure 5.29 for an internal source in a duct with uniform flow and zero free-jet speed, for simplicity. Consider a noise source inside the nozzle with its wave-number vector **k** having an upstream facing component, $k_x < 0$, with phase velocity vector of magnitude c (local speed of sound in the jet) and group-velocity vector or acoustic ray velocity facing in the downstream direction obtained by vectorially adding **c** (= c**k**/|**k**|) and the local jet velocity vector **V**. We assume here that k_x is such that it does not correspond to total internal reflection. This downstream going ray in the jet finally interacts with the lip shear-layer, represented as a vortex-sheet, either directly or after reflecting from the duct-walls. At the vortex-sheet between the ambient and the nozzle-jet, the equality of static pressure implies that the x-components of the wave-number vectors in the ambient and the jet must be equal, i.e., $k_{x1} = k_x$ where subscript 1 stands for flow outside the jet. Hence if k_x has an upstream facing component at the source $k_x < 0$, then $k_{x1} < 0$ too, and the far-field ray in the quiescent ambient will propagate in the upstream quadrant. With a free jet flow present and $V_{fj} > 0$ this far-field ray will be further deflected due to convection, as already discussed using Figure 5.25. While a vortex-sheet model was used here for convenience, this whole argument is also true for a thin lip shear-layer with constant static pressure within its thickness because the x-component of the wave-number vector, k_x, remains constant throughout the shear-layer thickness.

In summary, only downstream going rays from internal sources within the jet, which do not correspond to total internal reflection angles, can radiate outside the nozzle; all upstream going rays from internal sources within the jet are trapped inside the nozzle. As a special and important subset of these rays, only the downstream going rays from the internal source within the jet which correspond to upstream facing wave-number vectors at the source will radiate into the upstream far-field quadrant when no free jet flow is present.

With this new diagnostic method in hand, let us examine the high NPR condition TO #3 because it showed better invariance of PWL-spectrum than TO #1 which corresponds to low NPR.

5.4.3 Application to Operating Condition TO # 3

Figure 5.30 shows the comparison of polar SPL at a 150 ft radius inside the free-jet for mixer 12UH at free-jet Mach numbers of 0.0, 0.2, and 0.3 at the "shifted" emission angles obtained from the equation of the previous section or Table 5.1. Here, the reference case is taken to be at $\theta_{20} = 90°$ for $M_{fj} = 0.0$ (the "static" angle). Since we are using emission angles we obtain, from Table 5.1, $\theta_2 = 90°$ also for both $M_{fj} = 0.2$ and 0.3 as the "shifted" angle. In this case data is indeed available exactly at 90° for $M_{fj} = 0.2$ and 0.3 and, hence, the error in the angle for which data is plotted is zero. This error in angle is shown in brackets after the corresponding shifted angle in the legend of Figure 5.30. We follow this nomenclature in this section. We see that frequencies beyond 1000 Hz do not change significantly (they are all within the margin of error for SPL)

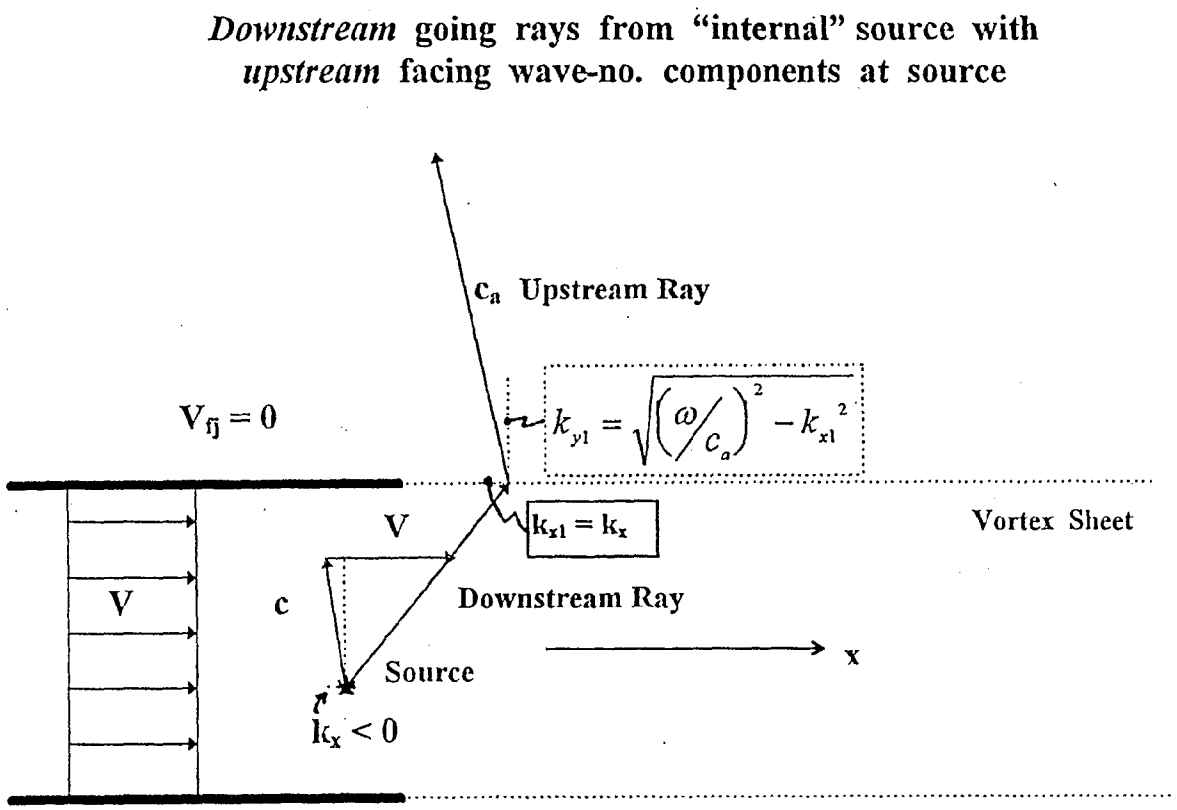

Figure 5.29 Upstream far-field propagation of rays from sources inside the nozzle.

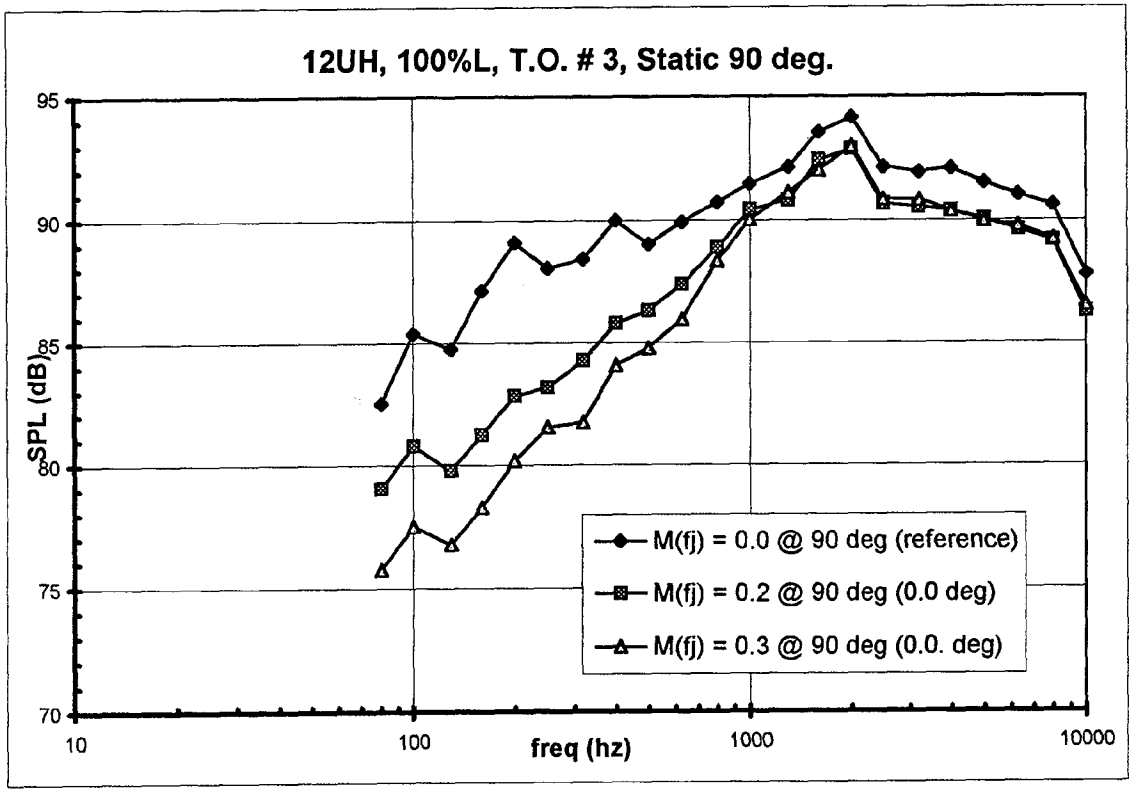

Figure 5.30 "Shifted-angle comparison" at different free-jet Mach numbers, M(fj), for 12UH mixer at static 90 degs.

with changing M_{fj}. This implies that the invariant high-frequency noise at angles at 90° is most likely associated with "excess" noise sources lying either inside the nozzle or close to the exit plane and is due to the turbulence caused by the axial vortices generated between the fan and core streams. We unfortunately do not have the plume data at the exit plane for this condition to nail down the excess sources any further as "internal" or "external."

Let's examine the "shifted" SPL's at different angles.. In Figure 5.31(a) the data at "static" angles of 80° and 100° are compared to appropriately shifted angles for the various free-jet Mach numbers tested. The shifted angles, θ_{2r}, for both free-jet Mach numbers are also 80° and 100° respectively from Table 5.1. It appears that at 80° the SPL's for frequencies around 2000 Hz are quite invariant for the two free-jet Mach numbers, implying that internal and/or external excess sources are responsible for these frequencies at this angle. The downstream angle associated with 100° does not show as much invariance at higher frequencies. If we further compare in the upstream quadrant at angles 85°, 75° and 55°, as shown in Figure 5.31(b), then the previous invariance of SPL appears to hold good at intermediate frequencies near 2000 Hz. For angles less than 70° or more than 95° this SPL invariance appears to falter. Hence, it appears that at least for a certain angular range near 90° the internal and/or external excess sources are, indeed, responsible for the noise at frequencies near 2000 Hz and higher. For the corresponding range of angles near 90° for M_{fj} = 0.2, the resulting PNL is within 3 to 4 PNdB of the peak PNL value for mixer 12UH (see Figure 5.18) and, hence, the excess noise source should be a significant contributor to EPNL.

We have analyzed all the mixers at operating condition TO #3 using the diagnostic technique of comparing SPL's at "shifted" angles for different M_{fj}'s. Some of these results are attached in Appendix D and show comparisons at "static" angles of 75°, 90° and 100° and corresponding "shifted" angles at higher M_{fj}'s. (Note from table 5.1 that the corresponding shifted angles are also approximately 75°, 90° and 100° respectively.) Examination of all these figures given in Appendix D shows the following:

1. All lobed mixers show strong invariance of SPL at mid-to-high frequencies for "static" 75° when M_{fj} is varied from 0.0 to 0.2 to 0.3 similar to the 12UH mixer discussed earlier. Actually this was seen to hold good for a small range of angles in the upstream quadrant near 90°.

2. In the downstream quadrant away from 90° the SPL invariance breaks down.

3. In the scalloped lobe mixers 12CL and 20DH although the SPL variation at higher frequencies was less that at low frequencies, clean SPL-invariance was not observed even at 90°. That is, compared to the SPL invariance in unscalloped mixer 20UH, the SPL's for 12CL and 20DH mixers at shifted angles varied more than 20UH for high frequencies when M_{fj} was varied.

4. The sound pressure levels of the confluent mixer (CONF) do not show invariance at "shifted" angles for different free jet Mach numbers at any frequency. This means that the dominant noise sources are either not the internal or the external excess noise sources, or that if any excess noise sources are present then they have merged with the free jet outside

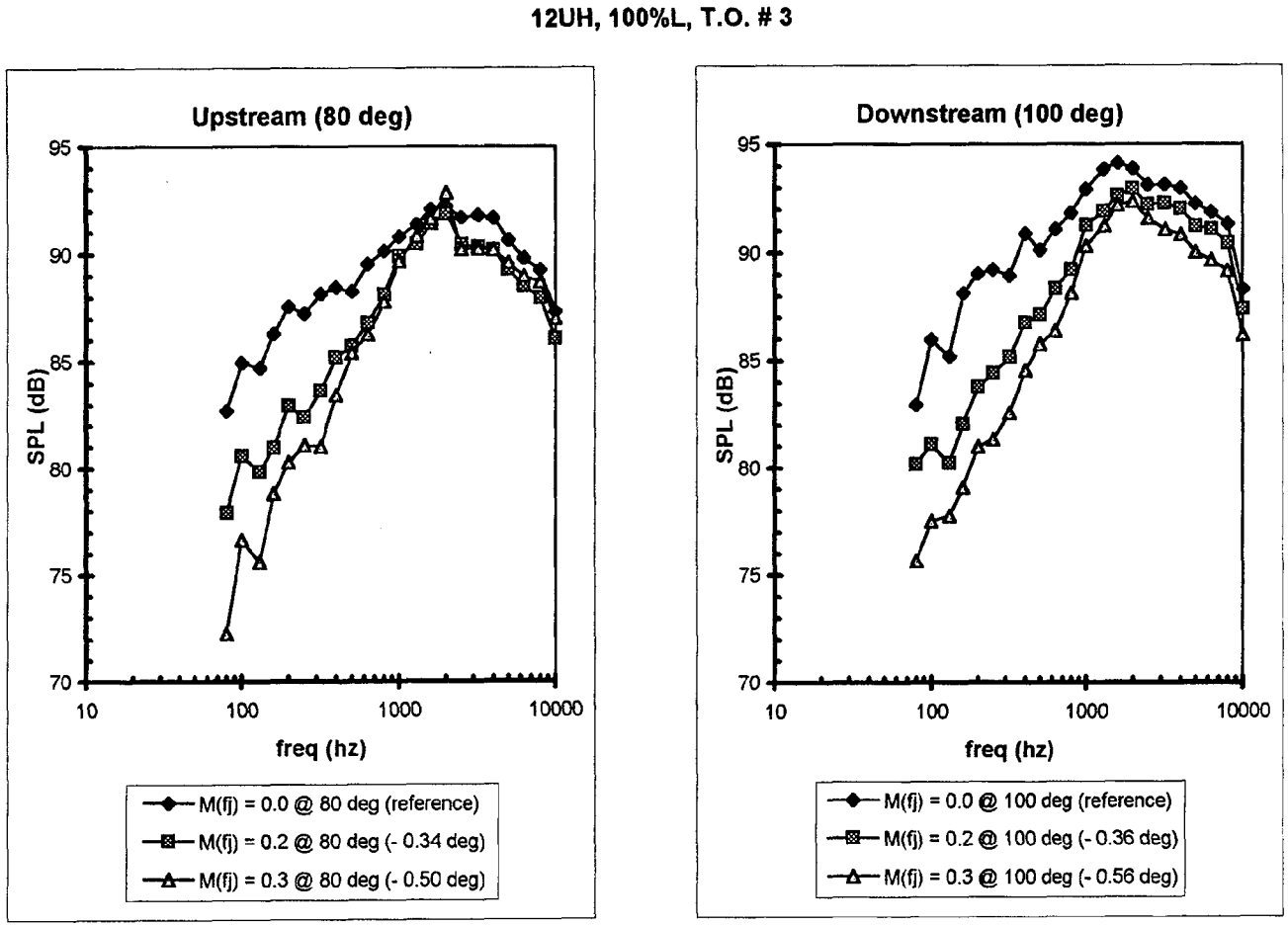

Figure 5.31(a) "Shifted-angle comparison" at different free-jet Mach numbers for 12UH mixer at 80 degs and 100 degs.

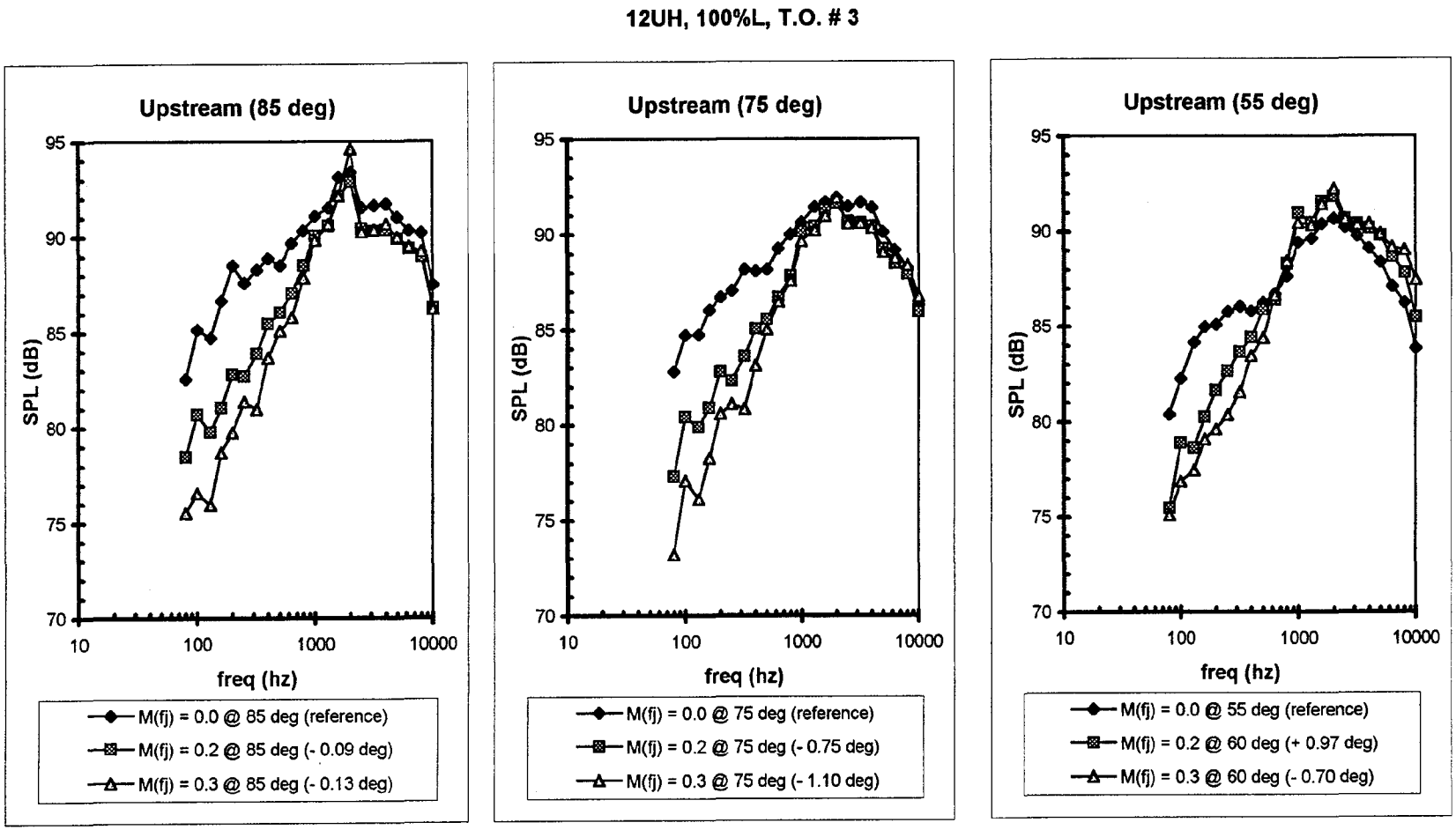

Figure 5.31(b) "Shifted-angle comparison" at different free-jet Mach numbers for 12UH mixer at various upstream angles.

the nozzle. This configuration does not produce axial vorticity structures and little mixing occurs inside the nozzle. The fan/core flow mixing outside the nozzle near the exit-plane, which is away from the free-jet, is a region which is not a dominant noise producing region as explained in the model of a coplanar coaxial jet for the "initial" region contained in Fisher et al[17].

In summary, application of the new diagnostic technique at operating condition TO #3 shows that all unscalloped mixers (12UH, 16UH, 20UH) appears to have "excess" noise sources which emit noise at upstream angles close to 90°. These excess sources can be either inside the nozzle duct or close to the nozzle exit plane near the jet axis representing partial fan/core stream mixing. The turbulence generated by the strong axial vortices found in these forced lobed mixer configurations is the probable candidate for the excess source. Perturbation of streamwise vortices which have convoluted vortex surfaces with normals in the transverse plane will emit the strongest sound in the radial direction or at $\theta \approx 90°$ which is what has been observed. However, the deeply scalloped mixer (20DH) and the cutout mixer (12CL) do not show this behavior clearly. Hence, their excess sources, if any, are either weak or they interact with the free-jet/model-jet shear layer to change the far-field SPL's at "shifted" angles, as observed. 20DH mixer also typically shows fairly uniform velocity profiles at the nozzle exit plane, except for a small hump at the center (see Figure 4.13). Hence, its internal noise sources must be weak radiators. Recall that 20DH and 12CL are also the quietest mixers, especially in the mid-to-high frequency range (see Figures 5.19, 5.16). Thus, this "shifted" angle SPL comparison in a way complements the previous acoustic findings.

We have applied this technique also at the lower NPR condition, TO #1, to all mixers, and the results do not show much SPL invariance with free jet Mach number, implying that these "excess" sources become less important at the lower jet speeds (830 ft/s) associated with this operating condition.

5.5 Effect of Nozzle-Length

In this section acoustic data is presented and analyzed for mixers with different nozzle-lengths. The nozzles tested varied the mixing-length or the distance between the mixer exit plane to the nozzle exit plane, L, between 50%, 75% and 100% of the baseline mixing length. These correspond, respectively, to $L/D_{mp} = 0.55$, 0.83 and 1.10 where D_{mp} is the mixing-plane diameter. The 75%L configuration was tested in conjunction with only three of the available lobed mixers (12TH, 20UH, 20DH). In each case the nozzle exit plane diameter was kept the same, as shown in Figure A.5.

Since the recording microphones were at fixed locations in the APL dome, the distance between them and the nozzle exit plane changed slightly as the nozzle-length was varied. The changes in the nozzle-length, ΔL, are at most 5.5" (distance between the exit planes of 100%L and 50%L) and the microphones are at R = 48 ft. As a result, $\Delta R/L = 0.0095$ and the changes in the microphone angles and distances which are measured from the center of the baseline (100%L) nozzle are negligible.

Initially we examine the effect of nozzle-length on the overall acoustic metrics at all performance conditions. In the second section we examine the SPL-spectra at various angles. Finally we examine the

probable mechanism that produces the observed behavior.

5.5.1 Overall Acoustic Metrics

Earlier studies with the confluent nozzle (CONF) showed that the nozzle-length or mixing-length, L, did not make any difference in far-field noise. (Some results from 1995 tests for CONF mixer are reported in Mengle et al[16].) This is an expected result because CONF does not produce any appreciable internal mixing and, therefore, changing mixing lengths does not change the fan/core or jet/ambient mixing behavior. Hence, we will not deal with the length effects for CONF mixer. The focus here will be on mixing-length effects for the lobed mixers and the tongue mixer.

Figures 5.32 to 5.38 show the power spectrum, polar OASPL directivity and flyover PNL-directivity for, respectively, 12CL, 12UH, 12TH, 16UH, 20UH, 20MH and 20DH mixers at conditions TO #1, #2 and #3 with a free jet Mach number of M_{fj} = 0.2 for all nozzle-lengths tested. These are very comprehensive plots. Examination of these plots reveals the following interesting facts regarding mixing-length effects:

1. Reducing mixing length does not necessarily produce an increase in noise, as commonly believed. For example, for mixers 12TH, 20UH and 20DH at TO # 3 (Figures 5.34, 5.36, 5.38) both PNL and OASPL decreases at most angles as the mixing length is decreased from 100% to 75%L and then increases with further reduction to 50%L, showing a local minimum for noise. This is also true for mixer 12CL (Figure 5.32) where a reduction from 100%L to 50%L produces a decrease in noise for all the operating conditions. This noise decrease due to the reduction in L looks substantial and will be quantified in terms of EPNL later.

2. The reduction in noise with a decrease in L is not always observed for the lower NPR conditions for these mixers. For example, a noise increase is observed for mixer 12TH as the nozzle-length decreases for conditions TO #1 and #2. The PNL directivity of the 20 lobe mixer with deep scallops, 20DH, is essentially unchanged when the mixing-length is reduced from 100%L to 75%L at the lowest pressure ratio, TO #1. However as the NPR is increased, a PNL reduction is noted as the mixing length is reduced from 100%L to 75%L for configuration 20DH at angles less than or equal to 125°. However, 20UH shows a local minimum in noise at 75%L for all take-off conditions TO #1, #2 and #3.

3. The three mixers 12UH, 16UH and 20MH (Figures 5.33, 5.35, 5.37), for which no 75%L tests were done, always show an increase in noise when the mixing-length is reduced by half. Since all the other noise characteristics of these three high-penetration mixers are very much like those of 20UH, it is very likely that they too will show a local noise minimum if data were obtained at 75%L.

4. In terms of the PWL-spectra, changes in mixing-length produces substantial changes in the mid-to-high frequency range, but the low frequency is unchanged at all operating conditions for all mixers. Since near the peak PNL angle and upstream of it mid-to-high frequencies dominate, this spectral behavior is reflected as larger

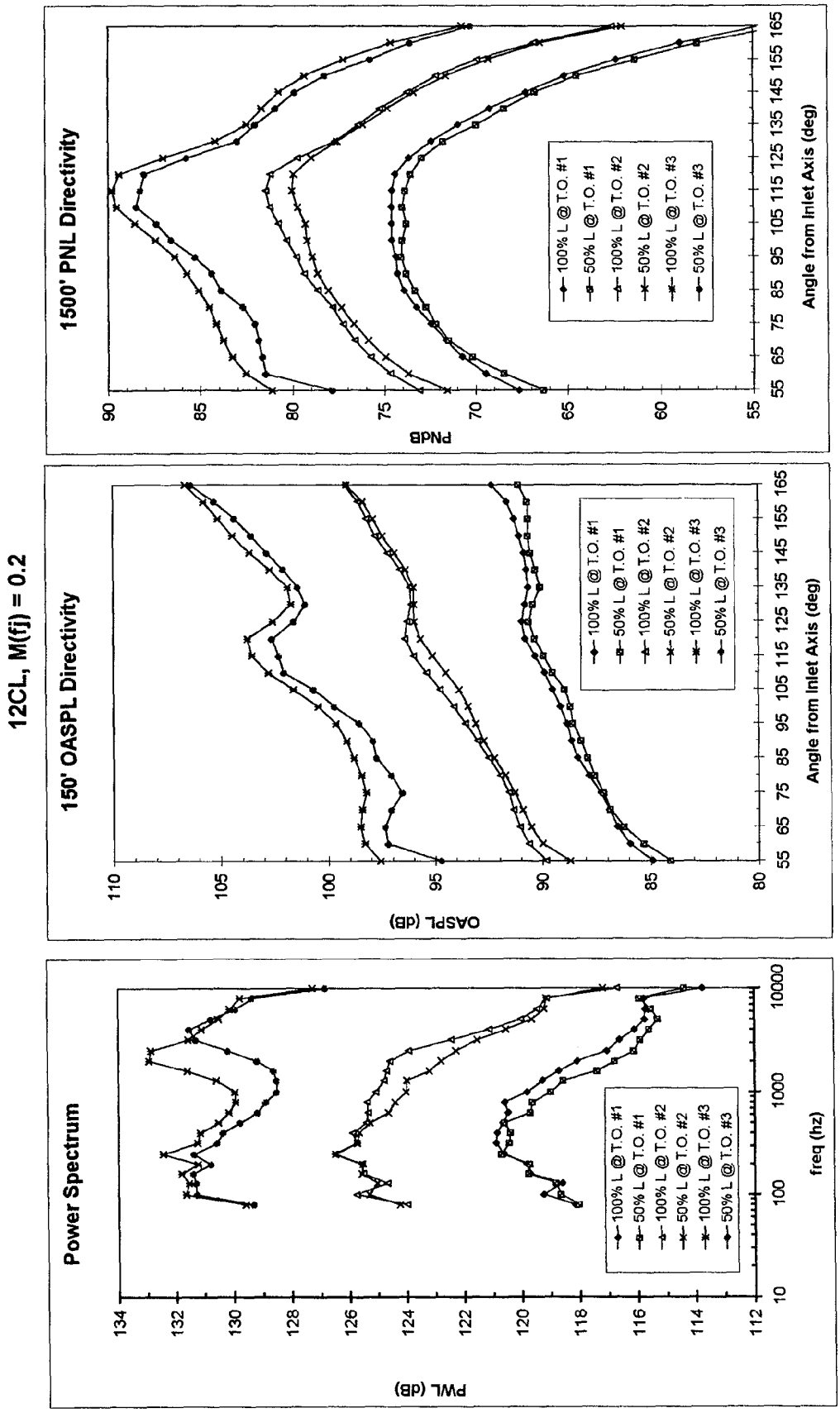

Figure 5.32 Effect of nozzle-length on Sound Power, OASPL and flyover PNL at different T.O. operating conditions on 12CL.

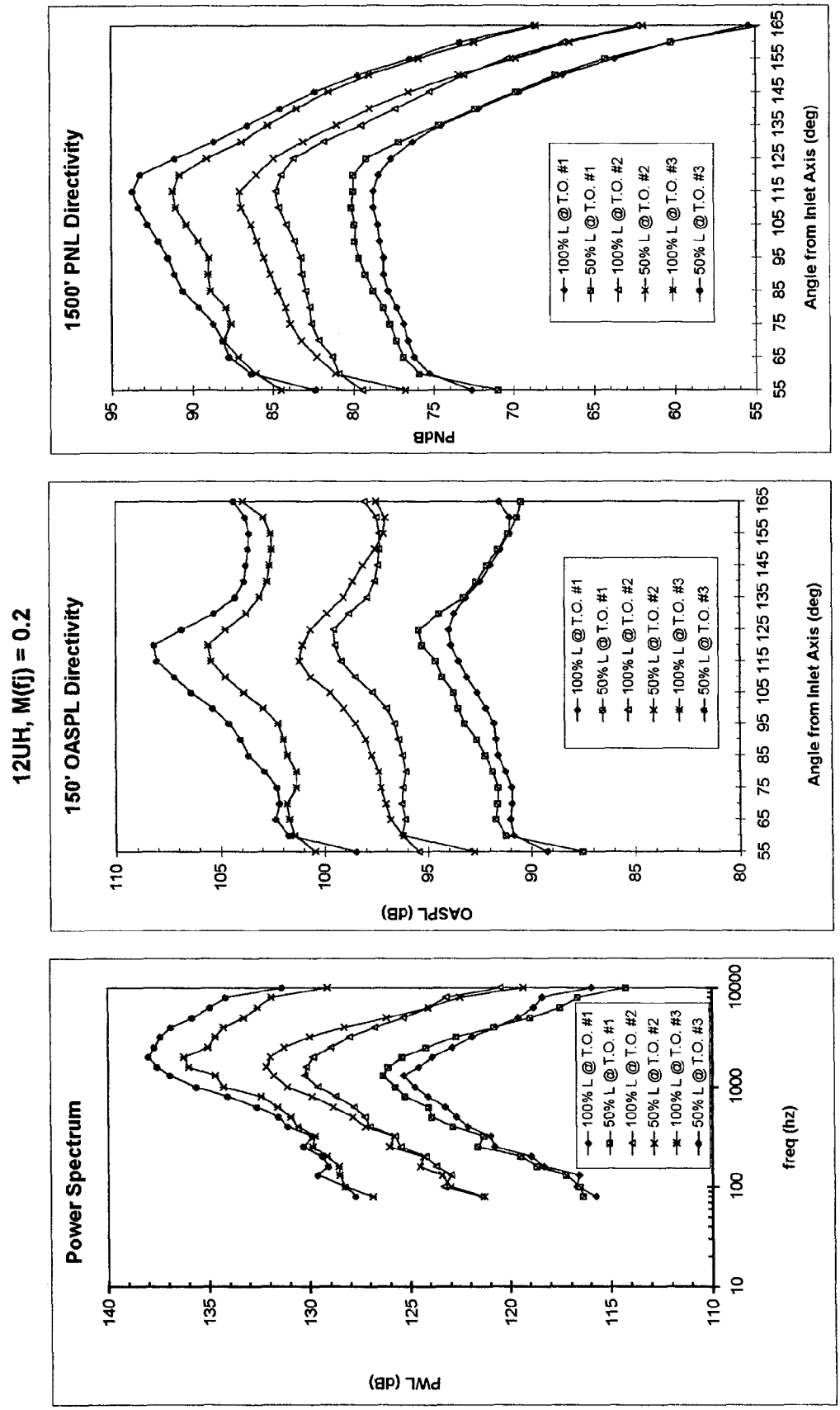

Figure 5.33 Effect of nozzle-length on Sound Power, OASPL and flyover PNL at different T.O. operating conditions on 12UH.

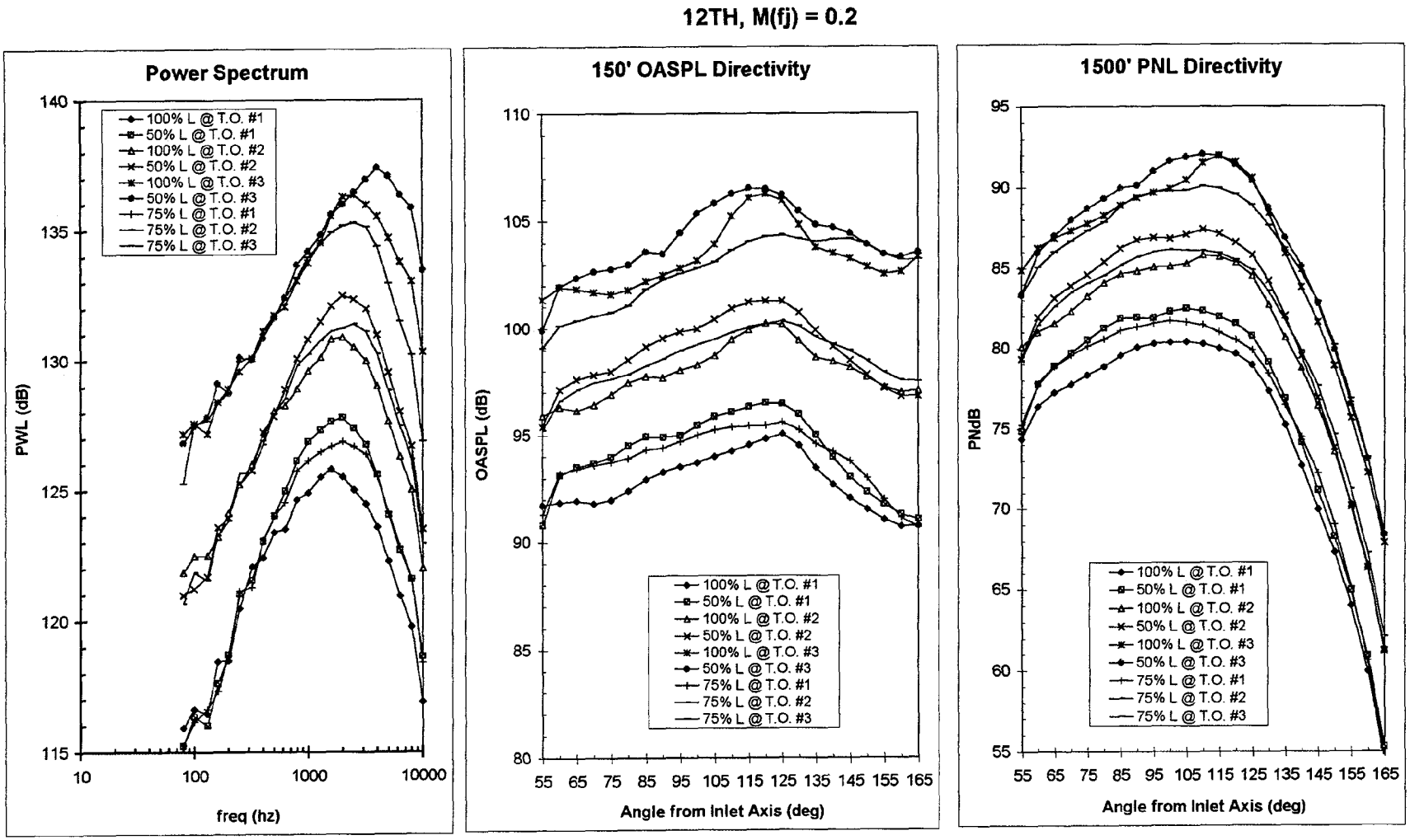

Figure 5.34 Effect of nozzle-length on Sound Power, OASPL and flyover PNL at different T.O. operating conditions on 12TH.

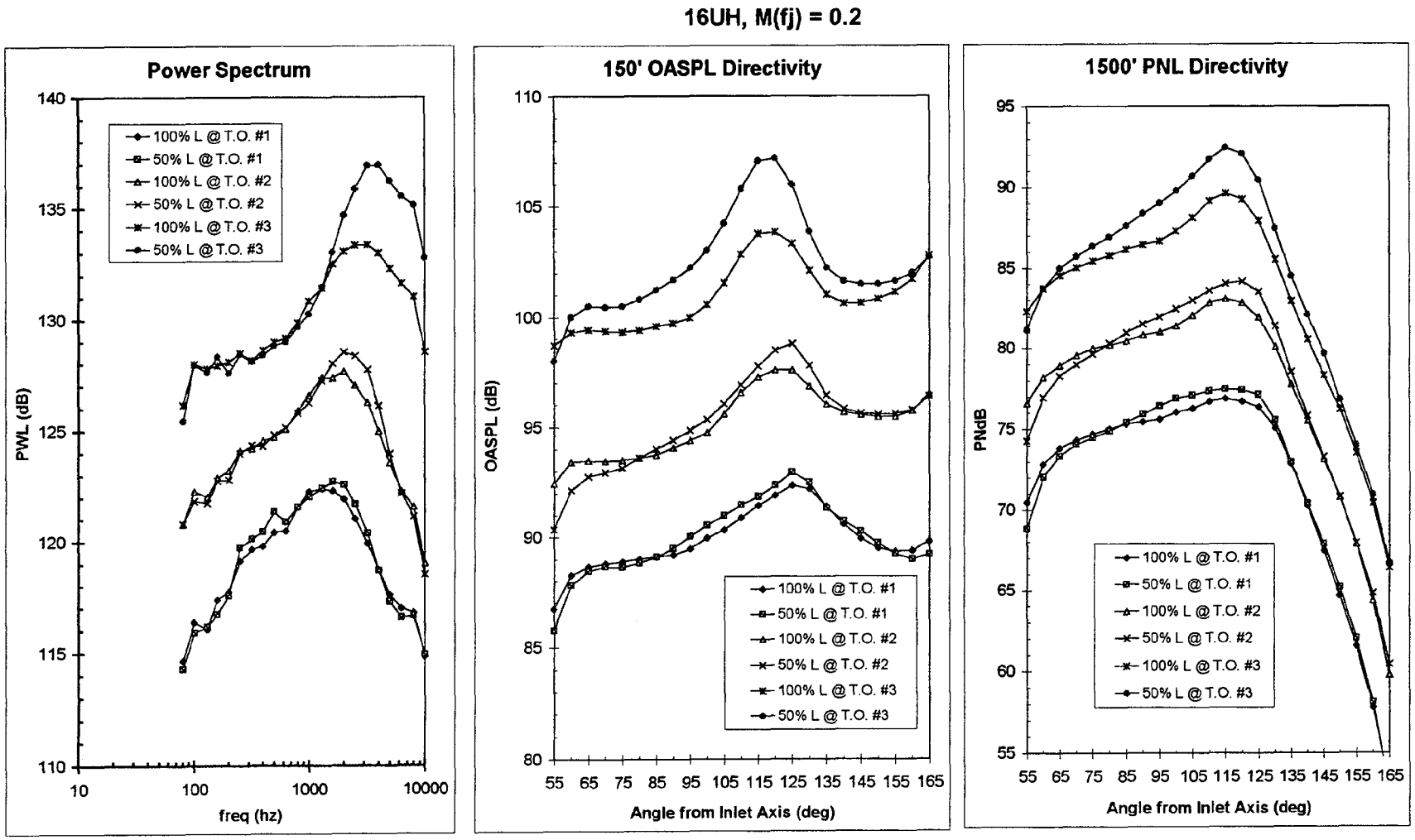

Figure 5.35 Effect of nozzle-length on Sound Power, OASPL and flyover PNL at different T.O. operating conditions on 16UH.

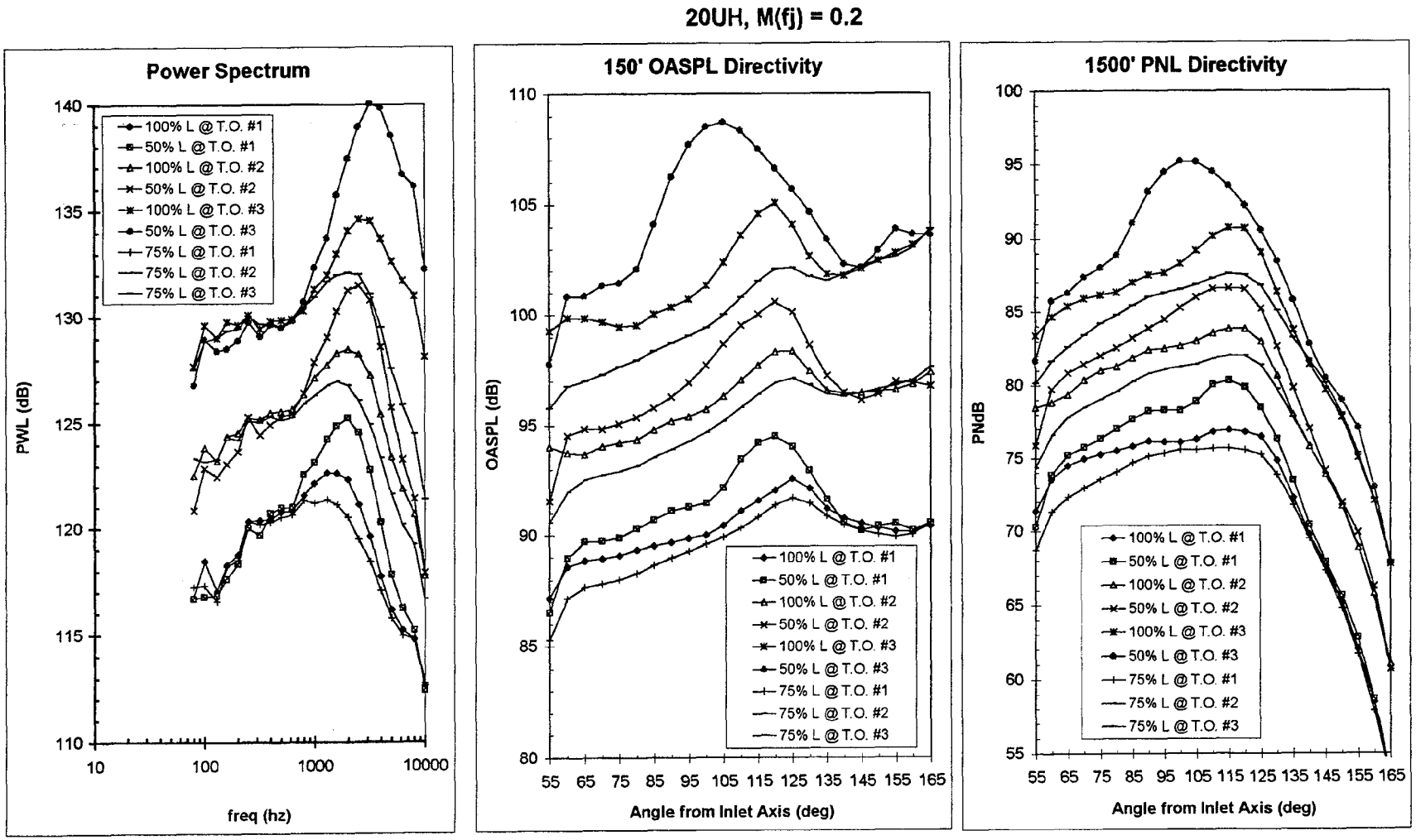

Figure 5.36 Effect of nozzle-length on Sound Power, OASPL and flyover PNL at different T.O. operating conditions for 20UH.

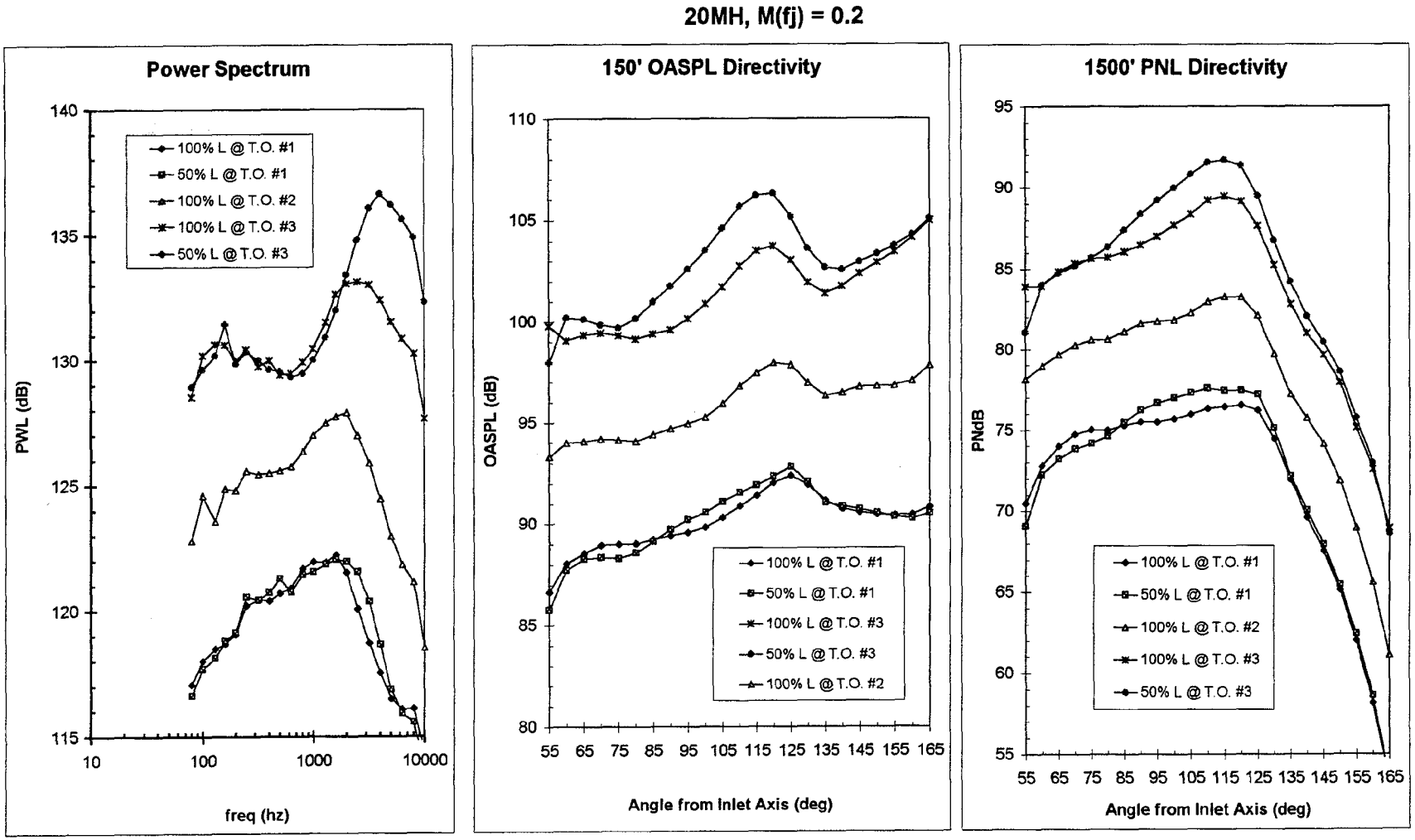

Figure 5.37 Effect of nozzle-length on Sound Power, OASPL and flyover PNL at different T.O. operating conditions for 20MH.

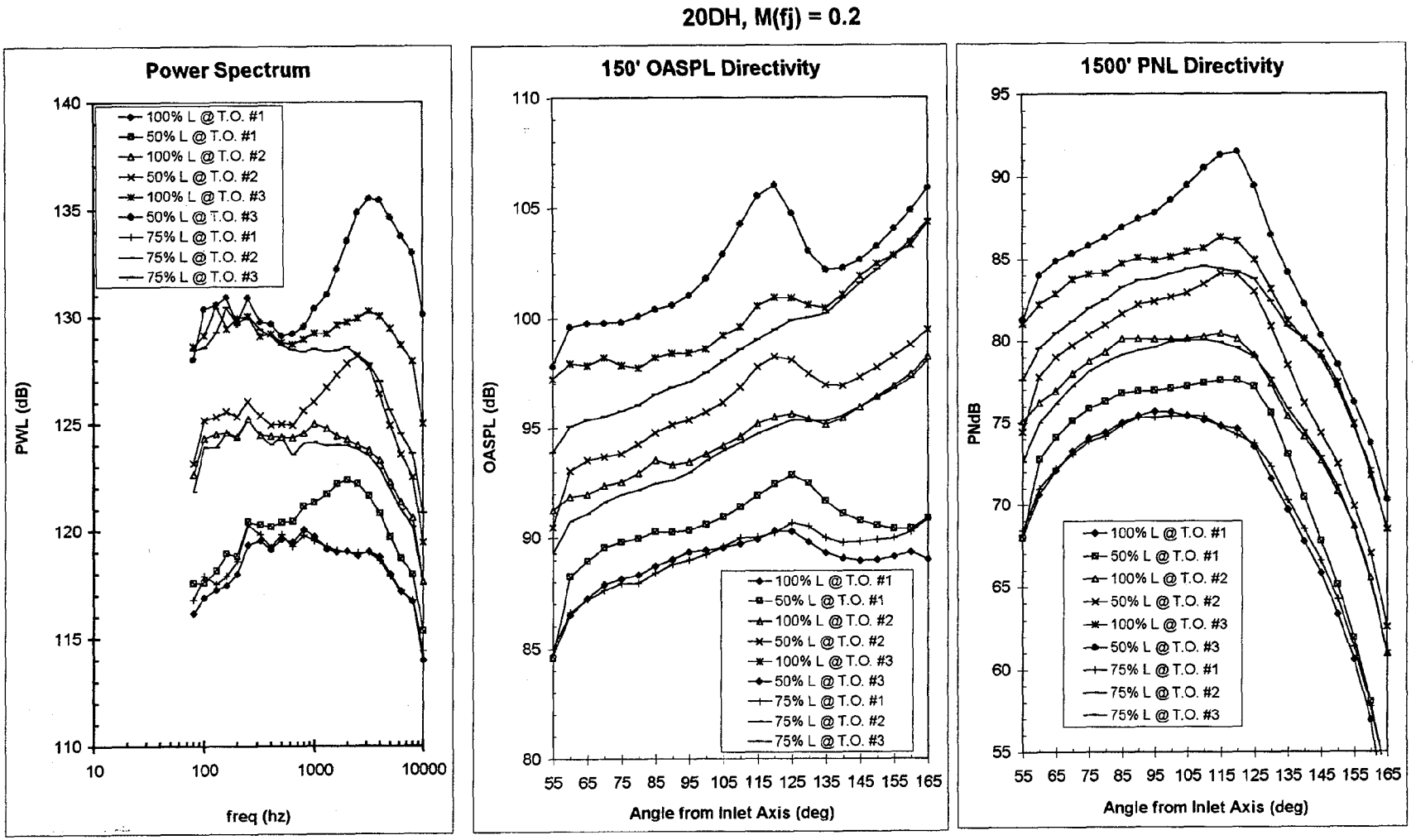

Figure 5.38 Effect of nozzle-length on Sound Power, OASPL and flyover PNL at different T.O. operating conditions for 20DH.

changes in PNL in the corresponding angular regions and smaller changes at the shallow angles. Similar changes were noted in the OASPL directivity. Thus, using 20UH as an example (Figure 5.36), large changes in peak PWL at 2000-3000 Hz are reflected as large changes in peak PNL at 100°-115°. Consequently if there is a reduction in the PWL-spectra at 2000 Hz going from 100% to 75%L then it also appears as a reduction in the PNL at the corresponding angles near the peak PNL angle.

5. The striking independence of low frequency PWL on mixing-length for all mixers at all conditions implies that the far downstream plume decay must be independent of the mixing length.

Any reduction in noise with decrease in nozzle length is always welcome from the point of view of nozzle weight but its effect on thrust should also be considered. We will investigate the reasons for this interesting acoustic behavior by scrutinizing the polar SPL-spectra in the next section.

5.5.2 Polar SPL-Spectra

Figures 5.39 to 5.45 show the 150 ft polar SPL-spectra for all nozzle lengths at 60°, 90° and 115° for the lobed mixers 12CL, 12UH, 12TH, 16UH, 20UH, 20MH and 20DH respectively for all operating conditions and at M_{fj} = 0.2. These Figures correspond to those in the previous section for each mixer and should be used for reference.

Examination of these SPL-plots reveals the following:

1. Changes in OASPL due to mixing-length changes at a given angle arise mainly due to changes in SPL in the mid-to-high frequency spectra. The low frequency portion of the SPL is almost invariant to nozzle-length changes at all angles. The very high frequency spectra also appears insensitive to nozzle-length, particularly at the low nozzle pressure ratio of TO #1. This spectral behavior is reflected in the PWL spectra discussed in the last section.

2. Using mixer 20UH at operating condition TO #2 as an example (Figures 5.43 and 5.36), the changes in OASPL or PNL at 115° due to mixing-length changes must be due to frequencies larger than 800 Hz since frequencies lower than 800 Hz do not change. Hence changes in the flow structures that cause the mid-to-high frequency sources must also be the dominant reason for changes in PNL or OASPL due to mixing-length changes. Earlier (Section 5.4.3 and Figure D.5) we have found that internal and external "excess" noise sources contribute largely to this mid-to-high frequency range at angles near 90° at M_{fj} = 0.2, and that the turbulence in the axial vortices are the likely noise generators. Interaction of these vortex structures with the free-jet in the nozzle lip-shear layer or further downstream near the end of the jet "core" will also produce mid-to-high frequency noise at other angles, e.g., where PNL peaks.

3. In order to understand why a local minimum for sound exists when mixing-length is decreased, we focus on a fixed frequency, say, at or near the spectral peak and see how its SPL changes at all angles. Recall that the polar SPL being examined is in the

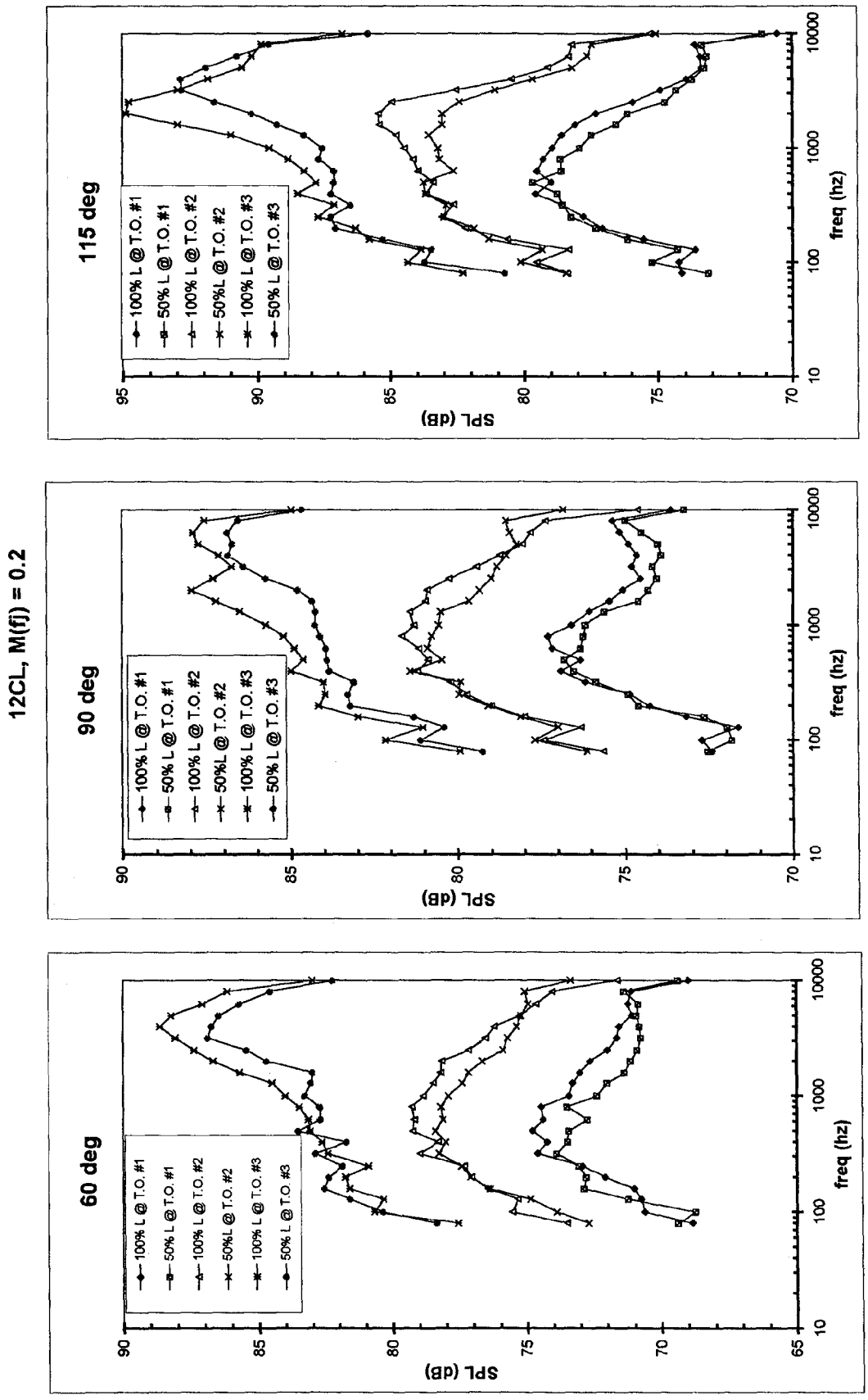

Figure 5.39 Effect of nozzle-length on 150' SPL spectra at different T.O. operating conditions and M(fj) = 0.2 for 12CL.

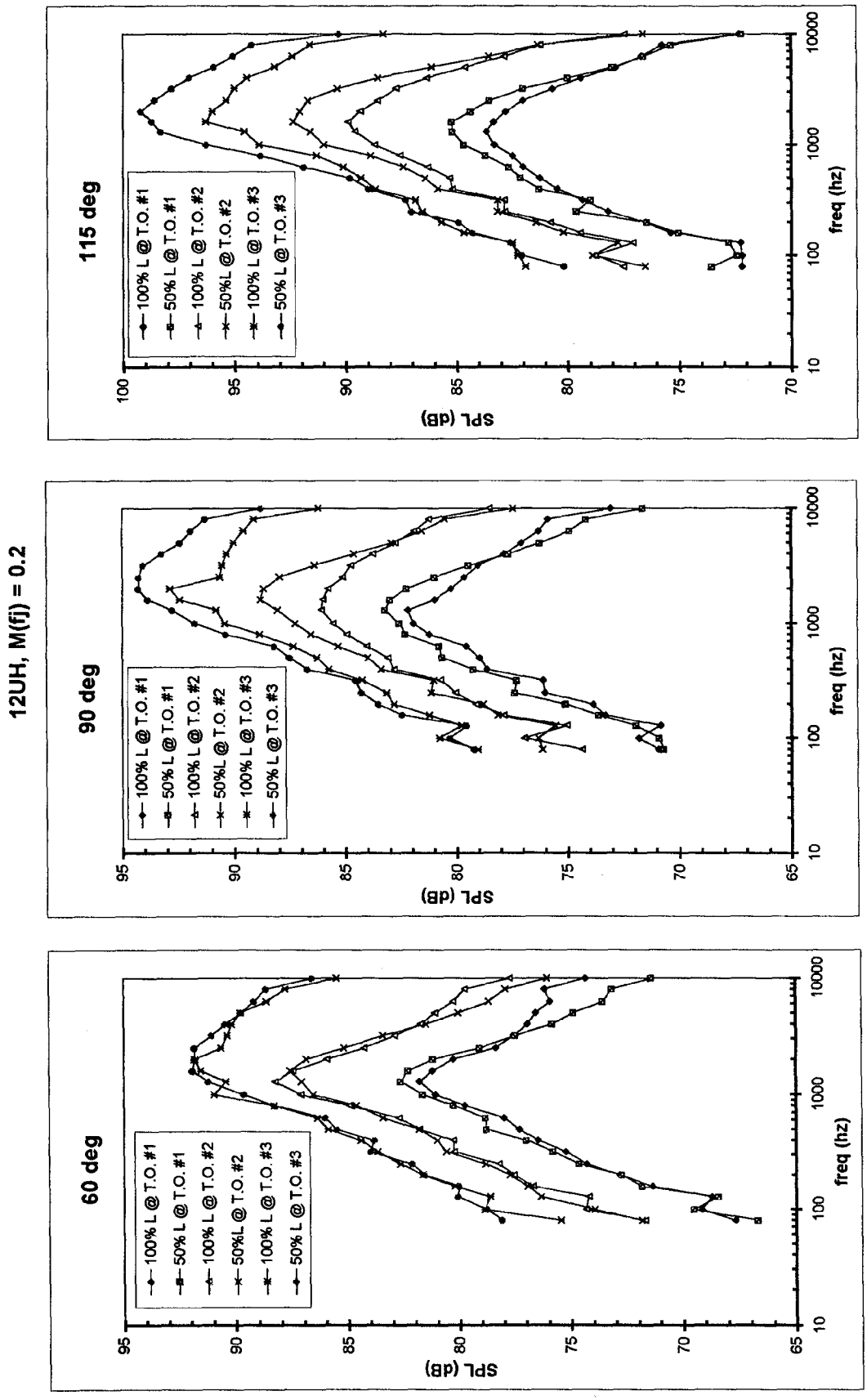

Figure 5.40 Effect of nozzle-length on 150' SPL spectra at different T.O. operating conditions and M(fj) = 0.2 for 12UH.

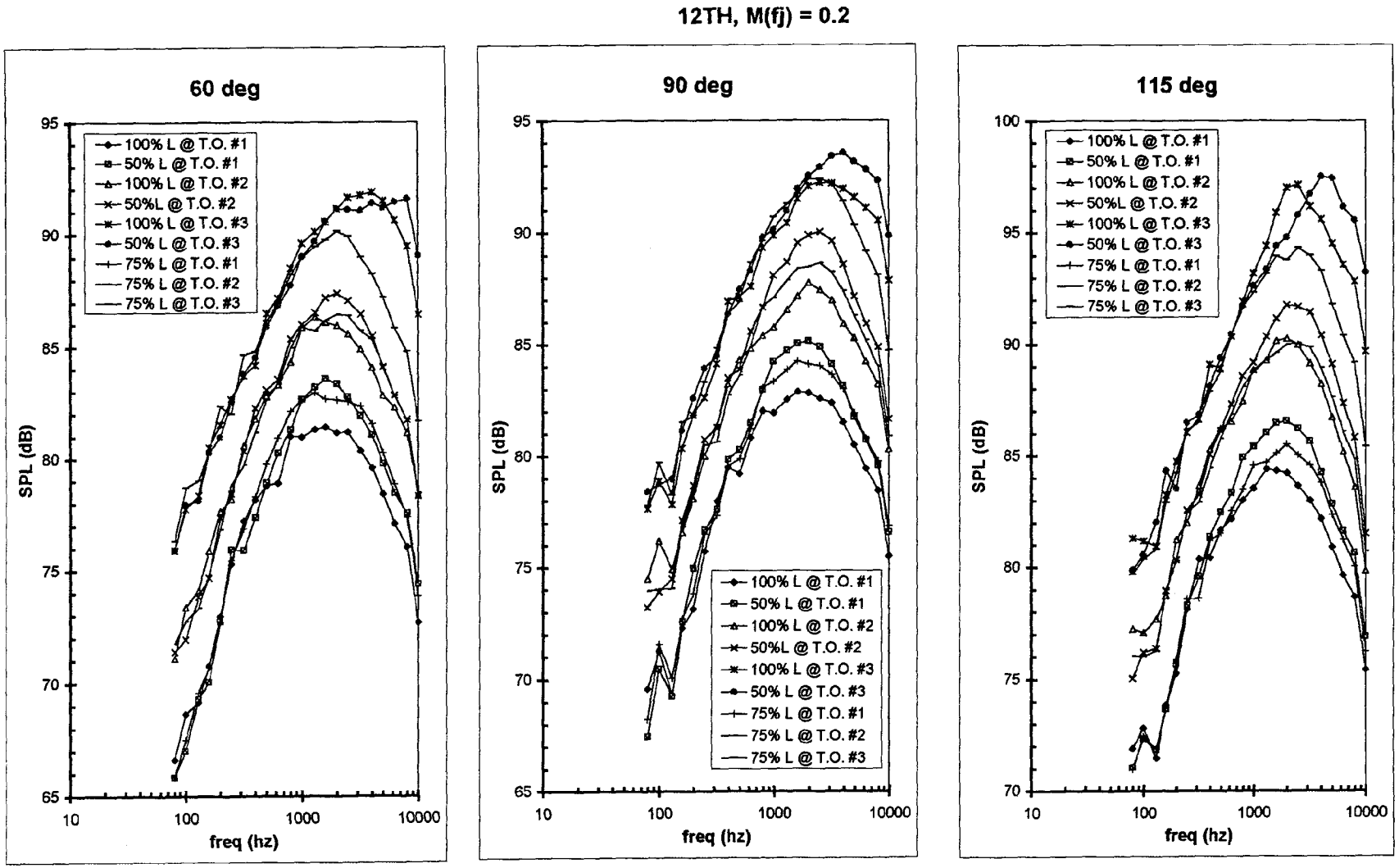

Figure 5.41 Effect of nozzle-length on 150' SPL spectra at different T.O. operating conditions and M(fj) = 0.2 for 12TH.

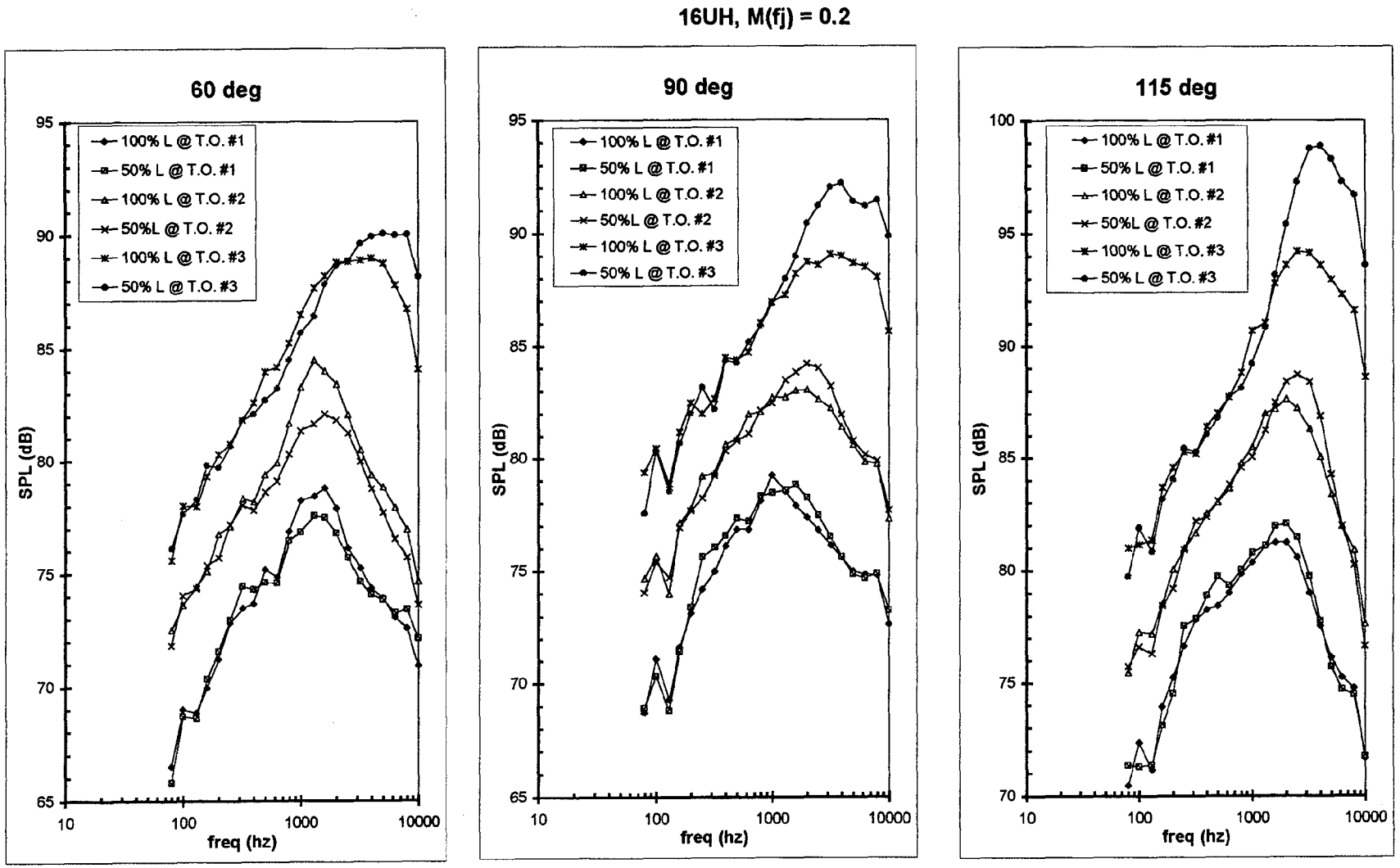

Figure 5.42 Effect of nozzle-length on 150' SPL spectra at different T.O. operating conditions and M(fj) = 0.2 for 16UH.

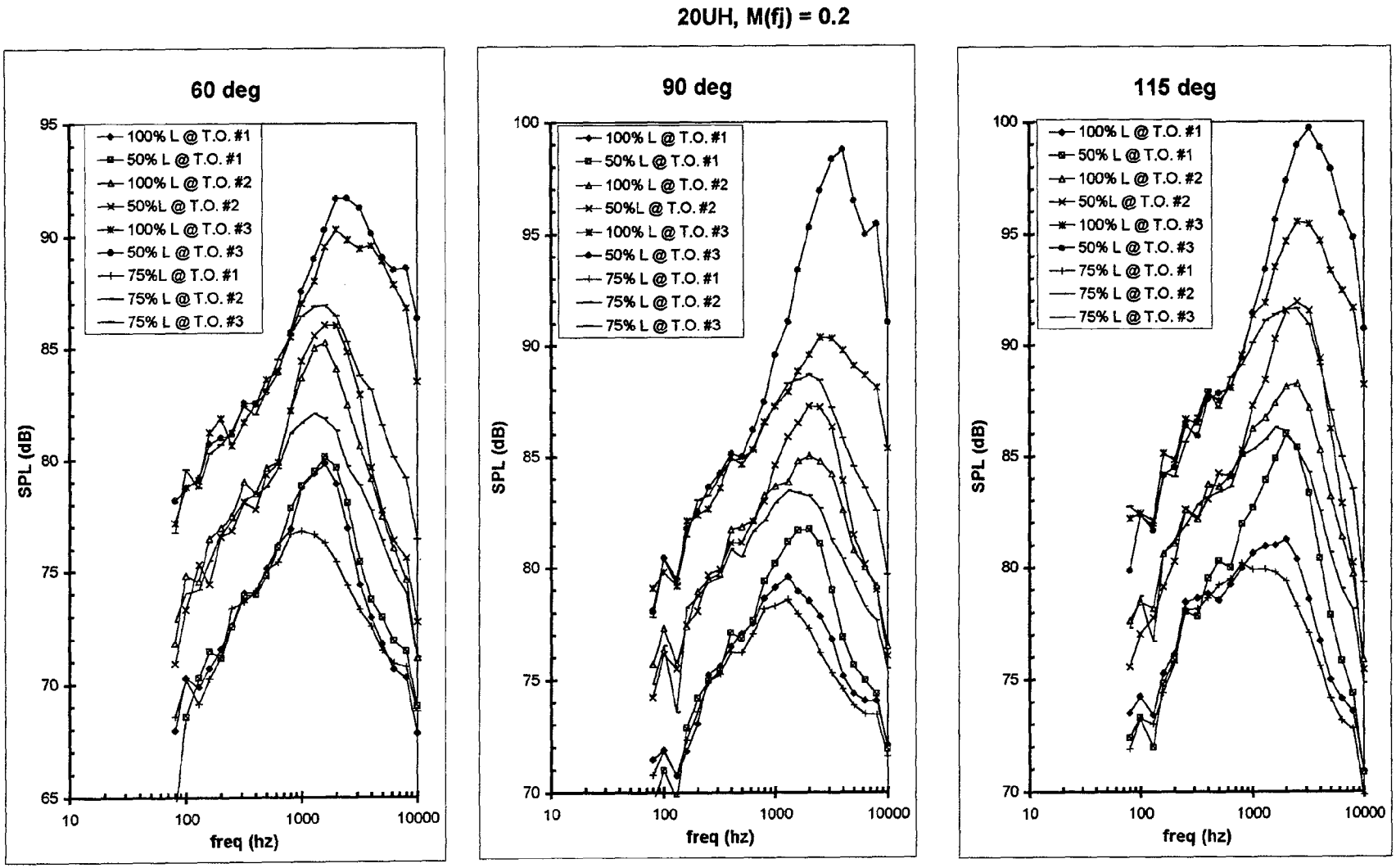

Figure 5.43 Effect of nozzle-length on 150' SPL spectra at different T.O. operating conditions and M(fj) = 0.2 for 20UH.

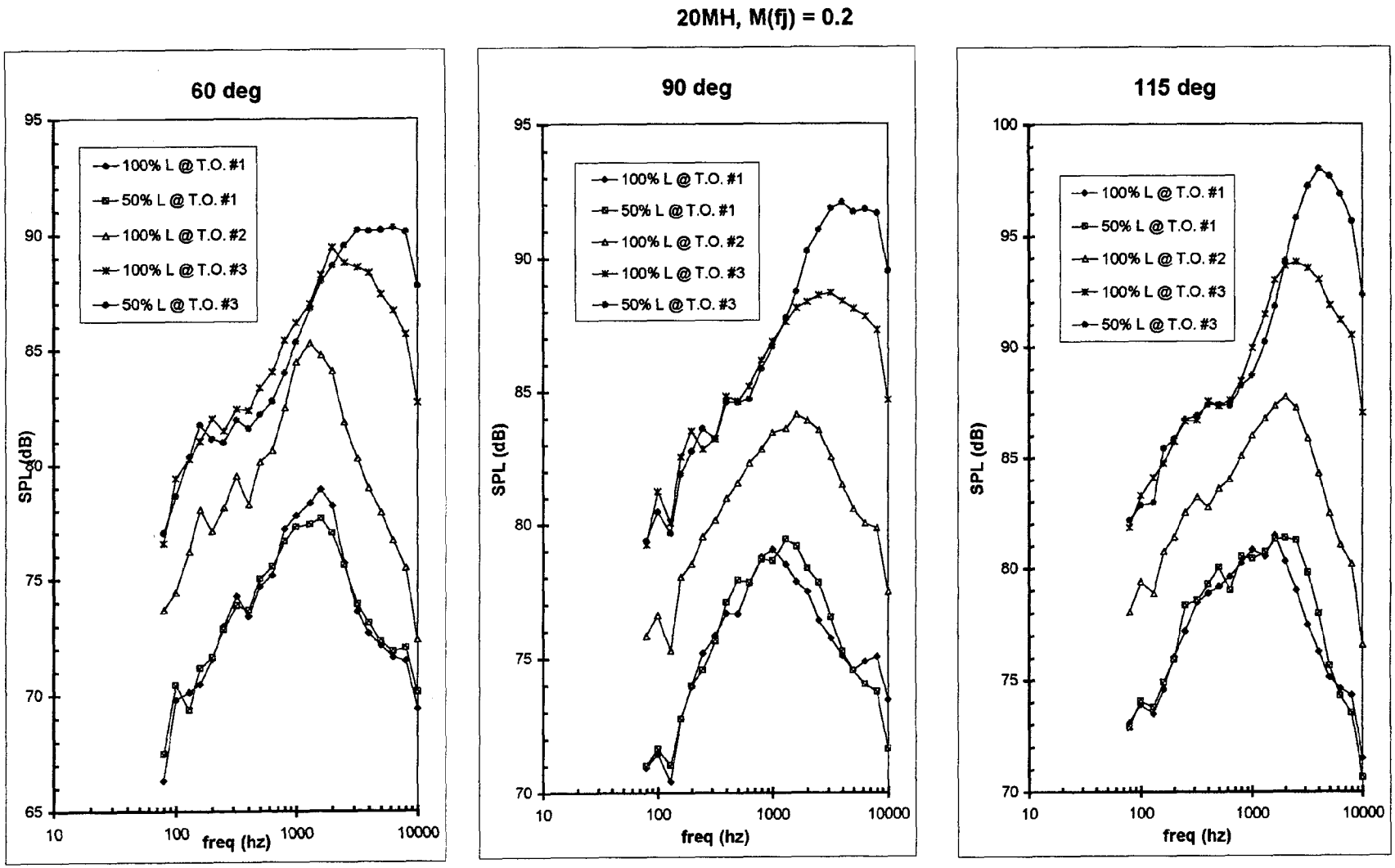

Figure 5.44 Effect of nozzle-length on 150' SPL spectra at different T.O. operating conditions and M(fj) = 0.2 for 20MH.

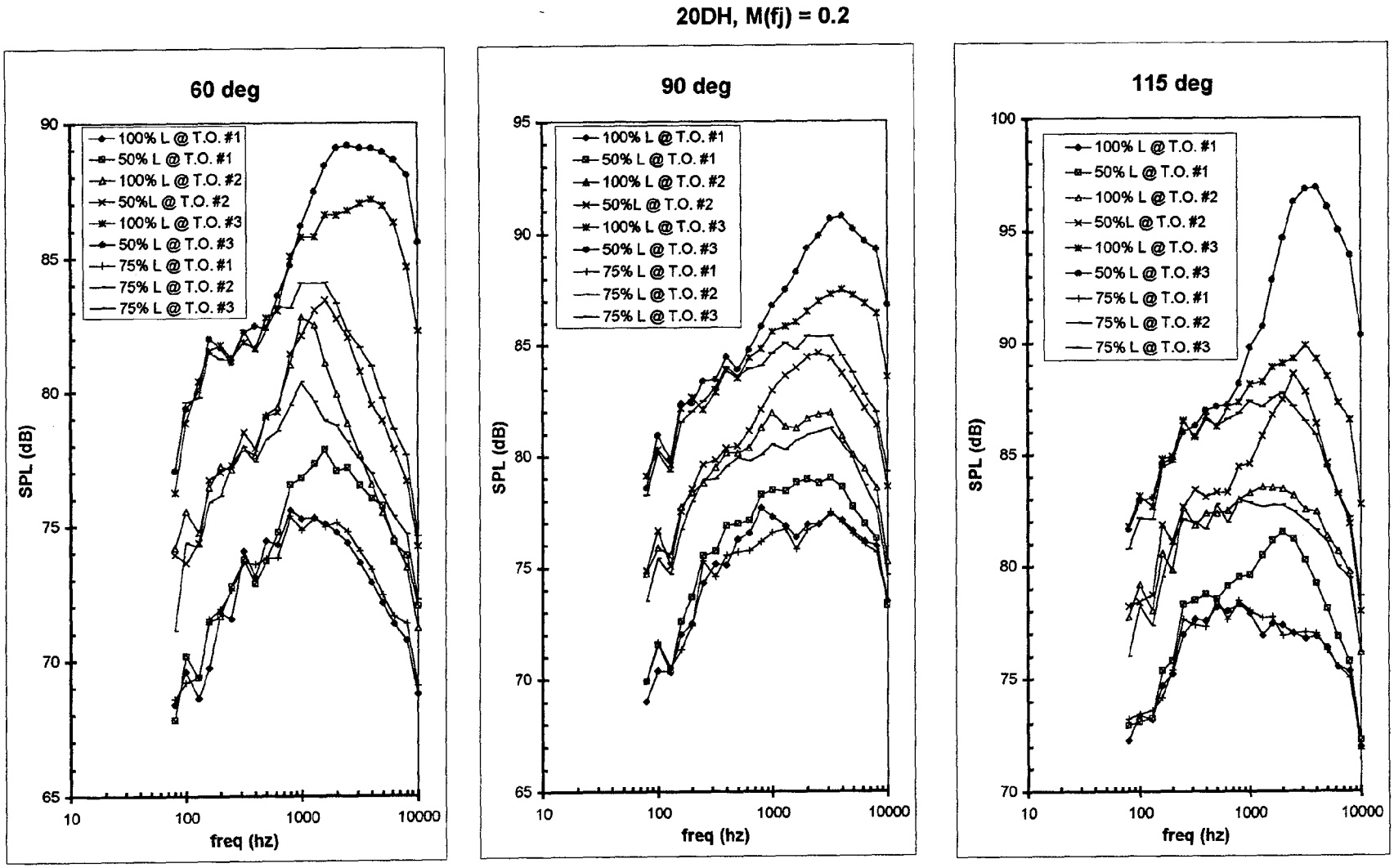

Figure 5.44 Effect of nozzle-length on 150' SPL spectra at different T.O. operating conditions and M(fj) = 0.2 for 20DH.

reference frame of the nozzle so that we do not need to Doppler-shift the frequency at different angles for comparison. Again using 20UH as an example (Figure 5.43), we see that the 2000 Hz component of SPL decreases by similar amounts at all angles when the mixing-length is reduced from 100% to 75%. This is also true for all the neighboring frequencies in the mid-to-high frequency bands. Since the far-field radiated sound due to a source can be thought to be made up of the product of an amplitude factor (intensity) and a directivity factor, this observation at all angles implies that the source producing these mid-to-high frequencies is decreasing in intensity as the length is decreased from 100% to 75%. Since the turbulence in the axial vortex structures is the cause for this frequency range, this turbulence intensity which is related to the strength of the axial vortices must be getting weaker. It was also noted previously that the noise starts increasing when the mixing-length is reduced further to 50%L. This suggests the presence of "competing" mechanisms – one which decreases noise and the other which increases it when the mixing length is reduced. We explore the competing mechanisms in the next section.

4. From Figure 5.45A it is also observed that as the mixing length is decreased from 100%L to 75%L the peak SPL frequency (in terms of 1/3rd octave-band center frequency) generally decreases, and when the mixing length is further decreased to 50%L the peak SPL frequency always increases, thus exhibiting a local minimum in the peak SPL frequency at a given angle. This curious fact is worthy of attention because one would otherwise expect that as the nozzle length is decreased the peak SPL frequency ought to *monotonically* increase due to more and more exposure of the smaller eddies produced by the mixing of fan and core streams. Also the decrease in peak SPL frequency for 75% L takes it away from the most annoying spectral region of 3000-4000 Hz. This combined with its reduced intensity, observed earlier, no doubt will reduce the perceived noise levels for 75% L. Such perceived noise levels will be studied in Section 5.6.

5. With a free-jet Mach number of M_{fj} = 0.2 in the above data, changing the nozzle length by a few inches also changes the boundary-layer thickness on the outside of the nozzle wall at the exit-plane by a small amount. It can be argued that this change in boundary layer thickness can affect the evolution of the jet plume downstream of the nozzle exit and, hence can affect this peculiar phenomenon of "local minimum of noise." In order to check if this unique phenomenon exists without any external boundary layer, we examine the static case, M_{fj} = 0, where there is no external boundary layer. Figure 5.46 shows the static polar SPL's for 20UH at TO #3 with different nozzle-lengths. We see that 75% nozzle-length again shows a local minimum in SPL at mid-to-high frequencies, as well as a local minimum for the frequency of peak SPL as before. This implies that the effect of the external boundary-layer is not an important part of the mechanism which produces the local noise minimum.

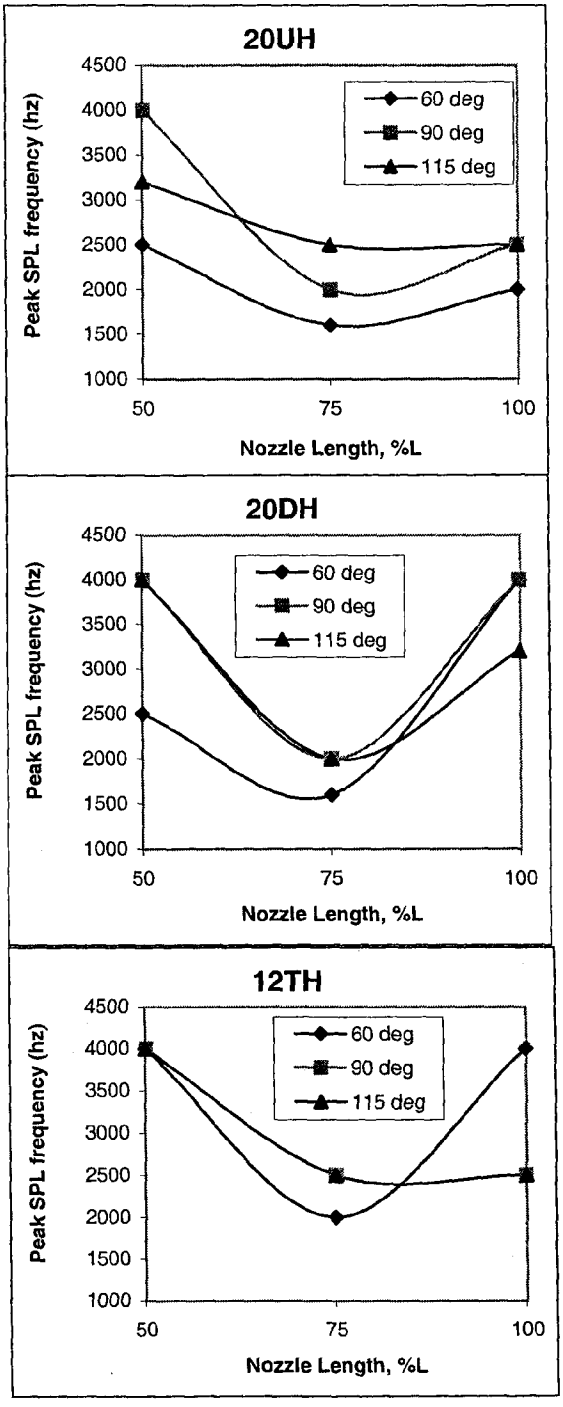

Figure 5.45A Variation of peak SPL frequency with mixing length at TO #3, M(fj) = 0.2.

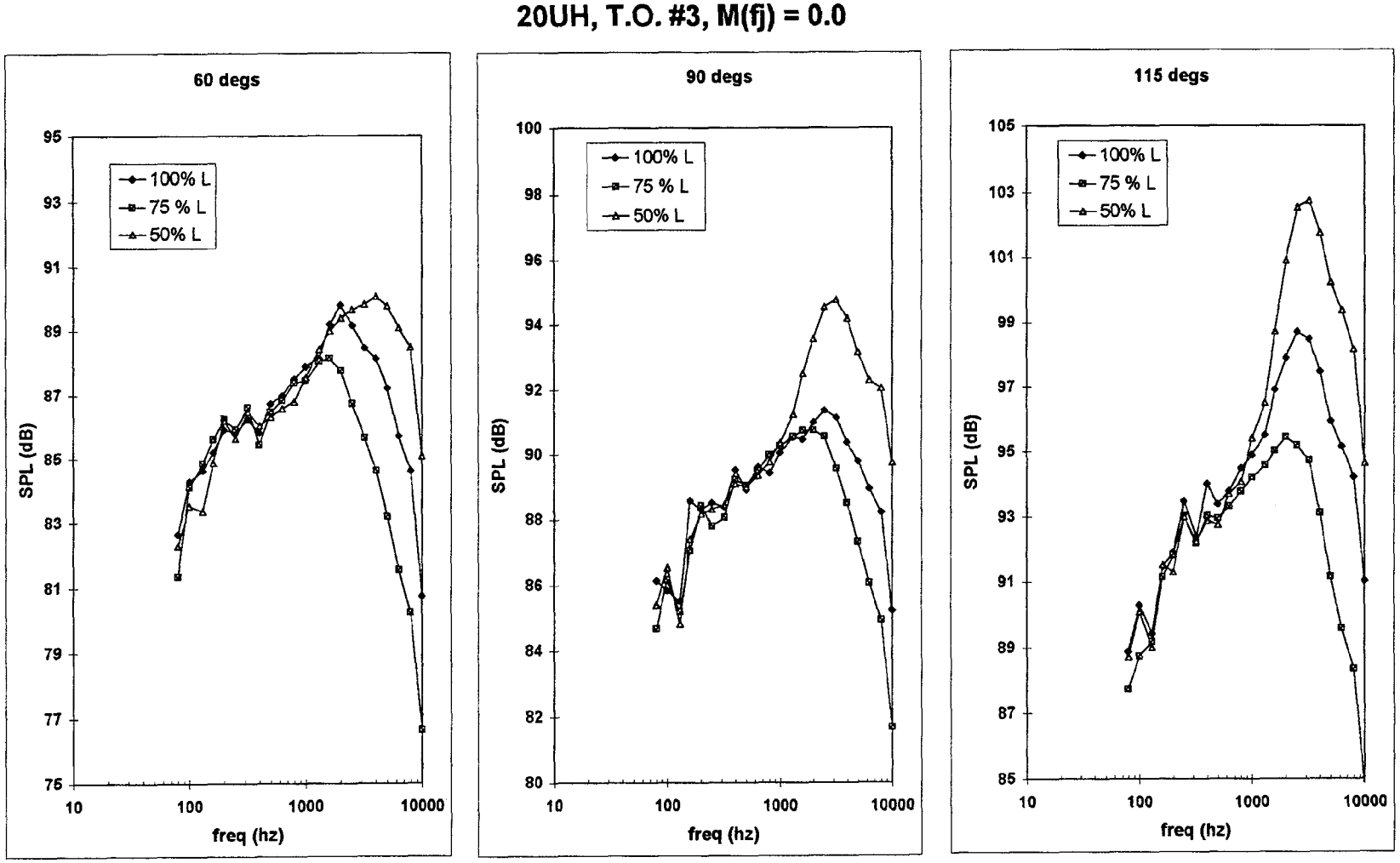

Figure 5.46 Static SPL spectral comparison for different nozzle lengths for 20UH Mixer at different angles.

5.5.3 Competing Mechanisms for Local Minimum of Noise

We have observed from Figures 5.41, 5.43 and 5.45 that all the lobed mixers tested with all three mixing lengths showed a local minimum for noise at some of the operating conditions. A local minimum exists when there are at least two competing mechanisms which are functions of the parameter being varied -- one which increases noise and the other which decreases it. We discuss the probable reasons for this behavior.

It is not difficult to see why noise for configurations with lobed mixers should increase when the mixing length is decreased. As we have shown earlier, these flows are dominated by axial vorticity and the consequent turbulent mixing between fan and core flows inside the nozzle duct. These turbulent vortices comprise the internal noise generator. When the duct length is decreased the sources in the aft portion are acoustically exposed or "acoustically unshielded" as shown in Figure 5.47. For a "shielded" source inside the duct, like A in Figure 5.47, all upstream going rays from it are trapped and only downstream going rays can be radiated outside the nozzle, if their wave-number vector angles do not correspond to total internal reflection angles, as discussed before. For an unshielded source, like B in Figure 5.47, rays over a much larger propagation angle range can reach the far-field. For the example of source B in Figure 5.47, the angle between the limiting rays is greater than 180° and is limited by only total internal reflection angles. Thus, a higher percentage of the total acoustic power of the source is radiated in the far field. Hence, if this source is dominated by mid-to-high range frequencies then there will be an increase in noise in that spectral range in the far-field. With many such sources being "unshielded" a higher percentage of their total acoustic power will be radiated to the far-field. However, the total far-field noise will go up only if the strength of these sources remains the same after reducing the mixing-length. If their strengths can decrease then a competing mechanism which can lead to a local minimum in noise has been identified. Let's explore that possibility.

When the nozzle length is reduced, the mixing length, L, is reduced but the nozzle diameter D is kept the same. This leads to "squeezing" of the flow in a shorter distance which would increase the acceleration in a subsonic flow more than before. But, more importantly, the "pressure release" condition to the ambient pressure applied at the nozzle lip on this squeezed flow now occurs earlier. This "squeeze and early release" mechanism now exposes axial vortex flow structures to the ambient pressure which would have been otherwise in a bounded duct-flow environment, as also explained earlier in Section 4.1.4. What the previous SPL data (§ 5.5.2) suggests is that when this happens the noise source intensity and, hence, the turbulent intensity of these "exposed" axial vortex flow structures can decrease. These same "exposed" weaker axial-vortex flow structures convect downstream, so that now, with reduced mixing length, there are weaker noise sources further downstream at the same axial distance from the mixer-exit plane than when the nozzle length is longer. This we will call as the "aerodynamic unshielding" effect. In order for the total noise to decrease, as observed for the 75%L cases, the weakening of these noise generators must exceed the increase in noise due to the "acoustic unshielding" mechanism discussed earlier by referring to Figure 5.45. We emphasize that this weakening of axial-vortex flow structures is only implied by the SPL data; we do not

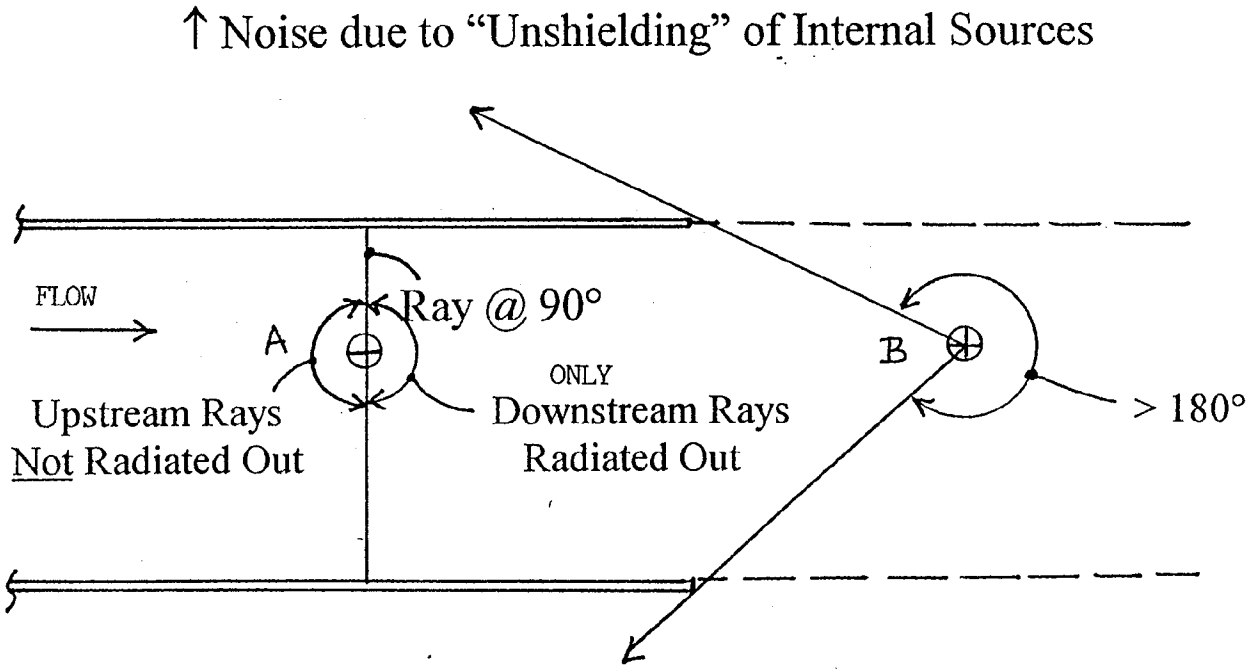

Figure 5.47 Acoustic unshielding of sources outside the nozzle-duct.

have definite plume turbulence intensity data or spectral data to prove this hypothesis.

Recall that for 12CL mixer the jet "mean" flow data in the transverse plane at X/D = 0.2 (ref. 100%L nozzle) and center-line velocity beyond X/D = 4 (see Figures 4.16, 4.17) did not show much change between 100%L and 50%L cases when compared at the same distance from the mixer exit plane. This means that the changes in noise source strengths speculated here must occur upstream of X/D = 0.2 (referred to nozzle exit plane of 100%L), that is, upstream of X/D = 1 when referred to the nozzle exit plane of 50%L. This calls for more scrutiny of the full plume data in future experiments near the nozzle exit plane and also inside the nozzle.

The "optimal" length of the nozzle where the local noise minimum occurs depends on the turbulence intensity governed by the strength of these axial vortex structures which in turn depends on the geometry of the lobed mixer. Hence, for example, the optimal mixing-length may vary for the 20UH and 12CL mixers, which produce streamwise vorticity of different strengths. The optimal nozzle length can also vary according to the operating condition, since this also affects the strength of the axial vortices, as seen in the noise of 20DH with differing nozzle-lengths (Figure 5.38). For lengths less than the optimal length, the initial vortices which are the strongest (as seen from the CFD simulations (see Figures 2.22, 2.25)) are no longer acoustically shielded, allowing the first mechanism to dominate the second quieting mechanism, thus producing an increase in overall noise. How this can produce the observed minimum in peak SPL frequency with changes in nozzle length needs to be scrutinized in the future.

In summary, to explain the existence of a local noise minimum with decreasing nozzle-length in lobed mixers two competing mechanisms are proposed: (i) "acoustic unshielding" of axial-vortex flow structures which increases the far-field radiated noise, and (ii) "aerodynamic unshielding" which decreases the turbulence intensity of the "exposed" axial-vortex flow structures due to earlier pressure release to the ambient conditions which decreases the far-field noise. The second mechanism especially needs to be verified.

5.6 Flyover EPNL

Effective perceived noise level or EPNL is an integral measure of noise observed at a stationary location over a finite time-interval as an aircraft flies by. We obtain EPNL in this section for a constant altitude flyover at 1500 ft flight-profile assuming a non-reflecting ground. EPNL is found from the PNL-data presented in the previous section after correcting it for "tones" and "duration" as is implied in the definition of EPNL[24] . With a single acoustic metric in hand, it becomes easier to compare the acoustic performance of one mixer to another over a range of operating conditions.

We first examine the effect of free-jet Mach number (or flight effect) on EPNL for a given mixer and see if it collapses with any particular choice of the horizontal coordinate in the EPNL plots. Having observed such a collapse with a particular coordinate, we then compare EPNL of one mixer against the other at different operating conditions. This comparison brings out the "relative noise merit" of each mixer and tells us the acoustic "winners" and "losers" amongst the mixers tested at different thrust levels or jet speeds.

5.6.1 Effect of Free-Jet Mach Number

EPNL can be plotted against a number of variables representing the operating condition. For example, the operating condition can be represented by the gross thrust, net thrust (which removes the ram drag), effective mixed velocity, effective mixed Mach number, or some other variable. (Here, effective mixed velocity is defined as the ratio of gross thrust to total mass-flow rate.) There is no agreement in the literature on this and different variables can be suitable for different purposes. For example, it can be argued that the noise from different mixers used in nozzles of the same diameter should be compared at the same thrust level for application to engines. In single stream nozzles of different sizes the jet velocity, which is specific thrust or thrust per unit mass-flow rate, is often used for noise comparison leading to Lighthill's well-known eighth-power law of noise in subsonic jets, for example. Effective mixed jet velocity, on the other hand, may not be the right choice for the horizontal coordinate for two-stream nozzles since at a fixed mixed velocity, different mixers can have different total mass-flow rates which would imply that their thrust would be different. Comparison of noise of two different mixer-nozzle configurations of same size but producing different thrusts does not seem appropriate to us.

5.6.1.1 Effect of Observable Angular Limits on EPNL

In this section, we try several horizontal coordinates and look for a collapse of the EPNL-data when the free-jet Mach number is varied. Before presenting such plots, however, it is important to examine the errors incurred in calculating EPNL from the current data set. As an example of a potential source of error, the limit on observation angles may not allow PNL to reach a full 10 dB below the peak for some of the mixer configurations as required in the definition of EPNL[24].

Figure 5.48 shows a typical plot of PNL versus Receiver Time for all the mixers at operating condition TO #3 and M_{fj} = 0.2 based on the available emission angles of 55° to 165°. The stark contrast in the noise signatures between confluent mixer (CONF) and forced lobe mixers is brought out in this Figure. The confluent mixer (CONF) has a long duration correction because its noise dies out very gradually and it has a relative low peak PNLT. All the lobed mixers show a sharp rise and a sharp fall with, typically, a higher peak PNLT (with the exception of 20DH). EPNL calculations need PNLT data 10 PNdB below the peak PNLT. We see that the data for the CONF mixer, with a peak PNLT of 86.8 PNdB does not reach the 10 dB down points at either end of the "event" (which translates back to upstream- and downstream-angles). The PNLT time history for the confluent mixer is much flatter (lower rate of change) at the later times after the aircraft has passed overhead than in the initial interval before the aircraft arrives at the observer location. As a result, failure to reach the 10 dB down point during the receding portion of the flyover will produce a larger EPNL error than a similar occurrence during the initial interval. On the other hand, since the noise of lobed mixers falls sharply on the downstream side of the peak, sufficient data exists to reach 10 PNdB below peak PNLT. However, we lack some data in the beginning or front quadrant for these lobed mixers; but, since the PNLT rises sharply the error incurred by neglecting data below 55° will be small compared to that for CONF.

An estimate of the "relative" error in EPNL between two mixers due to the neglection of

Figure 5.48 1500' Flyover PNLT vs Receiver Time
T.O. # 3 and M(fj) = 0.2

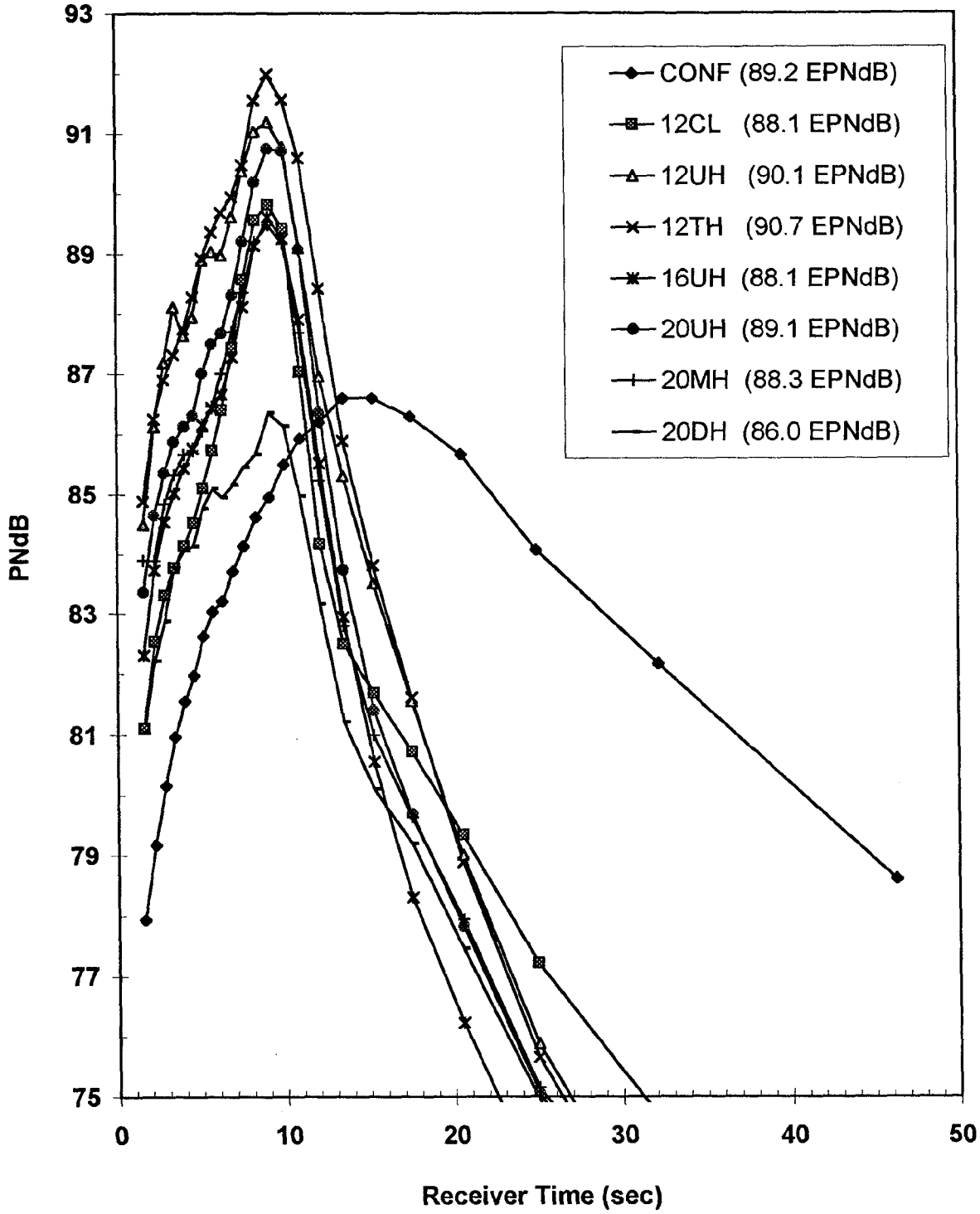

PNLT-data beyond the observed angles can be made as follows. Using the definition of EPNL[24] , we can show that the relative error between two mixers (denoted by subscripts 1 and 2 below) is:

$$\Delta EPNL = 10\log\left[\frac{1+\Delta A_1/A_1}{1+\Delta A_2/A_2}\right]$$

where A = area under $10^{PNLT/10}$ versus receiver time curve for available data, and ΔA = additional area needed to reach 10 PNdB below peak PNLT.

Note that the y-coordinate of the curve under which the area is being found is $10^{PNLT/10}$ and not PNLT itself. Due to the appearance of PNLT in the exponent, the peak PNLT value contributes the most to A and much lower values of PNLT than the peak will have a much smaller effect on A. In any case, if $\Delta A_1/A_1 \cong \Delta A_2/A_2$ then there is no relative EPNL error and ΔEPNL = 0. However, as an example, if $\Delta A_1/A_1 = 5.0\%$ and $\Delta A_2/A_2 = 2.5\%$, then ΔEPNL = 0.1 dB. Due to the flatness of the PNLT curve for CONF in the final stages of the flyover event we expect its EPNL error to be higher than for the lobed mixers. This error analysis shows, however, that the "relative" error in EPNL between two mixers due to lack of acoustic data at extreme angles will be very small indeed.

Next let us consider the error made in one of the possible candidates for the horizontal coordinate, namely thrust, by using unmixed thrust or separate flow thrust versus the actual thrust. All the acoustic data was collected in the NASA APL's NATR but simultaneous thrust measurements were not done because the thrust balance was not working properly. However, accurate individual mass-flow rates for the fan and core flow allow unmixed thrust to be calculated. The gross thrust coefficient C_{tr} , defined as the ratio of actual thrust to the unmixed thrust, gives a good measure of this error. As we saw in the previous chapter (see Table 4.1), for the lobed mixers tested at the static thrust-stand in FluiDyne, the deviation of actual thrust from the unmixed thrust captured in ΔC_{tr} loss = $(1-C_{tr})$ is generally less than 1% at TO conditions. For higher nozzle pressure ratios and hot total temperature ratios the C_{tr} loss decreases to less than 0.5%. Moreover the "relative" error in thrust between two mixers due to the use of unmixed thrust instead of actual thrust is even smaller than this because C_{tr}'s for all mixers are closer to each other than they are to 1.0. This means that using unmixed thrust for EPNL plots instead of actual thrust values will not create significant errors when examining a range of thrusts.

In summary, our error analysis shows that the "relative" error in EPNL due to limits on observable angles is small and the "relative" error in thrusts made by using unmixed thrust values instead of actual values in the EPNL plots is also very small.

5.6.1.2 Collapse of EPNL Plots

We examine the change in EPNL, across a whole range of operating conditions, due to changes in free-jet Mach number by plotting it against four variables:

(i) Normalized Separate Flow Gross Thrust - This is calculated from

$$\left[m_f V_{f\,ideal} + m_c V_{c\,ideal}\right] P_{ref}/P_{amb}$$

where m_f, m_c are the observed mass-flow rates for the fan and core passages at test-day ambient pressure, P_{amb}; velocities $V_{f\ ideal}$, $V_{c\ ideal}$ are

calculated for fan and core streams when each expands isentropically/ ideally and separately (unmixed) to the ambient pressure from the known total pressure and total temperature. The last factor is used to "normalize" the thrust to remove day to day variation in P_{amb} (this formula can be easily proved from the definition of the thrust coefficient, C_{tr}, which itself does not vary with P_{amb}).

(ii) Normalized Separate Flow Net Thrust - This is defined as:

Normalized Separate Flow Gross Thrust - $(m_f + m_c) V_{fj} [P_{ref}/P_{amb}]$

where V_{fj} = free-jet speed. That is, for net thrust calculations we remove the "ram drag" from the gross thrust.

(iii) Effective Mixed Velocity, V_{mix}, defined as the ratio of separate flow gross thrust to the observed total mass flow rate. This is the same as the mass-averaged separate flow velocity:

$$V_{mix} = \frac{m_f}{m_f + m_c} V_{fideal} + \frac{m_c}{m_f + m_c} V_{cideal}$$

(iv) V_{mix}/c_{amb}, a non-dimensional variable to remove day-to-day ambient temperature effects.

Figures 5.49, 5.50 and 5.51 display EPNL as a function of the above four variables across the whole range of operating conditions (including approach and all take-offs) with M_{fj} = 0.2 and 0.3 for, respectively, mixers 12CL, 12UH and 12TH with the baseline nozzle length. Only when EPNL is displayed as a function of net thrust, the variation with free jet Mach number collapses into a single curve. This behavior is not observed when any of the other parameters are selected as the independent variable. This is a significant new discovery. It is expedient to examine this behavior for all other mixers.

Figures 5.52(a) and (b) shows the EPNL versus net thrust plots for all the mixers studied with the baseline nozzle and M_{fj} = 0.2 and 0.3. Excellent collapse is observed for 12UH, 12TH, 16UH, 20UH and 20MH. However, the collapse does not appear as good for 20DH and at the low thrust conditions for 12CL. In addition, the EPNL curves for the CONF mixer are close to each other for the two free-jet Mach numbers but the collapse is not nearly as good as for the lobed mixers.

A couple of remarks are in order here:

(i) In constructing the previous plots, EPNL is assumed to vary smoothly and uniquely with net thrust. This implies that interpolation between calculated points is acceptable. However, the operating condition which will produce the required thrust at some intermediate interpolated point is not well defined. That is to say, although the thrust is known, the operating condition which will produce this thrust is not unique. One way to minimize this problem is to obtain noise data at closely spaced points on the operating line of the engine/nozzle.

(ii) The normalized separate flow net thrust can be further "non-dimensionalized" by $(m_f+m_c)c_{amb}$ which essentially gives the "relative" mixed Mach number defined as

$$M_{mix\ relative} = (V_{mix} - V_{fj})/c_{amb}$$

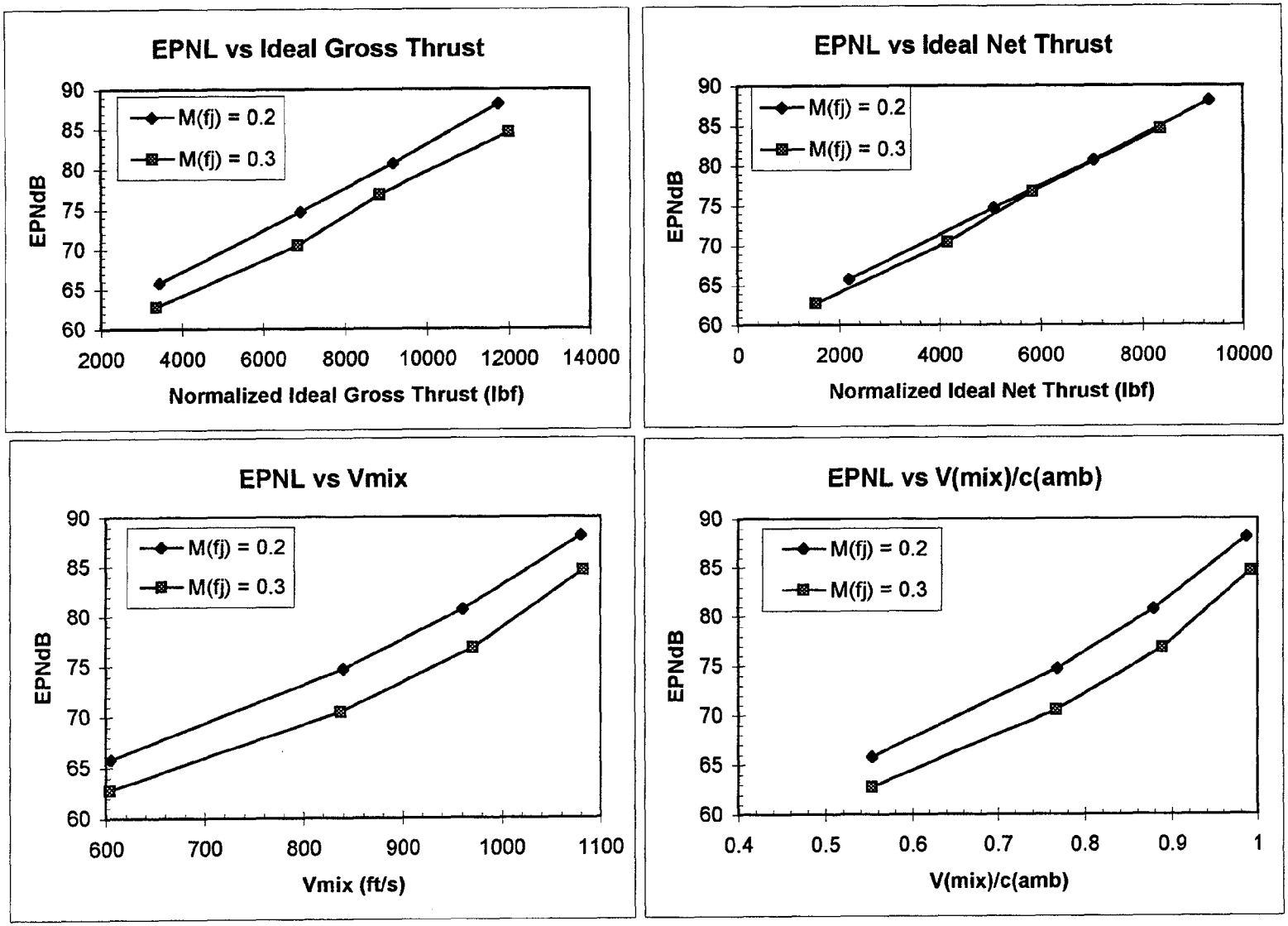

Figure 5.49 Collapse of flyover EPNL with ideal net thrust for the effect of free-jet Mach number for 12CL.

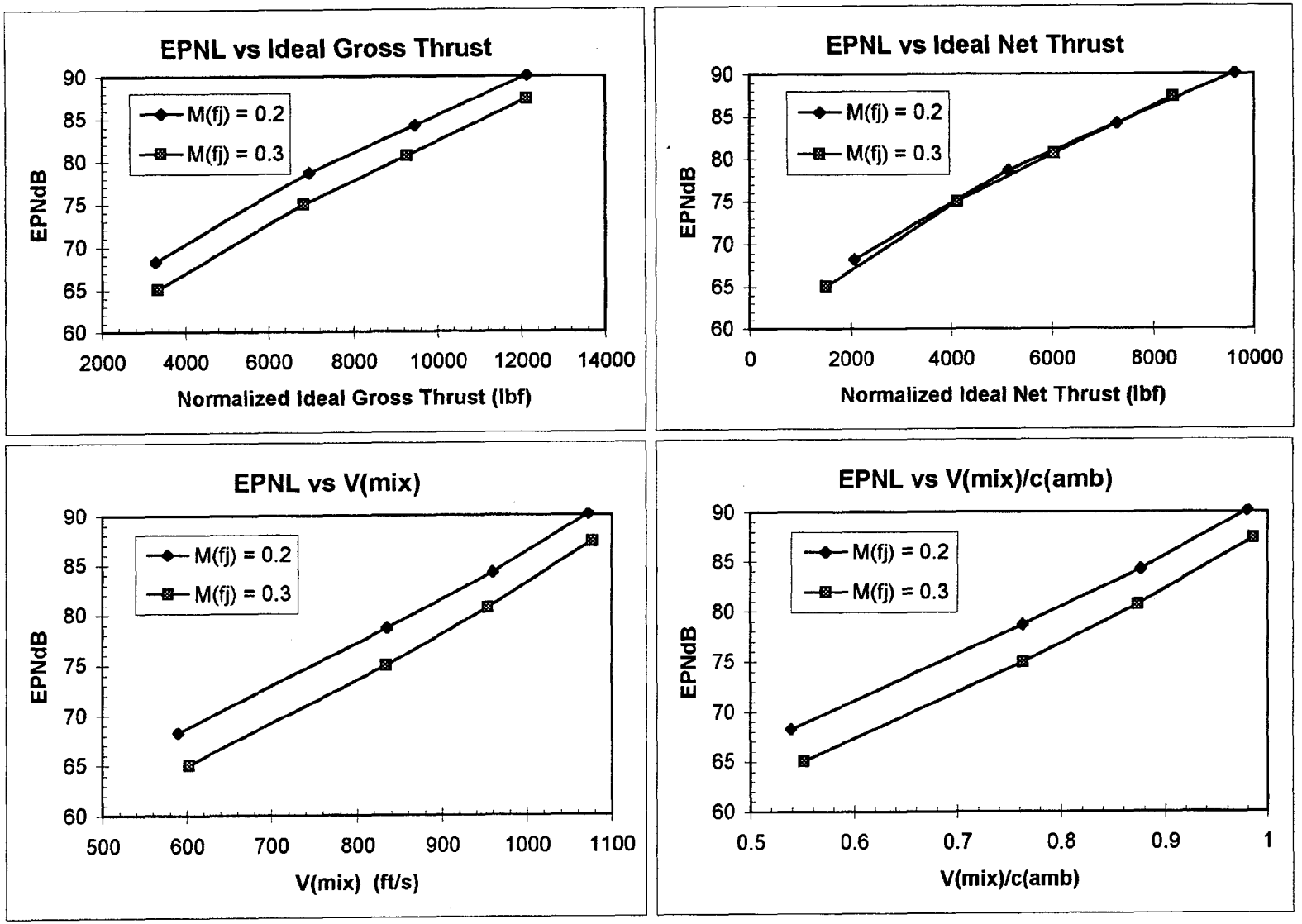

Figure 5.50 Collapse of flyover EPNL with Ideal Net Thrust for the effect of free-jet Mach number for 12UH.

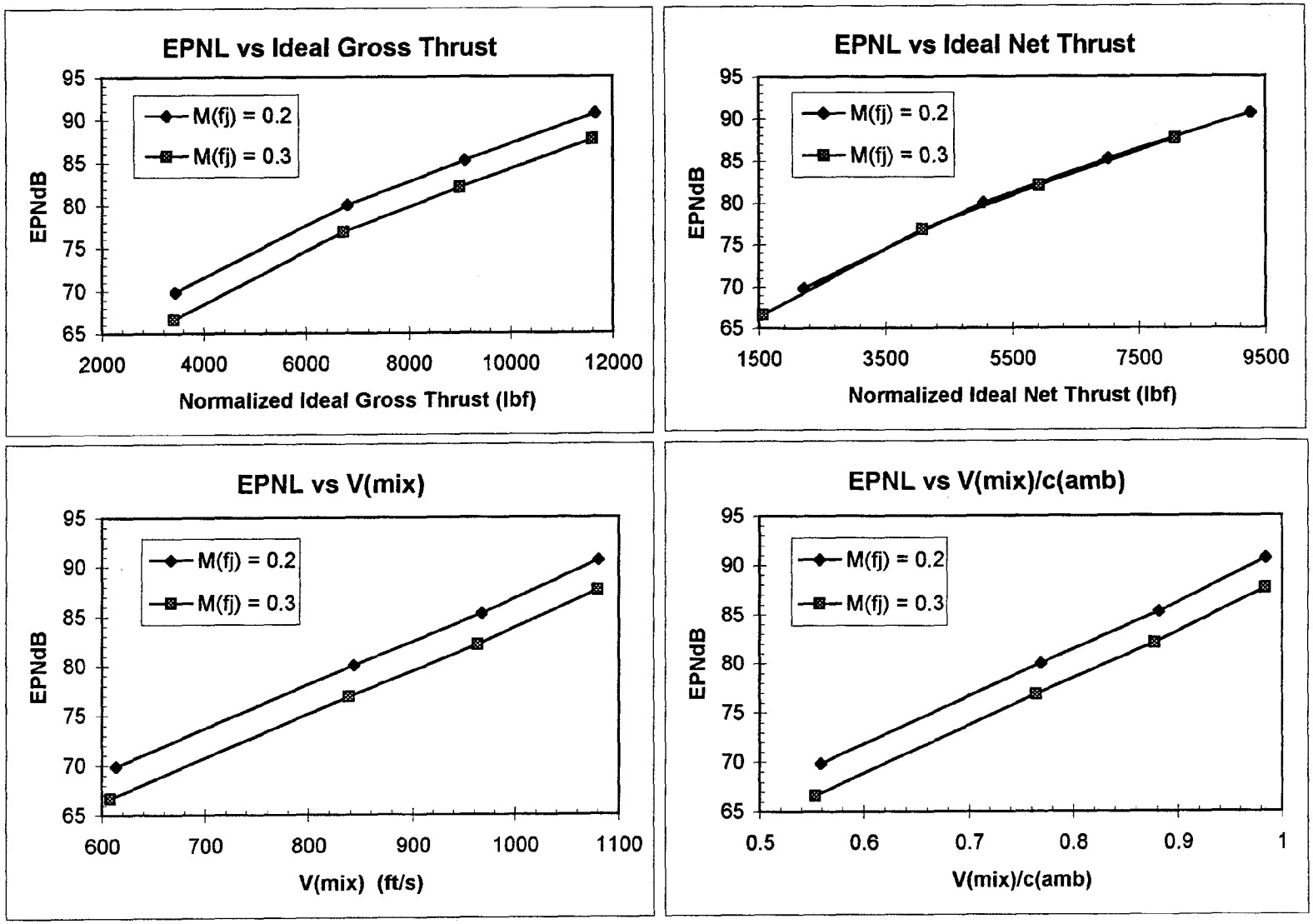

Figure 5.51 Collapse of flyover EPNL with Ideal Net Thrust for the effect of free-jet Mach number for 12TH.

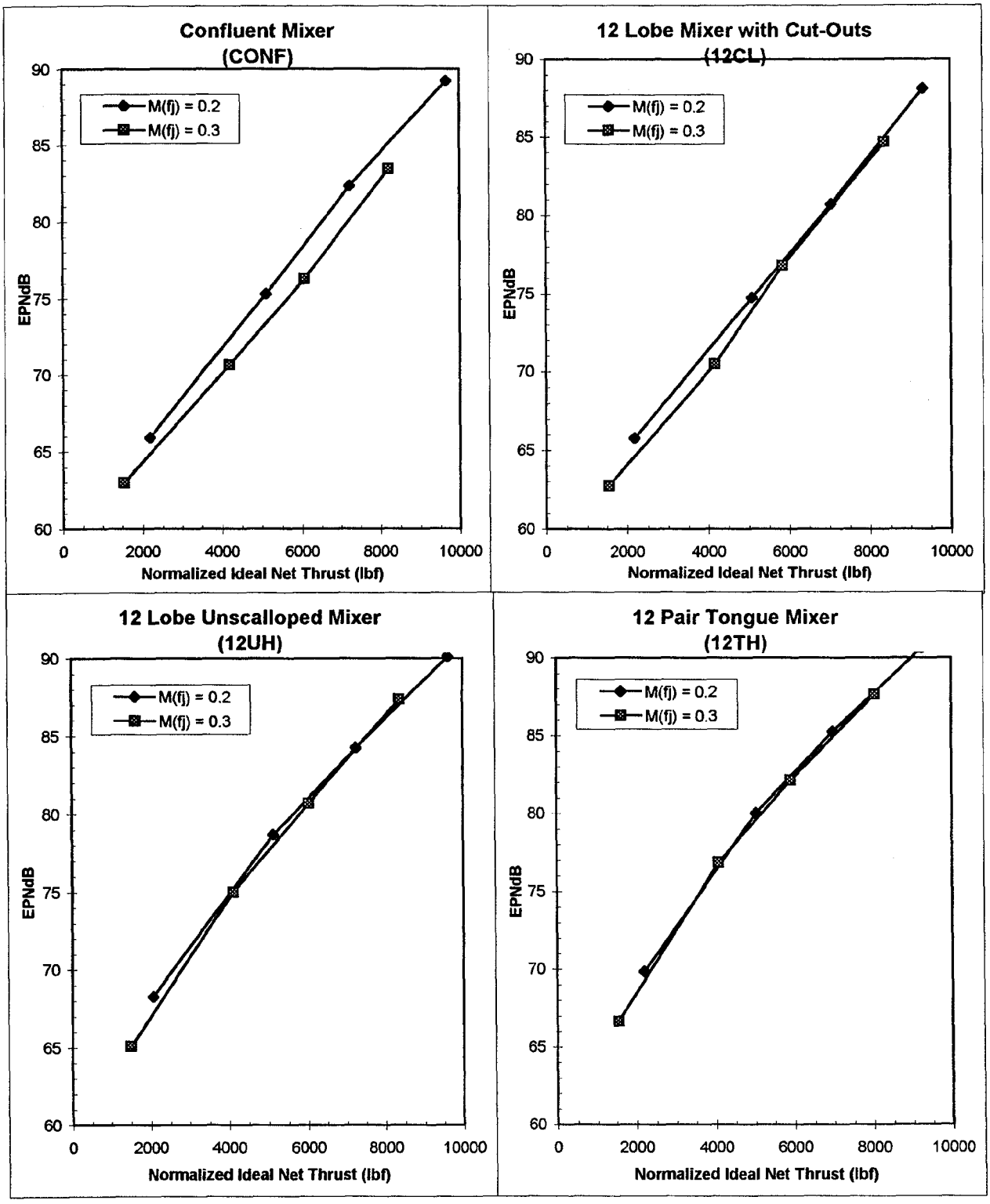

Figure 5.52(a) Collapse of EPNL vs Normalized Net Ideal Thrust data with free-jet Mach numbers.

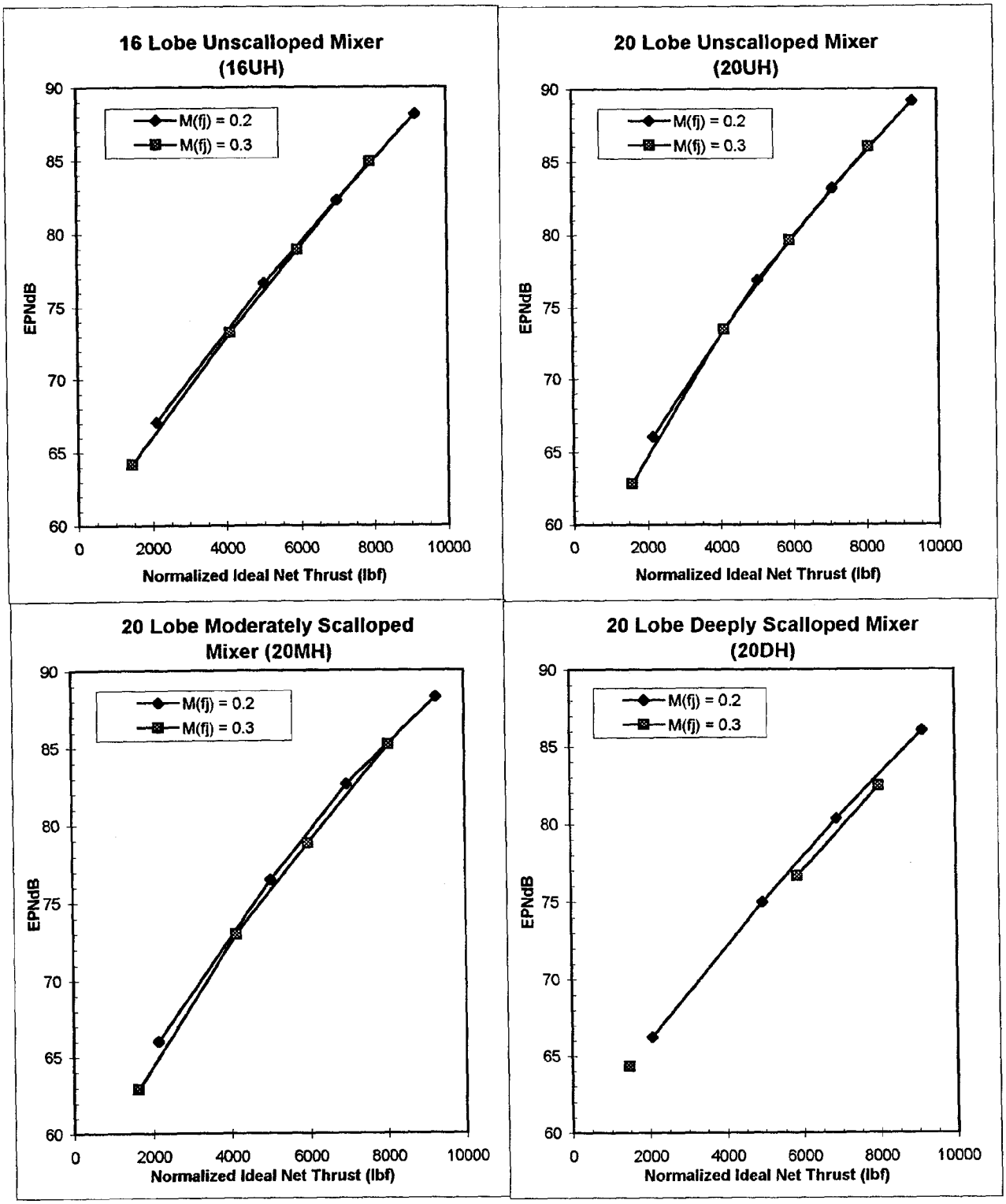

Figure 5.52(b) Collapse of EPNL vs Normalized Net Ideal Thrust data with free-jet Mach numbers.

The EPNL variation with free jet Mach numbers can also be expected to collapse with this $M_{mix\ relative}$ similar to the collapse of EPNL versus net thrust plots. However, for nozzles of same size the comparison between mixers for their noise merit should still be done on equal net thrust basis rather than the relative mixed Mach number.

The collapse of EPNL with net thrust for varying free-jet speeds can be used to advantage. Let us assume that EPNL has been obtained at various operating conditions with known total mass-flow rates, and one free-jet speed, V_{fj}. Then we can find the EPNL at a slightly different free-jet speed $V_{fj} + \Delta V_{fj}$, at the same operating conditions as before, as shown in Figure 5.53 due to the invariance of the EPNL with net thrust. The scaling of EPNL with net thrust implies we only need to know the net thrust at the new free-jet speed and the same operating condition. Since the free-jet speed does not significantly alter the total mass-flow rate at a given operating condition (see Figure 4.5 for BPR, for example), the difference in net thrust at the reference V_{fj} condition and at the new free-jet speed, $V_{new} = V_{fj} + \Delta V_{fj}$, is approximately [$m_{total}\Delta V_{fj}$]. Since we are using pressure normalized quantities on the net thrust axis, we assume that a factor of (P_{ref}/P_{amb}) is absorbed while calculating m_{total} above from the known total mass-flow rate at V_{fj} and P_{amb}. Once the net thrust has been calculated at the new free-jet speed then the corresponding EPNL can be quickly read off the EPNL-axis as shown in Figure 5.53. If $\Delta V_{fj} = V_{new} - V_{ref}$ is positive then the new net thrust is less than the reference free-jet case and we move to the left of the reference thrust; if $\Delta V_{fj} > 0$ then we move to the right. This shows that, at least, for those mixers for which collapse has been observed we do not need acoustic data at multiple free-jet speeds; only one free-jet speed will suffice; noise at the other free-jet speeds can be deduced. This will reduce the test-matrix considerably for these mixers, as well as for other similar mixers which are expected to have same behavior.

As an example of application of this method consider the case of 20UH mixer with known results of 1500 ft flyover EPNL versus net thrust for $M_{fj} = 0.2$ (see Figure 5.52(b) for 20UH). At the four operating conditions (see Table 3.1) for which noise data has been collected the total mass-flow rates at $M_{fj} = 0.2$ are also known. Now let us say we want to find the 1500 ft flyover EPNL at a different free-jet Mach number at TO #3 only by using this curve for $M_{fj} = 0.2$. First to verify this method let us find the EPNL at $M_{fj} = 0.3$ for which the actual EPNL is known and then we find it for $M_{fj} = 0.25$ for which there is no data.

At TO #3, $M_{fj} = 0.2$ we have $T_{amb} = 495.2$ °R, $P_{amb} = 14.48$ psia and $m_{total} = 21.69$ lb/s from the scaled nozzle data. This corresponds to $V_{fj} = 218.1$ ft/s and normalized unmixed net thrust of 9192 lb. Hence, at TO #3 but $M_{fj} = 0.3$, we get $V_{fj} = 327.2$ ft/s at same $T_{amb} = 495.2$ °R and the normalized net thrust difference from that at $M_{fj} = 0.2$ at full scale (scale factor of 4) as $m_{total}*\Delta V_{fj}(P_{ref}/P_{amb})=(4*21.69/32.2)*(327.2 - 218.1)*(14.7/14.48) = 1193.7$ lb. This means a normalized net thrust of (9192 – 1194) = 7998 lb at $M_{fj} = 0.3$ and TO #3. Reading the EPNL for this net thrust from the EPNL plot in Figure 5.52(b), we get 86 EPNdB approximately. The actual data for TO #3 at $M_{fj} = 0.3$ gives EPNL of 86.02 EPNdB. Thus the method gives fairly accurate results.

Now let us find EPNL at $M_{fj} = 0.25$ for the same TO #3 condition. Going through the same process as above, we get for $M_{fj}= 0.25$: normalized net thrust difference = 597 lb for

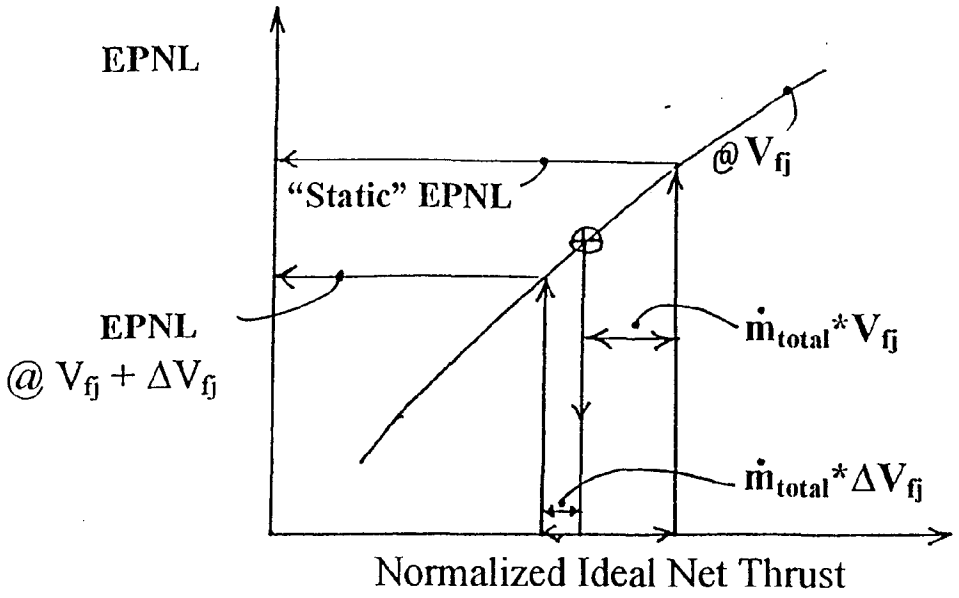

Figure 5.53 Use of collapsed EPNL plots.

which net thrust = 8595 lb and EPNL is read off as 87.5 EPNdB. This process of reading off from the EPNL versus net thrust curve for a given net thrust can be automated by using a curve-fit for the EPNL versus net thrust plot at the reference free-jet Mach number rather than the graphical method used here for demonstration purposes.

Another concept that we introduce here due to this scaling of EPNL with net thrust is the idea of an equivalent "static" EPNL, as also shown on Figure 5.53. This is simply the value obtained from the EPNL versus net thrust curve using gross thrust value at that operating condition as opposed to net thrust. The corresponding "static" EPNL is then read off from the y-axis on this curve. Note that calculation of EPNL always needs a non-zero aircraft speed or non-zero free-jet speed - that is, the aircraft needs to move relative to the observer for PNLT to fall by 10 PNdB, leading to a finite EPNL number. If the aircraft did not move the usual definition of EPNL will, of course, lead to an infinite value of EPNL. So this new concept of "static EPNL" is, at best, an artifice and is to be considered as some sort of datum for a given operating condition for examining the flight effect and no more. It would be difficult to give any physical interpretation for EPNL values corresponding to net thrust greater than the gross thrust. This also implies that such EPNL inferences by using this extrapolation method must be limited to some small finite interval of free-jet Mach numbers around the reference M_{fj}.

5.6.2 Effect of Nozzle-Length

Figures 5.54 to 5.58A show the effect of nozzle length on EPNL for free-jet Mach

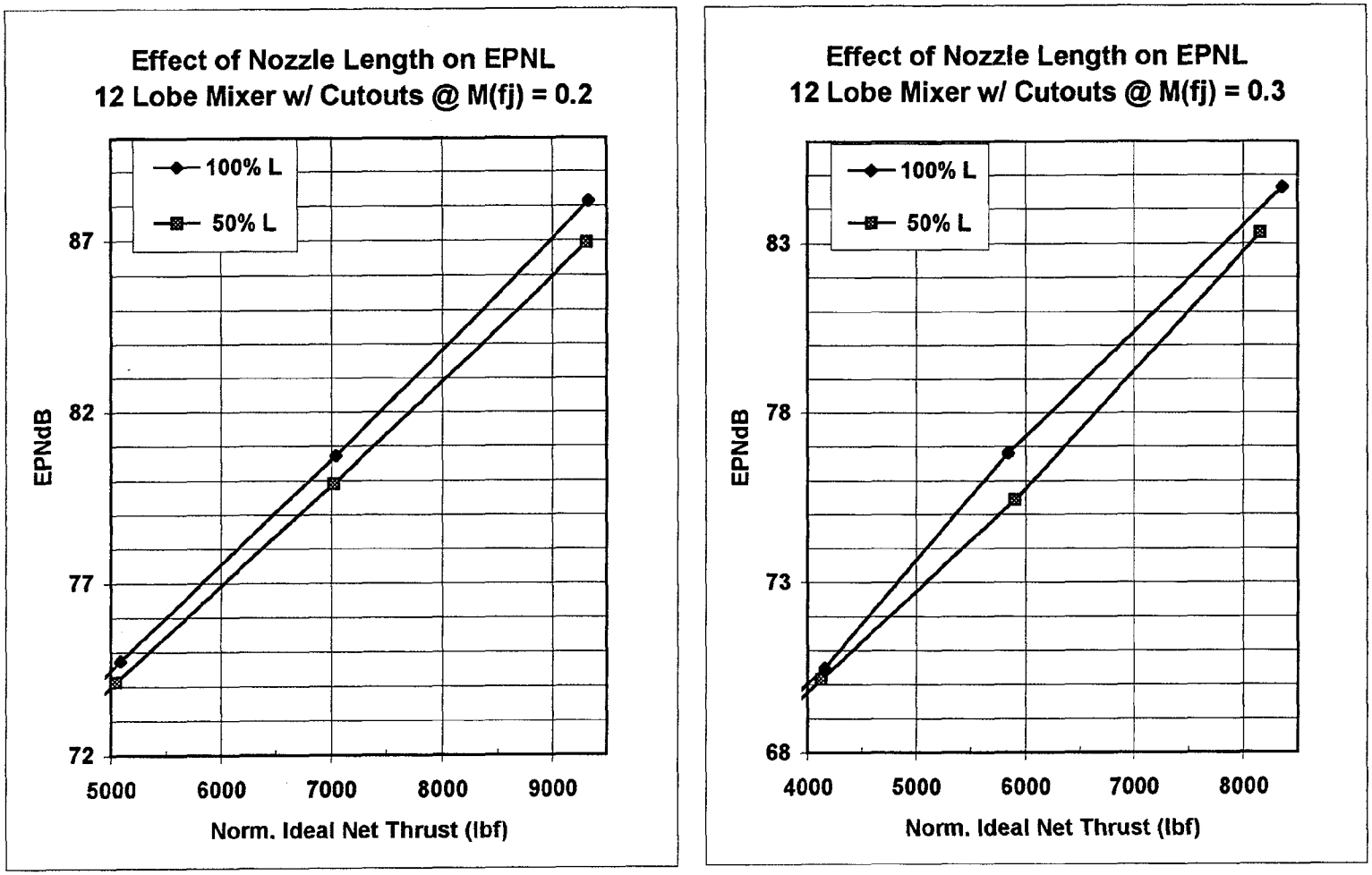

Figure 5.54 Effect of nozzle-length on flyover EPNL for 12CL at M(fj) = 0.2 and 0.3.

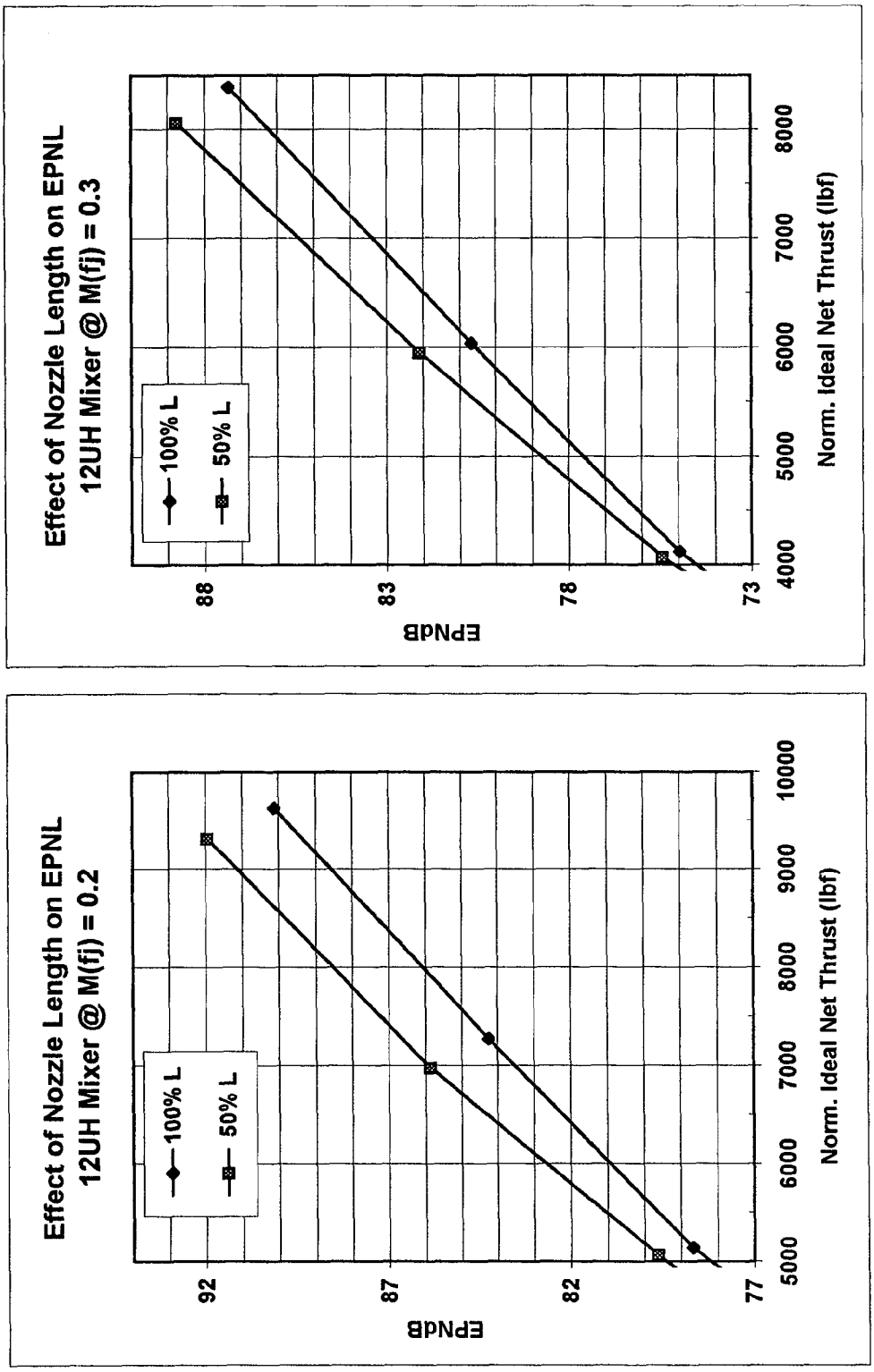

Figure 5.55 Effect of nozzle-length on flyover EPNL for 12UH at M(fj) = 0.2 and 0.3.

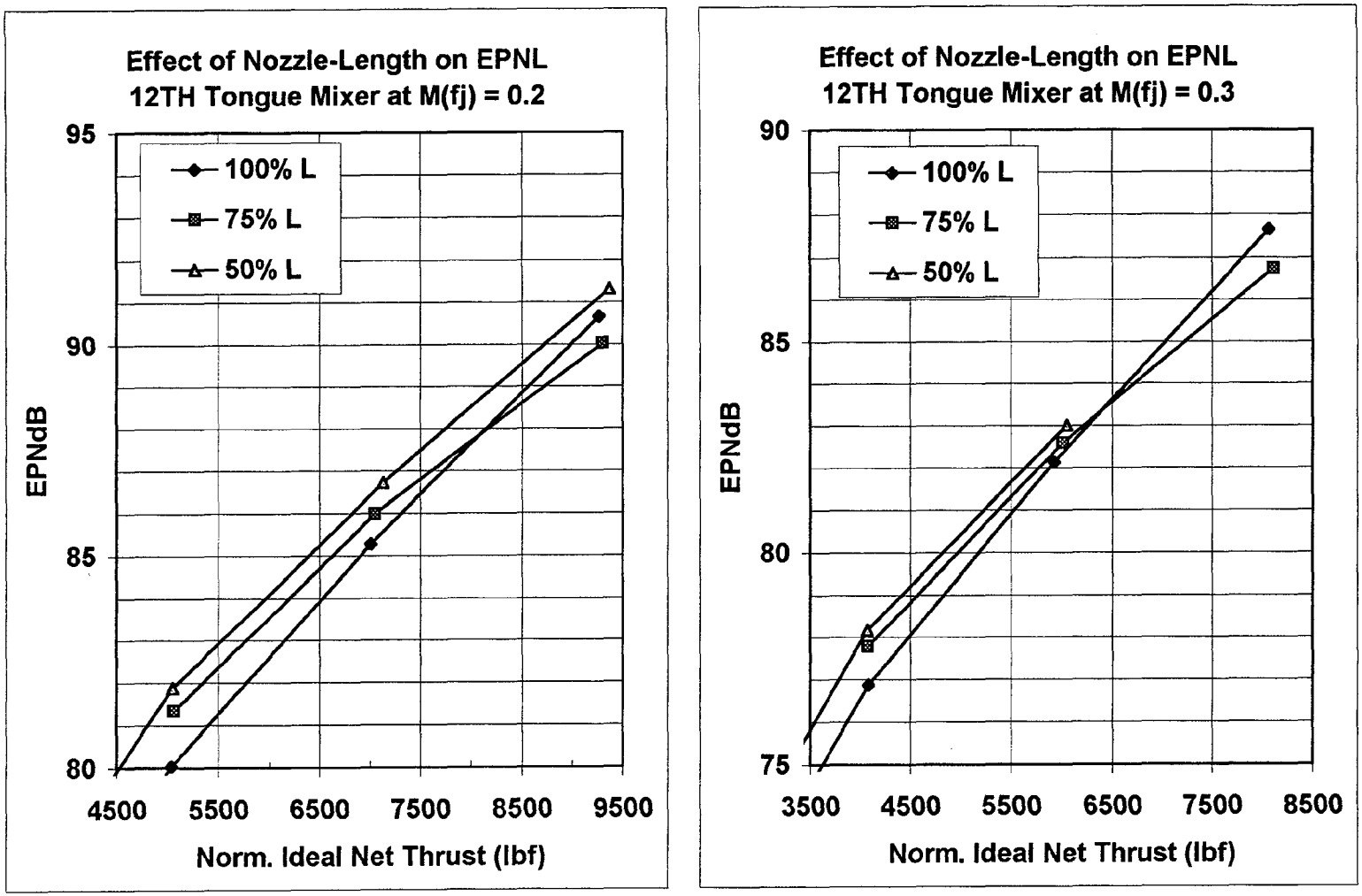

Figure 5.56 Effect of nozzle-length on flyover EPNL for 12TH at M(fj) = 0.2 and 0.3.

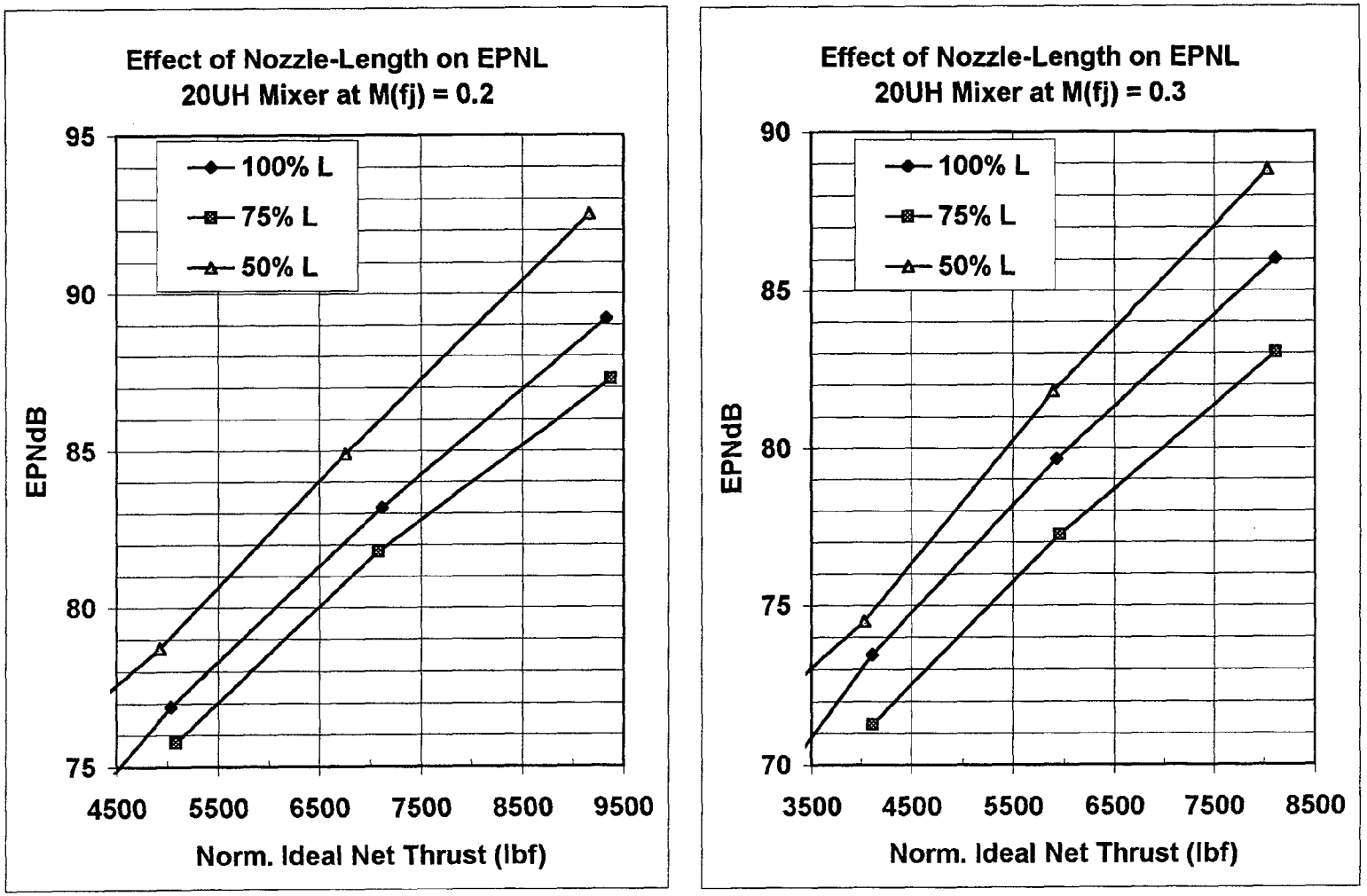

Figure 5.57 Effect of nozzle-length on flyover EPNL for 20UH at M(fj) = 0.2 and 0.3.

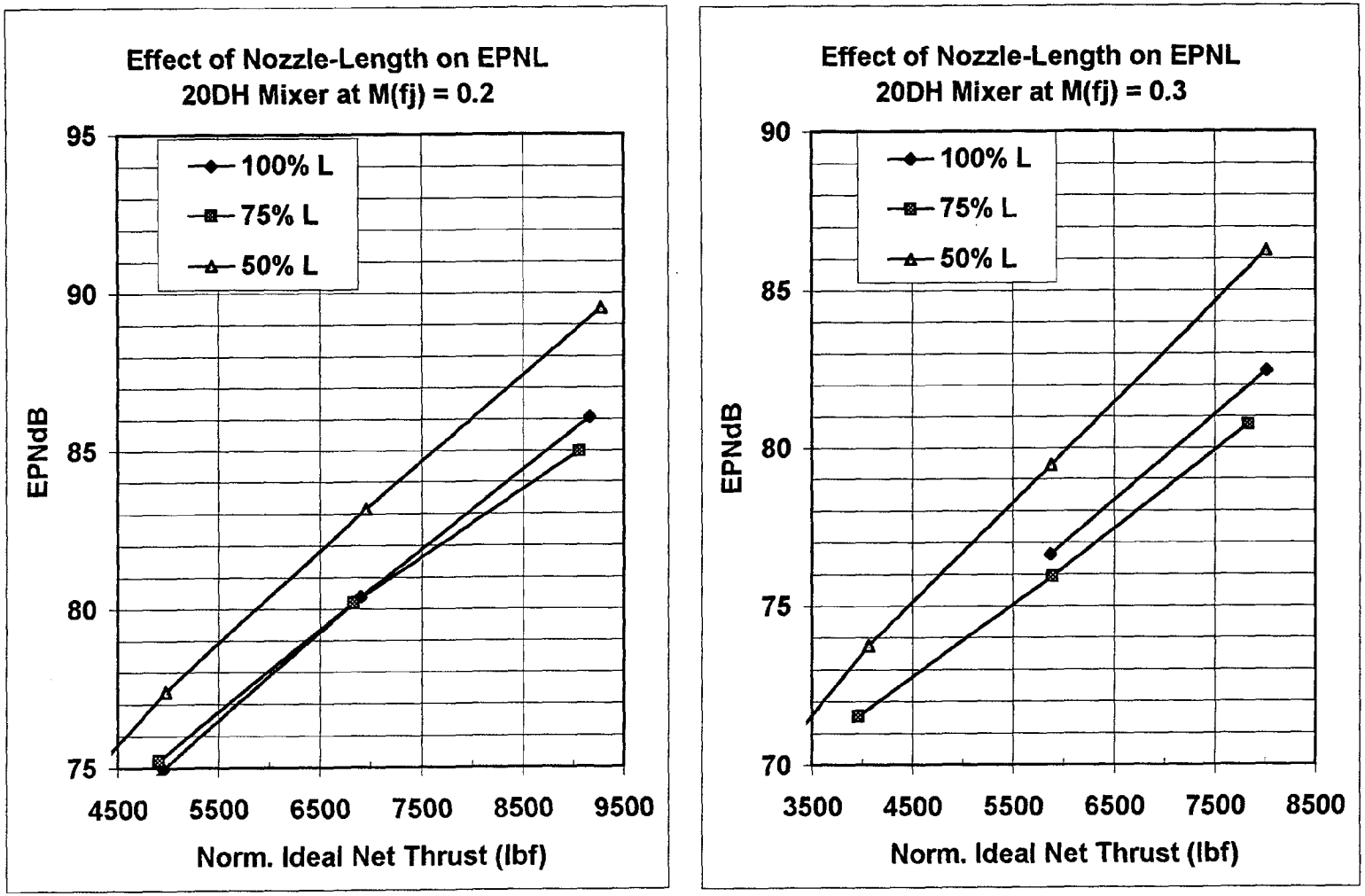

Figure 5.58 Effect of nozzle-length on flyover EPNL for 20DH at M(fj) = 0.2 and 0.3.

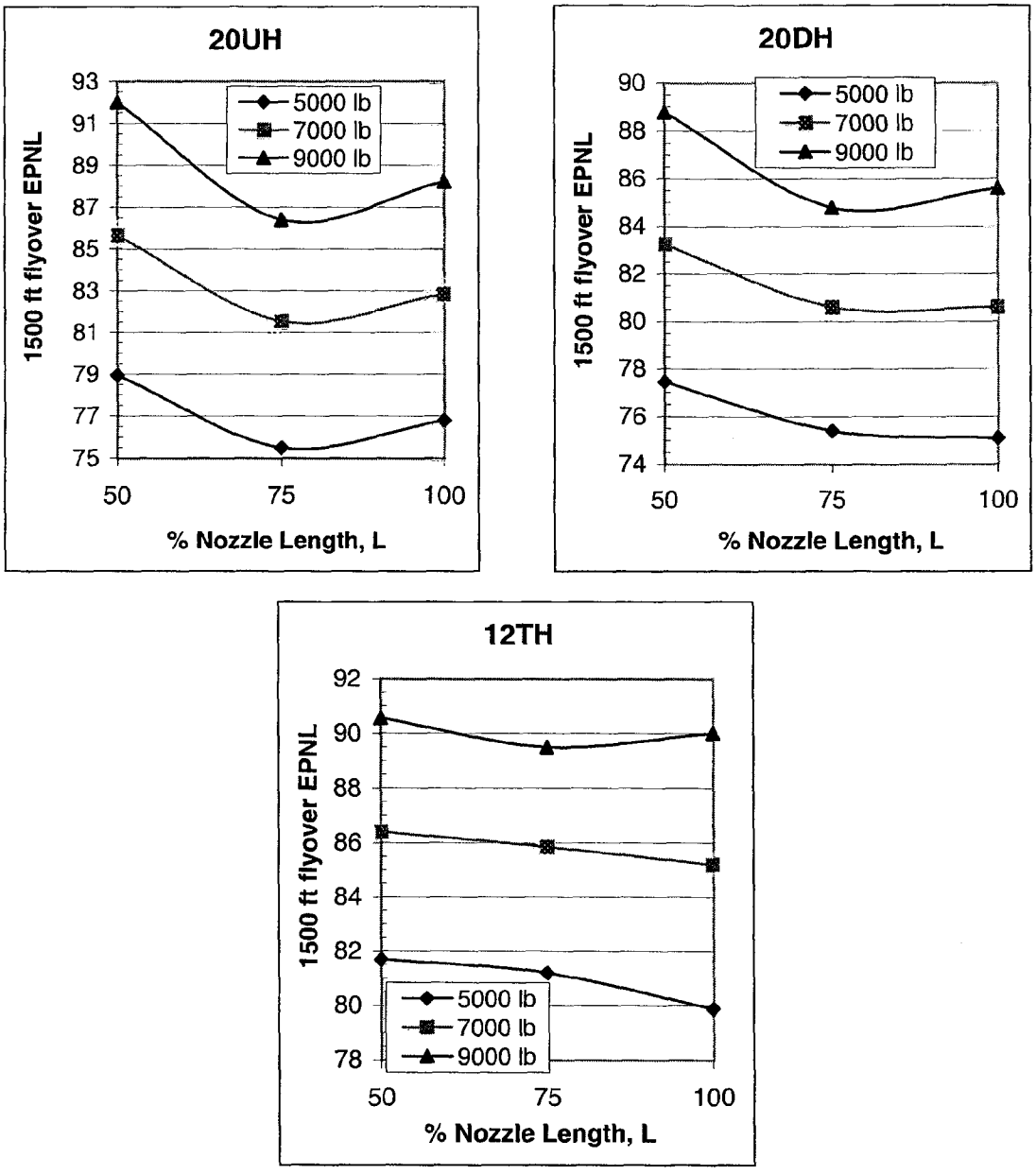

Figure 5.58A. Flyover EPNL vs nozzle length at various net thrust levels (shown in legend) for 20UH, 20DH and 12Th mixers at M(fj) = 0.2.

numbers of M_{fj} = 0.2 and 0.3 for mixer configurations 12CL, 12UH, 12TH, 20UH and 20DH for the three TO conditions.

- For configuration 12CL a noise benefit of more than 1 EPNdB is observed at the highest thrust conditions and M_{fj} = 0.2 by reducing the mixing-length by half (Figure 5.54); at M_{fj} = 0.3 a benefit of more than 1.5 EPNdB is obtained at mid-thrust conditions by reducing the mixing-length in half.
- 12UH (Figure 5.55), on the other hand, becomes considerably noisier when its mixing-length is reduced by half for both M_{fj} = 0.2 and 0.3.
- For the tongue mixer, 12TH, reducing the mixing length from 100% to 75% produces little less than 1 EPNdB noise reduction (see Figures 5.56 and 5.58A) at the highest thrust conditions for free-jet Mach numbers of M_{fj} = 0.2 and 0.3. At the lower thrust conditions reducing the nozzle length from the baseline (100%) length produced a noise increase for all free-jet conditions. Since the observed differences in EPNL are significantly larger than the error associated with the EPNL calculation method, the trends are deemed to be real.
- The data of Figures 5.57 and 5.58A for configuration 20UH clearly captures a local minimum in noise with a change in the mixing length at all thrust conditions and both M_{fj} = 0.2 and 0.3. This was, of course, suspected from the PNL-directivities and SPL-spectra discussed earlier where the competing mechanisms which create this phenomenon were provided. Note, for example, that 20UH benefits anywhere from 1 to 2 EPNdB by reducing its mixing-length by 25% from the baseline length at M_{fj} = 0.2. At the higher M_{fj} = 0.3, the benefit is even higher - about 2.2 to 3 EPNdB. This is a significant reduction in noise and it is obtained by a reduction in nozzle-length. Due to the excellent static cruise thrust performance of the unscalloped, high-penetration mixer 20UH (see Figure 4.2(b)) this is a phenomenon worthy of attention and future scrutiny.
- Figures 5.58 and 5.58A for mixer configuration 20DH again clearly illustrate the existence of a local noise minimum with decreasing mixing-length, especially at the higher thrust end. At M_{fj} = 0.2 the decrease in noise is as much as 1 EPNdB and at M_{fj} = 0.3 it is as much as 1.2 EPNdB when the mixing-length is decreased by 25% from the baseline length.

5.6.3 Comparison of EPNL Between Mixers

To sort out the effect of individual lobe mixer geometric parameters, the EPNL net thrust variation is displayed for each group of mixers, with the confluent configuration, CONF, as the baseline. It is important to recall that although the comparison is made on an equal net thrust basis, some of the mixers have very different area ratios (see Tables 2.1, 2.2). As a result, there is a significant bypass ratio variation between the various mixers, even at constant net thrusts as mentioned earlier (see Figures 4.6 and 4.7).

Figure 5.59 shows the EPNL plot for the 12-lobed mixers at M_{fj} = 0.2 and two different nozzle-lengths, 100% and 50%. As expected from the PNL-directivity curves discussed earlier, the 12CL mixer is the quietest, with 12UH second and 12TH being the noisiest . Only slight relief is obtained for the tongue mixer with the 50% L nozzle at the highest thrust condition as compared to 12UH. However, for both nozzle-lengths 12CL is the only configuration quieter than the baseline CONF mixer; but even that

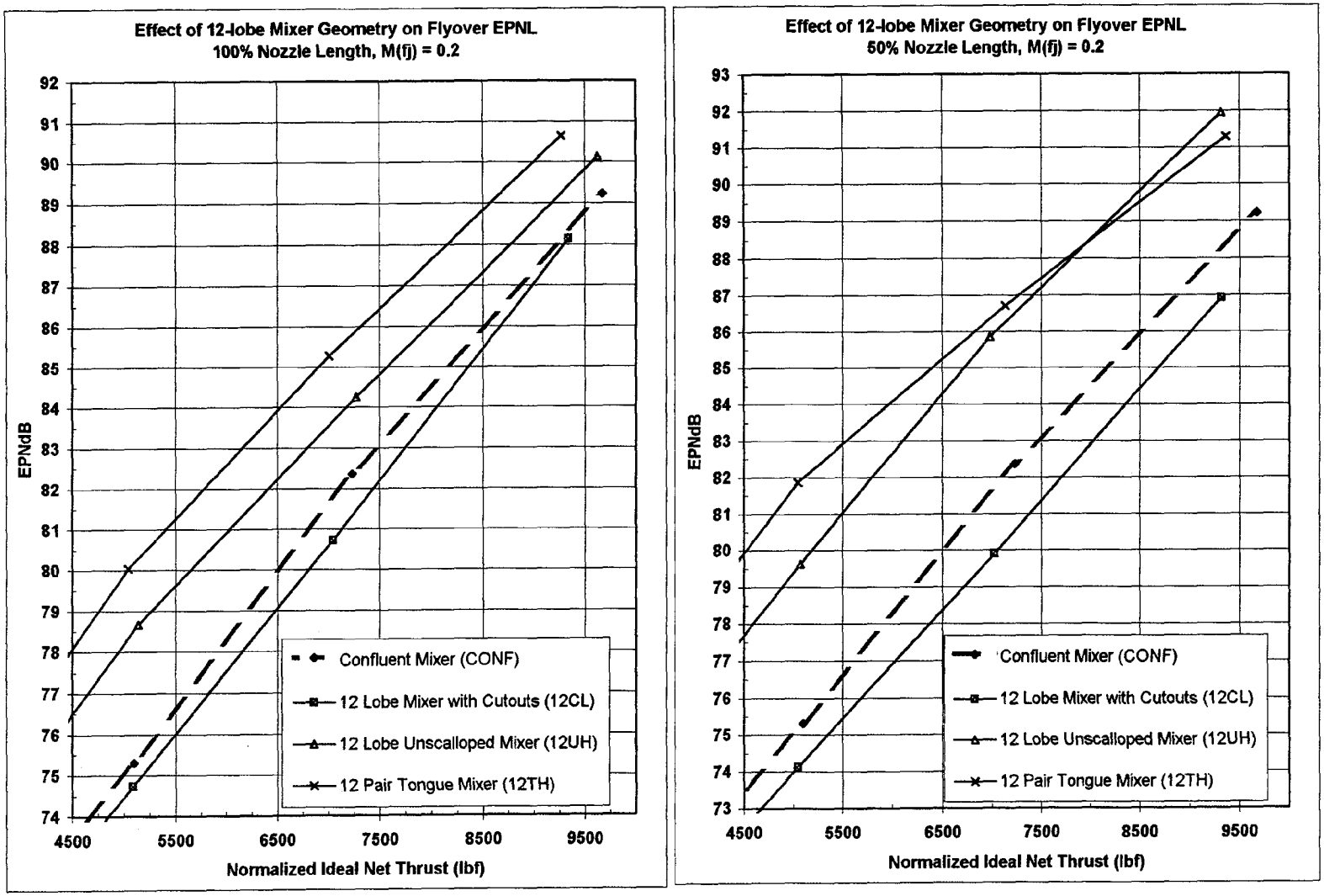

Figure 5.59 Effect of 12-lobe mixer geometry on flyover EPNL at M(fj) = 0.2 and two different nozzle-lengths.

effect appears to die out at high thrusts for 100% L. The maximum benefit of 12CL compared to CONF is about 1.8 EPNdB at TO #2 (at about 7000 lb net thrust) with the short (50%) nozzle. It is important to compare 12UH and 12CL on an equal net thrust basis because of certain advantages of no-scalloping in 12UH: With the 100%L nozzle-length 12CL is nearly 3.75 EPNdB quieter than 12UH near the reference TO #1 condition which corresponds to 5000 lb net thrust. This difference jumps to 5.4 EPNdB when the comparison is made with the 50% nozzle-length at the same net thrust. The noise benefit of 12CL compared to 12UH decreases slightly as net thrust increases for the baseline 100% nozzle-length. With a higher cruise thrust coefficient for a "cleaner" version of 12CL than 12UH (see table 4.1) and such excellent noise suppression, the 12-lobed low penetration mixer with cutouts (12CL) is clearly superior to the high-penetration unscalloped mixer (12UH).

Figure 5.60 shows the effect of number of lobes for the second group of mixers (12UH, 16UH, 20UH). Comparing 12UH versus 20UH, the mixer with the higher number of lobes (20UH) is quieter than 12UH at 100% nozzle-length but the noise benefit decreases considerably as the thrust increases. It is significant to note that 20UH has a slightly higher cruise thrust coefficient than 12UH and it is also quieter at the baseline TO #1 condition by 1.2 EPNdB. However, it is equally significant to note that none of these lobed mixers, all of them "unscalloped," were quieter than CONF mixer either at 100%L or 50%L. Even 16UH, with its very high bypass ratio is noisier than CONF at all thrusts. Their unscalloped lobes with high penetration are the controlling negative factors from the viewpoint of noise suppression.

Figure 5.61 shows the effect of scalloping on EPNL by comparing mixer configurations 20UH, 20MH and 20DH. At 100% nozzle-length, deep scalloping produces a benefit that ranges from about 1.7 EPNdB at low thrust (5000 lb) to 2.8 EPNdB at high thrust (9200 lb) compared to the unscalloped mixer. However, the considerable loss in cruise thrust coefficient due to deep scalloping (20DH versus 20UH) of about 0.38% (see Table 4.1) should also be kept in mind for applications to engines.

Figure 5.61A shows that compared to CONF the noise benefit of the deeply scalloped mixer (20DH) with 100% nozzle-length increases with thrust, ranging from negligible improvement at TO #1 to about 1.8 EPNdB at 9000 lb net thrust. At 100% L the benefit of "moderate" scalloping (20MH) over unscalloped mixer is also negligible at low thrusts and improves to only about 0.8 EPNdB at the highest thrust. From Figure 5.61A we observe that with half the nozzle length (50%L) none of the 20-lobed mixers are quieter than CONF, but moderate scalloping is quieter than both deeply scalloped and unscalloped mixers at all thrust levels. This shows that there is an "optimal depth of scalloping" for shorter nozzles. But for longer nozzles the noise benefits of scalloping appear monotonic.

Also note from Figure 5.61A that the unscalloped mixer, 20UH, is quieter than CONF by approximately 1 EPNdB only with 75% L at the highest thrust level (9000 lb); otherwise with either the shortest or the longest nozzle 20UH is noisier than CONF at all thrust levels. Since 20UH also has the highest cruise thrust coefficient such a minimization of its noise by fine tuning the nozzle length can be used in engine applications where cruise thrust efficiency cannot be sacrificed.

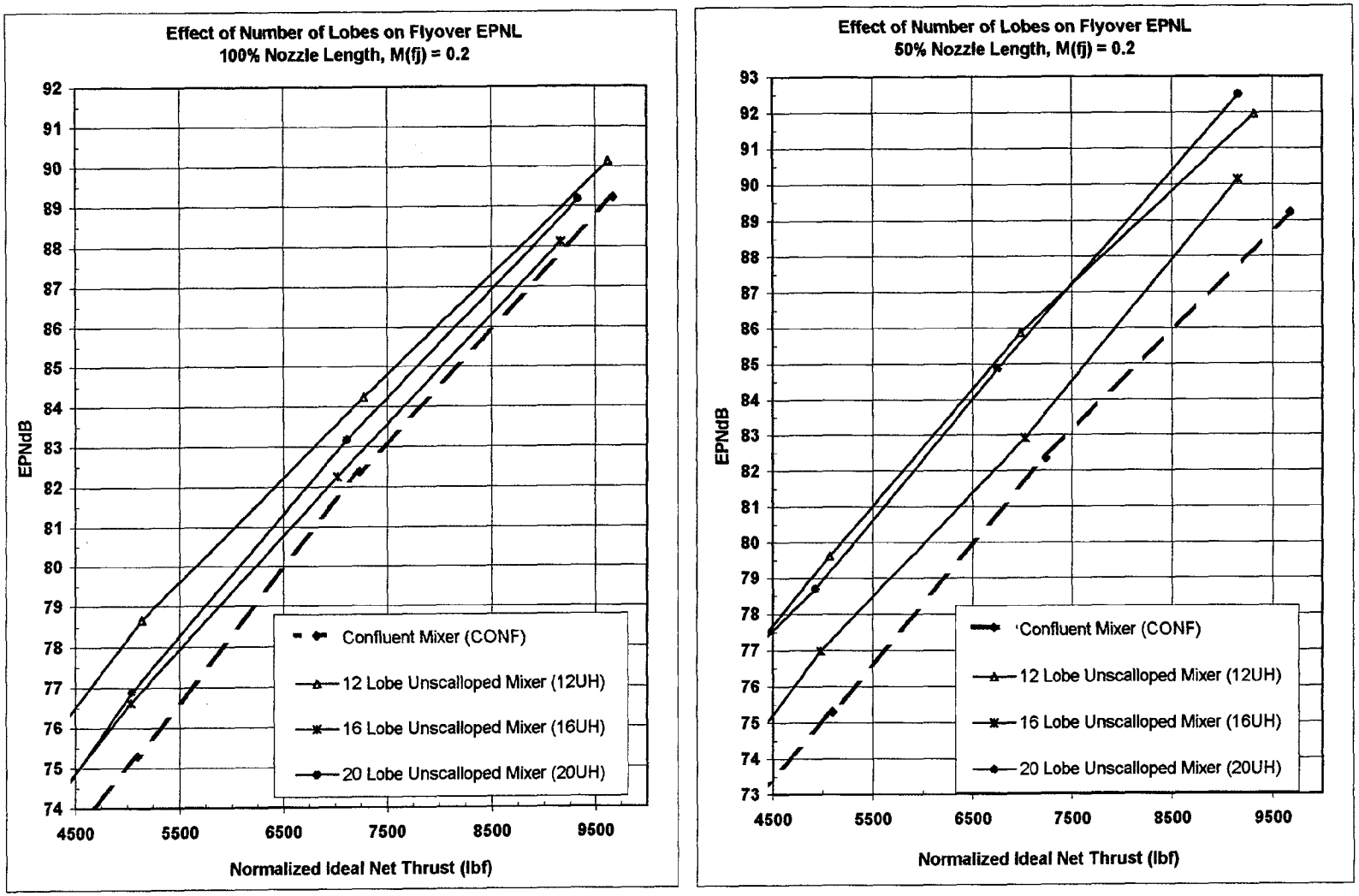

Figure 5.60 Effect of lobe number on flyover EPNL at M(fj) = 0.2 and two different nozzle-lengths.

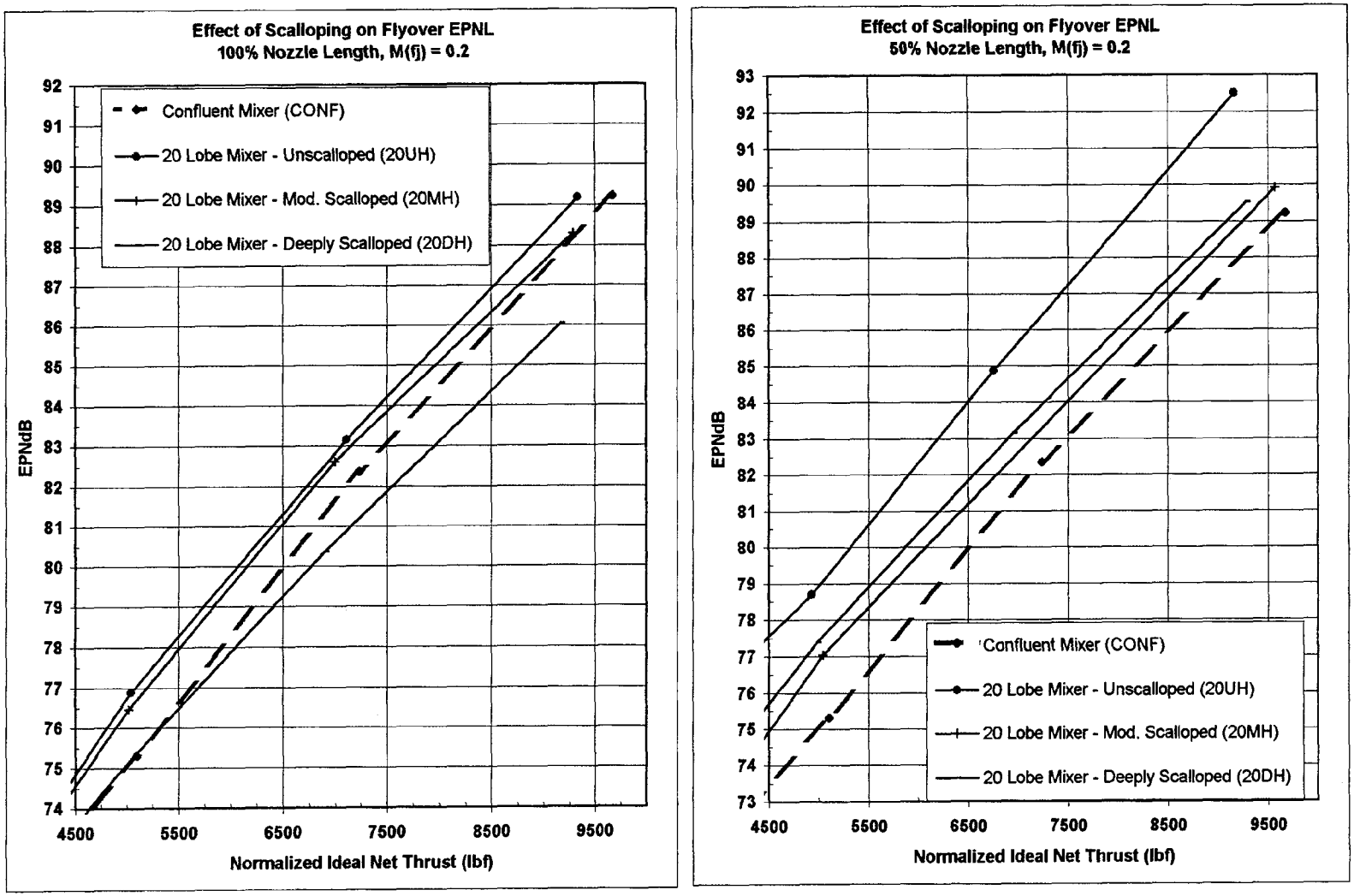

Figure 5.61 Effect of scalloping on flyover EPNL at M(fj) = 0.2 and two different nozzle-lengths.

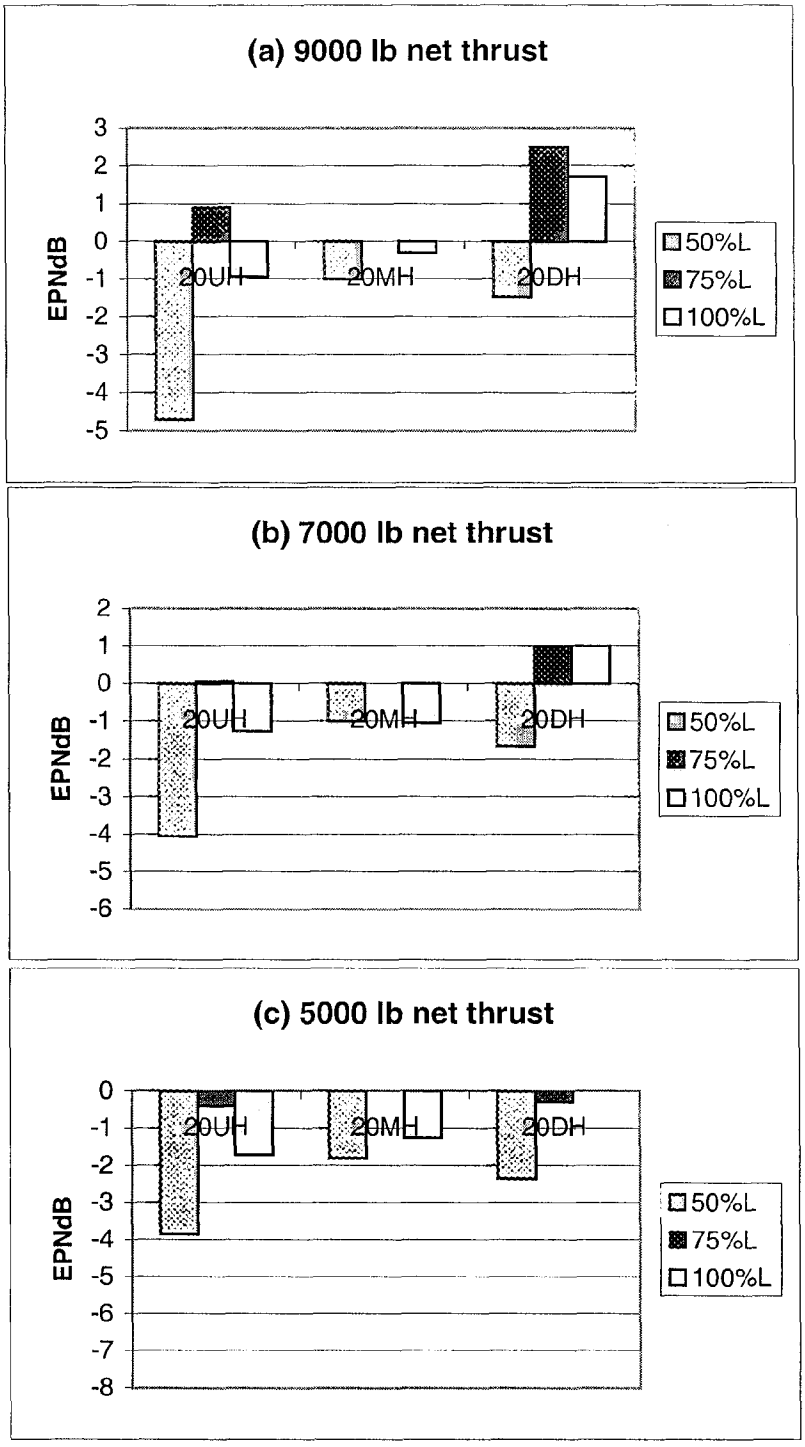

Figure 5.61A Effect of scalloping and nozzle length on flyover EPNL benefit compared to CONF at different net thrust levels and M(fj) = 0.2.

Figure 5.62 summarizes the EPNL comparison of all the mixers with baseline nozzle-length at M_{fj} = 0.2 on one plot. It clearly shows that out of all the mixers tested only 12CL and 20DH are quieter than CONF, with 12CL being more beneficial at low thrust conditions (TO #1). Both are equally beneficial at mid-thrust condition (TO #2) and 20DH is the best noise suppressor at the highest thrust conditions (TO # 3).

Figure 5.63 summarizes the EPNL for all mixers at M_{fj} = 0.2 with the shortest nozzle length (50%L), except CONF which has 100%L but whose behavior is not expected to change with nozzle length, as discussed earlier. This Figure clearly shows that at 50%L only the 12CL mixer remains quieter than the CONF configuration throughout.

Figures 5.64 and 5.65 summarize the EPNL for all mixers at an increased free-jet Mach number of 0.3 for 100% and 50% nozzle length respectively. At this high M_{fj} none of the lobed mixers is quieter than the simple confluent nozzle. 12CL produces only a marginal benefit at 50%L and low thrust (Figure 5.65) but the differences observed are within the margin of error for calculating EPNL. Thus, the high free-jet speed of M_{fj} = 0.3 produces so much noise reduction in the confluent mixer that all the intricacies of spectral changes and reductions in noise of lobed mixers is of no use at this scale factor.

5.6.4 Quietest Mixer-Nozzle Combinations

Figures 5.66(a) and (b) show the quietest mixer-nozzle combinations compared to the baseline confluent nozzle in terms of EPNL versus Net thrust and EPNL versus V_{mix}, respectively, at a free-jet Mach number of 0.2. Table 5.2 summarizes the noise benefits in terms of ΔEPNdB on the basis of equal net thrust, as well as, equal mixed jet velocity compared to CONF at three different thrusts and jet velocities. Note that the noise benefit at the highest thrust level of 9500 lb for 20DH with 75% L is obtained by linear extrapolation of EPNL data in Figure 5.66(a). Comparing ΔEPNdB at same jet velocity increases it by about 1 EPNdB (anywhere from 0.8 to 1.1 EPNdB) over suppression obtained on the basis of same net thrust. Although the values of ΔEPNdB benefit depend on whether we compare the mixer-nozzles on the basis of net thrust or jet velocity, the following trends are common to both:

(i) Only scalloped or cutout mixers (12CL or 20DH) prove to be the quietest at all thrust levels tested.

(ii) Noise suppression increases with thrust or jet velocity. At low thrusts the 12-lobe mixer with cutouts (12CL) produces a 1 EPNdB reduction with the 50%L nozzle. At high thrust, the deeply scalloped 20 lobe mixer (20DH) produces approximately 3.0 EPNdB noise reduction with the 75%L nozzle. When compared on the basis of equal jet velocity, these translate into 1.8 EPNdB benefit at the lower jet speeds and about 4.0 EPNdB at the higher jet speeds. Since the EPNL curves for the confluent nozzle and the 20DH-75%L configuration diverge from each other at higher thrust levels the noise benefits will be even more at higher thrusts or jet-speeds.

(iii) In all cases, the maximum noise reduction with a forced mixer was obtained with a nozzle shorter than the baseline length of L/D_{mp} = 1.10.

It is worth noting that only these two quietest mixer configurations, namely, 12CL and 20DH were also successful at reducing the low frequencies without too much increase in the annoying mid-to-high

Figure 5.62 1500 ft Flyover EPNL vs Ideal Net Thrust Comparison
100% Nozzle Length, M(fj) = 0.2

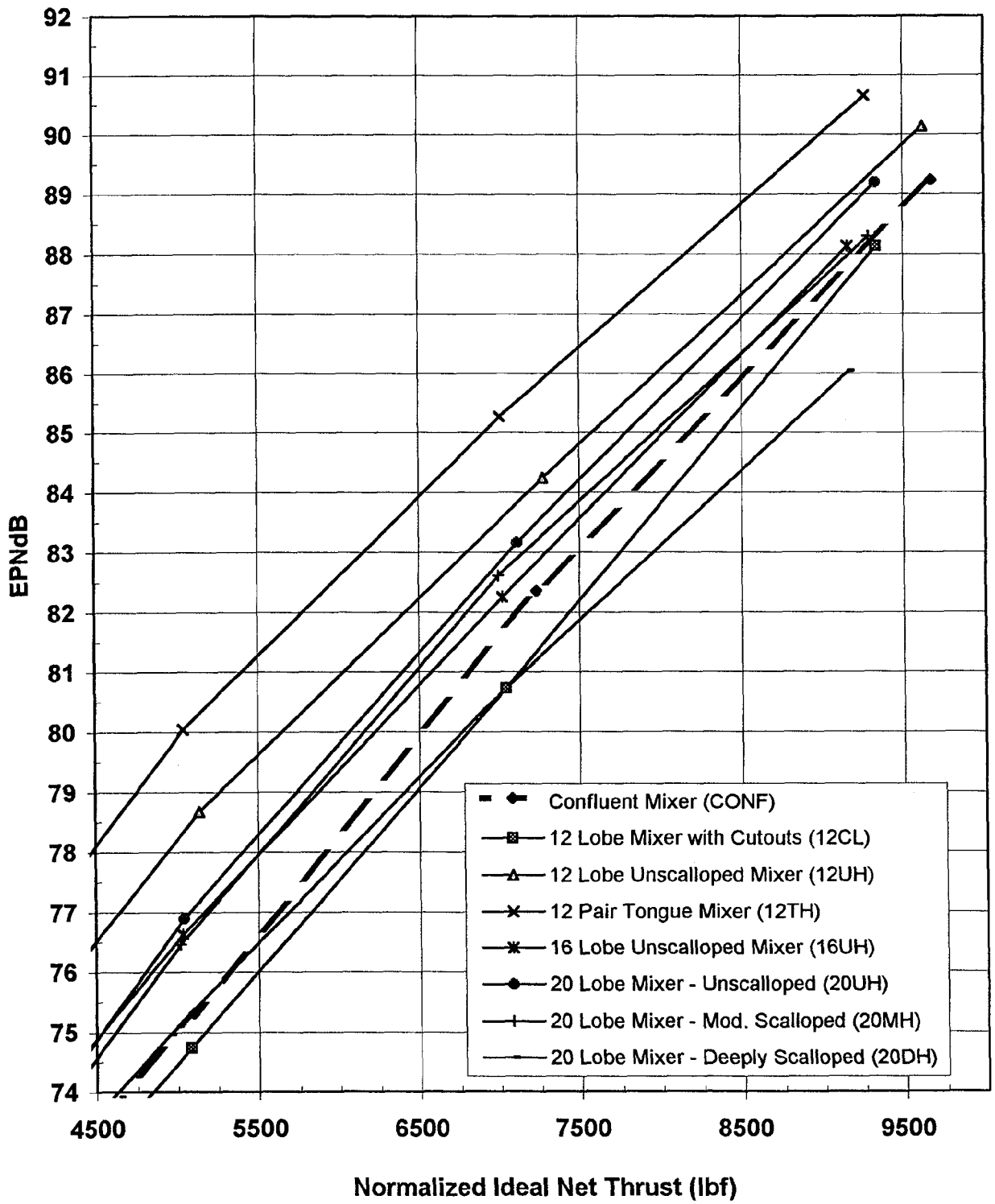

Figure 5.63 1500 ft Flyover EPNL vs Ideal Net Thrust Comparison
50% Nozzle Length, M(fj) = 0.2

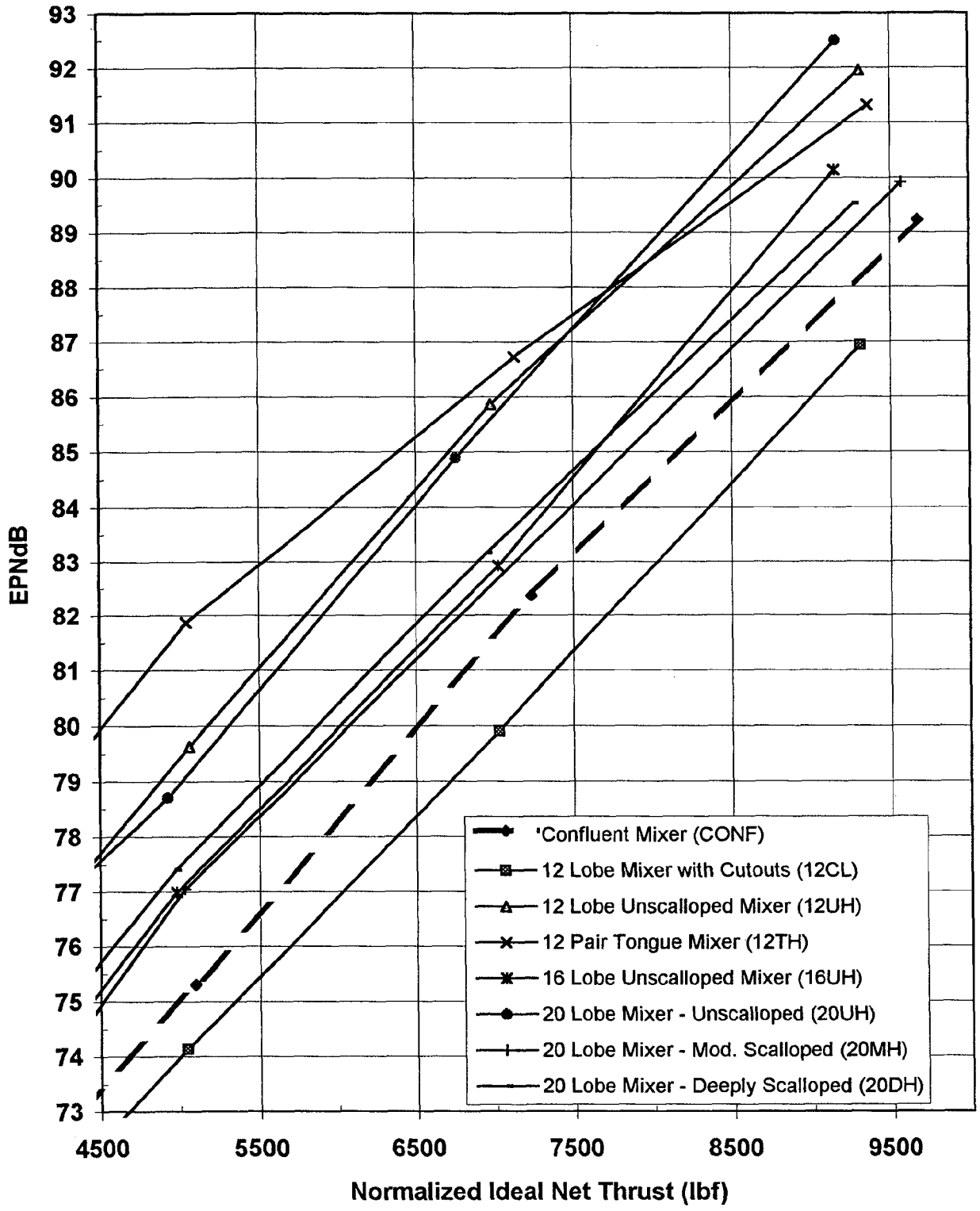

Figure 5.64 1500 ft Flyover EPNL vs Ideal Net Thrust Comparison
100% Nozzle Length, M(fj) = 0.3

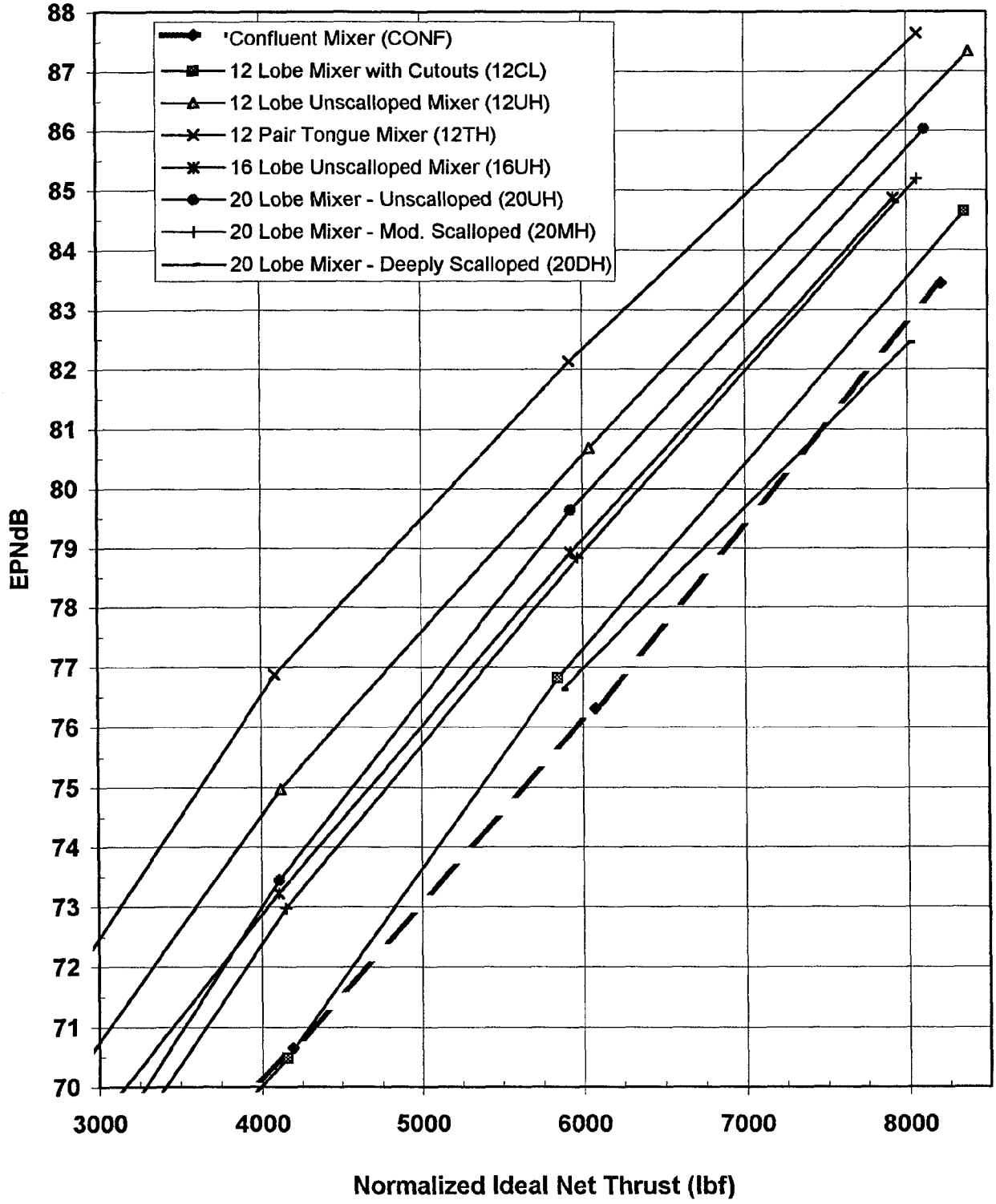

Figure 5.65 1500 ft Flyover EPNL vs Net Ideal Thrust Comparison
50% Nozzle Length, M(fj) = 0.3

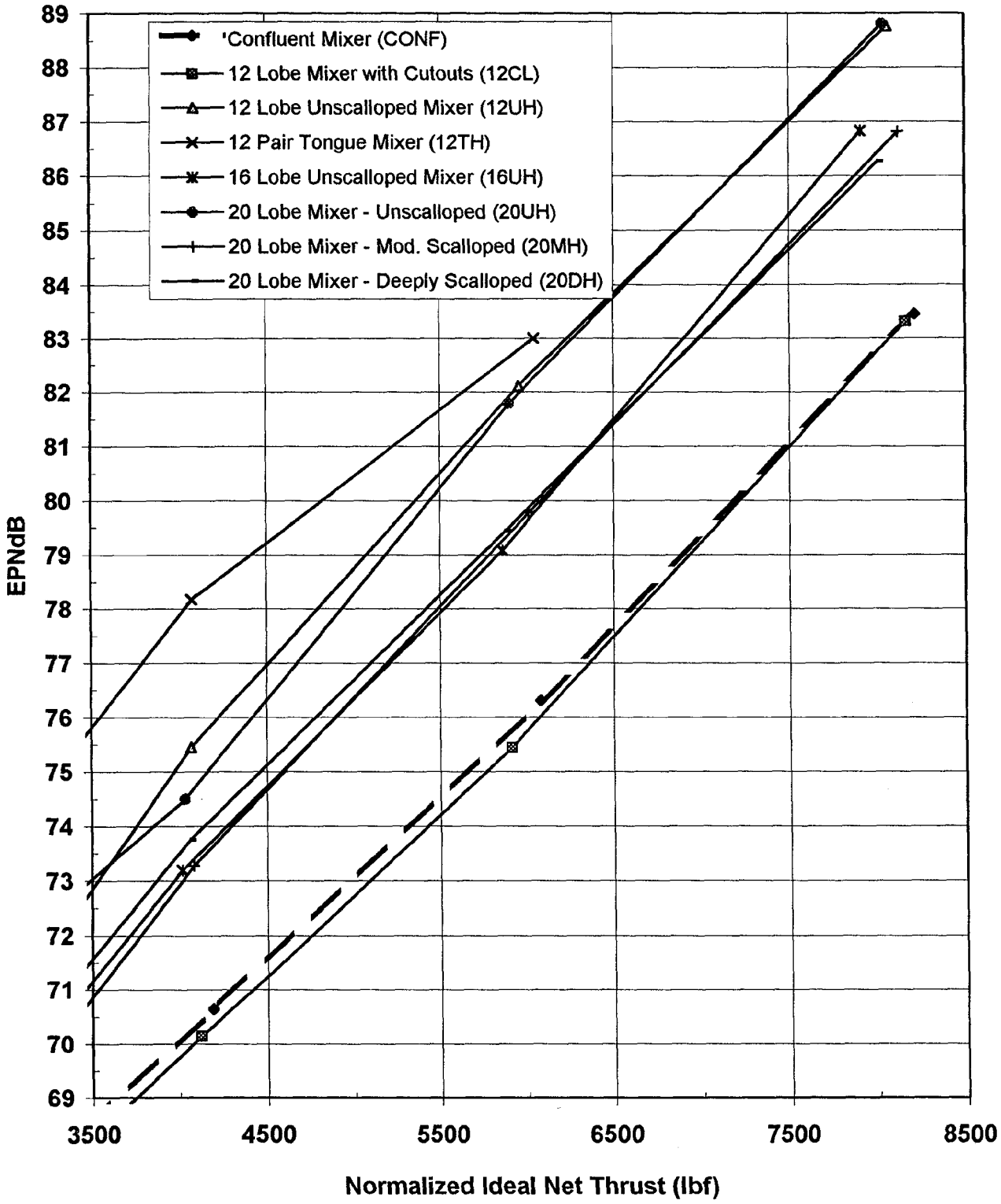

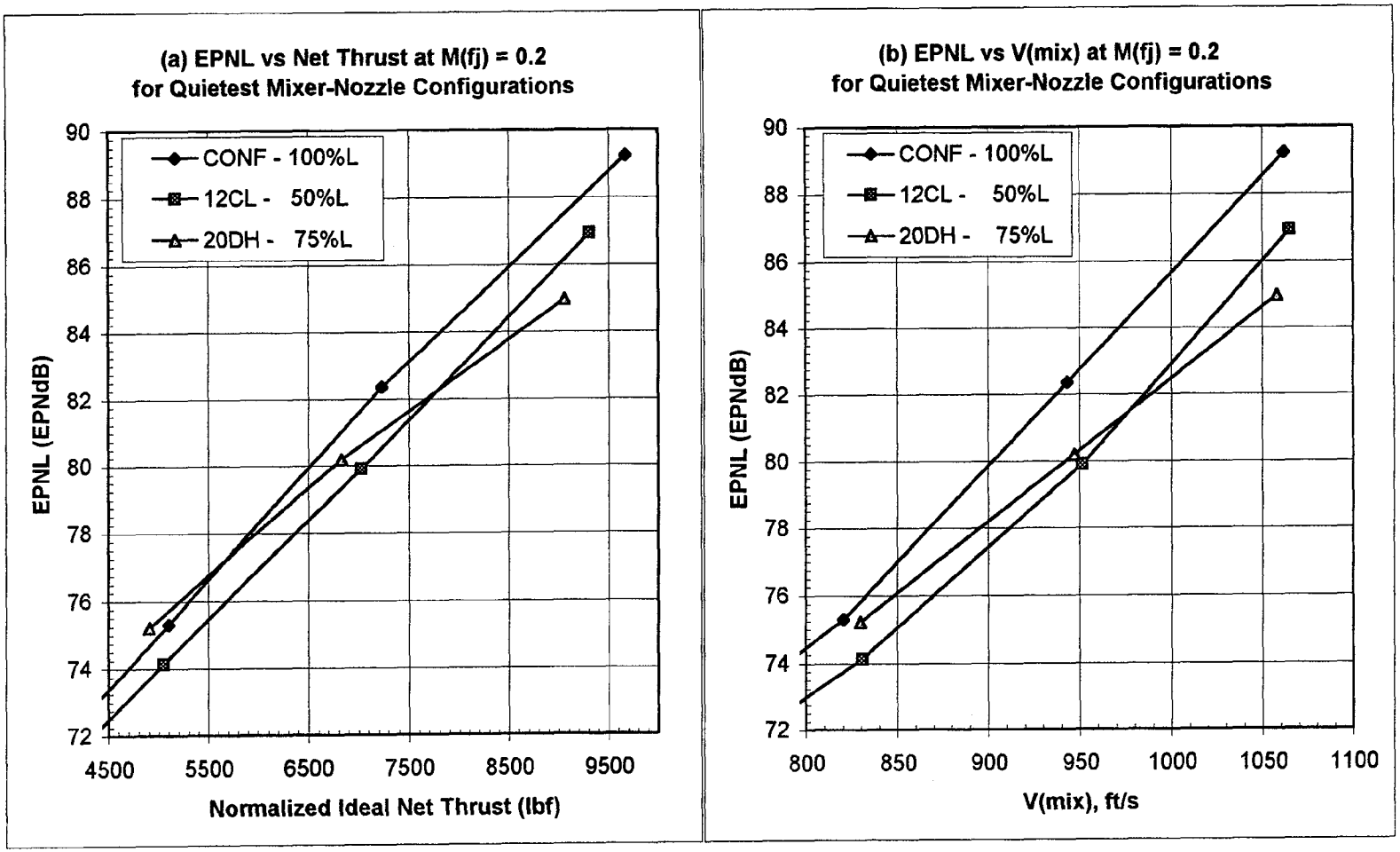

Figure 5.66 EPNL for the quietest mixer-nozzle combinations plotted against (a) Net Thrust and (b) V(mix)

Table 5.2 Quietest Mixer-Nozzle Combinations at M_{fj} = 0.2

Normalized Net Thrust (lb)	Mixer	Nozzle Length (L)	ΔEPNdB Benefit*
5000	12CL	50%	1.0
7000	12CL	50%	1.8
9500#	20DH	75%	3.0

V_{mix} (ft/s)	M_{mix} (= V_{mix}/c_{amb})	Mixer	Nozzle Length (L)	ΔEPNdB Benefit*
830	0.76	12CL	50%	1.8
950	0.87	12CL	50%	2.9
1060	0.97	20DH	75%	4.0

* ΔEPNdB Benefit = EPNL(Confluent) – EPNL(Mixer)
# After linear extrapolation of EPNL plot for 20UH+75%L

frequency noise compared to CONF. Hence, we conclude that at lower net thrusts a forced mixer using scallops/cutouts combined with low lobe penetration and fewer numbers of lobes will produce a noise reduction. At high net thrust, higher numbers of lobes and lobe scalloping helps. However, the noise benefits must be balanced against thrust losses at cruise conditions. In that regards, the fine tuning of the nozzle length for the most thrust efficient unscalloped lobe mixer 20UH to reduce noise below CONF should also be borne in mind although 20UH is noisier than 20DH or 12CL.

As a final note, it is appropriate to point out that the results presented in the report are somewhat scale sensitive. This is directly related to the frequency-weighting noy function applied to the SPL spectra in the definition of PNL. As the scale factor is increased or decreased from the value of 4 used throughout this report, key spectral features will translate to new frequency bands. Depending on the scale factor used, the resulting weighting factor applied to these features may alter their importance at the new scale. As a result, generalizations of the conclusions contained in this report to applications of different size should be undertaken with caution.

Chapter 6

Concluding Remarks

A comprehensive test database for the acoustic, aerodynamic and plume flow characteristics of model scale forced lobe mixers has been created for nozzles with bypass ratio of 5 to 6. The operating conditions for acoustic tests ranged from typical approach through take-off points with effective jet speeds from 600 ft/s to 1080 ft/s. Forward flight effects were simulated through the use of a separate free jet flow, with data obtained at free jet Mach numbers between 0.0 and 0.3. The static thrust performance was measured at cruise, as well as, at most of the take-off conditions.

The data was scaled to a nozzle exit diameter of 29 inches (scale factor of 4), representative of small-to-medium thrust turbofan engines. The effect of several mixer and nozzle parameters was analyzed: scalloping/cutouts in lobe side-walls, number of lobes, mixing length, and also lobe penetration and fan-to-core area ratio. Several new concepts, methods and mechanisms were identified during the conduct of this project which helped us explain some of the observed results and these ideas can be applied to the design of jet noise suppressors.

We summarize below some of the new concepts and important findings:

New Concepts/Methods

1. *Gradual* introduction of vorticity and the "trailing-edge" rule for scalloping leading to "boomerang" scallops to reduce internal fan/core mixing noise.
2. "Tongue" mixer - a unique limiting case of deep scalloping.
3. Comparison of noise for different free-jet Mach numbers at "shifted" angles to examine "excess" internal noise from fan-core mixing.
4. Extrapolation of flyover EPNL for lobed mixers from data known at one free-jet speed to another speed.

New Generic Findings

1. Horizontal flyover EPNL for different aircraft speeds was found to correlate with "net" thrust and not gross thrust or absolute jet speed. The collapse of the EPNL versus net thrust curves for different aircraft speeds was found to be good for most lobed mixers but less impressive for the confluent configuration.
2. Using the "shifted" angle comparison method for several free-jet speeds, it was found that the annoying mid-to-high frequencies upstream of the peak PNL angle were the result of "excess" noise sources which could be either "internal" to the nozzle duct or "external" to it but close to its exit plane. This was particularly notable in the unscalloped lobe mixers and the tongue mixer, and was less important in the two scalloped mixers which were also the quietest. The annoying excess noise spectra was deemed to be produced by the turbulence in the strong streamwise vortices from the forced mixers.

Important Specific Findings

1. Forced lobe mixers reduce noise in comparison to a coaxial jet by significantly reducing the low frequency contribution but, if not designed properly, such mixers can lead to an increase in the mid-to-high frequency sound which is heavily weighted for annoyance.
2. Sudden introduction of streamwise vorticity inside the nozzle as with unscalloped, high-penetration lobe-mixers is not a desirable feature from the point of view of noise suppression because of increases in the annoying spectral component which nullifies any benefit accrued by decreasing the low frequency spectra. On the other hand, *gradual* introduction of axial vorticity, as with "boomerang" scallops, is preferable on an overall basis even though it may not benefit the lower frequencies as much.
3. The most prominent geometric feature of the lobed mixers for reducing the annoying portion of the spectral band is "scalloping" of the lobes, but lobe-penetration and lobe count also have a role. For the size of engine considered (29 in. diameter), a scalloped lobe mixer with fewer lobes and lower penetration is the most effective mixer at low net thrusts (5000 lb), producing a maximum benefit of 1 EPNdB. At higher net thrusts (9500 lb) a deeply scalloped lobe mixer with higher number of lobes and higher lobe penetration is the most effective mixer, producing a maximum noise benefit of about 3 EPNdB. In all cases, noise reduction is measured against a coaxial or confluent configuration. These noise benefits increase by about one more EPNdB when compared on the basis of equal mixed jet velocity rather than equal net thrust.
4. For a given lobe mixer, an optimal mixing length was found to exist from the point of view of noise suppression. That is, decreasing the mixing length (or nozzle length) from the baseline length of $L/D_{mp} = 1.1$ also decreased the noise up to a local minimum value and any further decrease in nozzle length increased the noise. For unscalloped mixers such a decrease in mixing length gave a noise benefit of as much as 3 EPNdB at high nozzle pressure ratios. A working hypothesis in terms of two competing mechanisms is proposed, and a deeper look at this new and interesting phenomenon is required. It is obviously beneficial from the viewpoint of weight but its repercussions on the external boat-tail angle and consequent cruise thrust performance must also be considered.
5. At low to medium thrust levels, unscalloped lobe mixers with high lobe penetration do not reduce noise below that of a coaxial jet regardless of the number of lobes and nozzle-length. However, at higher thrusts fine tuning of nozzle length for a 20 lobe unscalloped mixer produced a 1 EPNdB benefit. The cruise thrust coefficient and the thrust-mixing efficiency of such unscalloped mixers are typically higher than scalloped lobe mixers. Hence, in applications where thrust efficiency is of more importance than noise suppression minimizing noise of unscalloped lobe mixers by adjusting the nozzle length may be a good alternative.
6. It should be noted, however, that the 12-lobe cutout mixer with low penetration has a good noise benefit throughout the jet-speeds tested, as well as, one of the highest cruise thrust performance. Scalloped lobe mixers, in

general, still have far better cruise thrust coefficients and thrust mixing efficiencies than a coaxial jet and are the quietest mixers. For certain nozzle lengths the moderate scalloping was better than unscalloped or deeply scalloped mixers. Thus the amount of scalloping can be used as a trading parameter between noise suppression and cruise thrust loss.

7. The tongue mixer model, designed for proof-of-concept in this task, provided the maximum suppression of the low frequency spectra amongst all the mixers, but this was accompanied by an unacceptable increase in the annoying mid-to-high frequency noise making it one of the noisiest mixers. It also produced low thrust coefficients. The primary reason for this behavior is its smaller fan-to-core area ratio and, hence, smaller bypass ratio. However, its simplicity of manufacturing, reduced weight and ease of reparability demand a second look at this concept after appropriately sizing it with a larger fan-to-core area ratio.

This tongue mixer concept has also been extended by Rolls-Royce Allison for use in externally mixed or separate flow nozzles under a separate NASA Contract NAS3-27720 to General Electric Company [25], and it has shown noise benefits of about 2 EPNdB over coaxial jets when applied to larger engines with higher jet speeds (see figure 87, Ref. 25). In this regard, it should be noted that in applications to real engines the concepts that produce large decrease in low frequency noise but moderate increase in mid-to-high frequency noise may not be so bad if the latter frequency range is dominated by other engine noise sources, such as, fan tones. This shows that the tongue mixer is, indeed, a viable concept from noise suppression point of view and should be further explored for application to full-scale engines.

Chapter 7

References

1. Packman, A. B. and Eiler, D. C. (1977): *Internal Mixer Investigation for JT8D Engine Jet Noise Reduction, Vol. I - Results.* U. S. Dept. of Transportation, Federal Aviation Administration Report No. FAA RD-77-132.1, Dec. 1977.
2. Shumpert, P. K. (1980): *An Experimental Model Investigation of Turbofan Engine Internal Exhaust Gas Mixer Configurations.* AIAA Paper 80-0288, AIAA 18th Aerospace Sciences Mtg., Jan. 14-16, 1980.
3. Kuchar, A. (1980): *Scale Model Performance Test Investigation of Exhaust System Mixer for an Energy Efficient Propulsion (E^3) System.* AIAA Paper 80-0229, AIAA 18th Aerospace Sciences Mtg., Jan. 14-16, 1980.
4. Larkin, M. J. and Blatt, J. R. (1984): *Energy Efficient Engine Exhaust Mixer Model Technology Report Addendum, Phase III Test Program.* NASA CR 174799, April 1984.
5. Saiyed, N. H., Bridges, J. E. and Krejsa, E. A. (1996): *Core and Fan Stream's Mixing Noise outside the Nozzle for Subsonic Jet Engines with Internal Mixers.* AIAA Paper 96-1667, AIAA Aeroacoustics Conference, May 6-8, 1996.
6. Booher, M. E., Kwon, O., Barta, A. B., Vittal, B. R. and Krishnan, M. R. (1993): *Development of an Advanced Exhaust Mixer for a High Bypass Ratio Turbofan Engine.* AIAA Paper 93-2435, 29th AIAA/ASME/SAE/ASEE Joint Propulsion Conference, June 28-30, 1993.
7. Barta, A. B., Vittal, B. R. and Dalton, W. N. III (1997): *Experimental Verification of the Mixing Process in Turbofan Engine Exhaust Systems.* AIAA Paper 97-2640, AIAA/ASME/SAE/ASEE Joint Propulsion Conference, July 6-9, 1997.
8. Meade, J. P. (1994): *Acoustic Evaluation of a Forced Mixer on a High Bypass Ratio Engine.* AIAA Paper AIAA-94-2954, 30th AIAA/ASME/SAE/ASEE Joint Propulsion Conference, June 27-29, 1994.
9. Elliott, J. K., Manning, T. A., Qiu, Y. J., Greitzer, E. M. and Tan, C. S. (1992): *Computational and Experimental Studies of Flow in Multi-Lobed Forced Mixers.* AIAA Paper 92-3568, 28th AIAA/ASME/SAE/ASEE Joint Propulsion Conference, July 6-8, 1992.
10. McCormick, D. C. and Bennett, J. C. (1993): *Vortical and Turbulent Structure of a Lobed Mixer Free-Shear Layer.* AIAA Paper 93-0219, 31st AIAA Aerospace Sciences Mtg., Jan. 11-14, 1993.
11. Belovich, V. M., Samimy, M. and Reeder, M. F. (1994): *Dual Stream Axisymmetric Mixing in the Presence of Axial Vorticity.* AIAA Paper 94-3084, 30th AIAA/ASME/SAE /ASEE Joint Propulsion Conference, June 27-29, 1994.
12. The NPARC Alliance (1996): **A User's Guide to NPARC Version 3.0.** Arnold Engineering Development Center, Tullahoma, Tennessee, Sept. 1996.
13. Pointwise, Inc.: **GRIDGEN User's Guide.**, Bedford, Texas 76095.
14. Castner, R. S. (1994): *The Nozzle Acoustic Test Rig - An Acoustic and Aerodynamic Free-Jet Facility.* NASA

TM 106495, 1994.

15. Ahuja, K. K., Tester, B. J. and Tanna, H. K. (1978*): The Free Jet as a Simulator of Forward Velocity Effects on Jet Noise.* NASA-CR-3056, Oct. 1978, 324 p.
16. Mengle, V. G., Dalton, W. N., Bridges, J. C. and Boyd, K. C. (1997): *Noise Reduction with Lobed Mixers: Nozzle-Length and Free-Jet Speed Effects.* AIAA Paper 97-1682, 3rd AIAA/CEAS Aeroacoustics Conference, May 12-14, 1997.
17. Fisher, M. J., Preston, G. A. and Bryce, W. D. (1993): *A Modelling of the Noise from Simple Co-axial Jets.* AIAA Paper 93-4413, 15th AIAA Aeroacoustics Conference, Oct. 25-27, 1993.
18. Balsa, T. F. and Gliebe, P. R. (1977): *Aerodynamics and Noise of Coaxial Jets.* **AIAA J.**, Vol. 15, No. 11, Nov. 1977, pp. 1550-1558.
19. Yu, S. C. M., Yip, T. H. and Liu, C. Y. (1997): *Mixing Characteristics of Forced Mixers with Scalloped Lobes.* **J. Propulsion & Power**, Vol. 13, No. 2, March-April 1997, pp. 305-311.
20. Abramovich, G. N. (1963): **The Theory of Turbulent Jets.** M.I.T. Press, Cambridge, MA, Chapter 5.
21. Candel, S. M. (1972): *Acoustic Transmission and Reflection by a Shear Discontinuity Separating Hot and Cold Regions.* **J. Sound and Vibration**, Vol. 24(1), pp. 87-91, 1972.
22. Lighthill, James (1978): **Waves in Fluids.** Cambridge University Press, Cambridge, Great Britain.
23. Thompson, R. J. (1971): *Ray Theory for an Inhomogeneous Moving Medium.* **J. of the Acoustical Society of America**, Vol. 51, No. 5 (part 2), 1971, pp. 1675-1682.
24. Society of Automotive Engineers (1973): *Definitions and procedures for Computing the Effective Perceived Noise Level for Flyover Aircraft Noise.* ARP 1071.
25. Janardan, B. A., Hoff, G.E., Barter, J. W., Martens, S., Gliebe, P. R., Mengle, V.G. and Dalton, W.N. (1998*): Separate Flow Exhaust System Noise Reduction Concept Evaluation.* Final Report, NAS3-27720, Area of Interest 14.3, NASA CR (to be numbered), GEAEA Report No. R98AEB152, May 1998, 273 p.

Appendix A

Geometrical Details of Mixers and Nozzles

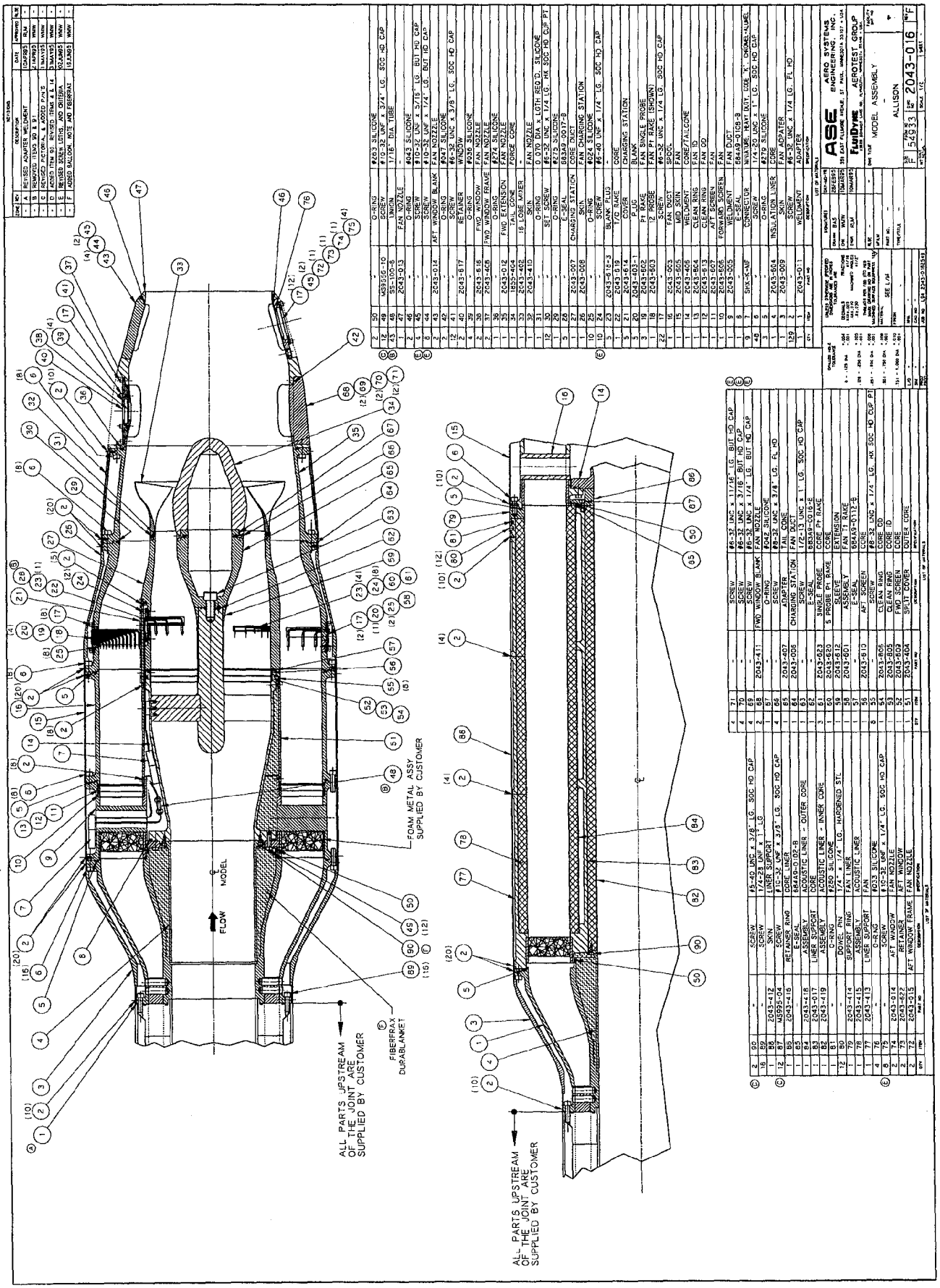

Figure A.1 Model assembly for use in NASA's NATR jet rig acoustic tests.

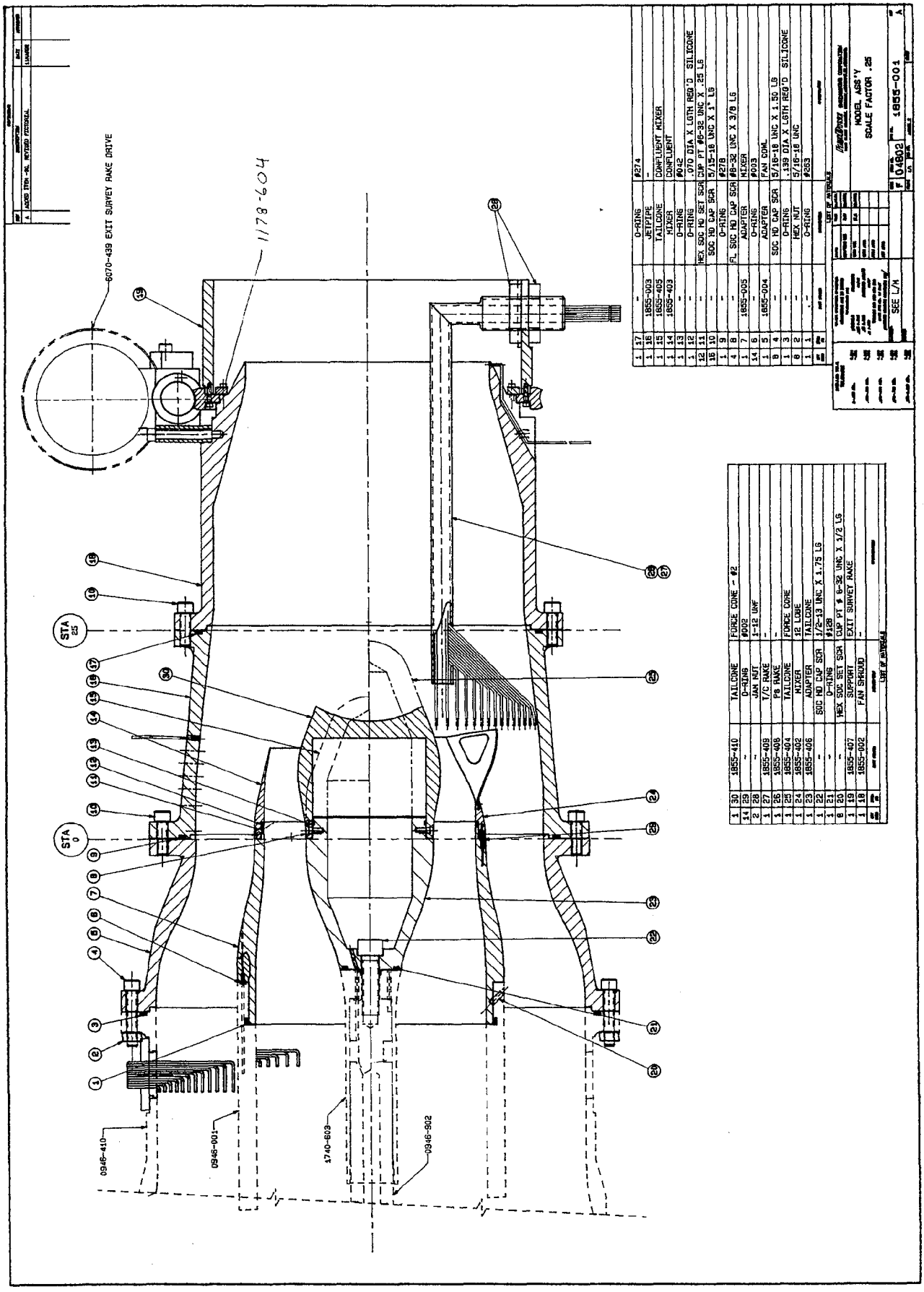

Figure A.2 Model assembly for use in FluiDyne's facility for aerodynamic performance tests.

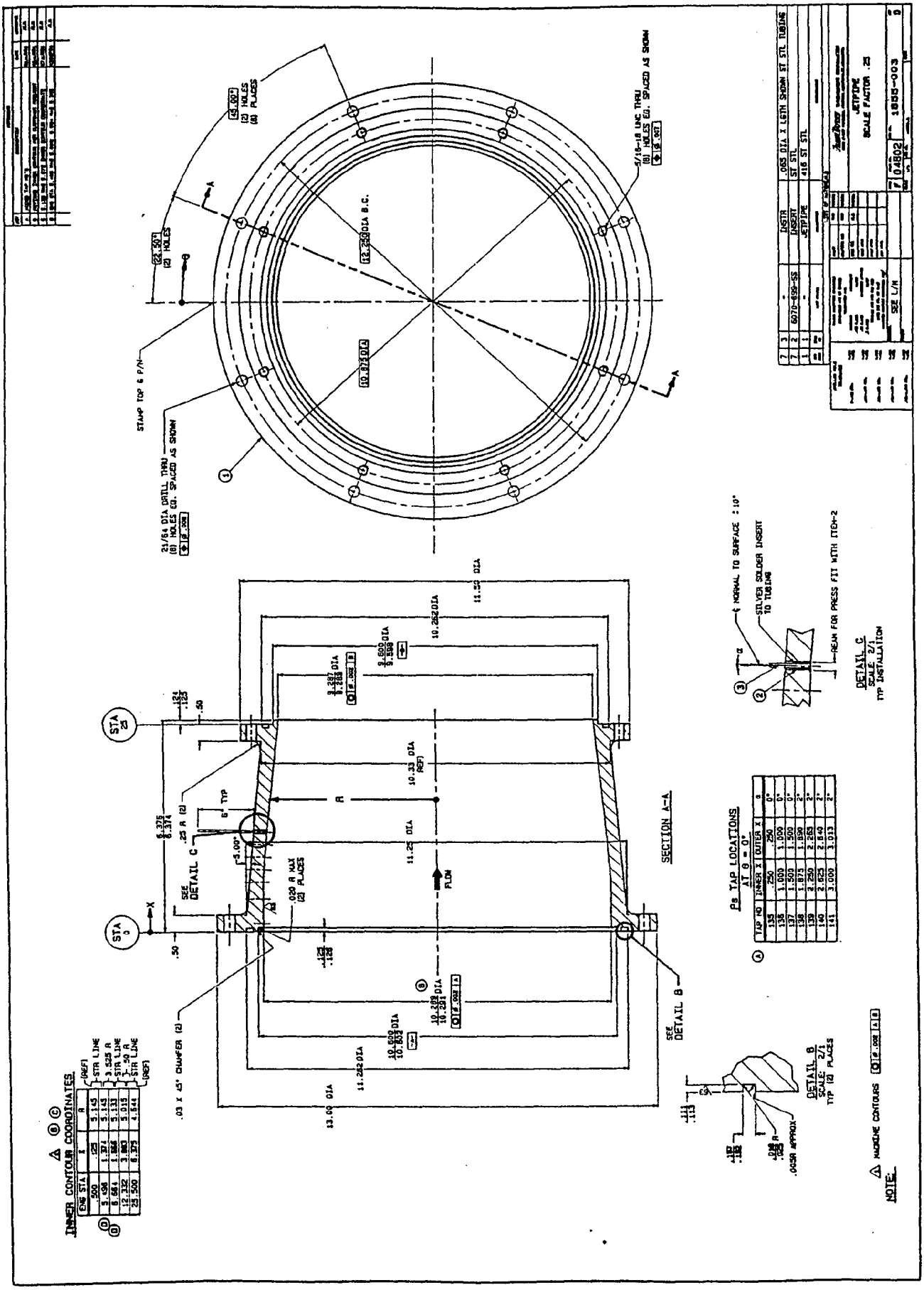

Figure A.3 Geometry of a section of the nozzle-duct.

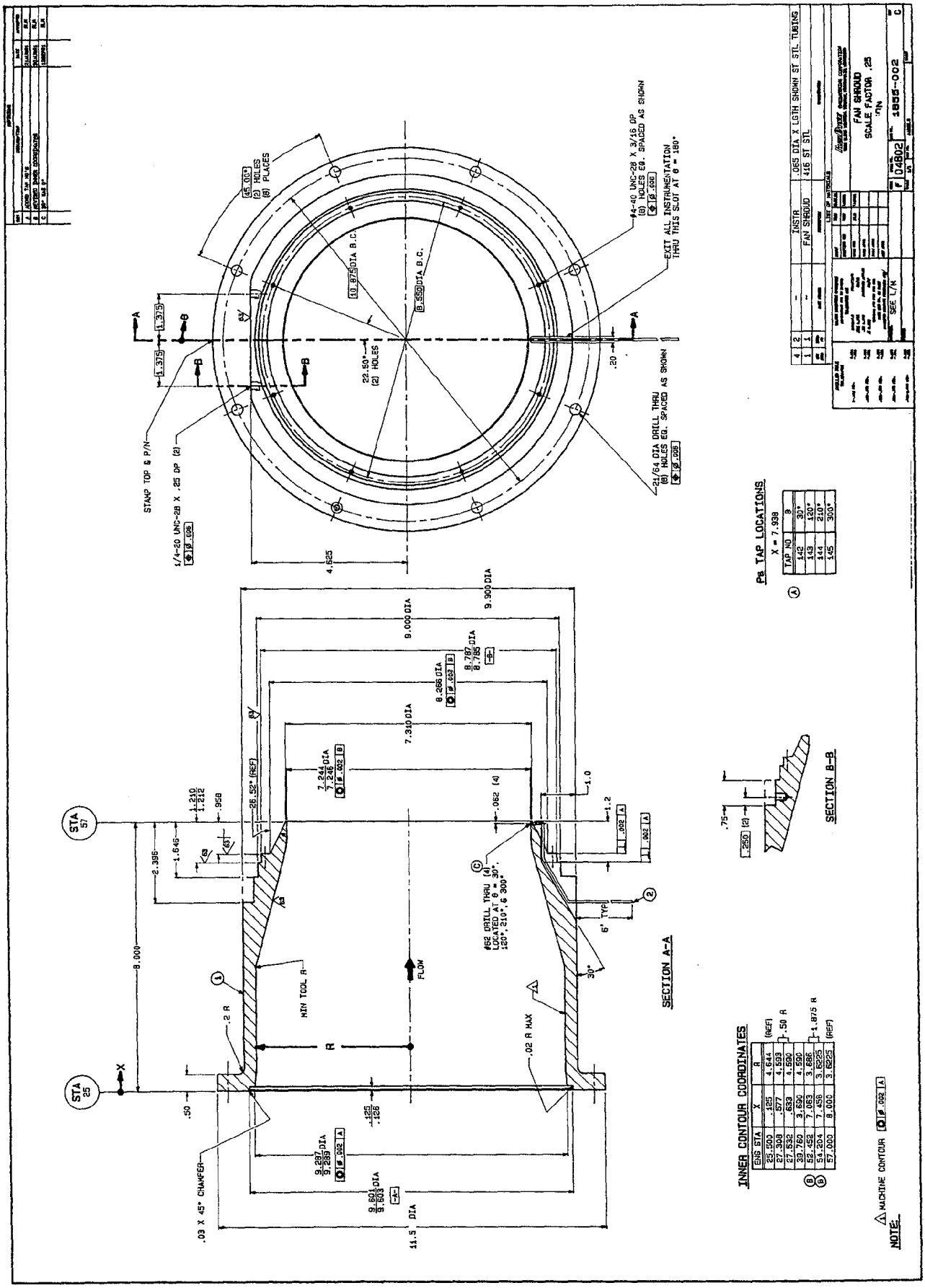

Figure A.4 Geometry of the end-section of the nozzle-duct.

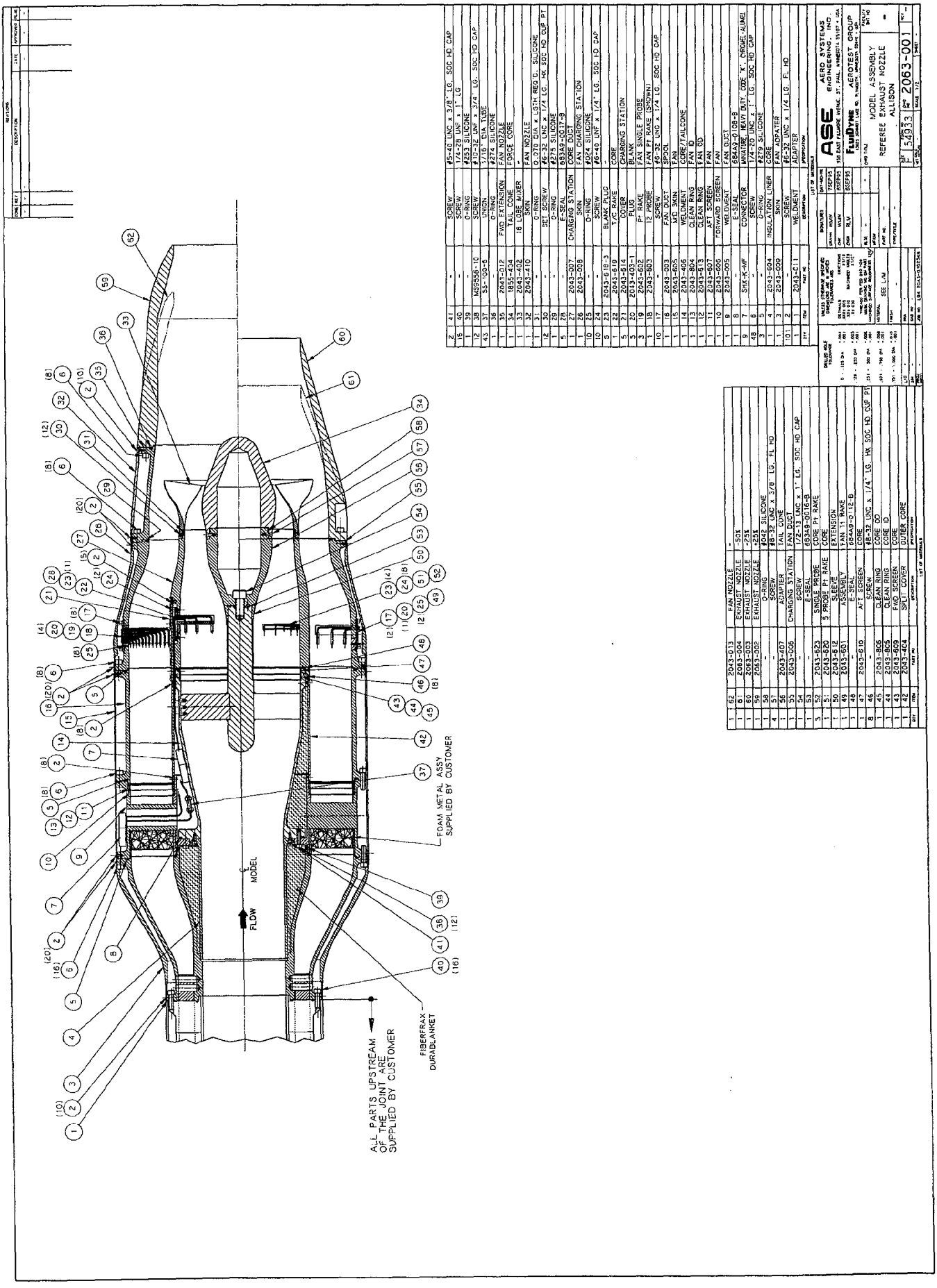

Figure A.5 Model assembly with different nozzle-lengths for NASA tests.

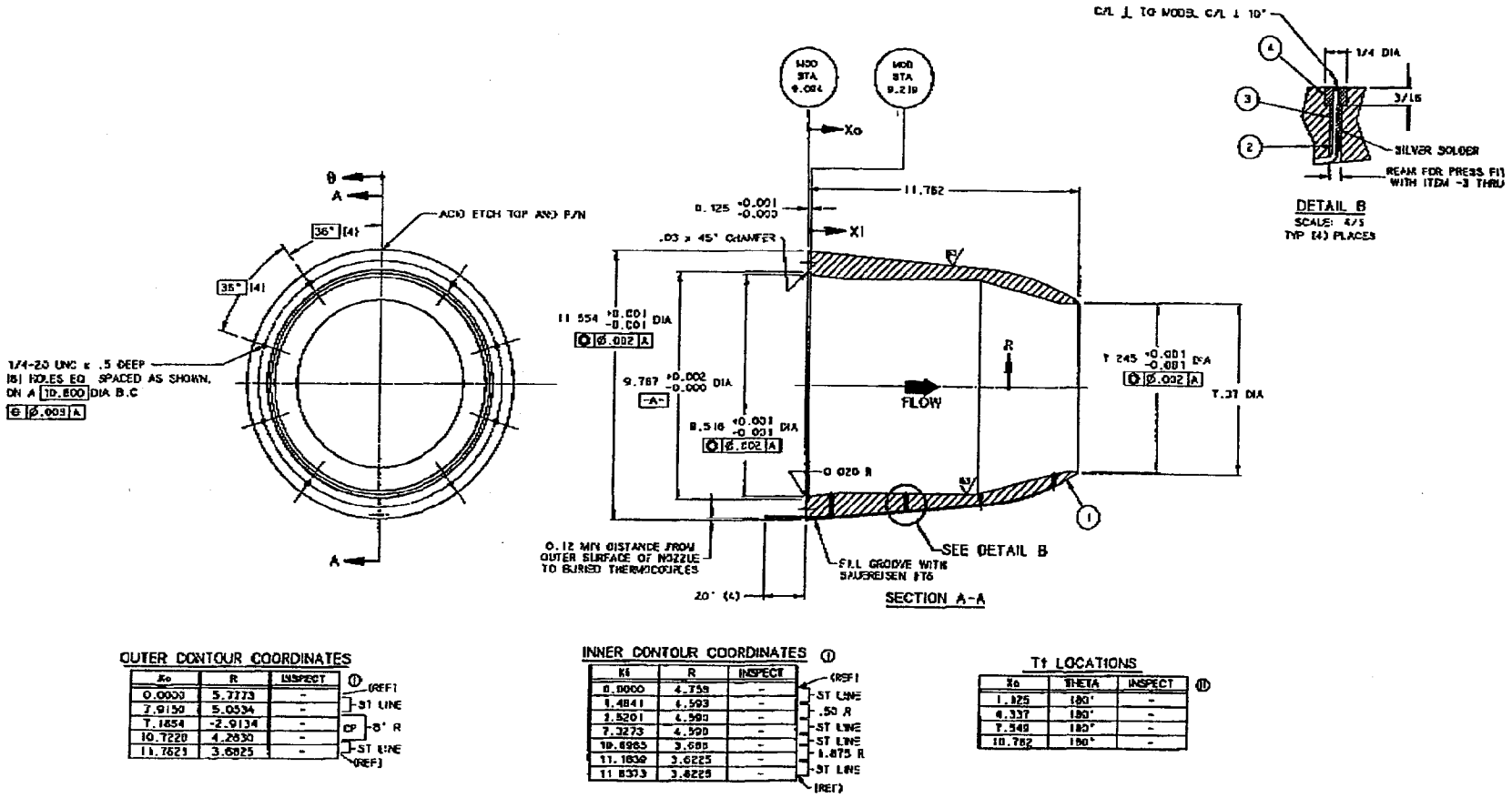

OUTER CONTOUR COORDINATES ①

Xo	R	INSPECT	
0.0000	5.7773	-	(REF)
2.9150	5.0534	-	ST LINE
T.1854	-2.9134	-	CP 8° R
10.7220	4.2830	-	ST LINE
11.7621	3.6825	-	(REF)

INNER CONTOUR COORDINATES ①

Xi	R	INSPECT	
0.0000	4.759	-	(REF)
1.4841	4.593	-	ST LINE
3.5201	4.593	-	.50 R
7.3273	4.593	-	ST LINE
10.6965	3.685	-	ST LINE
11.1830	3.6225	-	1.875 R
11.8313	3.6225	-	ST LINE
			(REF)

T† LOCATIONS ⑪

Xo	THETA	INSPECT
1.825	180°	-
4.337	180°	-
7.549	180°	-
10.782	180°	-

Figure A.6 Geometry of +25% nozzle-length.

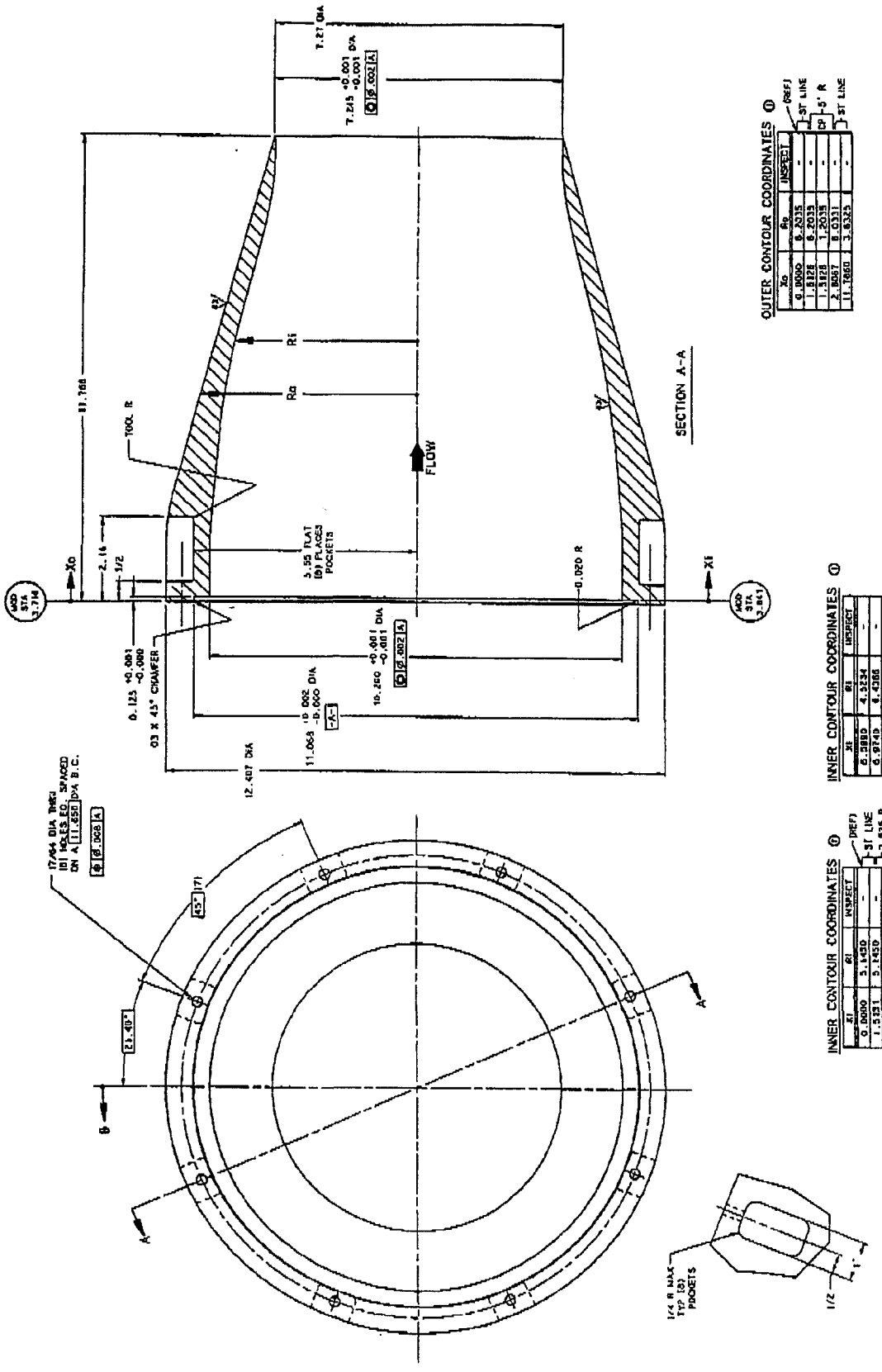

Figure A.7 Geometry of -25% nozzle-length.

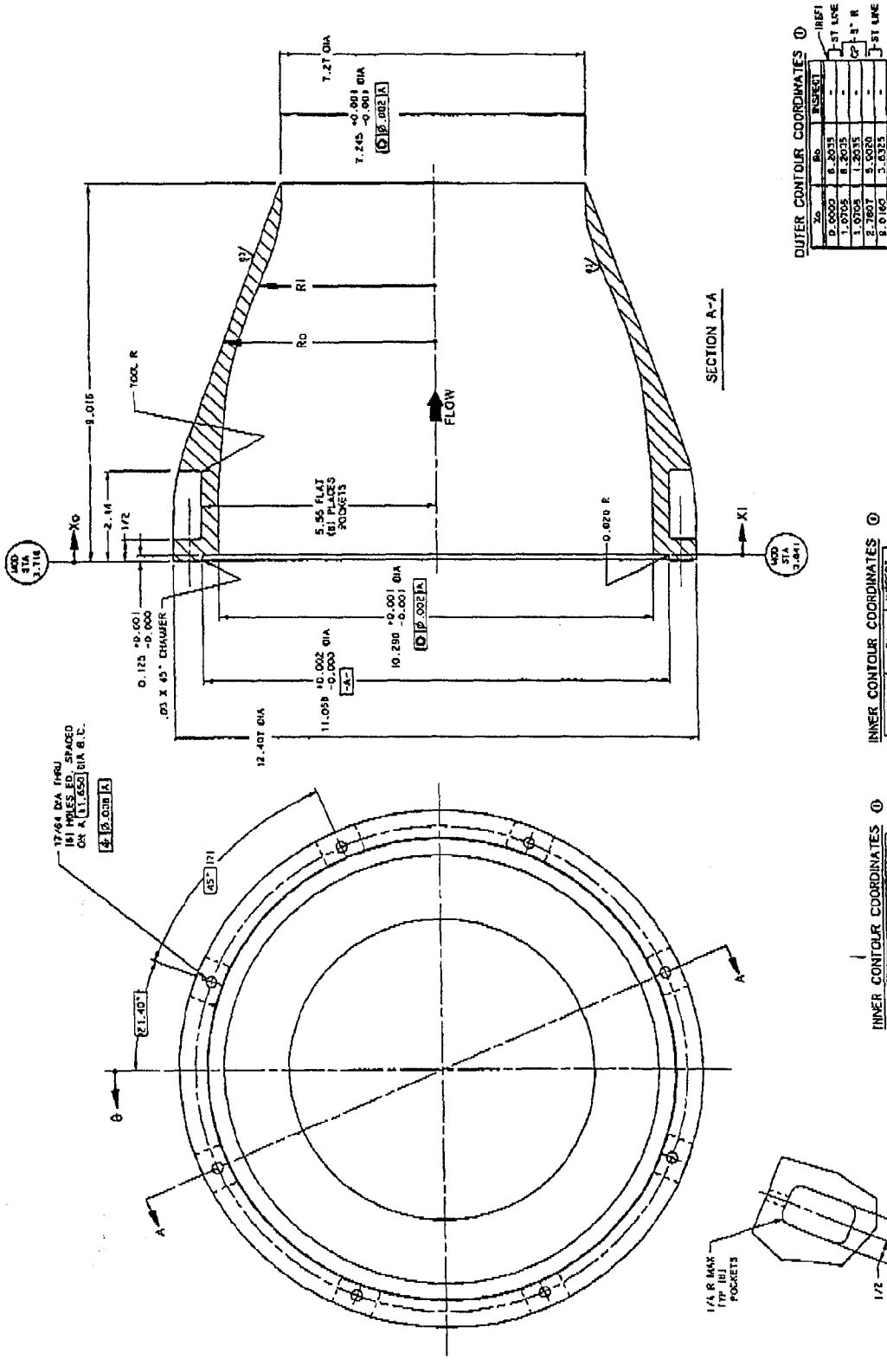

Figure A.8 Geometry of -50% nozzle-length.

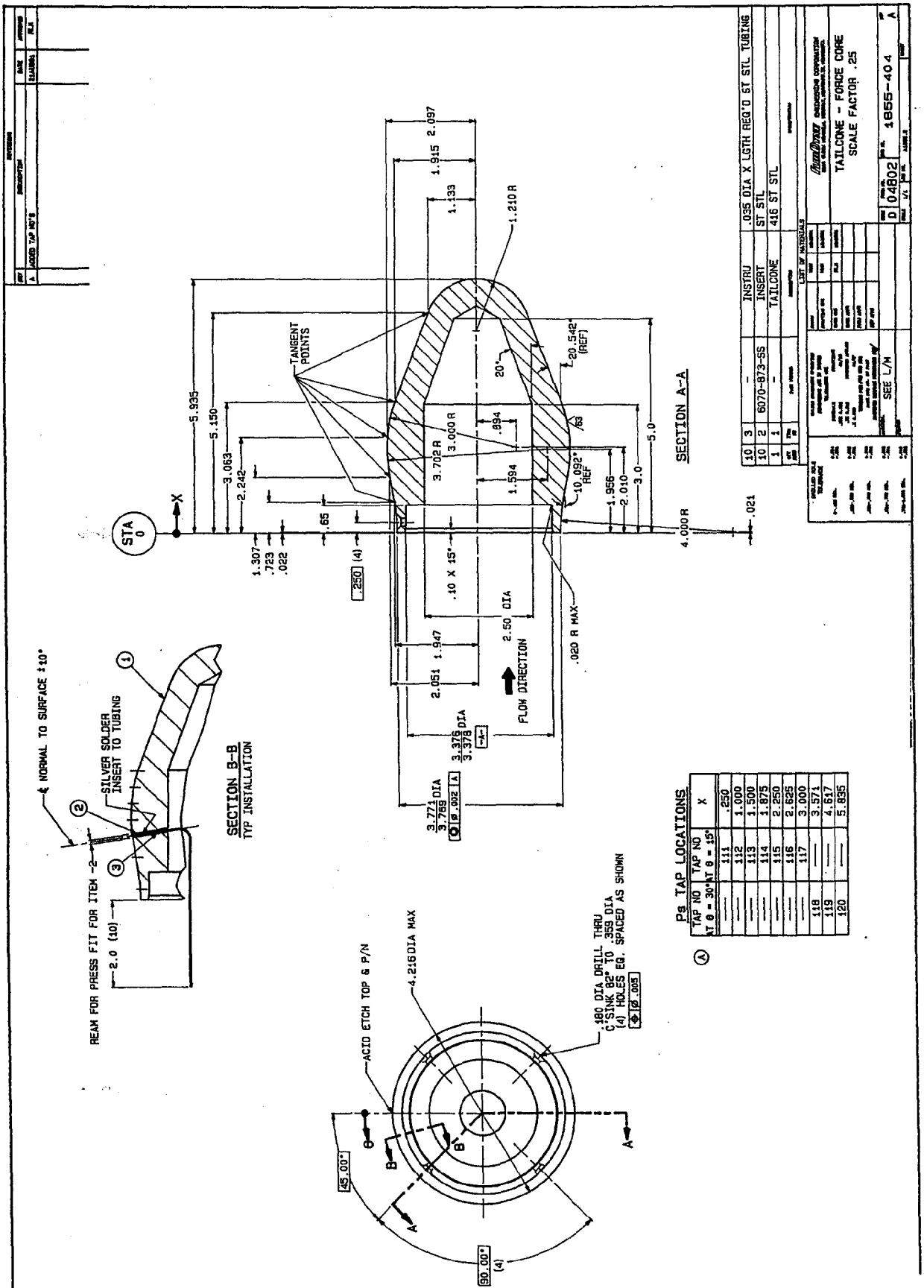

Figure A.9 Geometry of tail-cone for lobed mixers.

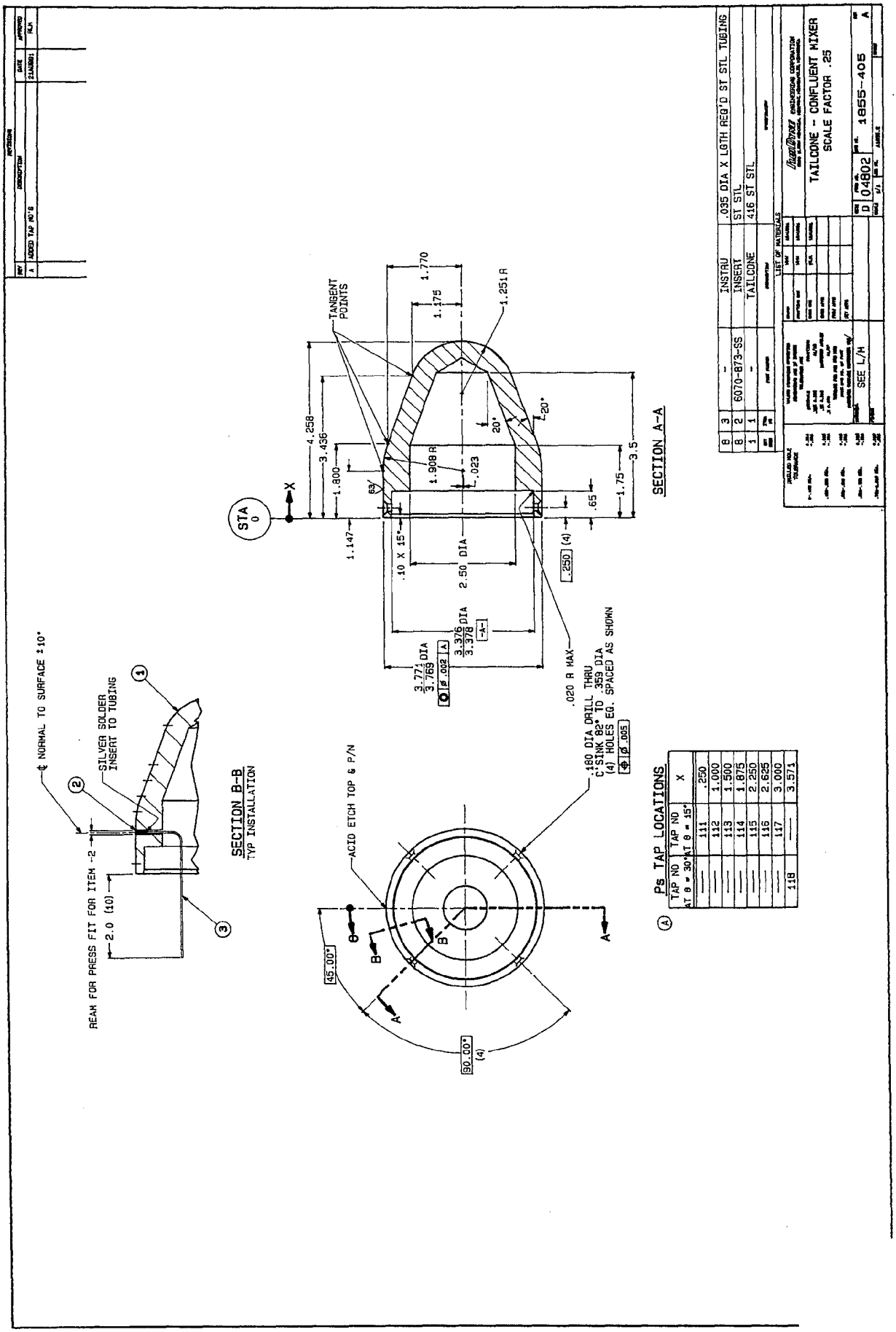

Figure A.10 Geometry of tail-cone for confluent mixer.

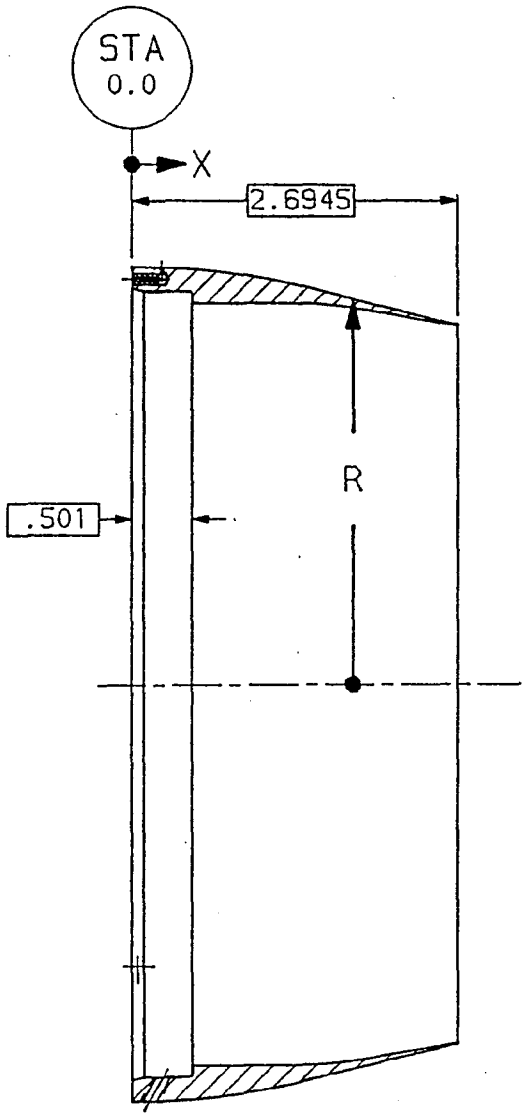

OUTER CONTOUR COORDINATES

ENG STA	X	R	R (INSP)
2.000	.50	3.415	3.418
5.672	1.418	3.268	3.273
8.112	2.028	3.118	3.124
10.544	2.636	2.969	2.973

INNER CONTOUR COORDINATES

ENG STA	X	R	R (INSP)
3.000	.75	3.135	3.133
7.924	1.981	3.074	3.0733
9.220	2.305	3.000	3.014

Figure A.11 Confluent mixer co-ordinates (CONF).

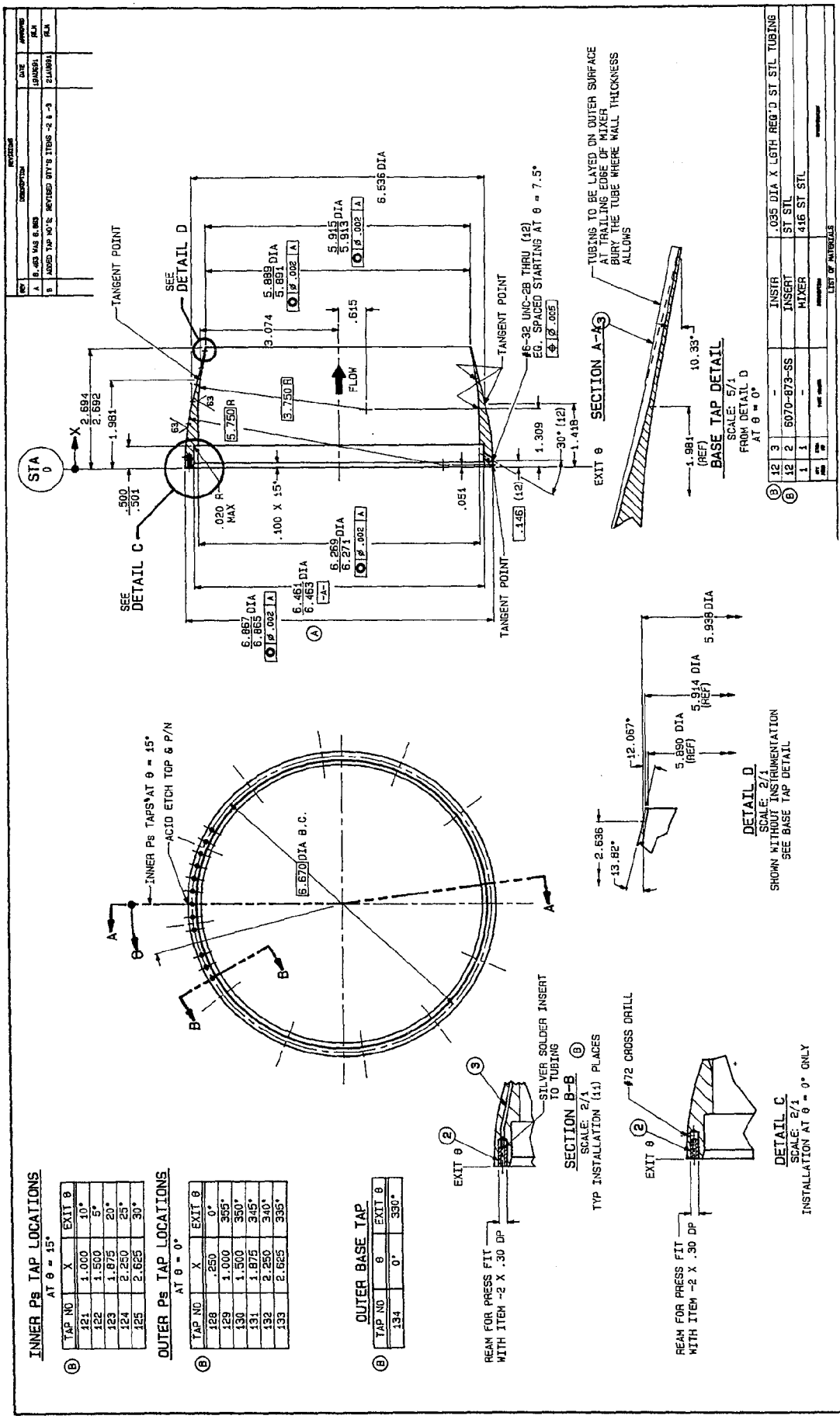

Figure A.12 Confluent mixer (CONF) details.

OUTER LOBE HILITE TABLE

LOBE #	R	R(INSP)
1	3.789	3.7929
2	3.789	3.7862
3	3.789	3.7890
4	3.789	3.7883
5	3.789	3.7863
6	3.789	3.7859
7	3.789	3.7876
8	3.789	3.7892
9	3.789	3.7885
10	3.789	3.7879
11	3.789	3.7871
12	3.789	3.7893

INNER LOBE HILITE TABLE

LOBE #	R	R(INSP)
A	2.343	2.3325
B	2.343	2.3381
C	2.343	2.3411
D	2.343	2.3429
E	2.343	2.3423
F	2.343	2.3438
G	2.343	2.3413
H	2.343	2.3430
I	2.343	2.3440
J	2.343	2.3416
K	2.343	2.3435
L	2.343	2.3430

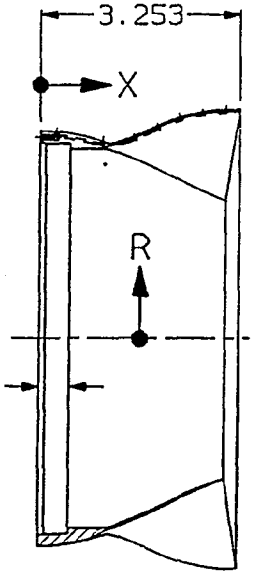

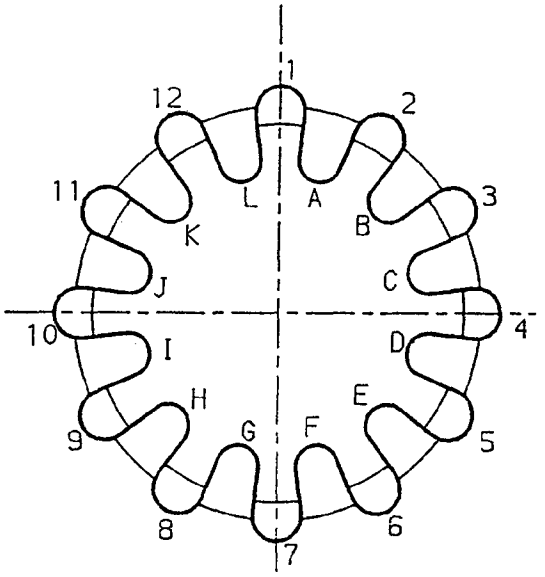

OUTER LOBE

OUTER CONTOUR 90° LOBE

X	R	R(INSP)
.155	3.430	3.4300
.530	3.392	3.3933
1.147	3.228	3.2309
1.780	3.467	3.4671
2.530	3.733	3.7318
3.155	3.800	3.7970

INNER CONTOUR 90° LOBE

X	R	R(INSP)
-	-	-
.530	3.135	3.1351
1.147	3.193	3.1893
1.780	3.432	3.4301
2.530	3.698	3.6981
3.155	3.765	3.7791

INNER LOBE

INNER CONTOUR 75° LOBE

X	R	R(INSP)
.750	3.138	3.1388
1.665	2.990	2.9845
2.155	2.736	2.7336
2.655	2.483	2.4789
2.905	2.372	2.3752

OUTER CONTOUR 75° LOBE

X	R	R(INSP)
.750	3.347	3.3483
1.665	3.028	3.0229
2.155	2.776	2.7743
2.655	2.522	2.5176
2.905	2.403	2.4057

Figure A.13 12 lobe mixer (12CL) co-ordinates.

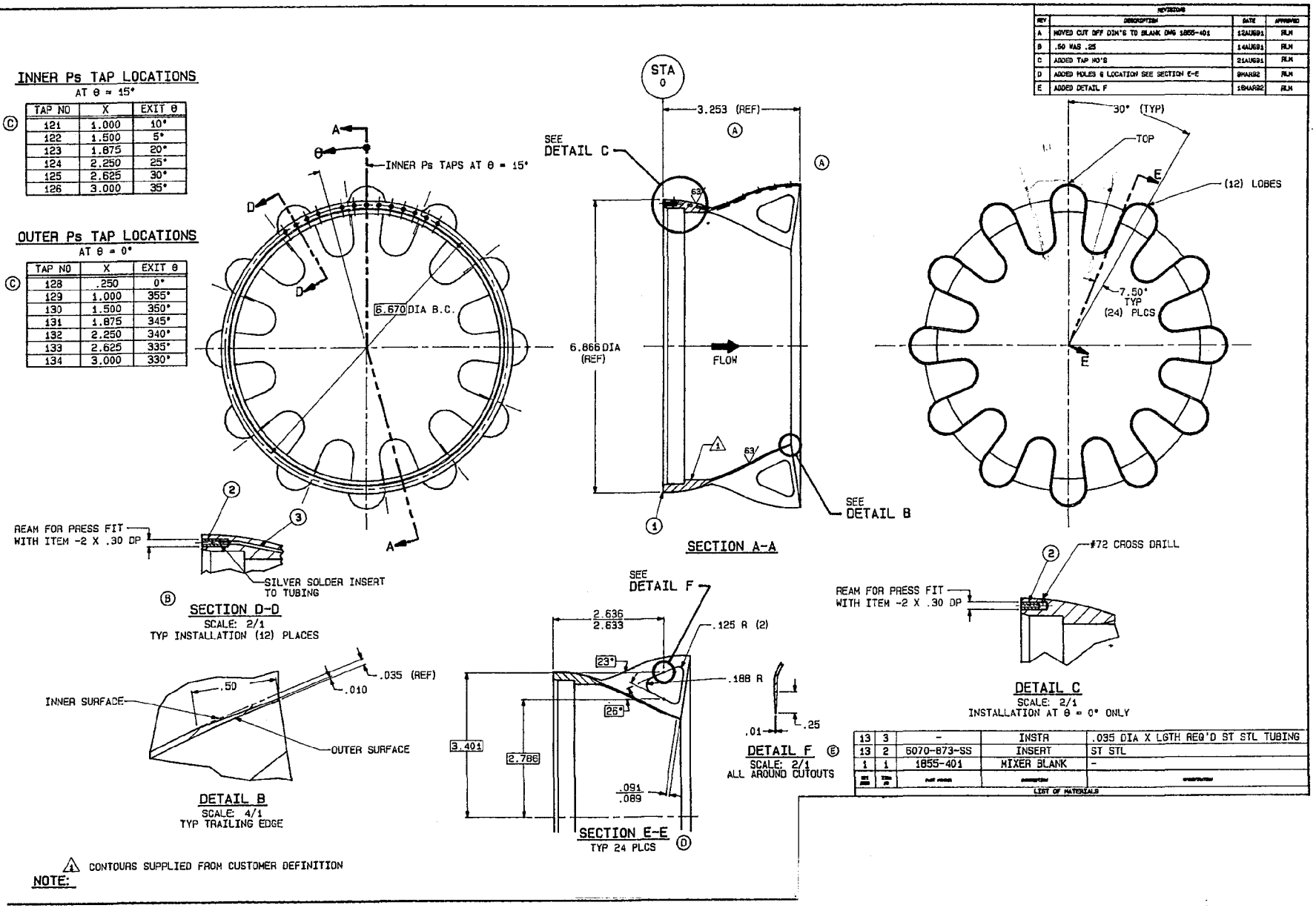

Figure A.14 12-lobe mixer with cut-outs (12CL) - details.

RADIUS AT LOBE EXIT (CROWN)

θ	R
0°	4.2802
30°	4.2805
60°	4.2789
90°	4.2791
120°	4.2787
150°	4.2805
180°	4.2798
210°	4.2803
240°	4.2798
270°	4.2797
300°	4.280
330°	4.2802

RADIUS AT LOBE EXIT (TROUGH)

θ	R
15°	2.2488
45°	2.2483
75°	2.2462
105°	2.2469
135°	2.2498
165°	2.2505
195°	2.2495
225°	2.2485
255°	2.2492
285°	2.2485
315°	2.2485
345°	2.2494

AT θ = 90° OUTER CROWN CONTOUR

X	R	R INSP
.300	3.4301	3.4291
.600	3.4027	3.4032
.900	3.3967	3.395
1.200	3.4215	3.4205
1.500	3.4726	3.4718
1.800	3.5636	3.5638
2.100	3.7262	3.7272
2.400	3.9503	3.9505
2.700	4.1232	4.1246
3.000	4.2332	4.2336

AT θ = 105° OUTER TROUGH CONTOUR

X	R INSP
.300	3.4295
.600	3.4013
.900	3.3337
1.200	3.2391
1.500	3.1228
1.800	2.9798
2.100	2.8105
2.400	2.622
2.700	2.4396
3.000	2.2754

AT θ = 90° INNER CROWN CONTOUR

X	R INSP
.800	3.1367
1.000	3.1292
1.200	3.1108
1.400	3.3084
1.600	3.3957
1.800	3.4972
2.000	3.6178
2.200	3.7608
2.400	3.9069
2.600	4.0341
2.800	4.1289

AT θ = 105° INNER TROUGH CONTOUR

X	R INSP
.800	3.1743
1.000	3.2087
1.200	3.2469
1.400	3.0753
1.600	3.0234
1.800	2.9346
2.000	2.8226
2.200	2.7011
2.400	2.576
2.600	2.4532
2.800	2.3366

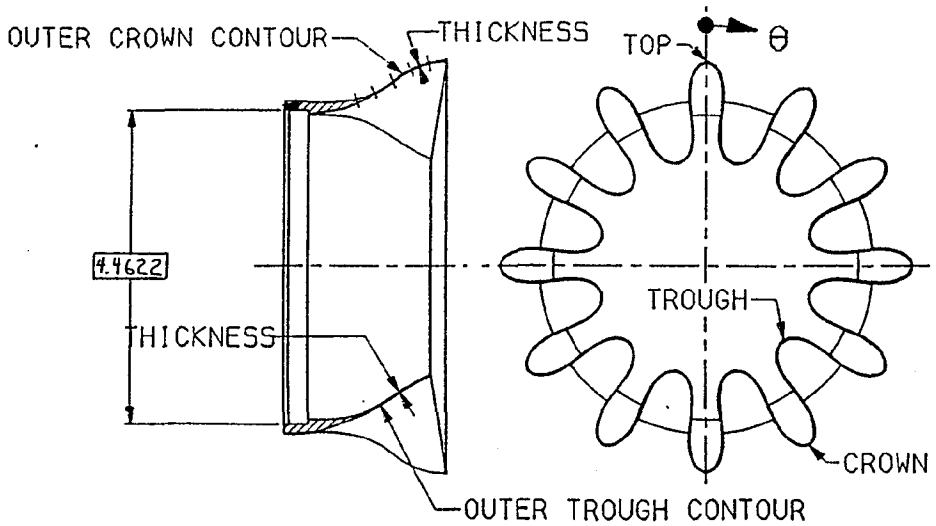

Figure A.15 12-lobe unscalloped mixer (12UH) co-ordinates.

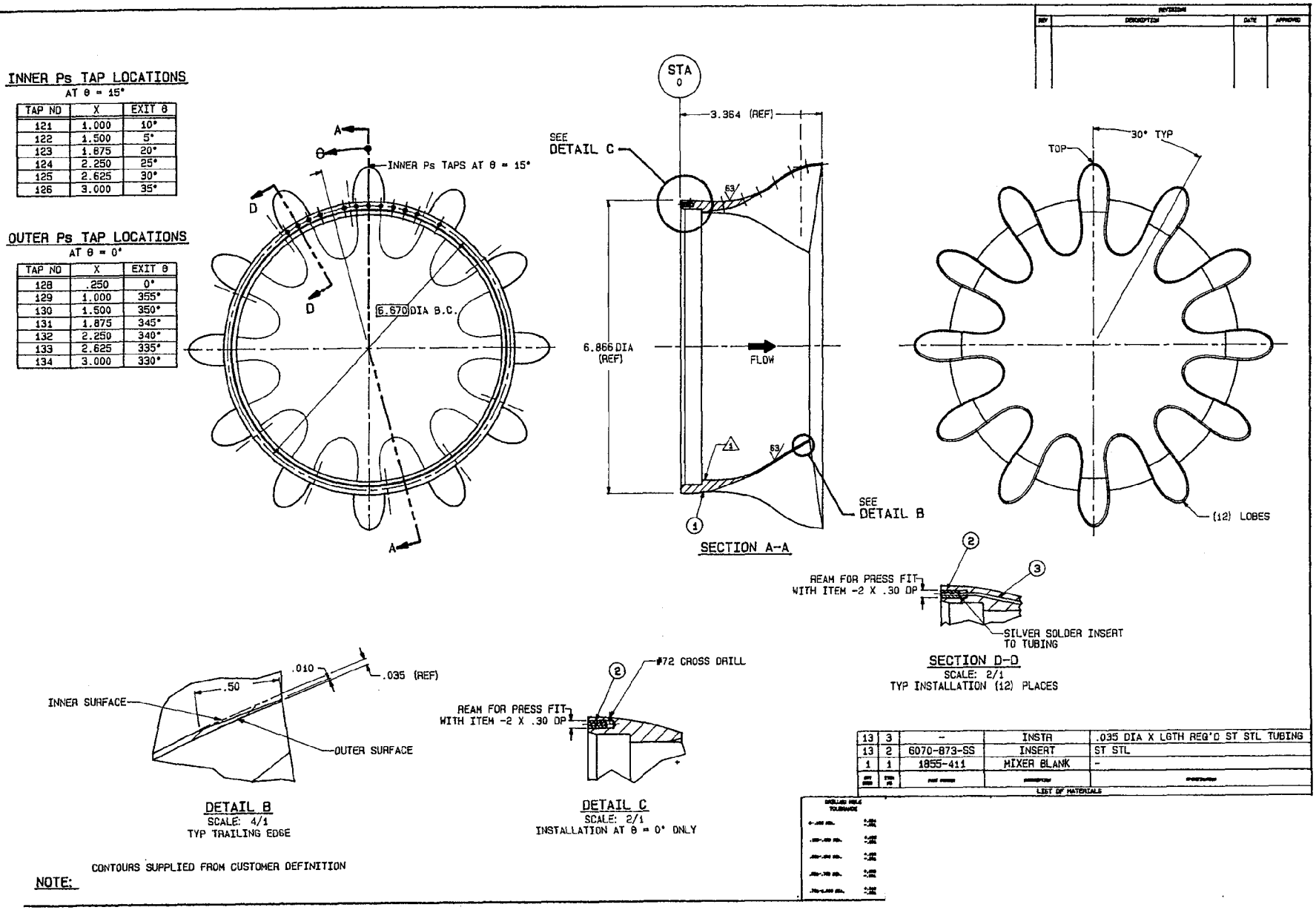

Figure A.16 12-lobe unscalloped mixer (12UH) - details.

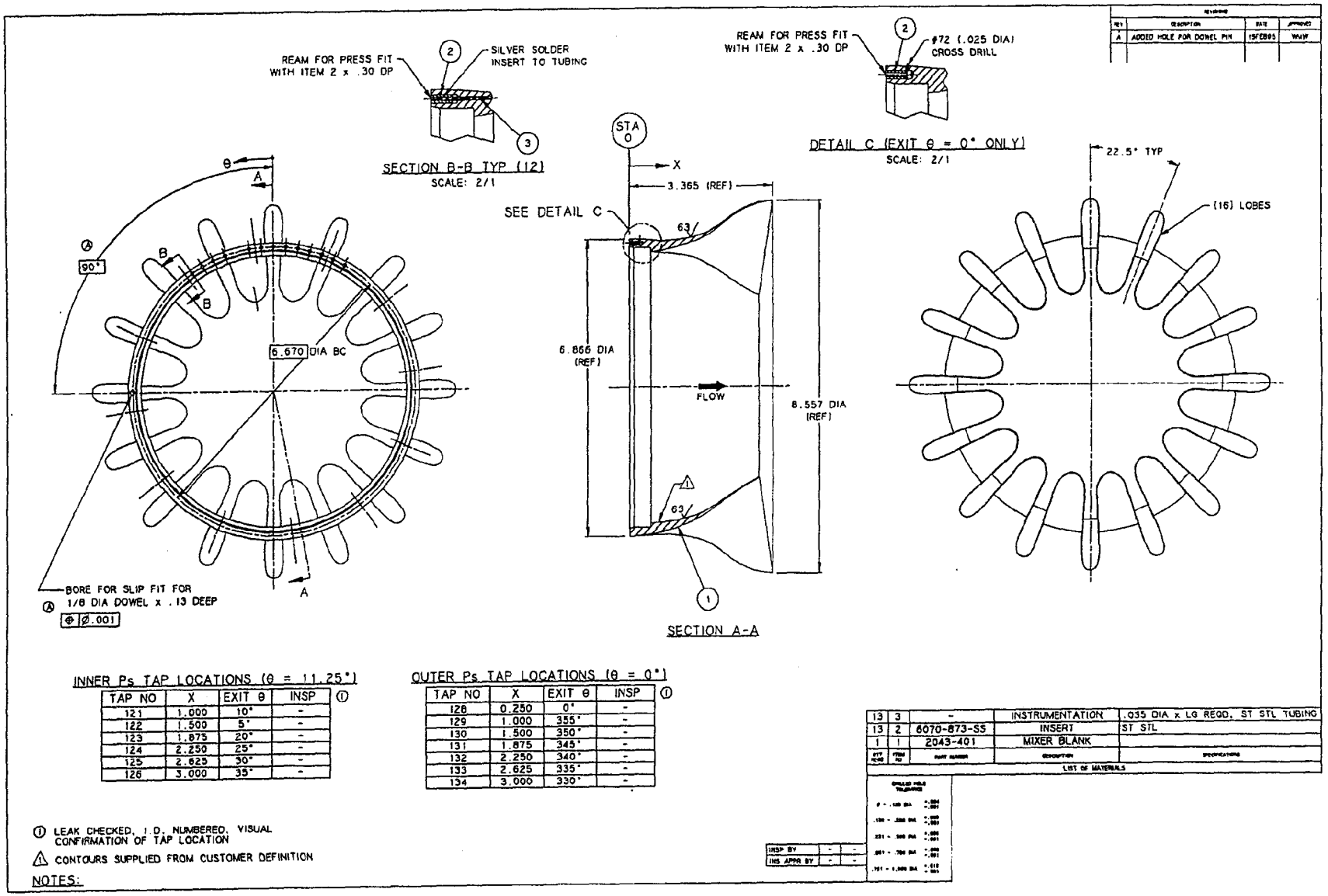

TAP NO	X	EXIT θ	INSP
121	1.000	10°	-
122	1.500	5°	-
123	1.875	20°	-
124	2.250	25°	-
125	2.625	30°	-
126	3.000	35°	-

TAP NO	X	EXIT θ	INSP
128	0.250	0°	-
129	1.000	355°	-
130	1.500	350°	-
131	1.875	345°	-
132	2.250	340°	-
133	2.625	335°	-
134	3.000	330°	-

Figure A.17 16-lobe unscalloped mixer (16UH) - details.

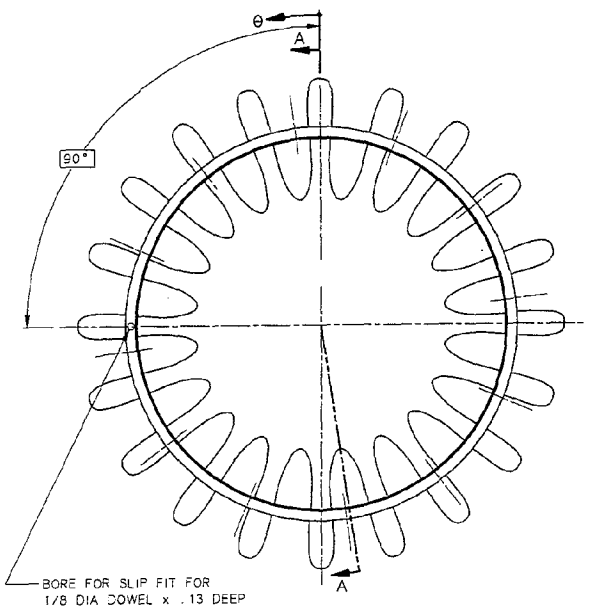

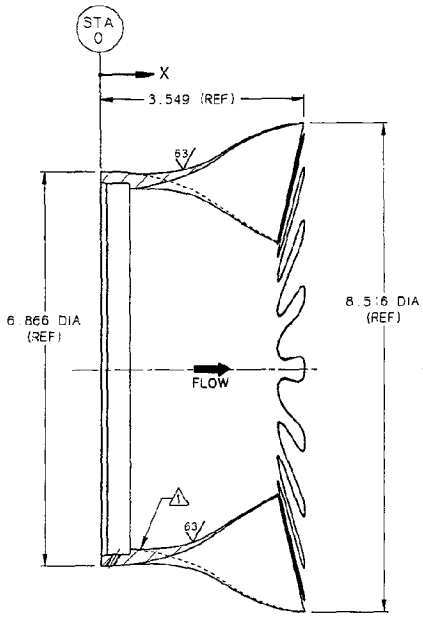

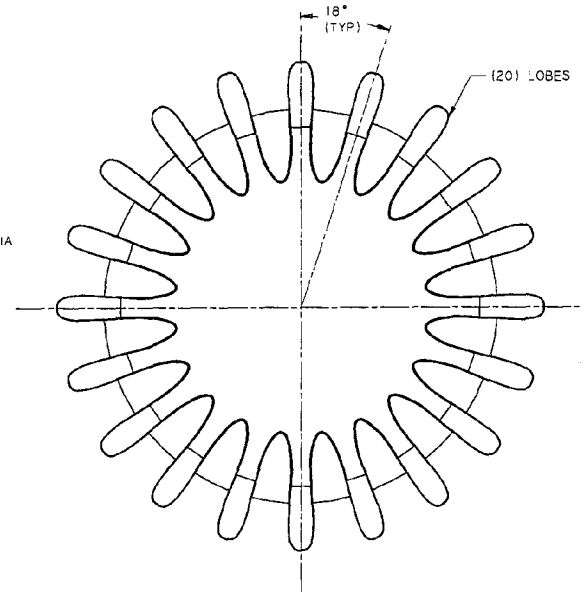

SECTION A-A

CROWN INSPECTION TABLE

X	R	THETA 0°	THETA 126°	THETA 234°
0.1861	3.4320	3.4310	3.4311	3.4313
0.5579	3.4070	3.4066	3.4061	3.4069
0.9235	3.3989	3.4009	3.3998	3.4003
1.2993	3.4360	3.4377	3.4370	3.4378
1.6633	3.5165	3.5204	3.5191	3.5205
2.0028	3.6658	3.6695	3.6684	3.6688
2.3208	3.8602	3.8618	3.8605	3.8609
2.6520	4.0288	4.0314	4.0306	4.0302
2.9998	4.1614	4.1628	4.1630	4.1631
3.3632	4.2385	4.2412	4.2418	4.2429

VALLEY INSPECTION TABLE

X	R	THETA 9°	THETA 135°	THETA 243°
0.8650	3.3835	3.3830	3.3813	3.3813
0.9950	3.3186	3.3189	3.3168	3.3172
1.3230	3.2235	3.2237	3.2214	3.2227
1.6440	3.0966	3.0939	3.0905	3.0914
1.9376	2.9170	2.9174	2.9137	2.9163
2.2208	2.7291	2.7282	2.7255	2.7300
2.5008	2.5461	2.5451	2.5421	2.5470
2.7858	2.3746	2.3774	2.3734	2.3848

WALL THICKNESS INSPECTION TABLE

X	THETA 0°	THETA 9°	THETA 180°	THETA 189°
2.0	0.052	0.043	0.050	0.049
2.5	0.024	0.024	0.025	0.024
3.0	0.023	0.027	0.021	0.025

⚠ CONTOURS SUPPLIED FROM CUSTOMER DEFINITION

NOTES:

REVISIONS					
ZONE	REV	DESCRIPTION	DATE	APPROVED	RLSE
-	A	ADDED INSPECTION TABLES	18OCT96	RLM	-
-	B	ADDED INPECTED VALUES	18OCT96	RLM	-

SIGNATURES		DAY-MO-YR
DRAWN	WMW	12AUG96
CHK	WMW	16SEP96
ENGR	RLM	16SEP96
RLSE	-	-
MFLM		
PART NO.	-	
TYPE/TITLE	-	

UNLESS OTHERWISE SPECIFIED DIMENSIONS ARE IN INCHES TOLERANCES ARE
DECIMALS .XXX ± .005, .XX ± .010, .X ± .030
FRACTIONS ± 1/16
MACHINING ANGLES ± 1/2°
THREADS PER FED STD H28
MARK DRAWING NO OR PART NO
MACHINED SURFACE ROUGHNESS 125
MATERIAL 2083-405
FINISH -
NHA -
CAD NO -
JOB NO L95-2083-167066

DRILLED HOLE TOLERANCE
0 - .125 DIA +.004 -.001
.126 - .250 DIA +.005 -.001
.251 - .500 DIA +.006 -.001
.501 - .750 DIA +.008 -.001
.751 - 1.000 DIA +.010 -.001

ASE AERO SYSTEMS ENGINEERING, INC.
358 EAST FILLMORE AVENUE, ST. PAUL, MINNESOTA 55107 • USA

FLUIDYNE AEROTEST GROUP
13525 SCHMIDT LAKE RD, PLYMOUTH, MINNESOTA 55446 • USA

DWG TITLE
20 LOBE MIXER
SCALE FACTOR 0.25
AADC

FACILITY SHT NO -

SIZE D | FSCM NO 54933 | DWG NO 2083-401 | REV B

WT (LB) ACTUAL - | SCALE 1/1 | SHEET -

Figure A.18 20-lobe mixer unscalloped mixer (20UH) - details.

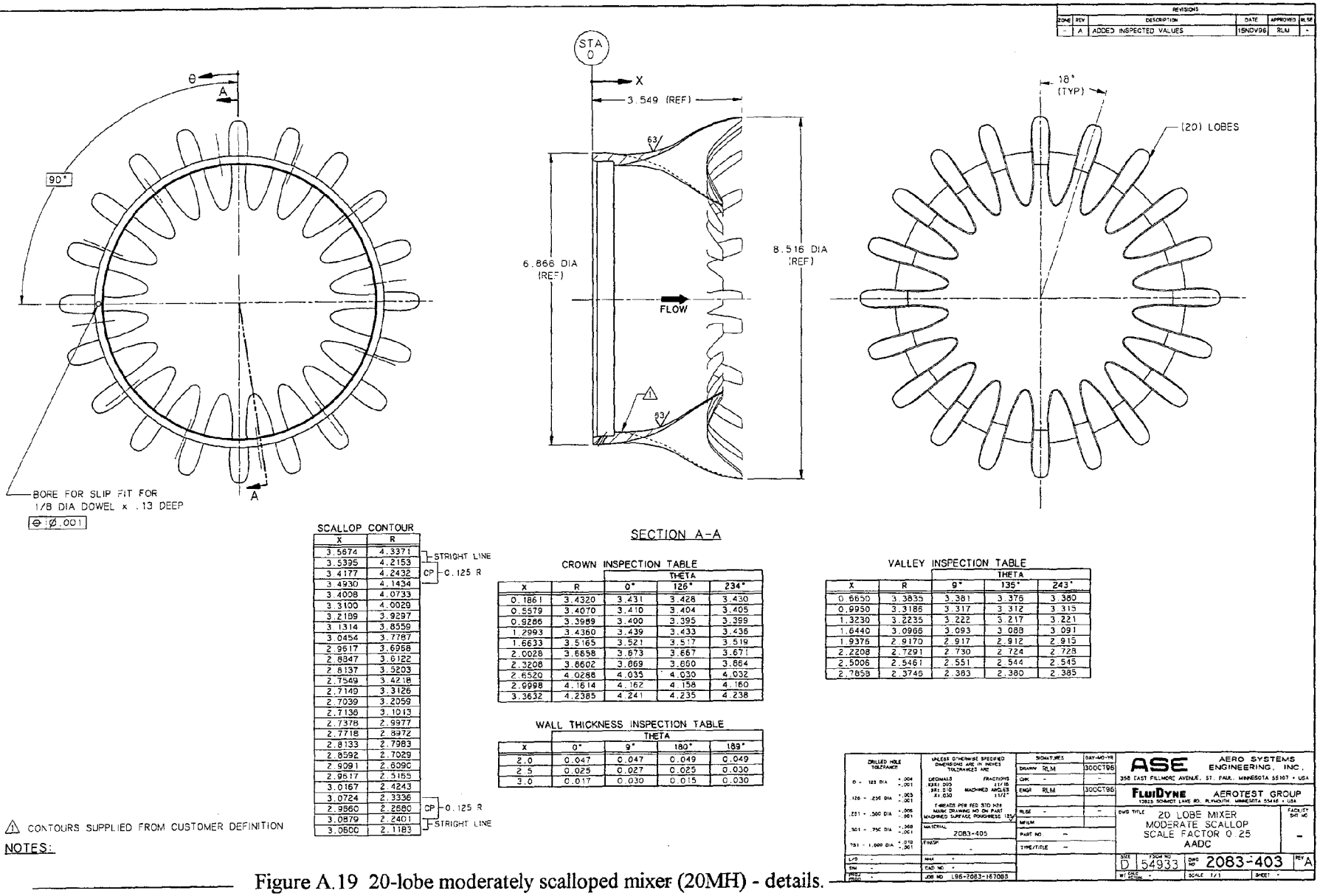

X	R
3.5674	4.3371
3.5395	4.2153
3.4177	4.2432
3.4930	4.1434
3.4008	4.0733
3.3100	4.0029
3.2189	3.9297
3.1314	3.8559
3.0454	3.7787
2.9617	3.6958
2.8847	3.6122
2.8137	3.5203
2.7549	3.4218
2.7140	3.3126
2.7039	3.2059
2.7136	3.1013
2.7378	2.9977
2.7718	2.8972
2.8133	2.7983
2.8592	2.7029
2.9091	2.6090
2.9617	2.5155
3.0167	2.4243
3.0724	2.3336
2.9860	2.2880
3.0879	2.2401
3.0600	2.1183

X	R	THETA 0°	126°	234°
0.1861	3.4320	3.431	3.428	3.430
0.5579	3.4070	3.410	3.404	3.405
0.9286	3.3989	3.400	3.395	3.399
1.2993	3.4360	3.439	3.433	3.436
1.6633	3.5165	3.521	3.517	3.519
2.0028	3.6658	3.673	3.667	3.671
2.3208	3.8602	3.869	3.860	3.864
2.6520	4.0288	4.035	4.030	4.032
2.9998	4.1614	4.162	4.158	4.160
3.3632	4.2385	4.241	4.235	4.238

X	R	THETA 9°	135°	243°
0.6650	3.3835	3.381	3.376	3.380
0.9950	3.3186	3.317	3.312	3.315
1.3230	3.2235	3.222	3.217	3.221
1.6440	3.0966	3.093	3.088	3.091
1.9376	2.9170	2.917	2.912	2.915
2.2208	2.7291	2.730	2.724	2.728
2.5006	2.5461	2.551	2.544	2.545
2.7858	2.3745	2.383	2.380	2.385

X	0°	THETA 9°	180°	189°
2.0	0.047	0.047	0.049	0.049
2.5	0.025	0.027	0.025	0.030
3.0	0.017	0.030	0.015	0.030

Figure A.19 20-lobe moderately scalloped mixer (20MH) - details.

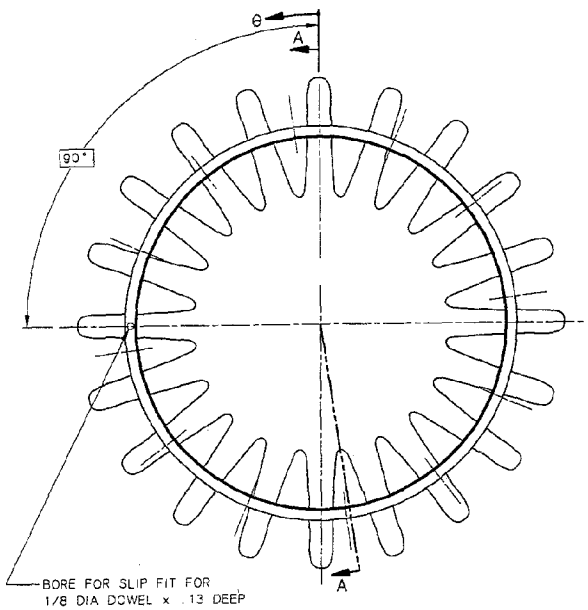

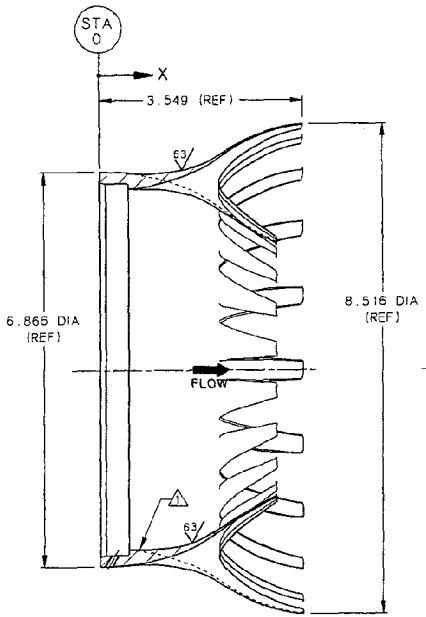

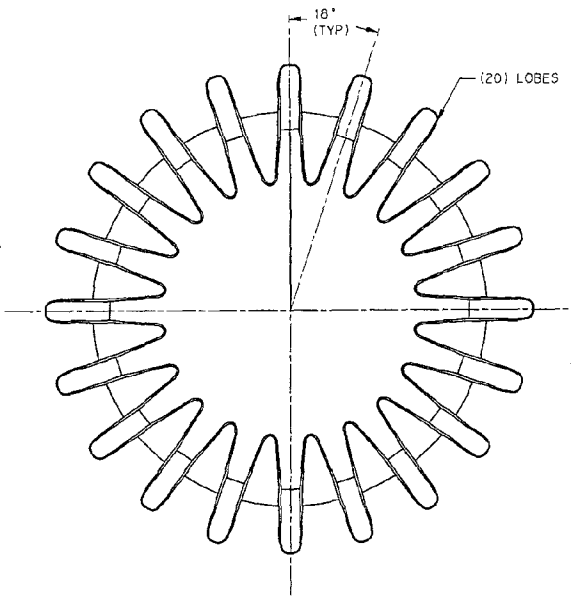

SCALLOP CONTOUR

X	R	
3.5574	4.3371	STRIGHT LINE
3.5389	4.2127	
3.4780	4.2267	CP 0.0625 R
3.4879	4.1650	
3.3211	4.1290	
3.1598	4.0779	
3.0021	4.0146	
2.8493	3.9416	
2.6991	3.8586	
2.5552	3.7676	
2.4176	3.6683	
2.2875	3.5580	
2.1721	3.4350	
2.0909	3.2868	
2.1129	3.1484	
2.1896	3.0306	
2.2853	2.9264	
2.3906	2.8295	
2.4984	2.7400	
2.6103	2.6526	
2.7251	2.5669	
2.8394	2.4832	
2.9544	2.3992	
3.0674	2.3148	
3.0295	2.2651	CP 0.0625 R
3.0904	2.2512	STRIGHT LINE
3.0512	2.0797	

SECTION A-A

CROWN INSPECTION TABLE

X	R	THETA 0°	THETA 126°	THETA 234°
0.1861	3.4326	3.4301	3.4327	3.4294
0.5579	3.4070	3.4053	3.4074	3.4040
0.9286	3.3989	3.4001	3.4002	3.3990
1.2993	3.4360	3.4382	3.4378	3.4368
1.6633	3.5165	3.5204	3.5211	3.5207
2.0028	3.6658	3.6700	3.6714	3.6708
2.3208	3.8602	3.8630	3.8629	3.8623
2.6520	4.0286	4.0310	4.0311	4.0311
2.9998	4.1614	4.1614	4.1632	4.1614
3.3632	4.2385	4.2401	4.2402	4.2391

WALL THICKNESS INSPECTION TABLE

X	THETA 0°	THETA 9°	THETA 180°	THETA 189°
2.0	0.060	0.058	0.060	0.061
2.5	0.035	0.038	0.034	0.039
3.0	0.030	0.030	0.032	0.029

VALLEY INSPECTION TABLE

X	R	THETA 9°	THETA 135°	THETA 243°
0.6650	3.3835	3.3822	3.3825	3.3833
0.9950	3.3186	3.3185	3.3203	3.3189
1.3230	3.2235	3.2244	3.2236	3.2233
1.6440	3.0966	3.0947	3.0955	3.0942
1.9376	2.9170	2.9195	2.9200	2.9190
2.2208	2.7291	2.7320	2.7281	2.7305
2.5006	2.5461	2.5474	2.5463	2.5468
2.7858	2.3746	2.3808	2.3785	2.3794

⚠ CONTOURS SUPPLIED FROM CUSTOMER DEFINITION

NOTES:

REVISIONS					
ZONE	REV	DESCRIPTION	DATE	APPROVED	RLSE
-	A	ADDED INSPECTED DIMENSIONS	1NOV96	RLM	-

DRILLED HOLE TOLERANCE

UNLESS OTHERWISE SPECIFIED DIMENSIONS ARE IN INCHES
TOLERANCES ARE
DECIMALS .XXX ±.005, .XX ±.010, .X ±.010
FRACTIONS 1/16
MACHINED ANGLES ±1/2°
THREADS PER FED STD H28
MASK DRAWING NO ON PART
MACHINED SURFACE ROUGHNESS 125
MATERIAL 2083-405
FINISH -

SIGNATURES	DAY-MO-YR
DRAWN RLM	10OCT96
CHK -	-
ENGR RLM	10OCT96
RLSE -	-
MFLM -	
PART NO -	
TYPE/TITLE -	

ASE AERO SYSTEMS ENGINEERING, INC.
358 EAST FILLMORE AVENUE ST. PAUL, MINNESOTA 55107 • USA

FLUIDYNE AEROTEST GROUP
13625 SCHMIDT LAKE RD. PLYMOUTH, MINNESOTA 55446 • USA

DWG TITLE 20 LOBE MIXER
DEEP SCALLOP
SCALE FACTOR 0.25
AADC

FACILITY DWG NO -

SIZE D | FSCM NO 54933 | DWG NO 2083-402 | REV A

WT SHT/TOTAL - | SCALE 1/1 | SHEET -

L/D -
DWG -
PROJ ENGR -

MFR -
CAD NO -
JOB NO L96-2083-167088

Figure A.20 20-lobe deeply scalloped mixer (20DH) - details.

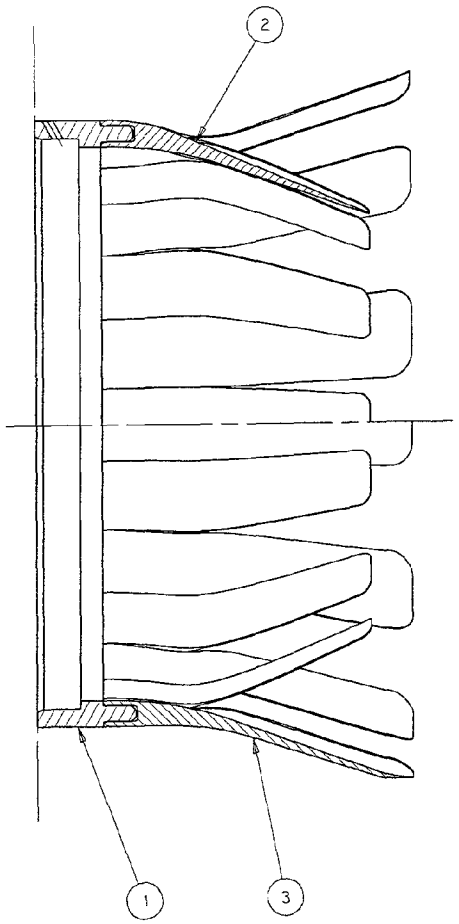

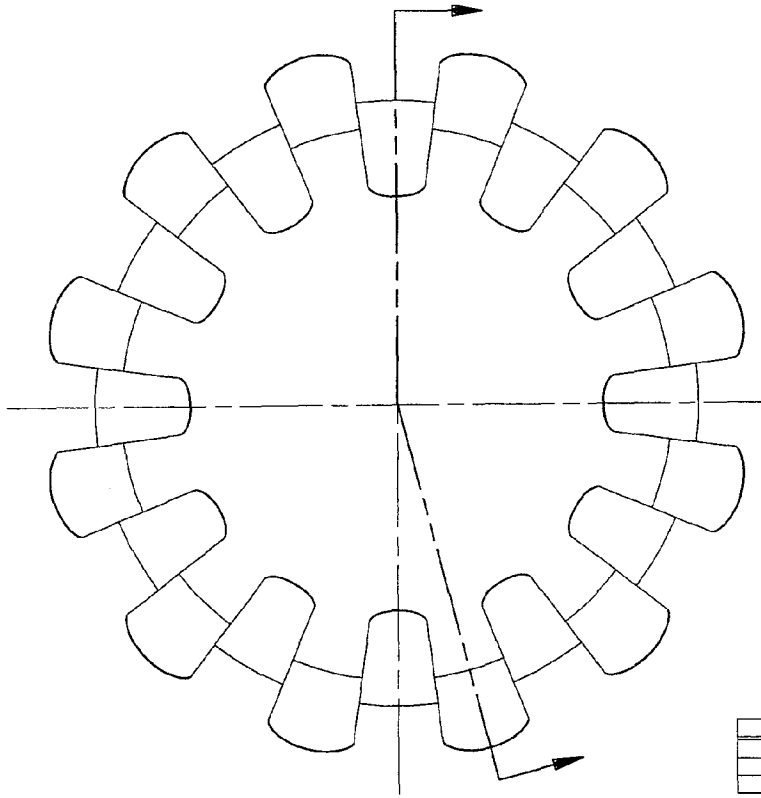

REVISIONS					
ZONE	REV	DESCRIPTION	DATE	APPROVED	RLSE
-	A	ADDED INSPECTED VALUES	26NOV96	RLM	-

CROWN INSPECTION TABLE

X	R	THETA 15°	THETA 195°
0.7500	3.4329	3.4298	3.4283
1.4754	3.4330	3.4290	3.4310
1.1118	3.4330	3.4300	3.4320
1.8371	3.4479	3.4434	3.4454
2.1941	3.5055	3.5010	3.5030
2.5427	3.6048	3.5990	3.6020
2.8868	3.7156	3.7100	3.7150
3.2318	3.8266	3.8200	3.8250
3.5767	3.9375	3.9305	3.9365
3.9222	4.0458	4.0380	4.0447
4.2840	4.0561	4.0495	4.0564

VALLEY INSPECTION TABLE

X	R	THETA 0°	THETA 180°
0.7500	3.4329	3.4310	3.4327
1.0772	3.4200	3.4208	3.4210
1.3958	3.3571	3.3600	3.3595
1.7036	3.2436	3.2490	3.2466
2.0035	3.1168	3.1240	3.1200
2.3045	2.9896	2.9974	2.9940
2.6068	2.8618	2.8693	2.8657
2.9079	2.7346	2.7427	2.7380
3.2074	2.6080	2.6170	2.6110
3.5087	2.4807	2.4880	2.4830
3.8104	2.3532	2.3563	2.3500

WALL THICKNESS INSPECTION TABLE

X	THETA 0°	THETA 15°	THETA 180°	THETA 195°
2.0	0.152	0.160	0.152	0.162
2.5	0.110	0.110	0.109	0.109
3.0	0.073	0.091	0.072	0.091

QTY	ITEM	PART NO	DESCRIPTION	SPECIFICATION
48	4	-	DOWEL PIN	1/8 Ø STAINLESS STEEL PIN X 3/8 LONG
12	3	2084-604	FAN EXPANSION LOBE	-
12	2	2084-603	CORE EXPANSION LOBE	-
1	1	2084-602	ADAPTER RING	-

LIST OF MATERIALS

1 MACHINE PARTS PER CUSTOMER SUPPLIED SURFACES

NOTE:

DRILLED HOLE TOLERANCE
0 - .125 DIA +.004 -.001
.125 - .250 DIA +.005 -.001
.251 - .500 DIA +.006 -.001
.501 - .750 DIA +.008 -.001
.751 - 1.000 DIA +.010 -.001

UNLESS OTHERWISE SPECIFIED DIMENSIONS ARE IN INCHES TOLERANCES ARE
DECIMALS XXX±.005 XX±.010 X±.030
FRACTIONS ±1/16
MACHINED ANGLES ±1/2°
THREADS PER FED STD H28
MARK DRAWING NO ON PART
MACHINED SURFACE ROUGHNESS 125
MATERIAL SEE LIST OF MATERIALS
FINISH -

SIGNATURES		DAY-MO-YR
DRAWN	RLM	18NOV96
CHK	-	-
ENGR	RLM	18NOV96
RLSE	-	-
MFLN		
PART NO	-	
TYPE/TITLE	-	

ASE AERO SYSTEMS ENGINEERING, INC.
358 EAST FILLMORE AVENUE, ST. PAUL, MINNESOTA 55107 • USA

FLUIDYNE AEROTEST GROUP
13825 SCHMIDT LAKE RD. PLYMOUTH, MINNESOTA 55445 • USA

DWG TITLE: TONGUE MIXER
AADC - TONGUE MIXER MODEL
FACILITY SHT NO: -

L/C	-	NHA	-
SIM	-	CAD NO	-
PROJ PROG	-	JOB NO	L96-2084-167091

SIZE F | FSCM NO 54933 | DWG NO 2084-605 | REV A
WT CALC ACTUAL - | SCALE 1/1 | SHEET -

Figure A.21(a) 12-pair tongue mixer (12TH) - co-ordinates.

REVISIONS					
ZONE	REV	DESCRIPTION	DATE	APPROVED	RLSE
-	-	-	-	-	-

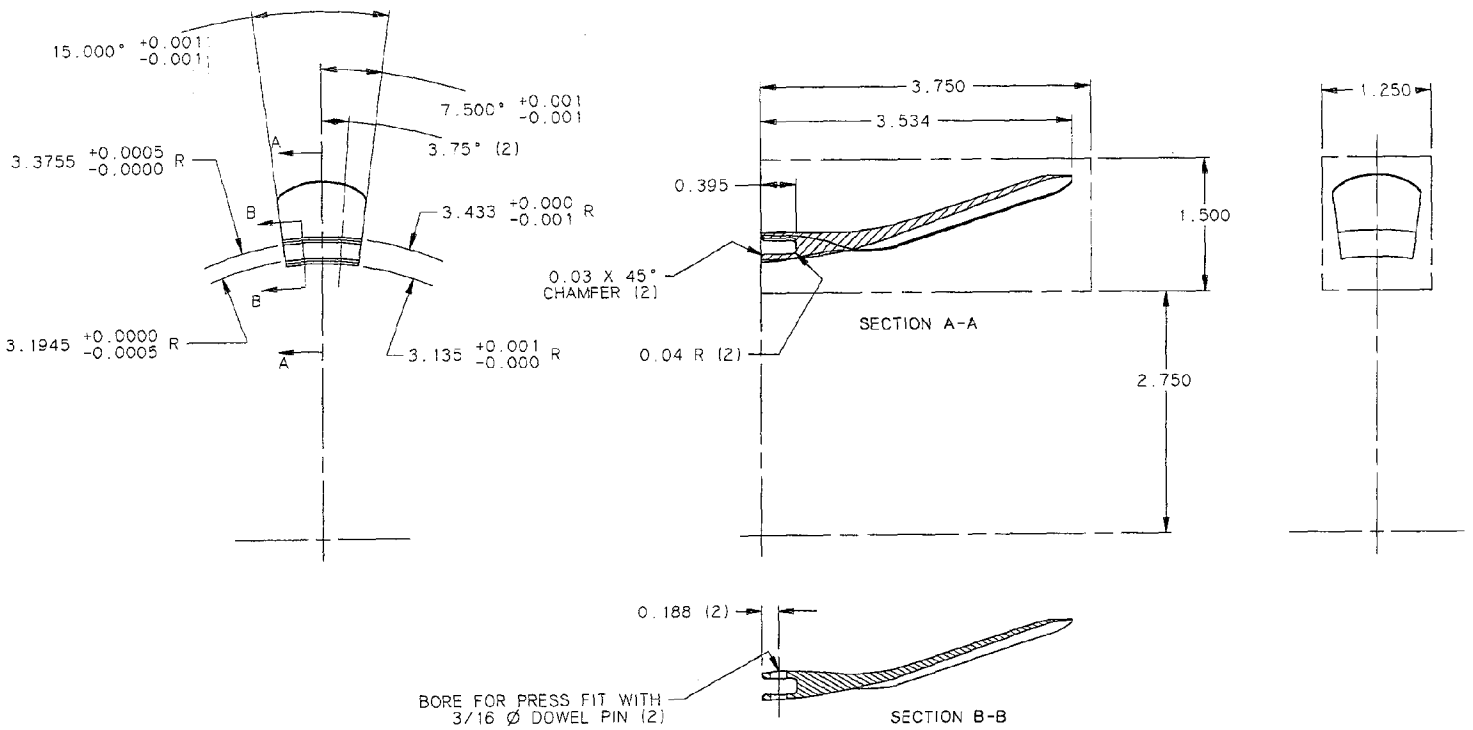

1 MACHINE PARTS PER CUSTOMER SUPPLIED SURFACES

NOTE:

Figure A.21(b) Top tongue details.

DRILLED HOLE TOLERANCE	
0 - .125 DIA	+.004 -.001
.126 - .250 DIA	+.005 -.001
.251 - .500 DIA	+.006 -.001
.501 - .750 DIA	+.008 -.001
.751 - 1.000 DIA	+.010 -.001

UNLESS OTHERWISE SPECIFIED DIMENSIONS ARE IN INCHES
TOLERANCES ARE
DECIMALS .XXX±.005 .XX±.010 .X±.030
FRACTIONS ±1/16 MACHINED ANGLES ±1/2°
THREADS PER FED STD H28
MARK DRAWING NO ON PART
MACHINED SURFACE ROUGHNESS 125
MATERIAL 416 STAINLESS STEEL
FINISH -

SIGNATURES		DAY-MO-YR
DRAWN	RLM	28OCT96
CHK	-	-
ENGR	RLM	31OCT96
RLSE	-	-
MFILM		
PART NO.	-	
TYPE/TITLE	-	

L/O	-	NHA	-
SIN	-	CAD NO	-
PROJ PROD	-	JOB NO	L96-2084-16709.1

ASE AERO SYSTEMS ENGINEERING, INC.
358 EAST FILLMORE AVENUE, ST. PAUL, MINNESOTA 55107 • USA

FLUIDYNE AEROTEST GROUP
13825 SCHMIDT LAKE RD. PLYMOUTH, MINNESOTA 55448 • USA

DWG TITLE
CORE EXPANSION LOBE
AADC - TONGUE MIXER MODEL

FACILITY SHT NO

SIZE	FSCM NO	DWG NO	REV
F	54933	2084-603	-

WT CALC ACTUAL - SCALE 1/1 SHEET -

REVISIONS					
ZONE	REV	DESCRIPTION	DATE	APPROVED	RLSE
-	-	-	-	-	-

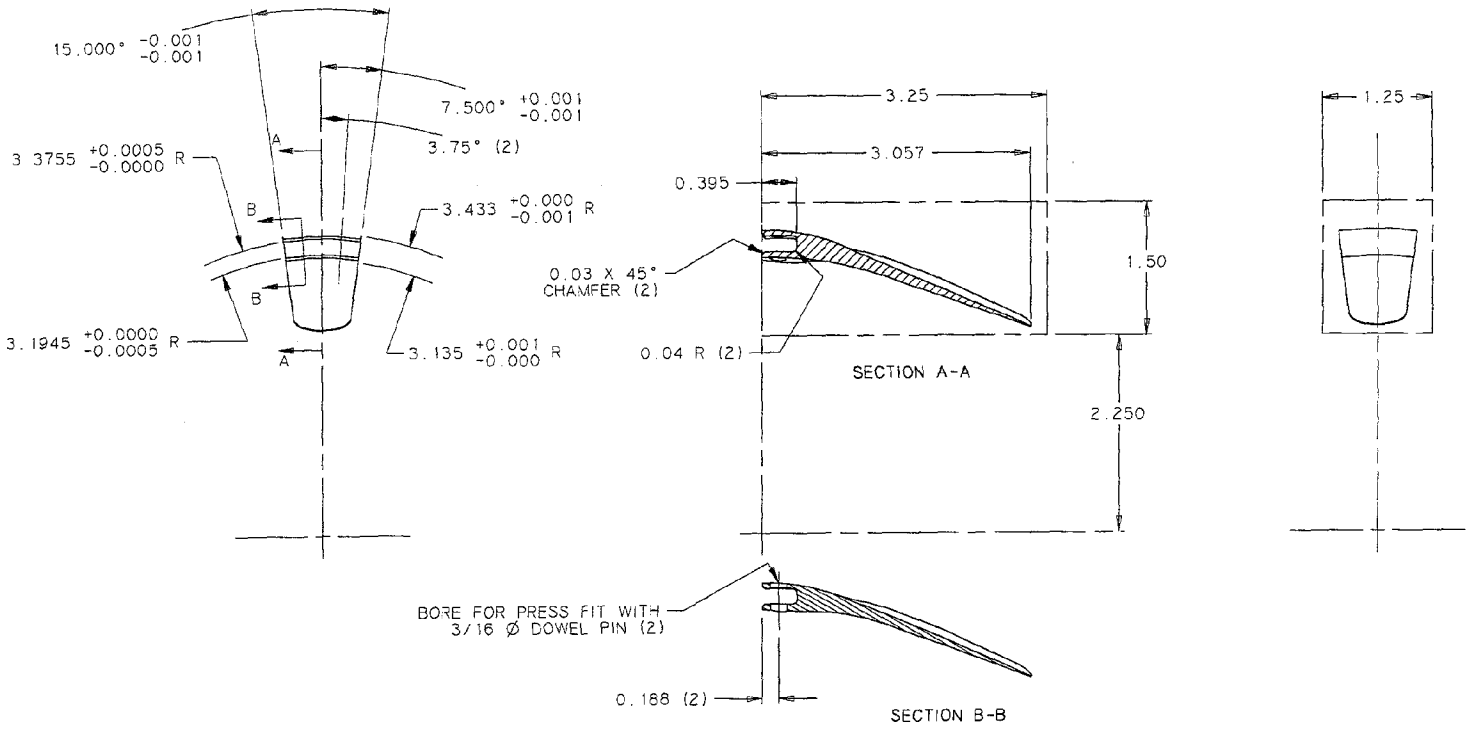

1 MACHINE PARTS PER CUSTOMER SUPPLIED SURFACES

NOTE:

Figure A.21(c) Bottom tongue details.

DRILLED HOLE TOLERANCE	
0 - .125 DIA	+.004 -.001
.126 - .250 DIA	+.005 -.001
.251 - .500 DIA	+.005 -.001
.501 - .750 DIA	+.008 -.001
.751 - 1.000 DIA	+.010 -.001

UNLESS OTHERWISE SPECIFIED DIMENSIONS ARE IN INCHES TOLERANCES ARE
DECIMALS .XXX± .005 .XX± .010 .X± .030
FRACTIONS ±1/16 MACHINED ANGLES ±1/2°
THREADS PER FED STD H28
MARK DRAWING NO. ON PART
MACHINED SURFACE ROUGHNESS 125
MATERIAL 416 STAINLESS STEEL
FINISH -

SIGNATURES		DAY-MO-YR
DRAWN	RLM	28OCT96
CHK	-	-
ENGR	RLM	31OCT96
RLSE	-	-
MFILM		
PART NO.	-	
TYPE/TITLE	-	

ASE AERO SYSTEMS ENGINEERING, INC.
358 EAST FILLMORE AVENUE, ST. PAUL, MINNESOTA 55107 • USA

FLUIDYNE AEROTEST GROUP
13625 SCHMIDT LAKE RD. PLYMOUTH, MINNESOTA 55446 • USA

DWG TITLE: FAN EXPANSION LOBE
AADC - TONGUE MIXER MODEL
FACILITY SHT NO: -

L/O	-	NHA	-
SIM	-	CAD NO	-
PROJ PROG	-	JOB NO	L96-2084-167091

SIZE F | FSCM NO 54933 | DWG NO 2084-604 | REV -
WT CALC ACTUAL - | SCALE 1/1 | SHEET -

Appendix B

Refraction Correction Procedure for Free-Jet/Ambient Shear-Layer and Angular Interpolation Scheme

When we have a free-jet facility of finite diameter surrounding the model jet to simulate aircraft forward speed effects, a shear-layer is created between the free-jet and the ambient quiescent atmosphere in the test cell. Sound from the model jet then refracts through this shear-layer before being recorded by the microphones which are outside the free-jet in the test cell. This shear layer is not present in the actual flyover case. In order to retrieve the original directivity of sound from the model jet we then need to account or correct for this refraction. This correction procedure is summarized below, as given to Rolls-Royce Allison by Dr. James Bridges of NASA Lewis Research Center. NASA has processed all the acoustic data using this procedure which forms part of the overall data processing scheme shown in Figure 3.5.

The free-jet shear-layer refraction correction is taken from Ahuja et al[15]. It is similar to the "Amiet" method with the main difference being that NASA has generalized the algorithm to work for narrow-band data instead of third octave spectra. In this method, one starts by considering the SPL of each frequency band (narrow-band) and each microphone individually. One assumes a location for the source of this sound and the location of the shear-layer based on the geometry and flow-conditions of the free-jet and the model. One also assumes that the shear-layer is infinitely thin, and use is made of acoustic ray theory, an assumption that was verified in Ahuja et al[15] for frequencies generated with a relatively small speaker. From this geometry the refraction that the sound underwent to reach the microphone is calculated and the original direction of the sound during propagation between model and free-jet/ambient shear-layer is found. This will not, in general, correspond to a location where a microphone exists. In fact, when a source location model is used, each frequency for a given microphone will have been directed to a unique angle because it originates from a different place. In addition, the difference between the geometric distance from the source to the microphone and the actual path-length that the sound traveled due to the refraction is calculated. This procedure of finding the original angle and the refracted path-length as a function of refracted angle is done for each frequency. Now if the attenuation due to spherical spreading over the refracted path-length is factored out, then one retrieves the original directivity of the jet as it would appear inside the free-jet. This is the same as the directivity in the reference frame of the nozzle.

As mentioned above, since we can assume that the effective source location is different for each frequency band, the directivity is known at different locations for each frequency band. To take this back to a common set of observer locations, the directivity of each frequency band is interpolated (in SPL) onto a convenient regular array, corresponding to an arc with 5 degrees intervals for this test. There are situations where sound at some frequencies are refracted strongly enough that none of the measured sound covers the interpolated array.

In this case, the data is set to "unknown" and is not used in the processing. In addition, for bands in which the data was not sufficiently above the background level or for which the microphone was found to be suspect in post-test analysis, the data was set to "unknown". This is generally a problem for high free-jet Mach numbers, low frequencies, and shallow angles, which have little impact on overall evaluation of noise.

Interpolation gives values only for those angles where sufficient information is known; data is never extrapolated outside the measured information. If insufficient data is available over a region because of background noise, then the whole region is taken as "unknown" in the interpolation scheme rather than filling in values based on very limited information. Specifically the algorithm calls for at least as many good points as unknown points in a region before the interpolating spline is evaluated for output. For example, if at the end of the array of N microphones a measured value exists at angle N but the two measurements at N-1 and N-2 were suspect while the measurement at N-3 was good, SPL values will be recorded as "unknown" for any locations which lie at angles greater than that of microphone N-3.

Interpolation of SPL between angles for a given frequency band is a required step and is not used for smoothing. The interpolation is done by strict cubic spline with zero derivative knots at the ends. Tests have shown this choice of interpolating polynomial to capture, but not overshoot, peaks very well, as opposed to linear interpolation which showed some smoothing. Interpolation can be performed on either SPL (in dB) or sound pressure (in Pascals squared). The final result will be affected by the choice, but again tests found that for representative spectra, sound power differences due to interpolation were less than 0.05 dB. Using the log scale makes it easier for the interpolating function to fit without spurious excursions, although it biases the error to the high side.

Because the source distribution is actually unknown and probably different for each jet, NASA has adopted as standard procedure the assumption that the sound sources for all frequencies is at the center of the nozzle exit plane. This is highly incorrect for low frequencies but without better information we prefer this simple model over an arbitrary one. This was mostly driven by the need to compare results with other facilities which have other shear-layer correction schemes. Data being compared came from G.E.'s Cell 41, Boeing's LSAF, NASA Ames' 40 x 80 wind-tunnel, NASA Langley's JNL Quiet Flow Facility, and NASA Lewis' APL. This source location assumption has been made for all NASA/Industry programs. However, until a better model comes up, this will remain an open issue.

Appendix C

Refraction Angle, Convection Angle and Transmission Coefficient Changes Due to Free-Jet Speed Changes

We extend Candel's analysis[21] to moving flows on *both* sides of a thin shear-layer represented by a thin straight vortex sheet at y = 0, x > 0 as shown in figure 5.25. In region 1, y > 0, the speed of sound is c_1 and the flow Mach number is M_1. In region 2, y < 0, the speed of sound is c_2 and the Mach number is M_2. The pressure fluctuations are $p_i\exp(-i\omega t)$, $Rp_r\exp(-i\omega t)$ and $Tp_t\exp(-i\omega t)$ for the incident, reflected and transmitted waves, respectively, and $v(x)\exp(-i\omega t)$ is the y-displacement of the vortex-sheet where ω is frequency, t = time and $i = \sqrt{-1}$. The incident wave has a normal direction ϕ_1; the reflected wave propagates in the direction $-\phi_1$, and the transmitted wave in the direction ϕ_2 (see figure 5.25):

$$p_i = \exp\left(-i\frac{k_1 x\cos\phi_1}{1-M_1\cos\phi_1} - i\frac{k_1 y\sin\phi_1}{1-M_1\cos\phi_1}\right)$$

$$p_r = \exp\left(-i\frac{k_1 x\cos\phi_1}{1-M_1\cos\phi_1} + i\frac{k_1 y\sin\phi_1}{1-M_1\cos\phi_1}\right)$$

$$p_t = \exp\left(-i\frac{k_2 x\cos\phi_2}{1-M_2\cos\phi_2} - i\frac{k_2 y\sin\phi_2}{1-M_2\cos\phi_2}\right)$$

$$k_1 = \omega/c_1, k_2 = \omega/c_2$$

$$0 < \phi_1 < \pi.$$

All waves have the same wave-number vector components in the x-direction:

$$\frac{k_1\cos\phi_1}{1-M_1\cos\phi_1} = \frac{k_2\cos\phi_2}{1-M_2\cos\phi_2}$$

This leads to the first useful relation between angles which denotes *pure refraction* effects:

$$\cos\phi_2 = \frac{(c_2/c_1)\cos\phi_1}{1-\cos\phi_1(M_1-(c_2/c_1)M_2)} \qquad (C.1)$$

We obtain ϕ_{20}, which is ϕ_2 for $M_2 = 0$, from above as:

$$\cos\phi_{20} = \frac{(c_2/c_1)\cos\phi_1}{1-M_1\cos\phi_1} \qquad (C.2)$$

Hence, ϕ_2 can be written directly in terms of ϕ_{20} without involving M_1 or ϕ_1 as:

$$\cos\phi_2 = \frac{\cos\phi_{20}}{1+M_2\cos\phi_{20}} \qquad (C.3)$$

And, from eqn (C.2), ϕ_1 can be found in terms of ϕ_{20} as:

$$\cos\phi_1 = \frac{\cos\phi_{20}}{\frac{c_2}{c_1}+M_1\cos\phi_{20}} \qquad (C.4)$$

To find the effect of *convection* of the refracted wave-fronts on the convected angle $\Delta\phi_c$ (see figure 5.25) we apply the sine-rule to the velocity triangle in region 2 which includes the transmitted ray and the refracted wave-front normal direction:

$$\frac{U_2}{\sin\Delta\phi_c} = \frac{c_2}{\sin(\pi-(\phi_2+\Delta\phi_c))}$$

This gives, after some manipulation, the second desired angular relation:

$$\tan \Delta\phi_c = \frac{M_2 \sin \phi_2}{1 - M_2 \cos \phi_2} \qquad \text{(C.5)}$$

The numerical results for these angles have been given in Table 5.1, plotted in figure 5.27 and discussed in the main text. As a further independent check on these calculations, we spot-checked it with values obtained from Thompson's ray equations (eqn. (12), Ref. 23) where the "generalized Snell's law of refraction" for moving media is derived by a wholly different method using ray-paths obtained from the characteristic *eikonal* equations. The values for the refracted ray angle, Φ_2, for given "static" ray-angles, ϕ_{20} , matched exactly with the ones given in Table 5.1.

To obtain the transmission coefficient T and reflection coefficient R, the conditions of continuity of pressure and particle displacement at the interface (vortex-sheet) must be applied:

$$(p_i + Rp_r)_{y=0_+} = (Tp_t)_{y=0_-}$$

$$\left(-i\omega + U_1 \frac{\partial}{\partial x}\right)^2 v(x) = -\frac{1}{\rho_1}\frac{\partial}{\partial y}(p_i + Rp_r)_{y=0_+}$$

$$-\left(-i\omega + U_2 \frac{\partial}{\partial x}\right)^2 v(x) = -\frac{1}{\rho_2}\frac{\partial}{\partial y}(Tp_t)_{y=0_-}$$

where ρ is density. Manipulation of these three equations with the previous result from the equality of x-component of the wave-number vector leads finally to the following relations between T and R:

$$1 + R = T$$

$$1 - R = \frac{\rho_1 {c_1}^2}{\rho_2 {c_2}^2}\frac{\sin 2\phi_2}{\sin 2\phi_1} T \qquad \text{(C.6)}$$

This yields:

$$T = \frac{2}{1 + \frac{\rho_1 {c_1}^2}{\rho_2 {c_2}^2}\frac{\sin 2\phi_2}{\sin 2\phi_1}} \qquad \text{(C.7)}$$

The static pressures on both sides of the interface are equal and consequently the ratio $\frac{\rho_1 {c_1}^2}{\rho_2 {c_2}^2}$ reduces, for perfect gases, to γ_1/γ_2, where γ is the ratio of specific heats. The final relation of the transmission coefficient T in terms of ϕ_2 and ϕ_1 is the same as in Candel[21]; however, the difference is in the relation between ϕ_2 and M_2, M_1 as derived in eqn (C.1).

In order to examine the effect of M_2 on the transmission coefficient T for a given incident wave angle ϕ_1 we can use equations (C.7) and (C.1) for some assumed values of flow in region 1. However, since ϕ_1 and ϕ_{20} have a one-to-one relation from eqn (C.2) and ϕ_{20} is the observable angle when no free-jet flow exists we will discuss the changes in T due to free-jet Mach numbers as function of ϕ_{20}. Thus for a given value of ϕ_{20} we first find ϕ_1 and ϕ_2 from eqns. (C.4) and (C.3) respectively and substitute that in eqn (C.7) to find T. We will also assume for simplicity that $\gamma_1/\gamma_2 = 1$. Figure C.1 shows a sample of plots of T Vs θ_{20} (= ϕ_{20}) for two typical cases (M_1 = 0.8, c_2/c_1 = 1.0) and (M_1 = 0.8 , c_2/c_1 = 0.8), for a range of M_2 values from 0.0 to 0.3. This is shown for a range of θ_{20} values from 0 to 180 degrees. A note on interpreting figure C.1: For a given ϕ_{20} the value for T for some parameter M_2 means the transmission coefficient for the corresponding refracted wave in region 2 whose angle is ϕ_2 .

Figure C.1 shows that the variation in the transmission coefficient T for a given θ_{20} (or incident wave) due to free-jet variations from

0.0 to 0.3 is fairly small in the angular range above 40° or so; below 40° the difference between the no free-jet flow case ($M_2 = 0$), and the $M_2 > 0$ case can be large. The values of θ_{20} above approximately 125° in Figure C.1(a) correspond to the "zone of silence." Our acoustic test data range varies from 55° to 165°. So it is of some interest to examine what the small differences in T from the no free-jet flow case in that range mean in terms of SPL differences in dB which is given by $20*\log(T(M_2)/T(M_2=0))$.

Figures C.2(a) and (b) show this SPL difference as a function of M_2 with θ_{20} (or ϕ_{20}) held fixed for a wide range of region 1 flow parameters. From these figures we can make the following general observations:

1. The SPL difference is no more than about 0.4 dB for the angular range investigated (60° to 110°) and is smaller for angles closer to 90°.
2. At 90° there is no SPL difference at different M_2 , and any M_1, c_1, c_2 value. This can be proven mathematically from the above formulae. That is, T = 1 for ϕ_{20} = 90° and the corresponding refracted wave-normal angle at any M_2 value, regardless of region 1 values.
3. Hotter the region 1 flow (lower the c_2/c_1 value) the smaller is the SPL difference.
4. The SPL difference is almost linear with M_2 in this range for a given value of ϕ_{20} . Thus, the smaller the M_2 value the smaller is the SPL difference from the static case $M_2 = 0$.

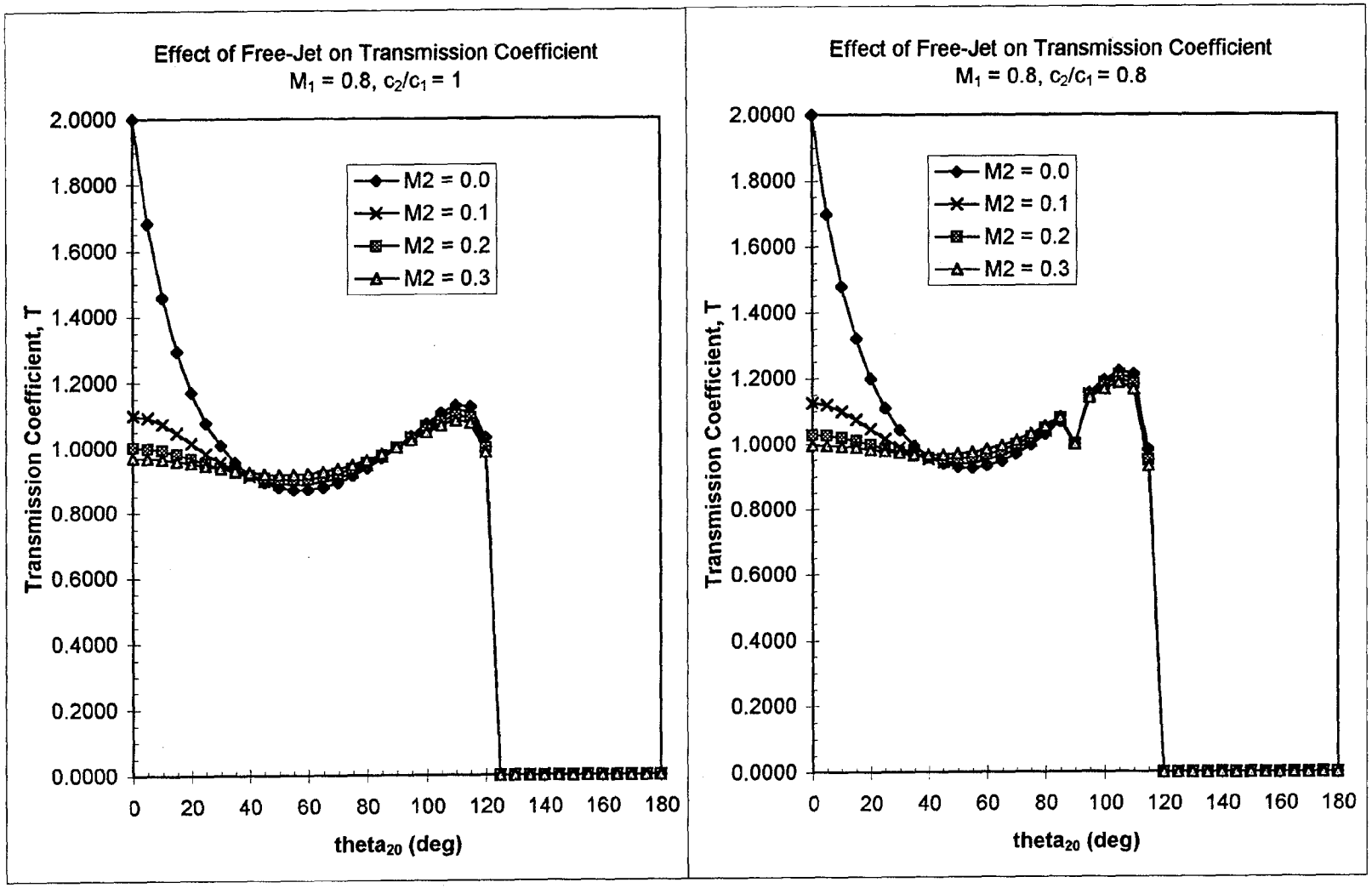

Figure C.1 Effect of free-jet Mach number (M2) on transmission coefficient at different "static" angles ($theta_{20}$) for two different combinations of model-jet Mach number (M1) and ratio of speeds of sound (c_2/c_1).

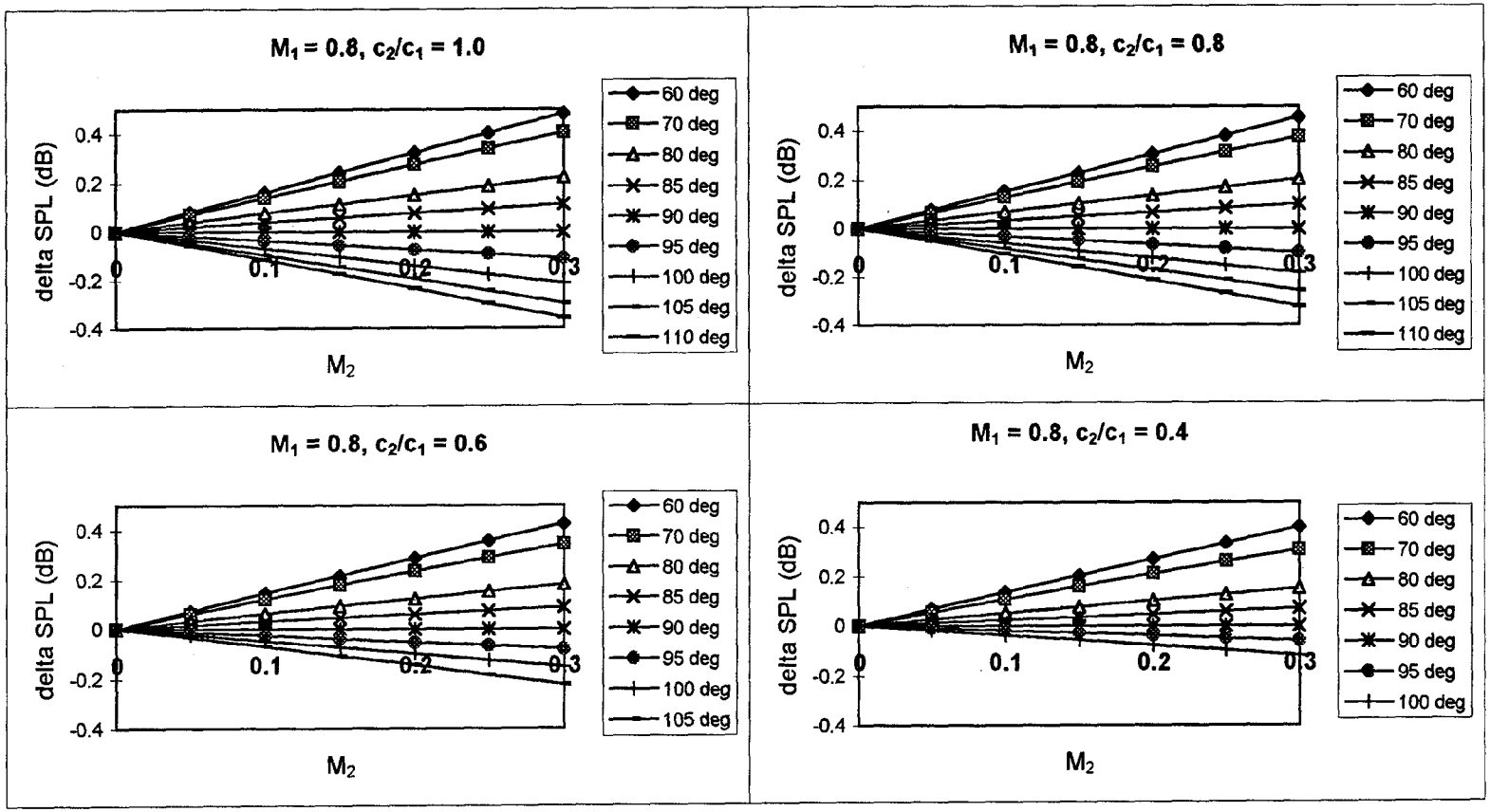

Figure C.2 Changes in transmission coefficient in dB's (with respect to static free-jet) due to changes in free-jet Mach no. for a fixed incident ray from a source inside the model jet which has Mach no. $M_1 = 0.8$ and different ratio of speeds of sound (c_2/c_1) varying from 1.0 to 0.4.

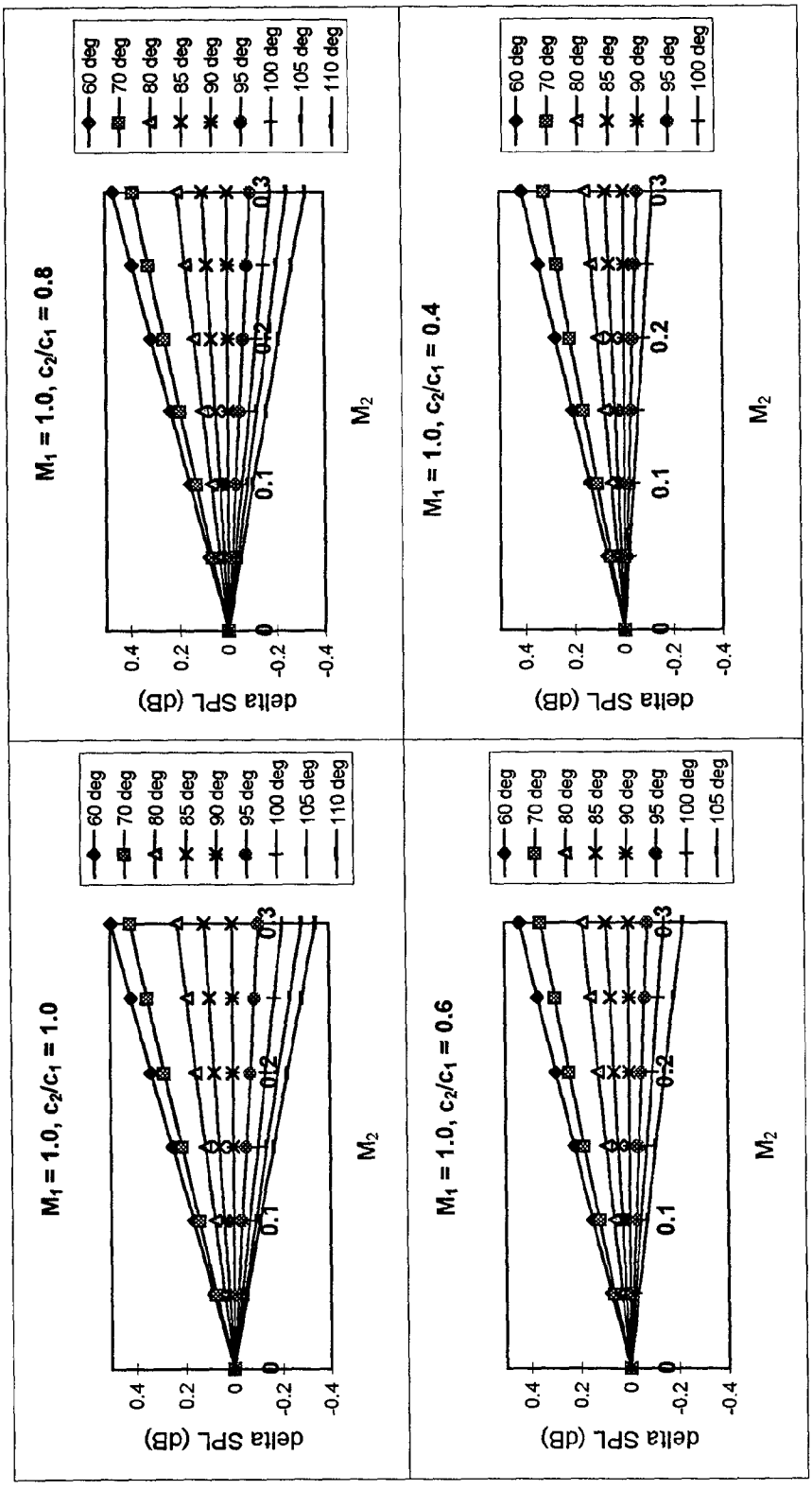

Figure C.3 Changes in transmission coefficient in dB's (with respect to static free-jet) due to changes in free-jet Mach no. for a fixed incident ray from a source inside the model jet which has Mach no. M_1 = 1.0 and different ratio of speeds of sound (c_2/c_1) varying from 1.0 to 0.4.

Appendix D

Comparison of SPL's at Different Free-Jet Mach Numbers and "Shifted" Angles for T.O. # 3

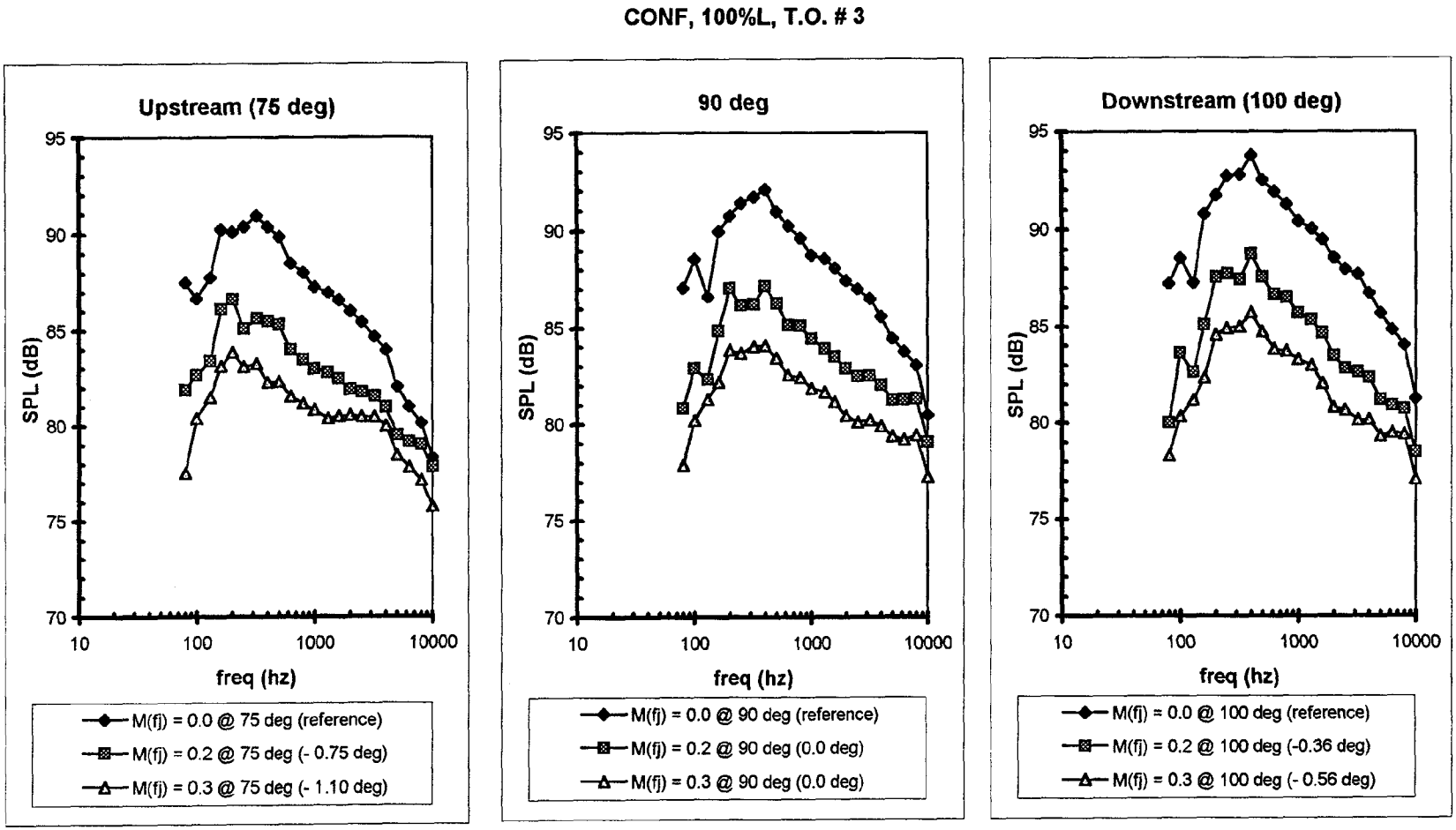

Figure D.1 Effect of free-jet Mach number, M(fj), on polar SPL at "shifted" wave-normal angles for CONF mixer.

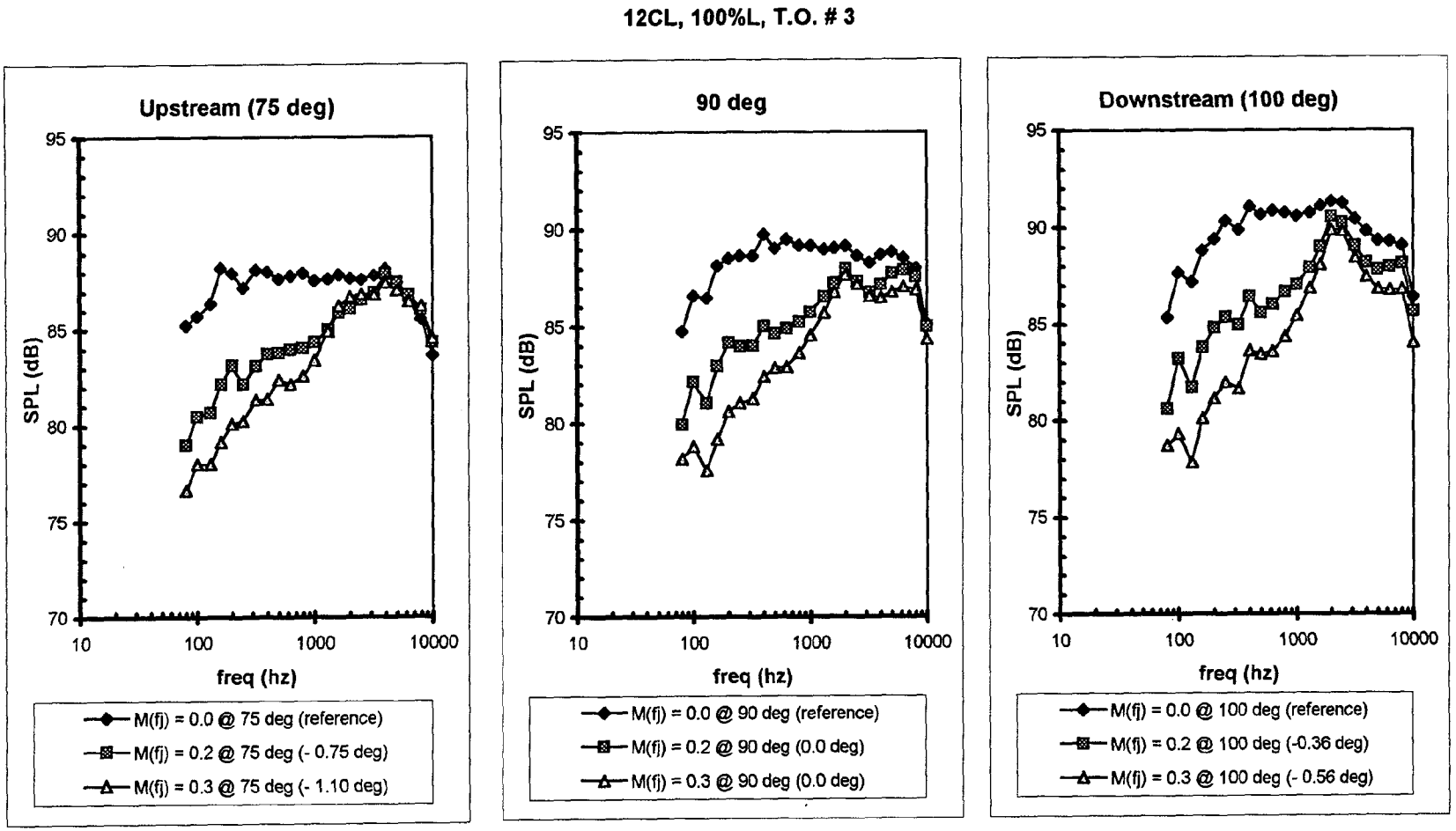

Figure D.2 Effect of free-jet Mach number, M(fj), on polar SPL at "shifted" wave-normal angles for 12CL mixer.

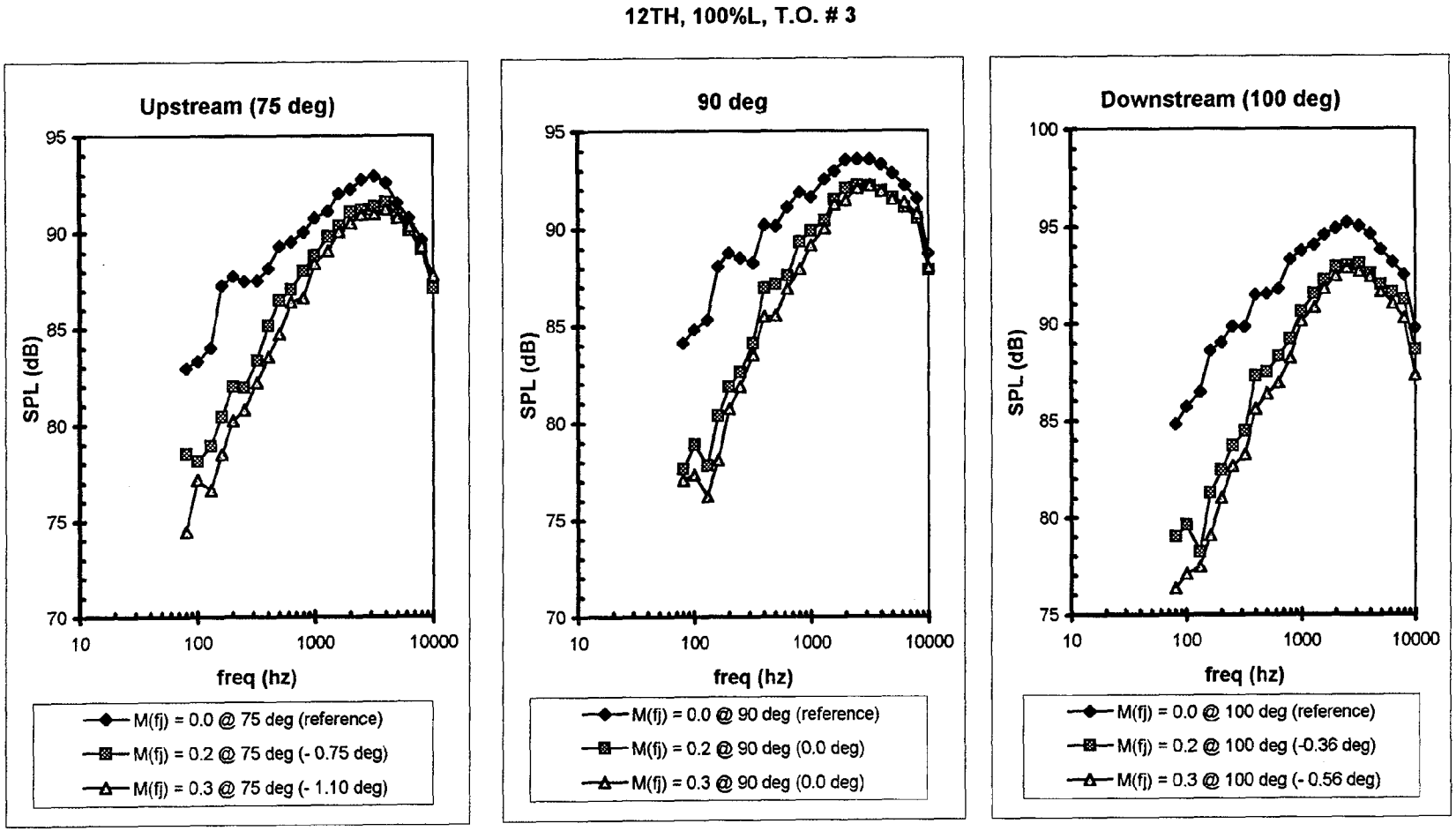

Figure D.3 Effect of free-jet Mach number, M(fj), on polar SPL at "shifted" wave-normal angles for 12TH mixer.

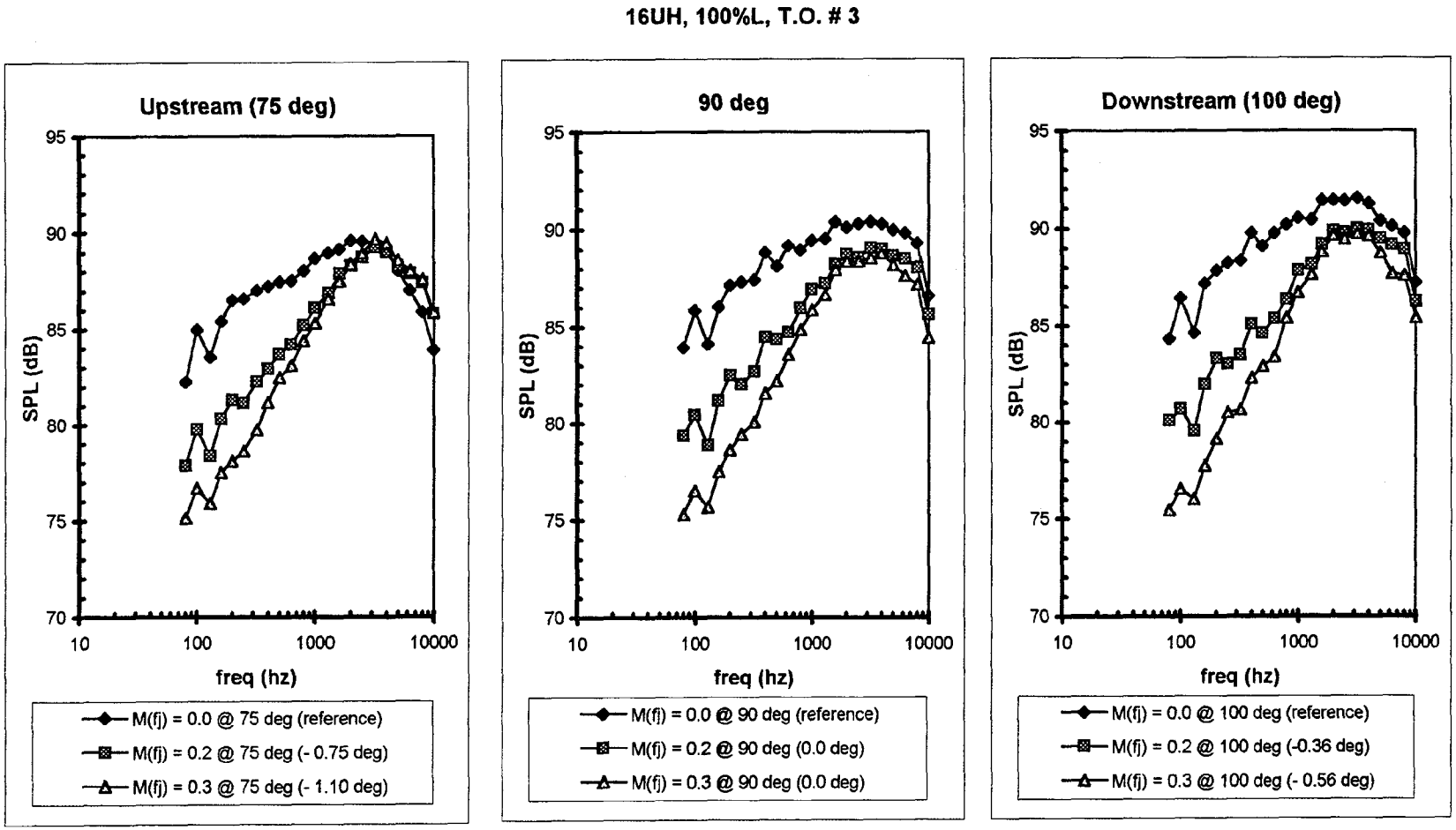

Figure D.4 Effect of free-jet Mach number, M(fj), on polar SPL at "shifted" wave-normal angles for 16UH mixer.

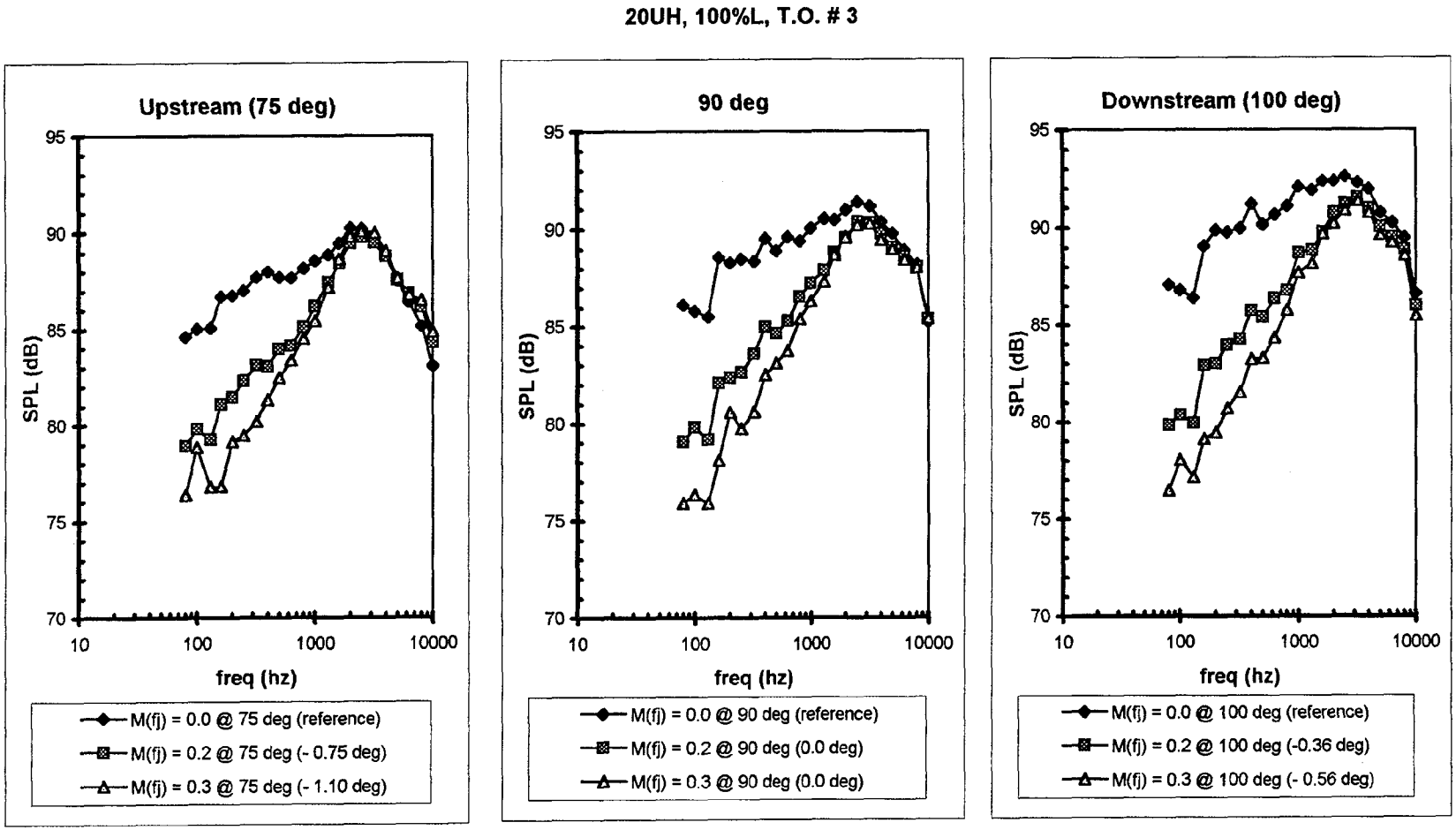

Figure D.5 Effect of free-jet Mach number, M(fj), on polar SPL at "shifted" wave-normal angles for 20UH mixer.

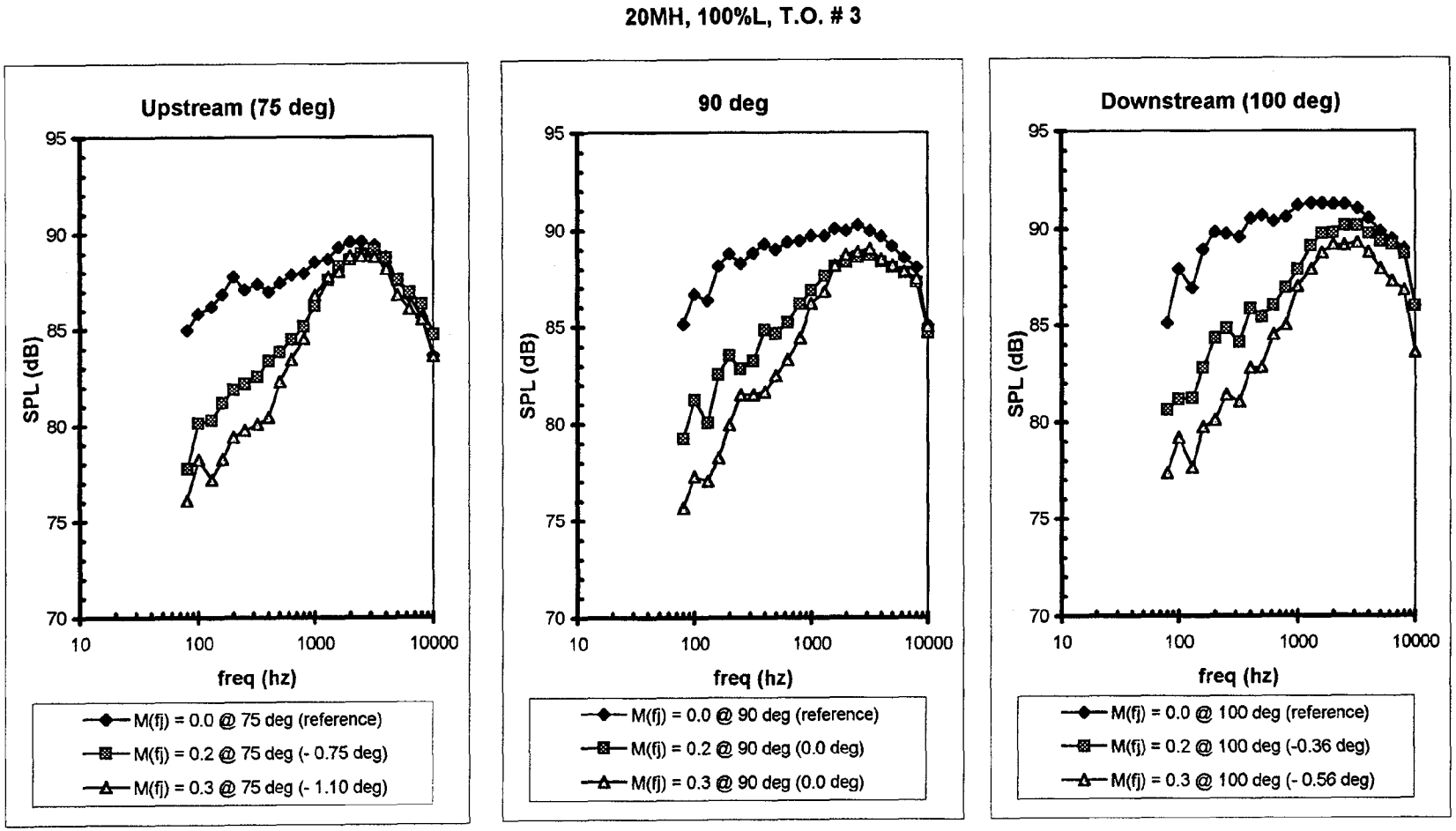

Figure D.6 Effect of free-jet Mach number, M(fj), on polar SPL at "shifted" wave-normal angles for 20MH mixer.

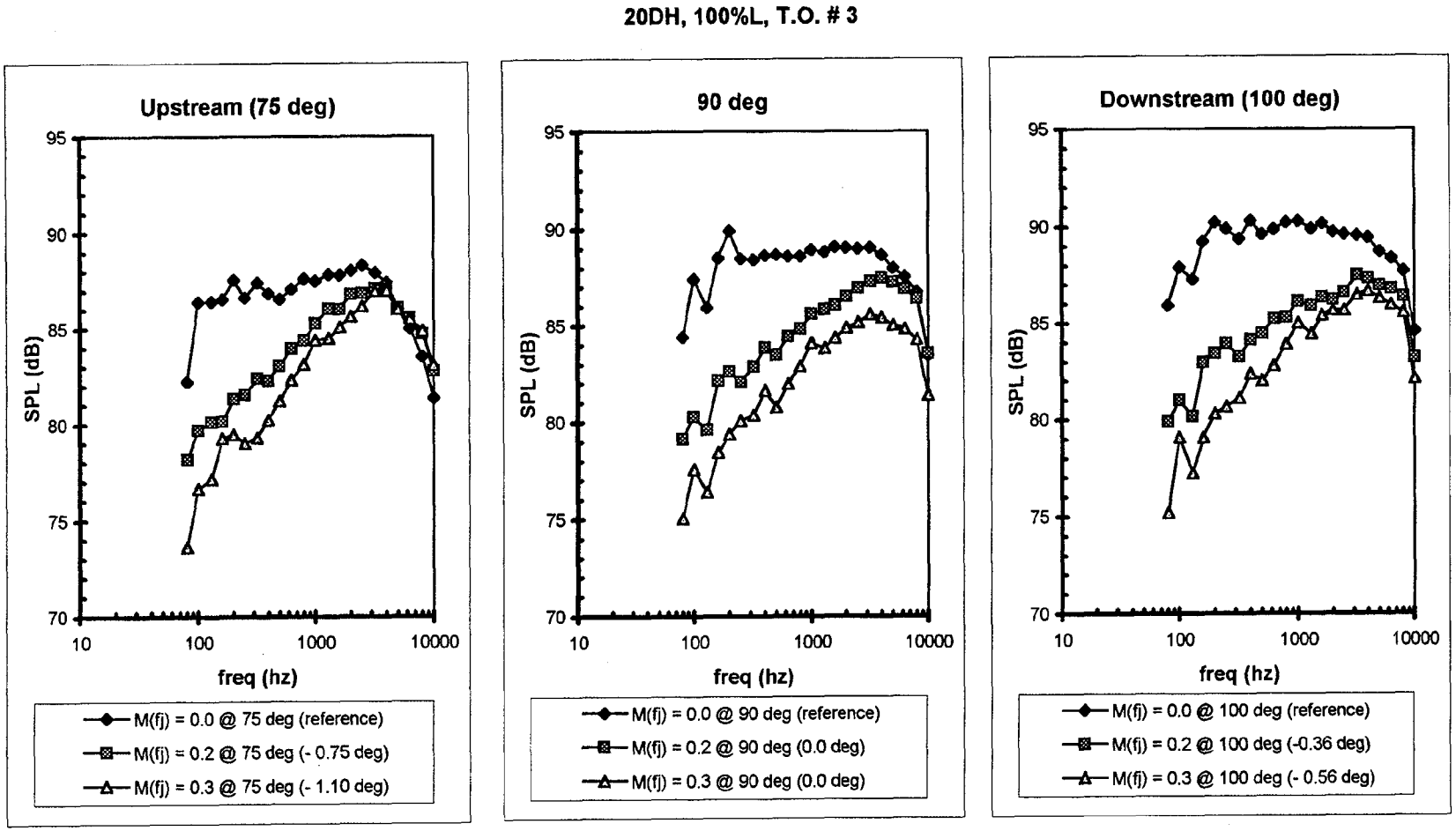

Figure D.7 Effect of free-jet Mach number, M(fj), on polar SPL at "shifted" wave-normal angles for 20DH mixer.

REPORT DOCUMENTATION PAGE

Form Approved
OMB No. 0704-0188

1. AGENCY USE ONLY (*Leave blank*)	2. REPORT DATE	3. REPORT TYPE AND DATES COVERED
	July 2002	Final Contractor Report

4. TITLE AND SUBTITLE

Lobed Mixer Design for Noise Suppression
Acoustic and Aerodynamic Test Data Analysis

5. FUNDING NUMBERS

WU–781–30–12–00
NAS3–27394
Task Order No. 6

6. AUTHOR(S)

Vinod G. Mengle and William N. Dalton

7. PERFORMING ORGANIZATION NAME(S) AND ADDRESS(ES)

Rolls Royce Allison
P.O. Box 420
Indianapolis, Indiana 46206–0420

8. PERFORMING ORGANIZATION REPORT NUMBER

E–12741–1

9. SPONSORING/MONITORING AGENCY NAME(S) AND ADDRESS(ES)

National Aeronautics and Space Administration
Washington, DC 20546–0001

10. SPONSORING/MONITORING AGENCY REPORT NUMBER

NASA CR—2002-210823-VOL1
EDR No. 18580

11. SUPPLEMENTARY NOTES

Contents were reproduced from the best available copy as provided by the authors. Project Manager, James Bridges, Structures and Acoustics Division, NASA Glenn Research Center, organization code 5940, 216–433–2693.

12a. DISTRIBUTION/AVAILABILITY STATEMENT

Unclassified - Unlimited
Subject Category: 07 Distribution: Nonstandard

Available electronically at http://gltrs.grc.nasa.gov/GLTRS

This publication is available from the NASA Center for AeroSpace Information, 301–621–0390.

12b. DISTRIBUTION CODE

13. ABSTRACT ***(Maximum 200 words)***

A comprehensive database for the acoustic and aerodynamic characteristics of several model-scale lobe mixers of bypass ratio 5 to 6 has been created for mixed jet speeds up to 1080 ft/s at typical take-off (TO) conditions of small-to-medium turbofan engines. The flight effect was simulated for Mach numbers up to 0.3. The static thrust performance and plume data were also obtained at typical TO and cruise conditions. The tests were done at NASA Lewis anechoic dome and ASK's FluiDyne Laboratories. The effect of several lobe mixer and nozzle parameters, such as, lobe scalloping, lobe count, lobe penetration and nozzle length was examined in terms of flyover noise at constant altitude. Sound in the nozzle reference frame was analyzed to understand the source characteristics. Several new concepts, mechanisms and methods are reported for such lobed mixers, such as, "boomerang" scallops, "tongue" mixer, detection of "excess" internal noise sources, and extrapolation of flyover noise data from one flight speed to different flight speeds. Noise reduction of as much as 3 EPNdB was found with a deeply scalloped mixer compared to annular nozzle at net thrust levels of 9500 lb for a 29 in. diameter nozzle after optimizing the nozzle length.

14. SUBJECT TERMS

Engine noise; Jet noise; Lobed mixers; Aeroacoustics; Internal noise; Excess noise; Nozzle length; Mixing length; Lobe scalloping; Thrust coefficient; Turbofan mixing; Jet plumes; Flight effect; Lobe count; Lobe penetration; Lobe scalloping

15. NUMBER OF PAGES

295

16. PRICE CODE

17. SECURITY CLASSIFICATION OF REPORT	18. SECURITY CLASSIFICATION OF THIS PAGE	19. SECURITY CLASSIFICATION OF ABSTRACT	20. LIMITATION OF ABSTRACT
Unclassified	Unclassified	Unclassified	